# "SYNTHESIS AND CHARACTERIZATION OF LANTHANIDES DOPED NANOFERRITES FOR EMR APPLICATIONS"

Thesis submitted to the Bharathidasan University for the award of the degree of DOCTOR OF PHILOSOPHY IN PHYSICS

By

Mrs. A. RAJESHWARI, M.Sc., B.Ed., (Ref.No.07311/Ph.D.K3/ Physics/Full-Time/Nov 2018)

# Under the Guidance of

Dr. I. KARTHARINAL PUNITHAVATHY, M.Sc., M.Phil., Ph.D., Associate Professor and Research Supervisor, PG and Research Department of Physics



# TRANQUEBAR BISHOP MANICKAM LUTHERAN COLLEGE, PORAYAR – 609 307

Affiliated to
BHARATHIDASAN UNIVERSITY
TIRUCHIRAPPALLI – 620 024
TAMILNADU – INDIA

FEBRUARY-2022

Dr. I. KARTHARINAL PUNITHAVATHY, M.Sc., M.Phil., Ph.D.,

Associate Professor and Research Supervisor,

Department of Physics,

T.B.M.L. College,

Porayar – 609 307,

Tamilnadu, India.

E-mail: profpunithaphysics@gmail.com

\_\_\_\_\_\_

**CERTIFICATE** 

This is to certify that the thesis entitled "SYNTHESIS AND

CHARACTERIZATION OF LANTHANIDES DOPED NANOFERRITES FOR

EMR APPLICATIONS" is a bonafide record of the original research work

carried out by Mrs. A. RAJESHWARI (Ref.No.07311/Ph.D.K3/Physics/

Full-Time/Nov 2018) under my supervision and guidance. The thesis has not

been formed the basis for the award of any degree, diploma, associateship,

fellowship or any similar titles.

Place: Porayar Dr. I.KARTHARINAL PUNITHAVATHY

Date: 03.02.2022 Research Supervisor

**DECLARATION** 

I, A. RAJESHWARI, declare that the thesis entitled "SYNTHESIS AND

CHARACTERIZATION OF LANTHANIDES DOPED NANOFERRITES FOR

EMR APPLICATIONS" is a bonafide record of the original research work

carried out by me. The thesis has not been submitted earlier elsewhere for the

award of any degree, diploma, associateship, fellowship or any other similar

titles.

**Place: Porayar** 

A. RAJESHWARI

Date: 03.02.2022

Dr. I. KARTHARINAL PUNITHAVATHY, M.Sc., M.Phil., Ph.D.,

Associate Professor and Research Supervisor,

Department of Physics,

T.B.M.L. College, Porayar – 609 307,

Tamilnadu, India.

E-mail: profpunithaphysics@gmail.com

\_\_\_\_\_

Date:03.02.2022

**CERTIFICATE ON PLAGIARISM CHECK** 

This is to certify that the thesis entitled "SYNTHESIS AND CHARACTERIZATION OF LANTHANIDES DOPED NANOFERRITES FOR EMR APPLICATIONS" in respect to Mrs. A. RAJESHWARI (Ref.No.07311/Ph.D.K3/Physics/Full-Time/Nov-2018) has been subjected to plagiarism check in the ouriginal software and the percentage of significance is 7%. The verified report is enclosed.

Signature of Research Supervisor with seal

# Curiginal

#### **Document Information**

Analyzed document A. Rajeshwari thesis.pdf (D126736517)

**Submitted** 2022-02-01T07:47:00.0000000

Submitted bySrinivasa ragavan SSubmitter emailbdulib@gmail.com

Similarity 7%

Analysis address bdulib.bdu@analysis.urkund.com

# Sources included in the report

W	URL: https://www.researchgate.net/publication/324036840_Effect_of_Neodymium_ion_on_the_S tructural_Electrical_and_Magnetic_Properties_of_Nanocrystalline_Nickel_Ferrites Fetched: 2020-04-12T22:21:07.0430000	88	26
W	URL: https://www.researchgate.net/publication/323950883_Structural_Electrical_and_Magnetic_Properties_of_NiLa_x_Fe_2-x_O_4_Nanoferrites Fetched: 2019-09-30T12:03:28.1700000	88	28
W	URL: https://www.researchgate.net/publication/322333655_Structural_optical_dielectric_and_magnetic_studies_of_Gadolinium-added_Mn-Cu_nanoferrites Fetched: 2019-09-30T12:03:38.5930000	88	17
W	URL: https://www.researchgate.net/publication/259513395_Impact_of_larger_rare_earth_Pr3_ions_on_the_physical_properties_of_chemically_derived_PrxCoFe2-xO4_nanoparticles Fetched: 2021-07-06T20:20:07.8900000	88	9
W	URL: https://www.researchgate.net/publication/223622944_Structural_analysis_of_nickel_doped_c obalt_ferrite_nanoparticles_prepared_by_coprecipitation_route Fetched: 2019-10-18T09:05:27.4070000	88	2
W	URL: https://www.researchgate.net/publication/225728396_Magnetic_properties_of_Resubstituted_Ni-Mn_ferrite_nanocrystallites Fetched: 2020-11-25T10:59:14.5300000	88	5
W	URL: https://www.researchgate.net/publication/327231845_Electrical_Magnetic_and_Structural_Properties_of_Polymer-Blended_Lanthanum-added_Nickel_Nano-ferrites Fetched: 2019-09-30T12:02:40.9230000	88	10
W	URL: https://www.researchgate.net/publication/319307642_Impact_of_Lanthanum_on_structural_optical_dielectric_and_magnetic_properties_of_Mn_1-x_Cu_x_Fe_185_La_015_O_4_spinel_nanoferrites Fetched: 2019-09-30T12:03:08.5770000	88	4
W	URL: https://link.springer.com/article/10.1007/s10967-019-06953-4 Fetched: 2021-06-04T08:35:19.6830000	88	1

# **CONTENTS**

CHAPTER No.	TITLES	PAGE No.
	PREFACE	i
	ACKNOWLEDGEMENTS	V
	LIST OF RESEARCH PUBLICATIONS	vii
	LIST OF FIGURES	viii
	LIST OF TABLES	xii
	LIST OF SYMBOLS	xiv
I	INTRODUCTION TO NANOFERRITES	1-25
	1.1 NANOMATERIALS AND NANOTECHNOLOGY	1
	1.2 CLASSIFICATION OF NANOMATERIALS	2
	1.3 PROPERTY ANALYSIS OF NANOMATERIALS	4
	1.3.1 Structural Properties	4
	1.3.2 Optical Properties	4
	1.3.3 Surface Morphology	5
	1.3.4 Electrical Properties	5
	1.3.5 Magnetic Properties	5
	1.4 FERRITES	7
	1.5 COBALT NANOFERRITES	14
	1.6 MANGANESE NANOFERRITES	16
	1.7 LANTHANIDES	17
	1.8 APPLICATIONS OF NANOFERRITES FERRITES	18
	1.9 AIM OF THE PRESENT INVESTIGATION	19
	REFERENCES	21
II	REVIEW OF LITERATURE	26-49
	2.1 INTRODUCTION	26
	2.2 LANTHANUM DOPED COBALT NANOFERRITES	26
	2.2 LANTHANUM DOPED MANGANESE NANOFERRITES	30
	2.4 GADOLINIUM DOPED COBALT NANOFERRITES	35
	2.5 GADOLINIUM DOPED MANGANESE NANO FERRITES	38
	2.6 CONCLUSION	44

	REFERENCES	45
III	EXPERIMENTAL METHODS AND CHARACTERIZATION TECHNIQUES	50-79
	3.1 INTRODUCTION	50
	3.2 CHEMICAL METHODS	51
	3.2.1 Hydrothermal Method	52
	3.2.2 Polyol or Gel-Evaporation Method	54
	3.2.3 Co-Precipitation Method	56
	3.2.4 Solvothermal Method	57
	3.2.5 Sol-Gel Method	59
	3.2.6 Advantages of sol-gel method	60
	3.3 EXPERIMENTAL TECHNIQUES	61
	3.3.1 Materials	61
	3.3.2 Synthesis of nanoferrites	61
	3.4 CHARACTERISATION TECHNIQUES	63
	3.4.1 X-ray Powder Diffraction	63
	3.4.2 Ultra-Violet Diffuse Reflectance Spectroscopy	65
	3.4.3 Fourier Transform Infrared Spectroscopy	66
	3.4.4 Morphology Studies	67
	3.4.5 Raman spectroscopy	68
	3.4.5.1 Raman scattering	68
	3.4.5.2 Working of Raman Spectroscopy	68
	3.4.6 X-ray Photoelectron Spectroscopy (XPS)	69
	3.4.7 Vibrating Sample Magnetometer	72
	3.4.8 Impedance Study	73
	3.4.9 Dielectric Study	73
	REFERENCES	75
IV	IMPACT OF LANTHANUM IONS ON MAGNETIC AND DIELECTRIC PROPERTIES OF COBALT NANOFERRITES	80-120
	4.1 INTRODUCTION	80
	4.2 MATERIALS AND EXPERIMENTAL PROCEDURE	82
	4.2.1 Materials	82
	4.2.2 Experimental Procedure	83

	4.2	3 Characterization of the CoLa <sub>x</sub> Fe <sub>2-x</sub> O <sub>4</sub> Nanoferrites	84
	4.3 RE	SULTS AND DISCUSSION	85
	4.3	.1 Structural Analysis	85
	4.3	.2 Optical Analysis	89
	4.3	.3 Functional Group Analysis	93
	4.3	.4 Surface Morphology with EDAX	95
	4.3	.5 XPS Analysis	96
	4.3	.6 Magnetic Analysis	98
	4.3	.7 Impedance Analysis	102
	4.3	.8 Dielectric Analysis	105
	4.3	.8(a) Dielectric Constant (ε')	105
	4.3	.8 (b) Dielectric Loss	107
	4.4 CO	ONCLUSION	109
	RE	FERENCES	116
V	STRUCT PROPER NANOFF	· · · · · · · · · · · · · · · · · · ·	
	5.1 IN	TRODUCTION	121
	5.2 MA	ATERIALS AND EXPERIMENTAL PROCEDURE	123
	5.2	.1 Materials	123
	5.2	.2 Experimental Procedure	123
	5.2	3 Characterization of MnLa <sub>X</sub> Fe <sub>2-X</sub> O <sub>4</sub> nanoferrites	125
	5.3 RE	SULTS AND DISCUSSION	125
	5.3	.1 Structural Analysis	125
	5.3	.2 Optical Analysis	130
	5.3	.3 Functional group analysis	133
		.4 Surface Morphology with EDAX	135
	5.3	.4 Surface Morphology with EDAA	133
	5.3 5.3	2 2	136
		.5 Magnetic Analysis	
	5.3	.5 Magnetic Analysis .6 Impedance Analysis	136
	5.3 5.3 5.3	.5 Magnetic Analysis .6 Impedance Analysis	136 139

	5.3.7 (c) Dielectric Loss	146
	5.3.7(d) AC Conductivity	147
	5.4 CONCLUSION	149
	REFERENCES	151
VI	EFFECT OF $Gd^{3+}$ IONS ON STRUCTURAL, OPTICAL, MAGNETIC AND DIELECTRIC PROPERTIES OF $CoGd_XFe_{2-X}O_4(0.00 \le X \ge 0.08)$ NANOFERRITES	158-196
	6.1 INTRODUCTION	158
	6.2 MATERIALS AND EXPERIMENTAL PROCEDURE	160
	6.2.1 Materials	160
	6.2.2 Experimental Procedure	160
	6.2.3 Characterization of the CoGd <sub>x</sub> Fe <sub>2-x</sub> O <sub>4</sub> Nanoferrites	161
	6.3 RESULTS AND DISCUSSION	162
	6.3.1 Structural Analysis	162
	6.3.2 Optical Analysis	167
	6.3.3 Functional Group Analysis	170
	6.3.4 Surface Morphology with EDAX	171
	6.3.5 Raman Spectroscopy Analysis	173
	6.3.6 Magnetic Analysis	175
	6.3.7 Impedance Analysis	179
	6.3.7 (a) Real part of impedance Spectroscopy	179
	6.3.7 (b) Imaginary part of impedance Spectroscopy	180
	6.3.7 (c) Cole - Cole plot	180
	6.3.8 Dielectric Analysis	182
	6.3.8 (a) Dielectric Constant (ε')	182
	6.3.8 (b) Dielectric Loss	184
	6.3.8 (c) AC Conductivity	186
	6.4 CONCLUSIONS	187
	REFERENCES	189
VII	INFLUENCE OF $Gd^{3+}$ IONS ON STRUCTURAL, OPTICAL, MAGNETIC AND DIELECTRIC PROPERTIES OF $MnGd_XFe_{2-x}O_4(0.0 \le x \ge 0.8)$ NANOFERRITES	197-234
	7.1 INTRODUCTION	197

	7.2 MATERIALS AND EXPERIMENTAL PROCEDURE	199
	7.2.1 Materials	199
	7.2.2 Experimental procedure	199
	7.2.3 Characterization of the MnGd <sub>x</sub> Fe <sub>2-x</sub> O <sub>4</sub> Nanoferrites	200
	7.3. RESULTS AND DISCUSSIONS	201
	7.3.1. Structural analysis	201
	7.3.2 Optical Analysis	205
	7.3.3 Functional Group Analysis	209
	7.3.4 Surface Morphology studies with EDAX	210
	7.3.5 Raman spectroscopy analysis	212
	7.3.6 Magnetic Analysis	214
	7.3.7 Impedance Analysis	217
	7.3.7 (a) The Real part of impedance spectroscopy	217
	7.3.7 (b) The Imaginary part of the impedance spectroscopy	218
	7.3.7(c) Cole-Cole plot	219
	7.3.8 Dielectric Analysis	220
	7.3.8 (a) Dielectric constant (ε')	221
	7.3.8 (b) Dielectric loss	223
	7.3.8 (c) A.C Conductivity	224
	7.4 CONCLUSION	226
	REFERENCES	228
VIII	SUMMARY AND CONCLUSION	235-244
	LIST OF PUBLICATIONS	245

#### **PREFACE**

Over the past few years, spinel ferrites have gained tremendous importance in recent times due to their potential applications in low loss magnetic core materials, microwave absorbing materials, transformer cores and antenna rods, etc. to perform a number of functions at high frequencies. The problem of Electromagnetic Interference (EMI) has attracted considerable attention due to a variety of applications in telecommunication systems such as mobile phones, computers and radar systems. The different kinds of electromagnetic waves shielding and absorbing devices have been developed to solve the problem of EMI by making use of the absorbing materials. The recent researches on microwave absorbing materials and to improve the properties have been reached and achieved with the better outcomes. Nowadays, the microwave-absorbing properties of rare-earth doped nickel ferrites are investigated in-depth due to the magneto crystalline anisotropy in the 4f (Lanthanides)–3d (Fe<sub>2</sub>O<sub>4</sub>) intermetallic compounds. The Lanthanides doped nanoferrites are interested in the current research due to the technological development in electronics and medicine.

In this study, four series of nanoferritesCoLa<sub>x</sub>Fe<sub>2-x</sub>O<sub>4</sub>, MnLa<sub>x</sub>Fe<sub>2-x</sub>O<sub>4</sub>(X=0.00, 0.02, 0.04, 0.06 and 0.08) and  $MnLa_xFe_{2-x}O_4(X=0.00, 0.02, 0.04, 0.06$  and 0.08) were prepared using solgel method, were investigated to explore their structural, optical, magnetic and electrical properties using X-ray diffraction (XRD), ultra violet-diffuse reflectance spectroscopy (UV-DRS), Fourier Transform Infrared Spectroscopy (FTIR), Field Emission Scanning Electron Microscopy (FESEM) coupled with energy-dispersive X-ray (EDAX) analysis, X-ray Photoluminence Spectroscopy (XPS), Vibrating Sample Magnetometer (VSM). Inductance Capacitance and Resistance (LCR) Hitester and electrochemical impedance spectroscopy. Lanthanumdoped Cobalt nanoferrites CoLa<sub>X</sub>Fe<sub>2-X</sub>O<sub>4</sub> (X=0.00 to 0.08) were synthesized by using solgel method. A cubic spinel structure was confirmed by using X-ray diffraction pattern. Fourier transform infrared spectrum confirmed the presence of metal oxide spinel nanoferrites. The bandgap energy has increased with addition of La<sup>3+</sup> ions by using ultraviolet diffuse reflectance spectrum. The grain boundary contribution is greater than that of grain contribution due to small crystal size, which was confirmed by an impedance analysis. The dielectric constant and dielectric losses were decreased

with increasing frequencies. The binding energy of La, Co, Fe and O were determined by X-ray photoelectron spectroscopy. The magnetic studies were made through vibrating sample magnetometer. The hysteresis loop revealed the soft ferromagnetic nature.

Lanthanum doped Manganese spinel nanoferrites (MnLa<sub>x</sub>Fe<sub>2-x</sub>O<sub>4</sub>) with series x=0.00, 0.02, 0.04, 0.06 and 0.08 were fabricated using sol-gel method. The fabricated samples were characterized to X-ray diffraction analysis for structural investigation and also it confirms single phase cubic structure. Fourier Transform Infrared Spectra were used to subject the chemical band of tetrahedral and octahedral sites in the spinel ferrites (FT-IR). Field Emission Scanning Electron Microscope revealed that the prepared samples attain spherical in shape. Energy dispersive X-ray spectra confirm the presence of Mn, La, Fe and O element with few impurities. The optical property for prepared nanoferrites was used to characterize Ultra-Violent diffuse reflectance spectroscopy. It reveals absorbance spectra are inversely proportional to band gap energy. The magnetic hysteresis curves measured at room temperature expose ferromagnetic behavior with decrease of saturation (M<sub>s</sub>) and increase of coercivity (Oe). The of the CoGdxFe2-xO4Nanoferrites e origin of ferromagnetism in La3+ doped Manganese nanoferrites were discussed in elaborate with reference to the allocation of Mn<sup>2+</sup> and Fe<sup>3+</sup>ion with in the spinel lattice. An impedance spectroscopy of the samples is performed in the frequency range 100 mHz -10 MHz at room temperature and also it is used to understand the dielectric parameters. The resistance of the grain and grain boundary is found to increase with La<sup>3+</sup> ion. The dielectric constant and dielectric loss decrease with increase of frequency.

Gadolinium doped Cobalt nanoferrites ( $CoGd_xFe_{2-x}O_4$ , where x=0.00, 0.02, 0.04, 0.06 and 0.08) were synthesized by sol-gel method. The structural effects of Gd doping in the nanoferrites were analysed by X-ray diffraction (XRD), Micro-Raman and FT-IR spectroscopic techniques. A well crystalline cubic phase was identified by XRD and the crystallite size was found to be lower for the Gd doped compositions. Spherical shaped particles were observed by field emission electron microscope and the elemental composition of the Gd doped ferrites was investigated using Energy

dispersive X-ray analysis (EDAX) technique. Ultra-Violet diffuse reflectance spectroscopy (UV-DRS) revealed that absorbance spectra were inversely proportional to band gap energy due to synergistic effect of the dopant. The magnetic hysteresis curves exposed soft ferromagnetic nature with increases of coercivity (Oe) and decreasing of saturation (M<sub>s</sub>) with increasing of doping (Gd<sup>3+</sup>) concentration. The impedance spectroscopy has been used to investigate the effect of Gd co-doping on the grain and grain boundary resistance of the nanoferrites. An improved dielectric property was found with increasing Gd<sup>3+</sup> concentration as a function of applied AC frequency (voltage).

Gadolinium doped manganese nanoferrites (MnGd<sub>x</sub>Fe<sub>2-x</sub>O<sub>4</sub>) (X = 0.00, 0.02, 0.04, 0.06 and 0.08) for microwave absorbers and storage devices were synthesized by using an effective sol-gel method. The structural parameters analysed using X-ray diffraction (XRD) revealed a well crystalline cubic phase with crystallite size being smaller in Gd doped compositions. The elemental compositions of the Gd doped ferrites were studied using energy dispersive X-ray analysis (EDAX) technique, and spherical-shaped particles were detected using a field emission electron microscopy (FESEM), UV diffuse reflectance spectroscopy (UV-DRS) revealed that the absorbance spectra were inversely related to bandgap energy due to the synergistic action of the dopant. The magnetic hysteresis curves demonstrated soft ferromagnetic nature with increasing coercivity (Oe) and decreasing saturation (M<sub>s</sub>). Gd co-doping altered the grain and grain boundaries resistance of nano ferrites and better dielectric characteristics were formed with increasing Gd<sup>3+</sup> concentration as AC frequency increased (voltage); they have strong microwave absorption capacity.

The aim of this research is to synthesize lanthanides doped nanoferrites with various X concentration (X= 0.00 to 0.08) to explore the properties are structural, magnetic, dielectric and microwave-absorption of the prepared nanoferrites. The thesis is compiled in the following manner.

**Chapter I** deals with the brief introduction of the research work presented along with the general introduction, classification, properties and application of the nanoferrites. The aim and scope of the present investigation is proposed here.

**Chapter II** deals with the literature survey on various synthesis methods of lanthanides doped cobalt and manganese nanoferrites.

**Chapter III** deals with the different methods and materials to prepare and characterize the lanthanides doped cobalt and manganese nanoferrites. And also, provides detailed information about the Sol-gel method and its advantages.

**Chapter IV** deals with the Impact of Lanthanum ion on Magnetic and Dielectric properties of Cobalt Nanoferrites.

**Chapter V** deals with the Dependance of Lanthanum ions on Structural, Magnetic and Electrical properties of manganese-based spinel nanoferrites.

**Chapter VI** deals with the Effect of  $Gd^{3+}$  ions on Structural, Optical, Magnetic and Dielectric Properties of  $CoGd_XFe_{2-X}O_4$  (0.00  $\leq X \geq$  0.08) Nanoferrites.

**Chapter VII** deals with the Influence of  $Gd^{3+}$  ions on Structural, Optical, Magnetic and Dielectric properties of  $MnGd_XFe_{2-X}O_4$  (0.00  $\leq x \geq$  0.08) Nanoferrites, along with their applications.

**Chapter VIII** deals with the summary and conclusion of the findings in the present investigation. The promising future of the research work is also highlighted at the end of the chapter.

#### **ACKNOWLEDGEMENTS**

I express my sincere thanks to my Research Advisor **Dr. I. Kartharinal Punithavathy,** Associate Professor, Department of Physics, T.B.M.L College, Porayar for her valuable guidance, suggestions and discussions during my period of research. I greatly acknowledge her continuous support and warm care in all aspects whenever needed.

I sincerely thank **Dr. Gene George**, Principal, T.B.M.L College, Porayar for her valuable support throughout my research period.

My sincere and deep sense of gratitude is to the Doctoral committee members **Dr. S. Johnson Jeyakumar,** Research Advisor & Associate Professor Department of Physics, T.B.M.L College, Porayar. and **Dr. D. Benny Anbu Raj,** Head & Assistant Professor, Department of Physics, **DGGAC,** Mayiladuthurai.

I greatly acknowledge the help and guidance of all the **faculty members** of the Department of Physics, T.B.M.L College, Porayar throughout my research work.

I express my deep gratitude and respect to **Dr. M. JOTHIBAS**, Assistant Professor, T.B.M.L College, Porayar, for his keen interest, strong motivation and constant encouragement during the course of the work. I thank him for his great patience, constructive criticism and myriad useful suggestions apart from invaluable guidance to me.

I am grateful to **Dr. T.C Sabari Girisan**, Assistant professor, Department of Physics, Bharathidasan University, Trichy, for the support and facilities extended to me for pursing my research work.

I convey my heartiest gratitude to, **Dr. Lenin**, Assistant Professor, KSR Institute of technology, Erode, **S. Ajithkumar & B. Vigneshwaran** Research Assistant, IRTC, Sathyabama University, Chennai, who were the bone back of my research work, teaching me various aspects of research, continuous support, inspiration, critical comments without which completion of my work would have not been possible.

I am grateful to Dept of nanoscience and Technology, SAIIF, **IIT** Chennai, Dept of Physics, **Karunya University**, Coimbatore, IRC, **Sathyabama University**, Chennai for the support and facilities extended to me for pursing my research work.

I specially thank my friends Mrs. P. Jamila Jayanthi, Dr. B. Arunkumar, Dr. R. Radhika, Dr. J. Divya Maglin, Dr. S. Suganya, Mr. M. Sankar, Mrs. A. Sindhya, Mr. Paulson, Mr. S. Soorya, Miss. R. Priyadharshini, Miss. M. Agalya and Mr. Abishek David, Research Scholars, Department of Physics, T.B.M.L College, Porayar for their valuable associateship. It has been interesting and enjoyable working with them. I dedicate my thesis work to my research team.

I would like to extend personal thanks to my friends outside research area **Mr. R. Prakash**, for their warm support, word of encouragement in several aspects of my life.

I am grateful to my parents **S. Arumugam and A. Lakshmi** and my father-in-law **Mr. G. Rajarethinam**, Mother-in-law **A. Lakshmi**, Sister-in-law **R. Premi** and **R. Priyadharshini** and my beloved brothers and sisters and also my dear relatives and friends for their understanding and support. I thank my beloved husband **Mr. R. Arunkumar** who has been behind me in all my initiatives and being a mentor. I express my love and appreciation to my dear children Ms. **A. Liya** and **A. Saagithya** who understands me and strengthen me to do my research work.

A. Rajeshwari

# LIST OF RESEARCH PUBLICATIONS

# **Peer reviewed international publications**

(UGC-CARE Approved; SCI/Scopus Indexed)

- 1. Impact of lanthanum ion on magnetic and dielectric properties of cobalt nanoferrites, I. Kartharinal Punithavathy, A. Rajeshwari, S. Johnson Jeyakumar, N. Lenin, B. Vigneshwaran, M. Jothibas, B. Arunkumar, Journal of Materials science: Materials in Electronics (2020), <a href="https://doi.org/10.1007/s10854-020-03523-3">https://doi.org/10.1007/s10854-020-03523-3</a> (Springer).
- 2. Dependance of lanthanum ions on structural, magnetic and electrical properties of manganese-based spinel nanoferrites. A. Rajeshwari, I. Kartharinal Punithavathy, S. Johnson Jeyakumar, N. Lenin, B. Vigneshwaran, Ceramics international (2020), <a href="https://doi.org/10.1016/j.ceramint.2019.11.180">https://doi.org/10.1016/j.ceramint.2019.11.180</a> (Elsevier).
- 3. CoGd<sub>X</sub>Fe<sub>2-X</sub>O<sub>4</sub> (0.00 ≤ X ≥ 0.08) Nanoferrites: Effect of Gd<sup>3+</sup> ions on Structural, Optical, Magnetic and Dielectric Properties, A. Rajeshwari, I. Kartharinal Punithavthy, S. Johnson Jeyakumar, M. Jothibas, S. Ajith Kumar, Journal of Materials science: Materials in Electronics (2021), <a href="https://doi.org/10.1007/s10854-022-07775-z">https://doi.org/10.1007/s10854-022-07775-z</a> (Springer).

#### List of articles under review/communicated in journals

1. Influence of  $Gd^{3+}$  ions on Structural, Optical, Magnetic and Dielectric properties of  $MnGd_XFe_{2-X}O_4(0.0 \le x \ge 0.8)$  Nanoferrites, A. Rajeshwari, I. Kartharinal Punithavthy, S. Johnson Jeyakumar, M. Jothibas, Journal of Surface and Interface(2021), (Elsevier). [Communicated]

# LIST OF FIGURES

FIGURE NO.	TITLE	PAGE NO.
1.1	Classification of Nanomaterials Based on Dimension	3
1.2	Schematic Representation of Top-down and Bottom-up Methods	6
1.3	Schematic Representation of Classification of Ferrites	7
1.4	Structure, Tetrahedral sites and Octahedral sites of Unit cell of Spinel Ferrite	8
1.5	Cation Distributions in Regular Spinel Ferrites	9
1.6	Cation Distributions in Inverse Spinel Ferrites	10
1.7	Cation Distributions in Mixed Spinel Ferrites	10
1.8	Garnet Ferrite: (a) Crystal Structure and (b) Interstice	11
1.9	Magneto plumbite (Hexagonal) Ferrites	12
1.10	Typical Hysteresis Loops for Both Soft and Hard Ferrites	14
1.11	Applications of Ferrites in Different Areas	19
3.1	Hydrothermal Synthesis	52
3.2	Gel-Evaporation Method	55
3.3	Co-precipitation Method	56
3.4	Solvothermal Process	58
3.5	Sol-gel Processes	60
3.6	The flow chart of detailed synthesis procedure	62
3.7	Illustration of x-ray scattering from crystal lattice	64
3.8	Block diagram of UV-DRS spectroscopy	66
3.9	Block diagram of FT- IR spectroscopy	66
3.10	Block diagram of FE-SEM	67
3.11	Rayleigh and Raman scattering mechanism of photons.	68
3.12	Block Diagram of Raman Scattering System	69
3.13	Block Diagram of XPS	70
3.14	Working Principal of XPS	71
3.15	Block Diagram of VSM	73
4.1	Schematic diagram for preparation of CoLa <sub>X</sub> Fe <sub>2-X</sub> O <sub>4</sub> nanoferrites	84
4.2	X-ray diffraction pattern of $CoLa_XFe_{2-X}O_4$ (X = 0.00 to 0.08) nanoferrites.	87
4.3	Absorbance spectra of CoLa <sub>X</sub> Fe <sub>2-X</sub> O <sub>4</sub> (X = 0.00 to 0.08) nanoferrites	90
4.4	Direct bandgap energy of $CoLa_XFe_{2-X}O_4$ (X = 0.00 to 0.08) nanoferrites	91

4.5	Indirect bandgap energy of $CoLa_XFe_{2-x}O_4$ (X = 0.00 to 0.08) nanoferrites.	92
4.6	FT-IR spectra of $CoLa_XFe_{2-X}O_4$ (X = 0.00 to 0.08) nanoferrites.	94
4.7	FESEM with EDAX images of the $CoLa_XFe_{2-x}O_4$ (X = 0.00 to 0.08) nanoferrites.	95
4.8	XPS spectra of the $CoLa_XFe_{2-X}O_4$ (X = 0.00 to 0.08) nanoferrites	97
4.9	Hysteresis loop of the $CoLa_XFe_{2-X}O_4$ (X = 0.00 to 0.08) nanoferrites.	99
4.10	Real part of impedance spectra of $CoLa_XFe_{2-X}O_4$ (X = 0.00 to 0.08) nanoferrites.	102
4.11	Imaginary part of impedance spectra of $CoLa_XFe_{2-X}O_4$ (X = 0.00 to 0.08) nanoferrites.	103
4.12	Nyquist plots of $CoLa_XFe_{2-X}O_4$ (X = 0.00 to 0.08) nanoferrites.	104
4.13	Dielectric constant of the $CoLa_XFe_{2-x}O_4$ (X = 0.00 to 0.08) nanoferrites.	105
4.14	Dielectric loss of the $CoLa_XFe_{2-X}O_4$ (X = 0.00 to 0.08) nanoferrites.	108
5.1	Flow chart for the sample preparation of $MnLa_XFe_{2-}$ $_XO_4nanoferrites$ .	124
5.2	X-ray diffraction pattern of MnLa <sub>X</sub> Fe <sub>2-X</sub> O <sub>4</sub> (X=0.00 to 0.08) nanoferrites.	129
5.3	Absorbance spectra of MnLa <sub>X</sub> Fe <sub>2-X</sub> O <sub>4</sub> (X= 0.00 to 0.08) nanoferrites.	131
5.4	Direct bandgap energy of MnLa <sub>X</sub> Fe <sub>2-X</sub> O <sub>4</sub> (X= 0.00 to 0.08) nanoferrites.	132
5.5	Indirect bandgap energy of MnLa <sub>X</sub> Fe <sub>2-X</sub> O <sub>4</sub> (X= 0.00 to 0.08) nanoferrites.	133
5.6	FT- IR spectra of $MnLa_XFe_{2-X}O_4$ (X = 0.00 to 0.08) nanoferrites	134
5.7	FESEM with EDAX images of prepared MnLa <sub>X</sub> Fe <sub>2-X</sub> O <sub>4</sub> (X =0.00to 0.08) nanoferrites	136
5.8	Hysteresis loop of $MnLa_XFe_{2-X}O_4$ (X = 0.00 to 0.08) nanoferrites.	137
5.9	Real part of impedance spectra of MnLa <sub>X</sub> Fe <sub>2-X</sub> O <sub>4</sub> (X=0.00 to 0.08) nanoferrites.	140
5.10	Imaginary part of impedance spectra of MnLa <sub>X</sub> Fe <sub>2-X</sub> O <sub>4</sub> (X=0.00 to 0.08) nanoferrites.	141
5.11	Nyquist plots of MnLa <sub>X</sub> Fe <sub>2-X</sub> O <sub>4</sub> (X= 0.00 to 0.08) nanoferrites.	142
5.12	Dielectric constant and Complex dielectric constant of the prepared $MnLa_XFe_{2-x}O_4$ (X = 0.00 to 0.08) nanoferrites.	143
5.13	Dielectric constant of the MnLa <sub>x</sub> Fe <sub>2-x</sub> O <sub>4</sub> (X = 0.00 to 0.08) nanoferrites.	145

		4 4 5
5.14	Dielectric loss of $MnLa_XFe_{2-X}O_4$ (X = 0.00 to 0.08) nanoferrites.	146
5.15	AC Conductivity vs Frequency of $MnLa_XFe_{2-X}O_4$ (X = 0.00 to 0.08) nanoferrites.	148
6.1	Flow chart for the preparation of CoGd <sub>x</sub> Fe <sub>2-x</sub> O <sub>4</sub> nanoferrites.	161
6.2	X-ray diffraction pattern of $CoGd_XFe_{2-X}O_4$ (X = 0.00 to 0.08) nanoferrites.	166
6.3	Absorbance spectra of $CoGd_XFe_{2-X}O_4$ (X= 0.00 to 0.08) nanoferrites.	167
6.4	Direct band gap energy of CoGd <sub>x</sub> Fe <sub>2-x</sub> O <sub>4</sub> (X= 0.00 to 0.08) nanoferrites	168
6.5	Indirect band gap energy of CoGd <sub>x</sub> Fe <sub>2-x</sub> O <sub>4</sub> (X= 0.00 to 0.08) nanoferrites	169
6.6	FTIR spectra of $CoGd_XFe_{2-X}O_4$ (X = 0.00 to 0.08) nanoferrites.	170
6.7	FESEM images of $CoGd_XFe_{2-X}O_4$ (X = 0.00 to 0.08) nanoferrites	172
6.8	EDAX images of $CoGd_XFe_{2-X}O_4$ (X = 0.00 to 0.08) nanoferrites	173
6.9	Raman studies of $CoGd_XFe_{2-X}O_4$ (X = 0.00 to 0.08) nanoferrites	174
6.10	Hysteresis loop of $CoGd_XFe_{2-X}O_4$ (X = 0.00 to 0.08) nanoferrites	176
6.11	Real part of impedance spectra of $CoGd_XFe_{2-X}O_4$ (X = 0.00 to 0.08) nanoferrites.	179
6.12	Imaginary part of impedance spectra of $CoGd_XFe_{2-X}O_4$ (X = 0.00 to 0.08) nanoferrites.	180
6.13	Nyquist plots of CoGd <sub>X</sub> Fe <sub>2-X</sub> O <sub>4</sub> (X= 0.00 to 0.08) nanoferrites	181
6.14	Equivalent circuit model of $CoGd_XFe_{2-X}O_4$ (X = 0.00 to 0.08) nanoferrites.	182
6.15	Dielectric constant of $CoGd_XFe_{2-X}O_4$ (X = 0.00 to 0.08) nanoferrites.	183
6.16	Dielectric loss of $CoGd_XFe_{2-x}O_4$ (X = 0.00 to 0.08) nanoferrites.	185
6.17	AC Conductivity vs Frequency of $CoGd_XFe_{2-X}O_4$ (X = 0.00 to 0.08) nanoferrites.	186
7.1	Flow chart for the sample preparation of MnGd <sub>x</sub> Fe <sub>2-x</sub> O <sub>4</sub> nano ferrites.	200
7.2	X-ray diffraction pattern of $MnGd_XFe_{2-x}O_4$ (X = 0.00 to 0.08) nanoferrites.	204
7.3	Absorbance spectra of $MnGd_XFe_{2-X}O_4$ (x= 0.00 to 0.08) nanoferrites.	206
7.4	Direct bandgap energy of MnGd <sub>x</sub> Fe <sub>2-x</sub> O <sub>4</sub> (X= 0.00 to 0.08) nanoferrites.	207
7.5	Indirect bandgap energy of MnGd <sub>x</sub> Fe <sub>2-x</sub> O <sub>4</sub> nano (X= 0.00 to 0.08) nanoferrites.	208
7.6	FTIR spectra of $MnGd_XFe_{2-X}O_4$ (X = 0.00 to 0.08) nanoferrites.	209

7.7	FESEM images of $MnGd_XFe_{2-X}O_4$ (X = 0.00 to 0.08) nanoferrites.	211
7.8	EDAX images of $MnGd_XFe_{2-X}O_4$ (X = 0.00 to 0.08) nanoferrites.	212
7.9	Raman studies of $MnGd_XFe_{2-X}O_4$ (X = 0.00 to 0.08) nanoferrites.	213
7.10	Hysteresis loop of $MnGd_XFe_{2-X}O_4$ (X = 0.00 to 0.08) nanoferrites.	215
7.11	Real part of impedance spectra of $MnGd_XFe_{2-X}O_4$ (X = 0.00 to 0.08) nanoferrites.	218
7.12	Imaginary part of impedance spectra of $MnGd_XFe_{2-X}O_4$ (X = 0.00 to 0.08) nanoferrites.	219
7.13	Nyquist plots of $MnGd_XFe_{2-X}O_4$ (X= 0.00 to 0.08) nanoferrites.	220
7.14	Dielectric constant of $MnGd_XFe_{2-X}O_4$ (X = 0.00 to 0.08) nanoferrites.	222
7.15	Dielectric loss of $MnGd_XFe_{2-X}O_4$ (X = 0.00 to 0.08) nanoferrites.	224
7.16	AC Conductivity vs Frequency of $MnGd_XFe_{2-X}O_4$ (X = 0.00 to 0.08) nanoferrites.	225

# LIST OF TABLES

TABLE NO.	TITLE	PAGE NO.
4.1	Structural parameters of CoLa <sub>X</sub> Fe <sub>2-X</sub> O <sub>4</sub> (X = 0.00 to 0.08) nanoferrites	89
4.2	Optical parameters of $CoLa_XFe_{2-X}O_4$ (X = 0.00 to 0.08) nanoferrites.	93
4.3	Functional parameters of $CoLa_XFe_{2-X}O_4$ (X = 0.00 to 0.08) nanoferrites.	94
4.4	Binding energy of CoLa <sub>X</sub> Fe <sub>2-X</sub> O <sub>4</sub> (X = 0.00 to 0.08) nanoferrites.	98
4.5	Magnetic parameters of $CoLa_XFe_{2-X}O_4$ (X = 0.00 to 0.08) nanoferrites.	101
4.6	Dielectric parameters of $CoLa_XFe_{2-X}O_4$ (X = 0.00 to 0.08) nanoferrites.	109
5.1	Structural parameters of $MnLa_XFe_{2-X}O_4$ (X = 0.00 to 0.08) nanoferrites	130
5.2	Optical parameters of $MnLa_XFe_{2-X}O_4$ (x = 0.00 to 0.08) nanoferrites.	133
5.3	Functional parameters of prepared MnLa $_X$ Fe $_{2-X}$ O $_4$ (X = 0.00 to 0.08) nanoferrites	135
5.4	Magnetic parameters of prepared MnLa <sub>X</sub> Fe <sub>2-X</sub> O <sub>4</sub> ( $X = 0.00$ to 0.08) nanoferrites.	139
5.6	Dielectrical parameters of $MnLa_XFe_{2-X}O_4$ (X = 0.00 to 0.08) nanoferrites.	149
6.1	Structural parameters of $CoGd_XFe_{2-X}O_4$ (X = 0.00 to 0.08) nanoferrites	167
6.2	Optical parameters of $CoGd_XFe_{2-X}O_4$ (X = 0.00 to 0.08) nanoferrites.	170
6.3	Functional parameters of $CoGd_XFe_{2-X}O_4$ (X = 0.00 to 0.08) nanoferrites.	171
6.4	Raman studies of $CoGd_XFe_{2-X}O_4$ (X = 0.00 to 0.08) nanoferrites.	175
6.5	Magnetic parameters of $CoGd_XFe_{2-X}O_4$ (X = 0.00 to 0.08) nanoferrites.	178
6.6	Dielectric parameters of $CoGd_XFe_{2-X}O_4$ (X = 0.00 to 0.08) nanoferrites.	187

7.1	Structural parameters of $MnGd_XFe_{2-X}O_4$ (X = 0.00 to 0.08) nanoferrites.	205
7.2	Optical parameters of MnGd <sub>x</sub> Fe <sub>2-x</sub> O <sub>4</sub> (X= 0.00 to 0.08) nanoferrites.	208
7.3	Functional parameters of $MnGd_XFe_{2-X}O_4$ (X = 0.00 to 0.08) nanoferrites	210
7.4	Raman studies of $MnGd_XFe_{2-x}O_4$ (X = 0.00 to 0.08) nanoferrites	214
7.5	Magnetic parameters of $MnGd_XFe_{2-X}O_4$ (X = 0.00 to 0.08) nanoferrites.	217
7.6	Dielectric parameters of $MnGd_XFe_{2-x}O_4$ (X = 0.00 to 0.08) nanoferrites.	228

# LIST OF SYMBOLS AND ABBREVIATIONS

 $\alpha$  - Alpha

AC - Alternative current

Å - Bohr magnetron

μ<sub>B</sub> - Capacitance

C - Capacitance

H<sub>c</sub> - Coercivity

 $\Omega$  - Conductivity

D - Crystallite Size

° - Degree

 $\delta$  - Delta

d<sub>xrd</sub> - Density

EMI - Electromagnetic interference

EMR - Electromagnetic radiation

emu - Electromagnetic unit

eV - Electron Volt

Eg - Energy bandgap

EDAX - Energy-dispersive X-ray Analysis

FESEM - Field Emission Scanning Electron Microscopy

FTIR - Fourier Transform Infra-Red

γ - Frequency

FWHM - Full Width Half Maximum

 $\gamma$  - Gamma

G - Gram h - Hour

LCR - Inductance Capacitance and Resistance

JCPDS - Joint Committee on Powder DiffractionStandards

K - Kelvin

keV - Kilo Electron Volt

kg - Kilo Gram kHz - Kilo Hertz mHz - Milli HertzMHz - Mega HertzkV - Kilo Voltλ - Lambda

γ-Fe2O3 - Maghemite Fe3O4 - Magnetite

m - Meter

mA - Milliampere

mg - Milligram
mm - Millimeter
nm - Nanometer

B-site - Octahedral site

Oe - Oersted  $\Omega$  - Ohm Pa - Pascal

% - Percentage

h - Planck constant

KBr - Potassium Bromide

pH - Potential of Hydrogen

 $M_r$  - Remanent magnetization  $M_s$  - Saturation magnetization

A-site - Tetrahedral site

 $\Theta$  - Theta

UV-DRS - Ultraviolet-Diffuse Reflectance Spectroscopy

VSM - Vibrating Sample Magnetometer

W - Watt

Wt% - Weight percentage
XRD - X-ray Diffraction

XPS - X-ray Photoluminous Spectroscopy

# CHAPTER – I

# INTRODUCTION TO NANOFERRITES

Nanotechnology is well developed day-by-day through the world-wide researches. The foundation of nano has been made in the voice of Richard Feynman in 1959. The sector of nanotechnology has included many technologies in its core. Because of this, results can be extended to any discussion on society and environment regards, specific to any particular application. In recent years, the nanotechnology is found to be a most significant and stimulating technology in Physics, Chemistry, Biology and Engineering. Coming years, nanotechnology will be upgrading in the path of the wide range of technological advances through some different applications. Worldwide research and development are being undertaken with the intension of assessing its potential for technological innovations. Nanotechnology deals with materials that the size of less than hundred nanometres, for governed by new characteristics and behaviour and also based on the recognition of nanostructure.

This chapter contains a brief overview of the research work given in this thesis, as well as a general introduction to nanoferrites, their classification, qualities, and applications. The significance of nanoferrites and lanthanides doped nanoferrites, as well as nanoferrites applications, are discussed. At the end of the chapter, the purpose of the current investigation is proposed, together with the specific objectives derived from it.

#### 1.1 NANOMATERIALS AND NANOTECHNOLOGY

The word "nano" comes from the Greek and means "dwarf." The ability to see, measure, manipulate, and synthesise materials at the nanoscale scale is a current field in nanotechnology. A nanometer (nm) is a SI unit of length equal to one billionth of a metre (10<sup>-9</sup>m). Nanotechnology (or "Nanotech") is the study of controlling matter at the atomic and molecular level. Nanotechnologies, in general, deal with a wide range of scientific fields, including physical, biological, and chemical qualities, phenomena, and processes in the nanoscale range. These materials and systems can be investigated for innovative and significant improvements. Because of their improved and diverse optical, magnetic, and electrical capabilities compared to their bulk structure, nanoparticles are regarded one of the most important materials. Because of their critical applications in highly efficient catalysts, low loss magnetic core materials, high-density recording media, electric generators, high-density data storage, microwave absorbing materials, magnetic resonance imaging, transformer core, and antenna rod, nanomagnetic particles have sparked a lot of interest. Due to the above properties or applications of nanoferrites are playing a key role in modern technology [Reghunadhan et.al., 2018, Bhagyaraj et.al., 2018, Oluwafemi et.al., 2018, Dolez et.al.,2015 & Ramsden et.al.,2009].

#### 1.2 CLASSIFICATION OF NANOMATERIALS

Figure 1.1 shows the dimension-based classifications of nanomaterials. The following are the dimensions that can be used to classify nanomaterials:

• **Zero-dimensional:** The materials have dimensions in all three directions that are in the nanoscale range (no dimensions). It can be spherical in

shape in general -quantum dots, silver nanoparticles, fullerenes, nanoporous silicon, nanograins, nanoshells, nanocapsules, nanorings, colloidal particles, activated carbon and quasicrystals.

- One-dimensional: These materials will have one dimension that is outside
  of the nanoscale range -nanowires, nanorods, nanofilaments, nanotubes
  and quantum wires.
- **Two-dimensional:** The nanoscale isn't the only place where two dimensions exist nanofilms, coatings, sheets, disc, platelets, superlattices, and quantum wells.
- Three-dimensional: Oils, nanocones, nanopillars, and nanoflowers all have three dimensions (Oluwafemi *et.al.*, 2018, Dolez *et.al.*, 2015 & Tiwari *et.al.*, 2012).

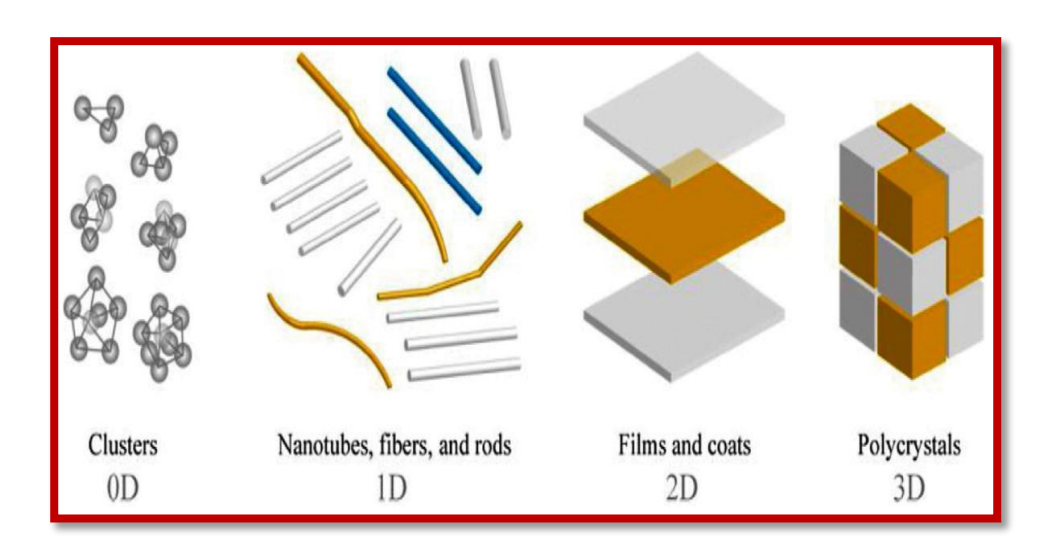


Figure 1.1 Classification of Nanomaterials Based on Dimension

#### 1.3 PROPERTY ANALYSIS OF NANOMATERIALS

Certain characteristics, such as crystallite size, specific surface area, shape, crystalline phase, crystallinity and defect structure, size distribution, aspect ratio, agglomeration/aggregation state, dustiness, particle and surface morphology/ topography, can change the properties of nanomaterials. To gain a better knowledge of nanoparticles, some of their impart properties are mentioned below.

# 1.3.1 Structural Properties

When it comes to minuscule dimensions like nanometers, the size and distribution of materials matter. The structural parameters of nanoparticles are their shape (including aspect ratios when appropriate), size, and morphological substructure of the substance. A nanomaterial's size is a criterion for evaluating its electrical, thermodynamic, and chemical properties. The shape, crystallinity, and structure lattice properties of a nanomaterial are affected by its size. The structural features are complexly formed from atomic and molecular origins. Nanomaterial cluster properties, for example, differ significantly from those of individual components in bulk or at extended surfaces [Vollath *et.al.*, 2008].

# **1.3.2 Optical Properties**

Nanomaterials' optical characteristics are responsive to UV and visible light at the same time (Reghunadhan *et.al.*, 2018). Nanoparticles have the ability to produce appealing colours. The optical characteristics of nanoparticles vary significantly depending on particle size and colour. The energies of the highest occupied molecular orbital (valence band) and the lowest empty molecular orbital are most affected by the reduced dimensionality of the small nanocluster's electronic structure (conduction band). During the electronic transition between these two states, optical features such as emission and adsorption occur [Bhagyaraj *et.al.*, 2018, & Oluwafemi *et.al.*, 2018].

# 1.3.3 Surface Morphology

The combined influence of the size, shape, and particular arrangement of the involved particles is known as surface morphology of nanomaterials. The crystallinity and synthesis process influence the development of surface morphology. The exposed surface of the materials generates this image [Kefeni *et.al.*, 2017].

# **1.3.4 Electrical Properties**

Nanomaterials have characteristics that differ dramatically from bulk materials due to the increased relative surface area and quantum effects of electrons. The attributes of reactivity, strength, and electrical characteristics can all be altered or improved by these parameters. In general, polarisation components such as ionic, space charge orientational, and electronic polarisation influence the dielectric characteristics of any material. At lower and higher frequency areas, however, electronic and space charge polarisation has been seen in synthesised nanomaterials [Hashim *et.al.*, 2013, Solymar *et.al.*, 2010 & Walsh *et.al.*, 2010].

# 1.3.5 Magnetic Properties

Classical ideas cannot explain the magnetic characteristics of nanoparticles. The interaction of magnetic moments of unpaired electrons in the presence of an external magnetic field is demonstrated by the unique magnetic characteristics of nanomaterials. Because of the huge surface-area-to-volume ratio of nanostructures, constituent atoms experience distinct magnetic interaction with nearby atoms, resulting in varied magnetic characteristics. Due to the fluctuation of magnetization, the magnetic anisotropy energy in magnetic nanoparticles may be slightly decreased [Bhagyaraj *et.al.*, 2018, Kelsall *et.al.*, 2005 & McHenry *et.al.*, 1999].

The confinement effect, crystal flaws, and surfaces all have a role in the characteristics of nanomaterials. Under varied situations, these factors are generally modified in the synthesis procedures. In general, top-down and bottom-up strategies were used to create nanomaterials. Bottom-up approaches are utilised to create smaller components with atomic or molecular dimensions that self-assemble. Top-down procedures are applied to a process that begins with a huge element and works its way down to smaller structures [Rosa *et.al.*, 2013]. Figure 1.2 shows a schematic depiction of top-down and bottom-up techniques.

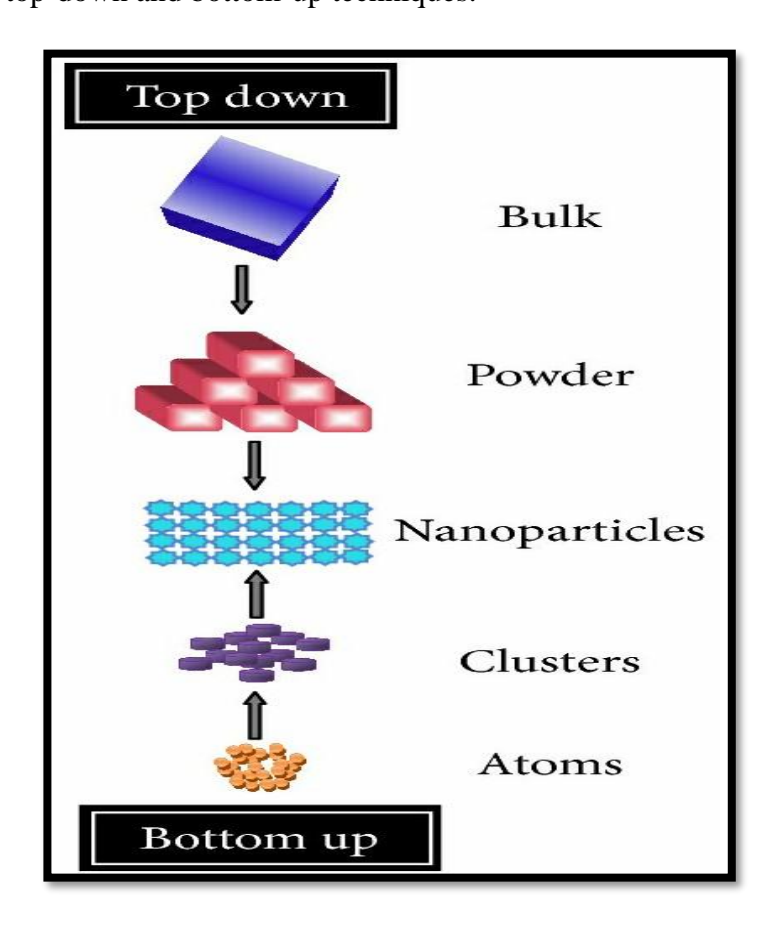


Figure 1.2 Schematic Representation of Top-down and Bottom-up Methods

#### 1.4 FERRITES

Ferrite is the name for a ferrimagnetic substance. Ferrites are a specific type of ferromagnetic substance. Except for the alignments of spin magnetic moments, ferrites and ferromagnetic materials have comparable properties. The ferromagnetic materials' spin magnetic moments are oriented in the same direction. The spin magnetic moments of ferrite materials, on the other hand, are not associated in the same direction. Some of them have a back-and-forth relationship. The term "ferrite" comes from the Latin word "ferrum." Ferrites are metal oxide mixtures with iron oxide as the major component. Throughout the last few decades, ferrites have played a critical part in numerous scientific and technological breakthroughs that have drastically altered our lives. According to their crystalline structure, ferrites can be categorised into Four categories: spinel, hexagonal, garnet, and magnet plumbites [Kaur et.al., 2016, Sharmaet.al., 2016, & Pullar et.al., 2012].

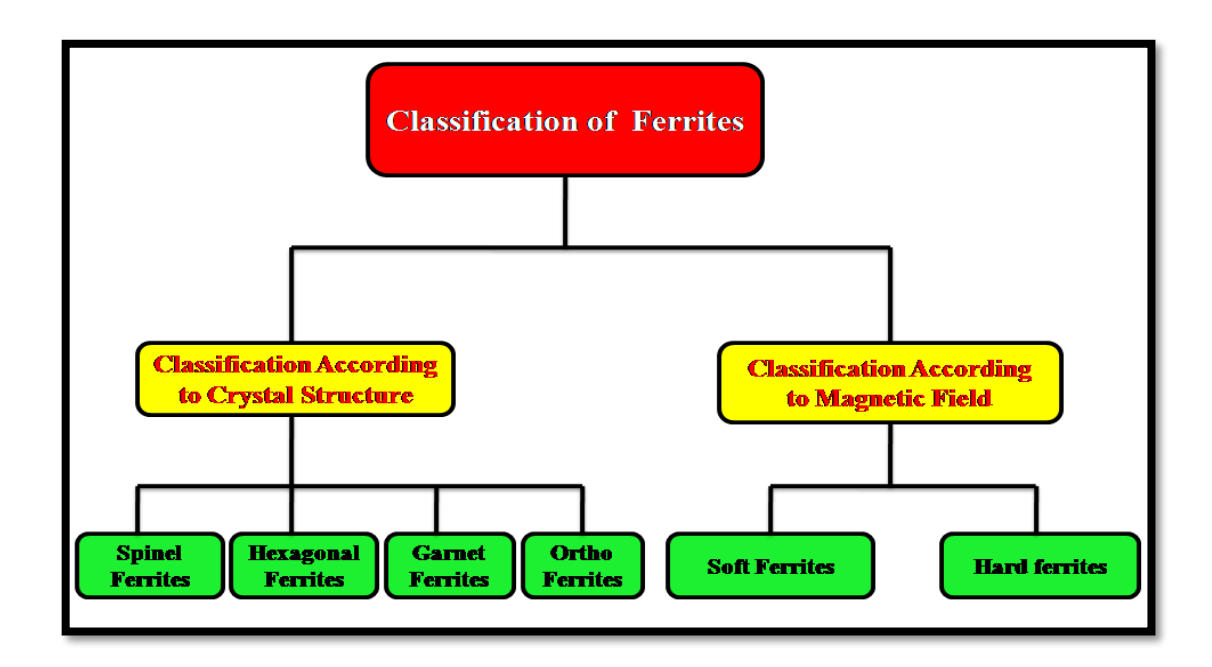


Figure 1.3 Schematic Representation of Classification of Ferrites

# • Spinel Ferrites

The first group of ferrites are those having the general chemical formula AB<sub>2</sub>O<sub>4</sub>, in which A and B represent tetrahedral and octahedral cation sites, respectively, and O represents the oxygen anion site. Magnetically, spinel ferrites are soft. It could be used instead of metal magnets like Fe and stacked Fe-Co &Mn alloys. Due to its exceptional magnetic characteristics, it usually performs better in applications. Spinel ferrites have excellent electrical resistivity and low magnetic losses, among other characteristics. The spinel ferrite family includes the two widely used magnets, Cobalt - Manganese ferrites and Manganese - Cobalt ferrites. They've piqued interest because of their high electrical resistivity, high magnetic permeability, and the capacity to modify intrinsic properties throughout a large range [Sharma et.al., 2016, Hazra et.al., 2014, Ghosh et.al., 2014, & Valenzuela et.al., 2012]. Figure 1.4 shows the structure of the spinel ferrite unit cell's tetrahedral and octahedral sites.

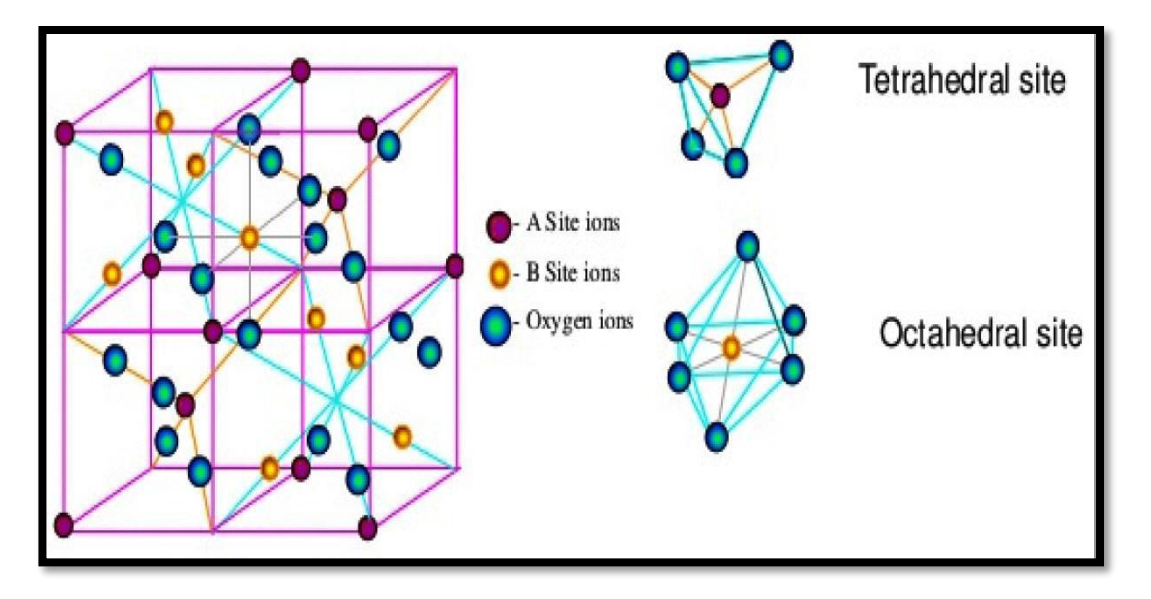


Figure 1.4 Structure, Tetrahedral sites and Octahedral sites of Unit cell of Spinel Ferrite

The oxygen anions form a close face-centered cube (FCC) packing in Figure 1.4, resulting in 64 tetrahedral sites (8 of which are occupied) and 32 octahedral sites (16 are occupied). Regular spinel ferrites, inverse spinel ferrites, and mixed spinel ferrites are the three forms of cation distribution.

• **Spinel Ferrites** (**Regular**): Divalent cations occupy the A-sites, while trivalent cations occupy the B-sites. Regular spinel is the name given to the ferrite. Magnetically,  $MgAl_2O_4$  and  $FeCr_2O_4$  are examples of normal spinel ferrites. Regular spinel ferrite has the structural formula  $M^{2+}$  (divalent ions)  $[Fe_2^{3+}]$   $O_4^{2-}$ , as shown schematically in Figure 1.5.

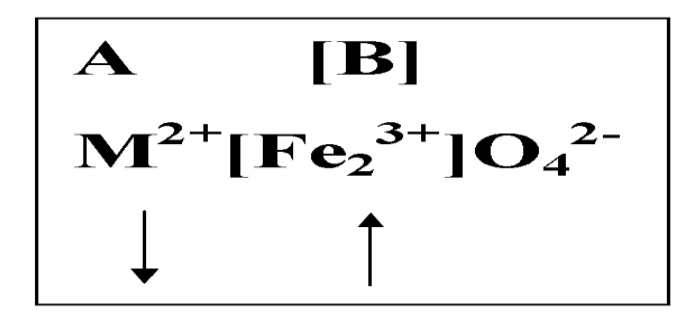


Figure 1.5 Cation Distributions in Regular Spinel Ferrites

- Inversed Spinel Ferrites: This ferrite has all divalent cations in B sites and trivalent cations evenly divided across A and B sites; the structure is called inversed spinel.
- The structural formula of inverse spinel ferrite is Fe<sup>3+</sup>[M<sup>2+</sup>Fe<sup>3+</sup>] O<sub>4</sub> is the structural formula for inverse spinel ferrite. Magnetite NiFe<sub>2</sub>O<sub>4</sub> and CoFe<sub>2</sub>O<sub>4</sub> are examples of inverse spinel ferrites. One half of Fe<sup>3+</sup> is put in A-sites and the other half in B-sites in inverted spinel ferrites. Figure 1.6 depicts the inverse spinel ferrite schematically.

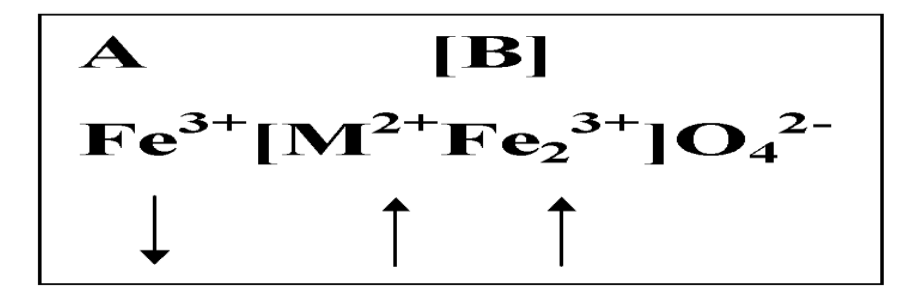
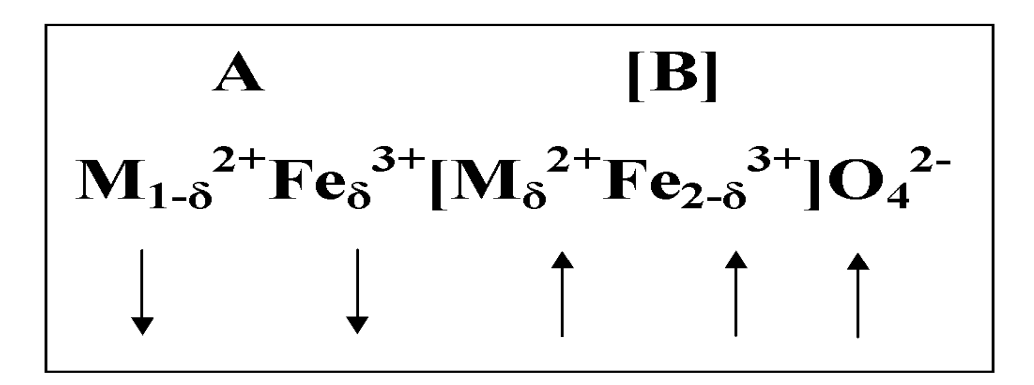


Figure 1.6 Cation Distributions in Inverse Spinel Ferrites

• Mixed Spinel Ferrites: Mixed spinel ferrites are formed when the cations  $M^{2+}$  and  $Fe^{3+}$  occupy both A and B sites.  $M1-\delta^{2+}Fe_{\delta}^{3+}$  [ $M_{\delta}^{2+}F_{2-\delta}^{3+}$ ]  $O_4$  is the structural formula for mixed spinel ferrite, where  $\delta$  is the degree of inversion [Valenzuela *et.al.*, 2012; Sharma *et.al.*, 2017]. Figure 1.7 shows a schematic representation of mixed spinel ferrite.



**Figure 1.7 Cation Distributions in Mixed Spinel Ferrites** 

# Garnet Ferrites

Mn<sub>3</sub>Al<sub>2</sub>Si<sub>3</sub>O<sub>12</sub> is an example of the garnet ferrites' crystal structure. The crystal structure is relatively complicated and possesses cubic symmetry. In garnet ferrites, there are three types of cation sites: dodecahedral (eightfold), octahedral (sixfold), and tetrahedral (fourfold). R ions, rare earth cations, occupy the greatest dodecahedral sites, while Fe<sup>3+</sup> cations are found in tetra- and octahedral sites. The cation

distribution is written as R3 (Fe<sub>3</sub>) [Fe<sub>2</sub>] O<sub>12</sub>, with brackets indicating dodecahedral sites, () parentheses indicating tetrahedral site occupancy, and square brackets indicating octahedral sites []. Tetrahedral cations are antiparallel, while dodecahedral and octahedral ions are parallel [Kaur *et.al.*, 2016 & Ozgur *et.al.*, 2009]. Figure 1.8 shows the garnet ferrite.

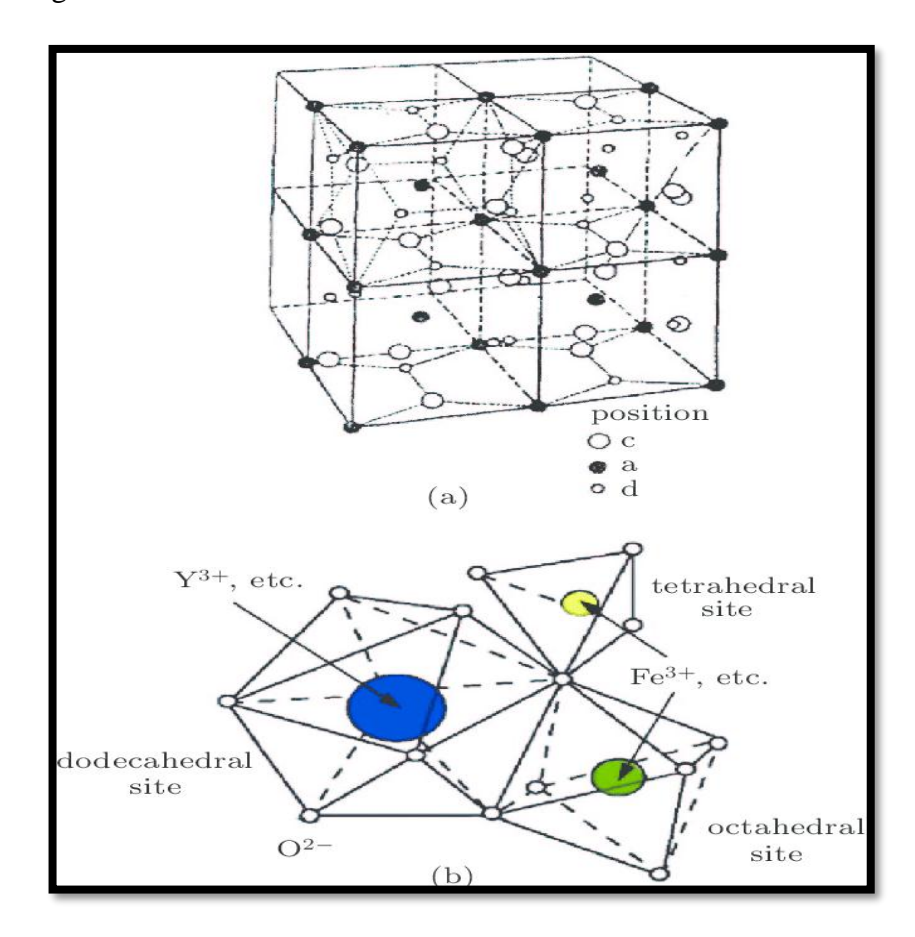


Figure 1.8 Garnet Ferrite: (a) Crystal Structure and (b) Interstice.

# • Magneto plumbite (Hexagonal) Ferrites

M<sup>2+</sup>Fe<sub>12</sub>O<sub>19</sub> (M= Mn, Ni, Co, Ba, Pb, Sr, etc.) is the typical composition of magneto plumbite. They're called hexagonal ferrites because the magneto plumbite structure is hexagonal. These ferrimagnetic oxides include a main component (Fe<sub>2</sub>O<sub>3</sub>) as well as divalent oxides (MnO, CoO or SrO). There are 64 atoms in a hexagonal ferrite unit-cell. Magneto plumbites ferrites contain a lot of uniaxial anisotropy, a lot

of magnetizations, and they're chemically stable. [Kaur *et.al.*, 2016, Morgan *et.al.*, 1982, and Cirlin *et.al.*, 1982] Magneto plumbite ferrites are ideally suited to the needs of recording technology. Figure 1.9 shows the magneto plumbite ferrite.

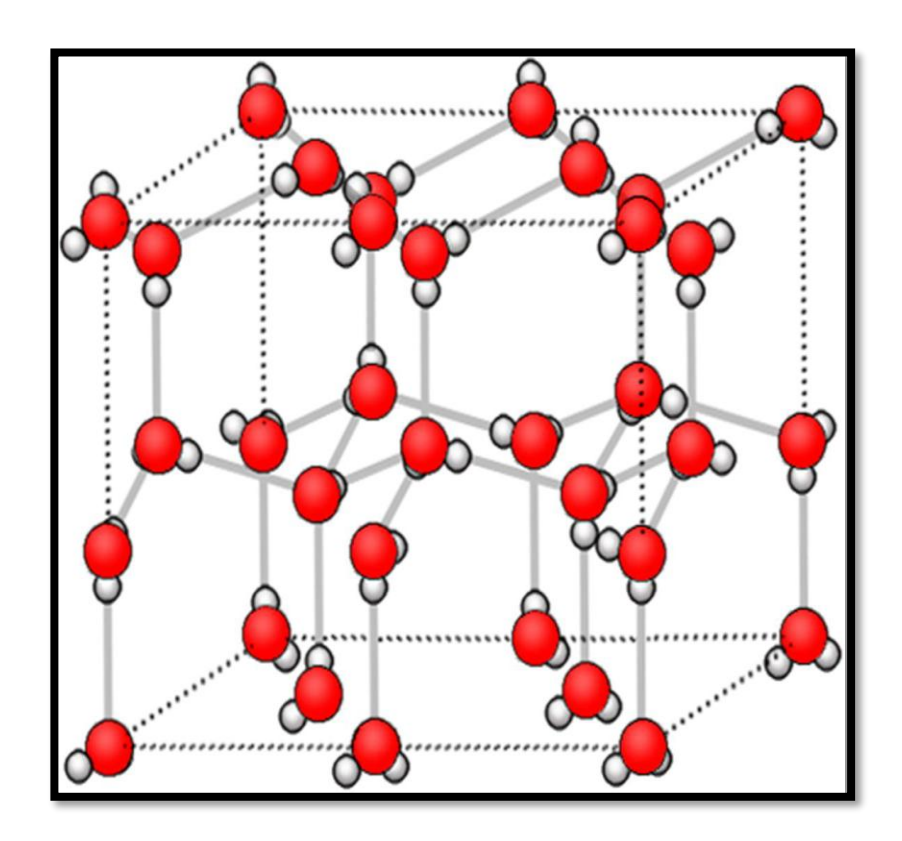


Figure 1.9 Magneto plumbite (Hexagonal) Ferrites

# **Classification of Ferrites**

Ferrites are often classified as "soft ferrites" and "hard ferrites." which refers to their low or high coercivity of magnetism, respectively.

➤ **Soft Ferrites:** Soft ferrites are ferrimagnetic materials with a cubic crystal structure, and their chemical formula is MFe<sub>2</sub>O<sub>3</sub>, where M is a transition metal ion such as Iron, Cobalt, Nickel, Manganese, Zinc, and so on. Manganese-Cobalt ferrites are a type of soft ferrites that can be employed in magnetic applications up to 10 MHz in frequency. The soft magnetic material can be

magnetised and demagnetized easily, allowing it to store and transfer magnetic energy in alternating or other shifting waveforms (sine, pulse, square, etc.). Due to eddy current losses, metallic soft magnetic materials cannot be employed at high frequencies. As a result, soft ferrites, which are ceramic insulators, have emerged as the material of choice for telephone signal transmitters and receivers, as well as switch mode power supply (referred to as DC-DC converters). The main factor for increasing frequency in this type of application is to allow miniaturisation [Hazra *et.al.*, 2014 & Ghosh *et.al.*, 2014, Jaswal *et.al.*, & Singh 2014, Goldman *et.al.*, 2006].

Hard Ferrites: Hard ferrites are used to make permanent ferrite magnets, which have a high coercivity and remanence after magnetization. Iron and barium or strontium oxides make up these ferrites. They conduct magnetic flux well and have a high magnetic permeability when magnetically saturated. This allows these ceramic magnets to store magnetic fields that are stronger than iron. They are inexpensive and commonly found in household items such as refrigerator magnets [Hazra et.al., 2014 & Ghosh et.al., 2014, Jaswal et.al., 2014, & Singh et.al., 2016, & Goldman et.al., 2006]. Figure 1.10 shows typical hysteresis loops for soft and hard ferrite.

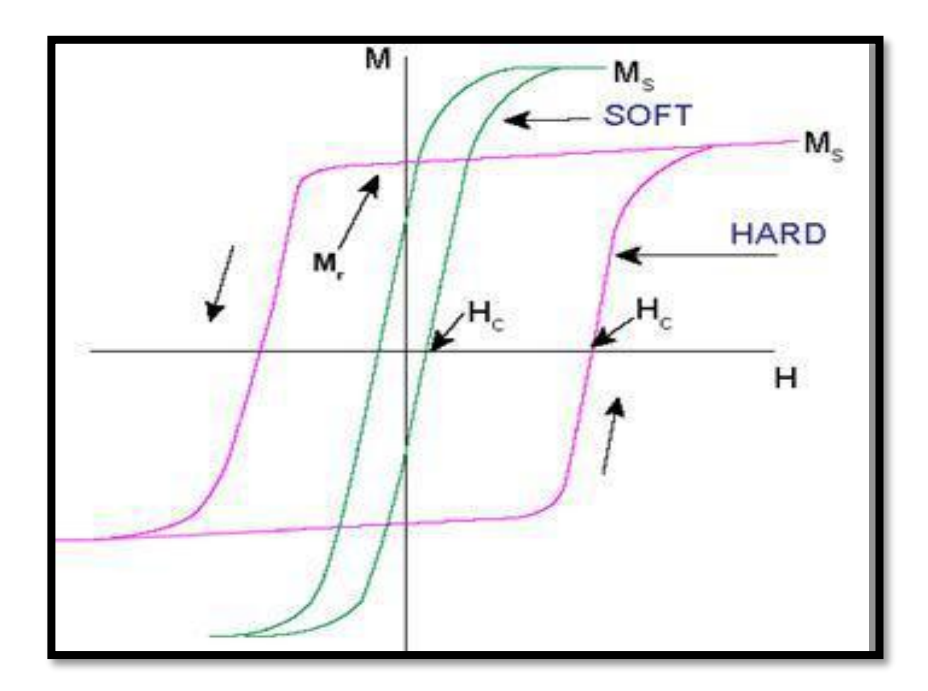


Figure 1.10 Typical Hysteresis Loops for Both Soft and Hard Ferrites

# 1.5 COBALT NANOFERRITES

Nanotechnology has advanced dramatically in the previous few decades, particularly in the physical sciences. Nano crystalline spinel ferrite forms play a significant role at the nano and subnano scales. Because of its typical ferrimagnetic properties, low conductivity, lower eddy current losses, and good electrochemical stability, cobalt nanoferrite (CoFe<sub>2</sub>O<sub>4</sub>) is one of the most versatile and technologically relevant soft ferrite materials.

Due to its outstanding magnetic, magneto resistive, and magneto-optical capabilities, magnetic resonance imaging enhancement, and magnetic high-density information storage properties, cobalt nanoferrites have shown a variety of uses [Shanmugavel *et.al.*, 2015 & Jie Tan *et.al.*, 2013]. Electric and magnetic properties are the most important attributes of cobalt nanoferrites, and they are affected by a variety of factors such as preparation circumstances, annealing temperature, cation

distributions, particle size, and chemical composition. Magnetic heads, inductors, magnetic refrigeration, and magnetic resonance imaging all require a different type of cobalt nanoferrite magnetic device. Modern uses of magnetic nano-particles include magneto-optical devices, contrast agents in magnetic resonance imaging, microwave industries, and ferrofluid technologies [El-Sayed *et.al.*, 2017, Prasad *et.al.*, 1998 & Gajbhiye 1998]. The type of cations and their distribution between the two interstitial sites determine the cobalt ferrites. Cobalt ferrites have different cation distributions than their bulk counterparts, which is highly interesting. The change in cation distribution from normal to mixed spinel-type, where Fe<sup>3+</sup> and Co<sup>2+</sup> ions occupy both positions, is related to the order of high-temperature cobalt ferrites. Co<sup>2+</sup> ions on B-sites and Fe<sup>3+</sup> ions spread equally among A and B-sites make CoFe<sub>2</sub>O<sub>4</sub> a well-known inverse spinel. Cobalt nanoferrites have a collinear spin arrangement in the core and a magnetic moment inclined to the magnetisation direction in the surface layer [Chinnasamy *et.al.*, 2001].

Because of its interaction with electric charges and magnetic dipoles present in the material, microwave radiation can be used to heat cobalt nanoferrites to high temperatures. Internal electric fields generated by microwaves penetrating and propagating through a magnetic dielectric material such as cobalt nanoferrite induce translational motions of free or bound charges (electrons or ions, rotate charge complexes, and electric and magnetic dipoles). Microwave processing [Sankaranarayanan *et.al.*, 2003, Sreekumar *et.al.*, 2003, Shi *et.al.*, 1999, & Shafi *et.al.*, 1997] is a rapid and efficient method for eliminating solvents and volatile species and sintering a wide range of materials.

#### 1.6 MANGANESE NANOFERRITES

Superparamagnetism, exchange bias, and disordered surface spins are among the unique features of spinel nanocrystalline cubic ferrites. Chemical compositions, preparation methods, dopant ions, particle sizes and shapes can all influence the optical, magnetic, and electrical properties of soft mixed nanoferrites [Kumar *et.al.*, 2010].

The soft Mn-Zn mixed nanoferrites feature a cubic inverse spinel structure with two distinct sublattice sites, namely tetrahedral-coordinated sites and octahedral-coordinated sites.

Because of their enormous size, all Co<sup>2+</sup> (0.65 Å) ions prefer to occupy tetrahedral positions in the spinel cubic structure, whereas Mn<sup>2+</sup> (0.83 Å) ions prefer to occupy octahedral sites. Although MnFe<sub>2</sub>O<sub>4</sub> nanoparticles generated by a variety of chemical processes are generally not complete inverse spinels, they do exist [Ghosh *et.al.*, 2019].

The type of dopant ions, preparation procedures, and cationic distribution between sublattices all have a big impact on the magnetic, optical, and dielectric properties of cubic spinel ferrites. Because diamagnetic Co<sup>2+</sup> ions occupy tetrahedral sites, Mn<sup>2+</sup> ions cannot migrate from octahedral locations. As a result, Mn<sup>2+</sup> ions enter octahedral sites, and the presence of diamagnetic Co<sup>2+</sup> ions in tetrahedral sites (50 percent) substantially changes different physical properties. In the nanoscale, cubic spinel Mn<sub>0.5</sub>Co<sub>0.5</sub>Fe<sub>2</sub>O<sub>4</sub> ferrite has dilute magnetic properties and good dielectric responses [Gopalan *et.al.*, 2010].

### 1.7 LANTHANIDES

Rare-Earth (RE) elements, which are f-block elements in the periodic table, are referred to as "lanthanides." These elements are not uncommon, but they are legally required to occur in equal amounts in nature and are difficult to distinguish from one another. In the periodic table, the RE elements have 15 Lanthanide elements with atomic numbers 57-71 [Cotton *et.al.*, 2006 & Kittel *et.al.*, 2005].

Spin coupling of the 3d electrons, which comes from Fe– Fe interactions, governs the conductivity and magnetic characteristics of spinel ferrites. The R–Fe interactions develop when Fe<sup>3+</sup> ions of spinel ferrites are partially substituted/replaced by rare earth ions (R<sup>3+</sup>), which belong to the 4f element series, resulting in 3d–4f coupling. The addition of rare-earth ions to these base ferrites significantly alters the ferrites' electromagnetic characteristics. The interaction between 3d–4f electrons caused by rare earth elements affects the ferrite's electrical and magnetic properties, resulting in magnetic anisotropy, also known as magneto-crystalline anisotropy. R can be divided into two groups based on their ionic radii. The radius of R<sup>3+</sup> ions is very near to that of Fe<sup>3+</sup> ions in the first class, and the rare-earth ions will enter the spinel lattice soon. The radius of R<sup>3+</sup> ions is greater than that of Fe<sup>3+</sup> ions in the second class, and the rare-earth ion cannot enter the spinel lattice unless a low quantity of R<sup>3+</sup> is utilised. When large concentrations of RE are used in the preparation of ferrites, secondary phases can occur [Ahmed *et.al.*, 2013].

In recent years, ferrite materials have been the subject of a slew of studies. The ferrite's exceptional features, including as high saturation magnetization, enormous

permeability at high frequencies, and remarkably high electrical resistivity, have been intensively explored. Electrical, dielectric, and magnetic properties of Co & Mn ferrites containing R [Lanthanum and Gadolinium] are important in the design of microwave, electronic, magnetic, and electrochemical devices, among other things. Rare-earth-doped cobalt and manganese ferrites have low eddy current losses; no other known material has as broad a range of uses in power production, conditioning, and conversion as rare-earth-doped cobalt and manganese ferrites. In such applications, boosting electrical characteristics and increasing the dielectric of rare-earth-doped cobalt and manganese ferrite at room temperature, on the other hand, are dependent on the synthetic condition, chemical composition, reactive/processing atmosphere, and the ions that substitute Fe<sup>3+</sup>/Fe<sup>2+</sup> ions [Opuchovic et.al., 2015, Inbanathan et.al., 2014, & Meng et.al., 2012].

### 1.8 APPLICATIONS OF NANOFERRITES FERRITES

Ferrites are widely employed as a vital component of electronic inductors, transformers, and electromagnets in our daily lives due to their high electric resistance, which results in very low eddy current losses. Ferrite powders, which have a spontaneous magnetic moment below the Curie temperature, are also utilised in the coatings of magnetic recording tapes, radars, and stealth-aircraft coatings. Because of their widespread use in our daily lives, more research is being conducted to determine their properties and applications in a variety of fields such as magnetic drug discovery, photocatalysis, and enzyme mimics. The role of ferrites and ferrates as adsorbents for the removal of environmental toxins is a novel application of ferrites and ferrates. As a result, Figure 1.11 depicts numerous ferrites applications.

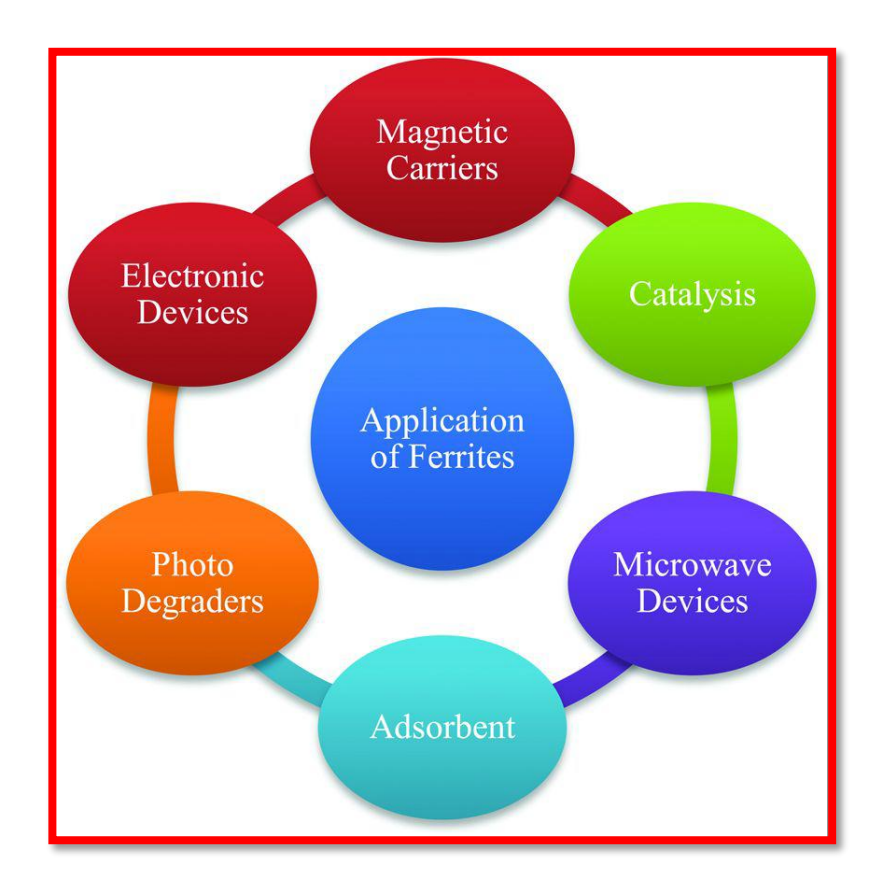


Figure 1.11 Applications of Ferrites in Different Areas

# 1.9 AIM OF THE PRESENT INVESTIGATION

The goal of this study is to produce lanthanides doped nanoferrites and investigate their microwave absorption, magnetic, and electrical properties. The goal of this study was based on the review fundamentals.

The following are the specific aim of this work:

- To make lanthanide-doped cobalt and manganese nanoferrites as  $CoLa_{X}Fe_{2-X}O_{4}, \quad MnLa_{X}Fe_{2-X}O_{4} \quad and \quad CoGd_{X}Fe_{2-X}O_{4}, \quad MnGd_{X}Fe_{2-X}O_{4} \\ (X=0.00,\,0.02,\,0.04,\,0.06,\,0.08 \,\, rare-earth \,\, concentration).$
- To investigate the structural, optical, magnetic, and electrical properties of lanthanide-doped cobalt nanoferrites.

- To investigate the electromagnetic absorption properties of cobalt and manganese nanoferrites doped with gadolinium.
- To evaluate the effect of addition of gadolinium to manganese nanoferrites
   on the improvement of magnetic, dielectric and optical properties of
   nanoferrites.

# REFERENCES

**Ahmed M.A**, Bishay S.T, Khafagy R.M & Saleh N.M, 'Promising waste water treatment using rare earth-doped nano ferrites', Journal of Magnetism and Magnetic Materials, 350 (2013) 73-80.

**Bhagyaraj S.M** & Oluwafemi O.S, 'Nanotechnology: The Science of the Invisible', Synthesis of Inorganic Nanomaterials, (2018) 1-18.

**Chinnasamy** C.N, Narayanasamy A, Ponpandian N, Chattopadhyay Shinoda K.K, Jeyadevan B, Tohji K & Nakatsuka K, Furubayash T & Nakatani I, 'Mixed spinel structure in nanocrystalline NiFe<sub>2</sub>O<sub>4</sub>', The American Physical Society, 63 (**2001**) 184108-184108.

**Cotton S**, 'Lanthanide and Actinide Chemistry', Uppingham School, Uppingham, Rutland, UK (2006).

**Dolez P.I**, 'NANOENGINEERING Global Approaches to Health and Safety Issues', CTT Group, St-Hyacinthe, Canada (2015).

**El-Sayed K**, Mohamed M.B, Hamdy S.H, & Ata-Allah S.S, 'Effect of synthesis methods with different annealing temperatures on micro structure, cations distribution and magnetic properties of nano-nickel ferrite', Journal of Magnetism and Magnetic Materials 423 (**2017**) 291-300.

Goldman A, 'Modern Ferrite Technology', Ferrite Technology Pittsburgh, USA (2006).

**Hashim M**, Alimuddin Shirsath S.E, Kumar S, Kumar R, Roy A.S, Shah J & Kotnala R.K, 'Preparation and characterization chemistry of nanocrystalline Ni–Cu–Zn ferrite', Journal of Alloys and Compounds, 549 (2013) 348-357.

**Hazra S** & Ghosh N.N, 'Preparation of nanoferrites and their applications', Journal of Nanoscience and Nanotechnology, 14 (**2014**) 1983-2000.

**Inbanathan S.S.R**, Vaithyanathan V, Chelvane J.A, Markandeyulu G & Bharathi K.K, 'Mossbauer studies and enhanced electrical properties of R (R=Sm, Gd and Dy) doped Ni ferrite', Journal of Magnetism and Magnetic Materials, 353 (**2014**) 41-46.

**Jaswala L** & Singh B, 'Ferrite materials: A chronological review', Journal of Integrated Science & Technology, 2 (2014) 69-71.

**Kaur M**, Kaur N, & Vibha, 'Ferrites: Synthesis and Applications for Environmental Remediation', American Chemical Society, 4 (**2016**) 113-136.

**Kefeni K.K**, Msagati T.A.M & Mamba B.B, 'Ferrite nanoparticles: Synthesis, characterization and applications in electronic device', Materials Science and Engineering vol. 215 (2017) 37-55.

**Kelsall RW**, Hamley, IW & Geoghegan M, 'Nanoscale Science and Technology', The University of Leeds, UK (2005).

**Kittel C**, 'Introduction to solid state Physics', University of California, Berkeley (2005).

**McHenry M.E**, Willard M.A, Laughlin D.E, 'Amorphous and nanocrystalline materials for applications as soft magnets', Progress in Materials Science, 44 (**1999**) 291-433.

**Meng Y.Y**, Liu Z.W, Dai H.C, Yu H.Y, Zeng D.C, Shukla S & Ramanujan R.V, Structure and magnetic properties of Mn (Zn)Fe<sub>2-x</sub> RE<sub>x</sub>O<sub>4</sub> ferrite nano-powders synthesized by coprecipitation and refluxing method', Powder Technology, 229 (**2012**) 270-275.

**Morgan P.E.D** & Cirlin E.H, 'The magneto plumbite crystal structure as a radwaste host', Communications of the American Ceramic Society, 65 (1982) c114-c115.

**Ozgur** U, Alivov Y & Morkoc H, 'Microwave ferrites, part 1: fundamental properties', J Material Science: Material Electronics, 20 **(2009)** 789-834.

**Prasad S**, & Gajbhiye N.S, 'Magnetic studies of nanosized nickel ferrite particles synthesized by the citrate precursor technique', Journal of Alloys and Compounds, 265 (1998) 87-92.

**Pullar R.C**, 'Hexagonal ferrites: A review of the synthesis, properties and applications of hexaferrite ceramics', Progress in Materials Science, 57 (2012) 1191-1334.

**Ramsden J**, 'Essentials of Nanotechnology', Ventus Publishing ApS (2009), ISBN 9788776814182.

**Reghunadhan A**, Kalarikkal N & Thomas S, 'Mechanical Property analysis of nanomaterials', characterization of Nanomaterials (**2018**) 191-212.

**Sankaranarayanan V.K** & Sreekumar C, 'Precursor synthesis and microwave processing of nickel ferrite nanoparticles', Current Applied Physics, 3 (2003) 205-208.

**Shafi K.V.P.M**, Koltypin Y & Gedanken A, 'Sonochemical Preparation of Nanosized Amorphous NiFe<sub>2</sub>O<sub>4</sub> Particles', The Journal of Physical Chemistry B, 01 (**1997**) 6409-6414.

**Shanmugavel T**, Gokul Raj S, Ramesh Kumar G & Rajarajan G & Saravanan D, 'Cost effective preparation and characterization of nanocrystalline nickel ferrites (NiFe<sub>2</sub>O<sub>4</sub>) in low temperature regime', Journal of King Saud University – Science, 27 (**2015**) 176-181.

**Sharma R**, Thakur P, Sharma P & Sharma V, 'Ferrimagnetic Ni<sub>2þ</sub> doped Mg-Zn spinel ferrite nanoparticles for high density information storage', Journal of Alloys and Compounds, 704 (**2017**) 7-17.

**Shi Y**, Ding J, Liu X & Wang J, 'NiFe<sub>2</sub>O<sub>4</sub> ultrafine particles prepared by co-precipitation/mechanical alloying', Journal of Magnetism and Magnetic Materials, 205 (**1999**) 249-254.

**Singh R.K**, Shah J & Kotnala R.K, 'Magnetic and dielectric properties of rare earth substituted Ni<sub>0.5</sub> Zn<sub>0.5</sub>Fe<sub>1.95</sub> R<sub>0.05</sub> O<sub>4</sub> (R=Pr, Sm and La) ferrite nanoparticles', Materials Science and Engineering B, 210 (**2016**) 64-69.

**Solymar** L & Walsh D, 'Electrical properties of materials', Oxford University, New York (2010).

**Tiwari J.N**, Tiwari R.N & Kim K.S, 'Zero-dimensional, one dimensional, two-dimensional and three-dimensional nanostructured materials for advanced electrochemical energy devices', Progress in Materials Science 57 (**2012**) 724-803.

**Valenzuela R**, 'Novel Applications of Ferrites', Physics Research International, Article ID. 591839 (2011).

**Vollath D**, 'An introduction to synthesis, properties and applications', Nano consulting, Germany (2008).

# **CHAPTER-II**

# **REVIEW OF LITERATURE**

### 2.1 INTRODUCTION

In recent years, rare earth doped nanoferrites with unique electronic and magnetic properties have drawn significant attention in different fields. As an important metallic material of the rare-earth nanoferrites reveal newly promising applications in several technical fields including Electro Magnetic Radiation, Telecommunication system, solar cell, gas sensing and electr magnetic sheilding. However, the synthesis of nanoferrites well supported nanoferrites remains a valued research area.

### 2.2 LANTHANUM DOPED COBALT NANOFERRITES

**Demirci et.al., (2018)** have investigated the structural, compositional, and magnetic properties as well as the AC magnetic hyperthermic response of  $CoFe_{2-x}La_xO_4$  (x=0.0, 0.2, 0.5) nanoparticles. They have studied the AC magnetic hyperthermia response. A series of temperature versus time measurements was done by varying the magnetic eld amplitude, the medium carrier viscosity, and the nanoparticles' concentration as parameters that governed the heating efficiency. A decrease of specific loss power was observed with an increase of the viscosity of the carrier medium for x=0 and x=0.25 substituted Co-ferrite nanoparticles. In contrast, a small increase was observed with the x=0.1 La<sup>3+</sup> substituted Co-ferrite nanoparticles. They have found that the La<sup>3+</sup> ions substituted into the Fe<sup>3+</sup> ion sites, resultingin increased magnetocrystalline anisotropy with x.

Lawrence Kumar et.al., (2012) synthesized CoFe<sub>2-x</sub>La<sub>x</sub>O<sub>4</sub> nanoparticles with different crystallite sizes by the citrate precursor method. All the XRD patterns could be analyzed by the Rietveld refinement technique. The cations distribution between the tetrahedral (A-site) and octahedral sites (B-site) has been estimated by Rietveld analysis. The refinement results show that La<sup>3+</sup> ions have strong preference for octahedral sites (B-sites). The presence of Co, Fe, La and O ions in the sample has been obtained by EDS with the help of FE-SEM. The saturation magnetization has been analyzed by the "Law of Approach (LA)" technique. They have found that the saturation magnetization, magnetic coercivity and magnetocrystalline anisotropy constants are found to decrease with the increase of La<sup>3+</sup> concentration.

Rajendran Indhrajothi et.al., (2015) have prepared the Mesoporous CoFe<sub>2</sub>O<sub>4</sub>, and lanthanum ion (La<sup>3+</sup>) substituted CoFe<sub>2</sub>O<sub>4</sub> nanoparticles of composition CoLa<sub>0.06</sub>Fe<sub>1.94</sub>O<sub>4</sub> were prepared by the citric acid and urea assisted combustion process. The citric acid, urea, and glycerol assisted the foam combustion process, respectively. The effect of lanthanum ion substitution on the crystallite size, the lattice parameter, the particle morphology and electrical properties of pristine CoFe<sub>2</sub>O<sub>4</sub> is studied using XRD, FTIR, SEM, TEM and impedance spectroscopy. Furthermore, half-cell charge/discharge performances are studied using cyclic voltammetry and charge/discharge cycling. They have recommended that; the rare earth ion substitution improves the structural stability of pristine CoFe<sub>2</sub>O<sub>4</sub> and enhances the oxidation reaction, maintaining lithium ions involved in the oxidation and reduction reactions. It also improved the battery performance; for instance, the specific capacity of La<sup>3+</sup>-ion-doped CoFe<sub>2</sub>O<sub>4</sub> is 188% compared to the new CoFe<sub>2</sub>O<sub>4</sub> anode even after 50 cycles.

NiCoZn-ferrites doped with La3b ions, Ni<sub>0.35</sub>Co<sub>0.15</sub>Zn<sub>0.5</sub>La<sub>x</sub>Fe<sub>2</sub>O<sub>4</sub> were prepared by *Xiaohu Ren et.al.*, (2014) using the sol-gel method. The effect of the La3b ions doping on the microstructure, complex permeability, Permittivity and microwave absorption of the samples was investigated. The results show that all samples exhibited a well-defined spinel phase when sintered at 1000 °C. With the increase of the substitution ratio of La3b ions the lattice parameters increased gradually, which resulted in the change of the particle shape and size. The magnetism data showed that the addition of La3b ions decreases saturation magnetization (Ms) and coercivity (Hc). They have reported that La3b ions doped in the ferrite not only improved complex Permittivity but also microwave absorbency.

*Bahhar et.al.*, (2018) were synthesized the (ZnFe<sub>2-x</sub>La<sub>x</sub>O<sub>4</sub> ferrite) nanoparticles with a magnetocaloric effect at low temperatures (≤10 K). Sol-gel technique was employed to synthesize ZnFe<sub>2-x</sub>La<sub>x</sub>O<sub>4</sub> (x=0.00, 0.001, 0.005 and 0.01) spinel. Structural, magnetic and magnetocaloric properties of ZnFe<sub>2-x</sub>La<sub>x</sub>O<sub>4</sub> spinel were investigated in detail. The XRD results show that the crystallite size was reduced with the increase in La<sup>3+</sup> cations. Magnetic properties and the magnetocaloric response of ZnFe<sub>2-x</sub>La<sub>x</sub>O<sub>4</sub> ferrite have been studied as a function of La<sup>3+</sup> concentration. They have found that the Neel temperature (TN) decreased slightly with the La<sup>3+</sup> content.

Furthermore, the magnetic moment decreased with the addition of  $La^{3+}$  cations. The peak of magnetic entropy changes slowly reduced. They suggested a notable difference in structural, magnetic and magnetocaloric properties of  $ZnFe_{2-}$   $_xLa_xO_4$  due to La doping.

La-doped nano spinel ferrite compounds were synthesized via the standardmicelle's method by *Ketan A. Ganure et. al.*, (2018). The prepared nano ferrites were characterized by spectrographic tools such as XRD, FTIR, TGA/DSC and EDAX, respectively. X-ray diffraction shows well defined cubic spinel structure with the secondary phase of ortho ferrite LaFeO<sub>3</sub>. Lattice parameter exhibited gradual increases with increasing in La<sup>3+</sup> ion concentrations FT-IR spectra recorded to detect vibrational bands. SEM analyzed surface morphology. TGA/DSC curves show calcination temperature, and EDAX confirmed stoichiometry of elements. They have found that synthesized particle size is in the range of a few nanometers with little agglomerations through TEM analysis.

*Kulkarni et.al.*, (2018) have prepared La substituted Ni-Co nanocrystalline ferrites via the sol-gel auto combustion method. Ni<sub>0.5</sub>Co<sub>0.5</sub>La<sub>x</sub>Fe<sub>2-x</sub>O<sub>4</sub> nanoparticles were drilled at different percentages of La<sup>3+</sup> compositions with analytical grade metal nitrate. The prepared samples were sintered at 400°C and characterized by XRD. The particle size was determined using Scherrer's formula. The nanoparticles size of NiCoFe<sub>2</sub>O<sub>4</sub> with the influence of La<sup>3+</sup> was found to be in the range of 23.30 to 32.31 nm. They have suggested that the average grain size is found to be constant with increasing La substitution.

Dascalu et.al., (2013) have been investigated the influence of rare earth (RE) addition on the structural, dielectric, magnetic and magneto resistive properties of cobalt ferrite bulk materials. Three lanthanide ions with different ionic radii and magnetic properties were dopants: Dy, Gd, La. The structural properties of the sintered samples were investigated using XRD, Raman spectroscopy and SEM. The

variation of the magnetoelectric response with the applied dc magnetic field was analyzed through VSM studies. They have reported that the insertion of rare earth elements influenced the structural characteristics of the samples and their magnetic and electric properties. And also, they have explained the weaker nature of the RE3þ–Fe3þ interaction compared to Fe3þ–Fe3þ interaction and to the antiferromagnetic alignment of the REFeO<sub>3</sub> second phase observed in the diffraction patterns after the sintering process.

Copper and rare-earth-doped (RE= La, Gd, Nd) CuFe<sub>1.85</sub>RE<sub>0.15</sub>O<sub>4</sub>nano ferrite were prepared by *Rajesh kanna et.al.*, (2018) using the sonochemical method. The effective doping of rare-earth (La<sup>3+</sup>, Nd<sup>3+</sup>, Gd<sup>3+</sup>) ions with copper nanoferrites were confirmed by X-ray diffraction. The tetrahedral and octahedral sites of the nanoferrites were identified through the FTIR spectra. The doping of rare-earth elements enhances the optical bandgap energy of the nanoferrites that are observed through Ultraviolet-DRS spectra. The SEM images indicate a spherical morphology with agglomeration to some elongate. They have suggested that values of dielectric constant and conductivity decrease considerably due to doping of rare-earth ions with copper nanoferrites.

### 2.3 LANTHANUM DOPED MANGANESE NANOFERRITES

Nanoferrites of Mn–Nd–Cu combinations were synthesized by *Rajesh kanna et.al.*, (2019) using the sonochemical method. The XRD pattern showed a cubic spinel structure with its appropriate lattice parameters. FTIR spectra showed the chemical bond of tetrahedral and octahedral sites in the spinel ferrites. The surface morphology and elemental composition were analyzed by SEM coupled with EDAX, which

showed elongated, spherical agglomeration with desired elemental peak. The optical bandgap energies increased with the inclusion of Nd<sup>3+</sup>, which was investigated using the UV-DRS. The dielectric parameter decreased with an increase in frequency. The relatively low AC conductivity values were obtained for the Mn–Nd–Cu nanoferrites. The hysteresis curve showed that the prepared nanoferrites had a soft magnetic material with ferromagnetic nature. They have reported that the enhanced optical bandgap, decreased dielectric loss, and low coercivity of NMC4 indicated that the prepared nanoferrites could be utilized at super-high frequencies in electronic gadgets.

Pure and La-doped zinc ferrites were synthesized by *Tholkappiyan et. al.*, (2014) through the combustion method using glycine as fuel. The prepared nanoparticles characterized using XRD revealed the formation of cubic spinel phase with high crystallinity. The average crystallite size, X-ray density and bulk density were found to decrease with an increase in La3p concentration. The chemical elements and states on the surface of these ferrites were determined using XPS. The magnetic behaviour of these nanoparticles was studied using a VSM and corresponding changes in the magnetic parameters. In the UV–DRS studies, the optical band gap was found to be in the range of 1.87–1.97eV. They documented that; the combustion method significantly produces a large number of products within a short time. Therefore, this method is potentially suitable for manufacturing industries for preparing magnetic nanoparticles.

Ahsan et. al., (2018) had synthesized manganese doped cobalt ferrite nanoparticles via standard solid-state reaction route. The XRD spectrum confirms the formation of the spinel structure of the synthesized samples. The average crystallite

size is estimated through FESEM. The energy dispersion spectrum showed the presence of Co, Mn, Fe and O in the prepared sample. Frequency-dependent dispersion exhibits strange behaviour. A pronounced leftward shift of relaxation peaks in the distribution was observed in the loss factor tanδ curve. The fabricated nanoparticles have shown semiconducting behaviour at a low-frequency regime but a purely insulating behaviour at a higher frequency regime, indicating a second-order phase transition. The magnetoresistance of Co<sub>1.125</sub>Mn<sub>0.125</sub>Fe<sub>1.875</sub>O<sub>4</sub> decreases monotonically with increasing magnetic field and hence bears the signature of semiconducting material. However, comparing the transverse and longitudinal magnetoresistance of the material, they have found that both the magneto resistive parameters are magnetic field dependent and hence bear the nature of mixed metallic and semiconducting material.

Elangbam Chitra Devi et. al., (2017) had successfully prepared the La-doped Mn ferrite MnLa<sub>x</sub>Fe<sub>2-x</sub>O<sub>4</sub> (x = 0.02, 0.04, 0.06, 0.08, 0.10) by adopting the chemical co-precipitation method. The prepared samples were characterized by analytical tools such as XRD, FTIR, EDAX and SEM, respectively. XRD and FTIR studies confirm the single spinel phase formation of the prepared nanoparticles up to 0.10 concentration of Lanthanum. SEM micrographs depicted the morphology of agglomerated nanoparticles. EDX confirmed the presence of the elements Mn, Fe, La and O. The behaviour of dielectric constant with the applied frequency follows the normal behaviour of ferrites and is explained in terms of Maxwell Wagner and Koop's model of dielectrics. The frequency variation of ac conductivity of all the samples further confirms the hopping mechanism of the conduction process in the

prepared nanoferrites. They had recommended that; this particular method is suitable for the effective synthesis method for preparing single spinel phase La-doped Mn ferrite nanoparticles at low cost and time.

*Humaira et. al.*, (2013) had effectively achieved the Mn-Zn doped with Cd<sup>2+</sup> (Mn<sub>0.5</sub>Cd<sub>x</sub>Zn<sub>0.5-x</sub>Fe<sub>2</sub>O<sub>4</sub>) nanoferrite powders using the sol-gel auto- combustion and coprecipitation methods. The effect of Cd<sup>2+</sup> doping on the crystalline phase was investigated by XRD, which confirms the spinel structure of prepared samples. Crystallite size was found to be lower for samples prepared by the coprecipitation method. The samples prepared using coprecipitation were found to be denser as compared to the sol-gel process. SEM analysis confirmed the nanostructure of the prepared samples. Dielectric properties were studied using impedance analyser and RF material analyser, respectively. DC electrical measurements showed a highly resistive nature of the prepared samples, and values are high for samples prepared from the sol-gel method. Impedance spectroscopic analysis for the prepared samples shows the resistance of grain boundary is more elevated than grains. They reported that the high resistance of samples is due to an increase in the number of grain boundaries in the nano synthesised samples.

*Prashant Thakur et. al.*, (2016) had prepared Mn<sub>0.5</sub>Zn<sub>0.5</sub>La<sub>x</sub>Fe<sub>2-x</sub>O<sub>4</sub> (x=0, 0.025, 0.050, 0.075, 0.1) nanoferrites by co-precipitation method. The structural, morphological and elemental study has been performed using XRD, FTIR, FESEM and EDS. Different structural parameters (crystallite size, interplanar spacing and lattice constant) have been calculated from XRD. The formation of cubical spinel structure has been confirmed from XRD and FTIR. Magnetic properties have been

investigated using VSM. Maximum saturation magnetization and magnetic moment have been obtained at x=0.050. The results are attributed to the solubility of La in Mn–Zn ferrite and the size of nanoparticles. For x=0.050, a blue shift in absorbance and photoluminescence measurements has been observed due to quantum confinement. They have concluded that the doping of La ions in Mn-Zn nanoferrites results in the Maximum saturation magnetization and magnetic moment.

Spinel Mn<sub>1-x</sub>Cu<sub>x</sub>Fe<sub>1.85</sub>La<sub>0.15</sub>O<sub>4</sub> nanoferrites were synthesised by **Rajesh Kanna** et al. (2017) via the sonochemical method. The effect of La<sup>3+</sup> on the structural, optical, dielectric and magnetic properties of Cu-Mn nanoferrites was investigated through various characterisation techniques. XRD results showed the prepared nanoferrites to have a face-centred cubic spinel structure with an average crystal size of 26–58 nm. The FTIR spectra showed the presence of two absorption bands related to tetrahedral (537, 588 and 700 cm<sup>-1</sup>) and octahedral (450 cm<sup>-1</sup>) group complexes within the spinel ferrite lattice system. XPS spectra confirmed the elements and oxidation states of Cu 2p, La 3d, Fe 2p, Mn 2p and O 1 s elements. The surface morphology of the nanoferrites revealed a spherical shape, and the elements of the prepared nanoferrites uniformly arose with the designed chemical formula, which SEM confirmed with EDAX analysis. The optical bandgap energy values (5.23–5.42 eV) of the nanoferrites were examined from the observed wavelength (228–237 nm) of UV-DRS. The dielectric measurements showed a low dielectric constant and dielectric loss. They had reported, these nanoferrites were made up of soft magnetic material and had a ferromagnetic nature.

La<sup>3+</sup> substituted Mn-Zn nanoferrites with composition Mn<sub>0.6</sub>Zn<sub>0.4</sub>La<sub>x</sub>Fe<sub>2-x</sub>O<sub>4</sub> (x = 0.0. 0.2) have been prepared by *Sanjeev Kumar et al.* (2017) using the sol-gel autocombustion technique. The structure of the synthesized samples has been analyzed using the XRD, which confirmed the single-phase formation. The augment trend in the lattice parameter (8.37-8.39 Å) has been observed with the substitution of La<sup>3+</sup> ions in the Mn-Zn nanoferrite. In addition, they had found that the investigation of dc resistivity shows the semiconducting nature of prepared nanoferrites.

### 2.4 GADOLINIUM DOPED COBALT NANOFERRITES

Asif Iqbal et. al., (2013) have been synthesized Li<sub>1.2</sub>Mg<sub>0.4</sub> Gd<sub>x</sub>Fe<sub>(2-x)</sub> O<sub>4</sub> (X= 0.00, 0.02, 0.04, 0.06, 0.08, 0.10) ferrites via sol-gel auto combustion technique and reported the Effect of Gd on physical and magnetic properties of Li–Mg ferrites. XRD analysis reveals the fcc phase in all the samples, along with a few traces of the second phase. Due to the Partial solubility of Gd-ions in the lattice, the constant lattice increases initially and then decreases with Gd's substitution. It is revealed from M (H)-loops that magnetization follows decreasing trend; however, coercivity increases with Gd substitution. The decreasing trend of saturation magnetization is attributed to the weakening of exchange interactions. However, the increase in coercivity with substitution of Gd concentration is attributed to the presence of an ultra-thin layer at the grain boundaries. They have found that Li–Mg ferrites have a high value of coercivity, can be suitable for high-frequency microwave absorption.

Muhammad Shahid et al. (2017) has been synthesized the Nanoparticles of gadolinium (Gd<sup>3+</sup>) and cobalt (Co<sup>2+</sup>) doped manganese spinel ferrites by the microemulsion method. TGA, XRD, magnetic hysteresis, FTIR and dielectric measurements were done to study the variation in manganese ferrite with Co<sup>2+</sup> and

Gd<sup>3+</sup> substitution and their effect on lattice parameters. The phase development identified by XRD showed the cubic nature of the fabricated material. Magnetic properties showed a definite S-shaped hysteresis loop at room temperature for all compositions. This increase could be explained by the substitution of Fe<sup>3+</sup> ions with Gd<sup>3+</sup> ions. Gd<sup>3+</sup> ions have a very high value of magnetic moment due to seven unpaired electrons. FTIR spectra exhibited two major frequency bands and confirmed cubic spinel structure. They achieved nanoparticles with a decrease in dielectric loss and dielectric constant with the increase in substitution.

Gadolinium substituted cobalt ferrite CoGd<sub>x</sub>Fe<sub>2-x</sub>O<sub>4</sub> (x=0, 0.04, 0.08) powders have been prepared by *QingLin et al.* (2015) through the sol-gel auto combustion method. XRD result indicates the production of a single cubic phase of ferrites. The lattice parameter increases, and the average crystallite size decreases with the substitution of Gd<sup>3+</sup>ions. SEM shows that the ferrite powers are nanoparticles. Mossbauer spectra display its ferromagnetic behaviour. They have found that the saturation magnetization decreases, and the coercivity increases by the Gd<sup>3+</sup> ions.

*Murugesan et al.* (2015) studied the influence of Gd<sup>3+</sup> substitution in the structural, magnetic and electrical properties of cobalt ferrite synthesized using the sol-gel auto combustion method. The XRD analysis reveals that the Gd-substituted cobalt ferrites crystallize in a single-phase spinel structure for lower concentrations of Gd<sup>3+</sup>, while a trace of GdFeO<sub>3</sub>appears as a minor phase for higher concentrations. Raman and FTIR spectra confirm the formation of spinel structure. Furthermore, Raman analysis shows that the inversion degree of cobalt ferrite decreases with Gd<sup>3+</sup> doping. The FE-SEM images show that the substitution of a small amount of Gd<sup>3+</sup>

causes a considerable grain size reduction. Studies on magnetic properties reveal that the coercivity of Gd substituted cobalt ferrites enhances, and the saturation magnetization decreases monotonically. The electrical properties show that the Gd<sup>3+</sup> doped samples exhibit high values of dielectric constant (616 at 100 Hz) and ac conductivity (4.83x10-5 S/cm at 100 Hz) at room temperature. The activation energy is found to decrease from 0.408 to 0.347 eV for the rise of Gd<sup>3+</sup> content. The impedance study brings out the role of bulk grain and grain-boundary towards the electrical resistance and capacitance of cobalt ferrite. They have found that the Gd-substitution and nano size of cobalt ferrite enhance the electrical and magnetic properties, which could ensure a higher memory storage capability.

*Erum Pervaiz et al.*, (2013) have been synthesized a series of  $Gd^{3+}$  doped nanocrystalline Co-ferrites  $CoGd_xFe_{2-x}O_4$  (x =0.0 to 0.1) by sol-gel auto combustion technique. Structural and morphology studies were performed using XRD and SEM, respectively. Indexed XRD patterns confirm the formation of the pure cubic spinel phase. Average crystallite sizes ranging from 16 nm to 25 nm ±2 was calculated from Sherrer's formula and Williamson Hall plots. Crystal strain increases with an increase in the doping amount of trivalent Gd ion. Lattice constant (a) and crystallite size D (311) increases with increase in  $Gd^{3+}$  concentration due to large ionic radii (0.94nm) of  $Gd^{3+}$  replacing  $Fe^{3+}$  (0.64nm). SEM images show the spherical morphology and uniform size distribution. Room temperature DC electrical resistivity decreases (~106) for x=0.025 then increases up to x=0.1 ~ (4.5x107). Dielectric properties have been studied using an RF Impedance/material analyzer in the frequency range of 1 MHz to 1GHz. All the studied samples show a semiconducting behaviour as Permittivity and tangent loss (tanδ) decreases with the substitution of  $Gd^{3+}$  in the

parent crystal structure. Magnetic studies by VSM shows that magnetization (Ms) decreases with an increase in  $Gd^{3+}$  concentration. They reported that the Coercivity (Hc) first decreases for x=0.025, after which it increases to 2308 Oe for x=0.1.

CoFe<sub>2-x</sub>Gd<sub>x</sub>O<sub>4</sub> ( $0.0 \le x \ge 0.1$ ) nanoparticles were synthesized by *Raghvendra Singh Yadav et. al.*, (2015) through the starch-assisted sol-gel auto-combustion method. Powder X-ray diffraction patterns revealed the formation of cubic spinel ferrite with the signature of the GdFeO<sub>3</sub> phase at a higher Gd<sub>3+</sub> concentration. The FESEM study demonstrated the spherical nanoparticle in size range 4–10nm. Raman and FTIR spectra supported the formation of the spinel ferrite structure in the nanocrystalline form. The XPS analysis confirmed the presence of Co<sub>2+</sub> and Fe<sup>3+</sup> at the octahedral site as well as the tetrahedral site in CoFe<sub>2-x</sub>Gd<sub>x</sub>O<sub>4</sub> (x = 0.05) nanoparticles. The distribution of Fe<sup>3+</sup> ions was obtained to be about 73 % in the octahedral sites and about 27 % in the tetrahedral sites. They have reported that the distribution of Co<sup>2+</sup> ions at the octahedral and tetrahedral sites were 78 and 22 %, respectively.

### 2.5 GADOLINIUM DOPED MANGANESE NANO FERRITES

Manganese (Mn<sup>+2</sup>) doped spinel cobalt ferrites nanoparticles (NPs) with composition (Mn<sub>x</sub>Co<sub>1-x</sub>Fe<sub>2</sub>O<sub>4</sub> where x = 0.2, 0.4, 0.6 and 0.8) were synthesized by *Rihab Jabbar et al.* (2019) through the sol-gel precipitation method. The structural, dielectric and magnetic properties were characterized via XRD, FTIR, LCR meter, and VSM, respectively. The average crystallite size (D) was found to increase from 10.79 nm to 14.18 nm with increasing the Mn<sup>+2</sup> doping ratio from (0.2 to 0.6) then decrease to 9.95 nm with further increasing of Mn<sup>+2</sup> to (0.8). FTIR spectrum

confirmed the formation of the spinal structure of ferrite, assigned to the octahedral complexes and (513.08 – 574.81 cm<sup>-1</sup>) assigned to tetrahedral complexes. The hysteresis loop obtained from VSM indicated the formation of soft magnetic material and the saturation magnetization decrease from 56 emu g<sup>-1</sup>. They have found that the dielectric properties of samples were decreased with increasing the doping ratio.

Undoped and rare earth substituted manganese ferrite (MF) nanoparticles, Mn<sub>0.9</sub>R<sub>0.1</sub>Fe<sub>2</sub>O<sub>4</sub> (where R = Nd, Pr, Eu and Gd) were synthesized by **Mohd Mohsin et. al., (2018)** via sol-gel technique. The structural, morphological and magnetic properties of the as-synthesized samples were determined and characterized by XRD, FTIR, TEM and VSM, respectively. The XRD spectra reveal the formation of the single-phase cubic spinel structure. The average crystallite size was found to be in the range of 8.19–21.4nm and is consistent with the results of TEM. Also, the lattice parameter increases with the rare earth (Pr, Nd, Eu, and Gd) substitution.

Furthermore, DC electrical resistivity as a function of temperature was studied using the two-probe technique and found to decrease with an increase in temperature, which reveals the semiconducting nature of the samples. Simultaneously, the optical analysis shows significant decreases in bandgap energy with rare-earth content and ranging from 2.03 to 1.73eV. It is also seen that rare earth substituted manganese ferrites show soft ferrimagnetic behaviour, and saturation magnetization decreases with the substitution of rare earth. They have suggested that this have expected application in magnetic hyperthermia for cancer therapy and various other applications.

 $Gd^{3+}$  ion-substituted manganese ferrite nanoparticles MnGd<sub>x</sub>Fe<sub>2-x</sub>O<sub>4</sub> (x=0.0, 0.05, and 0.1) were synthesized by *Murugesan et. al.*, (2015) using sol-gel auto

combustion method. TG-DTA result reveals that the prepared sample is thermally stable above 300°C. Structural and morphology studies were performed using XRD, FTIR and SEM, respectively. Indexed PXRD patterns confirm the formation of pure cubic spinel structure. The average crystallite sizes calculated using Sherrer's formula decreased from 47nm to 32nm, and the lattice constant was enhanced from 8.407Å to 8.432Å. The FTIR spectrum of manganese ferrite shows a high-frequency vibrational band at 564 cm<sup>-1</sup> assigned to the tetrahedral site. Alow-frequency vibrational band at 450 cm<sup>-1</sup> assigned to an octahedral site shifted to 556 cm<sup>-1</sup> and 439 cm<sup>-1</sup> for Gd<sup>3+</sup> substitution and confirm the incorporation of Gd<sup>3+</sup> into manganese ferrite. SEM analysis shows the presence of agglomerated spherical shaped particles at the surface. Room temperature dielectric and magnetic properties were studied using broadband dielectric spectroscopy (BDS) and vibrating sample magnetometry (VSM). They have found that the Frequency-dependent dielectric constant, ac conductivity and tan delta were found to increase with Gd<sup>3+</sup> ion substitution. They have found that the saturation magnetization decreases with an increase in Gd3+ concentration, and coercivity decreases gradually.

Nanocrystalline powders of Gadolinium ( $Gd^{3+}$ ) substituted nickel ferrite spinel (Ni $Gd_xFe_{2-x}O_4$ : x=0.00, 0.025, 0.050, 0.075 and 0.1) samples were synthesized via sol-gel Method by *Maria Lumina Sonia et. al.*, (2018). The structural, morphological, magnetic and dielectric properties of the synthesized nanoparticles were examined by XRD, FTIR, HRSEM, EDX, TEM, VSM and dielectric studies. The crystallite size of Ni $Gd_xFe_{2-x}O_4$  samples was found to decrease from 25 nm to 11 nm with an increase in  $Gd^{3+}$  content is well correlated with the data obtained from

HRTEM. Lattice parameters decrease, and lattice strain increases with the increase in Gd<sup>3+</sup> content in the sample. HRSEM images analysis confirms the stoichiometric presence of expected elements in the samples. Magnetic studies of the samples were performed magnetization values were achieved by using the "Law of Approach (LA) to Saturation magnetization" technique. Specific correlation between magnetic interaction and lattice strain was observed in VSM, in which magnetizations (Ms) decrease with an increase in Gd<sup>3+</sup> concentration from 36.51emu/gm to 19.69emu/gm. They have reported that the gadolinium content was gradually increased, coercivity and remnant magnetization were also decreased. Magnetic anisotropy of nickel ferrite was also found to decrease with increasing gadolinium content. Dielectric parameters such as dielectric constant and dielectric loss of the prepared samples decrease with the increase of applied frequency and Gd<sup>3+</sup> doping concentration.

Jagdish Chanda et. al., (2011) have been prepared MgGd<sub>x</sub>Fe<sub>2-x</sub>O<sub>4</sub> nanoparticles by solid-state reaction technique. The microstructures, electric, dielectric, and magnetic properties have been investigated using X-ray diffraction, Keithley 2611 system, impedance analyser, and VSM. Two orders of magnitude increase the dc resistivity as compared to Mg ferrite. Saturation magnetization has been increased by two times, and remnant magnetization has been increased by more than three times due to the doping of Gd<sup>3+</sup> ions in Mg ferrite. The relative loss factor was found to have very low values and is of the order of 10–4–10–5 in the frequency range 0.1–30 MHz. The variations of electric, dielectric and magnetic properties of the samples have been studied as a function of frequency and Gd<sup>3+</sup> ions concentration measured at room temperature. They have recommended that the addition of

Gadolinium in Mg ferrite has been shown to play a crucial role in enhancing the electric, dielectric and magnetic properties.

The dielectric and electrical properties of praseodymium substituted MnFe<sub>2</sub>O<sub>4</sub> ferrite as a function of frequency (1 MHz to 3 GHz) at room temperature have been studied by *Muhammad Tahir Farid et. al.*, (2017). The dielectric constant, complex dielectric constant and loss tangent of these samples decreased with an increase of the praseodymium concentration. The values of the activation energy, calculated from the direct current conductivity, increase with the substitution of praseodymium, which suggests that the conduction mechanism in the present ferrite system is due to polaron hopping. They have indicated that the prepared spinel ferrites are suitable for power applications and high-frequency multilayer chip inductors.

Mohd Mohsin et. al., (2018) were prepared the undoped and rare earth substituted manganese ferrite (MF) nanoparticles Mn<sub>0.9</sub>R<sub>0.1</sub>Fe<sub>2</sub>O<sub>4</sub> (where R=Nd, Pr, Eu and Gd) via synthesized by sol-gel technique. The structural, morphological and magnetic properties of the as-synthesized samples were determined and characterized by XRD, FTIR, TEM and VS, respectively. The XRD spectra reveal the formation of the single-phase cubic spinel structure. The average crystallite size evaluated from XRD data was found to be in the range of 8.19–21.4nm and is consistent with the results of TEM. In addition, the lattice parameter is found to increase with the rare earth (Pr, Nd, Eu, and Gd) substitution. DC electrical resistivity as a function of temperature was studied by using the two-probe technique and found to decrease with an increase in temperature, which reveals the semiconducting nature of the samples. Simultaneously, the optical analysis shows significant decreases in bandgap energy

with rare-earth content and ranging from 2.03 to 1.73eV. They have found that rare earth substituted manganese ferrites show soft ferrimagnetic behaviour and saturation magnetization decreases with the substitution of rare earth. Because of the soft ferrimagnetic behaviour, it has expected application in magnetic hyperthermia for cancer therapy and various other applications.

MnGd<sub>x</sub>Fe<sub>2-x</sub>O<sub>4</sub> nanoferrites with varying Gd concentration (x = 0.02, 0.04, 0.06, 0.08 and 0.10) were synthesized by *Elangbam Chitra Devi et. al.*, (2017) at low temperature facile co-precipitation method. XRD analysis of the prepared nanoferrites crystallizes in the spinel structure without any secondary phases. The observed increasing trend in the lattice constant reveals the partial substitution of  $Gd^{3+}$ ions in place of  $Fe^{3+}$  ions in the spinel structure. The frequency dependence of dielectric constant and dielectric loss tangent for all the compositions shows the usual dispersion behaviour at lower frequencies. The doping concentration of Gd also affects the dc resistivity of the nanoferrites. The overall dc resistivity of  $MnGd_xFe_{2-x}O_4$  nanoferrites increases with Gd concentration. They recommended that this particular method is a very simple and effective technique for synthesising pure spinel phase  $MnGd_xFe_{2-x}O_4$  nanoparticles.

Spinel ferrite  $Mn_{1-x}Cu_xFe_{1.85}Gd_{0.15}O_4$  (x = 0.2, 0.4, 0.6 and 0.8) was synthesized by *Rajesh Kanna et. al.*, (2018) using sonochemical method. The structure, optical, morphology, dielectric and magnetic properties of the prepared  $Mn_{1-x}Cu_xFe_{1.85}Gd_{0.15}O_4$  nanoferrites were exhaustively investigated using various characterization techniques. The phase purity, secondary phase and crystallite parameters were studied from XRD patterns. FTIR spectra showed two absorption

bands of transition metal oxides in the frequency range from 400 to 650 cm<sup>-1</sup>, which are related to asymmetric stretching modes of the spinel ferrites. Raman spectra have five active modes illustrating the vibration of O<sup>2+</sup> ions at both tetrahedral (A) site and octahedral (B) site ions. The presence of Mn, Cu, Gd, Fe, C and O elements in the composition were confirmed through XPS spectra. The influence of the Cu<sup>2+</sup> concentration in Mn<sub>1-x</sub>Cu<sub>x</sub>Fe<sub>1.85</sub>Gd<sub>0.15</sub>O<sub>4</sub> on the morphology, varying from nanorods, nanoflakes to spherical, was explored based on SEM images. UV-DRS studies indicated that the optical bandgap (5.12–5.32 eV) of the nanoferrites showed an insulating behaviour. The dielectric constant, loss tangent and complex dielectric constant values decreased with an increase in frequency with the addition of Gd<sup>3+</sup> content. VSM studies showed that the prepared nanoferrites had a soft ferromagnetic nature. The magnetic parameter changed markedly with an increase in the Cu content in Mn<sub>1-x</sub>Cu<sub>x</sub>Fe<sub>1.85</sub>Gd<sub>0.15</sub>O<sub>4</sub> nanoferrites. They have shown clearly that the optical, dielectric and magnetic properties were considerably enhanced with the addition of Gd<sup>3+</sup> ions in the spinel nanoferrites.

# 2.6 CONCLUSION

A detailed literary study of synthesis, properties and application of rare-earth doped nanoparticles was carried out in this chapter. Considerable particulars are collected on study methodology, structural, optical, morphological and photo catalytic study of sol-gel method of rare-earth doped nanoferrites and enlisted for the better understanding of the objectives formed.

# REFERENCES

**Ahsan M.Z**, Khan F.A, Structural and electrical properties of manganese doped cobalt ferrite nanoparticles, Journal of Material Science and Nanotechnology 2 (2018) 1-8.

**Asif Iqbal M**, Islam M.U, Ashiq M.N, Ali I, Iftikhar A, & Khan H.M, Effect of Gd-substitution on physical and magnetic properties of Li<sub>1.2</sub>Mg<sub>0.4</sub>Gd<sub>x</sub> Fe<sub>(2-x)</sub> O<sub>4</sub> ferrites, Journal of Alloys and Compounds 579 (2013) 181–186.

**Bahhar S**, Lemziouka H, Boutahar A, Bioud H, Lassri H & Hlil E.K, Influence of La<sup>3+</sup> site substitution on the structural, magnetic and magnetocaloric properties of ZnFe<sub>2-x</sub>La<sub>x</sub>O<sub>4</sub> (x=0.00,0.001,0.005 and 0.01) spinel zinc ferrites, Chemical Physics Letters,716 (2018).

**Dascalu G**, Popescu T, Feder M, Caltun O.F, Structural, electric and magnetic properties of CoFe<sub>1.8</sub>RE<sub>0.2</sub>O<sub>4</sub>(RE<sup>1</sup>/<sub>4</sub>Dy,Gd,La) bulk materials, Journal of Magnetism and Magnetic Materials, 333 (**2013**) 69-74.

Demirci **C.E**, Manna P.K, Wroczynsky Y, Akturk S, Van Lierop J, Lanthanum ion substituted cobalt ferrite nanoparticles and their hyperthermia efficiency, Journal of Magnetism and Magnetic Materials, 458 (**2018**) 253-260.

**Elangbam Chitra Devi** & Ibetombi Soibam, Structural and Electrical Studies of MnGd<sub>x</sub>Fe<sub>2-x</sub>O<sub>4</sub> Nanoparticles, Materials proceedings today 5 (2018) 2157-2162.

**Elangbam Chitra Devi**, Ibetombi Soibam, A Facile Low-Temperature Synthesis of MnLa<sub>x</sub>Fe<sub>2-x</sub>O<sub>4</sub> Nanoferrites with Structural and Electrical

Characterization, Journal of Superconductivity and Novel Magnetism, 31 (2018) 1615–1621.

**Erum Pervaiz** & Gul I.H, Influence of Rare Earth (Gd<sup>3+</sup>) on Structural, Gigahertz Dielectric and Magnetic Studies of Cobalt ferrite Journal of Physics: Conference Series 439 (**2013**) 012015.

**Humaira A** & Asghari M, Frequency dependent dielectric measurements of Cd<sup>2+</sup> doped Mn - Zn nano ferrites prepared by sol gel and coprecipitation methods, Journal of Physics: Conference Series, 439 (2013) 012014.

**Jagadesh Chand**, Kumar, Gagan, Kumar P, Sharma S.K, Knobel M, & Singh M, Effect of Gd<sup>3+</sup> doping on magnetic, electric and dielectric properties of MgGd<sub>x</sub>Fe<sub>2-x</sub>O<sub>4</sub> ferrites processed by solid state reaction technique, J. Alloys and Compds., 509 (**2011**) 9638-9644.

**Ketan A. Ganure**, Dhale L.A, Shirsat S.E & Lohar K.S, Morphological Study of Lanthanum-Doped Nano Spinel Ferrite via Normal Micelles Method, Journal of Inorganic and Organometallic Polymers and Materials 28 (**2018**) 1821-1828.

**Kulkarni V.D**, Bhujbal M.V, Rathod S.M, Influence of La<sup>3+</sup> Doped Ni-Co Nanoferrite and Magnetic Properties by Sol-Gel Auto Combustion Method, International Journal of Chemical and Physical Sciences, 5 (2016) 40-43.

**Lawrence Kumar**, Manoranjan Kar, Effect of La<sup>3+</sup> substitution on the structural and magneto crystalline anisotropy of nanocrystalline cobalt ferrite (CoFe<sub>2-x</sub>La<sub>x</sub>O<sub>4</sub>), Ceram. Int. 438 (**2012**) 4771-4778.

**Maria Lumina Sonia M**, Anand S, Maria Vinosel V, Asisi Janifer M, Pauline S & Manikandan A, Effect of lattice strain on structure, morphology and magneto-dielectric properties of spinel NiGd<sub>x</sub>Fe<sub>2-x</sub>O<sub>4</sub> ferrite nano-crystallites synthesized by sol-gel route, Journal of magnetism and magnetic materials 466 (**2018**) 238-251.

**Mohd Mohsin Nizam Ansari**, Shakeel Khan, Naseem Ahmad, Effect of R<sup>3+</sup> (R=Pr, Nd, Eu and Gd) substitution on the structural, electrical, magnetic and optical properties of Mn-ferrite nanoparticles, Journal of Magnetism and Magnetic Materials, 465 (**2018**) 81-87.

**Muhammad Tahir Farid**, Ishtiaq Ahmad, Muddassara Kanwal, Ghulam Murtaza, Irshad Ali, Muhammad Naeem Ashiq, Sajjad Ahmad Khan, Synthesis, Electrical and Magnetic Properties of Pr-Substituted Mn Ferrites for High-Frequency Applications, Journal of Electronic Materials 46 (**2017**) 1826-1835.

**Murugesan** C & Chandrasekaran G, Impact of Gd<sup>3+</sup> substitution on the structural, magnetic and electrical properties of cobalt ferrite nanoparticles, RSC Advances. **5 (2015)** 73714-73725.

**Murugesan** C, Sathyamoorthy C & Chandrasekaran G, Structural, dielectric and magnetic properties of Gd substituted manganese ferrite nanoparticles, Physica Scripta 90 (2015) 085809.

**Prashant Thakur**, Rohit Sharma, Manoj Kumar, S.C. Katyal, Nagesh Negi, N. Thakur, Vineet Sharma, Pankaj Sharma, Superparamagnetic La doped Mn–Zn nano ferrites: dependence on dopant content and crystallite size, Mater. Res. Express 3 (**2016**) 075001.

**Qing Lin**, Jinpei Lin, Yun He, Ruijun Wang, & Jianghui Dong, The Structural and Magnetic Properties of Gadolinium Doped CoFe<sub>2</sub>O<sub>4</sub> Nanoferrites, Journal of Nanomaterials (**2015**) 1-6.

**Raghvendra Singh Yadav**, Jaromir Havlica, Ivo Kuritka, Zuzana Kozakova, Eva Bartonickov, Jiri Masilko, Lukas Kalina, Jaromir Wasserbauer, Miroslava Hajduchov & Vojtech Enev, Structural and Magnetic Properties of  $CoFe_{2-x}Gd_xO_4$  ( $0.0 \le x \ge 0.1$ ) Spinel Ferrite Nanoparticles Synthesized by Starch-Assisted Sol–Gel Auto-combustion Method, Journal Superconductivity and Noval Magnetism, 28 (**2015**) 1797–1806.

**Rajendran Indhrajothi**, Prakash I, Venkateswarlu M & Satyanarayana N, Lanthanum ion (La<sup>3+</sup>) substituted CoFe<sub>2</sub>O<sub>4</sub> anode material for lithiumion battery applications, New Journal of Chemistry, 39 (**2015**) 4601-4610.

**Rajesh Kanna R**, Lenin N, Sakthipandi K, James Jebaseelan Samuel E, Neodymium doped on the manganese–copper nanoferrites: analysis of structural, optical, dielectric and magnetic properties, Journal of Materials Science: Materials in Electronics 30 (2019) 4473-4486.

**Rajesh Kanna R**, Lenin N, Sakthipandi K, Senthil kumar A, Doping effect of Rare-earth (lanthanum, neodymium and gadolinium) ions on the structural, optical, dielectric and magnetic properties of copper nanoferrites, Journal of Rare earth 3 (**2018**) 1299-1309.

Rajesh Kanna R, Lenin N, Sakthipandi K, Senthil Kumar A, Structural, optical, dielectric and magnetic studies of gadolinium - added Mn-Cu

Review of Literature Page 48

nanoferrites, Journal of Magnetism and Magnetic Materials,453 (2018) 78-90.

**Rajesh Kanna R**, Lenin N, Sakthipandi K, Sivabharathy M, Impact of Lanthanum on structural, optical, dielectric and magnetic properties of Mn<sub>1-x</sub>Cu<sub>x</sub>Fe<sub>1.85</sub>La<sub>0.15</sub>O<sub>4</sub> spinel nanoferrites, Ceram. Int. 43 **(2017)** 15868-15879.

**Rihab Jabbar,** Sabeeh S.H & Hameed A.M, Structural, Dielectric and Magnetic Properties of Mn<sup>+2</sup> doped Cobalt Ferrite Nanoparticles, Journal of Magnetism and Magnetic Materials, 494 (**2020**) 16572.

**Sanjeev Kumar**, Gagan Kumar, R. K. Kotnala, Arun Kumar, Pooja Dhiman, M. Singh, Effect of La<sup>3+</sup> ions on the Structural, Electrical and Magnetic Properties of Mn-Zn nanoferrites synthesized via Sol-Gel Auto Combustion Method, Applied Science Letters 3 (**2017**) 20-25.

**Tholkappiyan R**, Vishista K, Influence of lanthanum on the optomagnetic properties of zinc ferrite prepared by combustion method, Phys. B Condens. Matter 448 (**2014**) 177-183.

**Xiaohu Ren** & **Guangliang Xu**, Electromagnetic and microwave absorbing properties of NiCoZn-ferrites doped with La<sup>3+</sup>, Journal of Magnetism and Magnetic Materials, 354 (**2014**) 44-48.

Review of Literature Page 49

# **CHAPTER-III**

# EXPERIMENTAL METHODS AND CHARACTERIZATION TECHNIQUES

# 3.1 INTRODUCTION

The interest in research on nanoparticles is due to its unique properties in all sectors and also its resistivity, efficiency, strength, hardness, conductivity, chemical reactivity, various and versatile biological activity. The main reason for increase in interest in the nanoferrites, because the particles are widely used in semiconductor, catalysts, chemical sensing device, pharmaceutical applications and treatment, batteries, storage devices, cosmetics and microbiology.

Nanoferrites such cobalt, manganese and rare-earth have often attracted attention due to Electro Magnetic Radiation and Electro Magnetic Shielding properties which can be used in many applications. Nanoferrites with distinctive optical, electrical, magnetic and dielectric properties. It is used for various applications such as sensor, magnetic storage media, electronic and electrical materials, super capacitor and semiconductor. The preparation of these nanoferrites is one of the most important their sizes, controlling particles size, morphology and crystalline. The different preparation method was developed; some of the most well-researched approaches such as sonochemical method, Hydrothermal method, Solvothermal method, Co-Precipitation methos, Electro chemical method, Micro emulsion method, Chemical precipitation method, Microwave irradiation and Sol-gel method.

The synthesis methods are important for nanomaterial qualities since they allow for the control of nanoparticle size and shape, as well as the mechanical strength and solidity that these nanoparticles provide. Although numerous electrical resistance syntheses have been used to distinguish between the differences in the exhaustive compilation of nanoferrites and the general particle size of the product, the most appropriate ways are described below.

- Hydrothermal method
- Polyol or gel evaporation method
- Solvothermal method
- Spray pyrolysis method
- Sol-gel method

The Sol-gel method, in comparison to other approaches, uses an environmentally benign reaction medium and offers a number of advantages, including mild reaction conditions, low energy usage, and easy equipment. The present study used the sol-gel method to synthesise nanoferrites since it is a simple and cost-effective technology. The various materials and methods for preparing and characterising lanthanides doped cobalt and manganese nanoferrites are discussed in this chapter.

#### 3.2 CHEMICAL METHODS

Hydrothermal, Solvothermal Synthesis, Co-precipitation, Gel-Evaporation Method, and Sol-gel Method are some of the chemical processes utilised to prepare lanthanides doped cobalt and manganese nanoferrites.

# 3.2.1 Hydrothermal Method

The hydrothermal process is strongly linked to the appearance and development of nanomaterials. The first publication on the hydrothermal process is from the mid-nineteenth century, when quartz particles were submicrometric to nanometre-sized. The hydrothermal process produces nanomaterial at a range of temperatures from low to high. The hydrothermal technique is characterised as a broad-range chemical reaction in a solvent enclosed in sealed containers, in which the temperature of the solvents in this system produces heat at the same time as its stressed points. When water is utilised as a solvent, this sort of synthesis is known as the hydrothermal technique.

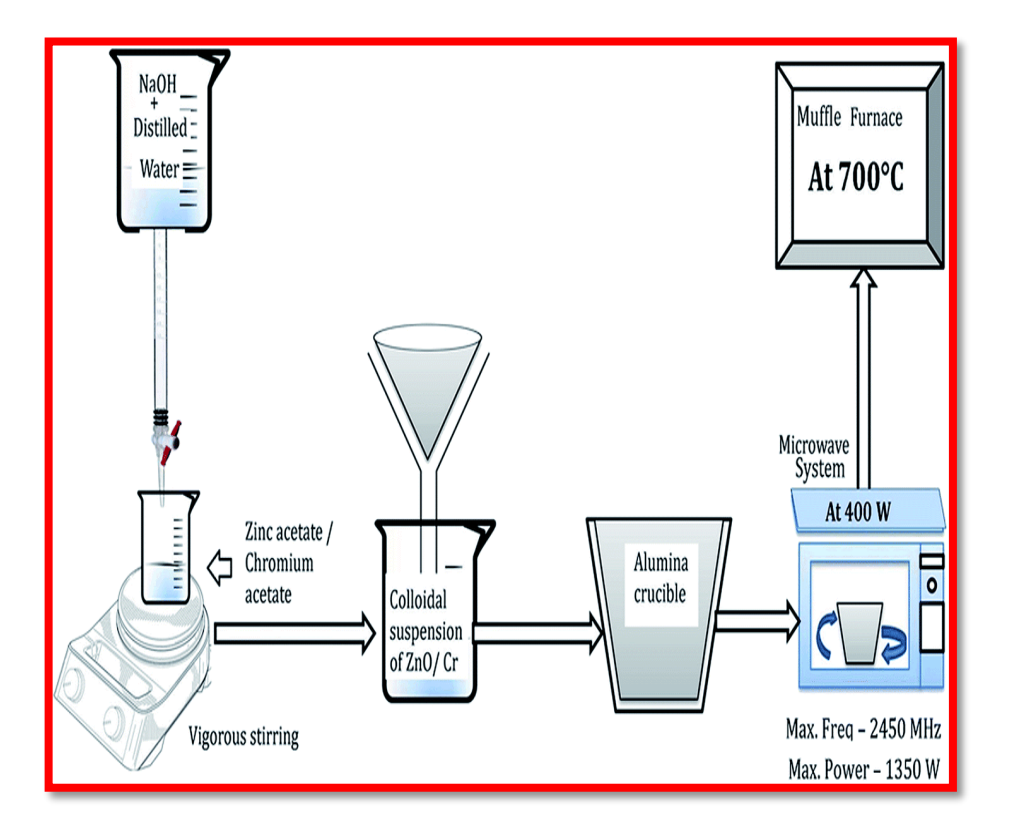


Figure 3.1 Hydrothermal Synthesis

The Hydrothermal method is rapidly becoming one of the most important instruments for advanced materials processing, particularly Experimental techniques, due to its suitability for processing nanostructured materials for a wide range of novel applications, including gadgets, optoelectronics, catalysis, ceramics, magnetic data storage, biomedical, biophotonics, and so on. The hydrothermal technique is a standout among the most appealing methods for processing nano-hybrid and nanocomposite materials because it not only aids in the preparation of monodispersed and highly homogeneous nanoparticles, but it also aids in the preparation of monodispersed and highly homogeneous nanoparticles. The phrase hydrothermal comes from the geological term hydrothermal. Any heterogeneous reaction in the presence of aqueous solvents or mineralizers at high pressure and temperature settings to dissolve and recrystallize materials that are generally intractable under ordinary conditions can be described as this process. (Byrappa K et.al., 2001). Any heterogeneous chemical reaction in the presence of a solvent above room temperature and a pressure greater than 1 atm in a closed system is defined as a hydrothermal reaction (Morey G. W et.al., 1913). It has an interesting edge over conventional technologies among the various breakthroughs available now in advanced materials processing.

This sophisticated materials approach has numerous benefits and can be used to achieve high product purity and homogeneity. Single-step processes, narrow particle size distributions, lower sintering temperature, a wide range of chemical compositions, sub-micron particles with a narrow size distribution, using simple equipment, lower energy requirements, fast reaction times, lowest residual time, polymorphic changes, with low to ultra-low solubility, and a large group of different

uses can all be achieved. This method relies on the solubility of practically all inorganic substances in water at high temperatures and pressures, which causes the dissolved material to crystallise and separate from the fluid. Water at high temperatures plays a crucial role in the transformation of precursor materials. The main parameters in hydrothermal processing are pressure, temperature, precursor concentration, and reaction time.

## 3.2.2 Polyol or Gel-Evaporation Method

The solid predecessor is liquid polyol, which is either very soluble (nitrate, acetate, and chloride) or relatively soluble (nitrate, acetate, and chloride) (oxide, hydroxide). The solution or suspension may be agitated at a specific temperature and is simple to convert to a metal that is less likely to lower the polyurethane reaction's boiling point at low temperatures. They are hydrogen-based fluids with strong permeability in water and monoalcohol because polyols are intriguing among non-aqueous solvents and can dissolve ionic mineral substances. Furthermore, while polyols and mono alcohols are fewer reducing agents, they can reduce atmospheric pressure by up to 250 degrees Celsius in solvents. Because of their chelating capabilities, polyols are comparable to diols in that they coordinate liquids with a wide range of complexity points. As a result, they can form reactive intermediate kinds on one side while preventing other liquids from collecting on the developing particles' surface.

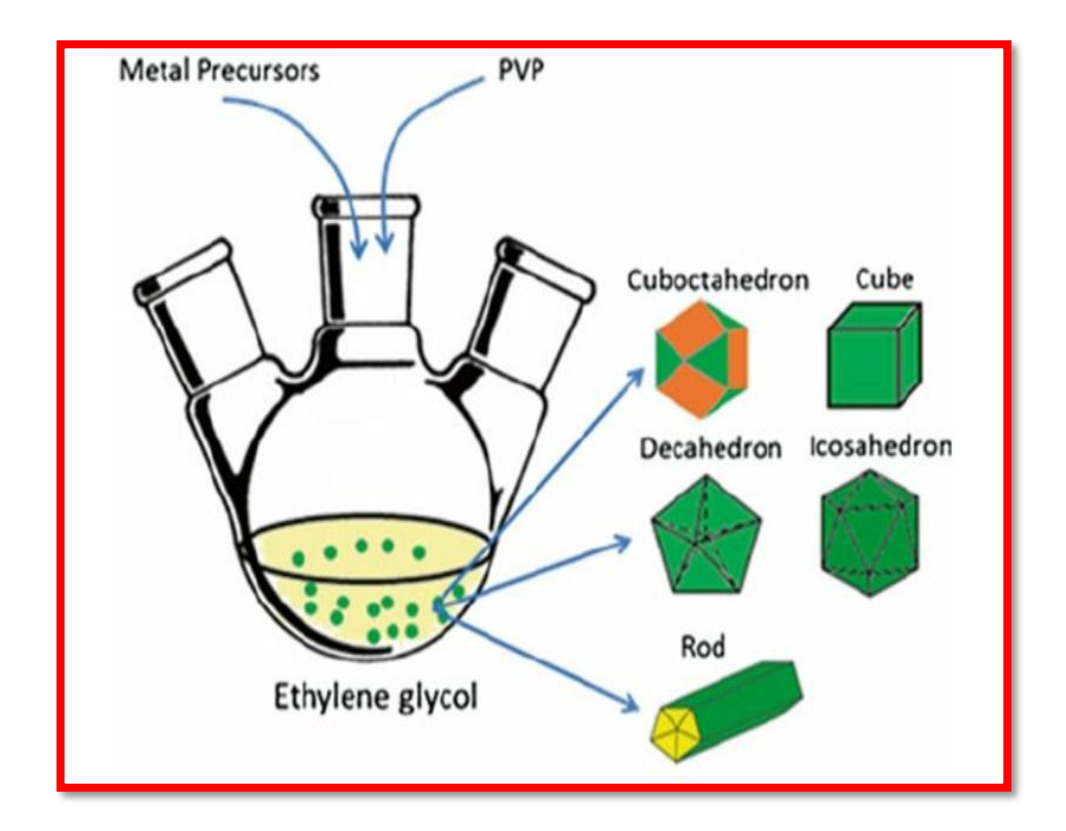


Figure 3.2Gel-Evaporation Method

When metal-containing compounds are combined in poly ethylene glycols, the ethylene glycol serves as both a dissolvable and a reducing agent. (Yugang Sun et.al.,2003). With the end objective of obtaining materials with well-defined particle size, morphology, stoichiometry, and polymorphic phase, maintaining control over the fundamental processes that regulate particle formation, namely nucleation, growth, and agglomeration, is critical. The local variables that each particle encounters in its environment have a significant impact on these basic procedures; every little temperature or chemical-specific fluctuation around the growing particle specifies new needs, forcing each particle toward a different shape, size, or phase. Indeed, by raising the batch size, for example, from a few millilitres to several litres, the precise local control over the transport processes is severely harmed. As a result, when things are scaled up, the optimum features of small-batch products vanish. As a

result, the option of boosting production by merely raising batch size while preserving quality is no longer viable: the reactor volume must be kept similarly modest.

# 3.2.3 Co-Precipitation Method

The needed metal products, known as soluble salts, are isolated from the general medium in the co-precipitation system, commonly as hydroxides, carbonates, oxalates, and citrates. In the case of oxidation and metal carbonates, because an acid dissolves them. To manufacture the final product of the residue acquired after drying, the required temperature in the atmosphere is required. The temperatures at which the precipitates degrade are superior to the high temperatures used in the ceramic approach. The co-precipitation process is a straightforward way to package powder.

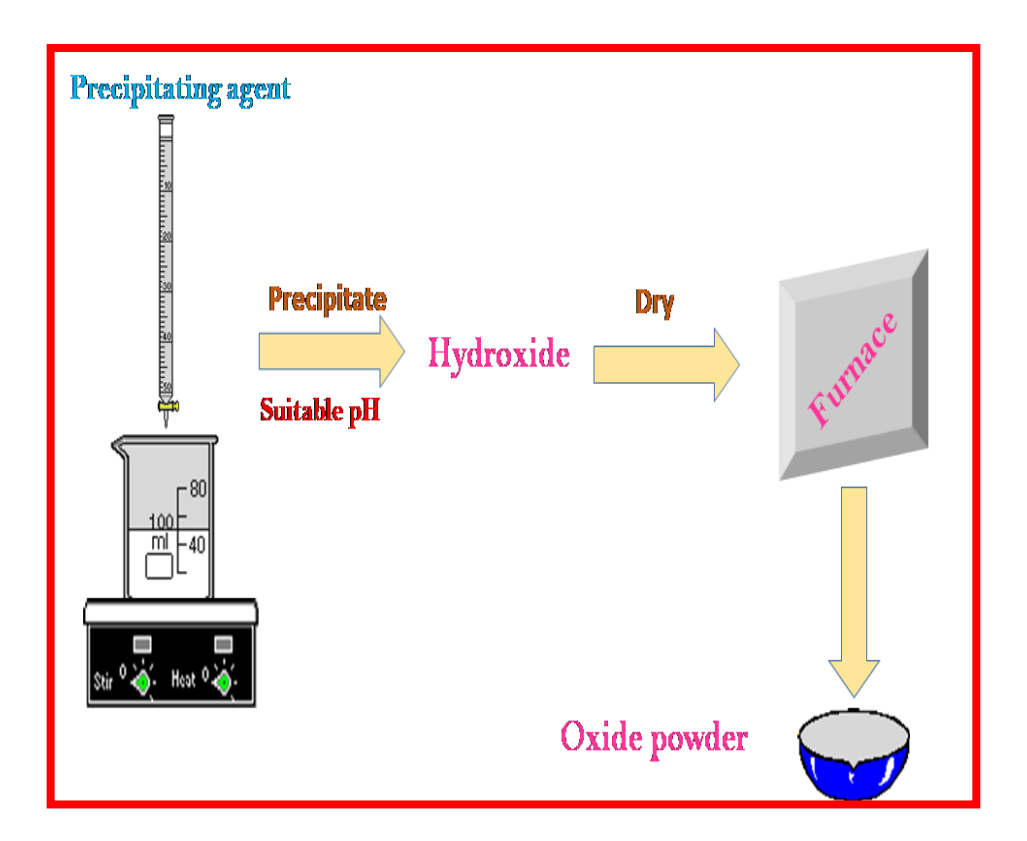
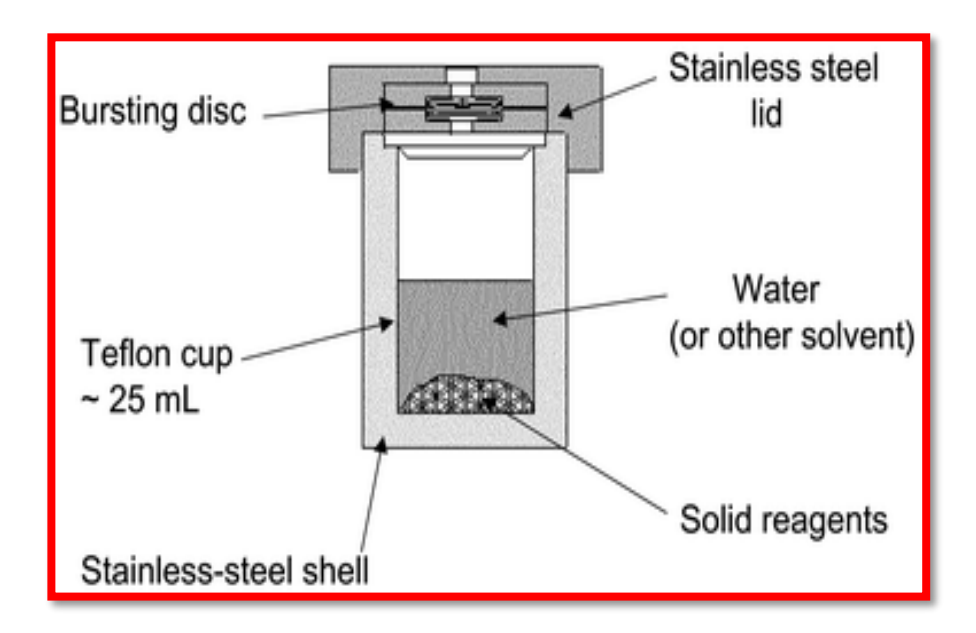


Figure 3.3 Co-precipitation Method

This method is a simple and flexible way to include nanomaterials from aqueous salt solutions to expand a base at room temperature or at a higher temperature in an inert atmosphere (*Ramasubba B et.al.*, 2014). The type of salts utilised (e.g., chlorides, sulphates, nitrates), the ratio, the reaction temperature, the pH value and ionic strength of the media, and the mixing rate with the base arrangement used to trigger the precipitation all influenced the form, size, and arrangement of the nanomaterials. Co-precipitation has been frequently used to deliver metal nanoparticles with precise sizes and antibacterial properties. Metallic oxide particles can also be utilised in high-speed compounds to promote continuous and large-scale collective precipitation.

# 3.2.4 Solvothermal Synthesis Method

The solvothermal method is similar to the hydrothermal method, except instead of water, organic solvents are utilised in the synthesis process. The reactions are also known as alcohothermal and glycothermal, respectively, because alcohols and glycerol are utilised as reaction mediums. These synthetic approaches are critical for creating NCs with good crystal characteristics. During the solvothermal approach, which uses a reaction mixture in sealed vessels, the chemical reaction dissolves at a temperature near boiling. This state improves solvent efficiency in dissolving solids and speeds up radical reactions. Precursors and other ventilators, such as solvents, are loaded at the precise rates in the autoclave of an oven arc at a specific temperature in everyday practise. The water and alcohols used by the samples are removed, dried, and vacuumed before the final product is formed. The main advantage of this method is to use any material to dissolve any motion by increasing temperature and pressure for its central point.



**Figure 3.4 Solvothermal Process** 

Solvothermal synthesis is a method for producing a wide range of materials, including metals, semiconductors, and pottery. (*Anandan K et.al.*, 2012). The procedure includes the utilization of a dissolvable under direct to high weight (regularly between 1 atm and 10,000 atm) and temperature (generally between 100 °C and 1000 °C) that encourages the connection of precursors during Synthesis. If water is utilized as the solvent, the method is called "hydrothermal synthesis." Under hydrothermal conditions, amalgamation is normally done below the water's supercritical temperature. (374°C).

The technique can be used to plan nanoparticles, bulk powders, single crystals, and nanocrystals, among other geometries. Furthermore, by manipulating solvent supersaturation, chemical of interest concentration, and kinetic control, the surface morphology morphologies of the crystals generated, such as sphere (3D), rod (2D), or wire (1D), may be regulated. The method can be used to create thermodynamically stable and metastable states, as well as unique materials that are difficult to build from

conventional materials. Many shapes, including spheres, rods, tetrapods, and teardrops, can be included into Quantum dots in this manner by manipulating the temperature, concentration, and reaction time. Furthermore, a shell of one composition (for example, Co) can be grown on top of a core of another nanocrystal (e.g., Mn). By adjusting the concentration after the initial growth, the core can also be used as a seed to generate larger particles. Many quantum dot applications are optimised by size and shape control in this technology, and solvothermal synthesis is a fundamental breakthrough for achieving this control.

#### 3.2.5 Sol-Gel Method

The solution eventually transforms into a gel-like diphasic system, containing both liquid and solid phases, in this chemical reaction. These two phases have morphologies that range from discrete particles to continuous polymer networks. The sol-gel strategy is a low-temperature method that is also inexpensive. The chemical makeup of the object can be adjusted using this method (Ghazaleh Allaedini *et.al.*, 2015). The arrangement can be doped with organic colours and rare earth elements using this technique. The dopants are evenly distributed throughout the finished product. This method can be used in the processing of ceramics and the production of metal oxide nanoparticles. This technique's nanomaterials have a wide range of applications in electronics, medicine, separation technology, and optics.

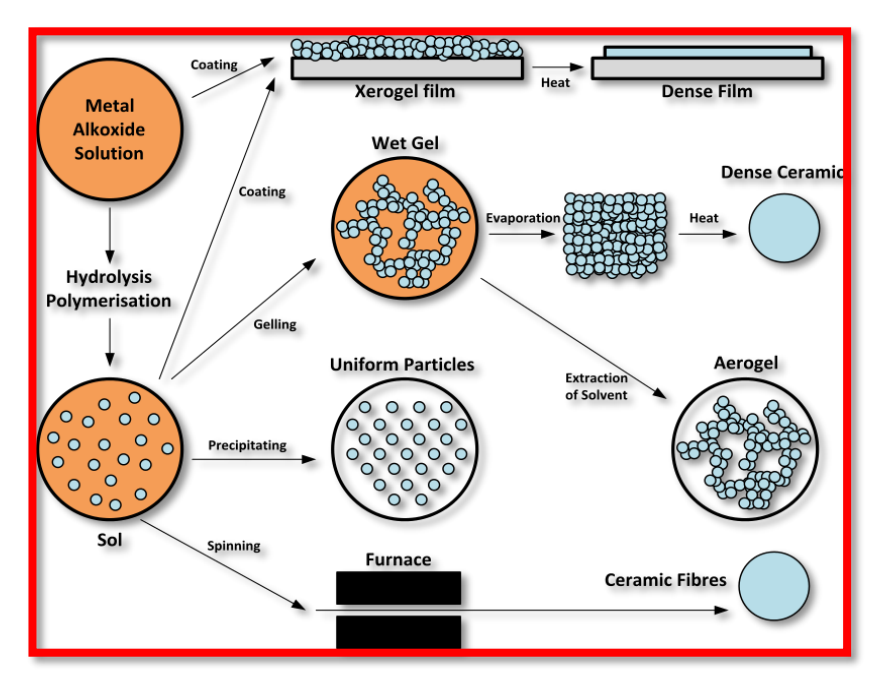


Figure 3.5 Sol-gel Processes

#### 3.2.6 ADVANTAGES OF SOL-GEL METHOD

The ability to synthesise nanoparticles of compounds that are unstable around the melting point, as well as the ability to synthesise high-quality nanoparticles, are two advantages of the sol-gel synthesis process.

The benefits of using the sol-gel process to prepare metals or metal oxides have recently become popular. This is because the resulting powder does not require any additional high-temperature calcinations, preventing contamination of the nanoparticles. Any operating temperature, pressure, or reaction way effects the shape and size of the particle during the time spent preparing nanopowder using the sol-gel process. The Sol-gel process has reached a desired operating condition, in which the materials attempt to avoid experiencing stage change as a result of varying temperatures and pressures, which would influence the shape of the created crystal in typical bunch tasks. Furthermore, in a supercritical environment, metal oxide dissolution is low, hydrolytic speed is high, nucleation during crystallisation is fast, and the diameters of produced crystals are small, providing substantial advantages as follows:

- > Environment friendly
- Control over the morphology (spheres, rod and discs etc.,)
- Easily scaled up for large Synthesis of nanoparticles
- ➤ No need of high temperature, pressure, energy and toxic chemicals
- ➤ More advantageous over use of micro-organisms by less elaborate process of maintaining cultures
- Reduce cost of micro-organism isolation and their culture media

# 3.3 EXPERIMENTAL TECHNIQUES

#### 3.3.1 MATERIALS

The following chemicals are used to Synthesis the nanoferrites(Analytical Grade, High Pure-Grade Merck). Lanthanum Nitrate hexahydrate(La(NO<sub>3</sub>)<sub>3</sub>.6H<sub>2</sub>O), Gadolinium Nitrate hexahydrate (Gd(NO<sub>3</sub>)<sub>3</sub>.6H<sub>2</sub>O), FerricNitrate Nanohydrate (Fe(NO<sub>3</sub>)<sub>3</sub>.9H<sub>2</sub>O), Cobalt Nitrate hexahydrate (Co(NO<sub>3</sub>)<sub>2</sub>.6H<sub>2</sub>O), ManganeseNitrate hexahydrate (Co(NO<sub>3</sub>)<sub>2</sub>.6H<sub>2</sub>O), citric acid (C<sub>6</sub>H<sub>8</sub>O<sub>7</sub>.H<sub>2</sub>O),ammonia (NH<sub>4</sub>OH) and distilled water were used as precursors.

### 3.3.2SYNTHESIS OF NANOFERRITES

A digital balance was used to measure the required stoichiometric amount of chemical powder (Analytical, Shimadzu). To make a homogenous precursor solution, the measured granules were combined with distilled water. For 1 hour, the combined solution was constantly agitated at 80°C. To achieve a pH of 7, more ammonia was added to the ferrite solution, one drop at a time. Finally, the dark solution was collected and dried for 24 hours in a hot air oven set to 60°C. The amorphous powders were collected and sintered for 2 hours at 500°C in a muffle furnace. The sintered nanopowders were then ground for 15 minutes to achieve a fine powder. As a result, the resulting nanopowders were calcined for further 24 hours at 1000°C. Finally, the nanoferrite was finely ground. Figure 3.6 depicts the synthesis technique as a flow chart.

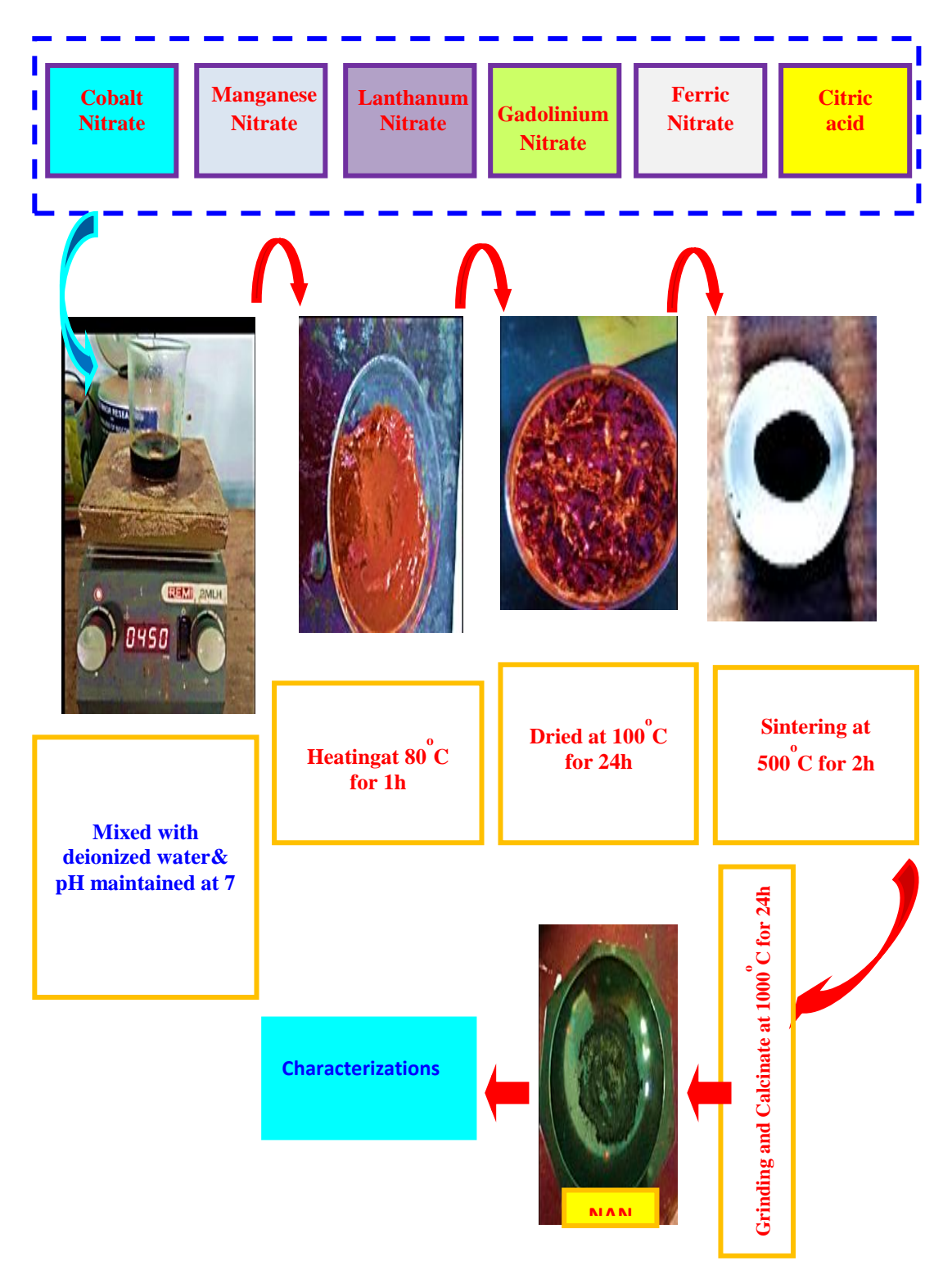


Figure 3.6The flow chart of detailed synthesis procedure.

The following nanoferrites were synthesised using the above-mentioned method.

- $\bullet$  CoLa<sub>X</sub>Fe<sub>2-X</sub> O<sub>4</sub> (X=0.00, 0.02, 0.04, 0.06 and 0.08)
- $\bullet$  MnLa<sub>X</sub>Fe<sub>2-X</sub> O<sub>4</sub> (X=0.00, 0.02, 0.04, 0.06 and 0.08)
- $\bullet$  CoGd<sub>X</sub>Fe<sub>2-X</sub> O<sub>4</sub> (X=0.00, 0.02, 0.04, 0.06 and 0.08)
- $\bullet$  MnGd<sub>X</sub>Fe<sub>2-X</sub> O<sub>4</sub> (X=0.00, 0.02, 0.04, 0.06 and 0.08)

# 3.4 CHARACTERISATION TECHNIQUES

The different characterisation techniques used to explore their structural, optical, dielectric and magnetic properties of the prepared nanoferrites were discussed in the following section.

- ❖ X-ray diffraction (XRD)
- ❖ Ultra Violet (UV) Diffuse Reflectance Spectroscopy (DRS)
- ❖ Fourier Transform Infrared Spectroscopy (FTIR)
- ❖ Field Emission Scanning Electron Microscopy (FESEM)
- ❖ Energy-Dispersive X-ray Analysis (EDAX),
- Raman Spectroscopy
- ❖ X-ray Photoelectron Spectroscopy (XPS)
- ❖ Vibrating Sample Magnetometer (VSM)
- Electrochemical Impedance Spectroscopy.
- ❖ Inductance Capacitance and Resistance (LCR) Hitester

# 3.4.1 X-ray Powder Diffraction

To identify the structural phase and the crystallite size of the prepared lanthanides doped cobalt and manganese nanoferrites were explored by the recorded XRD pattern (X'Pert PRO; PANalytical, the Netherlands). A CuKα radiation source

(λ=1.5406 Å) was used as a source to analyse the nanoferrites at the diffraction angle (2θ) position from 10° to 80° with a scanning rate of 0.05° s-1. Source was an operated at voltage and current ratings of 40 kV and 30 mA, respectively. The Scherrer formula was used to calculate the average crystallite size (D) of the prepared nanoferrites by measuring the full-width at half-maximum (FWHM) and Bragg's diffraction angle of diffraction peaks [Chand *et.al.*, 2017, Amer *et.al.*,2018, Ciocarlan*et.al.*,2016 & Sakthipandi *et.al.*, 2013]:

$$D = \frac{k \lambda}{\beta Cos\theta} 3.1$$

where  $\lambda$  is the wavelength of the x-ray,  $\theta$  the Bragg's diffraction angle and k are the FWHM.

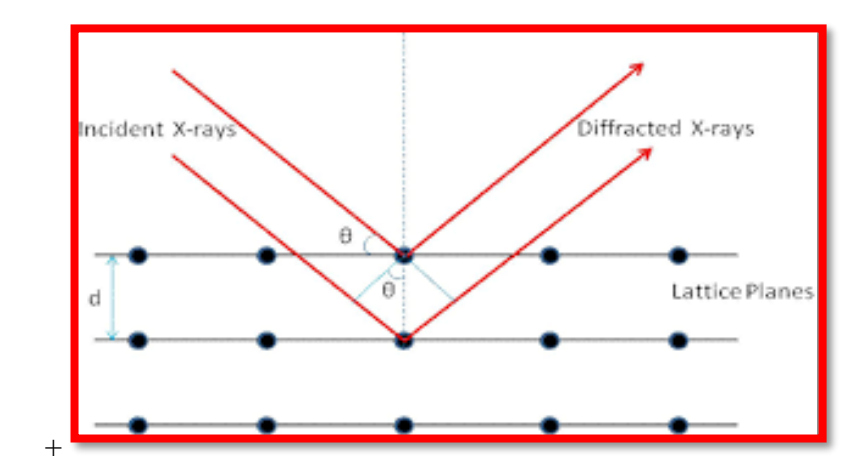


Figure 3.7Illustration of x-ray scattering from crystal lattice.

The lattice constant (a) was calculated using the standard equation [Sharma et.al., 2014]:

$$a = d_{hkl}\sqrt{h^2 + k^2 + l^2} 3.2$$

where d is the inter-planner spacing and hkl is the Miller indices of the XRD diffraction plane. The density  $(\rho_{xrd})$  of the prepared nanoferrites was determined

through X-ray measurements using the following relation [Sakthipandi *et.al.*,2011 & Shinde *et.al.*,2012]:

$$\rho xrd = \frac{8m}{Na^3}$$
 3.3

where M is the molecular weight of the prepared nanoferrites and N the Avogadro's number.

#### 3.4.2 Ultra-Violet Diffuse Reflectance Spectroscopy

A UV-DRS was used to determine the optical characteristics of the produced nanoferrites (2450, Shimadzu, USA). The wavelength-dependent absorption of nanoferrites was measured using UV-DRS spectra from 200 to 800 nm. The Eg of the manufactured nanoferrites is calculated using the following energy-dependence relationship:

$$E_g = \frac{hc}{\lambda}$$
 3.4

where h is Planck's constant, c is the velocity of light and  $\lambda$  is corresponds to the minimum dip of the absorption wavelength.

The band gap values were calculated using the following relation:

$$h\gamma\alpha = (h\gamma - E_{gap})^n 3.5$$

where h is the Planck constant, v is the frequency,  $\alpha$  is the absorption coefficient,  $\lambda$  is the wavelength of absorption and n is the different types of electronic transitions ( $n=\frac{1}{2}$  and 2 for direct and indirect transition, respectively) [Singh et.al., 2017, Moslehet.al., 2016, Singh et.al., 2015, Tholkappiyan et.al., 2014 & Tehrani et.al., 2012].

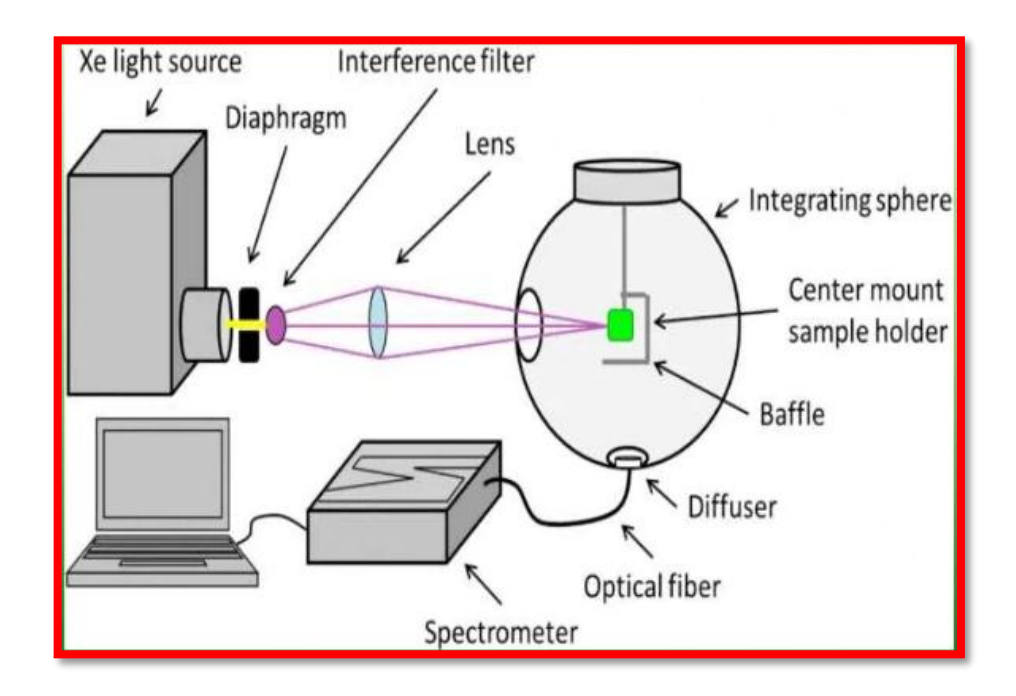


Figure 3.8Block diagram of UV-DRS spectroscopy

# 3.4.3 Fourier Transform Infrared Spectroscopy

FTIR spectra acquired with a Perkin Elmer Spectrometer (Spectrum 100, USA) in the wave number range of 4000–400 cm<sup>-1</sup> at room temperature were used to identify the functional groups and chemical bonds present in the produced nanoferrites. For FTIR spectral investigation, a pellet made of 95% KBr and 5% produced nanoferrites was manufactured. (Sudalai Muthu *et. al.*, 2013, Srivastava *et.al.*, 2009 & Ganure *et.al.*, 2017).

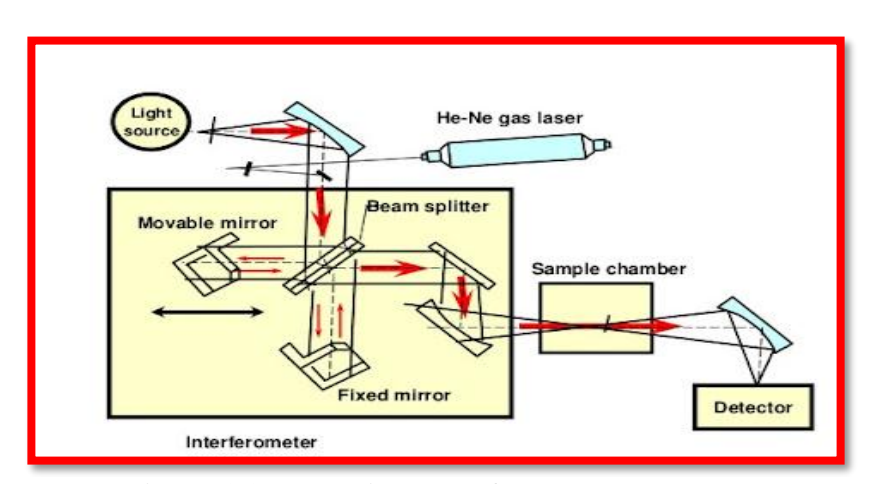


Figure 3.9Block diagram of FTIR spectroscopy

# 3.4.4 Morphology Studies

The surface morphology and elemental composition of prepared CoLa<sub>x</sub>Fe<sub>2-x</sub>O<sub>4</sub> and MnLa<sub>x</sub>Fe<sub>2-x</sub>O<sub>4</sub> nanoferrites were characterized using Field Emission Scanning Electron Microscopy (Quanta FEG 250,Germany). The spectrometer was operated at an accelerating voltage from 10to 20 kV with a magnification from ×5 to ×100,000. The surface morphologyand elemental composition of prepared CoGd<sub>x</sub>Fe<sub>2-x</sub>O<sub>4</sub>and MnGd<sub>x</sub>Fe<sub>2-x</sub>O<sub>4</sub> nanoferrites were characterized using FESEM (Carl Zeiss SEM EVO 18, Germany) coupled with an energy-dispersive analysis spectrum. The elemental composition of the nanoferrites was determined by X-ray fluorescence spectrum (EDX-720; Shimadzu, Japan). The SEM was operated at an accelerating voltage of 5 kV with a magnification from ×5 to ×3,000 KX.

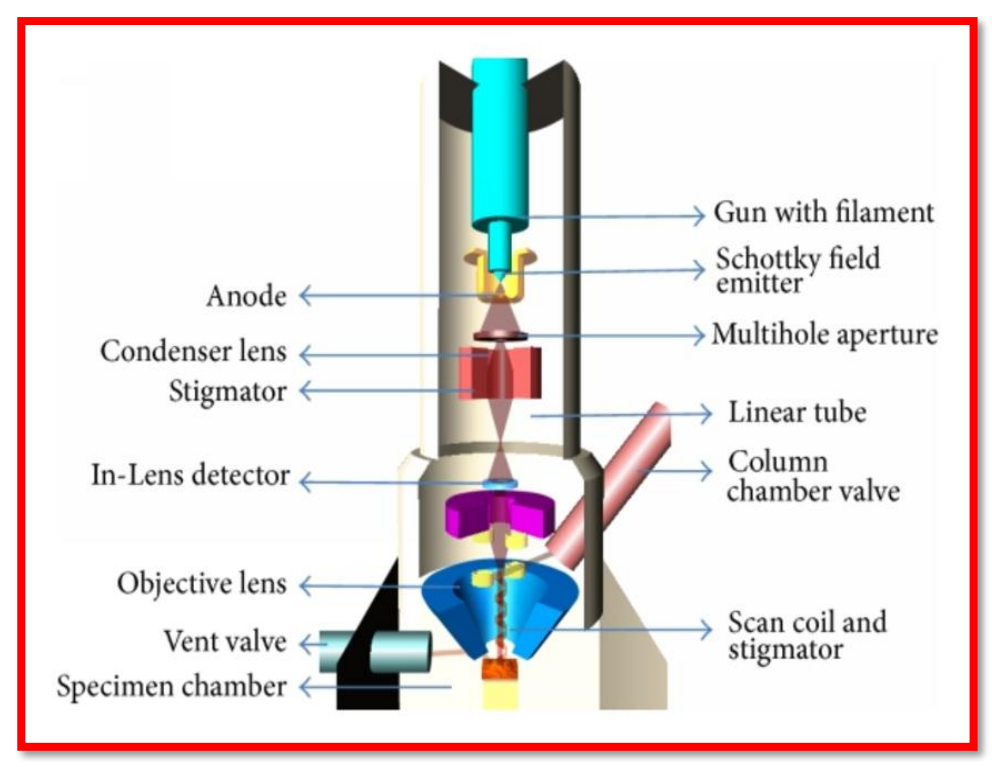


Figure 3.10 Block diagram of FESEM

#### 3.4.5 Raman spectroscopy

# 3.4.5.1 Raman scattering

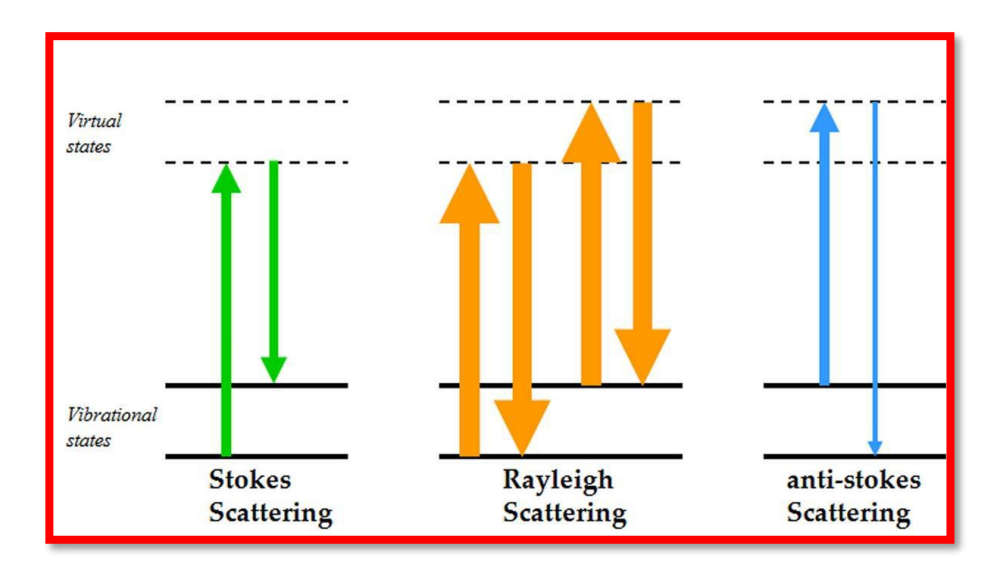


Figure 3.11 Rayleigh and Raman scattering mechanism of photons.

When light of a known frequency is shone on a medium, molecules scatter it. Rayleigh scattering occurs when photons are elastically dispersed from molecules and have the same wavelength as the incident one (Figure 3.11). Raman scattering occurs when photons are elastically scattered from molecules and have a longer (stokes) or shorter (anti-stokes) wavelength than the incident photons. The Raman shift is the frequency difference between an incident and Stokes scattering Raman scattering. Over a range of wave numbers, the Raman spectrum records the intensity of the Raman shift.

#### 3.4.5.2 Working of Raman Spectroscopy

Figure 3.12 shows a schematic diagram of the Renishaw micro-Raman system, which includes a laser source, sample lighting and collecting system, microscope, spectral analyzer, detector, and data processing system. After passing through a neutral density (ND) filter and a spatial filter, a laser beam became a single

wavelength, which was then focused on the sample by a microscope. Rayleigh light is blocked by a holographic filter, leaving only Raman scattered light. A diffraction grating is used to select the discrete wavelength of Raman scattered light. The CCD detector detects a finite range of Raman signal.

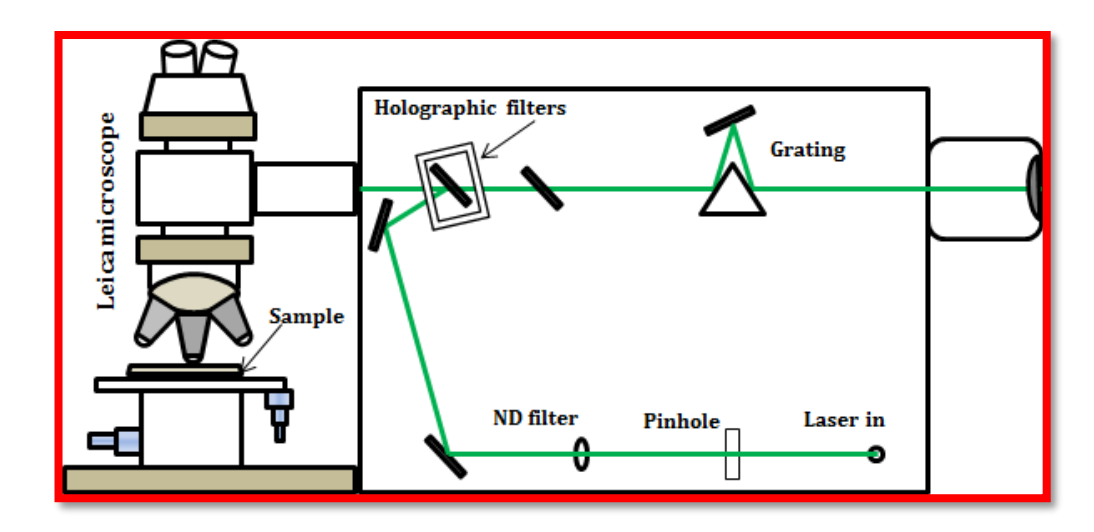


Figure 3.12 Block Diagram of Raman Scattering System

The Raman Effect is highly sensitive to molecular bonds and variations in bond-length. It can provide molecular structural information in different environments [M. Pelletier et.al.,1999, Lewis et.al.,2001].

#### 3.4.6 X-ray Photoelectron Spectroscopy (XPS)

Because it can be applied to a wide range of materials and provides valuable quantitative and chemical state information from the surface of the material being studied, X-ray Photoelectron Spectroscopy (XPS), also known as Electron Spectroscopy for Chemical Analysis (ESCA), is the most widely used surface analysis technique. For an XPS measurement, the average depth of analysis is about 5 nm. PHI XPS equipment may produce spectra with a lateral spatial resolution of as little as 7.5 m. By scanning the sample surface with a tiny focussed x-ray beam, spatial

distribution information can be collected. Combining XPS measurements with ion milling (sputtering) to describe thin film structures can yield depth distribution information. Many industrial and research applications where surface or thin film composition plays a critical role in performance, such as nanomaterials, photovoltaics, catalysis, corrosion, adhesion, electronic devices and packaging, magnetic media, display technology, surface treatments, and thin film coatings used for a variety of applications, benefit from the information provided by XPS.

XPS is commonly performed by bombarding a sample surface with monoenergetic Al k x-rays, which cause photoelectrons to be released. The energy of the released photoelectrons is measured using an electron energy analyser. The elemental identity, chemical state, and quantity of a detected element can be calculated using the binding energy and intensity of a photoelectron peak, as shown in Figure 3.13.

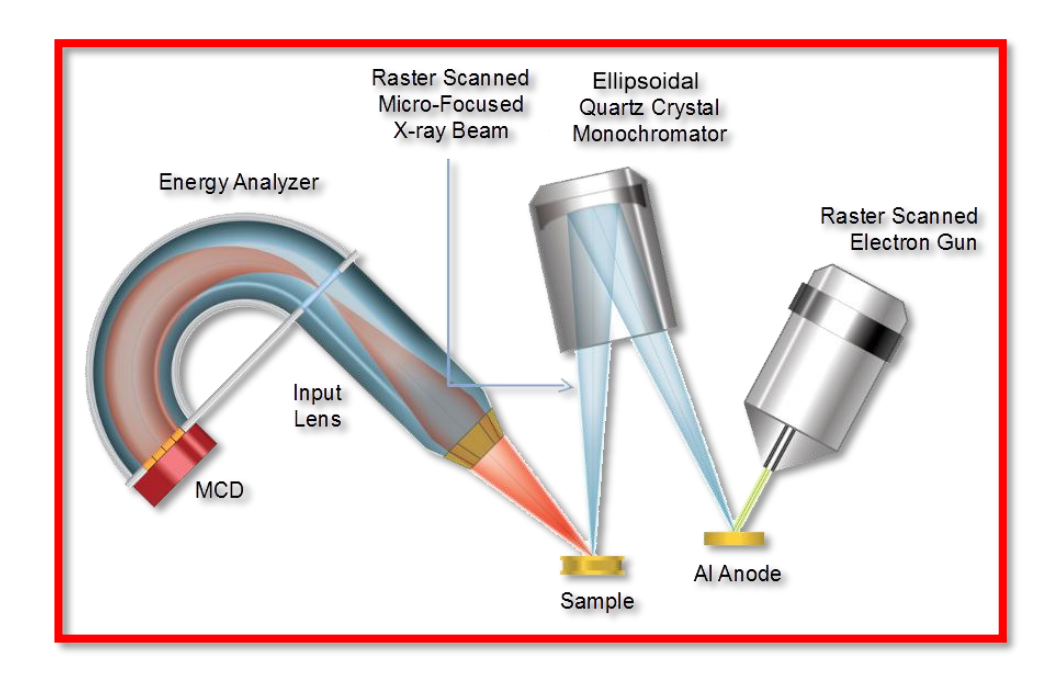


Figure 3.13 Block Diagram of XPS

The efficiency with which electrons are sampled by a spectrometer is highly dependent on these lens functions, and an instrument's performance might be significantly hampered without appropriately adjusted lens functions. Even with a well-tuned system, collection efficiency varies across the different operating modes, necessitating the use of a corresponding transmission function for each of the lens modes and energy resolutions to define an instrument.

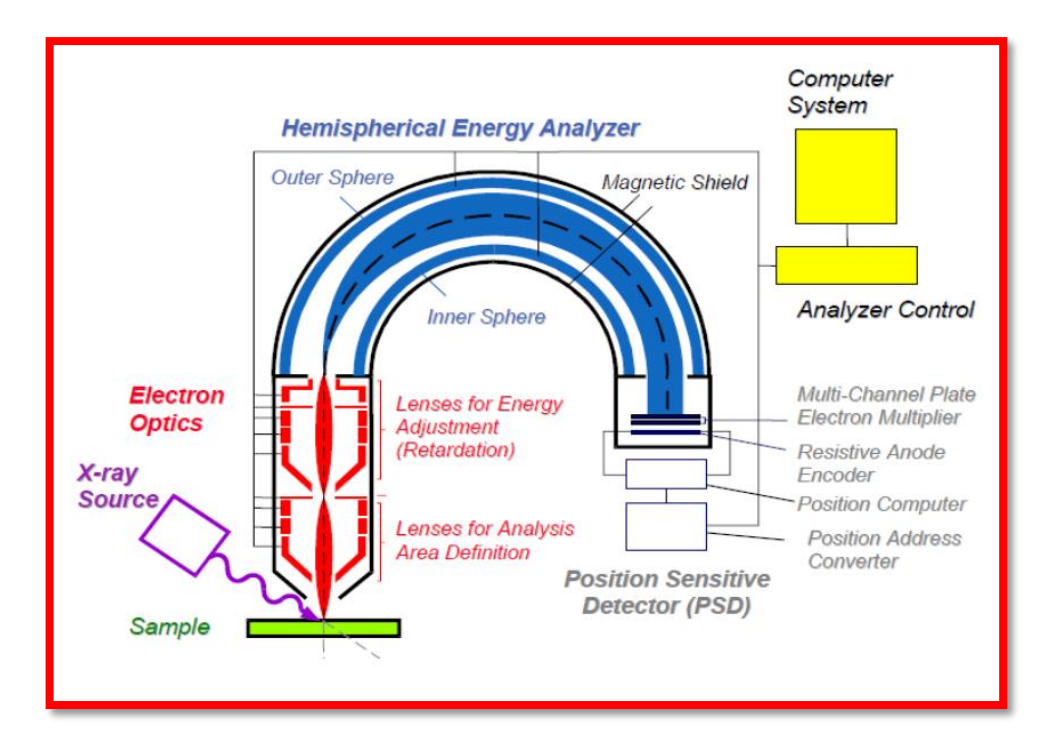


Figure 3.14Working Principal of XPS

Fixed Analyzer Transmission (FAT), also known as Constant Analyzer Energy (CAE), and Fix Retard Ratio (FRR), also known as Constant Retard Ratio, are two modes in which a hemispherical analyser and transfer lenses can be used (CRR). In FAT mode, the analyser's pass energy is kept constant, and the transfer lens system's sole responsibility is to retard the given kinetic energy channel to the analyser's acceptable range. FAT is used to acquire the majority of XPS spectra. The FRR mode scans the lens system while also adjusting the analyser pass energy to keep

the quantity "initial electron energy" / "analyser PE" constant, as shown in Figure 3.9. This mode is commonly employed for Auger spectra because the detection system's energy interval (i.e., resolution) grows with kinetic energy and recovers weak peaks at high kinetic energies while limiting the powerful low energy background that could harm the detection system. [Ray et.al., 2011&Yang et.al., 2018]

# **3.4.7 Vibrating Sample Magnetometer**

As shown in Figure 3.15, the saturation magnetization (M<sub>s</sub>), remnant magnetization or retentivity (M<sub>r</sub>), and coercivity (H<sub>c</sub>) in the produced nanoferrites were measured using a vibrating sample magnetometer (7404; Lake Shore, USA). At ambient temperature, the hysteresis loop was recorded with a magnetic field of -20 to +20 kOe. To determine the quality of the magnetic characteristics of the produced nanoferrites, the squareness ratio and the anisotropy constant (K) were computed using the following formulae. (Ribeiro *et.al.*, 2018, Sabikoglu *et.al.*,2015, Iqbal *et.al.*,2011 & Rezlescu *et.al.*,2004):

Squarness ratio = 
$$M_r/M_s$$
 3.6

Further, the Bohr magneton ( $\eta_B$ ) and Yafet–Kittel ( $\alpha_{Y-K}$ ) angles were calculated from the following equations (Sharma *et.al.*, 2017, Sarveena *et.al.*,2016, Thakur*et.al.*,2016, Zhou*et et.al.*, 2015 & Anwar *et.al.*,2012)

$$\eta_{B} = M_x M_s / 5585$$
 3.7

and,

$$\alpha_{Y-K} = \cos^{-1} \left[ 5 (1-x) + \eta_B/(6+x) \right]$$
 3.8

where M is the molecular weight and x is the concentration of rare-earth ion.

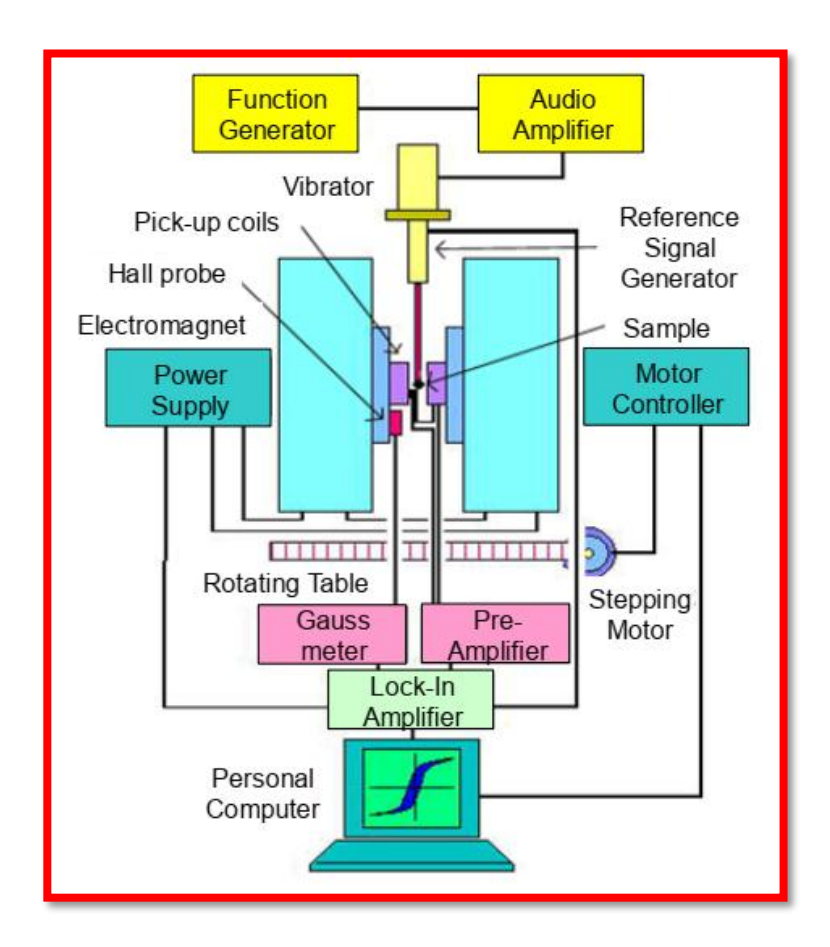


Figure 3.15 Block Diagram of VSM

# 3.4.8 Impedance Study

The spectrum was evaluated using electrochemical impedance spectroscopy to investigate the conductivity of the produced nanoferrites (PGstat302N; Autolab, the Netherlands). The conductivity measurements provided the Warburg values, which were utilised to determine the capacitance/resistance behaviour of the produced nanoferrites. (Ali *et al.* 2013 & Yu *et al.* 2011).

# 3.4.9 Dielectric Study

Using a Hitester (3532-50; HIOKI, Japan) inductance capacitanceand resistance meter, dielectric parameters such as the dielectric constant ( $\epsilon$ '), the dielectric loss or loss tangent ( $\tan \delta$ ) and the complex dielectric constant( $\epsilon$ ") were

measured. The pellet was prepared for dielectric measurements using the prepared nanoferrite powders. The  $\epsilon'$  of the prepared nanoferrites were calculated using the following formula:

$$\epsilon' = Cd/A$$
 3.9

where C is the capacitance, d the thickness of the pellet, A the cross-sectional area and  $\varepsilon_0$  the permittivity of free space. The dielectric loss and  $\varepsilon''$  values of the prepared nanoferrites were measured using the following equations:

$$\tan\delta = 1/2\pi\epsilon_0\epsilon'\rho \qquad \qquad 3.10$$
 and, 
$$\epsilon'' = \epsilon'\tan\delta \qquad \qquad 3.11$$

where  $\rho$  is the resistivity and f are the frequency of the applied field (Prasad *et.al.*,2017, Jnaneshwara *et.al.*,2014 & Anwar *et.al.*,2012).

In this research, the synthesised nanoferrites; lanthanides doped Cobalt and manganese nanoferrites were subjected to the aforementioned experimental techniques. The structural, optical, magnetic, and dielectric properties of microwave-absorbing materials, electrical, and magnetic devices were investigated using characterisation techniques such as XRD, UV-DRS, FTIR, FESEM coupled EDX, XPS, VSM, dielectric spectroscopy, and electrochemical impedance spectroscopy and measurements.

#### REFERENCES

**Ali I.O**, 'Sol–gel synthesis of NiFe<sub>2</sub>O<sub>4</sub> with PVA matrices and their catalytic activities for one-step hydroxylation of benzene intophenol', Journal of Thermal Analysis and Calorimetry, 116 (**2013**) 805-816.

**Amer M.A**, Matsuda A, Kawamura G, El-Shater R, Meaz T, & Fakhry F, 'Structural, magnetic, vibrational and optical studies of structure transformed spinel Fe<sup>2+</sup>-Cr nano-ferrites by sintering process', Journal of Alloys and Compounds, 735 (**2018**)975-985.

**Anwar H**& Maqsood A, 'Structural, Magnetic and Electrical Properties of Cu Substituted Mn–Zn Soft Nanoferrites', Journal of Superconductivity and Novel Magnetism, 25 (**2012**) 1913-1920.

**Anwar H**, & Maqsood A, 'Structural, Magnetic and Electrical Properties of Cu Substituted Mn–Zn Soft Nanoferrites', Journal of Superconductivity and Novel Magnetism, 25 (**2012**) 1913-1920.

**Chand P**, Vaish S & Kumar P, 'Structural, optical and dielectric properties of transition metal (MFe<sub>2</sub>O<sub>4</sub>; M= Co, Ni and Zn) nanoferrites', Physica B, 524 (**2017**) 53-63.

Ciocarlana R.G, Pui A, Gherca D, Virlan C, Dobromir M, Nica V, Craus M.L, Gostin I.N, Caltun O, Hempelman R & Cool P, 'Quaternary M<sub>0.25</sub>Cu<sub>0.25</sub>Mg<sub>0.5</sub>Fe<sub>2</sub>O<sub>4</sub> (M=Ni, Zn, Co, Mn)ferrite oxides: Synthesis, characterization and magnetic properties', Materials Research Bulletin, 81 (2016) 63-70.

Ganure K.A, Dhale L.A, Katkar V.T & Lohar K.S, 'Synthesis and Characterization of lanthanum-doped Ni-Co-Zn spinel ferrites

nanoparticles via normal micro-emulsion method', International Journal of Nanotechnology and Applications, 11(**2017**)189-195.

**Jnaneshwara D.M**, Avadhani D.N, Prasad B.D, Nagabhushana H, Nagabhushana B.M, Shanna S.C, Prashantha S.C & Shivakumara C, 'Role of Co<sup>2+</sup> ions substitution in magnetic and conductivity behaviour of nano CoFe<sub>2</sub>O<sub>4</sub>', Spectro chimica Acta Part A: Molecular and Biomolecular Spectroscopy, 132 (**2014**) 256-262.

**Lewis I.R**, and Edwards H.G.M, Handbook of Raman Spectroscopy, Marcel Dekker, New York, (2001).

**Li**, Yang, He, Yongyong, Qiu, Jianxun, Zhao, Jun, Ye, Qianwen, Zhu, Yijie, Mao, Junyuan, "Enhancement of Pitting Corrosion Resistance of Austenitic Stainless Steel Through Deposition of Amorphous/ Nanocrystalline Oxy-nitrided Phases by Active Screen Plasma Treatment". Materials Research, 21 (**2018**) ISSN 1516-1439.

**Mosleh M**, 'Synthesis, characterization and optical properties of neodymium doped nickel ferrite nanoparticles prepared by novel sol–gel method', Journal of Materials Science: Materials in Electronics, 27 (**2016**) 6703-670.

**Pelletier M**, Analytical Application of Raman Spectroscopy, Blackwell Science, Oxford, (1999).

**Prasada B.D**, H.Nagabhushanac & K.Thyagarajan, 'Transport and magnetic properties of nano compounds of nickel zinc ferrite for frequency reliant applications', Materials Today:Proceedings, 4 (2017) 12125-12129.

**Ray S**& Shard A.G, Quantitative Analysis of Adsorbed Proteins by X-ray Photoelectron Spectroscopy. Analytical Chemistry, 83(22) (2011) 8659-8666.

**Rezlescu N**, Rezlescu E, Sava C.L, Tudorache F, & Popa P.D, 'On the effects of Ga<sup>3+</sup> and La<sup>3+</sup> ions in MgCu ferrite:Humidity-sensitive electrical conduction', Crystal Research and Technology, 39 (**2004**) 548-557.

**Ribeiro U.L**, Nasar R.S, Nasar M.C & Araujoc J.H, 'Liquid phase sintering of ferrite of NiCuZn with low magnetic permeability for miniaturization', Ceramics International, 44(2018) 723-727.

**Sabikoglua I**, Paralo L, Malina O, Novak P, Kaslik J, Tucek J, Pechousek J, Navarik J & Schneeweiss O, 'The effect of neodymium substitution on the structural and magnetic properties ofnickel ferrite', Progress in Natural Science: Materials International,25 (**2015**) 215-221.

**Sakthipandi K**& Rajendran V, 'On-line phase transitions of bulk and nanocrystalline La<sub>1-x</sub>Pb<sub>x</sub>MnO<sub>3</sub> (x=0.3, 0.4, and0.5) perovskite manganite materials using ultrasonic Measurements', Materials Chemistry and Physics, 138 (**2013**) 581- 592.

**Sakthipandi K**, Rajendran V, Jayakumar T, Raj B & Kulandivelu P, 'Synthesis and on-line ultrasonic characterisation of bulk and nanocrystalline La<sub>0.68</sub> Sr<sub>0.32</sub> MnO<sub>3</sub>perovskite manganite', Journal of Alloys and Compounds, 509 (**2011**) 3457-3467.

**Sarveenaa G**, Kumar A, Kotnala R.K, Khalid M, Batoo M, &Singha M, 'Investigation of structural, magnetic and Mössbauer properties of

Co<sup>2+</sup>and Cu<sup>2+</sup> substituted Ni–Zn nanoferrites', Ceramics International, 42 (**2016**) 4993-5000.

**Sharma R**, Thakur P, Sharma P, & Sharma V, 'Ferrimagnetic Ni<sub>2b</sub> doped Mg-Zn spinel ferrite nanoparticles for high density information storage', Journal of Alloys and Compounds, 704 (**2017**) 7-17.

**Sharma R**, Thakur P, Sharma P, & Sharma V, 'Ferrimagnetic Ni<sub>2b</sub> doped Mg-Zn spinel ferrite nanoparticles for high density information storage', Journal of Alloys and Compounds, 704 (**2017**) 7-17.

**Shinde T.J**, Gadkari A.B & Vasambekar P.N, 'Influence ofNd<sup>3+</sup> substitution on structural, electrical and magnetic properties of nanocrystalline nickel ferrites', Journal of Alloys and Compounds, 513 (2012) 80-85.

**Singh A**, Singh A, Singh S, Tandon P, Yadav B.C, & Yadav R.R, 'Synthesis, characterization and performance of zinc ferritenanorods for room temperature sensing applications', Journal of Alloys and Compounds, 618 (2015) 475-483.

**Singh C**, Goyal A, Malik R, Bansal S & Singhal S, 'Envisioning the attachment of CdS nanoparticles on the surface of MFe<sub>2</sub>O<sub>4</sub> (M=Zn, Co and Ni) nanocubes: Analysis of structural, optical, magnetic and photocatalytic properties', Journal of Alloys and Compounds, 695 (**2017**) 351-363.

**Srivastava M**, Ojha A.K, Ojha S & Materny A, 'Synthesis and optical characterization of nanocrystalline NiFe<sub>2</sub>O<sub>4</sub> structures', Journal of Alloys and Compounds, 481 (**2009**) 515-519.

**Tehrani F.S**, Daadmehr V, Rezakhani A.T, Hosseini R, Akbarnejad S & Gholipour S, 'Structural, Magnetic, and Optical Properties of Zinc- and Copper-Substituted Nickel Ferrite Nanocrystals', Journal of Superconductivity and Novel Magnetism, 25 (2012) 2443-2455.

**Thakur A**, Kumar P, Thakur P, Rana K, Chevalier A, Mattei J.L & Queffélec P, 'Enhancement of magnetic properties ofNi<sub>0.5</sub>Zn<sub>0.5</sub>Fe<sub>2</sub>O<sub>4</sub> nanoparticles prepared by the co-precipitation method', Ceramics International, 42 (**2016**) 10664-10670.

**Tholkappiyan R**& Vishista K, 'Influence of lanthanum on the optomagnetic properties of zinc ferrite prepared by combustion method', Physica B, 448 (**2014**) 177-183.

Yu A, Sy A & Davies A, 'Graphene nanoplatelets supportedMnO<sub>2</sub> nanoparticles for electrochemical supercapacitor, Synthetic Metals, 161 (2011) 2049-2054.

**Zhou Y**, Chen W, Shen Y, Xuehang W.U, Wenwei W.U & Juan W.U, 'Lattice strains and magnetic properties evolution of copper-magnesium ferrite with lithium substitution', Journal of Magnetism and Magnetic Materials, 396 (**2015**) 198-203.

# **CHAPTER - IV**

# IMPACT OF LANTHANUM IONS ON MAGNETIC AND DIELECTRIC PROPERTIES OF COBALT NANOFERRITES

#### 4.1 INTRODUCTION

Recently, spinel nanoferrites have been used in numerous technological and scientific applications [Raghvendra Singh Yadava et.al., 2018] ie., low loss magnetic core materials, hyperthermia, memory devices, drug delivery, antenna rods, gas sensors, microwave-absorbing materials, super capacitors, solar cell and high frequency devices etc [Kovalenko et.al., 2016, Anantha ramaiah et.al., 2017, Lasheraset.al., 2016]. Basic formula of spinel nanoferrites is AB<sub>2</sub>O<sub>4</sub>, where A and B represents a divalent and trivalent metal cation [Lawrence Kumar et.al., 2012]. The spinel ferrites are classified into three types such as normal spinel structure, inverse spinel structure and intermediate spinel structure. In normal spinel ferrites, divalent ions are at tetrahedral A- site and trivalent ions are in octahedral B- site; at inverse spinel structure, where half of the trivalent ions are at B- site and half at A- site and the remaining ions are distributed in octahedral B- site whereas intermediate spinel structure possesses the intermediate stage between the normal and inverse spinel ferrites [Kunal Pubby et.al., 2018]. From the different spinel ferrite materials, CoFe<sub>2</sub>O<sub>4</sub> is the best challenging ferromagnetic material due to its better properties, as high Curie temperature, high coercivity, reasonable saturation magnetization, high mechanical and chemical stability [Lu et.al., 2015, Widatallah et.al., 2008]. Recent years, rare earth elements substituted spinel nanoferrites have special attention in developing their physical properties such as grain size and cation distribution at tetrahedral and octahedral sites [Gore et.al., 2017, Kamala Bharathi et.al., 2011]. The spinel nanoferrites are the best advisable materials used for absorption of electromagnetic radiation (EMR) in different ways such as ceramic tiles, sheets and powders [Leninet.al., 2018]. Electromagnetic interference (EMI) has got most promising applications in communication systems such as radar systems, computers, and mobile phones [Azadmanjiri et.al., 2007, Wang et.al., 2012]. The EMI affects electronically controlled systems and also damages human health. It causes device interrupt, generate distorted images, increase clutter on radar due to system-to-system interruption during EMI [Chaudhari et.al., 2013]. To circumvent these EMI troubles, EMR is preferred, which has the ability of absorbing unwanted electromagnetic signals. Rare earth doped nanoferrites have unique and important applications in electronic devices, transformer cores, magnetic recordings, radar signals, high frequency circuits and telecommunication. The doping of Lanthanum (La<sup>3+</sup>) ions which are having unpaired electrons in the 4f orbital tends normally to nonmagnetic state. However, replacing smaller ionic radii Fe<sup>3+</sup> ions into La<sup>3+</sup> ions at the octahedral site (B) to the ferrites leads to enhance the magnetic and electrical properties of the spinel nanoferrites used for microwave frequency applications [Roy et.al., 2007, Kadam et.al., 2012, Rajesh Kannaet.al., 2017]. The magnetic saturation (ms) decreases with an increase in the concentration of rare earth content in Li, Co, and Ni spinel nanaoferrites [Sakthipandi et.al., 2011]. From the literature, stability for transformer core where EMI is gently reduced and can avoid predicting false image in telecommunication system [Azadmanjiri et.al., 2007]. Lanthanum doped Cobalt ferrites are synthesized by various techniques such as the sonication technique [Rajesh Kannaet.al., 2017, Mechanical milling technique [Widatallah et.al., 2008],

Co-precipitate method [de Vicente *et.al.*, 2000], Sonochemical method [Raghvendra Singh Yadava *et.al.*, 2018], Hydrothermal method [Anwar *et.al.*, 2013] and Sol-gel technique [Zhikai Yan *et.al.*, 2015]. The spinel nanoferrites were synthesized by solgel technique which overcomes the difficulties in Co-precipitate technique [de Vicente*et.al.*, 2000].

In this study, Lanthanum doped Cobalt nanoferrites  $CoLa_XFe_{2-X}O_4$  (X = 0.00 to 0.08) were synthesized by using sol-gel method. The obtained Lanthanum doped cobalt nanoferrites were characterized by X-ray diffraction (XRD) for phase and structural identification, Ultra Violet diffuse reflectance spectroscopy (UV-DRS) to identify the optical properties and Fourier transform infrared spectroscopy (FTIR) for checking the metal oxides presence. The field emission scanning electron microscopy (FESEM) and energy dispersive X-ray analysis (EDAX) were used to understand the surface morphology and elemental analysis. Magnetic and Electrical properties were evolved using vibrating sample magnetometer (VSM) and Impedance spectroscopy. The obtained results were analyzed and utilized for the application of electronic devices in Micro-wave frequency.

#### 4.2 MATERIALS AND EXPERIMENTAL PROCEDURE

#### 4.2.1 Materials

High pure grade Merck precursors such as Cobalt nitrate (Co (NO<sub>3</sub>)<sub>2</sub>.6H<sub>2</sub>O), Lanthanum nitrate (La(NO<sub>3</sub>)<sub>3</sub>.6H<sub>2</sub>O), Ferric nitrate (Fe(NO<sub>3</sub>)<sub>3</sub>.9H<sub>2</sub>O), Ammonia (NH<sub>4</sub>OH), Citric acid (C<sub>6</sub>H<sub>8</sub>O<sub>7</sub>.H<sub>2</sub>O) and deionized water were used.

Impact of lanthanum ions on magnetic and dielectric Properties of cobalt nanoferrites

# **4.2.2 Experimental Procedure**

The CoLa<sub>X</sub>Fe<sub>2-X</sub>O<sub>4</sub> (x= 0.00, 0.02, 0.04, 0.06, 0.08) nanoferrites were synthesized by sol-gel technique in the following approach. The measured precursors were dissolved with 100 ml of de-ionized water to obtain a uniform mixture of the precursor materials. The final mixture was continuously stirred at a temperature of 80 °C for 1 hr. Further, ammonia was added drop wise to the ferrite solution to attain the pH value of 7. Finally, the dark solution was obtained and dried in hot air oven at fixed temperature of 60 °C for 24 hrs. The dried nanoparticles were collected and sintered in muffle furnace at 500°C for 2 hrs. At next, sintered nanopowders were grinded for 15 mins to obtain byproducts free nanoparticles. Thus, obtained nanopowders were calcined at 1000°C for 24 hrs. The schematic diagram of CoLa<sub>X</sub>Fe<sub>2-X</sub>O<sub>4</sub> nanoferrites were shown in Figure 4.1.

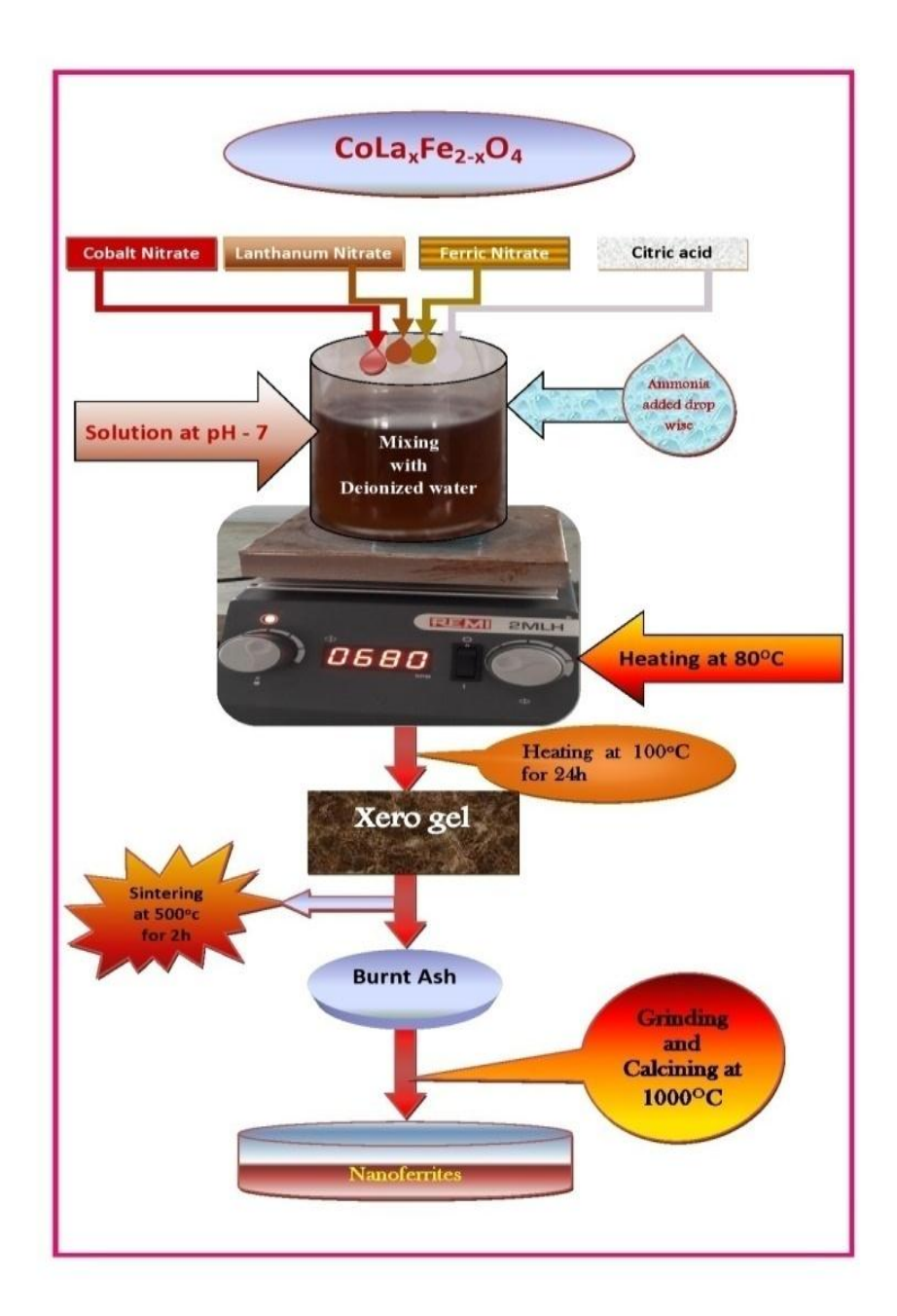


Figure 4.1 Schematic diagram for preparation of CoLa<sub>X</sub>Fe<sub>2-X</sub>O<sub>4</sub> nanoferrites.

# 4.2.3 Characterization of the CoLa<sub>x</sub>Fe<sub>2-x</sub>O<sub>4</sub> Nanoferrites

The crystallite size and structural properties of the prepared  $CoLa_XFe_{2-X}O_4$  (X = 0.00 to 0.08) nanoferrites were made by XRD (SHIMADZU-XRD 6000) technique with  $CuK\alpha$  radiation source, at the 20 range from 20° to 80°, operated at 40 kV and 30 mA. The chemical interaction and functional groups obtained in the

prepared CoLa<sub>x</sub>Fe<sub>2-x</sub>O<sub>4</sub> nanoferrites were determined by FTIR spectra (SHIMADZU-UV 18000) ranging from 4000 to 400 cm<sup>-1</sup> at RT (room temperature). The surface morphology and elemental composition were analyzed using FESEM with an EDAX (Quanta FEG 250). The optical properties of the synthesized samples were analyzed using an UV- DRS spectrum and the absorption wavelength was noted from 200 to 800 nm. The electrical property of the synthesized CoLa<sub>x</sub>Fe<sub>2-x</sub>O<sub>4</sub> nanoferrites was revealed using Impedance spectroscopy with the frequency range of 100mHz to 10MHz at Room temperature (30°C) (Biologic SP-300), Silver coating was applied to the pellet for good Ohmic contact. X-ray photoelectron spectroscopic (XPS) studies were made using an (ALU-PHI5000) AUG spectrometer with monochromatic Al Ka (26.00 eV) radiation. Magnetic studies were assessed using VSM (Lakeshore VSM 7140) at room temperature (RT) with an applied magnetic field of -15 to +15KOe.

## 4.3 RESULTS AND DISCUSSION

# 4.3.1 Structural Analysis

XRD patterns of  $CoLa_xFe_{2-x}O_4$  for all the samples with series of X=0.00 to 0.08, calcined at 1000 °C are shown in Figure 4.2. The obtained peaks are related to cubic spinel ferrites crystal structure and are matched with the standard JCPDS file No 22-1086. The peak 30.08°, 35.43°, 43.05°, 53.44° and 56.97° at corresponds to the crystal planes (220), (311), (400), (422) and (511) respectively [Sonia Gaba *et.al.*, 2004, Bensebaa *et.al.*, 2017].

The average crystallite size of the synthesized nanoferrites was estimated using Debye's Scherrer equation [Vigneshwaran *et.al.*, 2018].

$$D = \frac{k \lambda}{\beta Cos\theta} \tag{4.1}$$

where k is a Scherrer constant (0.9),  $\lambda$  is the wavelength of X-ray beam,  $\beta$  is the full width half maximum (FWHM) and  $\theta$  is the Braggs diffraction angle. The crystallite size of the ferrites decreases from 42 to 18 nm with increasing dopants concentration from X=0.00 to 0.08. The La<sup>3+</sup> ion having ionic radius of 1.06 Å has larger ionic radii compared with Fe<sup>3+</sup> ionic radius 0.67 Å. Therefore, it's difficult to displace Fe<sup>3+</sup> ion in CoFe<sub>2</sub>O<sub>4</sub> spinel cubic nanoferrites. So, few La<sup>3+</sup> ions could be present at grain boundaries. This larger ionic radius of La<sup>3+</sup> ions form pressure on the grains and therefore crystallite size deceases with increasing La content [Sattar *et.al.*, 2002]. The emergence of small amount of orthoferrite phase LaFeO<sub>3</sub> also appear with La<sup>3+</sup> content of (X = 0.02, 0.04, 0.08). The ionic radius of La<sup>3+</sup> ion is 1.06 Å, which is higher than that of the Fe<sup>3+</sup> ion (0.67 Å), and hence the amount of Fe<sup>3+</sup> ions replaced by La<sup>3+</sup> ions are limited and hence there is a solubility limit for the replacement of Fe<sup>3+</sup> ions by La<sup>3+</sup> ions. Thus, it is expected that an excess substitution of La<sup>3+</sup> ions tend to aggregate around the grain boundaries in the form of LaFeO<sub>3</sub>.

The lattice constant for the prepared nanoferrites is calculated using Nelson-raley function [Irshad Ali *et.al.*, 2013];

$$a = d_{hkl}\sqrt{(h^2 + k^2 + l^2)}$$
(4.2)

where d is inter planar distance, a is the lattice constant and (hkl) are Miller indices. The value of lattice constant is 8.37 Å which is in agreement with the reported value [Raghvendra Singh Yadav *et.al.*, 2015]. Lattice constant increases monotonically with increasing La<sup>3+</sup> ions which is due to the substitution of both Co<sup>2+</sup> ions with ionic radius of 0.78 Å and Fe<sup>3+</sup> ions with ionic radius of 0.67 Å by the larger La<sup>3+</sup> ions with ionic radius of 1.06 Å in Co-Fe-La spinel lattice [Peng *et.al.*, 2011]. The volume of unit cell increases from 587.3 to 600.9 Å with the increasing La<sup>3+</sup> concentration which occurs due to increase in the lattice constant.

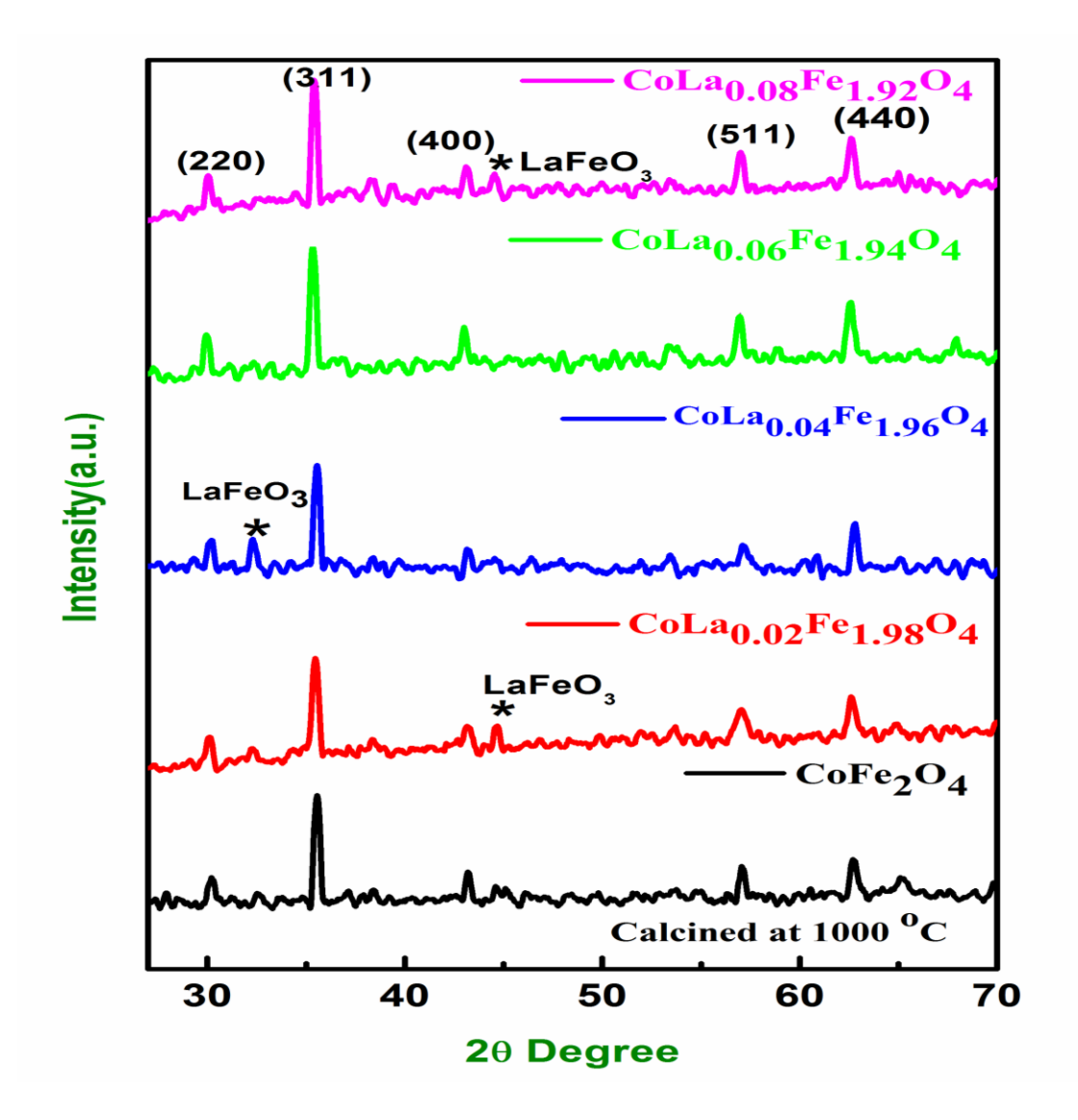


Figure 4.2 X-ray diffraction pattern of  $CoLa_XFe_{2-X}O_4$  (X = 0.00 to 0.08) nanoferrites.

X-ray density of the CoFe<sub>2</sub>O<sub>4</sub> nanoparticles was calculated following equation [Peng *et.al.*, 2011];

$$d_x = \frac{Zm}{Na^3} \tag{4.3}$$

where  $N_a$  is Avogadro's number, m is the molecular weight of the sample,  $a^3$  is the volume of the unit cell and Z is the basic unit cell for the cubic spinel structure which contains 8 ions.

X-ray density decreases from 5.685 to 5.403 g/cm<sup>3</sup> with increase of La<sup>3+</sup> ion concentration in cobalt ferrite nanoparticles, which may possibly due to the increase in unit cell volume. The volume of the unit cell is inversely propositional to the X-ray density. The bulk density (d<sub>B</sub>) was calculated using mentioned equation [Irshad Ali *et.al.*, 2013];

$$d_m = \frac{m}{\pi r^2 t} \tag{4.4}$$

where r is the radius of the pellet, m is the mass of the pellet, and t is the thickness of the pellet. The bulk density of Lanthanum doped cobalt nanoferrites was noticed to decrease from 2.6085 to 2.0173 g/cm<sup>3</sup> with increase of Lanthanum ions. As compared to X-ray density, bulk density was less due to the presence of pores which mainly depend on calcinated conditions [Ihsan Ali *et.al.*, 2013].

The surface area (S) was estimated using following expression [Ranjith Kumar *et.al.*, 2015].

$$S = 6/d_X D \tag{4.5}$$

where  $d_X$  is the X-ray density and D is the crystallite size of the nanoparticles. The surface areas (S) are increases with increase of  $La^{3+}$  ions which attribute to decrease in crystallite size.

The porosity (P) was calculated using following relation [Ranjith Kumar *et.al.*, 2015];

$$P = (1-d_B/d_X) \%$$
 (4.6)

Impact of lanthanum ions on magnetic and dielectric Properties of cobalt nanoferrites

The percentage of porosity increases from 5.0 to 6.4 % which may be due to decrease in bulk density with increase of La<sup>3+</sup> concentrations. Structural parameters such as X-ray density, crystallite size, dislocation density, microstrain, lattice constant, volume of unit cell, surface area, bulk density and porosity were determined and listed in Table 4.1.

Table 4.1 Structural parameters of  $CoLa_XFe_{2-X}O_4$  (X = 0.00 to 0.08) nanoferrites

Compositio	Crystallite size (D) (nm)	Dislocation density (δ) l/m <sup>2</sup> E+15	Micro strain (ε) X10 <sup>-3</sup>	Lattice constant (a) Å	Volume of unit cell (a³) Å	X-ray density (ρxrd) (g/cm³)	Surface area (S <sub>XRD</sub> ) (m <sup>2</sup> /g)	Bulk density (d <sub>B</sub> ) (g/cm <sup>3</sup> )	Porosity (%)
X =0.00	42	0.55	0.849	8.37	587.30	5.68	25.12	2.68	5.0
X = 0.02	37	0.72	0.977	8.37	589.30	5.64	28.72	2.61	5.2
X = 0.04	34	0.85	1.058	8.40	593.95	5.54	31.83	2.57	5.3
X = 0.06	25	1.56	1.429	8.42	596.96	5.47	43.81	2.45	5.6
X = 0.08	18	2.85	1.933	8.43	600.99	5.40	61.68	2.01	6.4

#### 4.3.2 Optical Analysis

The influence of Lanthanum on Cobalt nanoferrites were studied by using UV-DRS spectra are shown in Figure 4.3. The UV-DRS spectra has overcome UV-Visible absorption spectroscopy in its capability to evaluate the optical properties of powdered nanoparticles. UV-Visible absorption has larger scattering effect when compare to UV-DRS spectra [Rajesh Kanna*et.al.*, 2017]. The absorbance values are 226.6, 224.7, 223.3, 222.5 and 222.0 nm as shown in Figure 4.3. The E<sub>g</sub> of the prepared nanoferrites was obtained energy dependant relation as follows [Rajesh Kanna*et.al.*, 2017];

$$E_g = \frac{hc}{\lambda} \tag{4.7}$$

where c is the velocity of light, h is the Planck's constant and  $\lambda$  is the wavelength of the absorption.

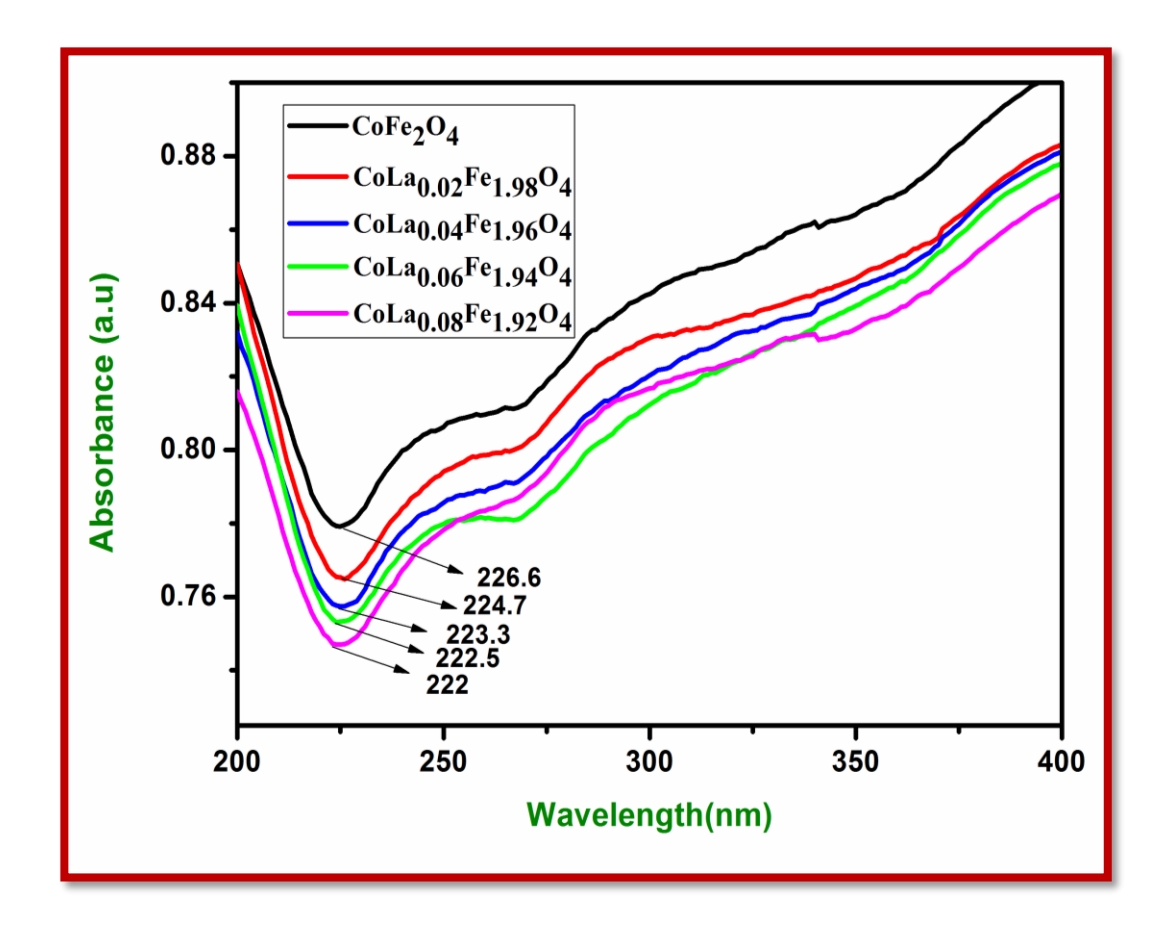


Figure 4.3 Absorbance spectra of  $CoLa_XFe_{2-X}O_4$  (X = 0.00 to 0.08) nanoferrites.

The indirect and direct band gap energy values of Lanthanum doped cobalt nanoferrites were calculated using the following relation [Rajesh Kanna *et.al.*, 2017];

$$h\gamma\alpha = (h\gamma - E_{gap})^n \tag{4.8}$$

where  $\gamma$  is the frequency, h is the plank's constant,  $\alpha$  is the absorbance coefficient and n are the different types of electronic transition (n=1/2 and 2) for bandgap (indirect and direct) transition respectively.

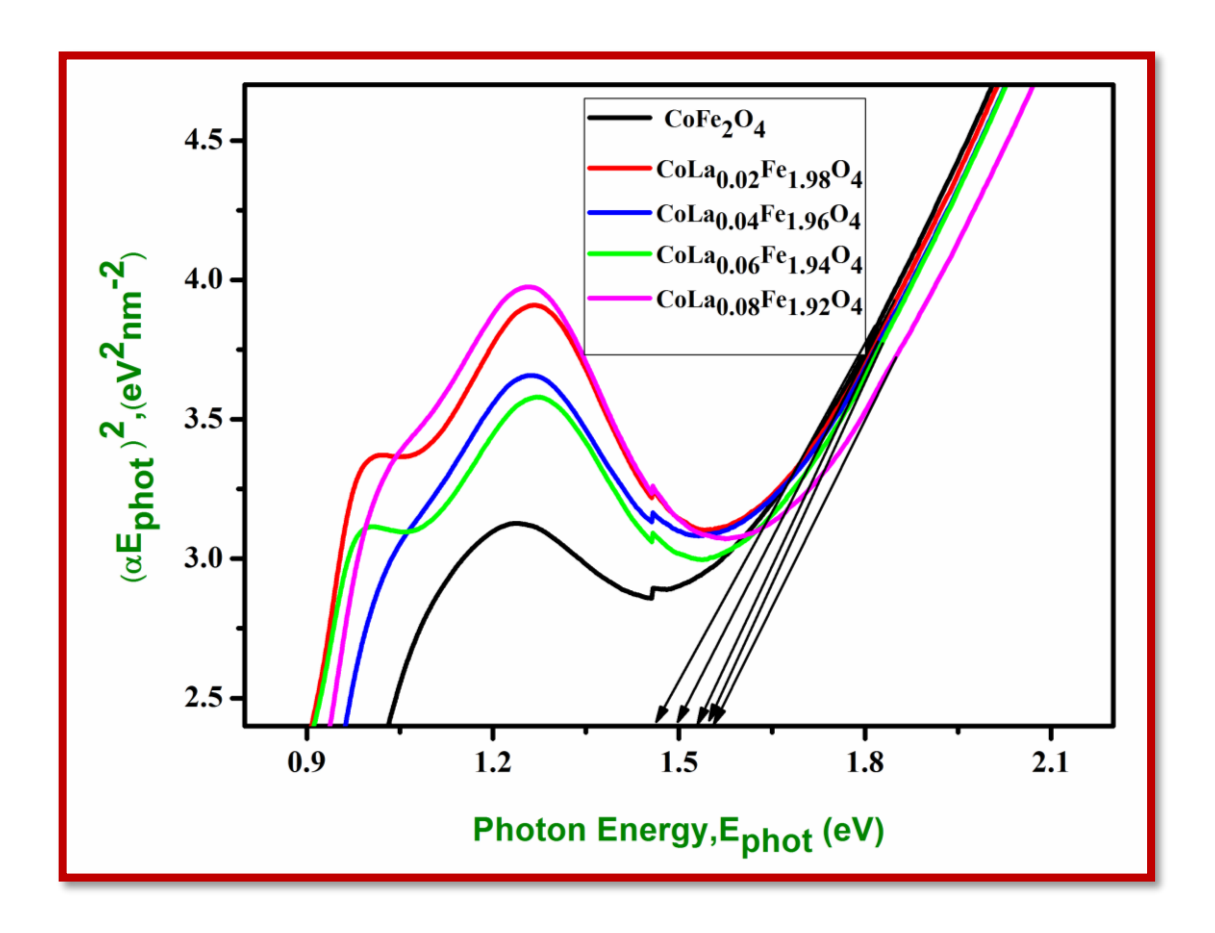


Figure 4.4 Direct bandgap energy of  $CoLa_XFe_{2-X}O_4\,(X=0.00\ to\ 0.08)$  nanoferrites

In Figure 4.4, direct bandgap energy demonstrates the Taue plot between  $(\alpha E_{photon})^2$  vs  $E_{phot}$  and the E values were 1.45, 1.50, 1.53, 1.55 and 1.56 eV. In Figure 4.5, indirect bandgap energy demonstrates the Taue plot between  $(\alpha)^{1/2}$  vs  $E_{phot}$  and the bandgap energy values of prepared nanoferrites were 1.73, 1.86, 1.93, 1.97 and 2.06 eV respectively.

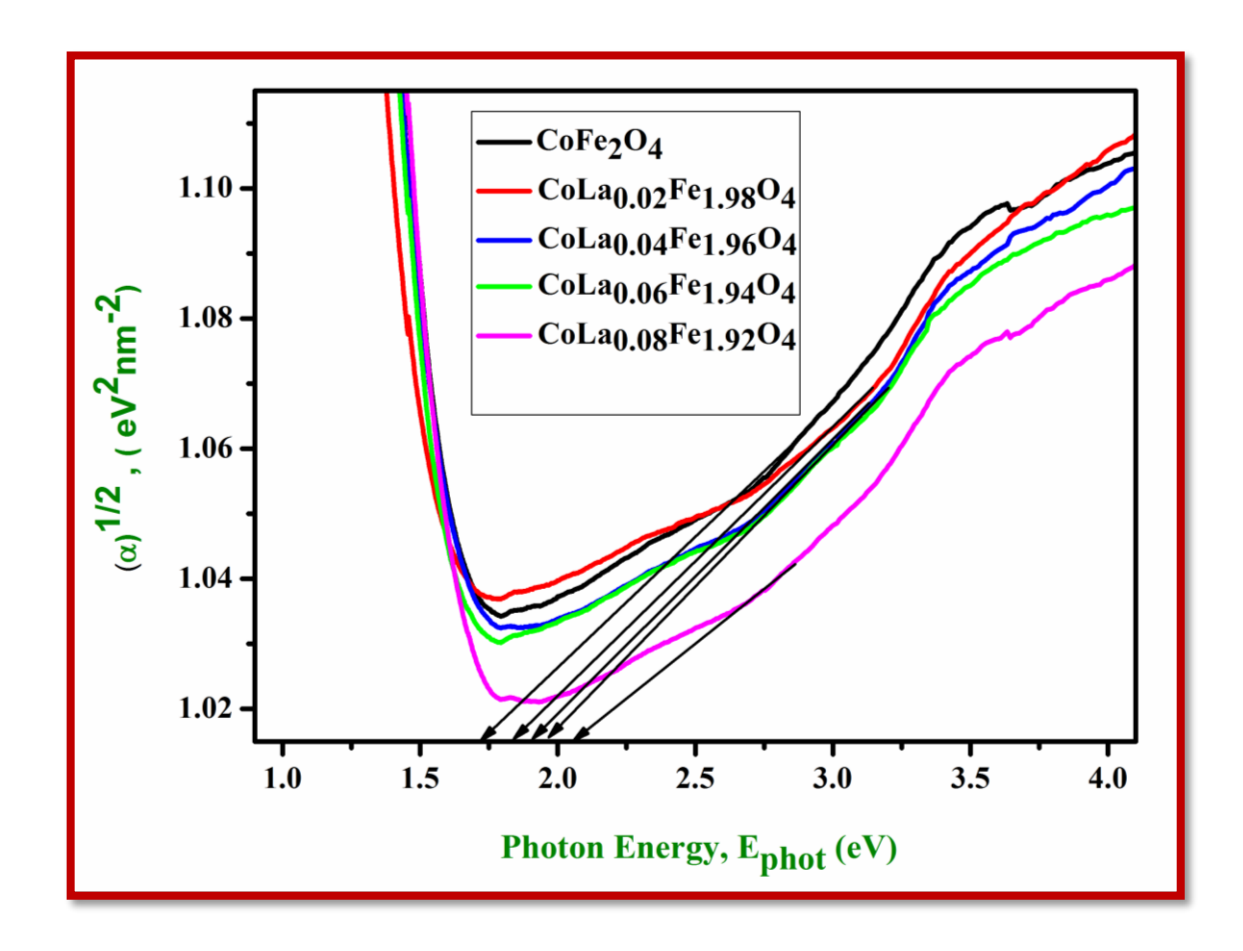


Figure 4.5 Indirect bandgap energy of  $CoLa_XFe_{2-X}O_4\,(X=0.00\ to\ 0.08)$  nanoferrites.

The absorbance and bandgap energy values of the Lanthanum doped cobalt nanoferrites are listed in Table 4.2. The bandgap energy shifts from red region to blue region for doped La<sup>3+</sup> ions. These shifts are attributed to 3d-4s spin interchange between Fe ions and La ions. However, the Lanthanum doped Cobalt nanoferrites bandgap energies vary based on the Brus equation [Saravanan *et.al.*, 2014].

Table 4.2 Optical parameters of  $CoLa_XFe_{2-X}O_4$  (X = 0.00 to 0.08) nanoferrites

Composition	Absorbance (nm)	Indirect bandgap energy (eV)	Direct bandgap energy (eV)
X=0.00	226.6	1.73	1.45
X=0.02	224.7	1.86	1.50
X=0.04	223.3	1.93	1.53
X=0.06	222.5	1.97	1.55
X=0.08	222.0	2.06	1.56

### 4.3.3 Functional Group Analysis

The FT-IR spectra of prepared nanoferrites were depicted in Figure 4.6. The transmittance spectra were obtained from the vibrational peaks appropriate to citric acid used in sol-gel technique which was acquired by stretching vibrations appropriate to metal- oxygen band of around 583 cm<sup>-1</sup> to form spinel cubic structure. The broad and strong stretching peak obtained which indicates the O-H stretching due to the available water vapour in the prepared sample at 3437 cm<sup>-1</sup> [Hankare *et.al.*, 2011]. The bending vibration of CH<sub>2</sub> carbon chain was observed with peak 2921 cm<sup>-1</sup>. The peaks are at 1745 cm<sup>-1</sup> corresponding to the C-H bending absorption of carboxyl group. Then 1149 cm<sup>-1</sup> is the C=O stretching vibration due to nitrogen group [Ghulam Mustafa *et.al.*, 2015]. In these cubic structure ferrites Fe<sup>3+</sup> ions placed tetrahedral Asites as well as Octahedral B- sites.

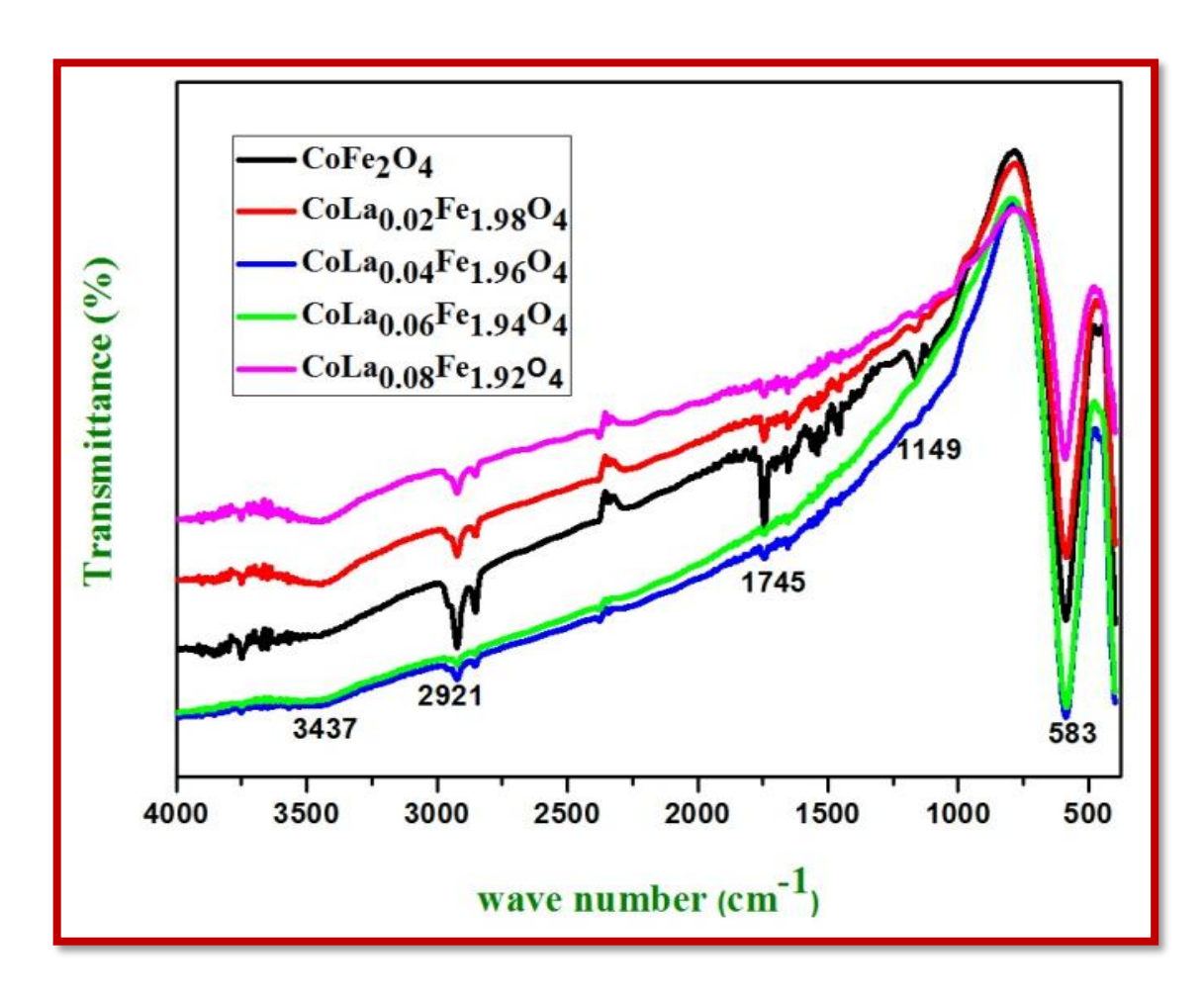


Figure 4.6 FT-IR spectra of  $CoLa_XFe_{2-X}O_4$  (X = 0.00 to 0.08) nanoferrites.

Table 4.3 Functional parameters of  $CoLa_XFe_{2-X}O_4$  (X = 0.00 to 0.08) nanoferrites

S.No	Vibrational assignments	Experimental absorption (cm <sup>-1</sup> )					
	vibrational assignments	X=0.00	X=0.02	X=0.04	X=0.06	X=0.08	
1	Metal - oxygen stretching vibration	583	583	583	583	583	
2	C=O stretching vibration	1149	1149	1149	1149	1149	
3	C - H bending vibration of carboxyl group	1745	1745	1745	1745	1745	
4	CH <sub>2</sub> bending vibration of carbon chain	2921	2921	2921	2921	2921	
5	O - H stretching vibration	3437	3437	3437	3437	3437	

## 4.3.4 Surface Morphology with EDAX

The FESEM images of Lanthanum doped cobalt nanoferrites were used to study surface morphology. Figure 4.7 denote that the prepared nanoferrites were spherical in shape with some agglomeration. This agglomeration of grain structure was mainly due to small crystallite size, calcinating process and magnetic nature of all the crystallites form together and promotes cluster and also gets agglomerated [Hankare *et.al.*, 2013, Peng *et.al.*, 2011]. Magnetic force or weak Vander Waals bonds play a major role in holding these agglomerations in contact [Aghav *et.al.*, 2011]. In the obtained result, grain size was decreased with increase of La<sup>3+</sup> ions.

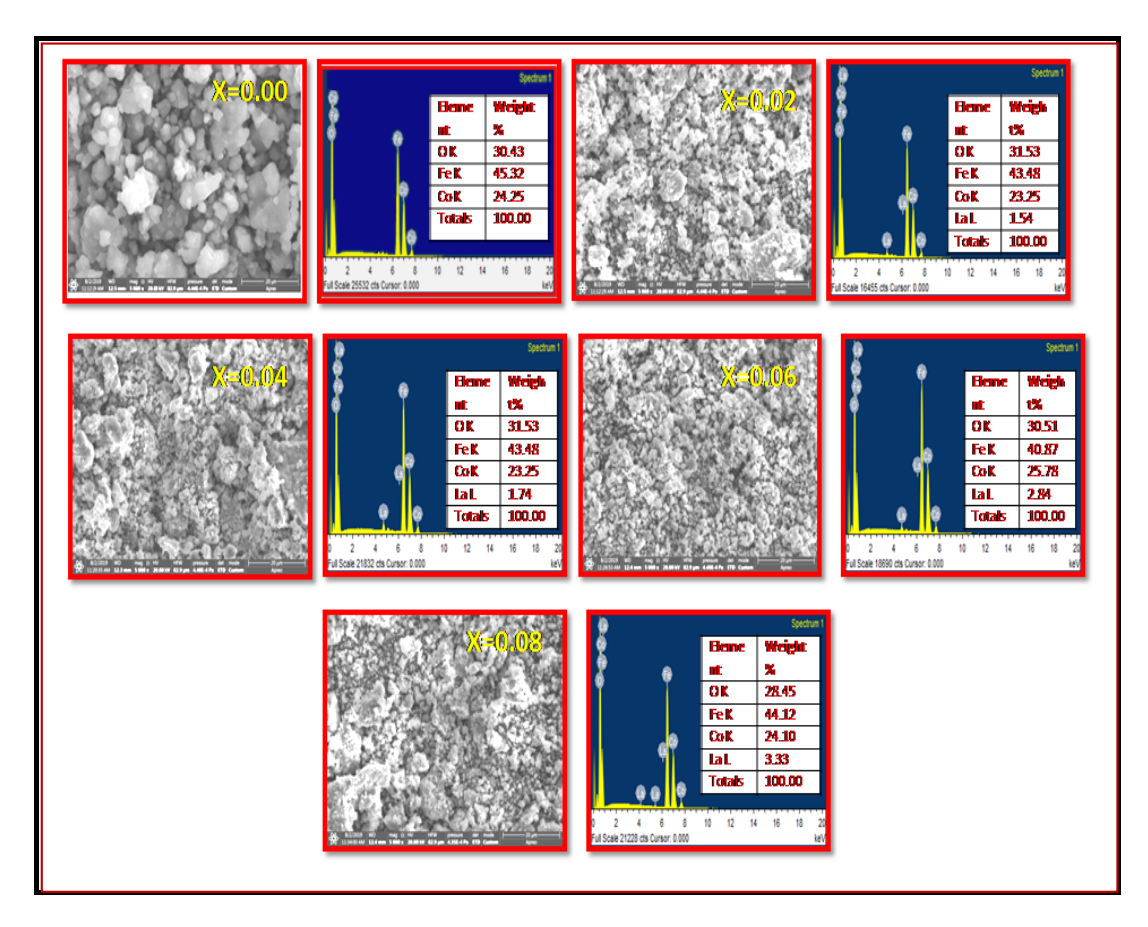


Figure 4.7 FESEM with EDAX images of the  $CoLa_XFe_{2-X}O_4$  (X = 0.00 to 0.08) nanoferrites

EDAX spectra of Lanthanum doped cobalt nanoferrites corresponds to the elements Fe, O, Co, and La, which is presented in Figure 4.7 (X=0.02 to 0.08) where absent of La peaks are observed for (X=0.00).

### 4.3.5 XPS Analysis

The X-ray photoelectron spectrocopy (XPS) analysis was used to investigate oxidation state and elemental composition of prepared nanoferrites. Figure 4.8(e) brings a wide scan spectrum of pure and Lanthanum doped Cobalt nanoferrites in the range of 0-980 eV. In the long range spectrum as shown in Figure 4.8(e), it can be clearly shown that the elemental and oxidation states of Co 2p, Fe 2p, La 3d, o 1s and c 1s are present. No other elements were found, which proves the purity of prepared nanoferrites. The narrow scan spectrum of O 1s shown in Figure 4.8(b), clearly indicate a peak at 529.06, 535.76 and 535.96 eV for pure and Lanthanum dopd Cobalt nanoferrites. These obtained peaks were due to the presence of O<sup>2-</sup> in the nanoferrites [Abdellatif et.al., 2017, Anandan et.al., 2017]. Th narrow scan spectrum of Co 2p as noticed from Figure 4.8(c), and corresponding two peaks at 778.93 and 786  $\pm$  0.4 eV. Similarly 785.11 eV and 790  $\pm$  15 were present for Co  $2p^{3/2}$  and Co  $2p^{1/2}$ , which confirms the oxidation state of Co<sup>2+</sup>. The narrow range spectrum of Fe 2p in nanoferrites revealed Fe  $2p^{3/2}$  and Fe  $2p^{1/2}$  binding energy peaks at 709.75 and 718  $\pm$ 0.8 eV for Fe  $2p^{3/2}$ , 723.54 and 725  $\pm$  14eV for Fe  $2p^{1/2}$  Figure 4.8(a), respectively. The peak at 718  $\pm$  0.8 eV is attained due to the Fe<sup>3+</sup> cation located at the octahedral site in the spinal ferrites, and the peak at  $725 \pm 14$ eV is attained due to the Fe<sup>2+</sup> cation located at the tetrahedral site in the spinal ferrites [Venkatesha et.al., 2015, Karakas et.al., 2015]. From the Figure 4.8(d), the narrow scan spectrum was obtained for La<sup>3+</sup> with binding energies of 833.18  $\pm$  0.69 eV for 3d<sup>5/2</sup> and 837.20  $\pm$ 0.12 eV for 3d<sup>3/2</sup>.

The obtained peaks were explained to the electron transfer of oxygen to the 4 f subshell of La<sup>3+</sup> ions due to photo-ionisation process [Anandan *et.al.*, 2017]. From XRD and XPS results, it was clearly noticed that the La<sup>3+</sup> ions were assimilated into Fe ions in cobalt nanoferrites. The observed binding energy of Oxygen, Cobalt, iron and Lanthanum were listed in Table 4.4.

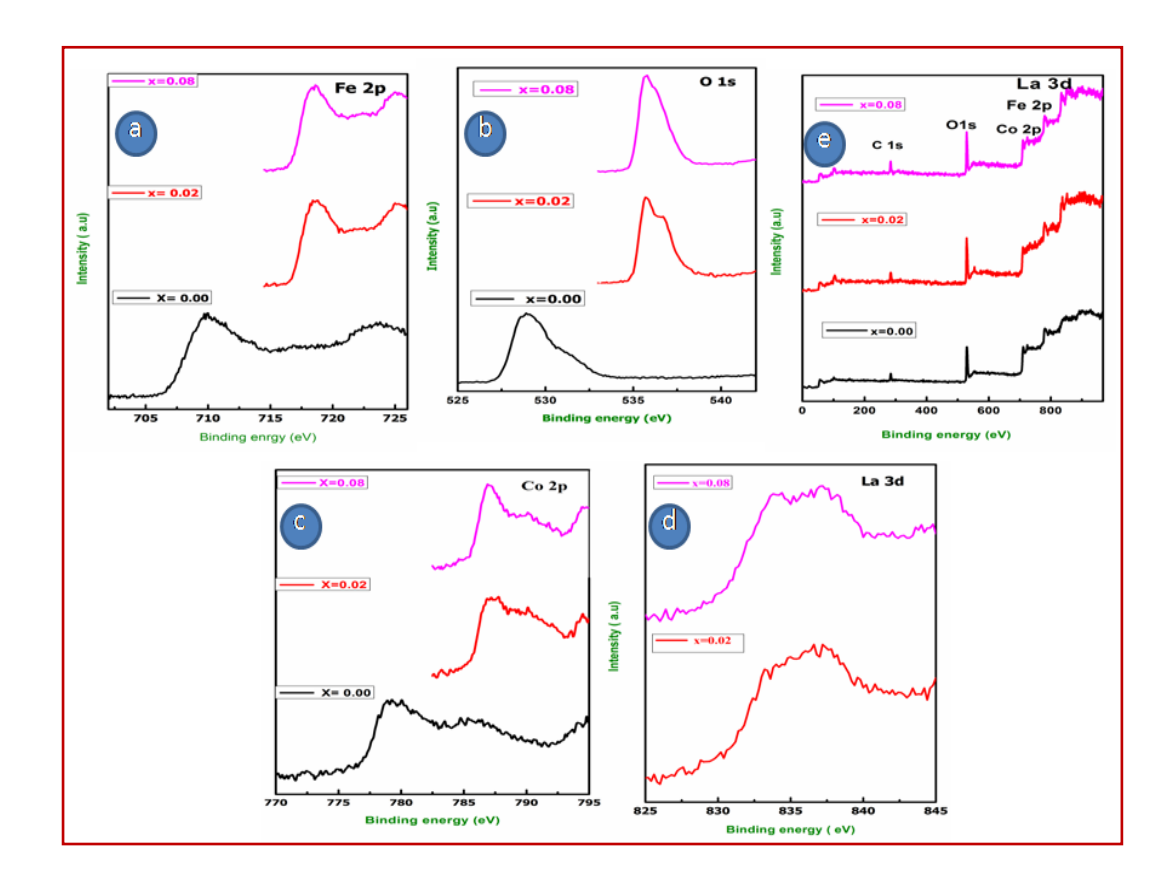


Figure 4. 8 (a-e). XPS spectra of the  $CoLa_XFe_{2-X}O_4\,(X=0.00\ to\ 0.08)$  nanoferrites.

Table 4.4 Binding energy of  $CoLa_XFe_{2-X}O_4$  (X = 0.00 to 0.08) nanoferrites.

Composition	O1s	Co 2p (eV)		Fe 2p (eV)		La 3d (eV)	
Composition	(eV)	2p <sup>3/2</sup>	2p 1/2	2p <sup>3/2</sup>	2p 1/2	3d <sup>5/2</sup>	3d <sup>3/2</sup>
X=0.00	529.06	778.93	785.11	709.75	723.58	-	-
X=0.02	535.76	786.98	790.28	718.49	725.16	833.18	837.20
X=0.08	535.96	787.12	790.43	718.57	725.30	833.87	837.32

# 4.3.6 Magnetic Analysis

The M-H loop for prepared CoLa<sub>X</sub>Fe<sub>2-X</sub>O<sub>4</sub> nanoferrites have been plotted with magnetic field maximum of 15,000 Oe at room temperature by VSM. From the Figure 4.9 S shaped hysteresis loops shows the soft magnetic nature of the prepared nanoferrites. The variation in magnetic parameters such as coercivity ( $H_C$ ), magnetic saturation ( $M_s$ ), retentivity ( $M_r$ ) and magnetic moment ( $\eta_B$ ) for prepared nanoferrites have been revealed to be dependent of number of factors such as grain growth, anisotropy, density, A-B exchange interaction, surface spin effect, synthesis techniques and chemical composition [Raghvendra Singh Yadav *et.al.*, 2017].

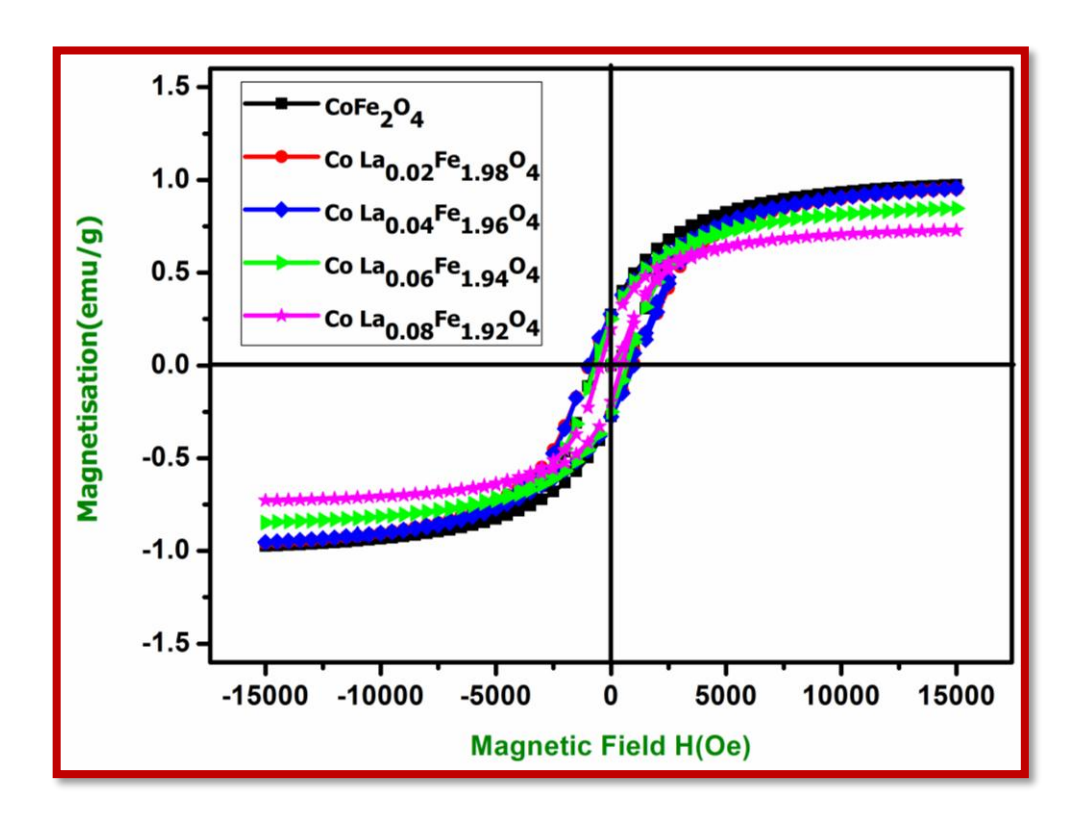


Figure 4.9 Hysteresis loop of the  $CoLa_XFe_{2-X}O_4$  (X = 0.00 to 0.08) nanoferrites.

From magnetic hysteresis loops, it is understood that the inclusion of La<sup>3+</sup>ions promote ferromagnetic nature. From Table 4.5, it is noticed the values of saturation magnetization decreases with increase of La<sup>3+</sup> ions in CoFe<sub>2</sub>O<sub>4</sub> nanoparticles which is could be explained by Neel's sub lattice model [Aziz *et.al.*, 2016]. From the Neel's sub lattice model, the magnetic moment of ions on the A site and B site sub lattices were aligned anti parallel to each other and their spins has a collinear structure.

The magnetic moment was calculated by using following equation;

$$\Pi_{B} = M_{B} - M_{A}$$
(4.9)

where  $M_A$  and  $M_B$  are [A] and [B] sub lattices [Dasan*et.al.*, 2017]. In general, magnetic super exchange interaction is based on the cation distribution between A site and B sites. This could be attained due to their larger ionic radii. Therefore, suggesting that the non-magnetic La<sup>3+</sup> could be replacing Fe<sup>3+</sup> ions from Octahedral

Impact of lanthanum ions on magnetic and dielectric Properties of cobalt nanoferrites

site (B) to tetrahedral site (A) [Santosh Bhukal*et.al.*, 2012]. Moreover, three types of exchange interaction would have happened between the magnetic ion at octahedral (B) and tetrahedral (A) site in spinel structure such as AA interaction, BB interaction, AB interaction.

Out of three, mentioned interactions AB interaction predominates over rest of other two interactions [Raghvendra Singh Yadav *et.al.*, 2017]. Further, the increase of La<sup>3+</sup> ions in CoLa<sub>x</sub>Fe<sub>2-x</sub>O<sub>4</sub> nanoparticles decreases the value of M<sub>s</sub> from 97.35 to 75.84 emu/g with decrease of crystal size from 42 to 18 nm, which result in increase in the surface effect [Dasan *et.al.*, 2017, Santosh Bhukal *et.al.*, 2012]. Decreasing crystallite size due to the substitution of La<sup>3+</sup> trends to the increase of disordered spins which implies in the decrease of magnetic saturation. The value of coercivity increases from 736.33 Oe to 1128.35 Oe with increase of La<sup>3+</sup> ions depend on crystal size, magnetic crystallite, cation distribution, strain, porosity and anisotropy [Joshi *et.al.*, 2017]. According to Brown's relation the coercivity is inversely proportional to the magnetic saturation. It was agreed for the prepared nanoferrites, where the coercivity increased with decreasing magnetic saturation for addition of La<sup>3+</sup> concentration.

The anisotropy constant and squareness ratio were estimated by using following equation [Anwar et.al.,2012, Zhou et.al., 2015];

squareness ratio = 
$$\frac{M_r}{M_s}$$
 (4.10)

$$K = \frac{H_c M_s}{0.98} \tag{4.11}$$

Impact of lanthanum ions on magnetic and dielectric Properties of cobalt nanoferrites

where  $M_r$  is the remanent magnetization or retentivity, K is the anisotropy constant. Further, Bohr magnetizations ( $\eta_B$ ) in magnetic moments ( $\mu_B$ ) were estimated from the following equation [Zhou *et.al.*, 2015];

$$\Pi_B = \frac{MXM_S}{5585}$$
(4.12)

where X is the concentration and M is the molecular weight of La<sup>3+</sup> ion content. The magnetic parameters such as magnetic saturation (M<sub>s</sub>), coercivity (H<sub>c</sub>), retentivity (M<sub>r</sub>), squareness ratio, anisotropic constant (k) and Bohr magnetron (n<sub>β</sub>) were noticed from M-H and measurements are listed in Table 4.5. This suggests that CoLa<sub>x</sub>Fe<sub>2-x</sub>O<sub>4</sub> nanoferrites have spin arrangements which are better on the B-site, leading to decrease in (A-B interaction) [Tholkappiyan *et.al.*, 2014, Kebede K. Kefeni*et.al.*, 2017]. It was observed that the addition of La<sup>3+</sup> ions in cobalt matrix improved to get soft ferrite behavior with good saturation magnetization and it has good suitability for electromagnetic application [Lily *et.al.*, 2008].

Table 4.5 Magnetic parameters of  $CoLa_XFe_{2-X}O_4$  (X = 0.00 to 0.08) nanoferrites

Composition	Magnetization (M <sub>s</sub> ) (emu/g)	Remanent magnetization (M <sub>r</sub> ) (emu/g)	Coercivity (Hc) (Oe)	Squareness ratio (M <sub>r</sub> /M <sub>s</sub> ) (No unit)	Anisotropy constant (K) (Oe)	Bohr magneton (η <sub>B</sub> ) (μ <sub>B</sub> )
x = 0.00	97.35	27.45	736.33	0.2819	73.14	0.4381
x = 0.02	95.62	26.75	958.91	0.2797	93.56	0.4273
x = 0.04	95.59	25.64	993.84	0.2683	96.90	0.4241
x = 0.06	94.66	25.04	1010.45	0.2645	63.60	0.3731
x = 0.08	75.84	19.45	1128.23	0.2564	34.94	0.3188

# 4.3.7 Impedance Analysis

Impedance spectroscopy is a well-known technique for complete understanding of electrical properties of spinel type ferrites, whose properties depend on their ceramic texture, impedance of electrodes, distribution of dopants and grain and grain boundary contributions [Azizar Rahman *et.al.*, 2014]. And it also provides information regarding imaginary and real components of the impedance property of a material. The Nyquist plot shows a complete contribution of grain and grain boundary resistance. Figure 4.12 shows that the applied frequency dependent imaginary (Z") and real (Z') part of impedance are decreases with increase of frequency. It denotes an increase in AC conductivity.

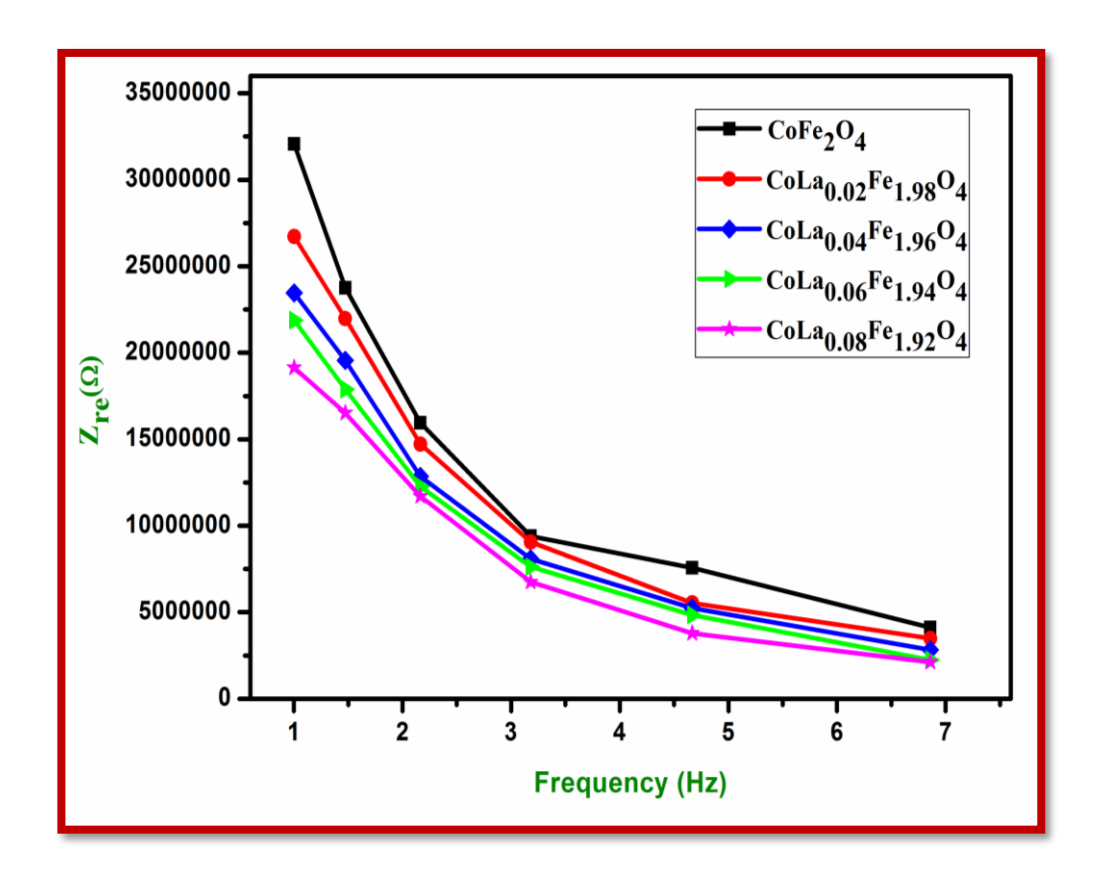


Figure 4.10 Real part of impedance spectra of  $CoLa_XFe_{2-x}O_4\,(X=0.00\ to\ 0.08)$  nanoferrites

The real part (Z') of the spectra values for all the prepared nanoparticles lead to lower values at higher frequency which implies release of space charges as a result of reduction in barrier properties of material [Azizar Rahman *et.al.*, 2014]. In Figure 4.10 impedance vs frequency plot gives an indication of increases of conduction with frequency, which infers that the ferrites to behave like a semiconductor material [Mangalaraja *et.al.*, 2002].

Figure 4.11, the imaginary part (Z") of the La<sup>3+</sup> doped cobalt nanoferrites decreases with increase of applied frequency and then remains low at high frequency. The imaginary part (Z") of the impedance spectra brings out relaxation peaks due to existence of space charge relaxation, associated with charge carries resulting from energy vacancies [Murugesan *et.al.*, 2015]. The Z" also decreases with increasing frequency due to the decreasing loss in the imaginary part of the nanoferrites.

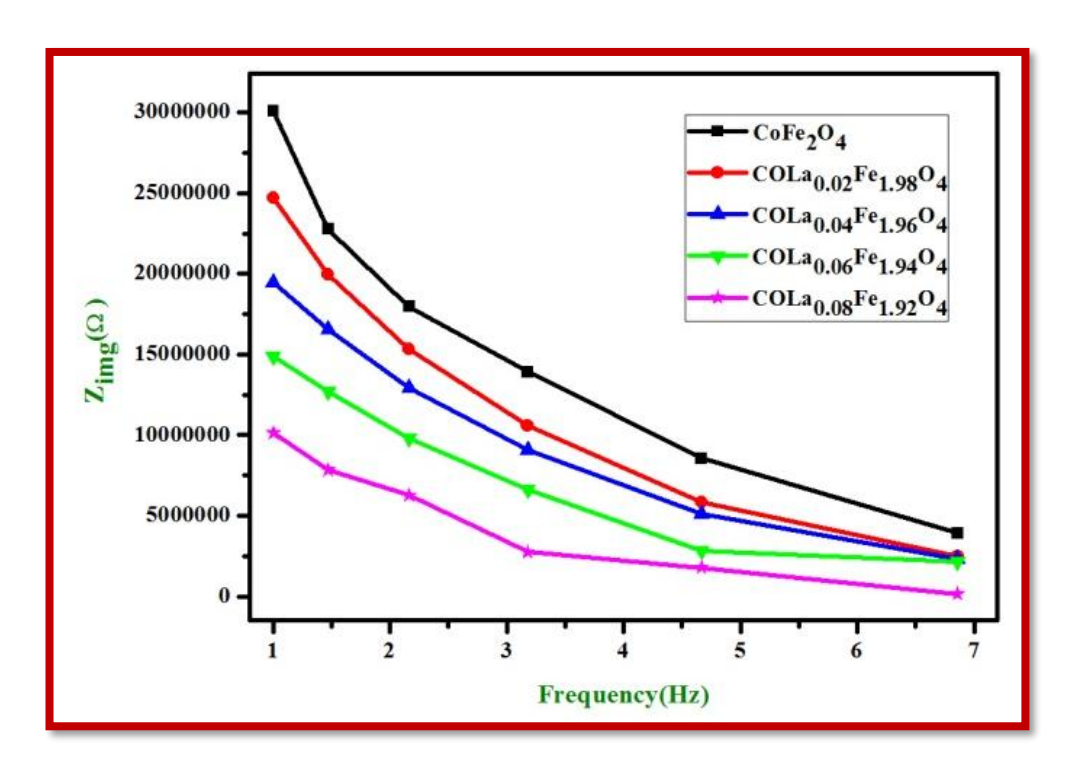


Figure 4.11 Imaginary part of impedance spectra of  $CoLa_XFe_{2-X}O_4$  (X = 0.00 to 0.08) nanoferrites.

Nyquist plot of impedance spectra as function of frequency for  $CoLa_xFe_{2-x}O_4$  nanoferrites are shown in Figure 4.12. Clear semicircle arcs were formed in high frequency for all the prepared nanoferrites with series of (X=0.00 to 0.08) because of the grain and grain boundary contributions to the conductivity. This also indicates that because of small crystallite size, the grain boundary contribution is higher than that of the grain contribution [Jnaneshwara *et.al.*, 2014]. Furthermore, it is observed that the value of Z' and Z'' in the impedance spectra for cobalt decreases with increasing  $La^{3+}$  concentration and it depicts that the overall resistance of the  $La^{3+}$  doped cobalt ferrite nanoparticles decrease, accordingly.

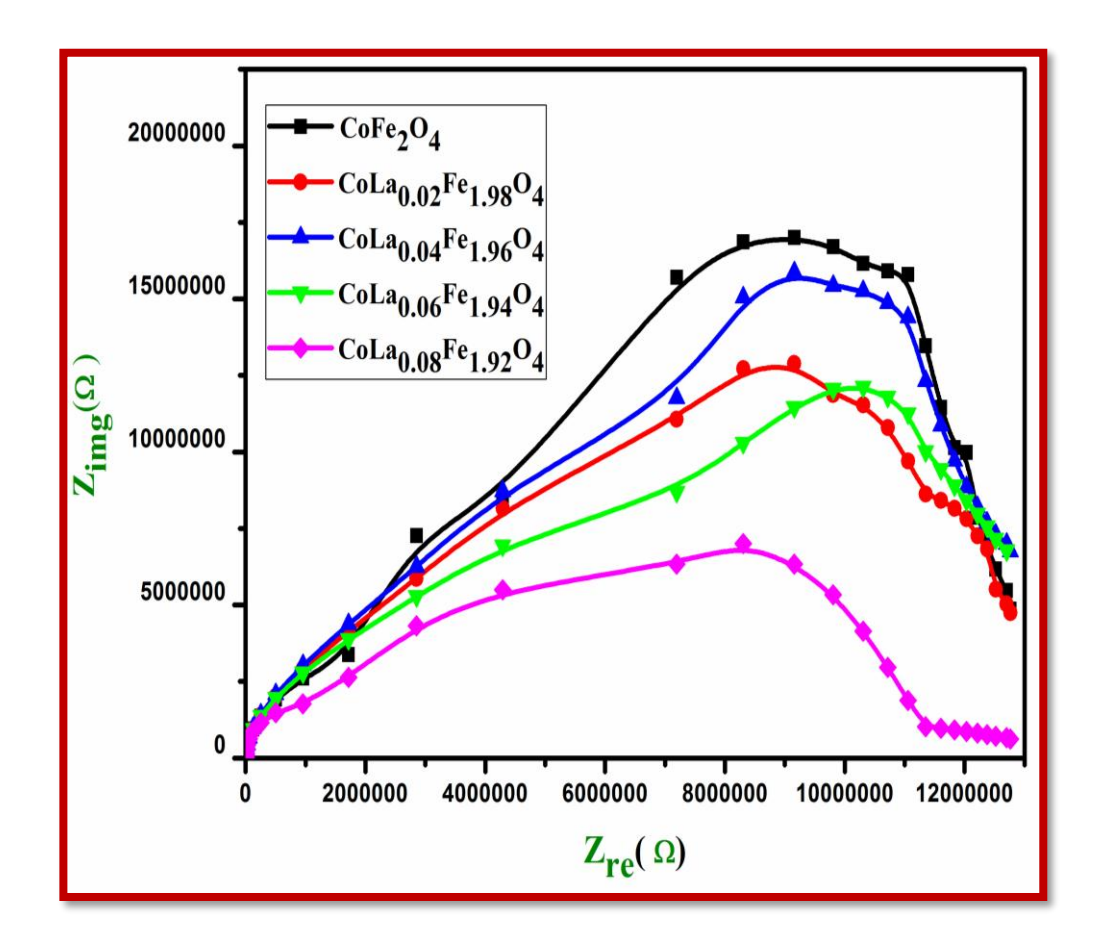


Figure 4.12 Nyquist plots of  $CoLa_XFe_{2-x}O_4$  (X = 0.00 to 0.08) nanoferrites

# 4.3.8 Dielectric Analysis

## **4.3.8(a)** Dielectric Constant ( $\mathcal{E}'$ )

The variation of dielectric constant ( $\mathcal{E}$ ') measured at the frequency in 100 mHz to 10 MHz at RT for the prepared nanoferrites as shown in Figure 4.13. The dielectric constant decreases with increase of Lanthanum content as a mechanism for the electrical conduction, which is same that of dielectric polarization. The dielectric constant was calculated using the following equation [Santosh Bhukal *et.al.*, 2012];

$$\varepsilon' = \frac{cd}{\varepsilon_0 A} \tag{4.13}$$

where  $\varepsilon$  is the dielectric constant, C is the capacitance of the pellet,  $\mathcal{E}_0$  is the permittivity of free space, A is the area of the CoLa<sub>X</sub>Fe<sub>2-X</sub>O<sub>4</sub> pellet and d is the thickness of the pellet. The values of dielectric constant both  $\varepsilon$ ' and  $\varepsilon$ " are higher at lower frequency and then decreases with increase in frequency for all the compositions (X=0.00 to 0.08).

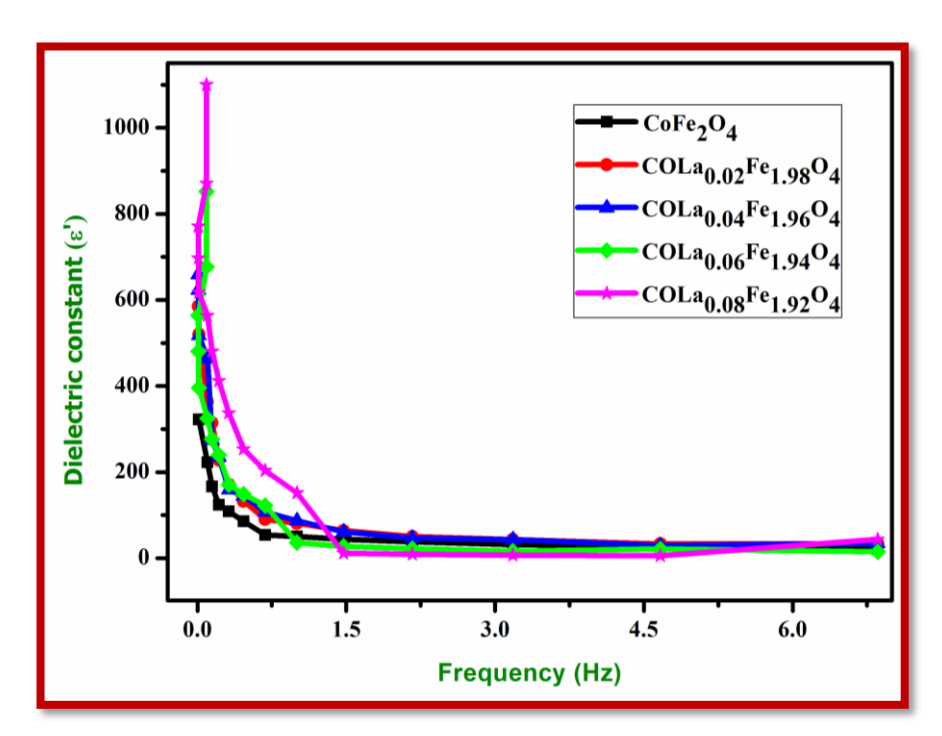


Figure 4.13 Dielectric constant of the  $CoLa_XFe_{2-x}O_4$  (X = 0.00 to 0.08) nanoferrites

The obtained dielectric constant and complex dielectric constant values are 321, 585, 659, 852, 1100 and 1150, 1921, 1874, 2190, and 2344 for all the compositions of X = 0.00, 0.02, 0.04, 0.06 and 0.08 respectively. The dielectric constants at lower frequency are based on some polarizations such as ionic, space charges and interface [Parashar et.al., 2015, Ravinder *et.al.*, 2003]. This type of behavior can be described based on Maxwell-Wagner interfacial polarization which is in agreement with Koop's theory [Mohan *et.al.*, 1999]. According to the Maxwell-Wagner model, the dielectric constant was due to high conductivity grains and poor conductivity grain boundaries.

In CoLa<sub>x</sub>Fe<sub>2-x</sub>O<sub>4</sub> spinal ferrites, the formation of Fe<sup>2+</sup> ions are due to interchange of electrons between Co<sup>2+</sup> and Fe<sup>3+</sup> to generate a pair of Co<sup>3+</sup> and Fe<sup>2+</sup> ions [Iqbal et.al., 2012]. The electron hopping between  $Fe^{2+} \leftrightarrow Fe^{3+}$  and hole hopping between  $Co^{3+} \leftrightarrow Co^{2+}$  ions and hence an applied electric field, the electrons pile up there, due to high resistance ultimately produces polarization. However, at high frequency the electron cannot move with fast changes due to the applied electric field because charge carries need sufficient time to transfer their orientation in react to the applied electric field. In general, the dielectric constant of any surface material depends on bulk polarization factor such dipolar, interfacial, ionic and electronic polarizations. In certain polarizations, dipolar and interfacial polarizations are real for the noticed behavior in dielectric constant at lower frequency, while electronic polarization is held responsible in the high frequency region [Kotnala et.al., 2013]. The decrease in both  $\mathcal{E}$ " and  $\mathcal{E}$ ' with frequency is due to the fact that any spices contributing to polarization is bound to slow the logging behind the applied field at high frequency [Hashim Alimuddin et.al., 2013, Mansour et.al., 2005]. Interestingly dielectric constant values decreased by more than 50% from 1100 (X = 0.08) to 321

(X=0.00) when the La<sup>3+</sup> increased less than 0.1% in CoLa<sub>X</sub>Fe<sub>2-X</sub>O<sub>4</sub>. The substitution of La<sup>3+</sup> ions in CoLa<sub>X</sub>Fe<sub>2-X</sub>O<sub>4</sub> nanoferrites tends to have significant variation in  $\epsilon'$  which improves the suitability of the nanoferrites for microwave frequency applications.

#### 4.3.8(b) Dielectric Loss

The variation of dielectric loss or loss tangent with variation of frequency is shown in Figure 4.14. It is evidently noticed that the loss tangent decreases with increase of La<sup>3+</sup> concentration. This can be mainly due to the increase in resistivity which results loss in tanδ. From the results, it is observed that the dielectric loss decreases with an increase of frequency at low frequency which decreased slowly in high frequency region before it become almost independence of the frequency in the higher frequency region. The dielectric loss is formulated with high resistivity at low frequency which is playing major role.

The dielectric loss and complex dielectric constant of nanoferrites were calculated using following equations [Veji et.al., 2009];

$$\tan \delta = \frac{1}{2\pi f \mathcal{E}_0 \mathcal{E}'} \tag{4.14}$$

$$\mathcal{E}'' = \mathcal{E}' \tan \delta \tag{4.15}$$

The dielectric losses of the nanoferrites are 3.583, 3.284, 2.844, 2.571 and 2.131 respectively. The electron interchange between Fe<sup>2+</sup> and Fe<sup>3+</sup> required more energy and accordingly more energy ions due to high resistivity of grain boundaries [Saafan*et.al.*, 2012]. Further, the electron interchange between Fe<sup>2+</sup> and Fe<sup>3+</sup> required loss of energy at high frequency of applied AC electric field which is equal to the hopping frequency of the charge carrier.

Impact of lanthanum ions on magnetic and dielectric Properties of cobalt nanoferrites

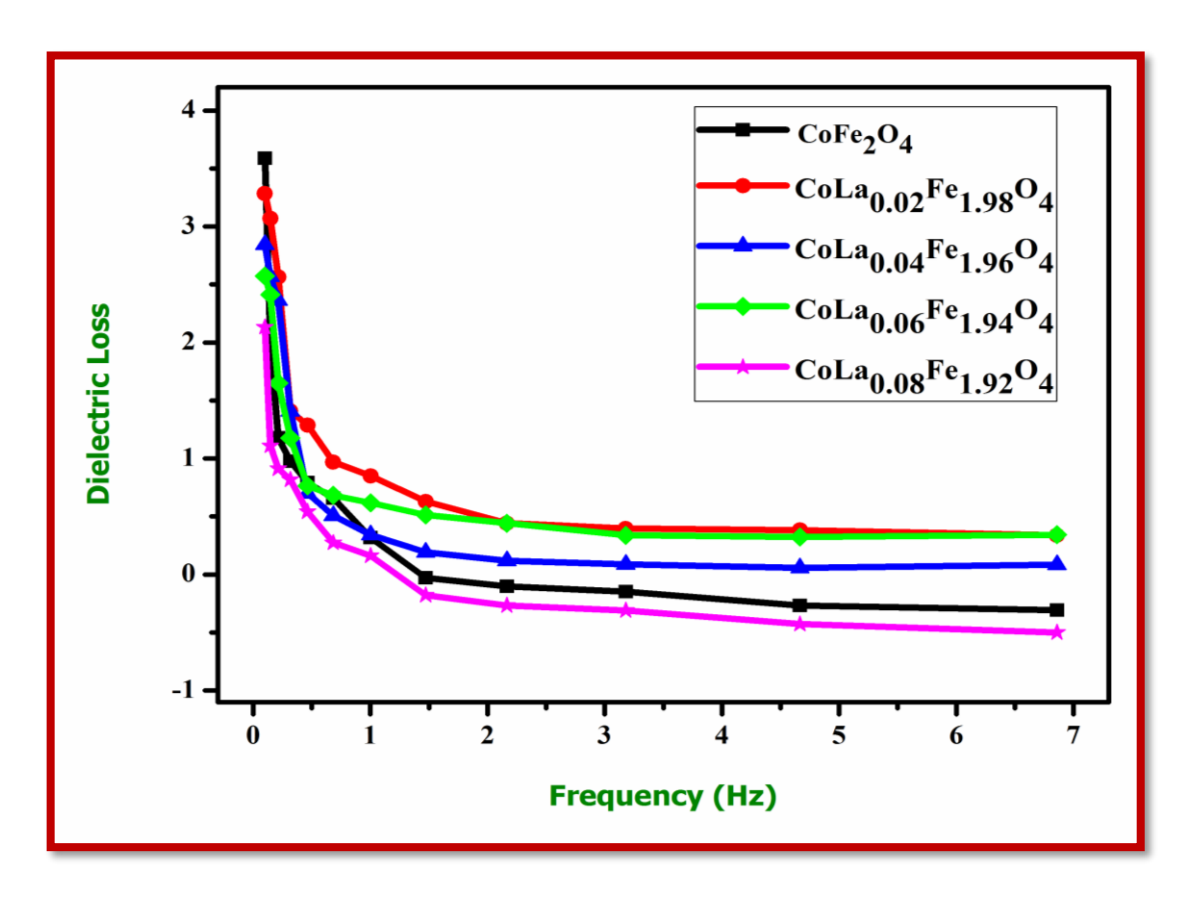


Figure 4.14 Dielectric loss of the  $CoLa_XFe_{2-X}O_4$  (X = 0.00 to 0.08) nanoferrites

The large amount of energy was thus recovered to transfer the oscillating ions and those by appearance of dielectric loss. The prepared material shows low dielectric loss is favorable for application in micro frequency devices. The electrical parameters such as dielectric constant, dielectric loss and complex dielectrics were listed in Table 4.6.

Table 4.6 Dielectric parameters of  $CoLa_XFe_{2-X}O_4$  (X = 0.00 to 0.08) nanoferrites

Composition	Dielectric Constant (ε')	Dielectric Loss (tanδ)	Complex dielectric constant (ε")
X=0.00	321	3.583	1150.14
X=0.02	585	3.284	1921.44
X=0.04	659	2.844	1874.19
X=0.06	852	2.571	2190.49
X=0.08	1100	2.131	2344.10

### **4.4 CONCLUSION**

Lanthanum doped Cobalt (CoLa<sub>x</sub>Fe<sub>2-x</sub>O<sub>4</sub>) nanoferrites with various composition for X = 0.00, 0.02, 0.04, 0.06, 0.08 were synthesized using simple and most effective sol-gel technique. XRD revealed cubic spinel structure with an average crystallite size of 31 nm. FTIR analyses confirmed the presence of metal at 583 cm<sup>-1</sup> corresponding to stretching M-O bond respectively. The lattice constant and volume of unit cell were increases with increase of La<sup>3+</sup> ions, whereas X-ray density and bulk density became inversely proportional to lattice constant. UV - diffuse reflectance spectra showed that the absorbance spectra of the CoLa<sub>x</sub>Fe<sub>2-x</sub>O<sub>4</sub> nanoferrite were varied from 226 to 222 nm. The value of indirect and direct energy bandgap varied from 1.73 to 2.06 eV and 1.45 to 1.56 eV. The obtained bandgap energy increased with increase of La<sup>3+</sup> concentrations. The obtained prepared nanaoferrites were identified with spherical morphology. XPS confirmed the presence of Co 2p, Fe 2p, La 3d and O 1s at octahedral [B] and tetrahedral [A] sites in CoLa<sub>x</sub>Fe<sub>2-x</sub>O<sub>4</sub> nanoferrites. The obtained VSM result showed that the prepared Lanthanum doped Cobalt nanoferrites has got a soft ferromagnetic nature. The saturation magnetization from 97.35 to 75.84 emu/g decreases with increase of La<sup>3+</sup> concentration. The higher coercivity (1128 Oe) with dielectric constant of the Lanthanum doped cobalt spinel nanoferrites is favorable for the applications in magneto recording devices. Impedance spectroscopy is used to identify grain contributions and grain boundary contributions to conductivity and utilized to estimate electrical response of Lanthanum doped cobalt nanoferrites. The frequency dependant dielectric constant, complex dielectric constant and dielectric loss decreases with increase of La<sup>3+</sup> ion. Behavior of dielectric constant and AC conductivity of Lanthanum doped cobalt nanoferrites was found to follow Maxwell-Wagner's model. Hence the combination of structural, magnetic, electrical and optical activities makes CoLa<sub>x</sub>Fe<sub>2-x</sub>O<sub>4</sub> (X = 0.00 to 0.08) nanoferrites highly useful for reducing false signals in the electronic devices and its highly suitable for Microwave frequency applications.

# REFERENCES

**Abdellatif M.H**, Innocenti C, Liakos I, Scarpellini A, Marras S, Salerno M, Effect of Jahn- Tellerdistortion on the short-range magnetic order in copper ferrite, J Magn Magn Mater. (**2017**) 424-402.

**Aghav P.S**, Vinod N. Dhage, Maheshkumar Mane L, Shengule D.R, Dorik R.G, Jadhav K.M, Effect of aluminium substitution on the structural and magnetic properties of cobalt ferrite synthesized by sol–gel auto combustion process, Physica B. 406 (**2011**) 4350–4354.

**Anandan S**, Selvamani T, Prasad G.G, Asiri A.M, Wu J.J, Magnetic and catalytic properties of inversespinel CuFe<sub>2</sub>O<sub>4</sub> nanoparticles, J Magn Magn Mater. (**2017**) 432-437.

**Anantharamaiah P.N**, Joy P.A, tuning of the magnetostrictive properties of cobalt ferrite by forced distribution of substituted divalent metal ions at different crystallographic sites, J. Appl. Phys. 121 (**2017**) 093904.

**Anwar H**, Maqsood A, Structural, magnetic and electrical properties of Cu substituted Mn Zn soft nanoferrites, J. Supercond. Nov. Magn. 25 (2012)1913-1920.

**Anwar**, Asghari Maqsood, Enhancement of electrical and magnetic properties of Cd<sup>2+</sup> doped Mn–Zn soft nanoferrites prepared by the sol–gel autocombustion method H. Journal of Magnetism and Magnetic Materials 333 (**2013**) 46–52.

**Azadmanjiri J**, Salehani H.K, Barati M.R, Farzan F, Preparation and electromagnetic properties of Ni<sub>1-x</sub>Cu<sub>x</sub>Fe<sub>2</sub>O<sub>4</sub> nanoparticle ferrites by solgel auto combustion method, Mater. Lett. 61 (**2007**) 84-87.

**Aziz H.S**, Rasheed S, Khan R.A, Rahim A, Nisar J, Shah S.M, Iqbal F, Khan A.R, Evaluation of electrical, dielectric and magnetic characteristics of Al–La doped nickel spinel ferrites.RSC Adv. 6 (**2016**) 6589–6597.

**Azizar Rahman M**, Akther Hossain A.K.M, Electrical transport properties of Mn–Ni–Zn ferrite using complex impedance spectroscopy, Phys. Scr. 89 (**2014**) 025803(8pp).

**Bensebaa F**, Zavaliche L, Ecuyer P, Cochrane R.W, and Veres T, Microwave Synthesis and Characterization of Co-Ferrite Nanoparticles. Journal of Colloid and Interface Science. (2004) 277, 104-110.

**Chaudhari V**, Shirsath S.E,.Mane M, Kadam R.H, Shelke S.B, Mane D.R, Crystallographic, magnetic and electrical properties of Ni<sub>0.5</sub>Cu<sub>0.25</sub>Zn<sub>0.25</sub>La<sub>x</sub>Fe<sub>2-x</sub>O<sub>4</sub> nanoparticles fabricated by solgel method, J. Alloys Compd. 549 (**2013**) 213-220.

**Dasan Y.K**, Guan B.H, Zahari Chuan M.H, Influence of La<sup>3+</sup> Substitution on Structure, Morphology and Magnetic Properties of Nanocrystalline Ni-Zn Ferrite, PLoS ONE. 12(1) (**2017**) e0170075.

**Ghulam Mustafa**, Islam M.U, Mukhtar Ahmad, Wenli Zhang, Yasir Jamil, Abdul Wahee, Anwar, Mudassar Hussain, Influence of the divalent and trivalent ions substitution on the structural and magnetic properties of Mg<sub>0.5-x</sub>Cd<sub>x</sub>Co<sub>0.5</sub>Cr<sub>0.04</sub>Tb<sub>y</sub>Fe<sub>1.96-y</sub>O<sub>4</sub> ferrites prepared by sol-gel method, Journal of Magnetism and Magnetic Materials. 387 (**2015**) 147–154.

Gore S.K, Jadhav S.S, Jadhav V.V, Patange S.M, Naushad Mu, Mane R.S, Kim K.H, The structural and magnetic properties of dual phase cobalt ferrite, Sci.Rep. 7 (2017) 2524.

**Hankare P. P**, Patil R. P, Jadhav A.V, Pandav R.S, Garadkar K.M, Sasikala R, and A.K. Tripathi, Synthesis and Characterization of Nanocrystalline Ti-Substituted Zn Ferrite. Journal of Alloys and Compounds. 509 (**2011**), 2160-2163.

**Hankare P.P**, Sanadi K.R, Garadkar K.M, Patil D.R, Mulla I.S, Synthesis and characterization of nickel substituted cobalt ferrite nanoparticles by sol-gel auto-combustion method, J. Alloys Compd. 553 (2013) 383–388.

**Hashim Alimuddin M**, Shirsath S.E, Kumar S, Kumar R, Roy A.S, Shah, J, Kotnala R.K, Preparation and characterization chemistry of nano-crystalline NiCuZn ferrite, J. Alloys Compd. 549 (**2013**) 348-357.

**Ihsan Ali**, Mukhtar Ahmad, Islam M. U, Awan M. S, Substitution effects of La<sup>3+</sup> ions on the structural and magnetic properties of Co<sub>2</sub>Y hexaferrites synthesized by sol–gel autocombustion method, Springer Science+ Business Media New York (**2013**).

**Iqbal M. J**, Khan R. A, Mizukami S, Miyazaki T, Mossbauer, magnetic and microwave absorption characteristics of substituted W-type hexaferrites nanoparticles, Ceramics International. 38 (**2012**) 4097–4103.

**Irshad Ali M**, Islam U, Ishaque Hasan M, Khan M, Muhammad Naeem Ashiq, Effect of Gd-substitution on physical and magnetic properties of Li<sub>1.2</sub>Mg<sub>0.4</sub>Gd<sub>x</sub>Fe<sub>(2-x)</sub>O<sub>4</sub> ferrites, Journal of Alloys and Compounds. (**2013**) 579, 181-186.

**Jnaneshwara D.M**, Avadhani D.N, Daruka Prasad B, Nagabhushana H, Nagabhushana B.M, Sharma S.C, Prashantha S.C, Shivakumara C, Role of Cu<sup>2+</sup> ions substitution in magnetic and conductivity behaviour of nano

CoFe<sub>2</sub>O<sub>4</sub>, Spectro chimica Acta Part A: Mole. Bimole. Spectroscopy. 132 (**2014**) 256-262.

**Joshi S**, Kumar M, Chhoker S, Kumar A, Singh M, Effect of Gd<sup>3+</sup> substitution on structural, magnetic, dielectric and opticalproperties of nanocrystalline CoFe<sub>2</sub>O<sub>4</sub> J. Magn. Magn. Mater.426 (**2017**) 252-263.

**Kadam M.R**, Patil R.P, Hankare P.P, Investigations on structural, electrical andmagnetic properties of nickel substituted La-ferrites, Solid State Sci. 14 (**2012**) 964-970.

**Kamala Bharathi K**, Tackett R.J, Botez C.E, Ramana C.V, Coexistence of spin glassbehavior and long-range ferromagnetic ordering in La- and Dy-doped Co ferrite, J.Appl. Phys. 109 (**2011**) 07A510.

**Karakas Z.K**, Boncukcuoglu R, Karakas I.H., The effects of heat treatment on the synthesis of nickel ferrite (NiFe<sub>2</sub>O<sub>4</sub>) nanoparticles using the microwave assisted combustion method. J.Magn. Magn. Mater. 374, (2015) 298–306.

**Kebede Kefeni K**, Titus Msagati A.M, Bhekie B. Mamba, Ferrite nanoparticles:synthesis, characterisation and applications in electronic device, Mater. Sci. Eng. B. 215 (**2017**) 37–55.

**Kotnala R.K**, Preparation and characterization chemistry of nanocrystalline NiCuZn ferrite, J. Alloys Compd. 549 (**2013**) 348-357.

**Kovalenko** A, Yadav R.S, Pospisil J, Zmeskal O, Karashanova D, Heinrichova P, Vala M, Havlica J, Weiter M, Towards improved efficiency of bulk-heterojunction. Solar cells using various spinel ferrite magnetic nanoparticles, Org. Electron. 39 (**2016**) 118–126.

**Kunal Pubby S**, Meena S, Yusuf S.M, Sukhleen Bindra Narang, Cobalt substituted nickel ferrites via Pechini's sol-gel route: X-band electromagnetic characterization, J. Magn. Magn. Mater. 466 (**2018**) 430–445.

**Lasheras X**, Insausti M, Gil de Muro I, Garaio E, Plazaola F, Moros M, Matteis L. De, de la Fuente J.M, Lezama L, Chemical synthesis and magnetic properties of monodisperse nickel ferrite nanoparticles for biomedical applications, J. Phys.Chem. C 120 (6) (**2016**) 3492–3500.

**Lawrence Kumar**, Manoranjan Kar, Effect of La<sup>3+</sup> substitution on the structural and magneto crystalline anisotropy of nanocrystalline cobalt ferrite (CoFe<sub>2-x</sub>La<sub>x</sub>O<sub>4</sub>), Ceram. Int. 438 (**2012**) 4771-4778.

**Lenin N**, Rajesh Kanna R, Sakthipandi K, Senthil Kumar A, Structural, Electrical and Magnetic Properties of NiLa<sub>x</sub>Fe<sub>2-x</sub>O<sub>4</sub> Nanoferrites, Mater. Chem Phy. 212 (**2018**) 385-393.

**Lily K**, Kumari K, Prasad R.N, Choudhary P, Impedance spectroscopy of (Na<sub>0.5</sub>Bi<sub>0.5</sub>) (Zr<sub>0.25</sub>Ti<sub>0.75</sub>)O<sub>3</sub> lead-free ceramic, J. Alloy. Compd. 453 (**2008**) 325–331.

**Lu L.T**, Dung N.T, Tung L.D, Thanh C.T, Quy O.K, Chuc N.V, Maenosono S, Thanh N.T.K, Synthesis of magnetic cobalt ferrite nanoparticles with controlled morphology, mono dispersity and composition: the influence of solvent, surfactant, reductant and synthetic conditions, Nanoscale 7 (**2015**) 19596.

**Mangalaraja R.V**, Ananthakumar S, Manohar P, Gnanam F.D, Magnetic, electrical and dielectric behaviour of Ni<sub>0.8</sub>Zn<sub>0.2</sub>Fe<sub>2</sub>O<sub>4</sub> prepared

through flash combustion technique, J. Magn. Magn. Mater. 253 (2002) 56–64.

**Mansour S.F**, Frequency and composition dependence on the dielectric properties for Mg–Zn ferrite, Egyptian Journal of Solids. 28 (2) (**2005**) 211–214.

**Mohan G.R**, Ravinder D, Reddy A.V.R, Boyanov B.S, Dielectric properties of polycrystalline mixed nickel–zinc ferrites, Materials Letters. 40 (**1999**) 39–45.

**Murugesan** C, and Chandrasekaran G, Impact of Gd<sup>3+-</sup>substitution on the structural, magnetic and electrical properties of cobalt ferrite nanoparticles, RSC Advances. **5** (**2015**) 73714-73725.

**Parashar J**, Saxena V.K, Jyoti D, Bhatnagar K.B, Sharma, Dielectric behaviour of Zn substituted Cu nano-ferrites. J. Magn. Magn. Mater. 394 (2015)105–110.

**Peng J**, Hojamberdiev M, Xu Y, Cao B, Wang J, Structural and Electrical Studies of MnGd<sub>x</sub>Fe<sub>2-x</sub>O<sub>4</sub> Nanoparticles, J.Magn. Magn. Mater. (**2011**) 323, 133–138.

**Peng J**, Hojamberdiev M, Xu Y, Cao B, Wang J, and Wu H, Hydrothermal synthesis and magnetic properties of gadolinium-doped CoFe<sub>2</sub>O<sub>4</sub> nanoparticles, Journal of Magnetism and Magnetic Materials. 323 (**2011**) 133–138.

Raghvendra Singh Yadav, Ivo Kuritka, Jarmila Vilcakova, Jaromir Havlica, Jiri Masilko, Lukas Kalina, Jakub Tkacz, Jiri Svec, Vojtech Enev and Miroslava Hajduchov, Impact of grain size and structural

changes on magnetic, dielectric, electrical, impedance and modulus spectroscopic characteristics of CoFe<sub>2</sub>O<sub>4</sub> nanoparticles synthesized by honey mediated sol-gel combustion method, Adv. Nat. Sci.: Nanosci. Nanotechnol. 8 (2017) 045002.

**Raghvendra Singh Yadav**, Jaromir Havlica, JiriMasilko, Lukas Kalina, Jaromir Wasserbauer, Miroslava Hajduchova, Vojtech Enev, IvoKuritka and Zuzana Kozakova, Impact of Nd<sup>3+</sup> in CoFe<sub>2</sub>O<sub>4</sub> spinel ferrite nanoparticles on cation distribution, structural and magnetic properties, Journal of Magnetism and Magnetic Material. (2015).

**Raghvendra Singh Yadava**, Ivo Kuritkaa, Jarmila Vilcakovaa, Jaromir Havlicab, Lukas Kalinab, Pavel Urbaneka, Michal Machovskya, David Skodaa, Milan Masara, Martin Holeka, Sonochemical synthesis of Gd<sup>3+</sup> doped CoFe<sub>2</sub>O<sub>4</sub> spinel ferrite nanoparticlesand its physical properties, Ultrasonics – Sonochemistry. 40 (2018) 773–783.

**Rajesh Kanna R**, Lenin N, Sakthipandi K, Sivabharathy M, Impact of Lanthanum on structural, optical, dielectric and magnetic properties of Mn<sub>1-x</sub>Cu<sub>x</sub>Fe<sub>1.85</sub>La<sub>0.15</sub>O<sub>4</sub> spinel nanoferrites, Ceram. Int. 43 (**2017**) 15868-15879.

**Rajesh Kanna R**, Lenin N, Sakthipandi K, Sivabharathy M, Impact of Lanthanum on structural, optical, dielectric and magnetic properties of Mn<sub>1-x</sub>Cu<sub>x</sub>Fe<sub>1.85</sub>La<sub>0.15</sub>O<sub>4</sub> spinel nanoferrites, Ceram. Int. 43 (**2017**) 15868-15879.

**Ranjith Kumar E**, Arunkumar T, Prakash T, Heat treatment effects on structural and dielectric properties of Mn substituted CuFe<sub>2</sub>O<sub>4</sub> and ZnFe<sub>2</sub>O<sub>4</sub> nanoparticles, J.Superlatt. Microstruct. 85 (**2015**) 530–535.

**Ravinder D**, Reddy P.V.B, High-frequency dielectric behaviour of Li–Mg ferrites, Materials Letters. 57 (**2003**) 4344–4350.

**Roy P.K**, Bera J, Enhancement of the magnetic properties of Ni-Cu-Zn ferrites with the substitution of a small fraction of lanthanum for iron, Mater.Res. Bull. 42 (**2007**) 77-83.

**Saafan S. A**, Assar S. T, Dielectric behavior of nano-structured and bulk LiNiZn ferrite samples, J. Magn. Magn. Mater. 324 (**2012**) 2989–3001.

**Sakthipandi K**, Rajendran V, Jayakumar T, Baldev Raj, Kulandivelu P, Synthesis and on-line ultrasonic characterisation of bulk and nanocrystalline La<sub>0.68</sub>Sr<sub>0.32</sub>MnO<sub>3</sub> perovskite manganite, J. Alloys Compd 509 (**2011**) 3457-3467.

**Santosh Bhukal T**, Sering Namgyal S, Mor S, Bansal, Sonal Singhal, Structural, electrical, optical and magnetic properties of chromium substituted Co–Zn nanoferrites Co<sub>0.6</sub>Zn<sub>0.4</sub>Cr<sub>x</sub>Fe<sub>2x</sub>O<sub>4</sub> (0 6 x 6 1.0) prepared via sol–gel auto-combustion method, Journal of Molecular Structure.1012 (**2012**) 162–167.

**Saravanan L**, Jayave R.l, Pandurangan A, Liu JH, Miao HY. Synthesis, structural and optical properties of Sm<sup>3+</sup> and Nd<sup>3+</sup> doped cadmium sulfide nanocrystals. Mater Res Bull. (**2014**), 52:128.

**Sattar A**, Samy A. M, El-Ezza R. S, Eatah A. E, Effect of rare-earth substitution on magnetic and electrical properties of Mn–Zn ferrites. Phys. Status Solid (a). (2002) 193(1), 86–93.

**Sonia Gaba**, Ashok Kumar, Pawan S. Rana, Manju Arora, Influence of La<sup>3+</sup> ion doping on physical properties of magnesium nanoferrites for

microwave absorption application, Journal of Magnetism and Magnetic Material. S0304-8853(**2017**) 32557.

**Tholkappiyan R**, Vishista K, Influence of lanthanum on the optomagnetic properties of zinc ferrite prepared by combustion method, Phys. B Condens.Matter. 448 (**2014**) 177-183.

**Veji Z.** C, Raki S, Jankov S, Skuban S, Kapor A, Dielectric properties and conductivity of zinc ferrite and zinc ferrite doped with yttrium, Journal of Alloys and Compounds. 480 (**2009**) 241–245.

**Venkatesha N**, Shivanad M. Pudakalakatti, Yasrib Qurishi, Hanudatta S. Atreya, Chandan Srivastava, MnFe<sub>2</sub>O<sub>4</sub>-Fe<sub>3</sub>O<sub>4</sub> core-shell nanoparticles as potential contrast agent for magnetic resonance imaging, RSC Adv. 5 (**2015**) 97807–97815.

**Vicente J. de**, Delgado A.V, Plaza R.C, Duran J.D.G, Gonzalez Caballero F, Stability of Cobalt ferrite colliodal particles. Effect of pH and applied magnetic fields, Langmuir. 16 (**2000**) 7954–7961.

**Vigneshwaran B**, Kuppusami P, Arunkumar Panda, Akash Singh and H.Sreemoolanadhan, Microstructure and optical properties of Ba<sub>0.6</sub>Sr<sub>0.4</sub>TiO<sub>3</sub> thin films prepared by pulsed laser deposition, Materials Research Express. 5 (**2018**) 0664.

**Wang H**, Guo H, Dai Y, Geng D, Han Z, Li D, Yang T, Ma S, Liu W, Zhang Z, Optimal electromagnetic-wave absorption by enhanced dipole polarization inNi/C nanocapsules, Appl. Phys. Lett. 101 (**2012**) 083116.

Widatallah H, Johnson C, Gismelseed A, Al-Omari I, Stewart S, Al-Harthi S, Thomas S, Sitepu H, Structural and magnetic studies of

nanocrystalline Mg-doped Li<sub>0.5</sub>Fe<sub>2.5</sub>O<sub>4</sub> particles prepared by mechanical milling, Journal of Physics D: Applied Physics, 41 (**2008**) 165006.

**Zhikai Yan**, Jianming Gao, Yang Li, Mei Zhang, Min Guo, Hydrothermal synthesis and structure evolution of metal-doped magnesium ferrite from saprolite laterite, RSC Adv. 5 (2015) 92778–92787.

**Zhou Y**, Chen W, Shen Y, Wu X, Wu W, Wu J, Lattice strains and magnetic properties evolution of copper-magnesium ferrite with lithium substitution, J. Magn. Magn Mater. 396 (**2015**) 198-203.

## **CHAPTER - V**

## DEPENDANCE OF LANTHANUM IONSON STRUCTURAL, MAGNETIC AND ELECTRICAL OF MANGANESE BASED SPINEL NANOFERRITES

#### **5.1 INTRODUCTION**

Nanomaterials have been showing excellent chemical and physical properties due to their smaller crystal size, high surface area, quantum confinement effect and high calcined ability. Recently, ferrite nanoparticles are used in many applications such as technological and fundamental reasons [Kryder et.al., 1996]. So that, these materials are of most challenging as magnetic memories, high density storage media, transformer cores, analogue devices, electron transport devices, electron magnetic interchange devices, choke coil and even in high - frequency device [Samoila et.al., 2015, Igbal et.al., 2012, Dixit et.al., 2013]. The properties attained by these ferrites are based on their cation distribution and chemical composition and in Octahedral Bsites and tetrahedral A-Site [Nitendar Kumar et.al., 1998]. Mn nanoferrites are one of the most important soft magnetic materials due to its high coercivity and low core losses [Katarzyna Winiarska et.al., 2012]. The rare earth iron play's vital role to change its magnetic properties involving large magneto crystalline anisotropy; a high magnetostriction and magnetic moment on adding of La<sup>3+</sup> ions with high ionic radii at very low temperature because of its localized nature of 4f electrons [Hemeda et.al., 2001]. La<sup>3+</sup> ions replace Fe<sup>3+</sup> ions at low concentration as they like to enter the octahedral site (B-site) [Nalbandian et.al., 2008, Wang et.al., 2004]. Micro strains are developed due to variation in the ionic radii between La<sup>3+</sup> and Fe<sup>3+</sup> ions which may

affect spinel structure that in turn influence the motion of domain wall. Lanthanum doped manganese nanoferrites are very helpful in preventing and extinguishing electromagnetic interference to electronic controlled system [Hasting *et.al.*,1956].

In recent years, the sol-gel method is used to prepare various mixed oxide, nanoporous oxides, nanoscale architectures, nanomaterials, inorganic and organic hybrids [Chinnasamy et.al., 2000]. The sol-gel method has got most admiring advantages such as small crystalline size and better homogeneity in the final product [Yang et.al., 2009]. Samolia.et.al. have reported magnetic and structural properties of Gd-doped Ni-Mn-Cr ferrites synthesized by sol-gel method and noticed that magnetization and coercivity decrease with the increase of Gd<sup>3+</sup> ions [Samoila et.al., 2015]. The rare earth element of Nd<sup>3+</sup> doped manganese zinc ferrite synthesized by using combustion method influences on the magnetic and structural properties and an increase in saturation magnetization with increase of Nd<sup>3+</sup> ions [Naiket.al., 2017]. Lanthanum doped manganese ferrites are prepared by enormous synthesize methods such as micro-emulsion auto-combustion, co-precipitation technique, wet chemical and sonication method [Shahul Hameed et.al., 2014, Fanet.al., 2012, Guoet.al., 2013]. Systematic studies on structural, electrical, optical and magnetic properties of La<sup>3+</sup> ion doped Manganese nanoferrites prepared by sol-gel method could not be found yet. In the present study, dependence of La<sup>3+</sup> ion substitution on the structural, optical, magnetic and electrical properties of manganese nanoferrites with particular series (X = 0.00 to 0.08) was noticed.

In this study, Lanthanum doped manganese nanoferrites  $MnLa_XFe_{2-X}O_4$  (X = 0.00 to 0.08) were prepared by sol-gel method. The obtained Lanthanum doped

cobalt nanoferrites were characterized by X-ray diffraction (XRD) for phase and structural identification, Fourier transform infrared spectroscopy (FTIR) for to identify organic and also some inorganic materials, Field Emission Scanning electron Microscopy (FESEM) coupled with energy dispersive X-ray analysis (EDAX) for surface morphology and elemental analysis, Ultra Violet (UV) diffuse reflectance spectroscopy (DRS) for optical properties and vibrating sample magnetometer (VSM) for magnetic measurements. The results are analyzed and the obtained results are identified towards utilized for the possible electronic devices in electromagnetic radiation applications.

#### 5.2 MATERIALS AND EXPERIMENTAL PROCEDURE

#### 5.2.1 Materials

High pure grade Merck precursors such as Manganese nitrate (Mn(NO<sub>3</sub>)<sub>2</sub>.6H<sub>2</sub>O), Lanthanum nitrate (La(NO<sub>3</sub>)<sub>3</sub>.6H<sub>2</sub>O), Ferric nitrate (Fe(NO<sub>3</sub>)<sub>3</sub>.9H<sub>2</sub>O), Ammonia (NH<sub>4</sub>OH), Citric acid (C<sub>6</sub>H<sub>8</sub>O<sub>7</sub>.H<sub>2</sub>O) and deionized water were used.

## **5.2.2 Experimental Procedure**

MnLa<sub>X</sub>Fe<sub>2-X</sub>O<sub>4</sub> (X=0.00, 0.02, 0.04, 0.06 and 0.08) nanoferrites were synthesized by sol-gel method. The precursors such as Lanthanum nitrate (La (NO<sub>3</sub>)<sub>3</sub>.6H<sub>2</sub>O), ferric nitrate (Fe (NO<sub>3</sub>)<sub>3</sub>.9H<sub>2</sub>O), manganese nitrate (Mn (NO<sub>3</sub>)<sub>2</sub>.6H<sub>2</sub>O), ammonia (NH<sub>4</sub>OH), citric acid (C<sub>6</sub>H<sub>8</sub>O<sub>7</sub>.H<sub>2</sub>O) and deionized water were used to prepare Lanthanum doped manganese nanoferrites. The measured precursors were dissolved with 100 ml of deionized water to attain homogeneous mixture of the precursor. The mixed solution was continuously stirred at 80°C for 1 hr. Further

ammonia was added drop by drop to the ferrite solution to attain the pH value of 7. Finally dark solution was collected and dried in a hot air oven at fixed temperature at 60°C for 24 hrs. The amorphous powders were collected and sintered in muffle furnace at 500°C for 2 hrs. Then the sintered nanopowders were grinded for 15 mins to reach a fine powder. Thus, obtained nanopowders were again well calcined at 1000°C for 24 hrs. Finally, obtained nanoferrite powders were grounded well. The Flow chart for sample preparation of MnLaxFe<sub>2-x</sub>O<sub>4</sub> nanoferrites was shown in Figure 5.1.

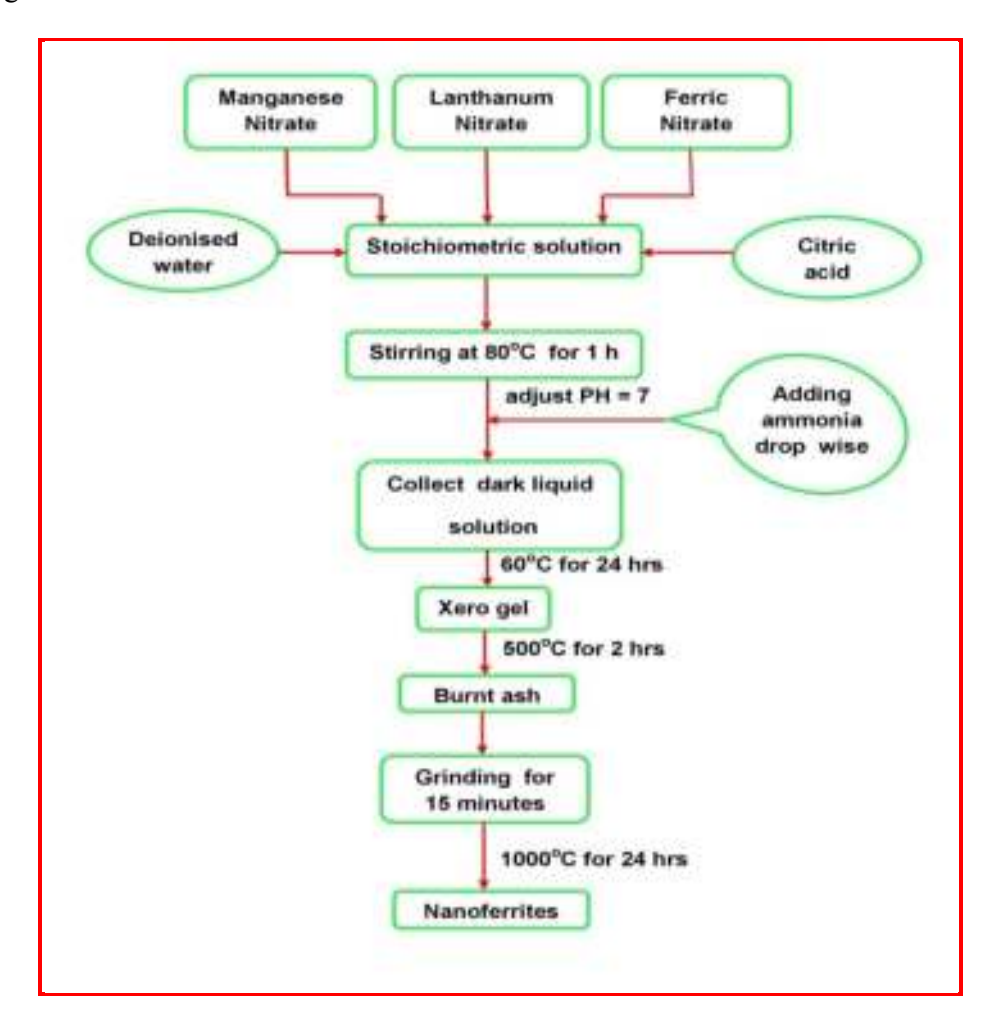


Figure 5.1 Flow chart for the sample preparation of MnLaxFe2-xO4 nanoferrites

## 5.2.3 Characterization of MnLaxFe2-xO4 nanoferrites

The structural analysis of the prepared MnLaxFe<sub>2-x</sub>O<sub>4</sub> (X= 0.00 to 0.08) nanoferrites were done by XRD (SHIMADZU-XRD 6000) technique. CuKα radiation source is used to discover the prepared nanoferrites at the 2θ range from 20° to 80°, operated at 40 kV and 30 mA. The functional groups and chemical interactions obtained in the prepared CoLaxFe<sub>2-x</sub>O<sub>4</sub> nanoferrites were examined by FTIR spectra (SHIMADZU-UV 18000) in the wavelength region of wave number ranges from 4000 to 400 cm<sup>-1</sup> at RT. The surface morphology and elemental composition were analyzed out using FESEM with an energy dispersive spectrum (Quanta FEG 250). The optical properties of the prepared samples were analyzed using the UV- DRS with absorption wavelength in the range of 200 to 800 nm. Impedance spectroscopy is used to examine the conductivity of the prepared MnLaxFe<sub>2-x</sub>O<sub>4</sub> nanoferrites (Biologic SP-300). Magnetic studies were assessed using VSM (Lakeshore VSM 7140) at RT with a magnetic field of -15 to +15 KOe.

#### 5.3 RESULTS AND DISCUSSION

### **5.3.1 Structural Analysis**

Figure 5.2 shows the structural XRD analysis of the Lanthanum doped manganese nanoferrites (MnLa<sub>X</sub>Fe<sub>2-X</sub>O<sub>4</sub>) with series X = 0.00 to 0.08 calcined at 1000°C. The peak positions appeared at 30.67°, 35.33°, 43.47°, 53.52° and 56.6° corresponds to (220), (311), (400), (422) and (333) planes respectively. All the obtained peaks are in good agreement with JCPDS card No (74-24023) and it is also revealed that the synthesized nanoferrites are in cubic structure [Devi *et.al.*,2017]. No other peaks related to either Lanthanum or other byproducts are observed. It confirms that the Lanthanum is doped in to the host Mn lattice.

The average crystallite sizes of the prepared nanoferrites are calculated using the well-known Scherrer formula [Vigneshwaran *et.al.*,2018];

$$D = \frac{K\lambda}{\beta Cos\theta}$$
 (5.1)

where K is a Scherrer constant (0.89),  $\lambda$ ,  $\beta$ ,  $\theta$  are the wavelength of x-ray used, Full Width at Half Maximum (FWHM) and Bragg's angle respectively. The crystallite size is calculated for the prepared nanoferrites which is decreasing from 26 to 12 nm with increase of La<sup>3+</sup> concentration from X=0.00 to 0.08. The decreasing crystallite sizes are mainly due to the difference in ionic radii of La<sup>3+</sup> ions and Fe<sup>3+</sup> ions [Irshad Ali *et.al.*,2012]. Therefore, it is difficult to replace La<sup>3+</sup> ion (1.06 Å) which has larger ionic radii as compared with Fe<sup>3+</sup> ions (0.67 Å) on the lattice strain. At the same time of substitution La<sup>3+</sup> ions to Fe<sup>3+</sup> ions on the lattice strain, few of the La<sup>3+</sup> ions may be settled on the grain boundaries and created pressure on the grain boundaries have arisen in smaller crystal size of La<sup>3+</sup> doped Mn ferrites in comparison with Gd, La doped Mn-Zn ferrites [Prashant Thakur et.al.,2016, Shahab Torkian *et.al.*,2016].

The lattice constant for the prepared nanoferrites is estimated through Nelson-relay function [Irshad Ali *et.al.*,2012];

$$a = d_{hkl}\sqrt{h^2 + k^2 + l^2} (5.2)$$

where d is inter planer distance, hkl are Miller indices and 'a' is the lattice parameter. The lattice constant increases linearly with increase of La<sup>3+</sup> ions for prepared nanoferrties. This may be due to La<sup>3+</sup> ions which possess a significant affinity to replenish the octahedral site due to their larger ionic radii (1.06 Å) than the

metal ion at the octahedral site  $Mn^{2+}$  (0.83 Å) and consequently occupies the octahedral sites [Zhang *et.al.*,2011].

The X-ray density was calculated by using the following equation [Tholkappiyan *et.al.*,2014];

$$d_{\chi} = \frac{Zm}{Na^3} \tag{5.3}$$

where m is the molecular weight of the sample N is Avogadro's number (6.022×10<sup>23</sup>) (particles/mole) a<sup>3</sup> is the volume of the unit cell, Z is the cubic unit cell which contains 8 atoms. X-ray density was decreases from 5.144 to 4.862 g/cm<sup>3</sup> with increase of La<sup>3+</sup> ions. This may be due to change in volume of unit cell and also The X-ray density is inversely proportional to the volume of the unit cell. The strains in the unit cell of the crystal increased with substitution of La<sup>3+</sup> ions due to the induced crystalline anisotrophy [Chaudhari *et.al.*, 2004].

The bulk density (d<sub>B</sub>) is evaluated using the mentioned equation [Tholkappiyan *et.al.*, 2014];

$$d_m = \frac{m}{\pi r^2 t} \tag{5.4}$$

where r is the radius of the pellet, m is the mass of the pellet and t is thickness of the pellet. The smaller value of bulk density than the X-ray density may be attained due to the existence of pores in the prepared ferrites [Rezlescu *et.al.*, 1998]. The doping of La ions activates the process in ferrites and leads to increase in density [Bobade *et.al.*, 2012]. The increase in bulk density is due to difference in atomic weight of Lanthanum (138.90 amu) and manganese (54.93 amu).

The surface area of the prepared nanoferrites is calculated using the following expression [Tholkappiyan *et.al.*, 2014];

$$S = 6/d_X D \tag{5.5}$$

where  $d_x$  is the X-ray density and D is the diameter of the particles. The surface area (S) increases from (44.85 to 102.16) which may be due to a decrease in crystallite size.

The porosity ( $\rho$ ) is calculated using following relation [Ranjith Kumar *et.al.*,2015];

$$P = (1-d_B/d_X) \%$$
 (5.6)

The porosity decreases from 6.737 to 4.431% which is attributed to the increase in bulk density with adding La<sup>3+</sup> ions. Here D<sub>B</sub> and d<sub>x</sub> are the bulk and X-ray densities for the prepared sample. Structural parameters such as crystallite size dislocation density, micro strain, lattice constant volume of unit cells, surface area, bulk density, X-ray density and porosity are listed in Table 5.1.

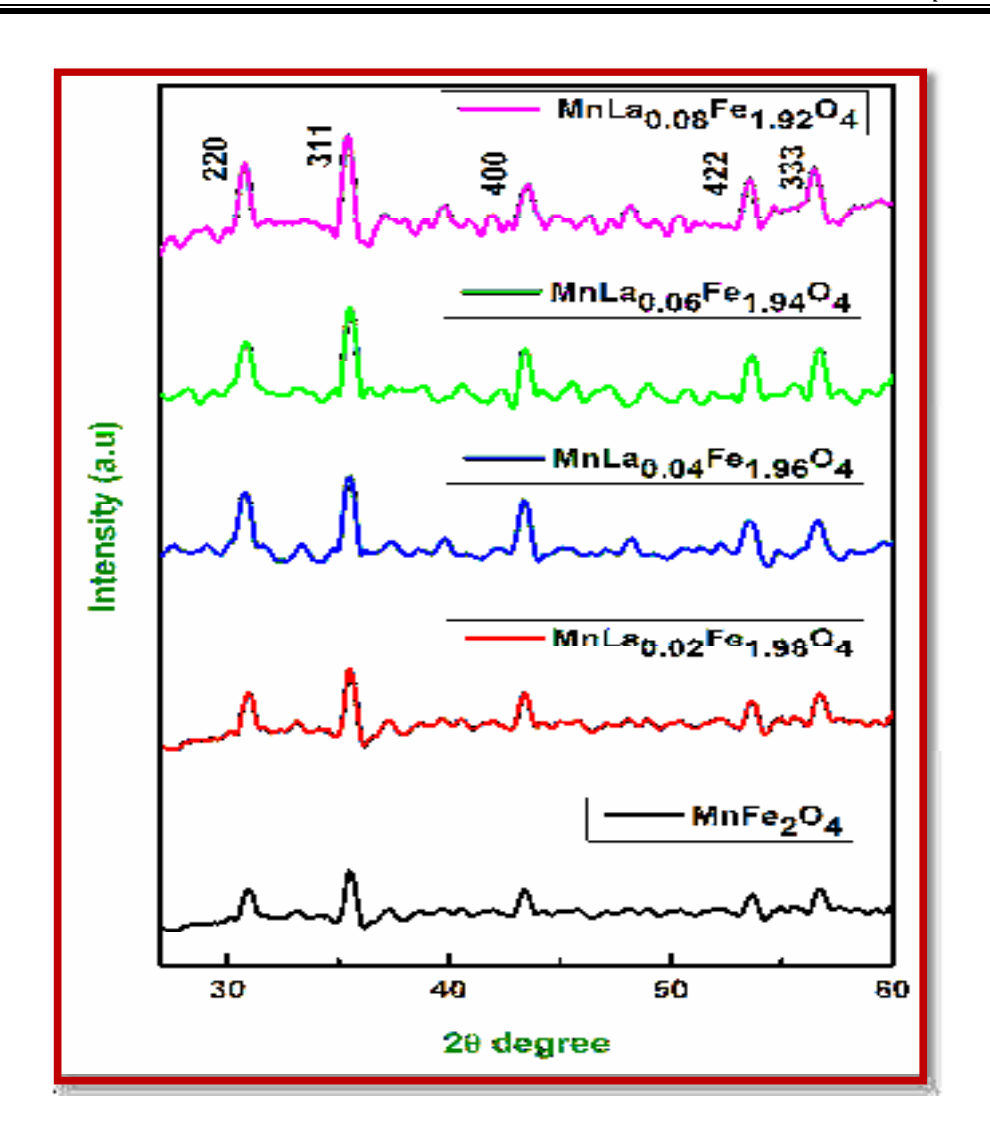


Figure 5. 2. X-ray diffraction pattern of MnLaxFe<sub>2-x</sub>O<sub>4</sub> (X=0.00 to 0.08) nanoferrites

Table 5.1. Structural parameters of MnLaxFe<sub>2-x</sub>O<sub>4</sub> (X = 0.00 to 0.08) nanoferrites

Composition	Crystal size (nm)	Lattice constant (a) Å	Volume of unit cell (a³) Å	X-ray density (ρxrd) (g/cm³)	Bulk density (d <sub>B</sub> ) (g/cm <sup>3</sup> )	Surface area (Sxrd) (m²/g)	Porosity (%)
X=0.00	26	8.7117	661.16	5.1448	1.6786	44.85	6.737
X=0.02	22	8.7515	670.26	5.0390	1.7888	54.12	6.450
X=0.04	18	8.7613	672.52	4.9869	1.8768	66.84	6.236
X=0.06	14	8.7777	676.30	4.9245	2.5383	87.03	4.845
X=0.08	12	8.7945	680.19	4.8662	2.7078	102.16	4.431

## **5.3.2 Optical Analysis**

The optical properties of prepared nanoferrties  $MnLa_XFe_{2-x}O_4$  with different composition X=0.00 to 0.08 were investigated using UV-diffuse reflectance measurement. The UV-DRS spectra recorded in the ranges from 200 to 800 nm could examine the band gap and electronic structure features. The optical absorbance is estimated using band gap energy  $(E_g)$  of the prepared Lanthanum doped manganese nanoferrties. The absorbance values are 228.12, 227.40, 226.10, 225.60 and 224.9 nm respectively with corresponding X=0.00 to 0.08 compositions.

The direct and indirect band gap energy values of prepared nanoferrites are calculated using relation between the absorption coefficient and the band [Mahulkar *et.al.*, 2009].

$$h\gamma\alpha = A(h\gamma - E_{gap})^n \tag{5.7}$$

where  $\alpha$  is the absorption coefficient, h is Planck's constant,  $\gamma$  is the frequency of light, A is a proportional constant, and  $E_g$  is the band gap and exponent n is the different type electronic transition n=1/2 and n=2 for direct and indirect band gap energy.

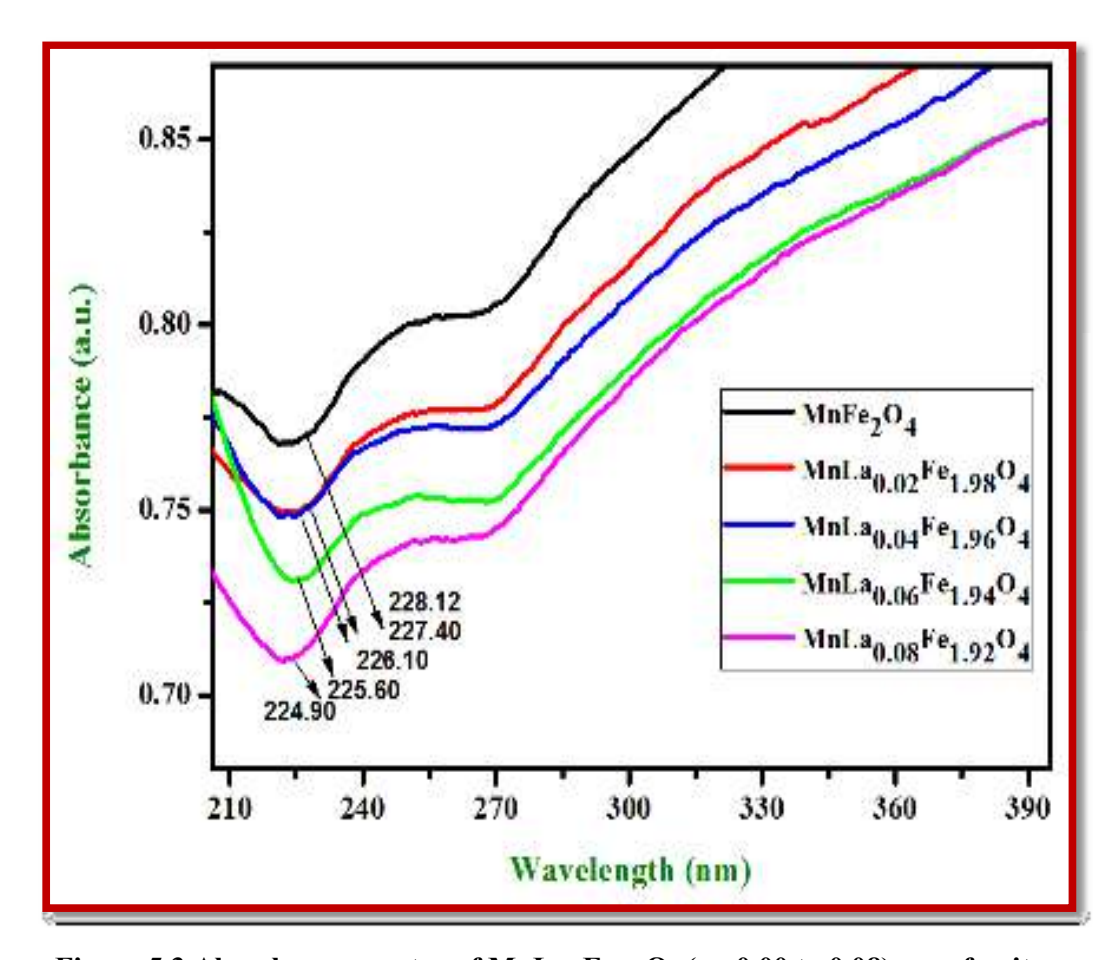


Figure 5.3 Absorbance spectra of MnLaxFe<sub>2-x</sub>O<sub>4</sub> (x= 0.00 to 0.08) nanoferrites

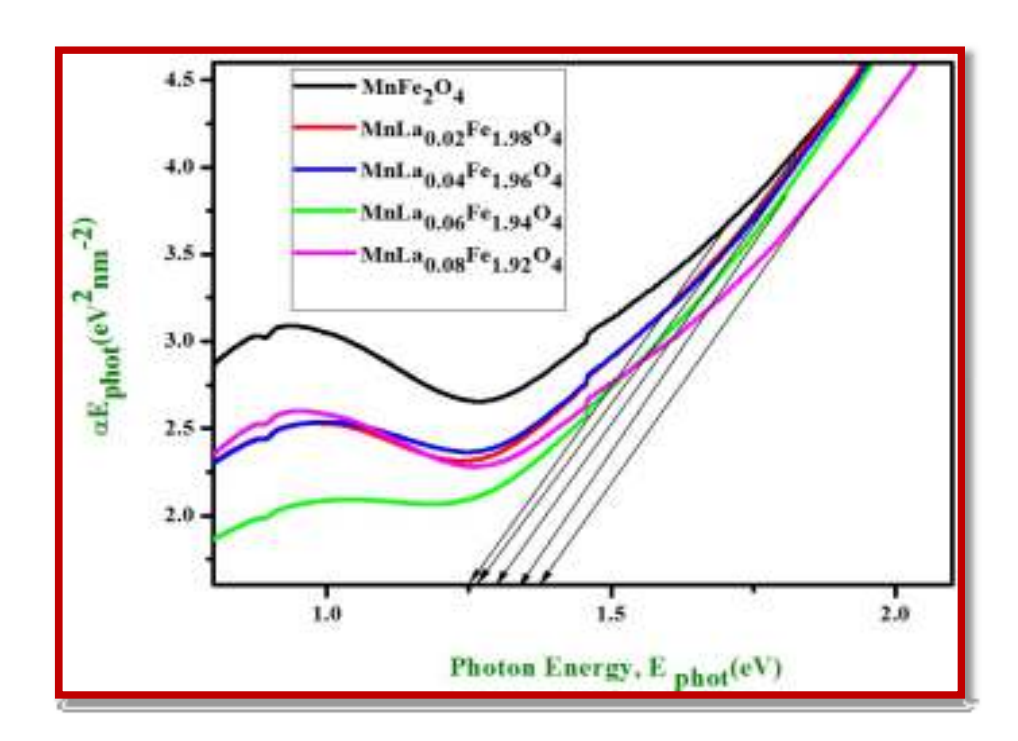


Figure 5.4 Direct bandgap energy of MnLaxFe<sub>2-x</sub>O<sub>4</sub> (X= 0.00 to 0.08) nanoferrites

Figure 5.4 associates the Tauc plot between  $(\alpha \ E_{photon})^2 \ Vs \ E_{photon}$  and the energy band gap values such as 1.25, 1.26, 1.30, 1.34 and 1.38 eV respectively. The band gap value of prepared Lanthanum doped manganese nanoferrites increases with increase  $La^{3+}$  ions concentration (X=0.00 to 0.08).

Figure 5.5 demonstrates the Tauc plot between  $(\alpha)^2$  vs E <sub>phot</sub> and the indirect energy band gap values of prepared nanoferrites such as 1.89, 1.98, 2.13, 2.27 and 2.35 eV respectively. The value of absorbance and bandgaps are listed in Table 5.3. The overview of result demonstrates that the improvement of energy levels or interface defects may be attributed to synergistic effect of Lanthanum with nanoferrites, and then recombination of decreased electron hole, which resulted in an increased band gap [Pinjari *et.al.*,2010].

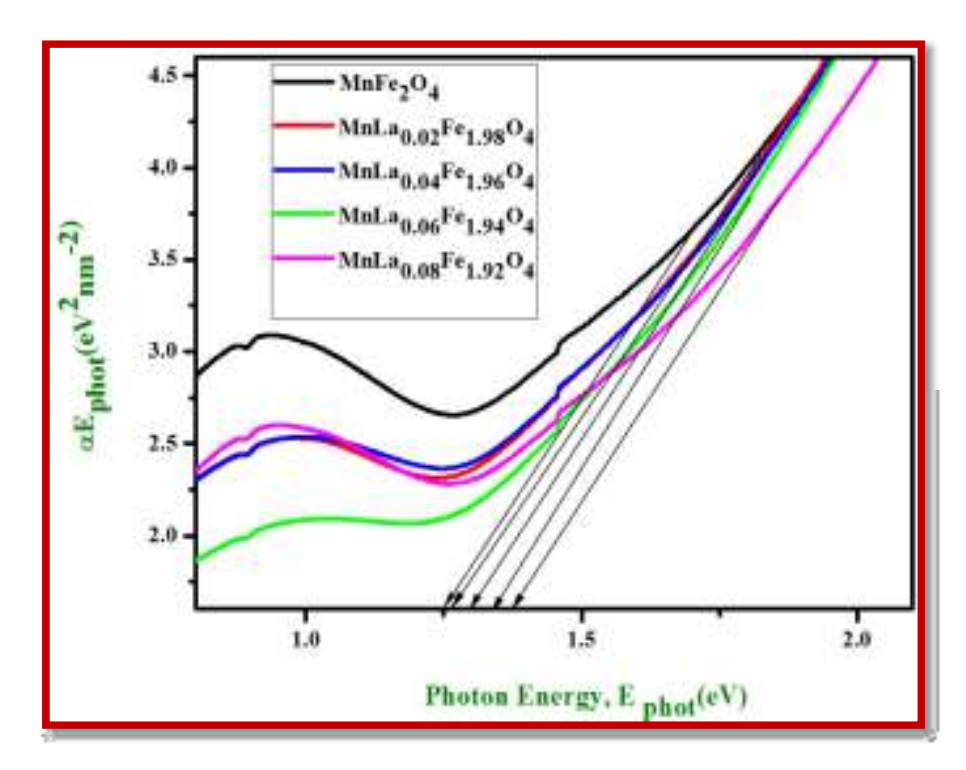


Figure 5.5 Indirect bandgap energy of MnLaxFe<sub>2-x</sub>O<sub>4</sub> (X= 0.00 to 0.08) nanoferrites

Table 5.2 Optical parameters of  $MnLaxFe_{2-x}O_4$  (x = 0.00 to 0.08) nanoferrites.

Composition	Absorbance (nm)	Indirect bandgap energy (eV)	Direct bandgap energy (eV)
X=0.00	228.12	1.89	1.25
X=0.02	227.40	1.98	1.26
X=0.04	226.10	2.13	1.30
X=0.06	22560	2.27	1.34
X=0.08	224.90	2.35	1.38

## **5.3.3 Functional Group Analysis**

Figure 5.6 shows the FT-IR spectra of Lanthanum doped manganese nanoferrites with different composition (X = 0.00 to 0.08) recorded by vibrational appropriate in the region 4000-400cm<sup>-1</sup>. FT-IR spectra are performed to give

information corresponding to the phase formation of spinel ferrites and other structural changes [Devi *et.al.*, 2017].

The band exists in the range of 562 cm<sup>-1</sup> may be due to the stretching vibration of metal oxygen in tetrahedral and octahedral sites. The band at 1366 cm<sup>-1</sup> represents for C-H bending bond due to carboxylic acid (Citric Acid). The wave number near at 2368 cm<sup>-1</sup> band is related C=N bond [Gupta *et.al.*, 2017]. The broad and strong band of oxygen hydrogen stretching vibration of remaining water appeared at wave number 3187 cm<sup>-1</sup> [Köseoglu *et.al.*, 2011].

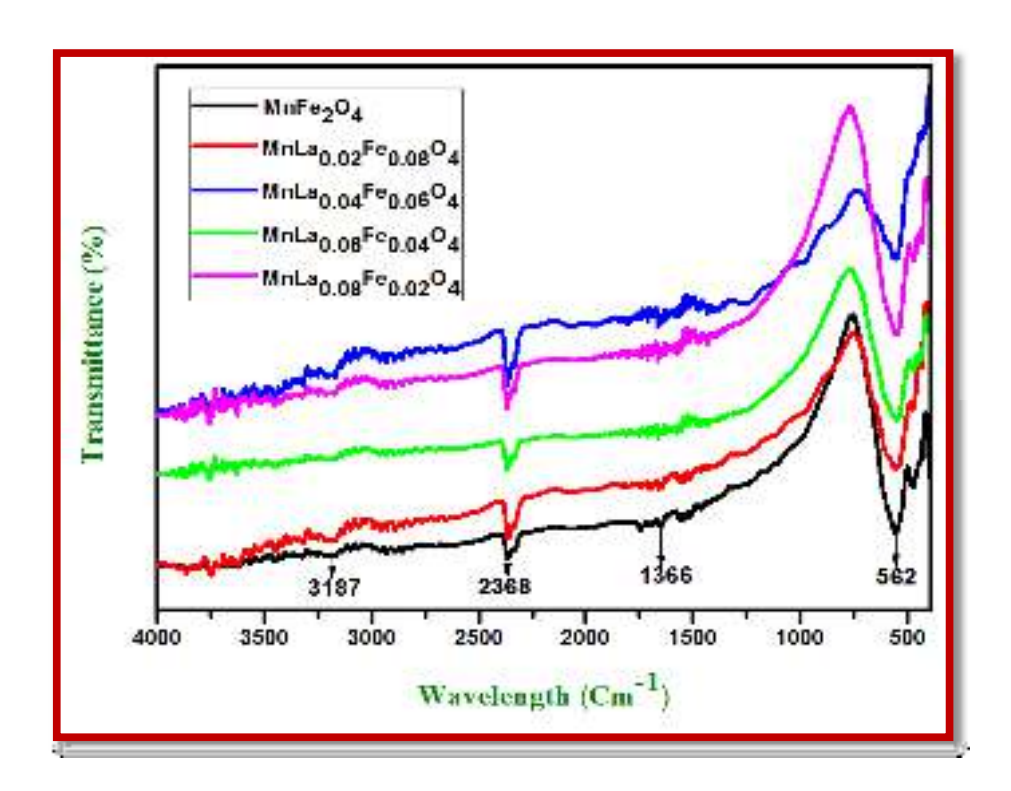


Figure 5.6 FT- IR spectra of MnLaxFe<sub>2-x</sub>O<sub>4</sub> (X = 0.00 to 0.08) nanoferrites

Table 5.3 Functional parameters of prepared MnLaxFe<sub>2-x</sub>O<sub>4</sub> (X = 0.00 to 0.08) nanoferrites

S.No	Vibrational	Experimental absorption (cm <sup>-1</sup> )					
	assignments	X= 0.00	X = 0.02	X = 0.04	X = 0.06	X = 0.08	
1	Metal - oxygen stretching vibration	562	562	562	562	562	
2	CH bending of carboxylic acid	1366	1366	1366	1366	1366	
3	Stretching vibration of C=N	2368	2368	2368	2368	2368	
4	O - H stretching vibration	3187	3187	3187	3187	3187	

## 5.3.4 Surface Morphology with EDAX

The morphology of prepared samples is obtained by FESEM which is shown in Figure 5.7. It reveals that spherical shape with uniform grain. This happened due to the diffusion of La<sup>3+</sup> ions mainly closer to the grain boundary, which exhibits ion and oxygen vacancies [Xing *et.al.*,2012]. There is some agglomeration occurred is obtained due to typical magnetic attraction of the spinel ferrites [Al-Ghamdi *et.al.*,2017]. Figure 5.7, depict EDAX spectra for a prepared sample which confirms the presence of Mn, La, Fe and O with few impurities.

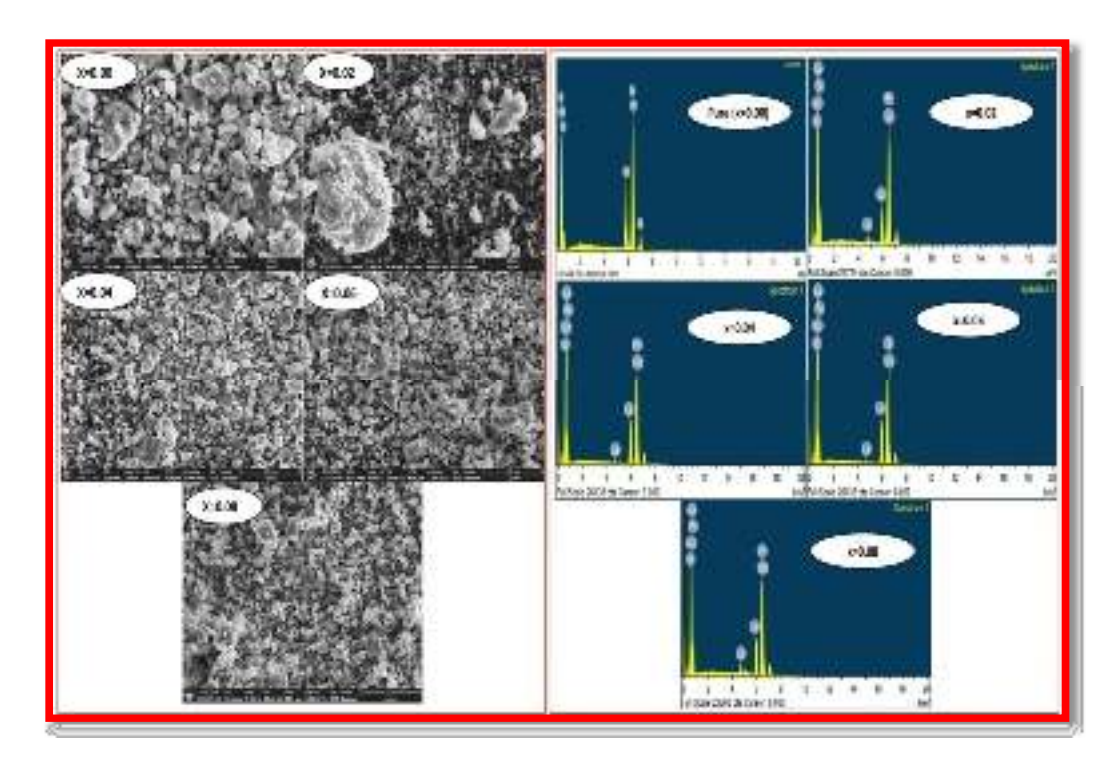


Figure 5.7 FESEM with EDAX images of prepared MnLaxFe<sub>2-x</sub>O<sub>4</sub>
(X = 0.00 to 0.08) nanoferrites

## 5.3.5 Magnetic Analysis

The M-H loop for the prepared Lanthanum doped Manganese nanoferrites MnLa<sub>X</sub>Fe<sub>2-x</sub>O<sub>4</sub> with series X=0.00 to 0.08 are plotted using Vibrating Sample Magnetometer (VSM). All the hysteresis loops are scanned up to 15,000 (Oe), recorded at room temperature. The shape and width of loops are based on few factors such as calcinating temperature, chemical composition, porosity, cation distribution and grain size etc. From Figure 5.8 it is learnt that S shaped hysteresis loops promote soft and ferromagnetic natures for prepared ferrites. The magnetic saturation (M<sub>S</sub>) in manganese ferrites decreases with decrease of crystallite size due to increase of surface effect [Cullity *et.al.*, 1978]. The values of saturation also decrease from 81.57 to 51.31 with increase in La<sup>3+</sup> ions which is attributed to smaller magnetic moment of

La (0 IB) than Fe (5 IB). In general, magnetic moment of rare earth ions is due to 4f-electrons [Shirsath 40 *et.al.*,2014].

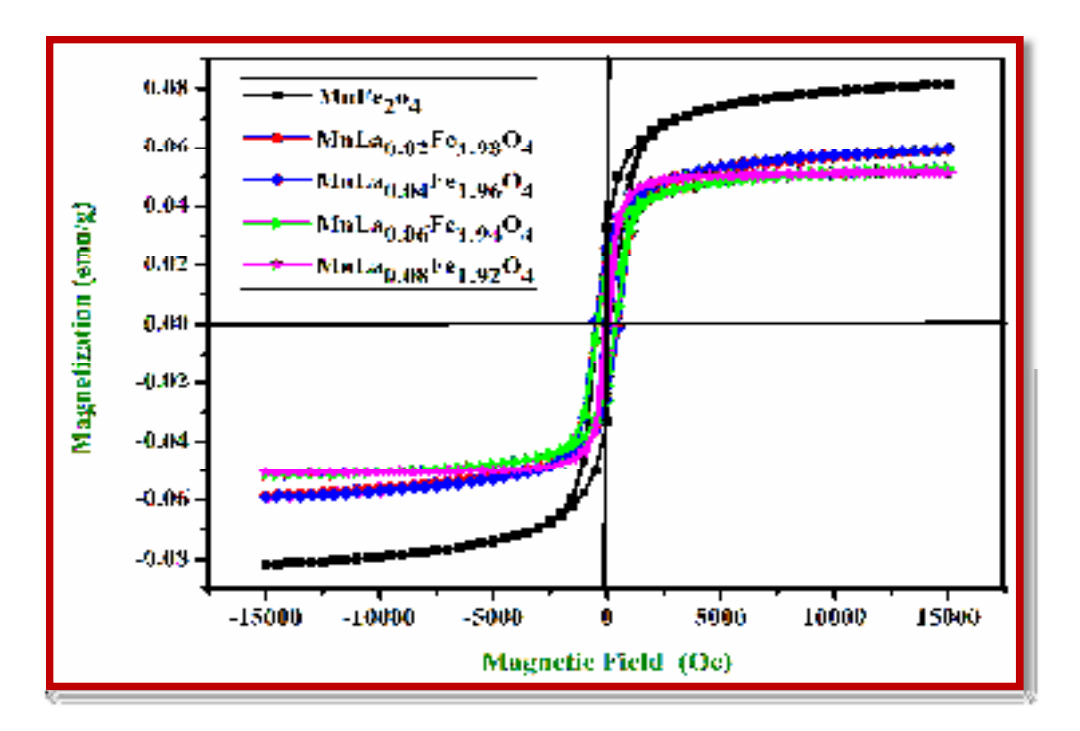


Figure 5.8 Hysteresis loop of  $MnLaxFe_{2-x}O_4$  (X = 0.00 to 0.08) nanoferrites

Magnetic saturation for spinel nanoferrites is adopted by the super exchange interaction between tetrahedral (A site) and Octahedral (B site) cations. Here three types of exchange interaction are placed between the magnetic ions at tetrahedral (A) and Octahedral (B) site in spinal structure such as A-A interaction, B-B interaction and A-B interactions. Among these A-B Interactions predominate the intra sub lattice than A-A, B-B interactions. The obtained A-B interaction is due to non-magnetic nature for La<sup>3+</sup> ions, which implies that exchange of ion interaction does not occur with closest neighbouring ions [John Jacob *et.al.*, 2010]. The values of coercivity 105 Oe to 517.37 Oe increases with increase of La<sup>3+</sup> ions for prepared nanoferrites. This effect on coercivity based on some factors like anisotrophy, magneto crystallinity,

magnetic particle and domain size of the material etc [Mathew George *et.al.*,2006]. The changes of coercivity with crystal size are due to the change in multi domain to single domain nature [Mathew George *et.al.*,2006]. The magnetic saturation and coercivity is inversely proportional to each other through Brown's relation [Razia Nongjai *et.al.*,2012]. The present work agrees this relation of decreasing magnetic saturation to Lanthanum concentrations. Earlier reports have explained that the larger lonic radii of rare earth substitution in spinel ferrites have increased the coercivity [Pachpinde *et.al.*,2014]. The squareness ratio and anisotrophy constant of MnLa<sub>x</sub>Fe<sub>2-x</sub>O<sub>4</sub> (X = 0.00, 0.02, 0.04, 0.06 and 0.08) nanoferrites are evaluated through below mentioned equations [Gupta *et.al.*,2017].

Squareness ratio = 
$$\frac{M_r}{M_s}$$
 (5.8)

$$K = \frac{H_c M_s}{0.98}$$
 (5.9)

where  $M_r$  is the remanent magnetization (or) retentivity, K is the anisotrophy constant and  $H_c$  is coercivity. The values of squareness ratio are less than 0.5 for all the prepared samples, which denotes uniaxial anisotropy contribution in the obtained nanoferrites [Tholkappiyan *et.al.*,2015]. Uniaxial anisotropy is a precondition for a hysteresis loop in ferromagnetic ferrites. Furthermore, Bohr Magnetization ( $\eta_{\beta}$ ) in magnetic moment ( $\mu_{\beta}$ ) is calculated using the following equation [Gupta *et.al.*,2017].

$$\Pi_B = \frac{MXM_S}{5585}$$
(5.10)

where x is the concentration and M is the molecular weight of  $La^{3+}$  ion substitution. The magnetic parameters such as magnetic saturation ( $M_s$ ) retentivity

 $(M_r)$ , coercivity  $(H_c)$ , squareness ratio  $(M_r/M_s)$ , anisotrophy constant (K) and Bohr magnetron  $(\eta_\beta)$  are observed from M-H measurements as listed in Table 5.4. In the present study, the value of coercivity is few hundred Oersteds (Oe) of prepared Lanthanum doped Manganese nanoferrites and with such a low value of coercivity nanoferrites materials are favorable for electromagnetic radiation materials [Azadmanjiri *et.al.*, 2004].

Table 5.4 Magnetic parameters of prepared MnLaxFe<sub>2-x</sub>O<sub>4</sub> (X = 0.00 to 0.08) nanoferrites.

Composition	Magnetization (M <sub>s</sub> ) (emu/g)	Remanent magnetization (M <sub>r</sub> ) (emu/g)	Coercivity (Hc) (Oe)	Squareness ratio (M <sub>r</sub> /M <sub>s</sub> ) (No unit)	Anisotrophy constant (K) (Oe)	Bohr magneton (η <sub>B</sub> ) (μ <sub>B)</sub>
x = 0.00	81.57	33.08	105.00	0.4055	87.39	0.3739
x = 0.02	59.56	26.03	392.55	0.4370	23.85	0.2711
x = 0.04	58.73	25.86	429.59	0.4403	25.74	0.2654
x = 0.06	52.00	21.15	516.93	0.4067	27.42	0.2334
x = 0.08	51.31	09.33	517.32	0.1818	27.08	0.2287

#### **5.3.6 Impedance Analysis**

Impedance spectroscopy is a useful technique which is widely used to separate real and imaginary part of the electrical parameter to propose the material's electrical properties. The impedance spectra values of prepared nanoferrites have capacitance and resistive components. Figure 5.11 clearly shows that successive semicircles represent electrical phenomena attributed to grain, grain boundaries and interfacial etc. In general, low frequency regions are effective in grain boundaries while the grains are effective in high frequency region. Thus, appearing of semi-circle in low frequency region enables the grain boundary contribution while grains are enabling to high frequency contribution. The real part (Z') of the spectra values for prepared

nanoferrites are corresponds low frequency to high frequency in the range of 100 mHz to 10 MHz at room temperature.

Figure 5.9 implies to impedance in frequency graph decreases with increase in applied frequency and then remain same at higher frequency. The constant Z' value at high frequency promotes the dominant contribution from grain boundary. The low value at high frequency implies the release of space charges and an improvement of the mobility of charge carrier [Kooti *et.al.*,2012].

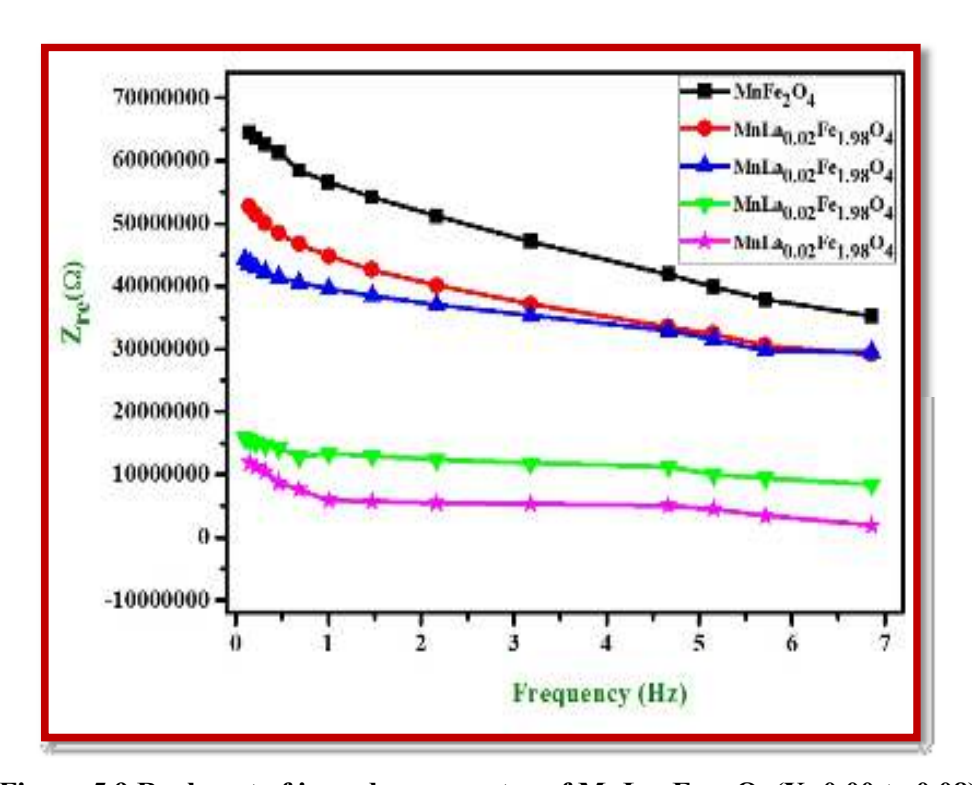


Figure 5.9 Real part of impedance spectra of MnLaxFe<sub>2-x</sub>O<sub>4</sub> (X=0.00 to 0.08) nanoferrites.

The imaginary part (Z'') of the Lanthanum doped manganese nanoferrites is represented in Figure 5.10. It decreases with increase of applied frequency and then merges at high frequency. The decrease in increasing frequency is due to the reduction loss in the resistive part of the prepared nanoferrites. The noticed peaks in

the imaginary part (Z") are one due to existence of the space charge relaxation attributed with the charge carriers concluding from oxygen vacancies [Azizar Rahman *et.al.*, 2014].

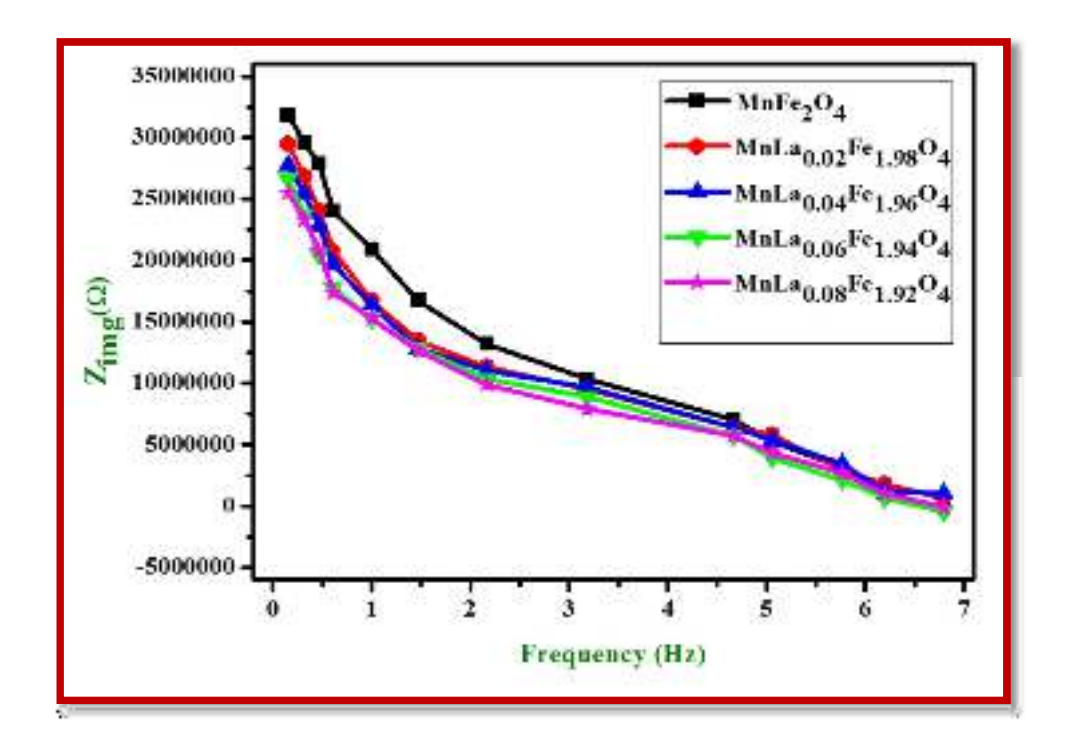


Figure 5.10 Imaginary part of impedance spectra of MnLaxFe<sub>2-x</sub>O<sub>4</sub> (X=0.00 to 0.08) nanoferrites

The Nyquist plot of impedance spectra for prepared Lanthanum doped manganese nanoferrites with series (X=0.00 to 0.08) are shown in Figure 5.11. The plot consists of clear semicircle arc which consists the grain and grain boundaries have contribution to the conductivity. These semicircles contain two types of relaxations with increase in La<sup>3+</sup> ion concentrations. The lower frequency side relaxation is attributed to grain boundary contribution and higher frequency grain contribution is mainly due to the effect of small crystal size from XRD. Furthermore, it is observed that the value of Nyquist plot decreases with increase of Lanthanum

concentrations which implies that impedance is inversely proportional to the conductivity, as the conductivity increases with increase of La<sup>3+</sup> ion. Hence this is well corroborated from conductivity values [Li *et.al.*, 2001].

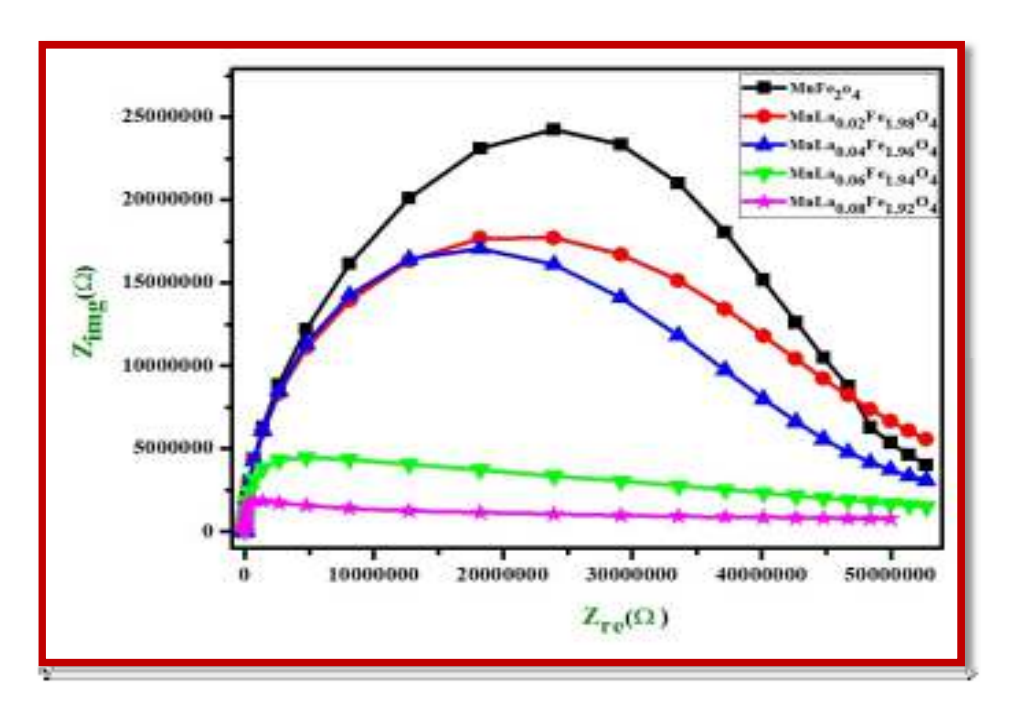


Figure 5.11 Nyquist plots of MnLaxFe<sub>2-x</sub>O<sub>4</sub> (X= 0.00 to 0.08) nanoferrites.

## **5.3.7 Dielectric Analysis**

The dielectric behavior of iron (Fe) oxide is attributed to the electric dipole created due to the charge ion exchange interaction between the divalent and trivalent metal cations with in the spinel structure, calcination temperature and time, method of preparation, chemical composition and occupancy of site in metal cation among the tetrahedral and octahedral sites on dielectric properties of ferrites [Ramana et.al.,2013, Rabia Pandit et.al.,2014]. The dielectric behavior of ferrites as a function of frequency gives important information of the behavior of the localized charge carriers and understanding the mechanism of dielectric polarization in ferrites [Pervaiz et.al.,2012].

# 5.3.7(a) compositional effect on dielectric constant ( $\epsilon$ ') and complex dielectric constant ( $\epsilon$ ")

The variation of dielectric constant ( $\epsilon$ ') and complex dielectric constant ( $\epsilon$ ") measured at the frequency in range 100 mHz to 10 MHz for Lanthanum doped manganese nanoferrites MnLa<sub>X</sub>Fe<sub>2-X</sub>O<sub>4</sub> with series X=0.00 to 0.08 at room temperature are depicted in Figure 5.12 (a,b) respectively. From the Figure, it can be noticed that both dielectric constant ( $\epsilon$ ') and complex dielectric constant ( $\epsilon$ ") increase with increase of La<sup>3+</sup> ions concentration.

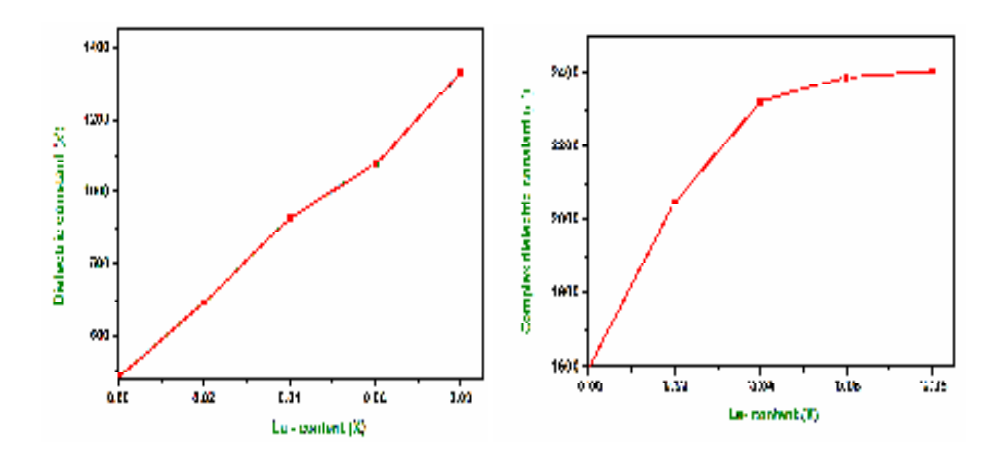


Figure 5.12 (a,b) Dielectric constant and Complex dielectric constant of the prepared  $MnLaxFe_2-xO_4$  (X=0.00 to 0.08) nanoferrites

The obtained results from electron interchange between  $Fe^{2+} \leftrightarrow Fe^{3+}$  in local displacement produce polarization of charges in these ferrites. Thus, it reveals number of ferrous ions on octahedral sites play a predominant in the process of conduction and dielectric polarization [Tatina *et.al.*,2007]. The hindrance of electron transfer between  $Fe^{2+}$  and  $Fe^{3+}$  ions are leading to decrease the polarization. The  $La^{3+}$  ion occupy octahedral sites owing to their larger ionic radius (1.06Å).

## 5.3.7(b) Dielectric Constant (ε')

Figure 5.13, shows the variation in the dielectric constant as a function of frequency for MnLa<sub>X</sub>Fe<sub>2-X</sub>O<sub>4</sub> nanoferrites with series X = 0.00 to 0.08 at room temperature. The value of dielectric constant for high frequency region dependent in the low frequency region while high frequency region it is frequency independent. The dielectric constants increase with increase of La<sup>3+</sup> ions for prepared Lanthanum doped manganese nanoferrties which is evaluated using the following relation [Gupta *et.al.*,2017];

$$\varepsilon' = \frac{cd}{\varepsilon_0 A} \tag{5.11}$$

where C is the capacitance of the pellet,  $\varepsilon_0$  is the permittivity of free space, A is the area of the pellet and d is the thickness of the pellet. The values of dielectric constant and complex dielectric constant are high at lower frequency and then decrease with increase in frequency for increasing La<sup>3+</sup> ions. The calculated dielectric constant values are 486, 692, 928, 1076 and 1333 with series X= 0.00, 0.02, 0.04, 0.06 and 0.08 respectively. The dielectric constant values decrease with increase of frequencies. This dispersion behavior in the ferrites can be explained with Maxwell Wagner type interfacial polarization in compliance with Koop's phenomenological theory [Hu Ping*et.al.*,2010, Pankhurst *et.al.*,2003]. According to Maxwell - Wagner type, dielectric differs for two-layer non-uniform medium, where first layer denotes high conducting grains at higher frequency, while second layer denotes poor conducting grain boundaries at low frequency [Hu Ping *et.al.*,2010]. The polarization can be occurred due to interchange of electrons between Fe<sup>2+</sup> and Fe<sup>3+</sup> on applying

field in ferrites, which follows the behavior of conducting mechanism [Tobias Neuberger *et.al.*,2005].

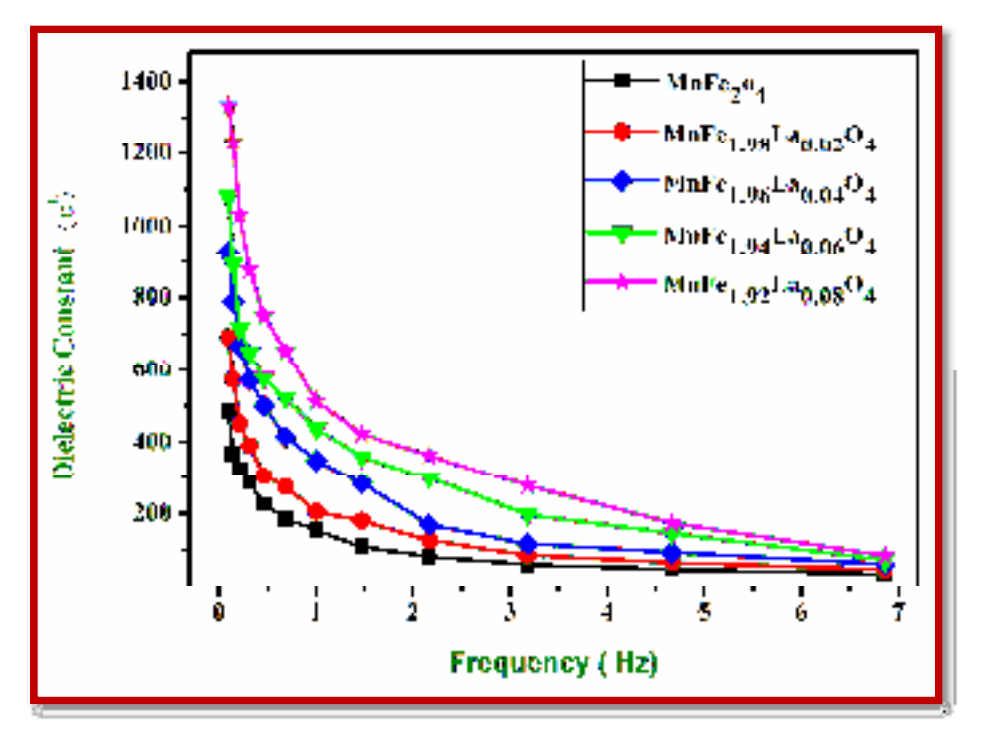


Figure 5.13 Dielectric constant of the MnLaxFe<sub>2-x</sub>O<sub>4</sub> (X = 0.00 to 0.08) nanoferrites

The decreasing polarization with increasing frequency leads to decrease in dielectric constant may be accumulated to decrease of electron exchange between Fe<sup>2+</sup> and Fe<sup>3+</sup> with applied field [Tobias Neuberger *et.al.*, 2005]. In spinel nanoferrites presence of La<sup>3+</sup> ions wish to occupy octahedral sites. Hopping between La<sup>3+</sup> and Fe<sup>3+</sup> increases at octahedral site with increase of La<sup>3+</sup> ion. Hopping of ion exchange between dissimilar metal is more effective when compared to similar metal ion [Bin Liu *et.al.*, 2007]. This mechanism gets activated to intensify the conduction while there is an increase of La<sup>3+</sup> ions. Thus, the dielectric constant increases with La content.

## 5.3.7 (c) Dielectric Loss

Variation of dielectric loss (or) tangent loss with frequency is depicted in Figure 5.14. From this it is clearly noticed that dielectric loss decreases with increase in frequency. This indicates a strong association in dielectric process and conduction process [Bin Liu *et.al.*, 2007]. The obtained dielectric loss decreases with increase of higher frequency. This dielectric loss may depend on certain factors such as composition, synthesis method and Fe<sup>2+</sup> content [Hu Ping *et.al.*, 2010].

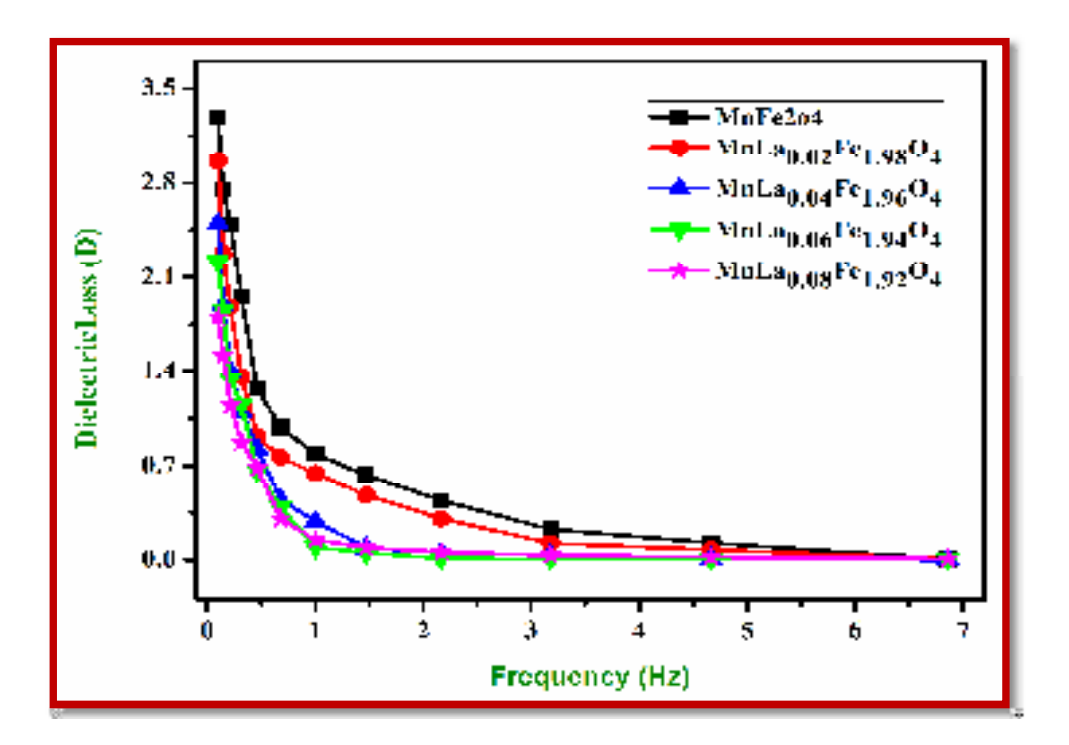


Figure 5.14Dielectric loss of MnLaxFe<sub>2-x</sub>O<sub>4</sub> (X = 0.00 to 0.08) nanoferrites

The dielectric loss and complex dielectric constant of prepared nanoferrites were estimated using the below mentioned relation [Gupta *et.al.*, 2017].

$$\tan \delta = \frac{1}{2\pi f \epsilon_0 \epsilon'} \tag{5.12}$$

$$\varepsilon'' = \varepsilon' \tan \delta$$
 (5.13)

The obtained dielectric loss values of the prepared nanoferrites are 3.28, 2.95, 2.50, 2.21 and 1.80 respectively. The tangent loss decreases with increase of La<sup>3+</sup> ions imply a decrease in total number of hopping mechanisms, as tangent loss is directly proportional to number of dipole available for relaxation [Iguchi *et.al.*, 1991]. This is agreed with impedance analysis; where the increase of La<sup>3+</sup> improves the resistive properties of materials thereby squash the Mn<sup>2+</sup>↔ Mn<sup>3+</sup> and Fe<sup>2+</sup>↔ Fe<sup>3+</sup> linkages [Pawan Kumara *et.al.*, 2010]. Even at higher frequencies, tangent loss is small which promote the application of these prepared ferrites is suitable to electromagnetic devices.

### 5.3.7(d) AC Conductivity

Figure 5.15 Shows AC conductivity of prepared nanoferrites shows increasing trend at low frequency region whereas the mentioned behavior is exhibit at high frequency range. Here, both Maxwell-Wagner model and Koop's phenomenological theories are confirming that ferrite material consists of conducting grains dispersive by resistive layer of grain boundary. This conduction process is related to the dielectric polarization [Koops *et.al.*,1951]. So that, all the prepared nanoferrites are affected by grain boundaries with high resistance at low frequency region. However, at high frequency region, effect due to grain and increasing trend of hopping of charge carriers Fe<sup>2+</sup>- Fe<sup>3+</sup> at adjacent octahedral sites influence the increasing of conductivity [Akther Hossain *et.al.*,2011].

Figure 5.15 shows that the increase in AC conductivity with increase of La<sup>3+</sup> ions. It reveals that the magnitude of electronic transfer is based on the concentration of Fe<sup>3+</sup>/ Fe<sup>2+</sup> ion pairs located at B-sites [Elkestawy *et.al.*, 2010]. From the graph, it is

noticed that the AC conductivity increases with increase of  $La^{3+}$  ions gradually. The value of AC conductivity increases from 0.014 to 0.134 ( $\Omega$ cm<sup>-1</sup>) with increase of  $La^{3+}$  ions (x = 0.00 to 0.08).

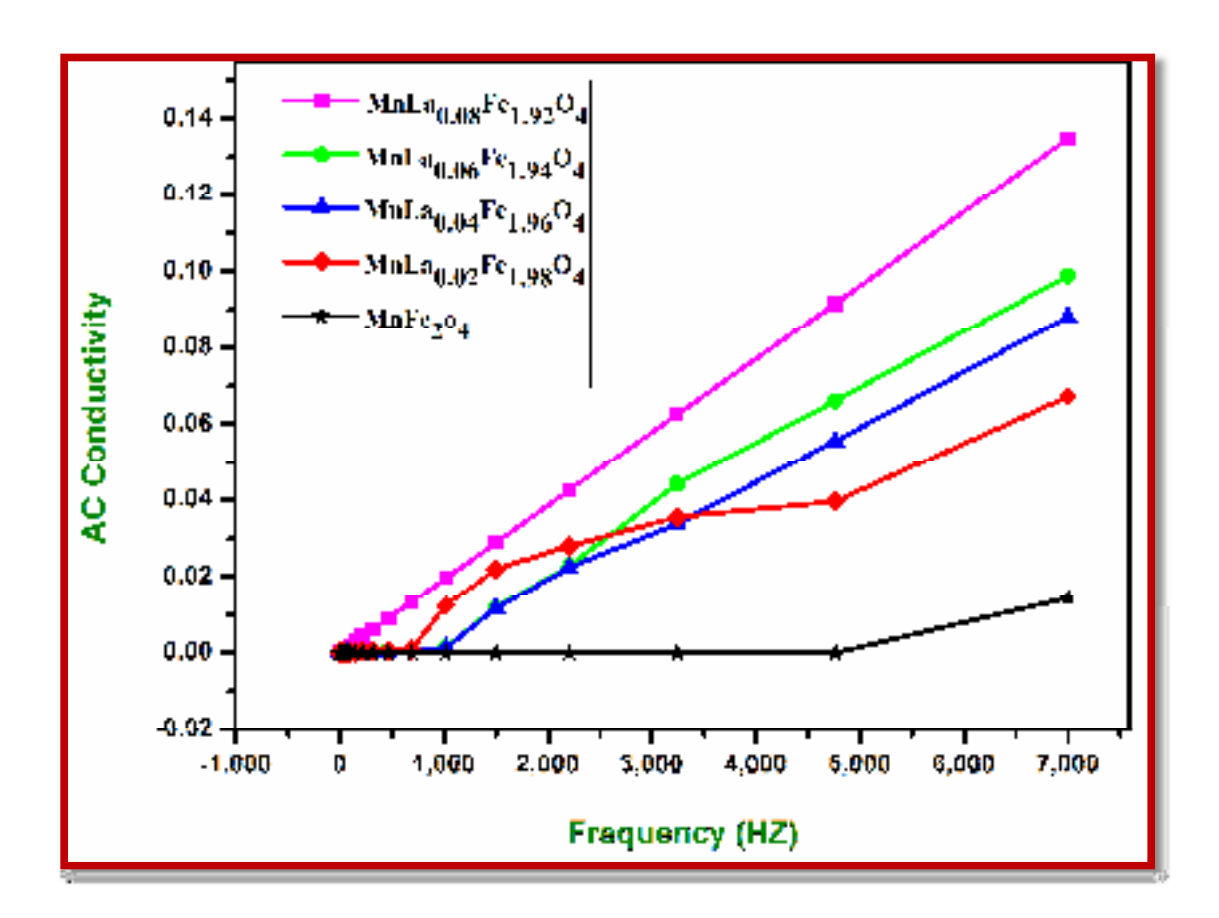


Figure 5.15 AC Conductivity vs Frequency of MnLaxFe<sub>2-x</sub>O<sub>4</sub> (X = 0.00 to 0.08) nanoferrites

The increase in AC conductivity is due to decrease in porosity confirms from XRD. It is noticed that at low frequency AC conductivity implies grain boundary contribution whereas high frequency can be attributed to the effect of grains [Navneet Singh *et.al.*, 2011, Bottger *et.al.*, 1985].

Table 5.5 Dielectric parameters of MnLaxFe<sub>2-x</sub>O<sub>4</sub> (X = 0.00 to 0.08) nanoferrites

Composition	Dielectric Constant (ɛ')	Dielectric Loss (tanδ) D	Complex Dielectric constant (ɛ")	AC Conductivity (ac) (Ωcm <sup>-1</sup> )
X=0.00	486.08	3.2839	1595.97	0.0134
X=0.02	692.37	2.9581	2048.09	0.0672
X=0.04	928.15	2.5017	2321.95	0.0882
X=0.06	1079.69	2.2128	2389.13	0.0989
X=0.08	1333.49	1.8039	2405.48	0.1347

#### **5.4 CONCLUSION**

Lanthanum doped Manganese nanoferrites were successfully synthesized by sol-gel method. These nanoferrites have cubic spinel structure with crystallite size from 26 to 12nm. The lattice constant and bulk density increased with increase of La<sup>3+</sup> ions, whereas X-ray density is inversely proportional to lattice constant and bulk density. The value of porosity decreases with increase of La<sup>3+</sup> ions. The absorption bands are noticed in the FTIR spectrum near 562 cm<sup>-1</sup>, which is confirms tetrahedral and octahedral stretching of Metal-Oxygen bond. The optical band gap values of the prepared Lanthanum doped Manganese nanoferrites are 1.89 - 2.35 eV, which improve with respect to the band gap 1.25 - 1.38 eV values of Mn nanoferrites due to impact of La<sup>3+</sup> ions. FESEM with EDAX reveals that the prepare nanoferrites have spherical morphology with few agglomerations and present elemental peaks attained consistently in all the compositions. The value of magnetic saturation is decreased from 81.5 to 51.3 emu/g and the value of coercivity increased from 105 to 517.32emu/g with increase of La<sup>3+</sup> ions whereas it showed magnetic saturation as inversely proportional to coercivity. VSM revealed that the prepared nanoferrites are

soft and ferromagnetic in nature. The dielectric constant and dielectric loss are decreased with increase of frequency and also dielectric constant and complex dielectric constant increased with increase of La<sup>3+</sup> ions. Impedance spectra reveal that the impedance response is over ruled by grain boundary behavior. The AC conductivity increases with increase of La<sup>3+</sup> ions. Hence, Lanthanum doped Manganese nanoferrites are favorable for electromagnetic applications.

## **REFERENCES**

**AktherHossain A.K.M,** Rahman M.A, Farhad S.F.U, Vilquinc B & Hidekazu Tanaka, 'Effect of Li substitution on the magnetic properties of LixMg<sub>0.40</sub>Ni<sub>0.60-2x</sub>Fe<sub>2+x</sub>O<sub>4</sub>ferrites', Physica B. 406 **(2011)** 1506–1512.

**Al-Ghamdi A.A,** Al-Hazmi F.S, Memesh L.S, Shokr F.S & Bronstein L.M, 'Evolution of the structure, magnetic and optical properties of Ni1-xCuxFe<sub>2</sub>O<sub>4</sub> spinel ferrites prepared by soft mechnochemical method', J. Alloys Compd. 712 **(2017)** 82.

**Azadmanjiri** J & Seyyed Ebrahimi S.A, 'Influence of stoichiometry and calcination condition on the microstructure and phase constitution of NiFe<sub>2</sub>O<sub>4</sub> powders prepared by sol gel autocombustion method', Phys. Status Solidi C. 1 (12) (2004) 3414.

**Azizar Rahman M** & Akther Hossain A.K.M, 'Electrical transport properties of Mn– Ni–Zn ferrite using complex impedance spectroscopy', Phys. Scr. 89 **(2014)** 025803 (8pp).

**Bin Liu** & Dieter K. Weller, 'Heat assisted magnetic recording film including superparamagnetic nanoparticles dispersed in an antiferromagnetic or ferrimagnetic matrix', U.S. Patent. 79(158) (2007) 346.

**Bobade D.H,** Rathod S.M & Maheshkumar L. Mane, Physica B. 407 (2012) 3700–3704.

**Bottger H** & Bryksin V.V, 'Hopping Conduction in Solids', (Akademie-Verlag, Berlin, **(1985).** 

**Chaudhari V,** Shirsath S.E, Mane M.L, Kadam R.H, Shelke S.B & Mane D.R, 'Crystallographic, magnetic and electrical properties of Ni<sub>0.5</sub>Cu<sub>0.25</sub> Zn<sub>0.25</sub>La<sub>x</sub>Fe<sub>2-x</sub>O<sub>4</sub> nanoparticles fabricated by sol-gel method', J. Alloys Compd. 549 **(2013)** 213e220.

**Chinnasamy C.N,** Narayanasamy A & Ponpandian N, 'Magnetic properties of nanostructured ferromagnetic zinc ferrite', J. Phys. Condens. Matter. 12 (2000) 7795.

Cullity B.D, 'Elements of X-Ray Diffraction', Addison-Wesley, Reading, MA, (1978).

**Devi** E.C & Soibam I, 'Structural and optical characterization of MnFe<sub>2</sub>O<sub>4</sub> nanoparticles', Adv. Mater. Proc. 2, 93–96 (2017).

**Devi E.C** & Soibam I, 'Effect of Zn doping on the structural, electrical and magnetic properties of MnFe<sub>2</sub>O<sub>4</sub> nanoparticles', Indian J. Phys. 91 **(2017)** 861–867.

**Dixit G,** Singh J.P, Srivastava R.C & Agrawal H.M, 'Magnetic resonance study of Ce and Gd doped NiFe<sub>2</sub>O<sub>4</sub> nanoparticles', J. Magn. Magn. Mater. 324 (2012) 479–483.

**Elkestawy M.A,** 'AC conductivity and dielectric properties of, Zn <sub>1-x</sub> Cu<sub>x</sub>Cr<sub>0.8</sub> Fe<sub>1.2</sub> O<sub>4</sub> spinel ferrites', J. Alloys Comp. 492 **(2010)** 616–620.

**Koops C.G,** 'On the Dispersion of resistivity and Dielectric constant of some semiconductors at audio frequencies', Phys. Rev. 83 (1951) 121.

**Fan G,** Tong J & Li F, 'Visible-light-induced photocatalyst based on cobalt-doped zinc ferrite nanocrystals', Ind. Eng. Chem. Res. 51 **(2012)** 13639–13647.

**Guo P,** Cui L, Wang Y, Lv M, Wang B & Zhao X.S, 'Facile synthesis of ZnFe<sub>2</sub>O<sub>4</sub> nanoparticles with tunable magnetic and sensing properties', Langmuir. 29 **(2013)** 8997–9003.

**Gupta N,** Jain P, Rana R & Shrivastava S, 'Current development in synthesis and characterization of nickel ferrite nanoparticle', Mater. Today-Proc. 4 **(2017)** 342–349.

**Hasting J.M** & Corliss L.M, 'An Antiferromagnetic Transition in Zinc Ferrite', Phys. Rev. 102 (6) (1956) 1460.

**Hemeda O.M,** Said M.Z, & Barakat M.M, 'Spectral and transport phenomena in Ni ferrite-substituted Gd O', J. Magn. Magn. Mater. 224 **(2001)** 132–142.

**Hu Ping**, Hai-bo Yang, De-a Pan, Hua Wang, Jian-jun Tian, Shen-gen Zhang, Xin-feng Wang & Alex A. Volinsky, 'Heat treatment effects on microstructure and magnetic properties of Mn–Zn ferrite powders', J. Magn. Magn. Mater. 322 **(2010)** 173–177.

**Iguchi E,** Kubota N, Nakamori T, Yamamoto N & Lee K.J, 'Polaronic conduction in *n*-type BaTiO<sub>3</sub> doped with La<sub>2</sub>O<sub>3</sub> or Gd<sub>2</sub>O<sub>3</sub>', Phys. Rev.B .43 (1991) 8646.

**Iqbal M.A,** Islam M, Ashiq M.N, Ali I, Iftikhar A & Khan H.M, 'Effect of Gd substitution on physical and magnetic properties of Li<sub>1.2</sub>Mg<sub>0.4</sub> Gd<sub>x</sub>Fe<sub>(2-x)</sub> O<sub>4</sub> ferrites', J. Alloy. Compd. 579 **(2013)** 181–186.

**Irshad Ali M.U,** Islam M, Ishaque & Hasan M. Khan, Muhammad Nazeem Ashiq, M.U. Rana, 'Structural and magnetic properties of holmium substituted cobalt ferrites synthesized by chemical co-precipitation method', Journal of Magnetism and Magnetic Materials. 324 **(2012)** 3773–3777.

**Islam R,** Hakim M.A, Rahman M.O, Das H.N & Mamun M.A, 'Study of the structural, magnetic and electrical properties of Gd-substituted Mn-Zn mixed ferrites', J. Alloys Compd. 559, 174–180 (2013).

**John Jacob M.A** & Khadar, 'Investigation of mixed spinel structure of nanostructured nickel ferrite', J. Appl. Phys. 107 **(2010)** 114310–114320.

**Katarzyna Winiarska,** Irena Szczygieł & Roman Klimkiewicz, 'Manganese-zinc ferrite synthesis by the sol-gel autocombustion method. Effect of the precursor on the ferrite's catalytic properties', Ind. Eng. Chem. Res. 52 **(2012)** 353–361.

**Kooti M** & Afshari M, 'Magnetic cobalt ferrite nanoparticles as an efficient catalyst for oxidation of alkenes', Sci. Iran. 19 (2012) 1991-1995.

**Köseogʻlu Y,** Bay M, Tan M, Baykal A, Sözeri H, Topkaya R & Akdogʻan N, 'Magnetic and dielectric properties of Mn<sub>0.2</sub>Ni<sub>0.8</sub>Fe<sub>2</sub>O<sub>4</sub> nanoparticles synthesized by PEG-assisted hydrothermal method', J. Nanopart. Res. 13 **(2011)** 2235–2244.

**Kryder M.H,** MRS Bull, Ultrahigh-Density Recording Technologies. 21 (1996) 17–19.

**Lawrence Kumar,** Manoranjan Kar, "'ffect of La<sup>3+</sup> substitution on the structural and magnetocrystalline anisotropy of nanocrystalline cobalt ferrite', Ceramics International. **(2012)** 4771-4782.

**Li C,** Wang J, Su E, Chen H, Zhong W & Zhang P, 'Effect of Mn<sup>2+</sup>on the electrical nonlinearity of (Ni, Nb)-doped SnO<sub>2</sub> varistors', Ceramics International. 27 (2001) 655.

**Mathew George,** Swapna S Nair, Asha Mary John, Joy P.A & Anantharaman M.R, 'Structural, magnetic and electrical properties of the sol-gel prepared Li0.5Fe2.5O<sub>4</sub> fine particles', J. Phys. D: Appl. Phys. 39 (2006).

**Mahulkar A.V,** Riedel C, Gogate P.R, Neis U & Pandit A.B, 'Effect of dissolved gas on efficacy of sonochemical reactors for microbial cell disruption: experimental and numerical analysis', Ultra Sonochem. 16 **(2009)** 635–643.

**Meaza T.M,** Attiab S.M & Abo El Ataa A.M, 'Effect of tetravalent titanium ions substitution on the dielectric properties of Co-Zn ferrites', J. Magn. Magn. Mater. 257 (2003) 296–305.

**Navneet Singh,** Ashish Agarwal & Sujata Sanghi, 'Dielectric relaxation, conductivity behavior and magnetic properties of Mg substituted Zn-Li ferrites', Curr. Appl. Phys. 11 **(2011)** 783–789.

**Naik P.P,** Tangsali R.B, Meena S.S & Yusuf S.M, 'Influence of rare earth (Nd<sup>+3</sup>) doping on structural and magnetic properties of nanocrystalline manganese-zinc ferrite', Mater. Chem. Phys. 191 **(2017)** 215–224.

**Nalbandian L,** Delimitis A, Zaspalis V.T, Deliyanni E.A, Bakoyannakis D.N & Peleka E.N, 'Hydrothermally prepared nanocrystalline Mn–Zn ferrites: Synthesis and characterization', Microporous Mesoporous Mater. 114 (2008) 465–473.

**Nitendar Kumar,** Pran Kishan, & Zaidi Z.H, 'Effect of Mg Ti and Zn Ti substitutions on electrical and magnetic properties of Li ferrite', Journal of Magnetism and Magnetic Materials. 184 (1998) 355-357.

**Pachpindec A.M,** Langade M.M, Lohar K.S, Patange S.M, & Shirsath S.E, 'Impact of larger rare earth Pr <sup>3+</sup> ions on the physical properties of chemically derived Pr<sub>x</sub>CoFe <sub>2-x</sub>O<sub>4</sub> nanoparticles', Chemical Physics. 429 **(2014)** 20-26.

**Pankhurst Q.A,** Connolly J, Jones S.K & Dobson J.J, 'Applications of magnetic nanoparticles in biomedicine', J. Phys. D: Appl. Phys. 36 (2003) R167.

**Pawan Kumar**, Sharma S.K, Knobel M & Singh M, 'Effect of La<sup>3+</sup> doping on the electric, dielectric and magnetic properties of cobalt ferrite processed by co precipitation technique', Journal of Alloys and Compounds. 508 **(2010)** 115–118.

**Pervaiz E** & Gul I.H, 'Structural, electrical and magnetic studies of Gd<sup>3+</sup> doped cobalt ferrite nanoparticles', International Journal of Current Engineering and Technology. 2 (2012) 377.

**Pinjari D.V** & Pandit A.B, 'Cavitation milling of natural cellulose to nanofibrils', Ultra Sonochem. 17 **(2010)** 845–852.

**Prashant Thakur,** Rohit Sharma, Manoj Kumar, Katyal S.C, Nagesh Negi, N. Thakur, Vineet Sharma & Pankaj Sharma, 'Superparamagnetic La doped Mn–Zn nano ferrites: dependence on dopant content and crystallite size', Mater. Res. Express. 3 (2016) 075001.

**Rabia Pandit,** Sharma K.K, Pawanpreet Kaur & Ravi Kumar, 'Cation distribution-controlled dielectric, electrical and magnetic behavior of In<sup>3+</sup> substituted cobalt ferrites synthesized via solid-state reaction technique', Mater. Chem. Phys. 148 **(2014)** 988-999.

**Ramana** C.V, Kolekar Y.D, Kamala Bharathi K, Sinha B & Ghosh K, 'Correlation between structural, magnetic, and dielectric properties of manganese substituted cobalt ferrite', Journal of applied Physics 114 (2013) 183907.

**Ranjith Kumar E,** Arunkumar T & Prakash T, 'Heat treatment effects on structural and dielectric properties of Mn substituted CuFe<sub>2</sub>O<sub>4</sub> and ZnFe<sub>2</sub>O<sub>4</sub> nanoparticles', J.Superlatt. Microstruct. 85 (2015) 530–535.

**Razia Nongjai,** Shakeel Khan K, Asokan, Hilal Ahmed & Imran Khan, 'Magnetic and electrical properties of in doped cobalt ferrite nanoparticles', journal of applied physics. 112 **(2012)** 084321.

**Rezlescu N,** Rezlescu E, Popa P.D & Rezlescu L, Effect of rare-arth oxides on physical properties of Li-Zn ferrite, J. Alloy. Comp. 275–277 (1998) 657–659.

**Samoila P**, Sacarescu L, Borhan A.I, Timpu D, Grigoras M, Lupu N, Zaltariov M & Harabagiu V, 'Magnetic properties of nanosized Gd doped Ni–Mn–Cr ferrites prepared using the sol–gel autocombustion technique', J. Magn. Magn. Mater. 378 **(2015)** 92–97.

**Shahab Torkian,** Ali Ghasemi, Reza Shoja Razavi, 'Structural and magnetic consequences of Mn<sub>0.6</sub>Zn<sub>0.4</sub>Fe<sub>2-x</sub>Gd<sub>x</sub>O<sub>4</sub> ferrite', J. Supercond. Novel Magn. 29 **(2016)** 1617–1625.

**Shahul Hameed A,** Bahiraei H, Reddy M.V, Shoushtari M.Z, Vittal J.J, Ong C.K & Chowdari B.V.R, 'Lithium storage properties of pristine and (Mg, Cu) co doped ZnFe<sub>2</sub>O<sub>4</sub> nanoparticles', ACS Appl. Mater. Interfaces. 6 **(2014)** 10744–10753.

**Shirsath S.E,** Mane M.L, Yasukawa Y, Liu X & Morisako A. 'Self-ignited high temperature synthesis and enhanced super-exchange interactions of Ho<sup>3+-</sup>Mn<sup>2+-</sup> Fe<sup>3+-</sup>O<sub>2</sub> ferromagnetic nanoparticles', Phys Chem. 16 (2014) 2347–57.

**Tatina brusentosva N,** Viatcheslva & kuznetsov D, 'Synthesis and investigation of magnetic properties of substituted ferrite nanoparticles of spinel systemMn<sub>1</sub>.  $_x$ Zn<sub>x</sub>[Fe<sub>2-y</sub>L<sub>y</sub>]O<sub>4</sub>', J.Magn. Magn. Mater. 311 (2007) 22–25.

**Tholkappiyan R** & Vishista K, 'Influence of lanthanum on the optomagnetic properties of zinc ferrite prepared by combustion method', Phys. B. 448 **(2014)** 177–183.

**Tholkappiyan R** & Vishista K, 'Structural, optical and magnetic properties of nanocrstalline Zinc ferrite particles from glycine assisted combustion' Effect of Sr<sup>2+</sup> dopant, Mater. Sci. Semicond. Process. 40 **(2015)** 631.

**Tobias Neuberger,** Bernhard Schopf, Heinrich Hofmann, Margarete Hofmann & Brigitte von Rechenberg, 'Superparamagnetic nanoparticles for biomedical applications: possibilities and limitations of a new drug delivery system', J. Magn. Magn. Mater. 293 (2005) 483–496.

**Torkain S,** Ghasemi A & Razavi R.S, 'Structural and magnetic consequences of Mn<sub>0.6</sub> Zn<sub>0.4</sub> Fe<sub>2-x</sub>Gd<sub>x</sub>O<sub>4</sub> ferrite', J. Supercond. Nov. Magn. 29, 1617–1625 (2016).

**Vigneshwaran B,** Kuppusami P, Arunkumar Panda, Akash Singh & H. Sreemoolanadhan, 'Microstructure and optical properties of Ba<sub>0.6</sub>Sr<sub>0.4</sub>TiO<sub>3</sub> thin films prepared by pulsed laser deposition', Mater. Res. Express 5, **(2018)** 066420.

**Wang J,** Zeng C, Peng Z.M & Chen Q.W, 'Synthesis and magnetic properties of Zn<sub>1-x</sub>Mn<sub>x</sub>Fe<sub>2</sub>O<sub>4</sub> nanoparticles', Physica B. 349 (2004) 124–128.

**Xing Q,** Peng Z, Wang C, Fu Z & Fu X, 'Doping effect of Y<sup>3+</sup> ions on the microstructural and electromagnetic properties of Mn–Zn ferrites', Physica B 407(3), 388–392 (2012).

**Yang M** & Yang K.L, 'An Optimal low - temperatue tartree precursor method for the synthesis of monophasic nanosized ZnFe<sub>2</sub>O<sub>4</sub>,' J. Nanopart. Res. 11 **(2009)** 1739.

**Zhang Y** & Wen D, 'Influence of RE/Mn (RE = La, Nd and Gd) ratios on the infrared absorption and emission properties of Co–Zn ferrites', Adv. Mater. Res. 218 (2011) 311–316.

### CHAPTER – VI

# EFFECT OF Gd<sup>3+</sup> IONS ON STRUCTURAL, OPTICAL, MAGNETIC AND DIELECTRIC PROPERTIES OF CoGd<sub>x</sub>Fe<sub>2-x</sub>O<sub>4</sub> (0.00 $\leq X \geq$ 0.08) NANOFERRITES

#### **6.1 INTRODUCTION**

In recent years, nanosized ferrites have immense applications in various fields with fast development microwave technology such as high frequency devices and their component, telecommunications devices, memory core devices, microwave absorption micro-oven, radar, antenna, sensor, magneto-resistive random-access memory (MRAM) devices, targeted magnetic tunnel junction and spintronics devices and drug delivery [Rashad et.al., 2009, Krishna et.al., 2012, El-Sheikh et.al., 2013, Kamar Tanbir et.al., 2020]. In electronic society, the usage of telecommunication and electronic equipment's has increased due to the problem raised in electromagnetic interference [Abbas et.al., 2007] as it generates false image, reduces the life time and efficiency of the instruments and also destroy the safety operation of many electronic devices. To overcome these problems, all electronic equipment's must be aware of electromagnetic damage [Che et.al., 2004, Huang et.al., 2007]. Now a day's research has been done for the improvement of latest microwave shielding materials which includes high efficiency, light weight, lifetime and high durability. Electromagnetic absorber solves such problems and also satisfies the above-mentioned parameters. Therefore, electromagnetic absorbers are highly needed and broad ranges of application have been taken out [Siddiqui et.al., 2012, Meshram et.al., 2004]. Some rare-earth element doping has been reported to play vital roles to amplify the

magnetic, structural and electrical properties. These properties can change based on the cation distribution, size, shape, concentration and lattice sites [Mritunjoy Prasad Ghosh et.al., 2020]. Spinel ferrites are one of the most absorbing materials in different forms such as paints, powder, ceramic filter and sheets, etc. [Lenin et.al., 2018]. The electrical and magnetic properties are superior when dopant of rare earth ions [Ahmed et.al., 2008]. Various efforts have been taken to develop techniques for the synthesis of nanoferrites such as co-precipitation [Lakshita PHOR et.al., 2020], sonochemical method [Lenin et.al., 2020], micro-emulsion technique [Muhammad Junaid et.al., 2020], hydrothermal [Bolarín-Miró et.al., 2011] and solvo thermal [Sivakumar et.al., 2007]. Among these, sol-gel method has emerged as a useful strategy for the preparation of nanoferrites. Sol-gel method allows control both size through structural properties and also homogeneity of particles. However, doping of rare earth along with large amount of Fe and some metal may result in unique properties [Ahmed et.al., 2006]. To our best of knowledge, a few researchers discussed the study of Gd in Co ferrites. Moreover, an elaborated study of magnetic and dielectric properties for spinel nanoferrites has been reported very rarely.

In current study  $CoGd_xFe_{2-x}O_4$  doped cobalt nanoferrites with various doping concentrations (x = 0.00, 0.02, 0.04, 0.06 and 0.08) were synthesized by sol-gel method. The impact of Gd incorporation on interconnected features such as structural, morphological, optical, and magnetic properties were investigated. The primary goal of the produced Gd doped cobalt nanoferrites (GNF) with varing different doping concentrations is to improve electromagnetic microwave absorption.

#### 6.2 MATERIALS AND EXPERIMENTAL PROCEDURE

#### **6.2.1 Materials**

A high pure nitrate precursors of the Cobalt, Iron, Gadolinium and salts such as Gadolinium nitrate (Gd (NO<sub>3</sub>)<sub>3</sub>.6H<sub>2</sub>O), and the commercial reagents Ammonia (NH<sub>4</sub>OH) and Citric acid (C<sub>6</sub>H<sub>8</sub>O<sub>7</sub>.H<sub>2</sub>O) were purchased from Merck.

## **6.2.2** Experimental Procedure

The  $CoGd_xFe_{2-x}O_4$ nanoferrites were synthesized by the well-known sol-gel method. The stoichiometric amount of nitrate was weighed and dissolved in 100 ml of de-ionized water until a mixture of the precursors. Then the mixture was constantly stirred at 80 °C for 1 hour. The ammonium hydroxide solution was further added in to the precursor solution drop by drop until the pH value of 7.

A dark sol suspension was obtained and the content was dried in oven at 60 °C for 24 hrs. The dried powder was kept for calcination in a muffle furnace at 500 °C for 2 hrs to obtain the by-products free nanoparticles. The prepared nanopowders were calcined at 1000 °C for 24 hrs. The schematic diagrams of preparation of CoGd<sub>x</sub>Fe<sub>2-x</sub>O<sub>4</sub> nanoferrites were shown in Figure 6.1.

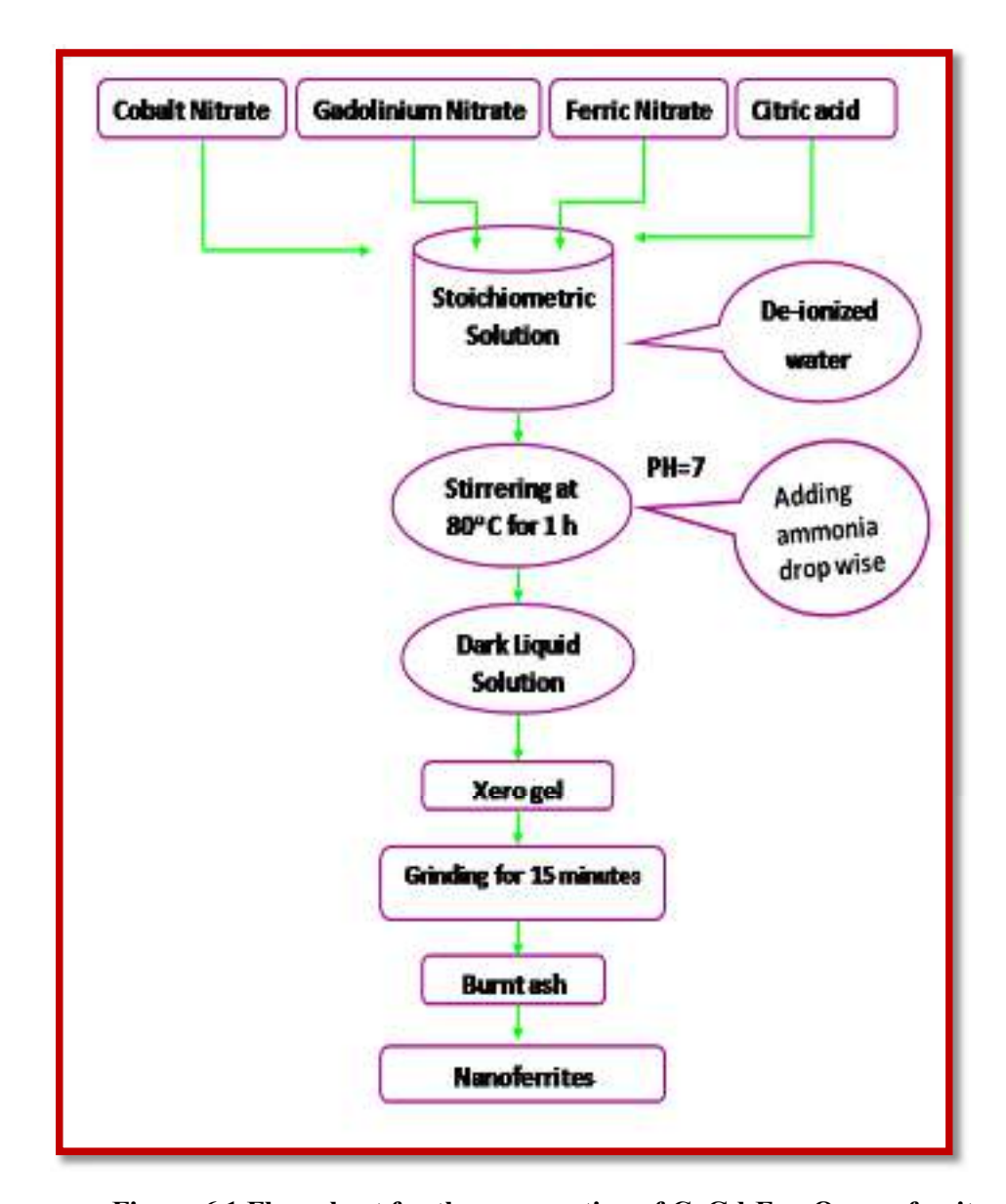


Figure 6.1 Flow chart for the preparation of CoGd<sub>x</sub>Fe<sub>2-x</sub>O<sub>4</sub>nanoferrites

# 6.2.3 Characterization of the CoGdxFe2-xO4Nanoferrites

The structural properties of the prepared  $CoLa_XFe_{2-x}O_4$  (X = 0.00 to 0.08) nanoferrites were characterized by XRD (SHIMADZU-XRD 6000) with  $CuK\alpha$  radiation source operated at 40 kV and 30 mA. The functional groups in the  $CoGd_xFe_{2-x}O_4$  nanoferrites were determined by FTIR spectra (SHIMADZU-UV 18000) ranging from 4000 to 400 cm<sup>-1</sup>. The morphology and elemental investigation

of the prepared material were analyzed by using FESEM with an EDAX (Quanta FEG 250). The optical properties were analyzed by using an UV- DRS for the prepared material. The Impedance spectroscopy with the frequency range of 100 mHz to 10 MHz at room Temperature (30 °C) (Biologic SP-300) was used to determine the electrical properties. Raman spectroscopy studies were made using an AUG spectrometer (ALU-PHI5000) with monochromatic Al Ka and 26.00 eV radiation. Magnetic properties were analyzed by using VSM (Lakeshore VSM 7140) with an applied magnetic field of -15000 to +15000Oe at room temperature.

#### 6.3 Results and Discussion

#### **6.3.1 Structural Analysis**

XRD spectra of  $CoGd_xFe_{2-x}O_4$  (x = 0.00 to 0.08) are shown in Figure 6.2. The observed reflections are (220), (311), (400), (422), and (511) of spinel ferrites which are matched with JCPDS card No 22-1056 [Bensebaa et.al., 2004]. The diffraction pattern confirms the formation of pure cubic structure of the spinel ferrites, without any secondary impurities. The method used for preparation ensures the substitution of  $Gd^{3+}$  ions into the spinel structure. The crystallite size was estimated from the basic Scherrer equation [Scherrer et.al., 1918];

$$D = \frac{K\lambda}{\beta \cos \theta} \tag{6.1}$$

where D is the average crystallite size, I is the x-ray wavelength, b is the width of the x-ray peak on the 2q axis, normally measured as full width at half maximum (FWHM) after the error due to instrumental broadening has been properly corrected (subtraction of variances), q is the Bragg angle, and K is the so-called Scherrer constant. K depends on the crystallite shape and the size distribution, indices of the

diffraction line, and the actual definition used for b whether FWHM or integral breadth [Langford et.al., 1978]. K can have values anywhere from 0.62 and 2.08. In this paper, K = X.X was used. Further, microstrain in the crystallite or nanocrystal also affects the width b, which needs to be considered in an accurate analysis. Spatial fluctuations in the alloy composition can also affect the width. In this work, the calculated values of D represent estimates. (Discussion on the accuracy of Equation [Scherrer et.al., 1918]; can be found in the literature, for example, in [Uvarov et.al., 2013]. The average crystallite size of the nanoferrites is decreases from 29 to 13 nm with increase of doping  $Gd^{3+}$ . The obtained results reveal that the average crystallite size of the prepared ferrites is highly influenced by the concentration of Gd concentration. This implies that the substitution of Fe ions with Fe ions hinders the grain growth. It can also be explained based on the difference between the ionic radii of Fe ions (0.67 Å) is smaller than that of Fe ions (0.938 Å) and, the substitution of rare earth ions shows limited solubility in spinel lattice and higher grain growth [Peng et.al., 2011].

The lattice constant of the prepared nanoferrites is calculated using below equation [Lenin et.al.,2021];

$$a = d_{hkl} \sqrt{(h^2 + k^2 + l^2)}$$
 (6.2)

where d is inter atomic spacing, a is the lattice constant and (hkl) are miller indices. The lattice constant was in the range of 8.50 ( $\pm$  0.002) Å to 8.59 ( $\pm$  0.002) Å (Table 6.1). It reveals that lattice constant increases with Gd<sup>3+</sup> substitution and when there is a replacement of rare earth ion in spinel ferrites, the lattice constant neither increases nor decreases [Rezlescu et.al., 1994]. The increase of lattice constant is

mainly due to incorrect occupancy of rare earth ions in the lattices [Rahman et.al., 2014]. In another way, the increase of lattice constant is due to replacement of ions in greater size of rare earth into transition element ions [Peng et.al., 2011]. In the current situation, the value of the lattice constant increases as the number of Gd<sup>3+</sup> ions increase, which is owing to the fact that Gd<sup>3+</sup> ions have a greater ionic radius (0.94 Å) than Fe<sup>3+</sup> ions in Octahedral locations, which causes the unit cell to expand, resulting in a larger lattice constant. [Peng et.al., 2011]. Thus, incorporation of Gd<sup>3+</sup> into cobalt nanoferrites was observed without any traces of secondary phase.

X-ray density of Gd<sup>3+</sup> doped CoFe<sub>2</sub>O<sub>4</sub> nanoferrites were estimated by the following equation [Lenin et.al., 2021];

$$d_x = Zm / Na^3 \tag{6.3}$$

where Z is basic unit cell of cubic structure contains eight ions, m is molecular weight of the ferrites, N is Avogadro's number and a<sup>3</sup> is volume of the unit cell. The observed X-ray density increases from 5.0 to 5.4 g/cm<sup>3</sup> with addition of Gd<sup>3+</sup> ion and it can be ascribed to the fact that the atomic weight of Gd<sup>3+</sup> is larger than that of Fe (55.84 g/mol). When the X-ray density increases the particles tend to acquire nanosize and tightly packed.

The bulk density (dB) was calculated by using specified equation [Lenin et.al., 2021];

$$d_{\rm B} = m / \pi r^2 t \tag{6.4}$$

where t is thickness, r is radius and m denote pellet's mass. The result revealed that the bulk density increases from 1.7 g/cm<sup>3</sup> to 2.7 g/cm<sup>3</sup> possibly as a result of

pores in the prepared nanoferrites. The place of Gd<sup>3+</sup> ions activate the calcinating condition thus trends to increase in densities [Bobade et.al., 2012]. The porosity (P) was estimated using following equation [Lenin et.al., 2021];

$$P = (1-d_B/d_X) \%$$
 (6.5)

where,  $d_x$  and  $d_B$  are X-ray density and bulk density of the ferrites. Table 6.1, infer that the porosity percentage was decreased from 6.9 to 4.7 with increase of  $Gd^{3+}$  ions which is due to increase in bulk density and also porosity behaves inversely proportional to each other.

The surface area (S) of the sample was calculated using subsequent expression [Lenin et.al., 2021];

$$S = 6 / d_X D \tag{6.6}$$

where, D is crystal size and  $d_X$  is the X-ray density of the ferrites. The surface area increases from 38 to 90 m<sup>2</sup>/g with addition of Gd<sup>3+</sup> ions are due to decrease in crystallite size. The results observed from all the structural parameters are listed in Table 6.1.

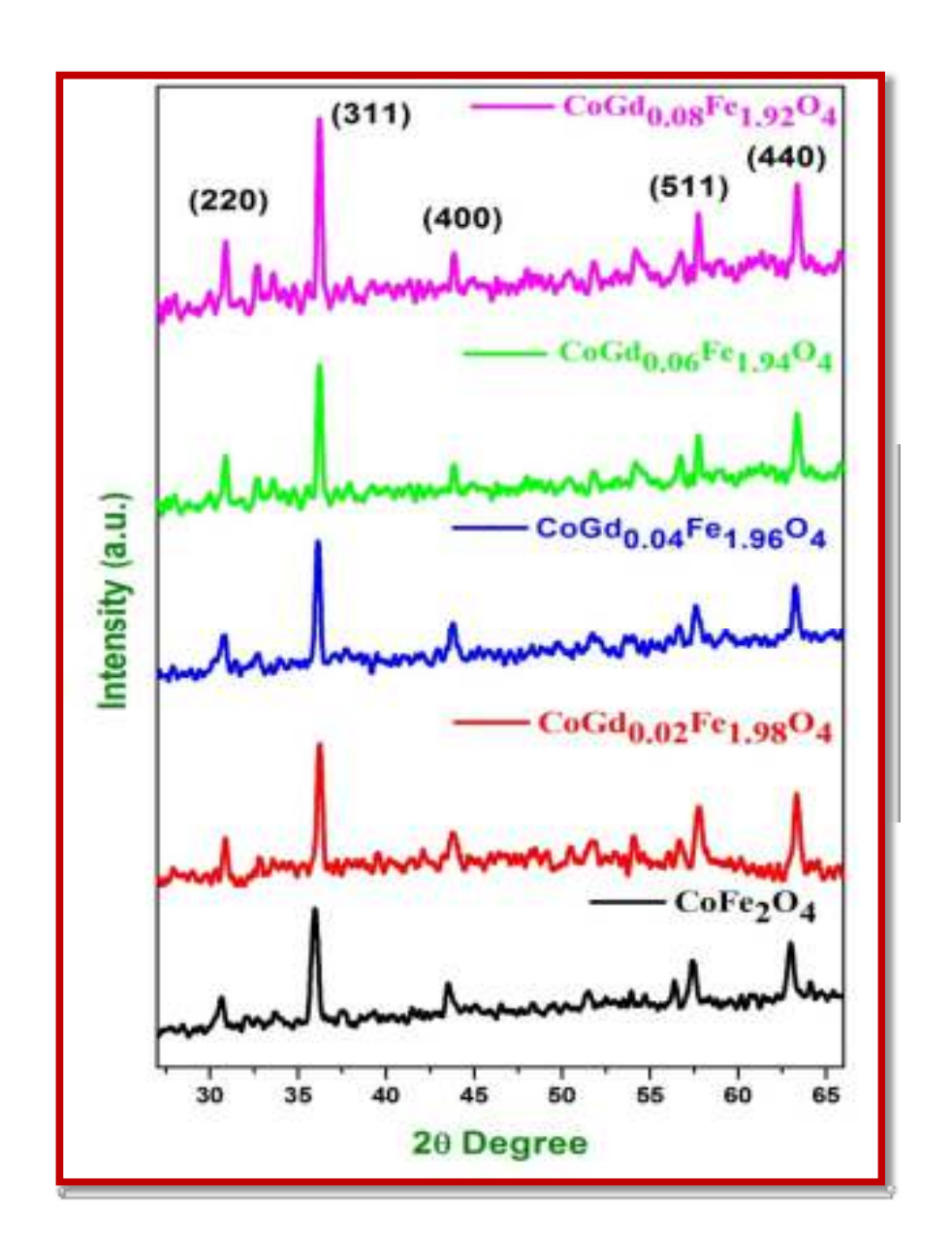


Figure 6.2 X-ray diffraction pattern of  $CoGd_XFe_{2-X}O_4$  (X = 0.00 to 0.08) nanoferrites.

Table 6.1. Structural parameters of CoGdxFe<sub>2-x</sub>O<sub>4</sub> (X = 0.00 to 0.08) nanoferrites

Composition	Crystallite size (nm) (± 0.03)	Lattice constant (a) Å (± 0.002)	Volume of unitcell (Å) (a³)	X-ray density (ρxrd) (g/cm³)	Bulk density (d <sub>B</sub> ) (g/cm <sup>3</sup> )	Surface area (Sxrd) (m²/g)	Porosity (%)
(G0) X=0.00	29	8.50	615.5	5.0	1.7	38	6.9
(G2) X=0.02	22	8.52	620.6	5.2	1.8	51	6.6
(G4) X=0.04	19	8.56	626.3	5.2	1.9	60	6.2
(G6) X=0.06	15	8.57	630.7	5.3	2.5	77	5.1
(G8) X=0.08	13	8.60	650.0	5.4	2.7	90	4.7

# 6.3.2 Optical Analysis

The impact of  $Gd^{3+}$  doping on the optical properties of  $CoGd_xFe_{2-x}O_4$  was carried out through diffuse reflectance (DR) UV spectrometer in the wavelength range of 200-800 nm as shown in Figure 6.3.

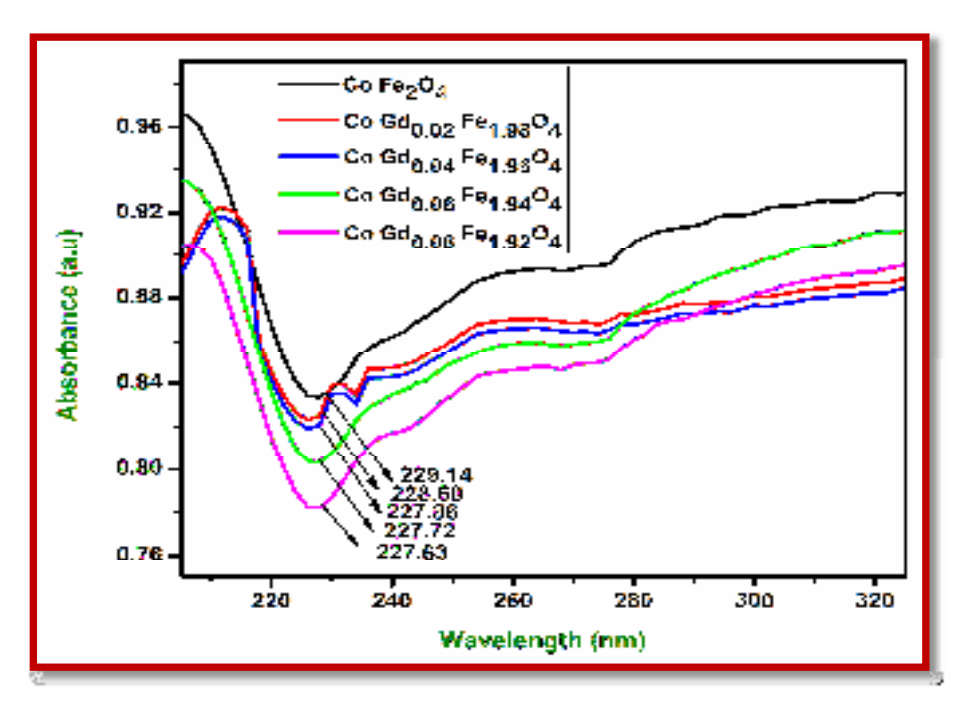


Figure 6.3 Absorbance spectra of CoGdxFe<sub>2-x</sub>O<sub>4</sub> (X= 0.00 to 0.08) nanoferrites

It can be clearly noticed that CoGd<sub>x</sub>Fe<sub>2-x</sub>O<sub>4</sub> nanoferrites exhibited absorption in the visible region. The absorption values of cobalt ferrites show visible light cut-off wavelength at 234 nm. As the Gd<sup>3+</sup> ions increasing, the absorptions were observed as 233, 232, 231 and 230 nm respectively. When compared to Gd<sup>3+</sup> doped ferrites, pure cobalt nanoferrites show better visible light absorption.

The optical bandgap energy was calculated following expression [Vigneshwaran et.al., 2018];

$$h\gamma\alpha = (h\gamma - E_{gap})^n \tag{6.7}$$

where the absorption coefficient is  $\alpha$ , the frequency of light is denoted by  $\gamma$ , the planks constant is h, and the bandgap is  $E_g$ . For indirect and direct bandgap energies, the exponents are 2 and  $\frac{1}{2}$ .

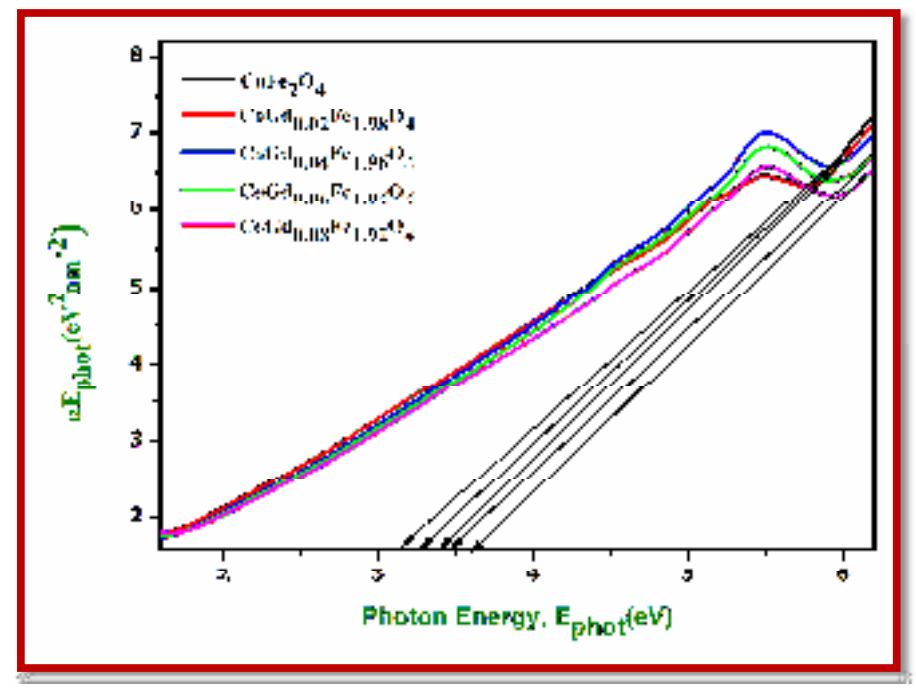


Figure 6.4 Direct bandgap energy of CoGdxFe<sub>2-x</sub>O<sub>4</sub> (X= 0.00 to 0.08) nanoferrites.

Figure 6.4 shows that the direct bandgap energy values are found as 3.14, 3.27, 3.39, 3.46 and 3.61 eV, which are relatively high with previous reports [Asiri et.al., 2018]. Figure 6.8 shows that the indirect bandgap values are 2.62, 2.73, 2.84, 2.96 and 3.09 eV respectively, which are also considerably higher values with previous reports [Alves et.al., 2017].

The optical bandgap energy increased as the concentration of  $Gd^{3+}$  grew (X = 0.00 to 0.08). This indicates an increase in energy level, which may be attributed to the synergistic impact of the  $Gd^{3+}$  ion, which reduces electron hole recombination and so increases the band gap [Li et.al., 2011]. Table 6.2 shows that the bandgap value has increased which exhibits an inverse relationship between bandgap and crystallite size as the lattice parameter is increased. [Kumar et.al., 2014].

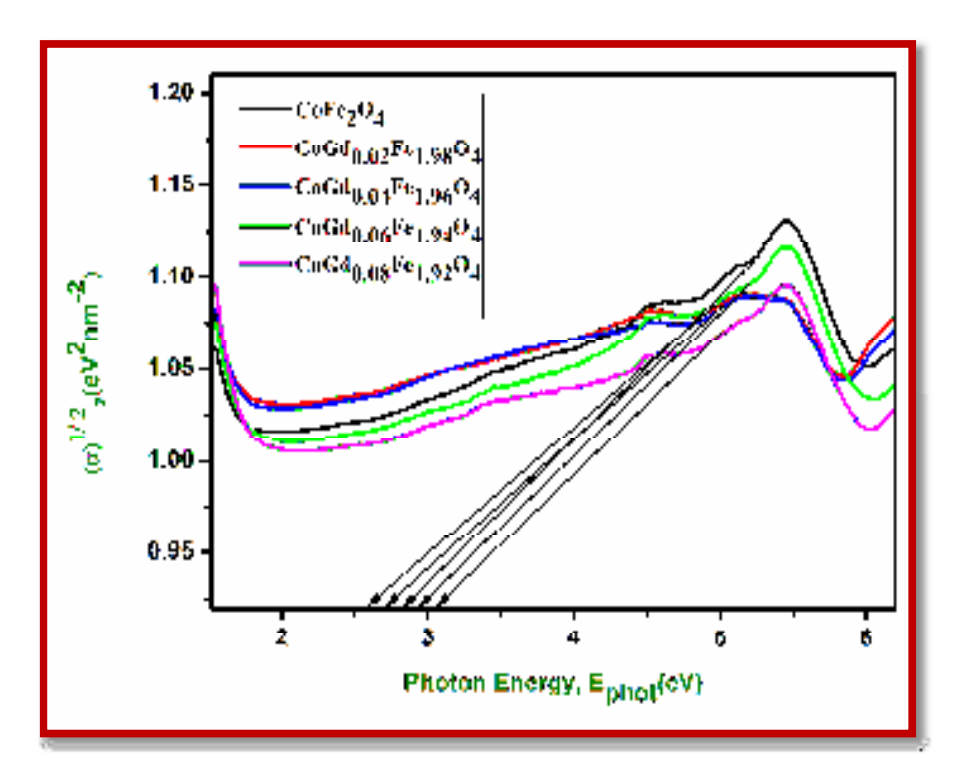


Figure 6.5 Indirect bandgap energy of CoGdxFe<sub>2-x</sub>O<sub>4</sub> (X= 0.00 to 0.08) nanoferrites

Table 6.2 Optical parameters of  $CoGdxFe_{2-x}O_4$  (X = 0.00 to 0.08) nanoferrites

Composition	Absorbance (nm)	Indirect band gap energy(eV)	Direct band gap energy (eV)
X=0.00	234	3.14	2.62
X=0.02	233	3.27	2.73
X=0.04	232	3.39	2.84
X=0.06	231	3.46	2.96
X=0.08	230	3.61	3.09

# **6.3.3 Functional Group Analysis**

Infrared Radiation (IR) transmittance spectra of these nanoferrites series are shown in Figure 6.6. The absorption of IR in molecular vibrations also confirms the formation of ferrites phase. The vibrational frequency at 585 cm<sup>-1</sup> represents stretching vibration of metal-oxygen bond.

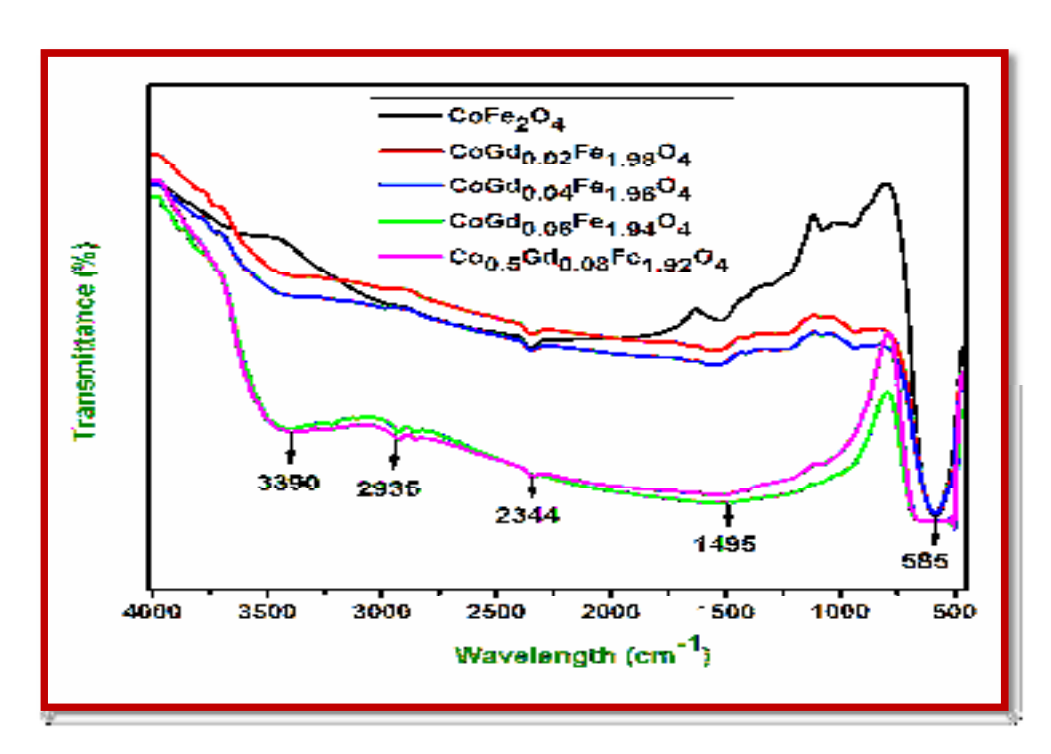


Figure 6.6. FTIR spectra of  $CoGd_XFe_{2-X}O_4$  (X = 0.00 to 0.08) nanoferrites

The broad and strong stretching peak at 3390 cm<sup>-1</sup> is due to stretching vibration of O-H bonds of water molecules coordinates to the ferrite structure [Purnama et.al., 2019]. The peak around at 1495 cm<sup>-1</sup> is due to stretching vibration of C-H bond [Wang et.al., 2011]. The peak appears around 2344 cm<sup>-1</sup> is due to stretching vibration of nitrate group, which indicates that nitrate ions are present in the starting precursors of all the samples [Sivakumar et.al., 2011]. The peak at 2935 cm<sup>-1</sup> was ascribed to symmetric and antisymmetric stretching modes of CH<sub>2</sub>, respectively [Zhang et.al., 2006].

Table 6.3 Functional parameters of CoGdxFe<sub>2-x</sub>O<sub>4</sub> (X = 0.00 to 0.08) nanoferrites

		Experimental absorption (cm <sup>-1</sup> )					
S.NO	Vibrational assignments	X= 0.00	X= 0.02	X= 0.04	X= 0.06	X= 0.08	
1	Metal - oxygen stretching vibration	585	585	585	585	585	
2	Stretching vibration of No <sub>3</sub>	1495	1495	1495	1495	1495	
3	Stretching vibration of C=N	2344	2344	2344	2344	2344	
4	C=H bending of carboxylic acid	2935	2935	2935	2935	2935	
5	O - H stretching vibration	3390	3390	330	3390	3390	

# **6.3.4 Surface Morpohology with EDAX**

The morphology studies can be determined by using FESEM as in Figure 6.7, which revealed that these nanoferrites have spherical in shape with few agglomerations which is due to the magnetic interactions between the particles increase in substitution of Gd<sup>3+</sup> ions [Ghodake et.al., 2016]. It was noticed that the substitution of Gd<sup>3+</sup> ion had insignificant effect on the material morphology, but

largely impact the average size of the ferrites, which implies that the average crystallite decreases with increase of dopant concentration [Peng et.al., 2011].

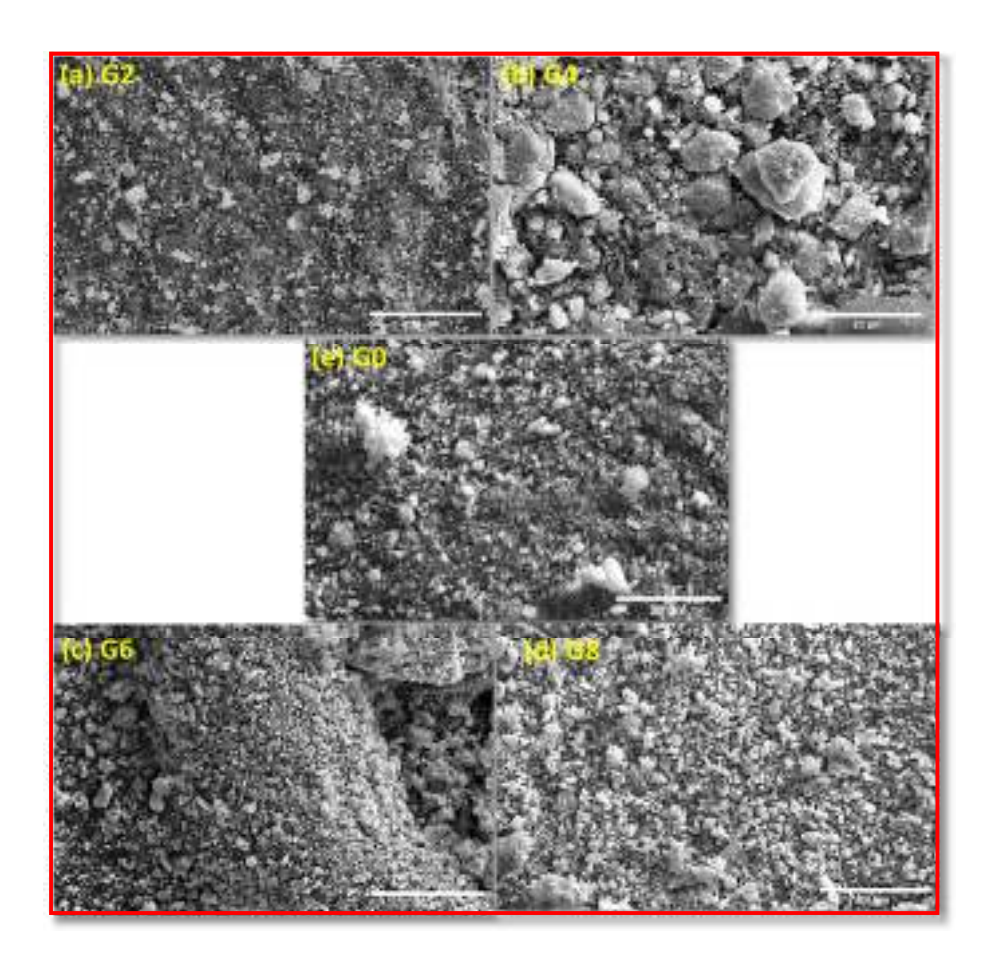


Figure 6.7 FESEM images of CoGdxFe<sub>2-x</sub>O<sub>4</sub> (X = 0.00 to 0.08) nanoferrites

EDAX analysis of CoGd<sub>x</sub>Fe<sub>2-x</sub>O<sub>4</sub> ferrites are shown in Figure 6.8. It is clearly seen that there is no formation of secondary impurity elements in the composition. The spectra also indicate that the incorporation of Gd<sup>3+</sup> was well incorporated in the ferrites as the Gd<sup>3+</sup> peaks appear as the intensities increase with increase of Gd<sup>3+</sup> ions. It's worth mentioning that the atomic weight percentages are closely matched with the theoretical stoichiometry which corresponds to the expected ratio of the concentrations.

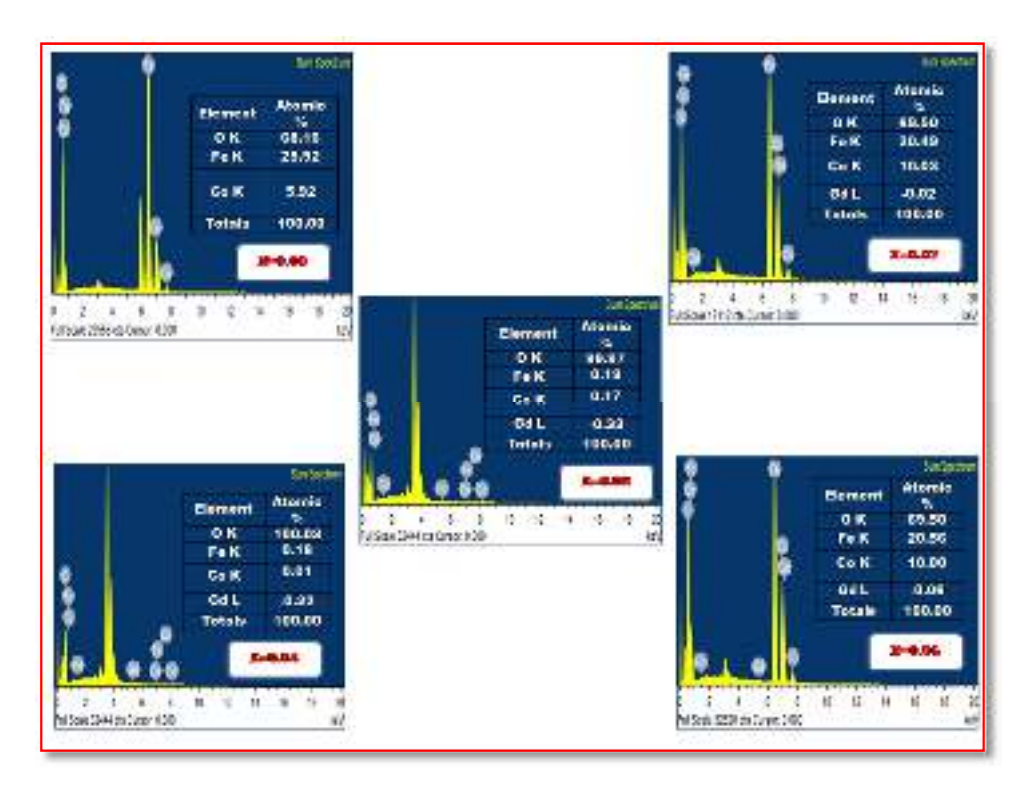


Figure 6.8. EDAX images of CoGdxFe<sub>2-x</sub>O<sub>4</sub> (X = 0.00 to 0.08) nanoferrites 6.3.5 Raman Spectroscopy Analysis

Raman spectroscopy analysis has been widely used to understand the key structural properties of the nanoparticles such as phase transition, structure and lattice distribution, spin-lattice, charge-lattice, couplings and magnetic ordering in nanoferrites [Yadav et.al., 2017]. Based on the group theory analysis of the lattice vibration, the cubic 3a spinel structure cobalt ferrite has vibrational Raman active modes of vibrations ( $A_{1g}+E_g+3T_{2g}$ ) [Yadav et.al., 2017, Yu et.al., 2002]. These modes are noticed due to the motion of anion and cation at A and B sites. The Raman spectra taken at room temperature in the wavelength range of 200 to 800 cm<sup>-1</sup> at CoGd<sub>x</sub>Fe<sub>2-x</sub>O<sub>4</sub> (X = 0.00 to 0.08) are shown in Figure 6.9. The  $A_{1g}$  mode is organized to symmetric stretching of the oxygen atom, the  $T_{2g}$  mode is associated to asymmetric stretching of oxygen atom with both octahedral and tetrahedral cation and  $E_g$  mode is

organized to symmetric bending of oxygen atom [Yu et.al., 2002]. The highest intensity of  $A_{1g}$  active mode split up into two modes ( $A_{1g}$ ) and ( $A_{2g}$ ) due to cation inversion [Saccone et.al., 2015]. The Raman modes at  $T_{2g}$  and  $E_g$  in the Gd doped cobalt nanoferrites are at lower frequency region described the stability of the spinel structure. Table 6.4 indicates the strong Raman mode above 600 cm<sup>-1</sup> represents to  $A_{1g}$  mode and it can be associated to the symmetric stretching of oxygen atoms along with metal oxygen (M-O) and Fe-O bonds at tetrahedral sites. The Raman mode  $T_{2g}$  (3) about 230 cm<sup>-1</sup> corresponds to 2g asymmetric bending of oxygen atom,  $T_{2g}$  (2) mode around 465 cm<sup>-1</sup> corresponds to asymmetric stretching of M-O and Fe-O at Octahedral site and  $T_{2g}$  (1) Raman mode around 535 cm<sup>-1</sup> is assigned to translation motion of tetrahedral. The Raman active mode of  $E_g$  (1) are located at 310 cm<sup>-1</sup> is linked with symmetric bending of oxygen with metal ion [Humbe et.al., 2017].

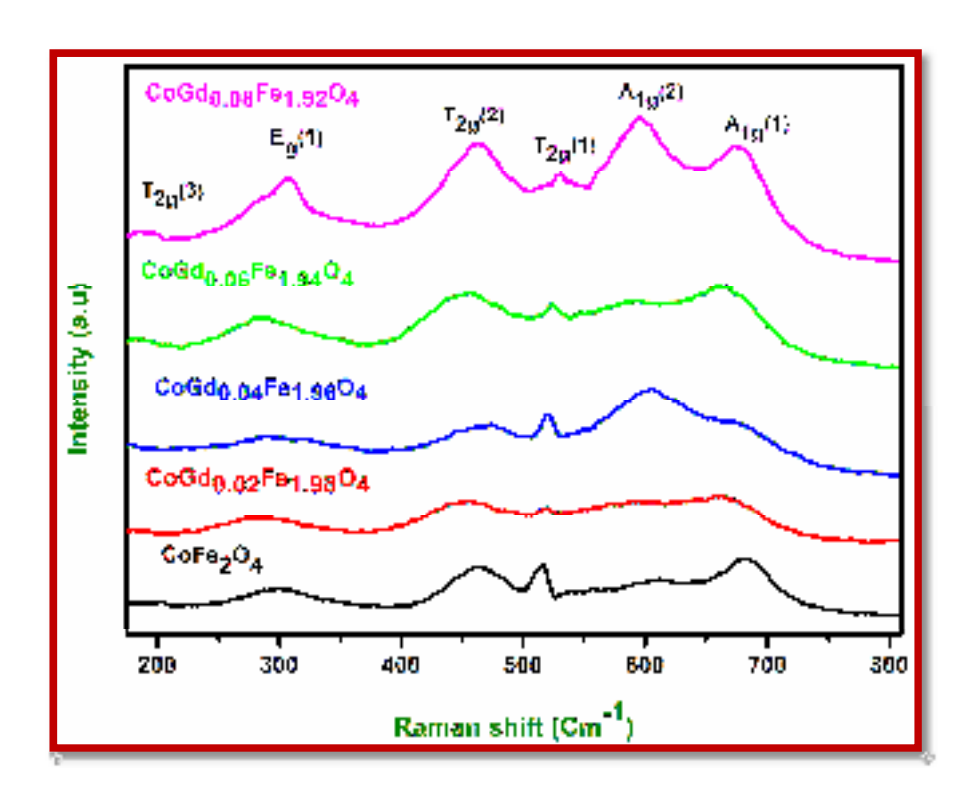


Figure 6.9 Raman spectra of CoGdxFe<sub>2-x</sub>O<sub>4</sub> (X = 0.00 to 0.08) nanoferrites

Table 6.4 Raman studies of CoGdxFe<sub>2-x</sub>O<sub>4</sub> (X = 0.00 to 0.08) nanoferrites

Composition	T <sub>2g</sub> (3)	E <sub>g</sub> (1)	T <sub>2g</sub> (2)	T <sub>2g</sub> (1)	A <sub>1g</sub> (1)	A <sub>1g</sub> (2)
CoFe <sub>2</sub> O <sub>4</sub>	199	305	462	517	614	683
CoGd <sub>0.02</sub> Fe <sub>1.98</sub> O <sub>4</sub>	222	284	450	520	604	666
CoGd <sub>0.04</sub> Fe <sub>1.96</sub> O <sub>4</sub>	197	285	459	519	608	679
CoGd <sub>0.06</sub> Fe <sub>1.94</sub> O <sub>4</sub>	207	291	455	524	601	668
CoGd <sub>0.08</sub> Fe <sub>1.92</sub> O <sub>4</sub>	195	308	462	532	599	679

In this study, the vibration modes above 600 cm<sup>-1</sup> are associated with  $A_{1g}$  symmetry of metal-oxygen bond at tetrahedral sites. The doping of  $Gd^{3+}$  ions are expected to occupy at the octahedral sites [G. Kumaret.al., 2014] by exchange of  $Co^{2+}$  from Octahedral to tetrahedral sites. And the vibrational frequency of Raman modes is moved to lower frequency region due to the crystallite size and cation redistribution of  $CoGd_xFe_{2-x}O_4$  (X=0.00 to 0.08) nanoferrites.

### **6.3.6 Magnetic Analysis**

Room temperature M-H loop study was carried out to analyze the magnetic behavior of CoGd<sub>x</sub>Fe<sub>2-x</sub>O<sub>4</sub> nanoferrites with applied magnetic field in the range of +15000 Oe as shown in Figure 6.10. The magnetic behavior of S shaped M-H hysteresis loops confirmed soft magnetic nature which can be associated to cubic spinel nanoferrites [Peijiang Liua et.al., 2016].

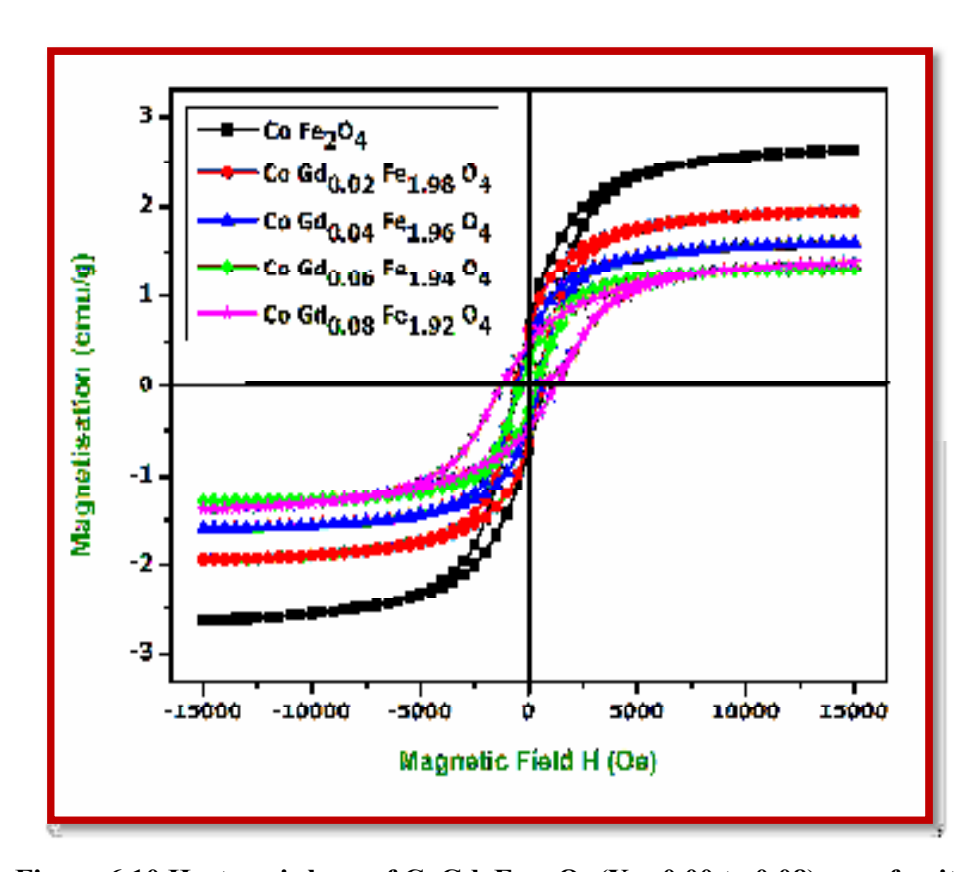


Figure 6.10 Hysteresis loop of  $CoGdxFe_{2-x}O_4$  (X = 0.00 to 0.08) nanoferrites

The hysteresis curve exhibits ferromagnetic behavior. The cation distribution in tetrahedral and octahedral nanocrystalline materials, chemical composition, synthesis process, and crystallite size all influence the magnetic characteristics of the material. [Dimri et.al., 2006, Lavanya Rathi et.al., 2021]. The magnetic parameters such as Retentivity ( $M_r$ ), Coercivity ( $H_c$ ), Magnetic saturation ( $M_s$ ), Anisotropy constant (K), squareness ratio and magnetic moment are evolved from the hysteresis loop and the variation of each magnetic parameters were listed in Table 6.5. The Magnetic saturation decreases from 26 to 13 (X = 0.00 to X = 0.08) with increment of  $Gd^{3+}$  ions in the cobalt ferrites due to decrease of crystallite size. This concept was explained from the theory of dead layer i.e core shell model [Peijiang Liu et.al., 2018].

In the core shell model, the magnetic particles are shielded inside the non-magnetic layer. And also, it can be discussed based on the changes in A-B exchange interaction between Octahedral (B) and tetrahedral (A) sub lattices. The cubic structure of spinel nanoferrites has various crystallographic sublattices for magnetic ions i.e Octahedral (B) and tetrahedral (A). Three types of magnetic interaction are involved among the magnetic ions i.e AA interaction, BB interaction and AB interaction. In spinel nanoferrites, magnetic order is strong because of superexchange interaction among the magnetic ions in the A and B sub lattices intermediate by oxygen ions. The surface effect for oxide nano material leads to decrease of magnetic saturation. The magnetic dead layer on the spin canting effect in the whole volume of the crystallite could be the reason for decrease in magnetic saturation [Amiri et.al., 2013].

Coercivity of the nanoparticles depends on defects, porosity, strain, synthesis process and magnetic crystalline anisotropy etc. The value of coercivity increased with increase of Gd<sup>3+</sup> ions as the crystallite size decreased. It can be clarified based on the Stoner Wohlforth theory, the coercivity value is correlated to the anisotropy constant (K) by the expression [Belavi et.al., 2012];

$$H_c = 0.98XK / M_S$$
 (6.8)

where K is the anisotropy constant,  $H_c$  is coercivity and  $M_s$  is magnetic saturation. In Table 6.5, it is noticed that anisotropic constant decreases with decrease of crystallite size from XRD, and it leads to an increase in coercivity. Based on this relation, Hc and K are inversely proportional to  $M_s$  which is constant with the results. The magnetic moment ( $\mu_B$ ) was estimated using relation [Kumari et.al., 2015].

$$\eta_{\rm B} = MXM_{\rm S} / 5585$$
 (6.9)

where M is the molecular weight of Gd<sup>3+</sup> ions, X is the concentration. Because Gd<sup>3+</sup> has a higher ionic radius than Fe<sup>3+</sup>, the magnetic moment in cobalt nanoferrites decreases as the amount of Gd<sup>3+</sup> ion increases. This is due to less magnetic contact between B and A sites. The presence of rare earth ions has been found to alter spin-orbit coupling. As Gd<sup>3+</sup> is a rare earth cation, it causes collinear ferromagnetic arrangements on B sites to change into non-collinear ferromagnetic orders of spins. The majority of Co<sup>2+</sup> ions occupy B sites in CoFe<sub>2</sub>O<sub>4</sub> ferrites, with the remainder Co<sup>2+</sup> ions occupying A sites. As a result of the Gd<sup>3+</sup> ions occupying B-sites, the collinear arrangements of spins are deformed, resulting in a drop-in saturation. The fact that the squareness ratio was so low, suggested the presence of single domain particles in these nanoferrites [Belavi et.al., 2012].

The addition of Gd<sup>3+</sup> ions in CoFe<sub>2</sub>O<sub>4</sub>, being as non-magnetic ion substitution in the spinel lattice, which decreases the magnetic exchange interaction between A and B site, leads to decrease in magnetic saturation. Smaller value of coercive field was achieved due to these nanoferrites which are applicable for magnetic shielding devices [Kadam et.al., 2013].

Table 6.5 Magnetic parameters of  $CoGd_XFe_{2-X}O_4$  (X = 0.00 to 0.08) nanoferrites

Composition	Magnetization (M <sub>s</sub> ) (emu/g)	Remanent magnetization (M <sub>r</sub> ) (emu/g)	Coercivityity (Hc) (Oe)	$\begin{array}{c} \text{Squareness} \\ \text{Ratio} \\ \text{(M}_{r}/\text{M}_{s}) \\ \text{(No unit)} \end{array}$	Anisotropy constant (K) (Oe)	Bohr magneton (η <sub>B</sub> ) (μ <sub>B</sub> )
X = 0.00	26.0	69.3	394.5	0.33	106.3	0.33
X = 0.02	19.5	62.4	520.5	0.32	85.3	0.24
X = 0.04	16.0	48.1	564.5	0.30	84.3	0.20
X = 0.06	13.9	45.2	600.5	0.26	80.0	0.17
X= 0.08	13.0	28.7	609.5	0.22	79.8	0.16

### 6.3.7 Impedance Analysis

Impedance spectroscopy is one of the most powerful tools for spectrum analysis which gives more information regarding real and imaginary part of an electrical component in nanoferrites and also effectively used for investigating electrical behaviors like electric, conductivity and relaxation characteristic in terms of the grain boundary and grain of the prepared nanoferrites.

# 6.3.7 (a) Real part of impedance Spectroscopy

The real part of impedance spectroscopy (Z') as a function of frequency is shown in Figure 6.11. From the figure, real part (Z') decreases with increase of frequency and then remains same at a higher frequency which implies increase in Ac conductivity. The real part of impedance decreases with increase of Gd<sup>3+</sup> ions and then tends to merge at high frequency. This is occurring because release of space charge can lead to reduction in barrier properties for material [Kumari et.al., 2008].

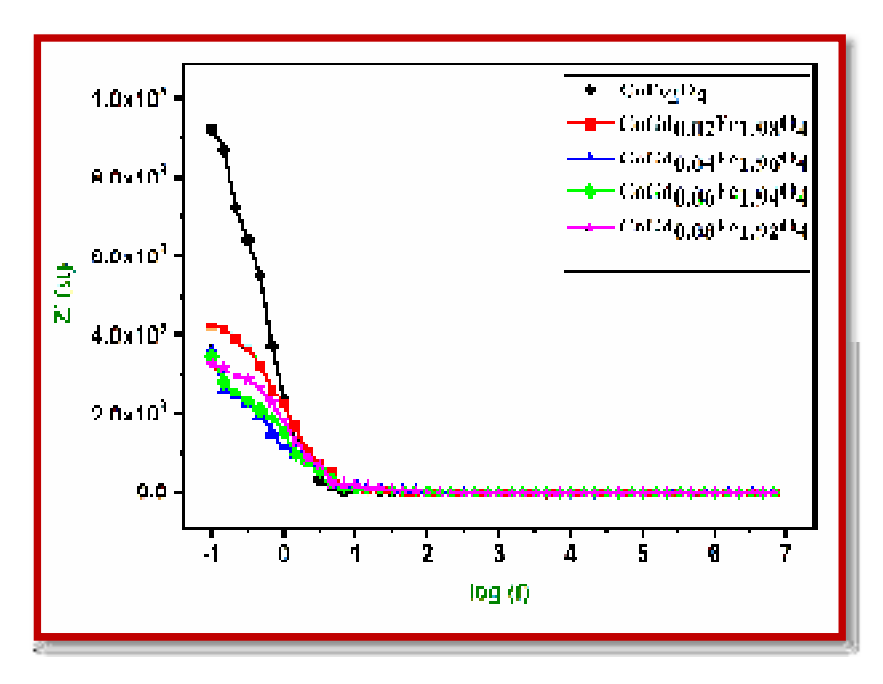


Figure 6.11 Real part of impedance spectra of  $CoGdxFe_{2-x}O_4$ (X = 0.00 to 0.08) nanoferrites

## 6.3.7 (b) Imaginary part of impedance Spectroscopy

The imaginary part of the impedance spectroscopy also decreases with increase of frequency and at last merges at higher frequency. The imaginary part of the impedance decreases with increasing of  $Gd^{3+}$  ions and then the curve tends to merge at higher frequencies as shown in Figure 6.12. The observed peak in the Z" parts are due to existence of the space charge relaxation, undertaken with the space charge carriers infer from oxygen vacancies [Rahman et.al., 2014]. Space charge polarization is found to be higher when the material is composed with grain and grain boundaries.

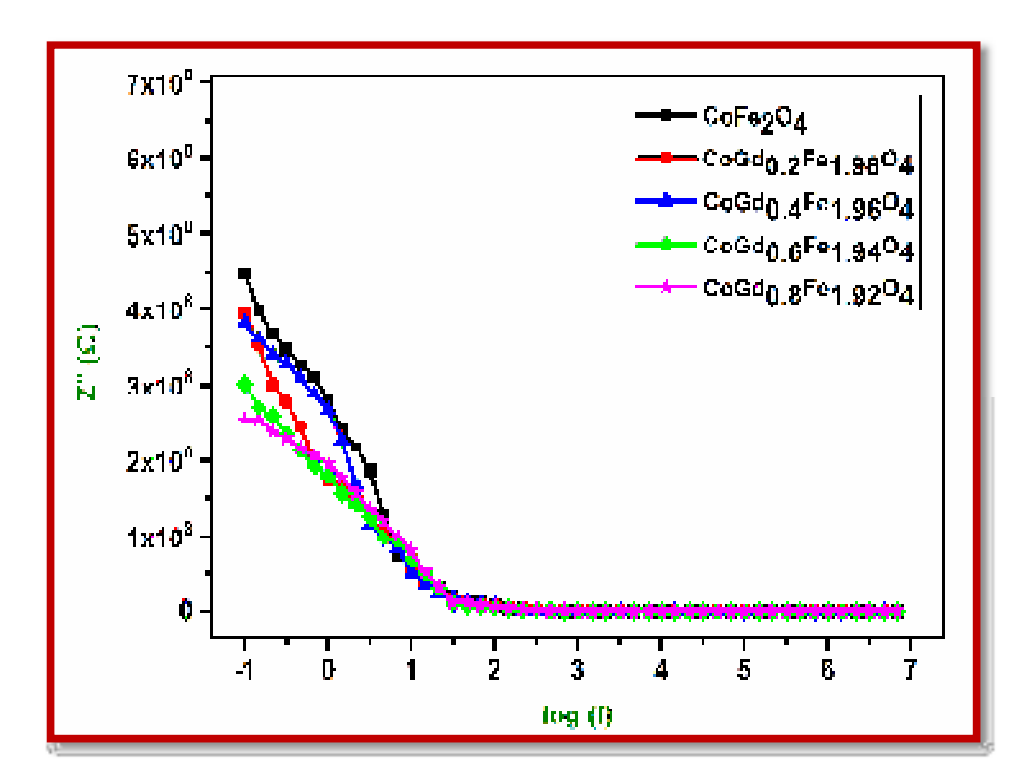


Figure 6.12 Imaginary part of impedance spectra of  $CoGdxFe_{2-x}O_4$ (X = 0.00 to 0.08) nanoferrites

#### **6.3.7** (c) Cole - Cole plot

Figure 6.13 shows the cole-cole plot for  $GdCo_XFe_{2-X}O_4$  with series of X = 0.00 to 0.08. The plot clearly shows semicircular arc, which denoted the electron interface

grain boundary and grain contribution to the conductivity [Ajith Kumar et.al., 2020]. The material's grain conduction mechanism, which is produced by a parallel combination of grain capacitance and grain resistance, is responsible for the appearance of a semicircle in the high frequency region. The semicircle symbolizes the low frequency area and is created by grain boundary conduction in materials, which happens when the material's grain boundary capacitance and grain boundary resistance are coupled in parallel [Kumar et.al., 2019].

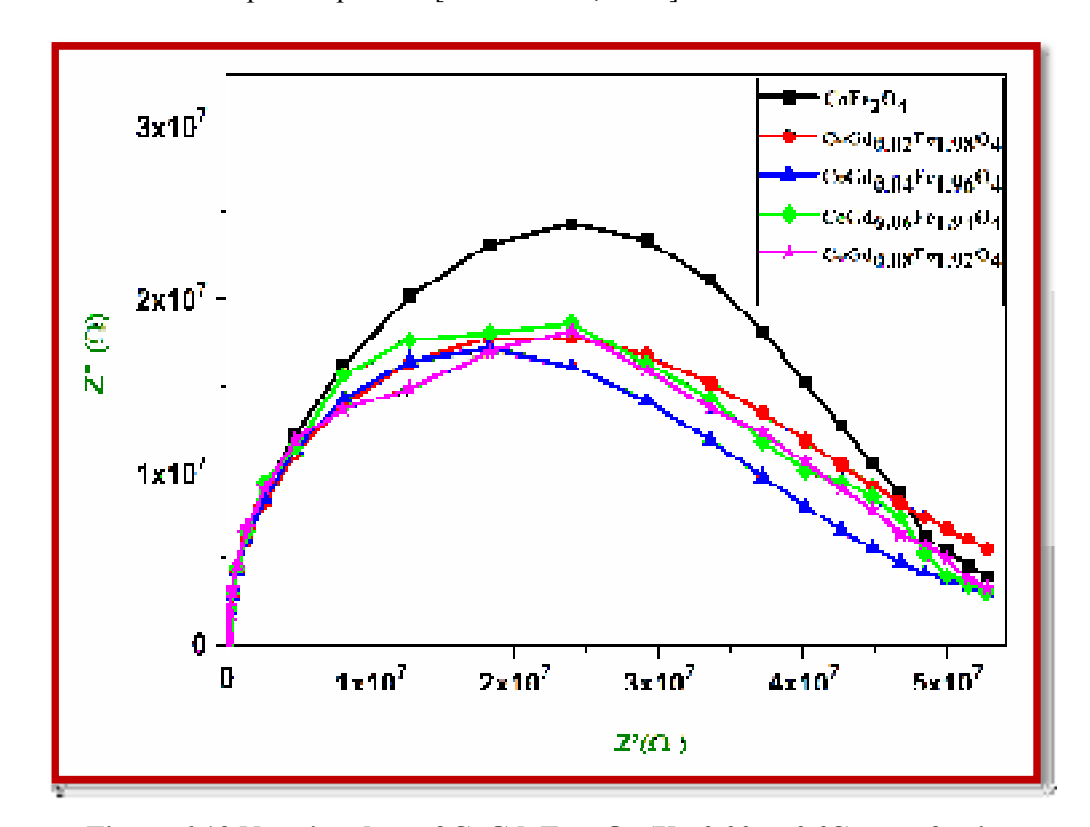


Figure 6.13 Nyquist plots of CoGdxFe<sub>2-x</sub>O<sub>4</sub> (X= 0.00 to 0.08) nanoferrites

The observed semicircle was successfully fitted by the equivalent circuit model as shown in Figure 6.14 In the present study, the major role in the conduction is observed to occur due to grain boundary contribution. Substitution of  $Gd^{3+}$  ions in cobalt ferrites increases the grain boundary resistance, where  $R_{gb}$  and  $R_{g}$  are the resistance of the grain boundaries and grains.  $CPE_{gb}$  and  $CPE_{g}$  are constant phase

element of grain boundaries and grains. This boundary is greater than that of the grain contribution which is occurred due to the effect of smaller crystallite size.

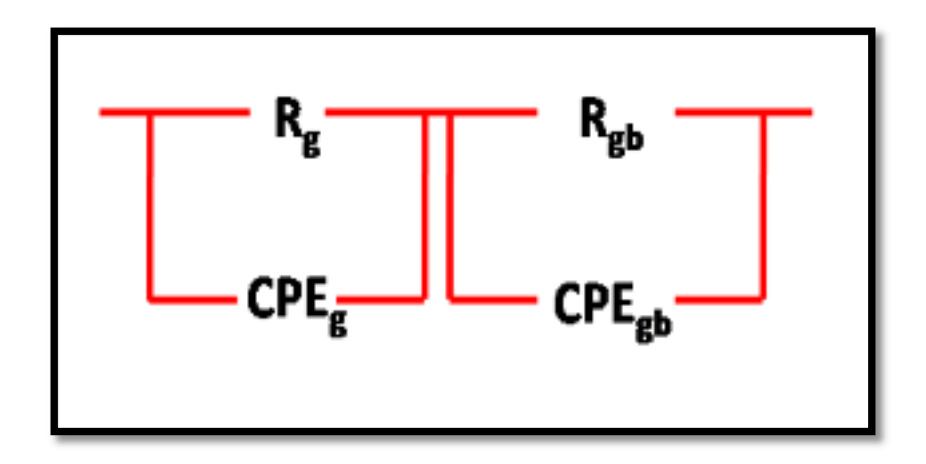


Figure 6.14 Equivalent circuit model of CoGdxFe<sub>2-x</sub>O<sub>4</sub>

(X = 0.00 to 0.08) nanoferrites

### **6.3.8 Dielectric Analysis**

### **6.3.8** (a) Dielectric Constant (ε')

Figure 6.15, shows the dielectric constant ( $\varepsilon$ ') measured to the material at the frequency range in 100 mHz to 10 MHz at room temperature. With the increase in frequency, the dielectric constants decrease. The dielectric constant declines sharply at low frequencies, but becomes frequency independent at high frequencies. The Maxwell-Wagner model of interfacial polarization, which agrees with the Koop model, is used to explain the fluctuation in dielectric constant. [Rahaman et.al., 2016]. The structure of spinel ferrites is assumed to have strongly conducted layers as grains in an insulating matrix with poor conduction layers as grain borders, according to Maxwell-Wagner. [Maxwell et.al., 1954]. At low frequencies, grain boundaries are more active than grains; hence the dielectric constant is higher at low frequencies and rapidly drops as frequency increases. [Kambale et.al., 2009]. As electrons are ready to

reach the poor conducting phase grain boundaries under the influence of an applied AC electric field. As a result, these electrons clump together, causing space charge polarization.

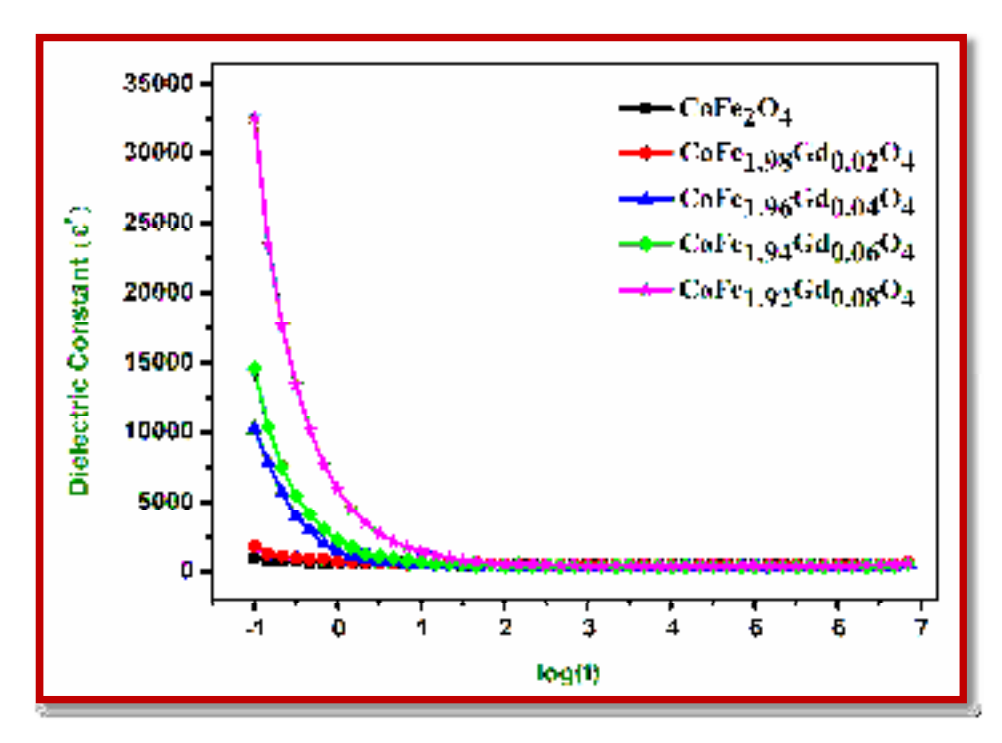


Figure 6.15 Dielectric constant of  $CoGdxFe_{2-x}O_4$  (X = 0.00 to 0.08) nanoferrites.

As a result, the dielectric constant is high at low frequencies and drops as frequency increases. In spinel ferrites, the formation of  $Fe^{3+}$  ions occur due to the exchange of electrons between  $Co^{2+}$  and  $Fe^{3+}$  to join a pair of  $Co^{3+}$  and  $Fe^{2+}$  [Igbal et.al., 2012].

The electron transfer from Fe<sup>3+</sup> to Fe<sup>2+</sup> causes a local displacement of the electron in the direction of the applied field, which explains ferrites' polarization. The polarization diminishes with increasing frequency until it reaches a constant value. As crystallite sizes shrink to the nanoscale, space polarization becomes increasingly important in determining the material's dielectric constant [Vigneshwaran et.al.,

2020]. The dielectric constant was evaluated using the below equation [Vigneshwaran et.al., 2020];

$$\varepsilon' = \operatorname{Cd} / \varepsilon_0 A \tag{6.10}$$

where C is the capacitance, d is thickness of the cylindrical pellet, A is area of the circular pellet,  $\varepsilon_0$  is permittivity of free space. In Table 6.6, the value of dielectric constant 949, 1799, 10223, 14588 and 32630 respectively increases with increase of  $Gd^{3+}$  ions. Furthermore, with increase of  $Gd^{3+}$  ions, the crystallite size decreases. Due to this, surface effects are increased the grain boundaries become highly active at lower frequency. The observed results showed increase in the value of dielectric constant, for these samples.

#### 6.3.8 (b) Dielectric Loss

The dielectric loss with respect to the frequency is shown in Figure 6.16. The dielectric losses are low at lower frequency and gradually increase with increase of frequency and also in the end, dielectric loss decreases at high frequency. This abnormal behavior of dielectric loss is due to dielectric relaxation peaks which could be described by Rezescu model [Rezlescu et.al., 1974]. In the view of Rezescu model, the dielectric relaxation peaks produce a combined involvement of N type and P type charge carriers. Beo et al. [Bao et.al., 2002] stated that the small polarons created in a material also associate to the polarization in addition to the N type charge carriers which exhibits to abnormal behavior of dielectric loss. Furthermore, the hopping frequency of localized charge carriers being linearly equal to the externally applied frequency and response occurring, resulting in the construction of the relaxation peak, can be linked to the establishment of the relaxation peak. The complex dielectric constant and dielectric loss are determined using the equations below [Vigneshwaran et.al., 2020].

$$\tan \delta = 1 / 2\pi f \varepsilon_0 \varepsilon' \qquad (6.11)$$

$$\varepsilon'' = \varepsilon ' \tan \delta \tag{6.12}$$

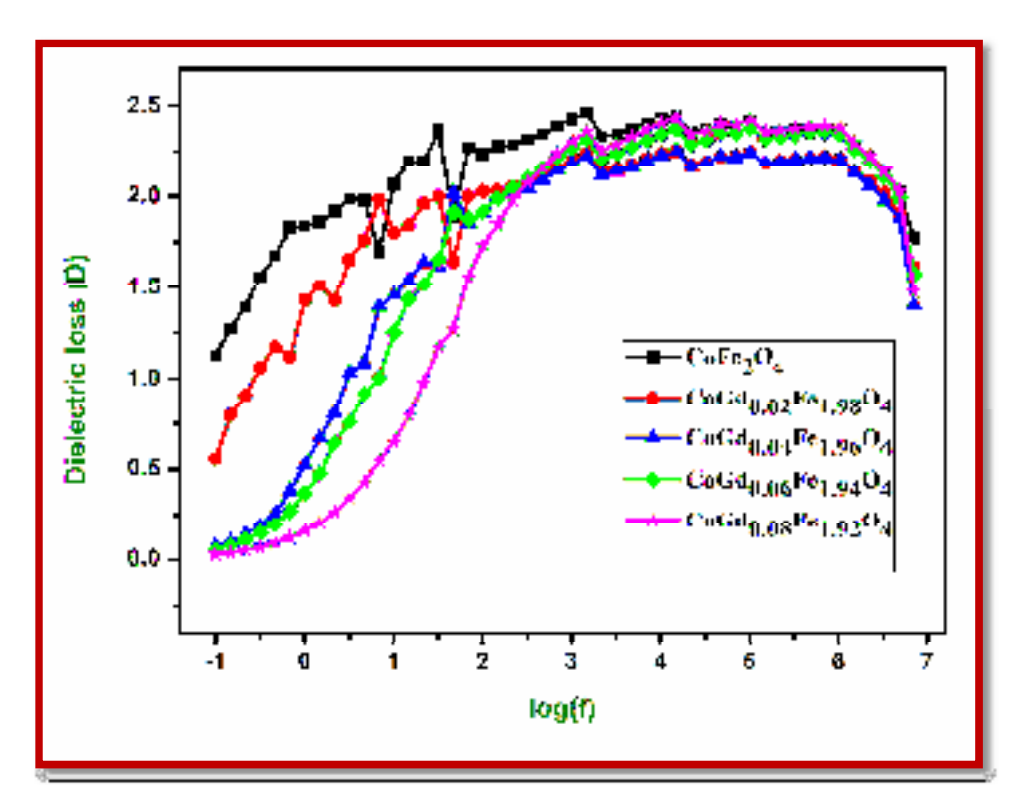


Figure 6.16 Dielectric loss of CoGdxFe<sub>2-x</sub>O<sub>4</sub> (X = 0.00 to 0.08) nanoferrites

The value of dielectric losses is 1.13, 0.56, 0.07, 0.06 and 0.03 respectively decreases with increasing of Gd<sup>3+</sup> ions. The electron exchanges between Fe<sup>3+</sup> and Fe<sup>2+</sup> need more energy and accordingly more energy loss occur due to high resistivity in grain boundaries. Furthermore, the amount of energy recovered was used to transfer the oscillating ions and these leads to dielectric loss.

#### 6.3.8 (c) AC Conductivity

Figure 6.17, shows the variation of Ac conductivity of the Gd<sup>3+</sup> doped Cobalt nanoferrites at various frequency (100 mHz to 10 MHz). In spinel nanoferrites the conduction mechanism can be explained by the Verwey mechanism [Gabal et.al., 2015].

The conduction is due to electron hopping between ions of the same element with various valence states at the octahedral (B) site, according to this mechanism. The following equation can be used to describe electron migration [Aziz et.al., 2016];

$$Co^{2+} + Fe^{3+} \leftrightarrow Co^{3+} + Fe^{2+}$$
 (6.13)

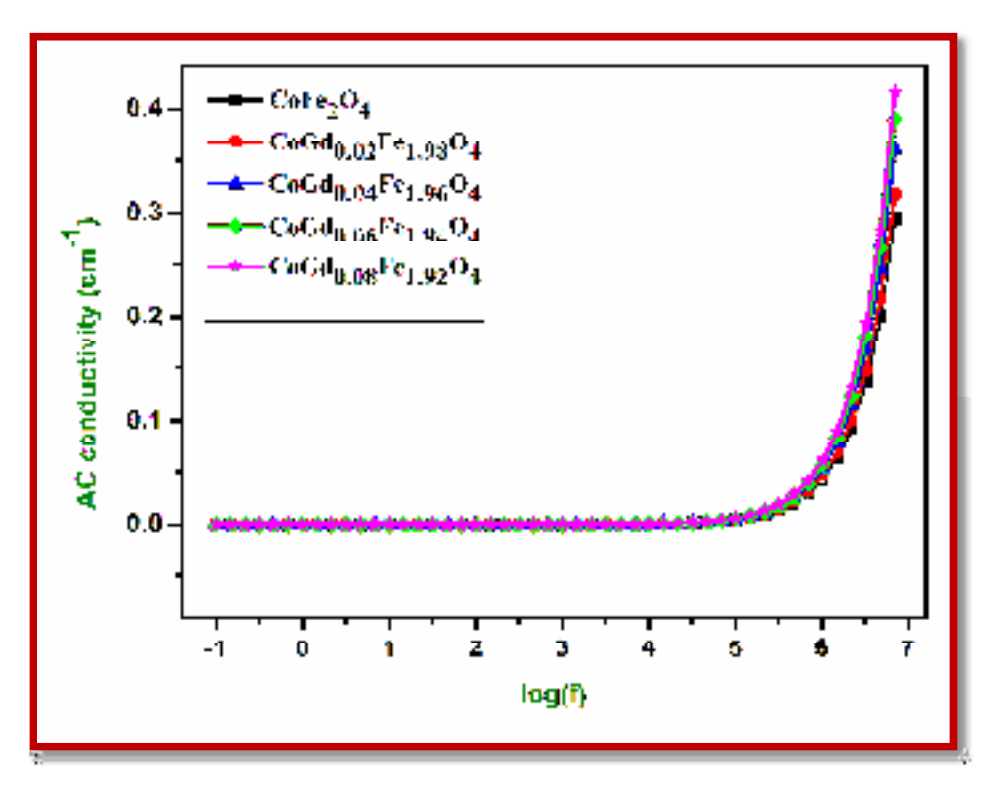


Figure 6.17 AC Conductivity vs Frequency of  $CoGdxFe_{2-x}O_4$ (X = 0.00 to 0.08) nanoferrites.

The migration of electron in between  $Fe^{3+}$  and  $Fe^{2+}$  present at the octahedral site in spinel ferrites is under the impact of applies Ac field and it owes to the electrical response of these ferrites. The electrical conductivity of nanoferrites is increased slowly at lower frequency, and then increases sharply at a higher frequency. Furthermore, in Table 6.6 an increase of conductivity in  $Fe^{3+}$  ions at the octahedral sites with the doping of  $Gd^{3+}$  ion in the cobalt ferrites, play a major role in enhancing the Ac conductivity of  $CoGd_XFe_{2-x}O_4$  nanoferrites (x = 0.00 to 0.08) [Murugesan et.al., 2015]. The dielectric parameters such as dielectric constant, complex dielectric constant, dielectric loss and AC conductivity were listed in Table 6.6.

Table 6.6 Dielectric parameters of  $CoGdxFe_{2-x}O_4$  (X = 0.00 to 0.08) nanoferrites.

Composition	Dielectric Constant (ε')	Dielectric Loss (tanδ)	Complex dielectric constant (ε")	AC Conductivity (Ω) (cm <sup>-1</sup> )
X=0.00	949	1.13	1070	0.30
X=0.02	1799	0.56	1002	0.32
X=0.04	10222	0.07	759	0.36
X=0.06	14588	0.06	817	0.39
X=0.08	32630	0.03	929	0.42

#### **6.4 CONCLUSIONS**

The prepared of  $Gd^{3+}$  doped cobalt nanoferrites of a spinel crystal  $CoGd_XFe_{2-}$   $_XO_4$  (X=0.00 to 0.08) via the sol-gel method is described briefly in this paper. The impact of  $Gd^{3+}$  ion substitutions in cobalt nanoferrites on structural, functional, optical, magnetic, and dielectric properties were examined. The cubic spinel structure of these nanoferrites was confirmed by X-ray diffraction patterns. In cobalt

nanoferrites, the average crystallite size falls as the number of Gd<sup>3+</sup> ions increase. Because of the change in ionic radius, the lattice constant and unit cell dimension rise as the number of Gd<sup>3+</sup> ions increase. The porosity reduces as the number of Gd<sup>3+</sup> ions increase, which is related to an increase in bulk density, but the surface area increases as the number of Gd<sup>3+</sup> ions fall, which is due to a reduction in crystallite size. The particles are spherical shaped grains with agglomeration, according to surface morphology.

The performance of grain and grain boundaries towards capacitance and resistance was shown by the Cole-Cole plot using impedance spectroscopy, implying that grain boundary contribution is higher than grain contribution. With increasing frequency, the variation of the dielectric constant diminishes. It is thought that the addition of Gd<sup>3+</sup> had a substantial impact on the Maxwell-Wagner interfacial charge polarization model, which agreed with the Koop model. The values of dielectric constant are increased with increase of Gd3+ ions. The value of dielectric losses decreases with increase of Gd3+ ions. The result also reveals abnormal behavior of dielectric loss and the same is due to relaxation peak. AC conductivity increases with increase of frequency as a function of increase with Gd3+ ions concentration as the spinels undergone Verwey mechanism. The very low dielectric loss and minimum magnetic saturation of these prepared nanoferrites has potential application in magnetic recording devices, magnetic shielding and microwave absorption devices. Further, reported sol-gel technique provides cost effective and green synthesis alternative for large scale production for industrial products and also for environmental advantages.

# REFERENCES

**Abbas S,** Chatterjee R, Dixit A, Kumar A, Goel T, Electromagnetic and microwave absorption properties of (Co<sup>2+</sup>–Si<sup>4+</sup>) substituted barium hexaferrites and its polymer composite, Journal of applied physics. 101(7) (2007) 074105.

**Ahmed M,** Ateia E, Salem F, Spectroscopic and electrical properties oMg–Ti ferrite doped with different rare-earth elements, Physica B: Condensed Matter. 381(1-2) (2006) 144-155.

**Ahmed M,** Okasha N, Kershi R, Influence of rare-earth ions on the structure and magnetic properties of barium W-type hexaferrite, Journal of Magnetism and Magnetic Materials. 320(6) (2008) 1146-1150.

**Ajith Kumar S,** Kuppusami P, Amirthapandian S, Fu Y.-P, Effect of Sm co-doping on structural, mechanical and electrical properties of Gd doped ceria solid electrolytes for intermediate temperature solid oxide fuel cells, International journal of hydrogen energy. 45(54) **(2020)** 29690-29704.

**Alves T,** Pessoni H, Franco Jr A, The effect of Y<sup>3+</sup> substitution on the structural, optical band-gap, and magnetic properties of cobalt ferrite nanoparticles, Physical Chemistry Chemical Physics. 19(25) (2017) 16395-16405.

**Amiri S,** Shokrollahi H, Magnetic and structural properties of RE doped Co-ferrite (RE: Nd, Eu, and Gd) nano-particles synthesized by co-precipitation, Journal of Magnetism and Magnetic Materials. 345 **(2013)** 18-23.

**Asiri S,** Sertkol M, Guner S, Gungunes H, Batoo K, Saleh T.A, Sozeri H, Almessiere M.A, Manikandan A, Baykal A, Hydrothermal synthesis of Co<sub>y</sub>Zn<sub>y</sub>Mn<sub>1-2y</sub>Fe<sub>2</sub>O<sub>4</sub> nanoferrites: magneto-optical investigation, Ceramics International. 44(5) **(2018)** 5751-5759.

**Aziz H.S,** Rasheed S, Khan R.A, Rahim A, Nisar J, Shah S.M, Iqbal F, Khan A.R, Evaluation of electrical, dielectric and magnetic characteristics of Al–La doped nickel spinel ferrites, RSC Advances. 6(8) (2016) 6589-6597.

- **Bao J,** Zhou J, Yue Z, Li L, Gui Z, Dielectric behavior of Mn-substituted Co<sub>2</sub>Z hexaferrites, Journal of Magnetism and Magnetic Materials. 250 (2002) 131-137.
- **Belavi P,** Chavan G, Naik L, Somashekar R, Kotnala R, Structural, electrical and magnetic properties of cadmium substituted nickel–copper ferrites, Materials Chemistry and Physics. 132(1) (2012) 138-144.
- **Bensebaa F,** Zavaliche F, L'ecuyer P, Cochrane R, Veres T, Microwave synthesis and characterization of Co–ferrite nanoparticles, Journal of colloid and interface science. 277(1) (2004) 104-110.
- **Bobade D,** Rathod S, Mane M.L, Sol–gel auto-combustion synthesis, structural and enhanced magnetic properties of Ni<sup>2+</sup> substituted nanocrystalline Mg–Zn spinel ferrite, Physica B:Condensed Matter. 407(18) (2012) 3700-3704.
- **Bolarín-Miró A.M,** Vera-Serna P, Sánchez-De Jesús F, Cortés-Escobedo C.A, Martínez-Luevanos A, Mechanosynthesis and magnetic characterization of nanocrystalline manganese ferrites, Journal of Materials Science: Materials in Electronics. 22(8) (2011) 1046-1052.
- Che R.C, Peng L.M, Duan X.F, Chen Q, Liang, XL, Microwave absorption enhancement and complex permittivity and permeability of Fe encapsulated within carbon nanotubes, Advanced Materials. 16(5) (2004) 401-405.
- **Dimri M.C,** Verma A, Kashyap S.C, Dube D, Thakur O, Prakash C, Structural, dielectric and magnetic properties of NiCuZn ferrite grown by citrate precursor method, Materials Science and Engineering:B. 133(1-3) (2006) 42-48.
- **El-Sheikh S.M,** Rashad M.M, Harraz F.A, Morphological investigation and magnetic properties of nickel zinc ferrite 1D nanostructures synthesized via thermal decomposition method, Journal of Nanoparticle Research. 15(10) (2013) 1-11.
- **Gabal M,** Al Angari Y, Al-Agel F, Cr-substituted Ni–Zn ferrites via oxalate decomposition. Structural, electrical and magnetic properties, Journal of Magnetism and Magnetic Materials. 391 **(2015)** 108-115.

**Ghodake J,** Kambale R.C, Shinde T, Maskar P, Suryavanshi S, Magnetic and microwave absorbing properties of Co<sup>2+</sup> substituted nickel–zinc ferrites with the emphasis on initial permeability studies, Journal of Magnetism and Magnetic Materials. 401 **(2016)** 938-942.

**Huang Y,** Li N, Ma Y, Du F, Li F, He X, Lin X, Gao H, Chen Y, The influence of single-walled carbon nanotube structure on the electromagnetic interference shielding efficiency of its epoxy composites, Carbon. 45(8) (2007) 1614-1621.

**Humbe A.V,** Nawle A.C, Shinde A, Jadhav K, Impact of Jahn Teller ion on magnetic and semiconducting behaviour of Ni-Zn spinel ferrite synthesized by nitrate-citrate route, Journal of Alloys and Compounds. 691 (2017) 343-354.

**Iqbal M.J,** Khan R.A, Mizukami S, Miyazaki T, Mössbauer, magnetic and microwave absorption characteristics of substituted W-type hexaferrites nanoparticles, Ceramics International. 38(5) **(2012)** 4097-4103.

**Kadam A,** Shinde S, Yadav S, Patil P, Rajpure K, Structural, morphological, electrical and magnetic properties of Dy doped Ni–Co substitutional spinel ferrite, Journal of Magnetism and Magnetic Materials. 329 **(2013)** 59-64.

**Kamar Tanbir**, Mritunjoy Prasad Ghosh, Rakesh Kumar Singh, Samrat Mukherjee, Gd-doped soft Mn–Zn nanoferrites: synthesis, microstructural, magnetic and dielectric characterizations, **J**ournal of Materials Science: Materials in Electronics. **(2020).** 

**Kambale R,** Shaikh P, Bhosale C, Rajpure K, Kolekar Y, Dielectric properties and complex impedance spectroscopy studies of mixed Ni–Co ferrites, Smart materials and structures. 18(8) (2009) 085014.

**KanYue,** Facile synthesis of ultrasmall Fe<sub>3</sub>O<sub>4</sub> nanoparticles on MXenes for high microwave absorption performance, Composites Part A: Applied Science and Manufacturing.115 (2018), 371-382.

**Krishna K.R**, Kumar K.V, Ravindernathgupta C, Ravinder D, Magnetic properties of Ni-Zn ferrites by citrate gel method, Advances in Materials Physics and Chemistry. 2(3) **(2012)** 149-154.

**Kumar G,** Shah J, Kotnala R, Dhiman P, Rani R, Singh V.P, Garg G, Shirsath S.E, Batoo K.M, Singh M, Self-ignited synthesis of Mg–Gd–Mn nanoferrites and impact of cation distribution on the dielectric properties, Ceramics International. 40(9) **(2014)** 14509-14516.

**Kumar** S.A, Kuppusami P, Vigneshwaran B, Fu Y.-P, Codoped Ceria  $Ce_{0.8}M_{0.1}Gd_{0.1}O_{2-\delta}$  (M= Sm<sup>3+</sup>, Sr<sup>2+</sup>, Ca<sup>2+</sup>) and Codoped Ceria–Na<sub>2</sub>CO<sub>3</sub> Nanocomposite Electrolytes for Solid Oxide Fuel Cells, ACS Applied Nano Materials. 2(10) (2019) 6300-6311.

**Kumari K,** Prasad K, Choudhary R, Impedance spectroscopy of (Na<sub>0.5</sub>Bi<sub>0.5</sub>) (Zr<sub>0.2</sub>5Ti<sub>0.75</sub>)O<sub>3</sub> lead-free ceramic, Journal of Alloys and Compounds. 453(1-2) (2008) 325-331.

**Kumari N,** Kumar V, Khasa S, Chemical synthesis and magnetic investigations on Cr<sup>3+</sup> substituted Zn-ferrite superparamagnetic nano-particles. Ceram Int. 41: **(2015)** 1907–1911.

**Lakshita PHOR**, Vinod KUMAR, Structural, thermomagnetic, and dielectric properties of Mn0.5Zn0.5GdxFe2-xO4 (x = 0, 0.025, 0.050, 0.075, and 0.1), Journal of Advanced Ceramics. **2020**, 9(2): 243–254.

**Langford J.I and Wilson A.J.C,** Scherrer after Sixty Years: A Survey and Some New Results in the Determination of Crystallite Size, J. Appl. Cryst. 11 102 (1978).

**Lavanya Rathi P,** Bharathi Ponraj and Deepa Seetharaman, Absorption-dominant Microwave Shielding Properties of Sn0.2Fe2.8O4-Graphite-PVDF Ternary Nanocomposite Films, Journal of Physics D: Applied Physics. **(2021).** 

**Lenin N,** Kanna R.R, Sakthipandi K, Kumar A.S, Structural, electrical and magnetic properties of NiLa<sub>x</sub>Fe<sub>2-x</sub>O<sub>4</sub> nanoferrites, Materials Chemistry and Physics. 212 **(2018)** 385-393.

**Lenin N,** Karthik A, Srither S.R, Sridharpanday M, Surendhiran S, Balasubramanian M, Synthesis, structural and microwave absorption properties of Cr-doped zinc lanthanum nanoferrites Zn<sub>1-x</sub>Cr<sub>x</sub>La<sub>0.1</sub>Fe<sub>1.9</sub>O<sub>4</sub> (*x*=0.09, 0.18, 0.27 and 0.36), Ceram Int. (2021).

**Lenin N,** Sakthipandi K, Kanna R.R, Rajkumar G, Electrical, magnetic and structural properties of polymer-blended lanthanum-added nickel nano-ferrites, Ceramics International. 44(17) (2018) 21866-21873.

**Li X,** Hou Y, Zhao Q, Wang L, A general, one-step and template-free synthesis of sphere-like zinc ferrite nanostructures with enhanced photocatalytic activity for dye degradation, Journal of colloid and interface science. 358(1) (2011) 102-108.

**M. Meshram,** Agrawal N.K, Sinha B, Misra P, Characterization of M-type barium hexagonal ferrite-based wide band microwave absorber, Journal of Magnetism and Magnetic Materials. 271(2-3) **(2004)** 207-214.

Maxwell J.C, Electricity and magnetism, Dover New York (1954).

**Mritunjoy Prasad Ghosh**, Samrat Mukherjee, Ce<sup>3+</sup>-doped nanocrystalline cobalt–zinc spinel ferrite: microstructural, magnetic, and optical characterizations, Journal of Materials Science: Materials in Electronics. (2020).

**Muhammad Junaid,** Muhammad Azhar Khan, Zubair Mahmood Hashmi, Gulfam Nasar, Nessrin A. Kattan, A. Laref, Structural, spectral, magnetic and dielectric properties of Bi substituted Li-Co spinel ferrites, Journal of Molecular Structure. 1221 **(2020)** 128859.

**Murugesan C,** Chandrasekaran G, Impact of Gd<sup>3+</sup> substitution on the structural, magnetic and electrical properties of cobalt ferrite nanoparticles, RSC Advances. 5(90) **(2015)** 73714-73725.

**Peijiang Liua,** Zhengjun Yaoa, Jintang Zhoua, Zhihong Yanga, Ling Bing Kongc, Small magnetic Co-doped NiZn ferrite/graphene nanocomposites and their dual-region microwave absorption performance, Journal of Materials Chemistry C. **(2016)** 1-39.

**Peng J,** Hojamberdiev M, Xu Y, Cao B, Wang J, Wu H, Hydrothermal synthesis and magnetic properties of gadolinium-doped CoFe<sub>2</sub>O<sub>4</sub> nanoparticles, Journal of Magnetism and Magnetic Materials. 323(1) **(2011)** 133-137.

**Peng Z,** Fu X, Ge H, Fu Z, Wang C, Qi L, Miao H, Effect of Pr<sup>3+</sup> doping on magnetic and dielectric properties of Ni–Zn ferrites by "one-step synthesis", Journal of Magnetism and Magnetic Materials. 323(20) (2011) 2513-2518.

**Purnama B,** Wijayanta A.T, Effect of calcination temperature on structural and magnetic properties in cobalt ferrite nano particles, Journal of King Saud University-Science. 31(4) (2019) 956-960.

**Rahaman M.D,** Mia M.D, Khan M, Hossain A.A, Study the effect of sintering temperature on structural, microstructural and electromagnetic properties of 10% Cadoped Mn<sub>0.6</sub>Zn<sub>0.4</sub>Fe<sub>2</sub>O<sub>4</sub>, Journal of Magnetism and Magnetic Materials. 404 **(2016)** 238-249.

**Rahman M.A,** Hossain A.A, Electrical transport properties of Mn–Ni–Zn ferrite using complex impedance spectroscopy, Physica Scripta. 89(2) (2014) 025803.

**Rahman M.T,** Ramana C, Gadolinium-substitution induced effects on the structure and AC electrical properties of cobalt ferrite, Ceramics International. 40(9) (2014) 14533-14536.

**Rashad M**, Elsayed E, Moharam M, Abou-Shahba R, Saba A, Structure and magnetic properties of Ni<sub>x</sub>Zn<sub>1-x</sub>Fe<sub>2</sub>O<sub>4</sub> nanoparticles prepared through co-precipitation method, Journal of Alloys and Compounds. 486(1-2) (2009) 759-767.

**Rezlescu N,** Rezlescu E, Dielectric properties of copper containing ferrites, physica status solidi (a). 23(2) (1974) 575-582.

**Rezlescu N,** Rezlescu E, Pasnicu C, Craus M, Effects of the rare-earth ions on some properties of a nickel-zinc ferrite, Journal of Physics: Condensed Matter. 6(29) (1994) 5707.

**Saccone F.D,** Ferrari S, Errandonea D, Grinblat F, Bilovol V, Agouram S, Cobalt ferrite nanoparticles under high pressure, Journal of applied physics. 118(7) (2015) 075903.

**Scherrer P,** Bestimmung der Grösse und der inneren Struktur von Kolloidteilchen mittels Röntgenstrahlen, Nachr. Ges. Wiss. Göttingen. 26 98 (1918).

**Siddiqui J.J,** Zhu K, Qiu J, Ji H, Sol–gel synthesis, characterization and microwave absorbing properties of nano sized spherical particles of La<sub>0.8</sub>Sr<sub>0.2</sub>Mn<sub>0.8</sub>Fe<sub>0.2</sub>O<sub>3</sub>, Materials Research Bulletin. 47(8) **(2012)** 1961-1967.

**Sivakumar N,** Narayanasamy A, Ponpandian N, Govindaraj G, Grain size effect on the dielectric behavior of nanostructured Ni<sub>0.5</sub> Zn<sub>0.5</sub>Fe<sub>2</sub> O<sub>4</sub>, Journal of applied physics. 101(8) **(2007)** 084116.

**Sivakumar P,** Ramesh R, Ramanand A, Ponnusamy S, Muthamizhchelvan C, Preparation and properties of nickel ferrite (NiFe<sub>2</sub>O<sub>4</sub>) nanoparticles via sol–gel autocombustion method, Materials Research Bulletin. 46(12) (2011) 2204-2207.

**Uvarov V. and Popov I,** Metrological characterization of X-ray diffraction methods for determination of crystallite size in nano-scale materials, Mater. Charac. 85 (111) **(2013).** 

**Vigneshwaran B,** Kuppusami P, Ajithkumar S, Sreemoolanadhan H, Study of low temperature  $\Box$  dependent structural, dielectric, and ferroelectric properties of Ba<sub>x</sub>Sr<sub>(1-x)</sub> TiO<sub>3</sub> (x = 0.5, 0.6, 0.7) ceramics, Journal of Materials Science: Materials in Electronics. 31 **(2020)** 10446–10459.

**Vigneshwaran B,** Kuppusami P, Panda A, Singh A, Sreemoolanadhan H, Microstructure and optical properties of Ba<sub>0.6</sub>Sr<sub>0.4</sub>TiO<sub>3</sub> thin films prepared by pulsed laser deposition, Materials Research Express. 5(6) (2018) 066420.

**Wang Z,** Xie Y, Wang P, Ma Y, Jin S, Liu X, Microwave anneal effect on magnetic properties of Ni<sub>0.6</sub>Zn<sub>0.4</sub>Fe<sub>2</sub>O<sub>4</sub> nano-particles prepared by conventional hydrothermal method, Journal of Magnetism and Magnetic Materials. 323(23) (2011) 3121-3125.

Yadav R.S, Kuritka I, Vilcakova J, Havlica J, Masilko J, Kalina L, Tkacz J, Svec J, Enev V, Hajdúchová M, Impact of grain size and structural changes on magnetic, dielectric, electrical, impedance and modulus spectroscopic characteristics of CoFe<sub>2</sub>O<sub>4</sub> nanoparticles synthesized by honey mediated sol-gel combustion method, Advances in Natural Sciences: Nanoscience and Nanotechnology. 8(4) (2017) 045002.

**Yu T,** Shen Z, Shi Y, Ding J, Cation migration and magnetic ordering in spinel CoFe2O4 powder: micro-Raman scattering study, Journal of Physics: Condensed Matter. 14(37) **(2002)** L613.

**Zhang L,** He R, Gu H.C, Oleic acid coating on the monodisperse magnetite nanoparticles, Applied Surface Science. 253(5) (2006) 2611-2617.

## **CHAPTER – VII**

# INFLUENCE OF GD<sup>3+</sup> IONS ON STRUCTURAL, OPTICAL, MAGNETIC AND DIELECTRIC PROPERTIES OF MNGd<sub>x</sub>Fe<sub>2-x</sub>O<sub>4</sub>(0.00 $\leq X \geq$ 0.08) NANOFERRITES

#### 7.1 INTRODUCTION

Ferrites are defined as materials that have both magnetic and electrical properties. Ferrites contain metallic oxides (such as MnO, CeO, ZnO, NiO, and others) and ferric oxides (such as Fe<sub>2</sub>O<sub>3</sub>). Man has known about the benefits of ferrites for millennia. The Chinese were well-versed in the use of inorganic substances in navigational compasses to signify a heavy load. [Smit et.al., 1953]. In recent years spinel ferrites are well known magnetic material having various tremendous magnetic and electrical properties. These features enable a wide range of applications in science and technology, including microwave devices, electronics power transformers, spintronics, antenna rods, gas sensors, and medication delivery, magnetic romance imaging (MRI) magnetic amplifier, electrical generator, biomedicines, transformer cores, and electromagnetic interference (EMI) [KárolyLázár et. al., 2002, Gadkari et.al., 2009, El-Sheikh et.al., 2013]

The rare earth elements belong to the lanthanide's series, which act as good electrically insulator substrates with high resistivity [Majid Niaz Akhtar et.al., 2017]. Comparing various spinel ferrite (MnFe<sub>2</sub>O<sub>4</sub>) is a particular type of soft ferrite material that is achievable athigh frequencies, with low coercivity and low dielectric losses. The substitution of smaller rare-earth of ion in ferrites nanoparticles affects its physical property such as structure, morphological, electrical and dielectric properties like loss and conductivity [Somnath et.al., 2017]. Rare-earth ions are well known for

the strong spin-orbit coupling but for Gd<sup>3+</sup> ions, due to half-filled 4f shell S(4f), the total magnetic moment has occurred from the unpaired spin part [Coey et.al., 2009]. Doping of rare-earth ions hinders crystal growth, thereby reducing the nano ferrite due to the significant size effect.

In general, ferrite nanomaterials have been synthesized from soft feasible method such as sol-gel [Wang et.al., 2016], co-precipitation [Stergiou et.al., 2011], solid-state reaction technique [Khan et.al., 2018], hydrothermal [Phumying et.al., 2013] and sono chemical method [Jing et.al., 2007]. Above all, owing to the tiny particle size, reducibility, high homogeneity, and increased purity of the produced nanoparticles, the sol-gel approach produces superior results. The microstructure, grain size, synthesis method, and cation distribution in the lattice sites all have a role in ferrites' relevance and use [Biao Zhou et.al., 2004].

The effect of gadolinium ions on the structural, optical, magnetic, and electrical properties of nanoferrites was investigated in this work. The crystal of the work is to achieve whether the dielectric constant of the materials can be improved compared to pure Mn ferrite while existing their insulating nature. There is limited literature on the magnetic response of Gd<sup>3+</sup>depending on Mn nano ferrites and their dielectric behavior.

In current study, MnGdFe<sub>2-x</sub>O<sub>4</sub>nano ferrites with different doping concentrations (x = 0.00, 0.02, 0.04, 0.06, and 0.08) were synthesized by sol-gel method. Modified structural, optical, magnetic and dielectric properties of prepared nanoferrites due to the substitution of the small amount of Gd<sup>3+</sup> ions have been examined by using XRD, FESEM with EDAX, UV-DRS, vibrating sample

magnetometer (VSM), Impedance spectroscopy and dielectric studies have been analyzed. It may be suitable for electric application in the microwave frequency region.

#### 7.2 MATERIALS AND METHODS.

#### 7.2.1 Materials

Gadolinium nitrate [Gd ( $NO_3$ )<sub>3</sub>.6H<sub>2</sub>O)] (99.99%), Iron nitrate [Fe ( $NO_3$ )<sub>3</sub>.9H<sub>2</sub>O)], Manganese nitrate [Mn ( $NO_3$ )<sub>2</sub>.6H<sub>2</sub>O)] (98%) and Citric acid [C<sub>6</sub>H<sub>8</sub>O<sub>7</sub>] (99.5%) are used as raw materials. All materials are obtained from Sigma Aldrich.

## 7.2.2 Synthesis procedure

The Stoichiometric ratios of nitrates were used for the synthesis of  $MnGd_XFe_{2-X}O_4$  (with X=0.00, 0.02, 0.04, 0.06 and 0.08). The estimated nitrate precursors are combined in deionized water through continuous stirring until a homogenous solution is formed.

A 1:1 molar ratio of citric acid to nitrate is dissolved in a deionized water solution of citric acid. With the aid of the ammonia solution, the pH of the solution is kept at 7. The temperature was raised to 80°C till the gel was formed. Then, the gel was held in an oven at 100°C temperature for 24 hrs to obtain the material in dry powder. And then, it was kept in a muffle furnace at 500 °C for 2hrs. Collected nano powder was grinded for 15 minutes to obtain by-product free nanoparticles. And then finally, the as he were calcined at1000 °C for 24hrs. The schematic diagram of prepared nano ferrites is shown in Figure 7.1.

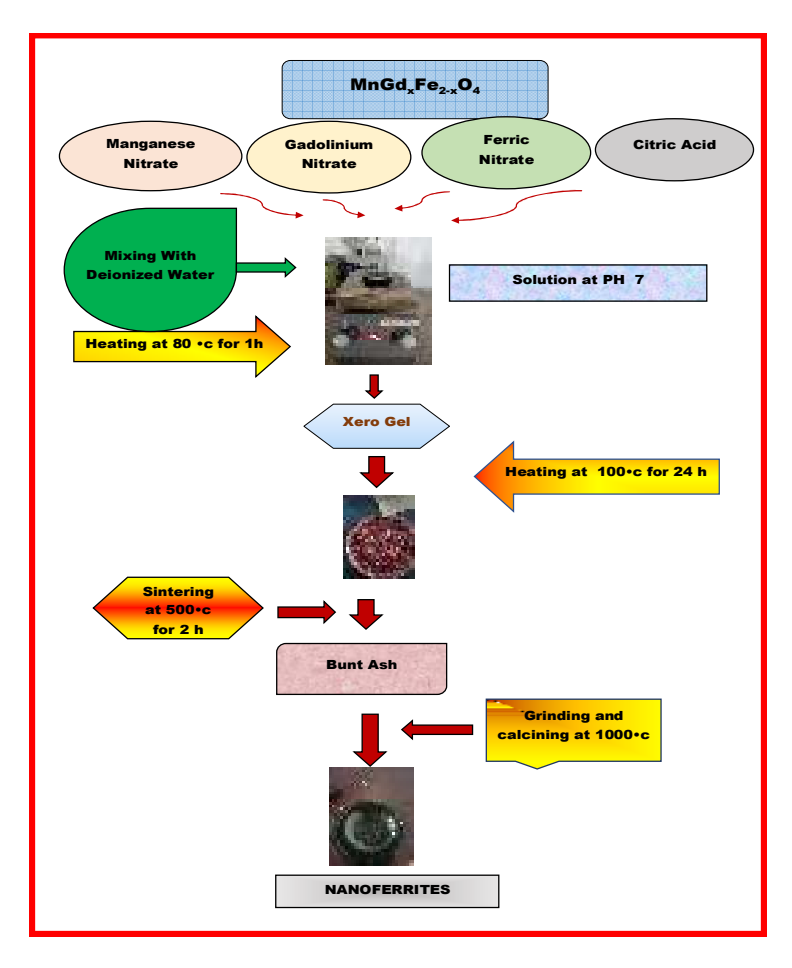


Figure 7.1 Flow chart for the sample preparation of MnGdxFe<sub>2-x</sub>O<sub>4</sub> Nanoferrites

### 7.2.3 Characterization Technique

The characterization techniques have been performed to evaluate the properties of these Gd doped Mn ferrites MnGd<sub>x</sub>Fe<sub>2-x</sub>O<sub>4</sub> (X=0.00, 0.02, 0.04, 0.06 and 0.08) samples. The XRD was been employed to find out the structural parameters in terms of lattice parameters, d-spacing, crystallite size, unit cell volume, and other parameters. The study was performed under SHIMADZU - XRD advance diffractometer with CuKα Radiations of 1.5406 Å wavelengths. FESEM determines the microstructure and elemental composition of all samples with an EDAX (JEOL JSM-6480 LV). The optical properties are employed using UV–DRS

spectrophotometer, and the wavelength was noted from 200 to 800nm. The spectroscopic vibrational studies of Gd doped Mn nanocrystalline ferrites have been performed on FTIR (Perkin Elmer L1600) between the wavenumber range of 4000–400 cm<sup>-1</sup>. Raman spectroscopy studies were made using an (ALU-PHI5000) AUG spectrometer with monochromatic Al Ka and 26.00 eV radiation. Magnetic characteristics of coercivity, saturation, and other parameters have been measured on VSM (Lake Shore 7404). The Impedance spectroscopy with the frequency range of 100 mHz to 10 MHz at room Temperature Biologic SP-300) was used to determine the electrical properties.

### 7.3. RESULTS and DISCUSSIONS

#### 7.3.1. Structural analysis

The XRD pattern of MnGd<sub>x</sub>Fe<sub>2-x</sub>O<sub>4</sub> ferrite with various Gd<sup>3+</sup> concentration namely x= 1.00, 0.02, 0.04, 0.06, and 0.08 are shown in Figure 7.2. The XRD pattern of prepared nano ferrites exposes that the presence of reflection planes having (hkl) values as (220), (311), (400), (333), and (440) are confirmed by JCPDS card No 74-2401[Mohd Mohsin Nizam Ansariet.al., 2020]. It is confirmed from JCPDS values that corresponding peak angles of 29.04°, 35.18°, 43.22°, 52.02°and 62.18°. These planes confirm the cubic structure of spinel ferrite without any additional, prominent impurities.

The average crystallite size (D) was estimated using the Scherrer formula [Kartharinal Punithavathy et.al., 2020].

$$D = \frac{\kappa\lambda}{\beta\cos\theta} \tag{7.1}$$

where, and k are the full width at half maximum, angle of diffraction, wavelength of the X-ray radiation and Scherrer constant (k=0.9). The average crystallite size decreases from 26 to 13 with an increase of Gd<sup>3+</sup> ions. The ionic radius of Gd<sup>3+</sup> ions (0.94 Å) is greater than that of Fe<sup>3+</sup> ions (0.65 Å). So, the replacement of rare-earth ions shows limited solubility in spinel lattice and inhibits grain growth [Penget.al., 2011].

The lattice constant for the prepared nano ferrites is calculated by using the following equation.

$$a = d_{hkl}\sqrt{h^2 + k^2 + l^2} \tag{7.2}$$

where a, d, hkl are the lattice constant, interatomic spacing and miller indices. The lattice constant monotonously increased from 7.820 to 8.928 with an increase of Gd<sup>3+</sup> concentration, which is an attribute to the larger ionic radius of Gd<sup>3+</sup> ions (0.94 Å) than that of Fe<sup>3+</sup> ions (0.65 Å) [Somnath et.al., 2017]. Thus, the Mn<sup>2+</sup>ions get incorporated into the lattice of Mn<sup>2+</sup> ions and Gd<sup>3+</sup> ions as the Octahedral site in a position of Fe<sup>3+</sup> ions, causing some internal stress that tends to expand unit cell [Lenin et.al., 2021]. Thus, incorporating Gd<sup>3+</sup> ion into manganese nano ferrites without any trace of secondary phase is further confirmed by the increase of the lattice constant. Additionally, the X-ray (dx) of the prepared nanoferrites was calculated [Kartharinal Punithavathy et.al., 2020];

$$d_{x} = \frac{8M}{Na^{3}} \tag{7.3}$$

where M, N and a<sup>3</sup> are the molecular weight of the ferrite, N is Avogadro's number, and a<sup>3</sup> is the volume of the cubic unit cell. The noticeable X-ray density decreases from 5.144to 4.862 with substitution Gd<sup>3+</sup> ions can be leads due to increase of lattice constant.

The bulk density  $(d_B)$  was estimated by using following relation [Kartharinal Punithavathy et.al., 2020];

$$d_B = \frac{m}{\pi r^2 t} \tag{7.4}$$

where t, r, m and  $d_B$  are the thickness of the pellet, radius of the pellet, the mass of the pellet ad bulk density. To infer that the bulk density increases from 2.470 to 2.971 with increased  $Gd^{3+}$  ion happens due to the atomic weight of the  $Fe^{3+}$  ion (55.84 g/mol) is smaller than that of the Gd ion (157.02 g/mol). The place of  $Gd^{3+}$  ions activate the sintering condition, thus resulting from increasing bulk density [Irshad Ali et.al., 2012]. Therefore, the X-ray density is more significant when compared to the bulk density due to presence of pores in the prepared nano ferrites.

The porosity (P) was estimated by using following relation.

$$P = \left(1 - \frac{d_B}{d_X}\right) \tag{7.5}$$

where dx, dB and Pare X-ray density, bulk density and porosity. The porosity percentage decreases from 0.585 to 0.280 % with the increase of Gd<sup>3+</sup> ion, which is attributed to an increase in bulk density. Hence the bulk density is inversely proportional to the porosity of the prepared ferrites.

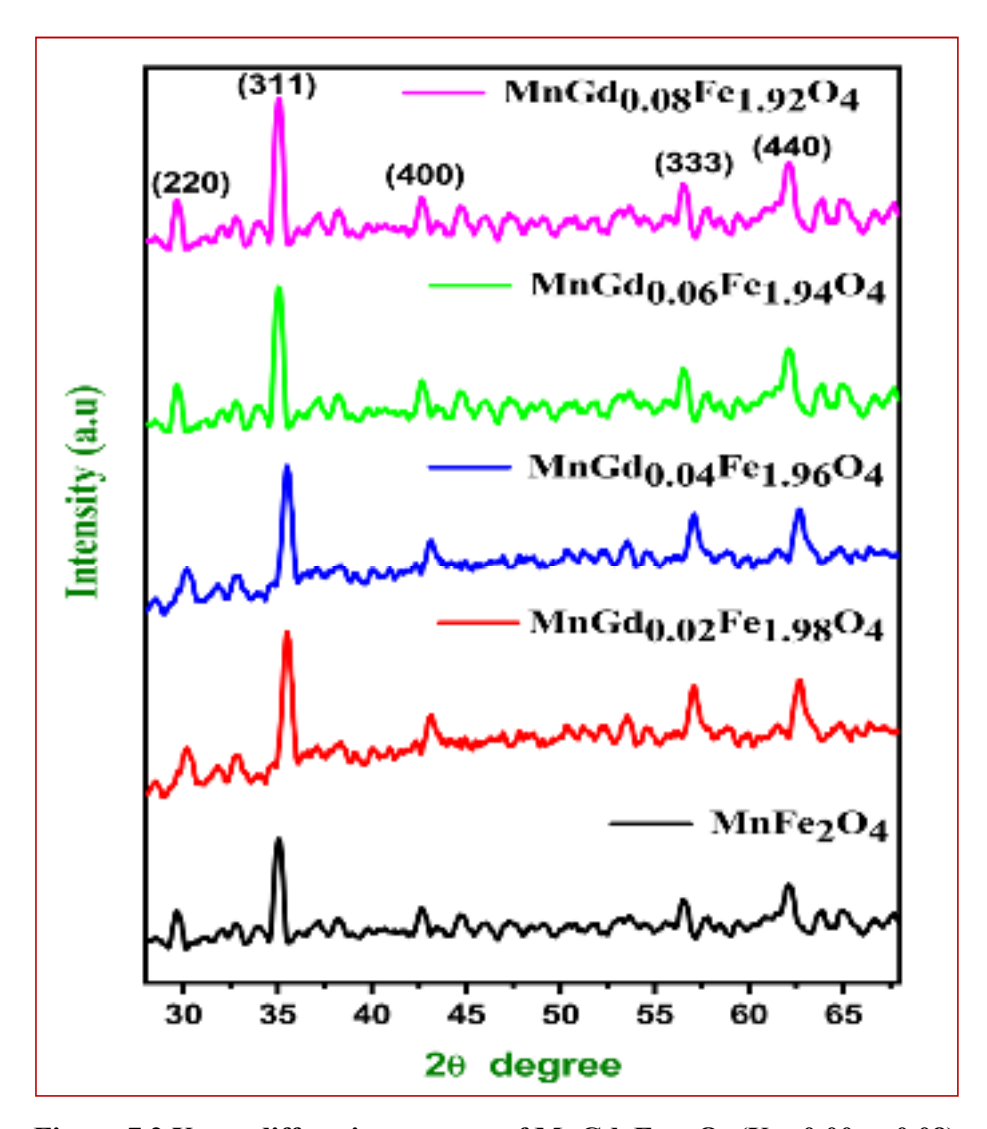


Figure 7.2 X-ray diffraction pattern of MnGdxFe<sub>2-x</sub>O<sub>4</sub> (X = 0.00 to 0.08)
nanoferrites

Table 7.1 Structural parameters of MnGdxFe<sub>2-x</sub>O<sub>4</sub> (X = 0.00 to 0.08) nanoferrites.

Composition	Crystallite size (nm) (± 0.02)	Lattice constant (a) (± 0.002) Å	Volume of unit cell (Å) (a³)	X-ray density (ρxrd) (g/cm³)	Bulk density (d <sub>B</sub> ) (g/cm <sup>3</sup> )	Surface area (S <sub>XRD</sub> ) (m <sup>2</sup> /g)	Porosity (%)
(G0) X=0.00	26	7.820	478.31	6.254	2.470	39.38	0.585
(G2) X=0.02	24	8.211	553.77	5.364	2.494	47.84	0.535
(G4) X=0.04	20	8.550	625.06	4.720	2.621	67.47	0.444
(G6) X=0.06	15	8.652	654.61	4.476	2.875	111.9	0.357
(G8) X=0.08	13	8.928	711.71	4.089	2.941	164.83	0.280

The surface area (S) was estimated by using the below expression [Kartharinal Punithavathy et.al., 2020].

$$s = \frac{6}{d_x} D \tag{7.6}$$

where D, dx and S are the crystallite size, X-ray density and surface area. The surface area increases from 39.38 to 164.83 with the substitution of Gd<sup>3+</sup> ion, which is due to a decrease in porosity and crystallite size. The results noticed from all the structural parameters are listed in Table 7.1.

## 7.3.2 Optical Analysis

The prepared nano ferrites optical properties were carried out using UV-DRS spectroscopy within the range of 200 – 800 nm at room temperature. It is used to estimate the bandgap to verify the semiconducting nature of the material. The absorbance usually depends on a few factors such as lattice parameter, bandgap, grain size, surface roughness and impurity centers [Gupta et.al., 1996]. Figure 7.3 clearly shows that the tremendous visible light region and the wavelength were decreased

with the increase of  $Gd^{3+}$  ion as 231.76 nm to 222.24 nm from X = 0.00 to 0.08, which is due to the decrease of crystallite size.

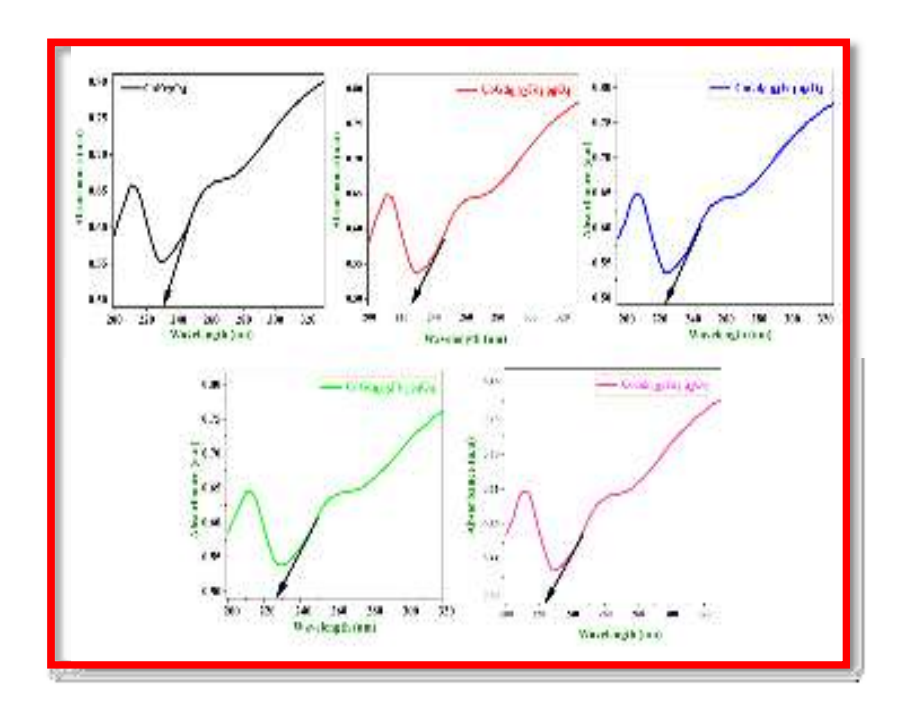


Figure 7.3 Absorbance spectra of MnGdxFe<sub>2-x</sub>O<sub>4</sub> (x= 0.00 to 0.08) nanoferrites

The optical band gap value of the ferrites was used to evaluate the classical Taue's equation [Vigneshwaran et.al., 2018];

$$\alpha h \gamma = A[h \gamma - E_g]^{\text{n}} \tag{7.7}$$

 $E_g$ , hy,  $\alpha$ , n, A is the bandgap, energy of the photon, absorption coefficient power index and probability transition constant, n depends on the nature of the electronic transitions, which have n= (1/2) for direct and indirect bandgap energies. From Figure 7.4 and 7.5, the direct and indirect bandgap values increase in the range of 2.36 to 2.96 eV and 3.25 to 3.76 eV increase of doping concentration  $Gd^{3+}$  ions as indexed in Table 7.2. The bandgap energy values obtained are consistent and function in a semiconducting nature [Almessiere et.al., 2019].

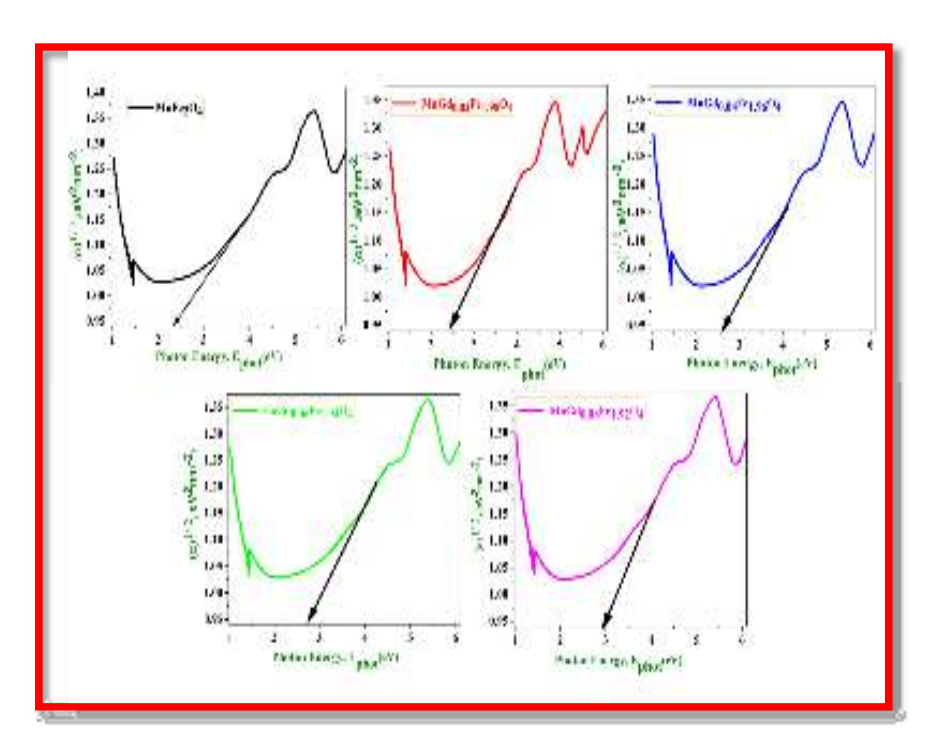


Figure 7.4 Direct bandgap energy of MnGdxFe<sub>2-x</sub>O<sub>4</sub> (X= 0.00 to 0.08) nano ferrites.

It is also noted that the bandgap of Mn ferrites has diverse nature by the small amount of Gd<sup>3+</sup> ions due to smaller crystallite size, lower concentration of Gd<sup>3+</sup> ions and movement of ions from valance band to conduction band. The bandgap increase is due to the synthetic effect of gadolinium and decreased electron-hole recombination, trends in a rise in bandgap [Li et.al., 2011].

The increase in direct bandgap with a rise in Gd<sup>3+</sup> ions can be explained by Burstein – Moss (B-M) shift which infers that as the Gd<sup>3+</sup> ions increase, donor electrons occupy the bottom states of the conduction band, effectively hindering the lower state of the conduction band increasing in the direct optical bandgap [Rana et.al., 2016]. It infers inverse variation of the bandgap with crystallite size obtained because of an increase in lattice parameters [Kumar et.al., 2014].

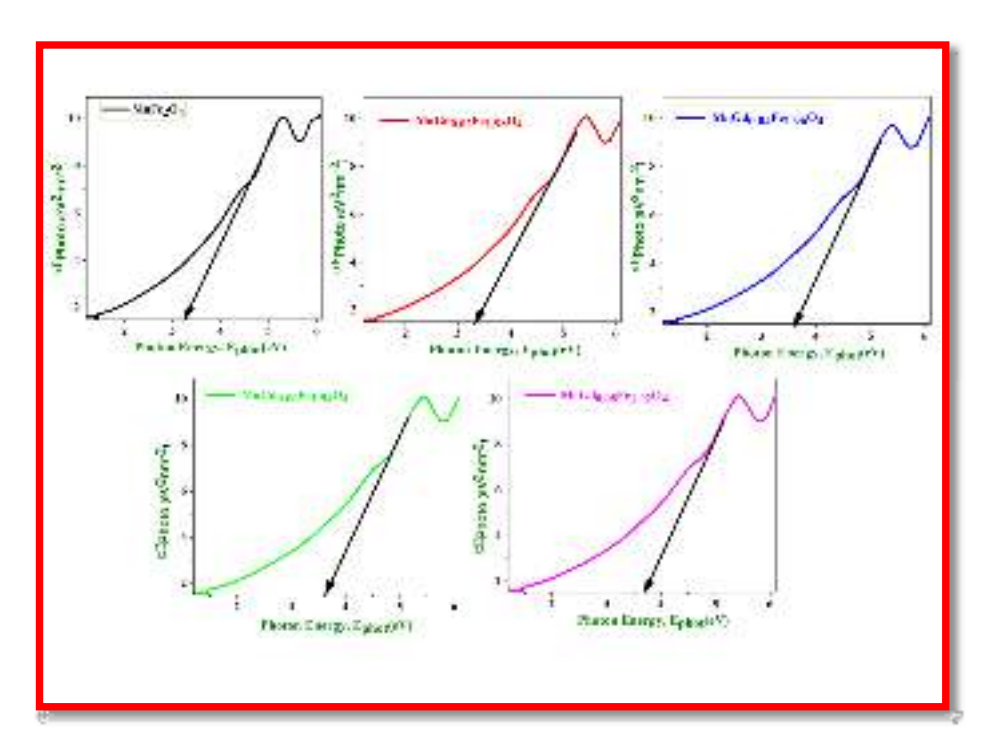


Figure 7.5 Indirect bandgap energy of MnGdxFe<sub>2-x</sub>O<sub>4</sub> (X= 0.00 to 0.08) nano ferrites

Table 7.2 Optical parameters of MnGdxFe<sub>2-x</sub>O<sub>4</sub> (X= 0.00 to 0.08) nanoferrites

Composition	Absorbance (nm)	Indirect bandgap energy (eV)	Direct bandgap energy (eV)	
X=0.00	231.76	3.25	2.36	
X=0.02	225.75	3.35	2.46	
X=0.04	223.80	3.55	2.62	
X=0.06	223.52	3.63	2.72	
X=0.08	222.24	3.76	2.96	

## 7.3.3 Functional Group Analysis

The FT-IR spectra were carried out in the range of 4000-400 cm<sup>-1</sup> at room temperature to identify chemical bonds and ensure the ferrite phase's successive formation. The vibrational frequency at 663 cm<sup>-1</sup>corresponds to the stretching vibration of Metal-Oxygen bond respectively [Gan et.al., 2020]. The observed peak around 1595 cm<sup>-1</sup> is assigned to the aromatic and aliphatic C–H bond stretching. The other observed peaks at around 2350 cm<sup>-1</sup> are attributed to the asymmetric and symmetric stretching vibration of CO<sub>2</sub> groups. As a result of the evaporation of CO<sub>2</sub>, these bands begin to separate for higher sintering temperatures. [Torkain et.al., 2016]. The stretching peak at 3781 cm<sup>-1</sup> corresponds to the stretching vibration of O-H bonds of water molecules [Gan et.al., 2020].

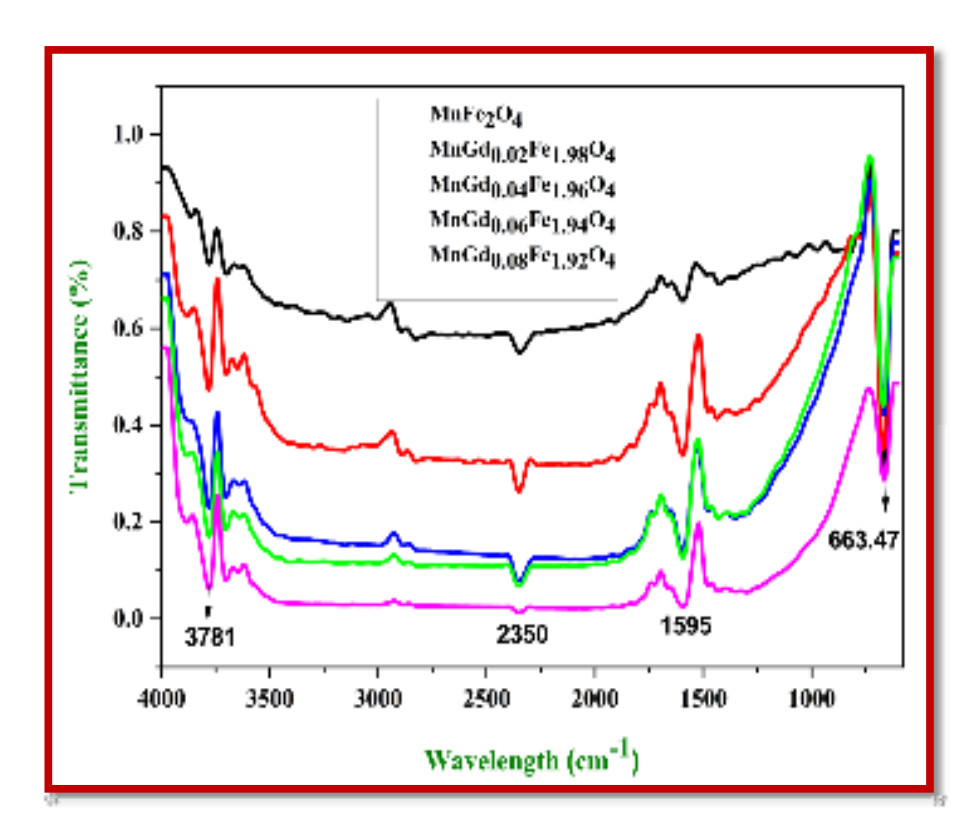


Figure 7.6 FTIR spectra of  $MnGdxFe_{2-x}O_4$  (X = 0.00 to 0.08) nanoferrites.

Table 7.3 Functional parameters of MnGdxFe<sub>2-x</sub>O<sub>4</sub> (X = 0.00 to 0.08) nanoferrites

S.		Experimental absorption (cm <sup>-1</sup> )					
No	Vibrational assignments	X= 0.00	X= 0.02	X= 0.04	X= 0.06	X= 0.08	
1	Metal - Oxygen stretching vibration	663.47	663.47	663.47	663.47	663.47	
2	C–H bond stretching	1595	1595	1595	1595	1595	
3	Symmetric stretching vibration of CO <sub>2</sub>	2350	2350	2350	2350	2350	
4	O - H stretching vibration	3781.00	3781.00	3781.00	3781.00	3781.00	

## 7.3.4 Surface Morphology with EDAX

The morphological studies of prepared nano ferrites are analyzed by using FESEM. In Figure 7.7, the aggregation of high crystalline spherical shape nanoparticles in a homogeneous distribution. Because of the high surface to volume ratio in their structure, agglomeration occurred owing to magnetic interactions among nanoparticles to reduce interfacial surface energy [Rahman et.al., 2005].

From XRD, the declination in crystallite size for X = 0.00 to X = 0.08 due to the small Gadolinium ion, which rare earth metal. Thus, X concentration leads to disorder in a lattice arrangement, and lattice stretches such restrains in crystallization and curbing in crystallite growth tend to diminution grain size [Yousuf et.al., 2019, Purnama et.al., 2019].

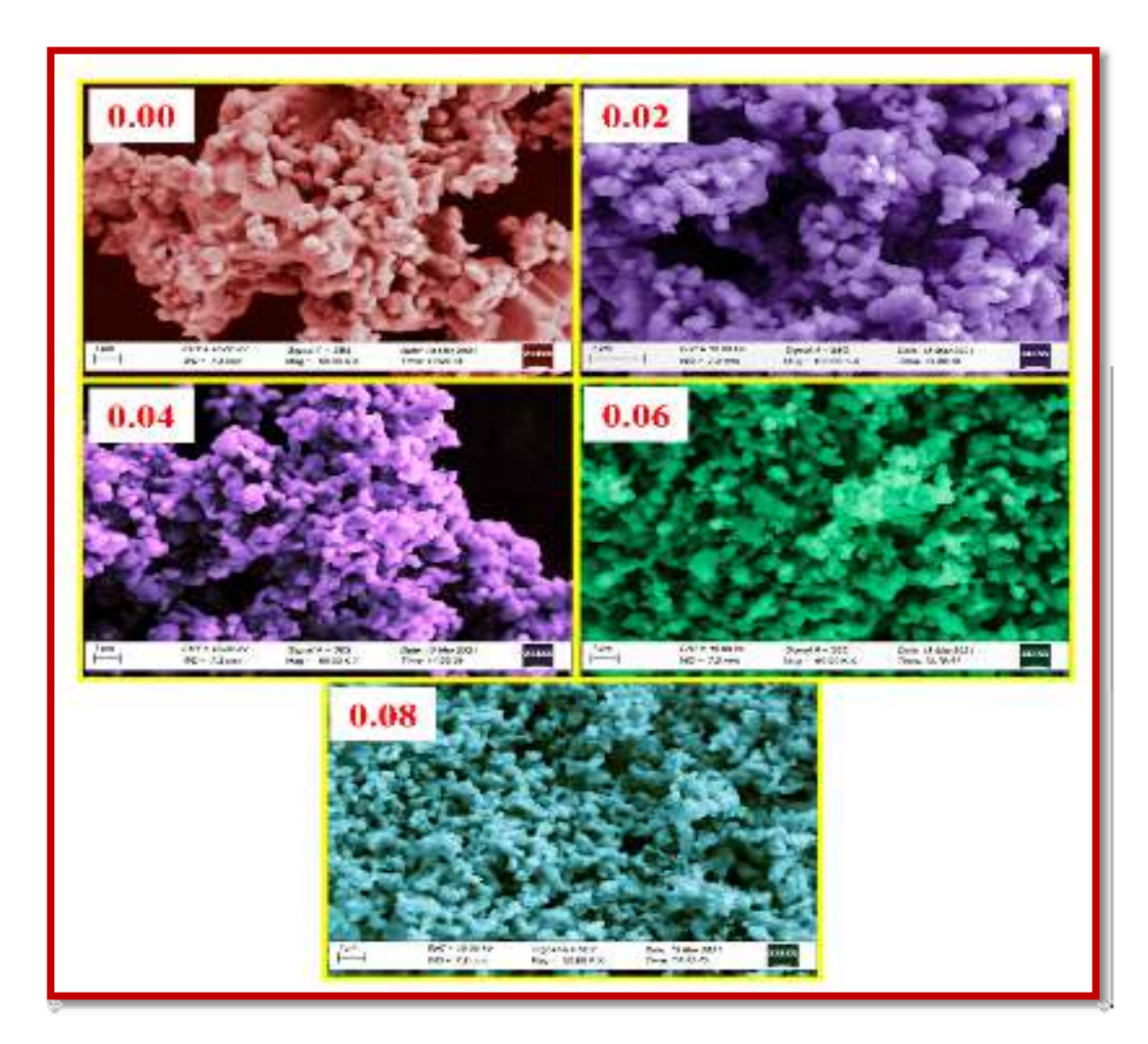


Figure 7.7 FESEM images of MnGdxFe<sub>2-x</sub>O<sub>4</sub> (X = 0.00 to 0.08) nanoferrites

EDAX analysis was used to estimate the compositions of fabricated nano ferrites. In Figure 7.8, shows the confirmation of accrued elements such as Fe, O, Mn and Gd. These spectra denote that the chemical reaction has been completed, closely matched with the atomic ratio of all the elements. For example, in X=0, there are no  $Gd^{3+}$  ions Which is the absence of impurity.

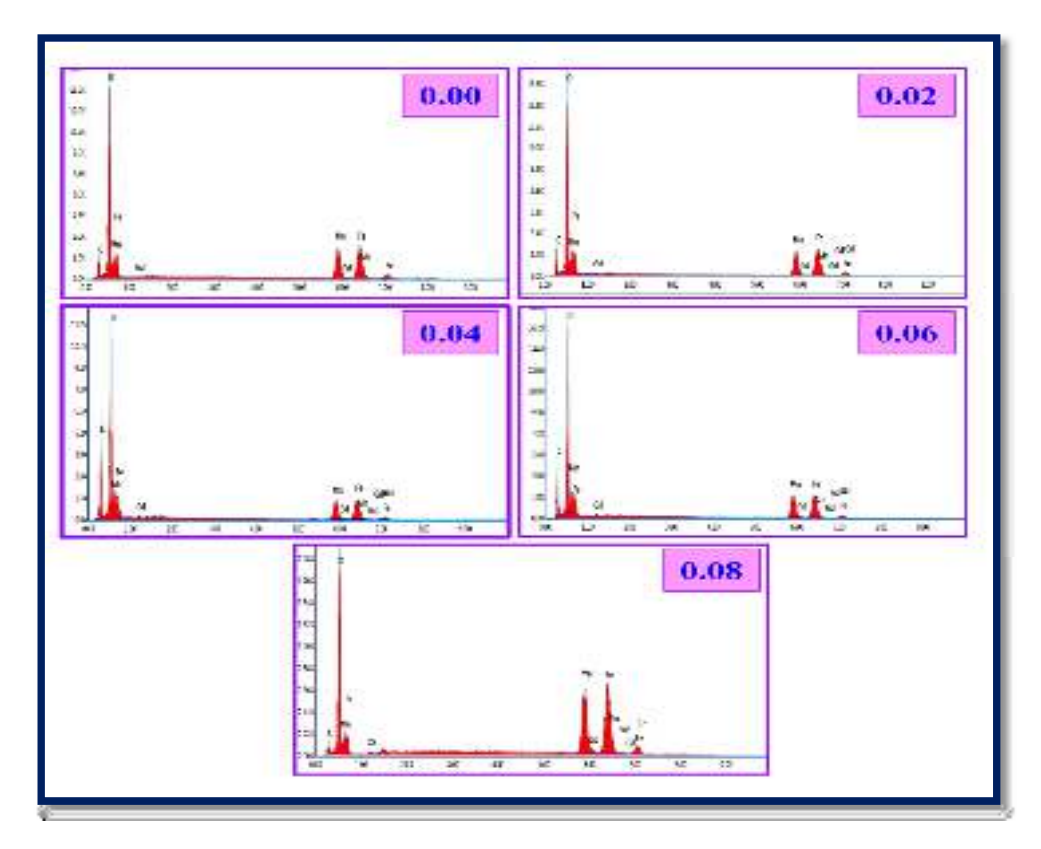


Figure 7.8 EDAX images of MnGdxFe<sub>2-x</sub>O<sub>4</sub> (X = 0.00 to 0.08) nanoferrites.

## 7.3.5 Raman spectroscopy analysis

Raman spectroscopy is a great way to figure out a material's crystal structure and vibrational bands. For example, thirty-nine vibration modes of spinel ferrite structures are estimated based on group theory research [Pawar et.al., 2018, Silva et.al., 2012].

$$T_{Raman} = A_{1g}(R) + E_{g}(R) + T_{1g} + 3T_{2g}(R) + 2A_{2U} + 2E_{U} + 4T_{1U}(1R) + 2T_{2U}$$
(7.8)

Five Raman active modes are observed, which are represented as  $(A_{1g}+E_g+3T_{2g})$ , and other modes are infrared operational modes. Here A, E, T denotes the 1D, 2-D and 3-D, respectively. The Raman active modes seen in the spinel ferrite structure are linked to the migration of  $O^{2-}$  ions and cations at tetrahedral (A-sites) and octahedral (B-sites). Raman band observed around 650 cm<sup>-1</sup> and 704 cm<sup>-1</sup> are assigned

to A<sub>1g</sub> (2) and A<sub>1g</sub> (1) modes vibration of the atom along Fe-O tetrahedral sub-lattice is the notice from Figure 7.9. E<sub>g</sub> is due to symmetric bending of O<sup>2-</sup> concerning Fe, and peaks located around 340cm<sup>-1</sup> to 343cm<sup>-1</sup>[Yadav et.al., 2017]; The Raman mode T<sub>2g</sub> (2) is an antisymmetric stretching of Fe and O, between 460 cm<sup>-1</sup> to 473 cm<sup>-1</sup>; T<sub>2g</sub> (1) is the translational motion of FeO, between 530 to 538 cm<sup>-1</sup> [Mohit et.al., 2014]. However, the Raman active bands for different doping Gd<sup>3+</sup> ions concentrations in the spinel structure appear to be slightly shifted, as listed in Table 7.4.

The doping of  $Gd^{3+}$  ions is expected to occupy the Octahedral site by exchanging  $Mn^{2+}$  from octahedral to tetrahedral sites. And the vibrational frequency of Raman modes is moved to the lower frequency region due to crystallite size and cation re-distribution of  $MnGd_xFe_{2-x}O_4$  (X=0.00 to 0.08) nano ferrites.

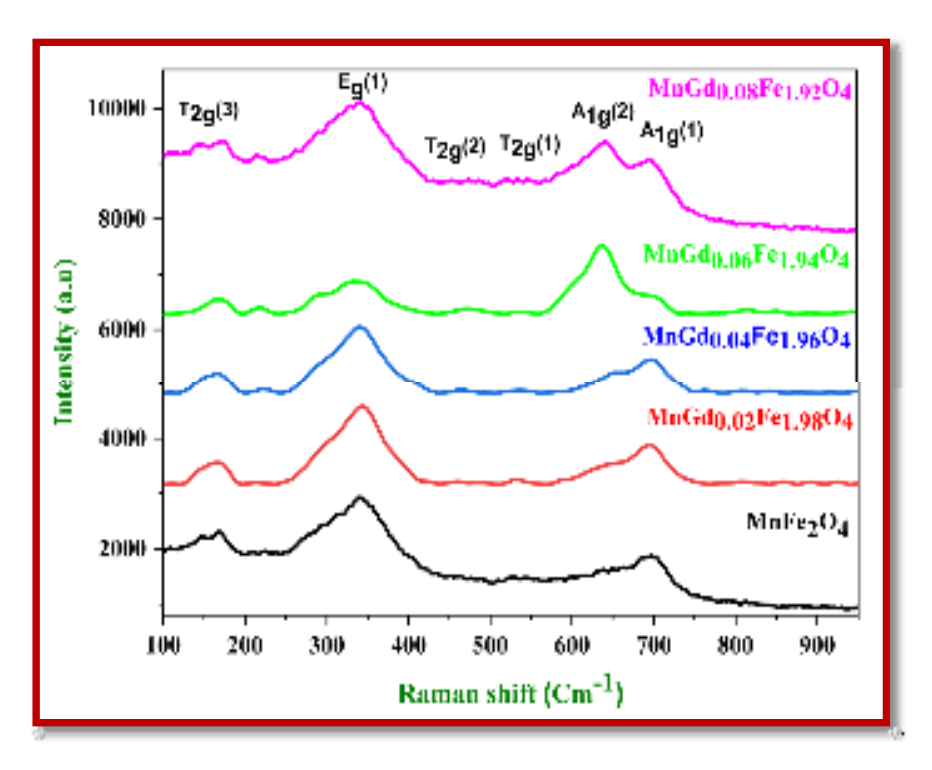


Figure 7.9 Raman spectra of MnGdxFe<sub>2-x</sub>O<sub>4</sub> (X = 0.00 to 0.08) nanoferrites

Table 7.4 Raman studies of  $MnGdxFe_{2-x}O_4$  (X = 0.00 to 0.08) nanoferrites

Composition	A <sub>1g</sub> (1)	A <sub>1g</sub> (2)	T <sub>2g</sub> (1)	T <sub>2g</sub> (2)	E <sub>g</sub> (1)	T <sub>2g</sub> (3)
MnFe <sub>2</sub> O <sub>4</sub>	700.01	634.42	536.10	462.14	343.68	171.71
MnGd <sub>0.02</sub> Fe <sub>1.98</sub> O <sub>4</sub>	703.84	634.42	538.91	473.02	339.45	168.71
MnGd <sub>0.04</sub> Fe <sub>1.96</sub> O <sub>4</sub>	699.44	651.86	537.51	469.49	341.39	167.30
MnGd <sub>0.06</sub> Fe <sub>1.94</sub> O <sub>4</sub>	698.03	648.87	531.69	463.85	342.27	169.60
MnGd <sub>0.08</sub> Fe <sub>1.92</sub> O <sub>4</sub>	696.62	646.57	530.99	460.86	340.86	170.30

# 7.3.6 Magnetic Analysis

Figure 7.10 demonstrates the room temperature magnetic field versus magnetic field loops (M-H) of Gd doped Mn nano ferrites using VSM with  $\pm$  15 Koe magnetic field. The obtained hysteresis loops are narrow in shape, indicating a soft ferromagnetic nature related to cubic spinel nano ferrites. The magnetic properties of ferrites are based on different factors, like cation distribution in the lattice structure, crystallite size, composition and production of defects in the lattice structure [Goodarz Naseri et.al., 2012].

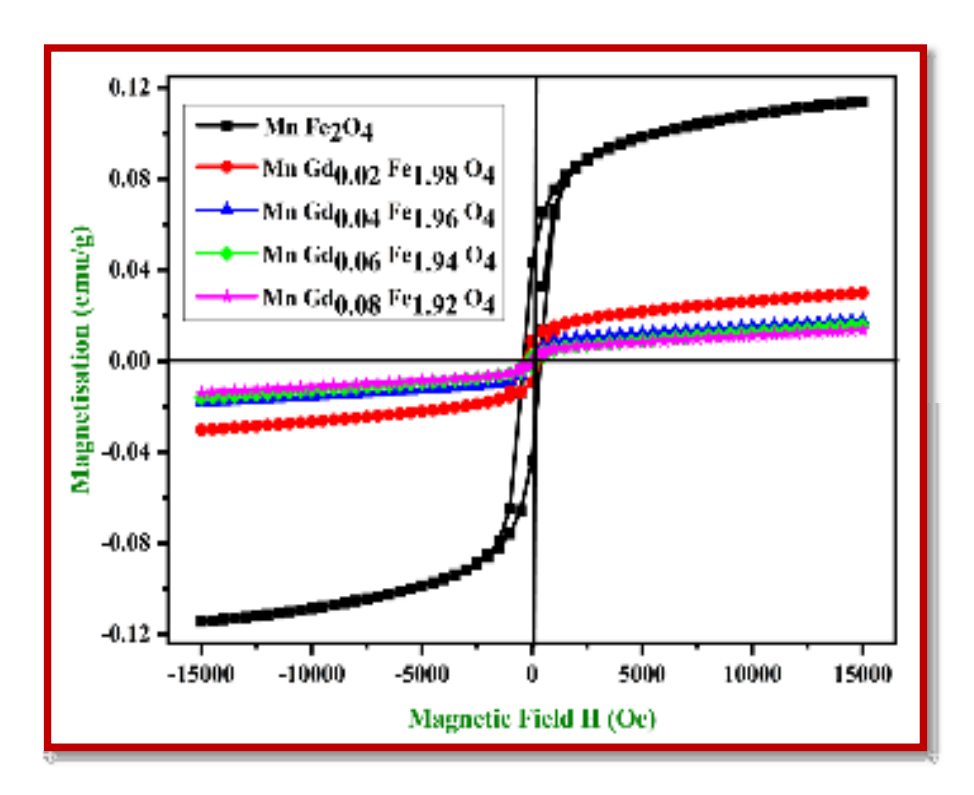


Figure 7.10 Hysteresis loop of  $MnGdxFe_2-xO_4$  (X = 0.00 to 0.08) nanoferrites

The magnetic saturation and retentivity decrease from 30.10 to 11.41 and 9.07 to 0.43 (X = 0.00 to 0.08) with an increase of  $Gd^{3+}$  ions due to a drop of crystallite size. The maximum value of  $M_S$  was attained for  $MnGd_xFe_{2-x}O_4$  at X=0.00. This exchange of  $Mn^{2+}$  and  $Gd^{3+}$  ions weakened the interaction of sublattice and decreased the magnetic moment of the unit cells, which in turn caused deduce in  $M_S$  values.

Three everyday super exchange interactions were attained in the  $AB_2O_4$  system between ions of the A and B sites. i.e., A-B, A-A and B-B interactions were involved. A-B interaction is strong because of super exchange interaction among the magnetic in the A and B sublattices intermediate by oxygen ions.

From Figure 7.10, it is clear that the value of coercivity increases with the increase of Gd<sup>3+</sup> ions. In general, Grain size, magneto-crystallinity anisotropy,

porosity, and strain are all factors that influence coercivity [Tholkappiyan et.al., 2015]. It can be explained based on the Stoner Wolfforth theory, the value of coercivity related to anisotropy constant (K) by the following expression [Lenin et.al., 2018];

$$H_C = \frac{0.98 \, K}{M_S} \tag{7.9}$$

where  $M_s$ , K, and  $H_c$  are magnetic saturation, anisotropy constant and coercivity. Table 7.5 infers that the anisotropic constant decreases with the decrease of crystallite size, increasing coercivity. Based on the equation  $H_c$  and K are inversely proportional to  $M_s$ , which agrees with the results. Neel's two sublattice model can also be used to describe the magnetic characteristics of spinel ferrites [Srinivas et.al., 2003]. The magnetic moment ( $\mu_B$ ) was calculated by using following relation [Lenin et.al., 2018].

$$\mu_{\rm B} = \frac{M \times Ms}{5585} \tag{7.10}$$

where  $M_s$ , X, M are magnetic saturation, X is concentration, and M is the molecular weight of rare-earth ions. The magnetic moment decreases with the increase of  $Gd^{3+}$  ion, which is an attribute to weaker magnetic interaction between B and A sites because  $Gd^{3+}$  has a more significant magnetic moment (7.9-8.0  $\mu_B$ ) ionic radius (0.94 Å) as compared to  $Fe^{3+}$  ions.

Also, it was observed that spin-orbit coupling is affected by the substitution of rare-earth ions. In Gd<sup>3+</sup> ions, the transformation of collinear ferromagnetic arrangement into non-collinear ferromagnetic order of spin on B sites. And also, Mn<sup>2+</sup> ions occupy B sites and the remaining Mn<sup>2+</sup> ion located on A sites distributed the

collinear arrangement of spin leads to the decrease of squareness ratio and anisotropy constant. The minimal value of the squareness ratio appreciates the existence of multidomain particles in nano ferrites [Belavi et.al., 2012]. The low weight of the coercive field was attained due to these nano ferrites and so are applicable for robust magnetic shielding devices [Kadam et.al., 2013]. The magnetic parameters are listed in Table 7.5.

Table 7.5 Magnetic parameters of MnGdxFe<sub>2-x</sub>O<sub>4</sub> (X = 0.00 to 0.08) nanoferrites

Composition	Magnetization (M <sub>s</sub> ) (emu/g)	Remanent magnetization (M <sub>r</sub> ) (emu/g)	Coercivity (Hc) (Oe)	Squareness ratio (M <sub>r</sub> /M <sub>s</sub> ) (No unit)	Anisotropy constant (K) (Oe)	Bohr magneton (η <sub>B</sub> ) (μ <sub>B)</sub>
X = 0.00	30.10	9.07	215.83	0.301	66.29	0.036
X = 0.02	18.09	4.61	245.30	0.254	62.00	0.022
X = 0.04	15.95	2.20	380.99	0.142	58.21	0.019
X = 0.06	13.75	1.96	385.47	0.137	54.08	0.017
X = 0.08	11.41	0.43	500.00	0.037	45.28	0.014

### 7.3.7 Impedance Analysis

Impedance analysis is a widely used technique for determining a material's conduction mechanism at the grain and grain boundary levels [Ahmad et.al., 2018]. It gives an idea about ferrites' resistive and reactive parts the resistive component acct as an imaginary part.

### 7.3.7 (a) The Real part of impedance spectroscopy

Figure 7.11 shows the room temperature variation of real part (Z') impedance with applied frequency. At lower frequency, Z' has higher values and gradually decreases and remains constant at a higher frequency. The decrease in Z' with increasing frequency indicates an increase in AC conductivity and supports space change, which leads to a drop in material behavior parameters [Zidi et.al., 2014]. And also, a real part of impedance decrement with an increment of Gd3+ ion and then inclined to merge at high frequency.

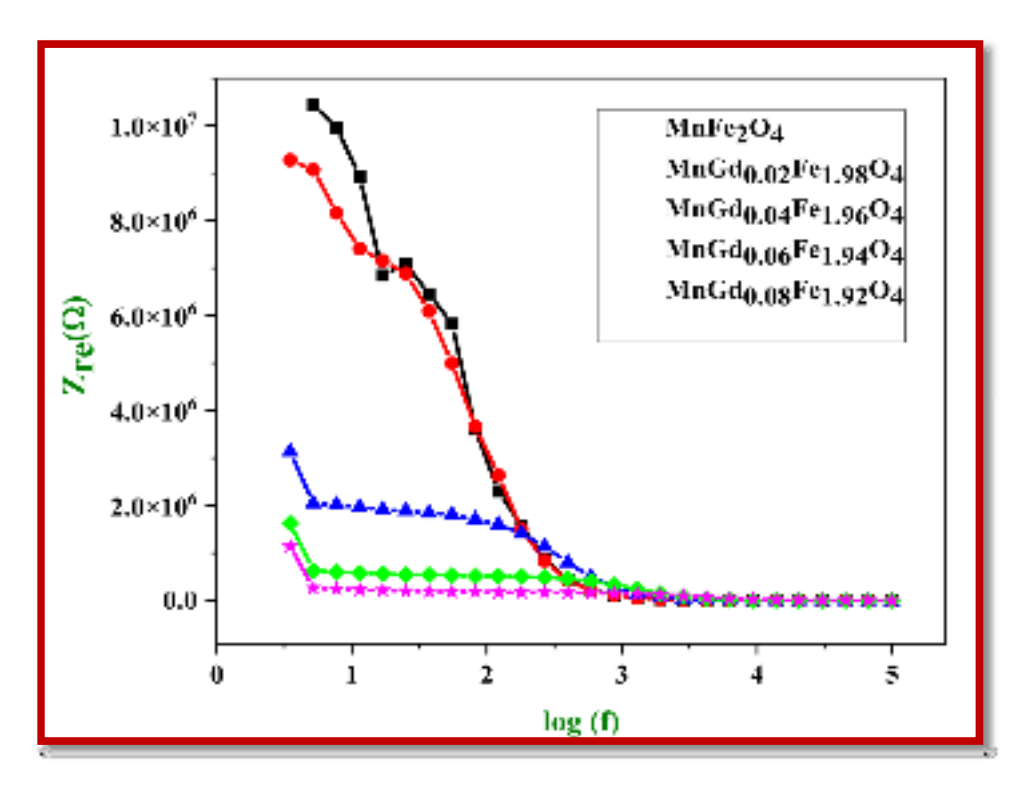


Figure 7.11Real part of impedance spectra of MnGdxFe<sub>2-x</sub>O<sub>4</sub> (X = 0.00 to 0.08) nanoferrites.

### 7.3.7 (b) The Imaginary part of the impedance spectroscopy

Impedance spectroscopy's reactive component (Z") decreases as the amount of Gd<sup>3+</sup> ion increases. Also, as the imaginary component (Z") of impedance drops monotonously with increasing frequency, a relaxation peak appears, and the broad peak emerges at higher frequencies. Due to the emergence of space charge polarization, this relaxation characteristic is accomplished [Rezlescu et.al., 1974, Ahmad et.al., 2015].

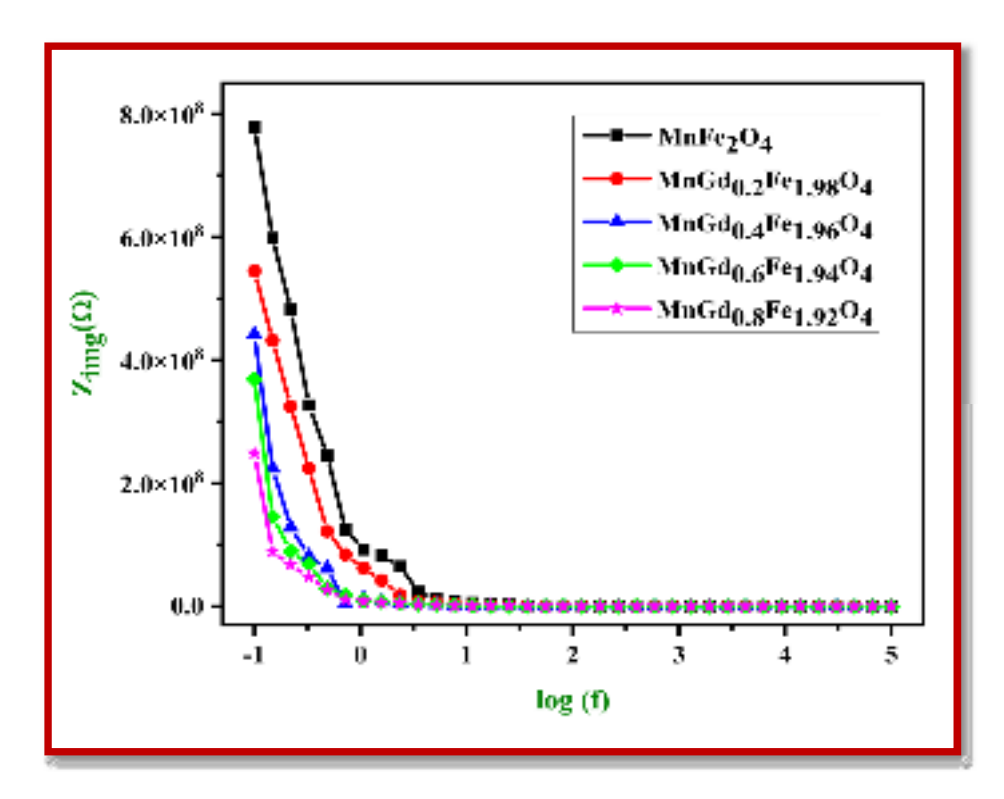


Figure 7.12Imaginary part of impedance spectra of MnGdxFe<sub>2-x</sub>O<sub>4</sub> (X = 0.00 to 0.08) nanoferrites.

## 7.3.8 (c) Cole-Cole plot

The cole-cole plot of nano ferrites clearly shows the semicircular arc, which attributes the electron interface grain boundary and grain contribution to the conductivity [Ajith Kumar et.al., 2020]. The poor conducting grain boundaries are more active at low frequency, and the hopping of Fe<sup>2+</sup> and Fe<sup>3+</sup> ions are ineffective. The semicircle arc found in the high-frequency range is attributed to the grain conduction mechanism of the material, which leads to the parallel combination of grain resistance and grain capacitance of the material. Because of the uneven arrangement and shortage of Fe atoms, the tiny grain size predicts a high density of grain borders. Only one semicircle arc is obtained in the Figure, and the conduction process is achieved to the grain boundaries [Pandit et.al., 2014]. Jump relaxation

activation energies, which are linked to the hopping process, can explain the observed spectra [Ortega et.al.,2008].

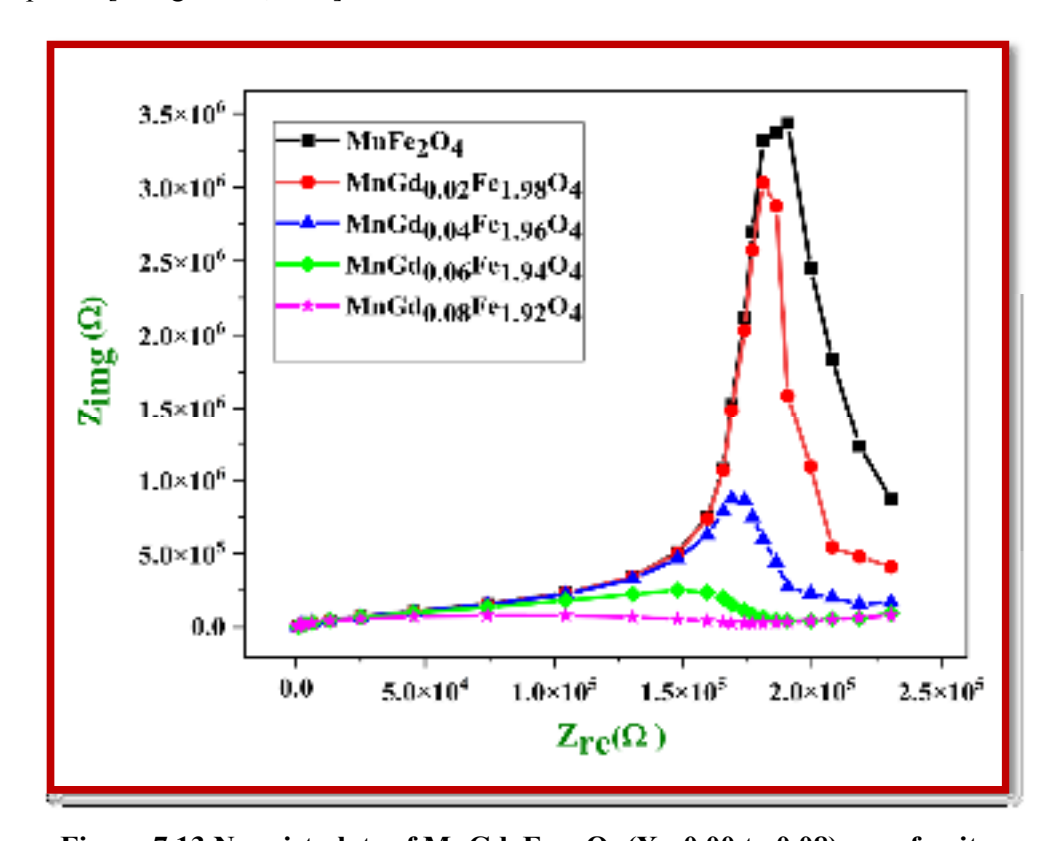


Figure 7.13 Nyquist plots of MnGdxFe<sub>2-x</sub>O<sub>4</sub> (X= 0.00 to 0.08) nanoferrites.

### 7.3.8 Dielectric Properties

The dielectric properties are fundamental in the microwave frequency region. These properties are helpful to examine the suitability of dielectric materials for application in microwave devices. In microwave devices, frequency stability is an important parameter, which needs a high dielectric constant with less dielectric loss. Dielectric characteristics in ferrites are determined by several parameters, including chemical composition, applied field, temperature, crystallite size, cation distribution, and production technique. The polarization-based Maxwell– Wagner model studied dielectric dispersion in ferrites [Han et.al., 2012, Khan et.al., 2014]. Dielectric

materials are those that, while being electrical insulators, exhibit polarization when exposed to an electric field.

#### 7.3.8 (a) Dielectric constant ( $\in$ ')

Figure 14, show the variation of €' with frequency in the range of 100 mHz to 10 MHz at room temperature. The dielectric constant of the prepared nano ferrites decreases slowly at a lower frequency and remain constant at a higher frequency [George et.al., 2007]. The continuous dielectric variation is explained by the Maxwell Wagner model and Koop's theory [Lakshmi et.al., 2016].

According to this concept, the dielectric constant of a spinel ferrites material is a mixture of two layers. The first of these two layers consist of grain boundaries, which are weak conductors (high resistance). Because of the high resistance, electrons pile up at grain boundaries, resulting in polarization. At high frequencies, this hopping frequency is unable to follow the fluctuation of the applied field. So that the dielectric constant at high frequency remains constant.

At high frequency where  $\omega < 1/\tau$  ( $\tau$  is relaxation time), dipoles cannot follow the applied field and lag behind the field, which informs a decrease in dielectric constant. In the case of low frequency where  $\omega \le 1/\tau$ , dipoles follow the applied field. The dielectric constant is generally influenced by four polarization factors: dipolar, ionic, space charge, and interfacial polarization. The dipolar polarization interfacial polarization is dominant at lower frequencies, while electric and ionic polarization plays an essential role at high frequencies [Phor et.al., 2019, Pradhan et.al., 2017].

The space charge polarization effects caused by charge carriers hopping between ions of the same element occurring in the minimum of two valence states can

be attributed to the high dielectric constant value at low frequency [Rezlescu et.al., 1974]. When the field is applied, electron hopping between Fe<sup>2+</sup> and Fe<sup>3+</sup> ions result in electron piling up at grain boundaries, resulting in space charge polarization. Moreover, when used frequency increases, the electron exchange between Fe<sup>3+</sup> and Fe<sup>2+</sup> ions cannot follow the various changing fields [Thorat et.al., 2018]. The dielectric constant was calculated using the following equation [Rajeshwari et.al., 2020];

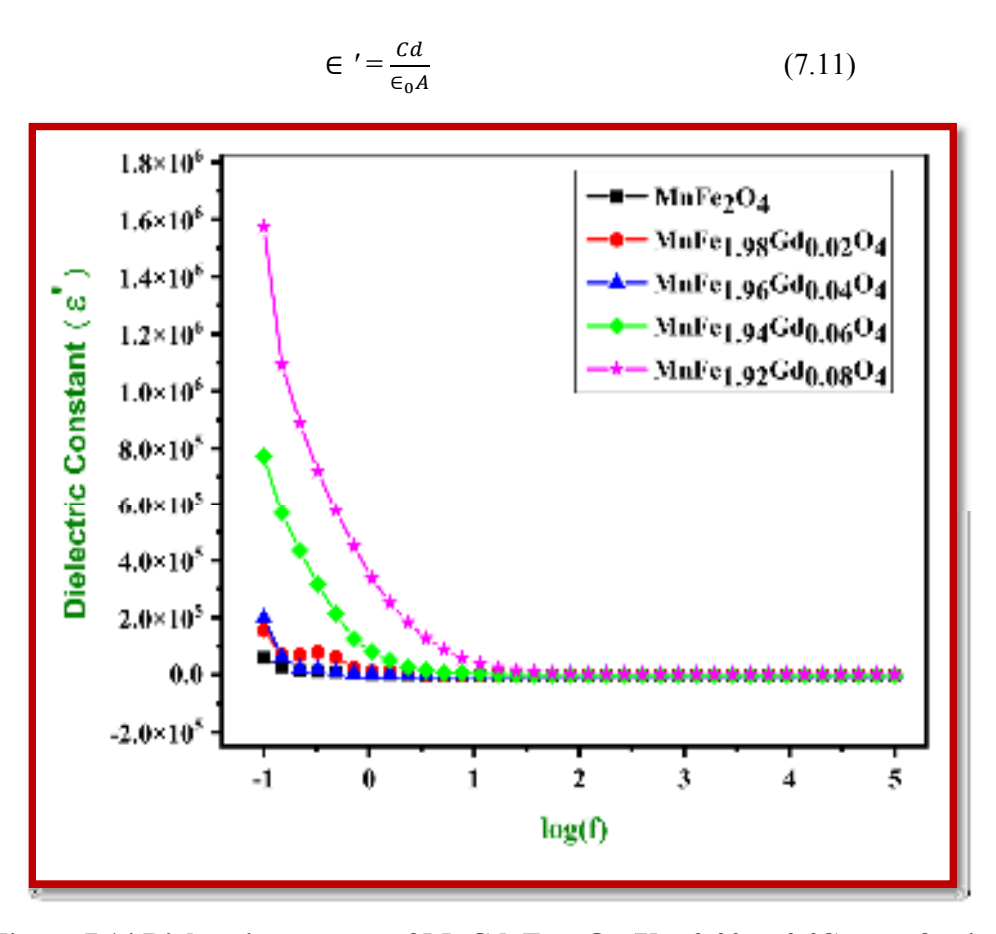


Figure 7.14 Dielectric constant of MnGdxFe<sub>2-x</sub>O<sub>4</sub> (X = 0.00 to 0.08) nanoferrites

where, A,  $\in_0$ , d, Cand A is an area of the pellet $\in_0$  is the permittivity of free space, d is the thickness of pellet, and C is capacitance. The dielectric constant value 60407.81, 154938.47, 198583.31,773908.62 and 1574426.14 are increases with

increases of  $Gd^{3+}$  ions. Because of the structural difference of  $Fe^{3+}$  at A-B sites, adding  $Gd^{3+}$  ions increase the dielectric constant significantly. The ferrites have dipolar properties due to the presence of  $Fe^{3+}$  and  $Fe^{2+}$  ions. The rotation of the  $Fe^{3+}$  and  $Fe^{2+}$  dipoles cause orientation polarization, as seen by the exchange of electrons between these ions, allowing for less polarization resistance and thus raising the dielectric constant [Panday et.al., 2016].

## 7.3.8 (b) Dielectric loss

In Figure 7.15, the dielectric loss peak is observed due to having maximum electron jump between Mn<sup>2+</sup> and Fe<sup>3+</sup> ion at the octahedral site in the following steps,

$$Fe^{3+} + Mn^{2+} \leftrightarrow Fe^{2+} + Mn^{3+}$$
 (7.12)

It reflects minimal dielectric loss at low frequencies but the substantial dielectric loss at higher frequencies. High resistive grain boundary effects play a critical role in the low-frequency domain helps explain this dielectric loss pattern. As a result, exchanging electrons between Fe<sup>2+</sup> and Fe<sup>3+</sup> requires more energy, resulting in a loss. In the high-frequency zone, on the other hand, low resistive grains become more efficient in the conduction process, requiring less energy to exchange electrons between Fe ions, resulting in the low dielectric loss. The dielectric loss and complex dielectric constant are estimated by the following equation [Panday et.al., 2016];

$$tan\delta = \frac{1}{2\pi f \epsilon_0 \epsilon'} \tag{7.13}$$

$$\in " = \in 'tan\delta \tag{7.14}$$

The value of the dielectric loss is 2.0214, 1.9945, 1.9524, 1.9125 and 1.8542, respectively. The dielectric loss decreases within the increase of Gd<sup>3+</sup> ion of the nano ferrites.

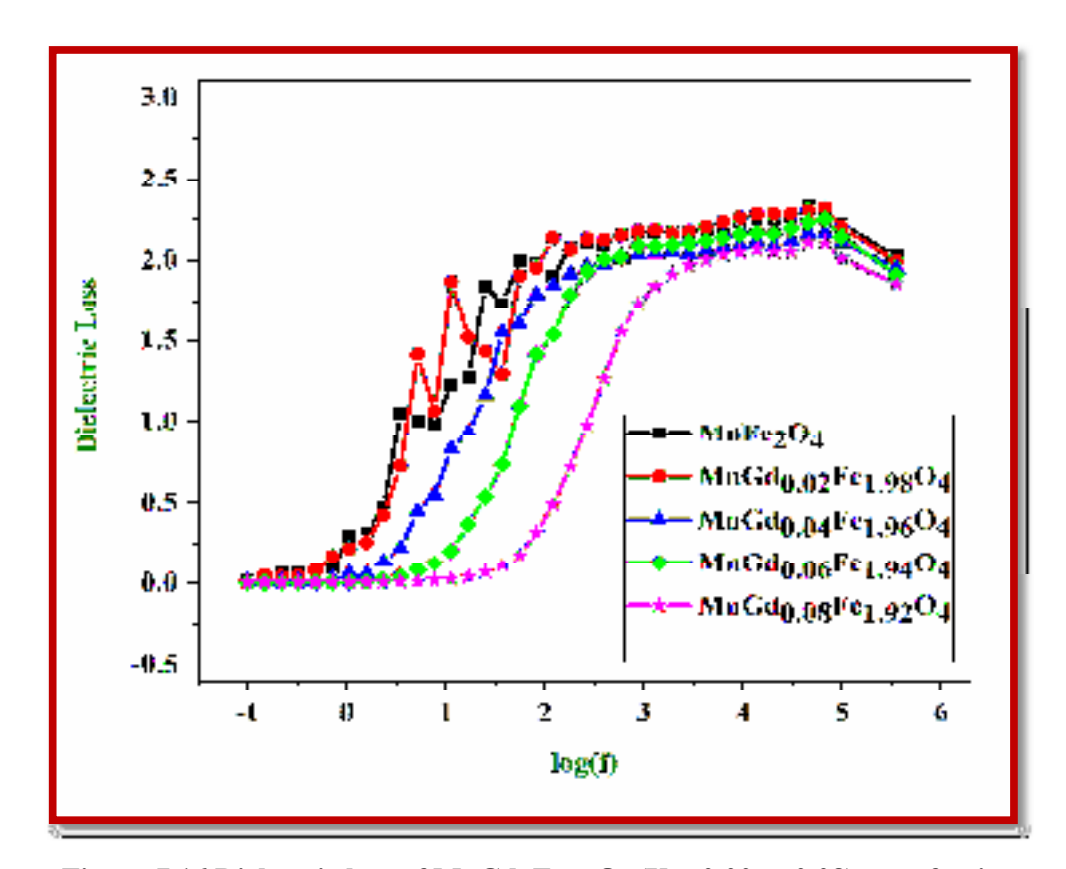


Figure 7.16 Dielectric loss of  $MnGdxFe_{2-x}O_4$  (X = 0.00 to 0.08) nanoferrites

## 7.3.8(c) A.C Conductivity

Variation of AC conductivity of Gd doped manganese nano ferrites at room temperature was shown in Figure 7.17. AC conductivity is calculated using the following relation [Vigneshwaran et.al., 2020];

$$\sigma_{ac} = 2\pi f \in \epsilon' \in 0 \ tan\delta \tag{7.15}$$

where  $\in_0$  is the permittivity of free space and frequency in H, ac conductivity constant at low frequency and then sharply increases at high frequency. In the context

of the Maxwell-Wagner model, this behavior makes sense. This is because the conduction process in the low-frequency area is solely due to inadequate conducting grain boundaries; however, conducting grain plays a substantial role at high frequencies.

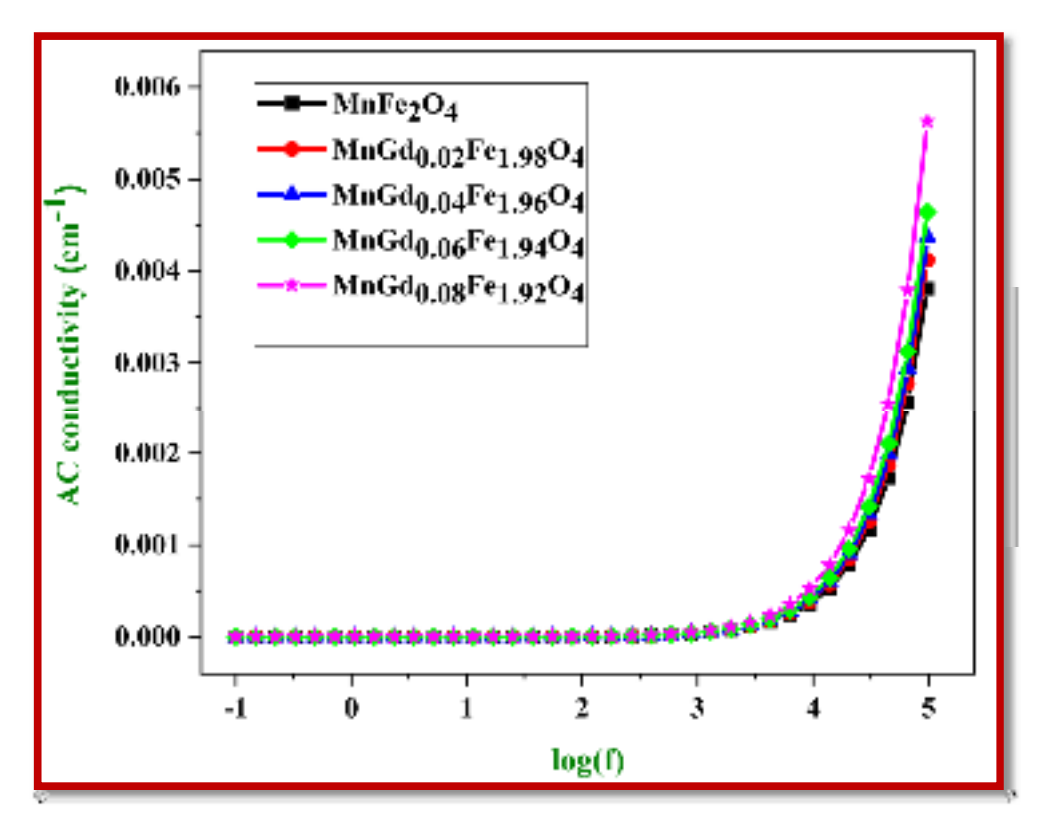


Figure 7.17 AC Conductivity vs Frequency of  $MnGd_XFe_{2-X}O_4$  (X = 0.00 to 0.08) nanoferrites

As a result, low conductivity values at low frequencies are attributed to highly resistive grain boundaries, which have a poor electron exchange rate. Conducting granules, on the other hand, enhance electron hopping at high frequencies [Kumari et.al., 2014]. Furthermore, an increase in AC conductivity is linked to an increase in charge carrier exchange rate. Because electrons follow the applied field, charge carrier exchanges rise as the frequency of the applied field increases [Chavan et.al.,

2017]. This implies a sharply increases in AC conductivity with applied frequency. In addition, the value of AC conductivity increases with the increase of Gd<sup>3+</sup> ions. The dielectric parameters such as dielectric constant, loss and AC conductivity are listed in the Table 7.6.

Table 7.6 Dielectric parameters of MnGdxFe<sub>2-x</sub>O<sub>4</sub> (X = 0.00 to 0.08) nanoferrites

Composition	Dielectric Constant (ε')	Dielectric Loss (tanδ)	AC Conductivity (ac) (Ωcm <sup>-1</sup> )	
X=0.00	60407.81	2.0214	0.00381	
X=0.02	154938.47	1.9945	0.00412	
X=0.04	198583.31	1.9524	0.00437	
X=0.06	773908.62	1.9125	0.00464	
X=0.08	1574426.14	1.9125	0.00563	

## 7.4 CONCLUSION

In summary, we have successfully synthesized  $MnGd_xFe_{2-x}O_4$  (X=0.00 to 0.08) nano ferrites using sol-gel technique. XRD pattern shows cubic spinel structure without any impurity peak. The crystallite size decreases from 26 to 13 with increases of  $Gd^{3+}$  ions. The Lattice constant increases with  $Gd^{3+}$  ions due to ionic radius FESEM shows spherical shape with agglomeration. The purity of the composition was confirmed from EDAX. The formation of spinel ferrites was confirmed from the absorption peak found from the FTIR spectra. The optical bandgap was inversely proportional to the absorbance of wavelength which in the range of semiconductor materials. Magnetic studies confirm S-shaped soft ferromagnetic material. The magnetic saturation decreases with the increase of  $Gd^{3+}$ ions due to a decrease in

crystallite size. The coercivity increases with Gd3+ ions, depending on grain size, magneto- crystallinity anisotropy constant, porosity and strain. And also, it can be explained based on Stoner Wohlforth theory. Raman spectroscopy attains five active modes  $[2A_{1g} + 3T_{2g} + E_g]$ . The Cole-Cole plot from impedance spectroscopy infers grain and grain boundaries towards capacitance and resistance, which denotes grain boundary greater than the grain contributions. The dielectric constant decreases with the frequency increase, which is explained based on the Maxwell-Wagner and Koop model. The value of the constant dielectric increases with the increase of Gd<sup>3+</sup> ion. The highest value of dielectric constant attains at X = 0.08. The value of dielectric loss decreases with increases of Gd<sup>3+</sup> ions. The results also express abnormal behavior dielectric loss. The low value of dielectric loss attains 0.08. AC conductivity linearly increases with the increase of frequency as well as increase with Gd<sup>3+</sup> ions. The investigation of Gd doped manganese nano ferrites (X= 0.00 to 0.08) reveals that the very low dielectric loss, saturation and minimum coercivity has finds potential application in storage devices, microwave absorption devices and also it can be used for various electronic applications.

#### REFERENCES

**Ahmad N**, Khan S, Ansari M.M.N, Optical, dielectric and magnetic properties of Mn doped SnO<sub>2</sub> diluted magnetic semiconductors, Ceram. Int. 44 **(2018)** 15972-15980.

**Ahmad R,** Gul I.H, Anwar H, Bilal M, Khan A, Author's accepted manuscript. Journal of Magnetism and Magnetic Materials. 405 (2015).

**Ajith Kumar S,** Kuppusami P, Amirthapandian S, Fu Y.-P, Effect of Sm co-doping on structural, mechanical and electrical properties of Gd doped ceria solid electrolytes for intermediate temperature solid oxide fuel cells, International journal of hydrogen energy. 45(54) **(2020)** 29690-29704.

**Almessiere M.A**, Slimani Y, Sertkol M, Khan F.A, Nawaz M, Tombuloglu H, Al-Suhaimi E.A, Baykal A, Ce–Nd Co-substituted nanospinel cobalt ferrites: An investigation of their structural, magnetic, optical and apoptotic properties, Ceram. Int. 45 **(2019)** 16147-16156.

**Almessiere M.A**, Slimani.Y, Korkmaz.A.D, Taskhandi.N, Sertkol.M, Baykal.A, Shirsath.S.E, Ercan.I, Ozçelik.B, Sonochemical synthesis of Eu<sup>3+</sup> substituted CoFe<sub>2</sub>O<sub>4</sub> nanoparticles and their structural, optical and magnetic properties, Ultrasonics Sonochemistry. 58 (2019) 104621.

**Belavi P**, Chavan G, Naik L, Somashekar R, Kotnala R, Structural, electrical and magnetic properties of cadmium substituted nickel–copper ferrites, Materials Chemistry and Physics. 132(1) **(2012)** 138-144.

**Biao Zhou**, Ya-Wen Zhang, Chun-Sheng Liao, Chun-Hua Yan, Liang-Yao Chen, Song-You Wang, J. Magn. Magn. Mater. 280 (2004) 327–333.

**Chavan P**, Naik L.R, Belavi P.B, Studies on electrical and magnetic properties of Mg-substituted nickel ferrites. J Electron Mater. 46 (2017) 188–198.

Coey J.M.D, Magnetism and Magnetic Materials (Cambridge University Press, Cambridge. (2009).

**da Silva S.W**, Nakagomi F, Silva M.S, Franco A, Garg V.K, Oliveira A.C, Morais P.C, Raman study of cations' distribution in Zn<sub>x</sub>Mg<sub>1x</sub>Fe<sub>2</sub>O<sub>4</sub> nanoparticles, J. Nanoparticle Res. 14 **(2012)** 798.

**El-Sheikh S.M,** Rabbah M, Novel low temperature synthesis of spinel nanomagnesium chromite's from secondary resources, Thermochim. Acta. 568 **(2013)** 13–19.

**Gadkari,** Shinde T, Vasambekar P, Structural analysis of Y<sup>3+</sup>doped Mg–Cd ferrites prepared by oxalate co-precipitation method, Mater. Chem. Phys. 114 **(2009)** 505–510.

**Gan G**, Zhang D, Li J, Wang G, Huang X, Yang Y, Rao Y, Xu F, Wang X, Zhang H, Equivalent permeability and permittivity of Sm substituted Mg–Cd ferrites for high-frequency applications, J. Alloys Compd. 819 **(2020)** 153059.

**George M**, Nair S.S, Malini K.A, Joy P.A, Anantharaman M.R, Finite size effects on the electrical properties of sol–gel synthesized CoFe<sub>2</sub>O<sub>4</sub> powders: deviation from Maxwell–Wagner theory and evidence of surface polarization effects, J. Phys. D Appl. Phys. 40 (2007) 1593–1602.

**Goodarz Naseri M**, Saion E.B, Kamali A, an overview on nanocrystalline ZnFe<sub>2</sub>O<sub>4</sub>, MnFe<sub>2</sub>O<sub>4</sub>, and CoFe<sub>2</sub>O<sub>4</sub> synthesized by a thermal treatment method, ISRN Nanotechnology. **(2012).** 

**Gupta V**, Mansingh A, Influence of postdeposition annealing on the structural and optical properties of sputtered zinc oxide film, J. Appl. Phys. 80 (2) **(1996)** 1063–1073.

**Han Q**, et al., Estimating the cation distributions in the spinel ferrites  $Cu_{0.5-x}Ni_{0.5}Zn_xFe_2O4$  (0.0 $\leq$ ;  $x\leq$  0.5)., J. Magn. Magn. Mater. 324 (12) (2012) 1975–1981.

**Irshad Ali**, Islam M.U, Ishaque M, Hasan Khan M, Muhammad Naeem Ashiq, Rana M.U, "Structural and magnetic properties of holmium substituted cobalt ferrites synthesized by chemical co-precipitation method," Journal of Magnetism and Magnetic Materials. 324 **(2012)** 3773–3777.

**Jing J**, Liangchao L, Feng X, Structural analysis and magnetic properties of Gd-doped Li-Ni ferrites prepared using rheological phase reaction method, J. Rare Earths. 25 **(2007)** 79-83.

**Kadam A,** Shinde S, Yadav S, Patil P, Rajpure K, Structural, morphological, electrical and magnetic properties of Dy doped Ni–Co substitutional spinel ferrite, Journal of Magnetism and Magnetic Materials. 329 **(2013)** 59-64.

**Károly Lázár**, Thomas Mathew, Zsuzsanna Koppány, János Megyeri, Violet Samuel, Subhash P. Mirajkar, Bollapragada S. Rao, László Guczi, Cu<sub>1-x</sub>Co<sub>x</sub>Fe<sub>2</sub>O<sub>4</sub> ferro spinels in alkylation: structural changes upon reaction, Phys. Chem. Chem. Phys. 4 **(2002)** 3530–3536.

**Kartharinal Punithavathy I**, Rajeshwari A, Johnson Jeyakumar S, Lenin N, Vigneshwaran B, Jothibas M, Arunkumar B, Impact of lanthanum ions on magnetic and dielectric properties of cobalt nanoferrites, Journal of Materials Science: Materials in Electronics. 31 (2020) 9783-9795.

**Khan A.A**, Satapathy S, Ahlawat A, Deshmukh P, Karnal A.K, Magnetodielectric coupling in SmFeO3: a study on anomalous dielectric, conductivity, impedance at spin reorientation temperature, Ceram. Int. 44 (2018) 12401-12413.

**Khan M.A**, High frequency dielectric response and magnetic studies of Zn<sub>1-x</sub>Tb<sub>x</sub>Fe<sub>2</sub>O<sub>4</sub> nanocrystalline ferrites synthesized via micro-emulsion technique, J. Magn. Magn. Mater. 360 (2014) 188–192.

**Kumar G,** Shah J, Kotnala R, Dhiman P, Rani R, Singh V.P, Garg G, Shirsath S.E, Batoo K.M, Singh M, Self-ignited synthesis of Mg–Gd–Mn nanoferrites and impact of cation distribution on the dielectric properties, Ceramics International. 40(9) **(2014)** 14509-14516.

**Kumari N,** Kumar V, Singh S.K, Synthesis, structural and dielectric properties of Cr<sup>3+</sup> substituted Fe<sub>3</sub>O<sub>4</sub> nanoparticles. Ceram Int. 40 **(2014)** 12199–12205.

**Lakshmi M**, Vijaya Kumar K, Thyagarajan K, Study of the dielectric behavior of Crdoped zinc nano ferrites synthesized by sol-gel method, Adv. Mater. Phys. Chem. 6 **(2016)** 141–148.

**Lenin N**, Kanna R.R, Sakthipandi K, Kumar A.S, Structural, electrical and magnetic properties of NiLa<sub>x</sub>Fe<sub>2-x</sub>O<sub>4</sub> nanoferrites, Materials Chemistry and Physics. 212 **(2018)** 385-393.

**Lenin N**, Karthik A, Srither S.R, Sridharpanday M, Surendhiran S, Balasubramanian M, Synthesis, structural and microwave absorption properties of Cr-doped zinc lanthanum nanoferrites Zn<sub>1-x</sub>Cr<sub>x</sub>La<sub>0.1</sub>Fe<sub>1.9</sub>O<sub>4</sub> (*x*=0.09, 0.18, 0.27 and 0.36), Ceram Int. **(2021)**.

**Li.X**, Hou.Y, Zhao.Q, Wang.L, A general, one-step and template-free synthesis of sphere-like zinc ferrite nanostructures with enhanced photocatalytic activity for dye degradation, Journal of colloid and interface science. 358(1) (2011) 102-108.

**Majid Niaz Akhtar,** Yousaf M, Khan S.N, Nazir M.S, Mukhtar Ahmad, Muhammad Azhar Khan, Ceram. Int. 43 **(2017)** 17032.

**Mohd Mohsin Nizam Ansari**, Shakeel Khan, Naseem Ahmed, Structural electrical transport and magnetic properties of Nd<sup>3+</sup> substituted Mn-Cu nanoferrites, Journal of alloys and compound. 831(2020) 154778.

**Mohit K,** Gupta V.R, Gupta N, Rout S.K, Structural and microwave characterization of Ni<sub>0.2</sub>CoxZn<sub>0.8</sub>-xFe<sub>2</sub>O<sub>4</sub> for antenna applications, Ceram. Int. 40 **(2014)** 1575–1586.

**Ortega N**, Kumar A, Bhattacharya P, Majumder S, Katiyar R, Impedance spectroscopy of multiferroic Pb Zr<sub>x</sub>Ti<sub>1-x</sub>O<sub>3</sub>/CoFe<sub>2</sub>O<sub>4</sub> layered thin flms, Phys. Rev. B. 77 **(2008)** 014111.

**Panday M,** Sridhar M, Vinoth M, Surendhiran S, Rajendran V, Susthitha Menon P, Investigation on electrical conductivity of strontium (Sr<sup>2+</sup>) influenced CaTi0. 8Fe0.2O3 polycrystalline perovskite, in: IEEE International Conference on Semiconductor Electronics. **(2016)** 192–195.

**Pandit R**, Sharma K, Kaur P, Kumar R, Cation distribution-controlled dielectric, electrical and magnetic behavior of In<sup>3+</sup> substituted cobalt ferrites synthesized via solid-state reaction technique, Mater. Chem. Phys. 148 **(2014)** 988–999.

**Pawar R.A,** Patange S.M, Shitre A.R, Gore S.K, Jadhav S.S, Shirsath S.E, RSC Advances Crystal Chemistry and Single-phase Synthesis of Enhanced Magnetic Properties. **(2018)** 25258-25267.

**Peng J**, Hojamberdiev M, Xu Y, Cao B, Wang J, Wu H, Hydrothermal synthesis and magnetic properties of gadolinium-doped CoFe<sub>2</sub>O<sub>4</sub> nanoparticles, Journal of Magnetism and Magnetic Materials. 323(1) (2011) 133-137.

**Phor L**, Kumar V, Structural, magnetic and dielectric properties of lanthanum substituted Mn<sub>0.5</sub>Zn<sub>0.5</sub>Fe<sub>2</sub>O<sub>4</sub>. Ceram Int. 45 **(2019)** 22972–22980.

**Phumying S**, Labuayai S, Swatsitang E, Amornkitbamrung V, Maensiri S, Nanocrystalline spinel ferrite (MFe<sub>2</sub>O<sub>4</sub>, M<sub>1/4</sub> Ni, Co, Mn, Mg, Zn) powders prepared by a simple aloe vera plant-extracted solution hydrothermalroute, Mater. Res. Bull. 48 **(2013)** 2060-2065.

**Pradhan D.K**, Kumari S, Puli V.S, Correlation of dielectric, electrical and magnetic properties near the magnetic phase transition temperature of cobalt zinc ferrite. Phys Chem Chem Phys. 19 **(2017)** 210–218.

**Purnama B**, Wijayanta A.T, Effect of calcination temperature on structural and magnetic properties in cobalt ferrite nano particles, Journal of King Saud University-Science. 31(4) (2019) 956-960.

**Rahman I.Z**, Ahmed T.T, a study on Cu substituted chemically processed Ni–Zn–Cu ferrites, J. Magn. Magn Mater. 290 (2005) 1576–1579.

**Rajeshwari** A, Punithavthy I.K, eyakumar S.J, Lenin N,Vigneshwaran B, Dependance of lanthanum ions on structural, magnetic and electrical of manganese based spinel nanoferrites, Ceramics International. 46(5) (2020) 6860-6870.

Rana M.P.S, Singh F, Negi.S, Gautam S.K, Singh R.G, Ramola R.C, Ceramic Int. 42 (2016) 5932.

**Rezlescu N**, ezlescu E, Dielectric properties of copper containing ferrites. Phys Stat Sol (a). 23 **(1974)** 575–582.

**Rezlescu N**, Rezlescu E, Dielectric properties of copper containing ferrites, Phys. Status Solidi. 23 (1974) 575-582.

**Smit J,** Wijn H, Ferrites, Philips technical library, Eindhoven, The Netherlands. **(1959)**, p. 278.

**Somnath**, Sharma I, Kotnala R.K, Singh M, Kumar A, Dhiman P, Singh V.P, Verma K, Kumar G, Structural, magnetic and Mossbauer studies of Nd-doped Mg-Mn ferrite nanoparticles, J. Magn. Magn Mater. 444 (2017) 77-86.

**Somnath**, Sharma I, Kotnala R.K, Singh M, Kumar A, Dhiman P, Singh V.P, Verma K, Kumar G, Structural, magnetic and Mossbauer studies of Nd-doped Mg-Mn ferrite nanoparticles, J. Magn. Magn Mater. 444 (2017) 77-86.

**Srinivas K**, Sarah P, Suryanarayana S, Impedance spectroscopy study of polycrystalline Bi <sub>6</sub>Fe<sub>2</sub>Ti<sub>3</sub>O<sub>18</sub>, Bull. Mater. Sci. 26 (2) **(2003)** 247–253.

**Stergiou C.A**, Litsardakis G, Electromagnetic properties of Ni and la doped strontium hexaferrites in the microwave region, J. Alloys Compd. 509 **(2011)** 6609-6615.

**Tholkappiyan R,** Vishista K, Combustion synthesis of Mg Er ferrite nanoparticles: cation distribution and structural, optical, and magnetic properties, Mater. Sci. Semicond. Process. 40 (2015) 631-642.

**Thorat L.M**, Patil J.Y, Nadargi D.Y, Co<sup>2+</sup> substituted Mg–Cu–Zn ferrite: Evaluation of structural, magnetic, and electromagnetic properties. J Adv Ceram. 7 (2018) 207–217.

**Torkain S**, Ghasemi A, Razavi R.S, Structural and magnetic consequences of Mn<sub>0.6</sub>Zn<sub>0.4</sub>Fe<sub>2-x</sub>Gd<sub>x</sub>O<sub>4</sub> ferrite. J. Supercond. Nov. Magn. 29 (2016) 1617–1625.

**Vigneshwaran B**, Kuppusami P, Ajithkumar S, Sreemoolanadhan H, Study of low temperature  $\Box$  dependent structural, dielectric, and ferroelectric properties of  $Ba_xSr_{(1-x)}$  TiO<sub>3</sub> (X = 0.5, 0.6, 0.7) ceramics, Journal of Materials Science: Materials in Electronics. 31 **(2020)** 10446–10459.

**Vigneshwaran B,** Kuppusami P, Panda A, Singh A, Sreemoolanadhan H, Microstructure and optical properties of Ba<sub>0.6</sub>Sr<sub>0.4</sub>TiO<sub>3</sub> thin films prepared by pulsed laser deposition, Materials Research Express. 5(6) (2018) 066420.

Wang Y, Wu X, Zhang W, Chen W, Synthesis and electromagnetic properties of Ladoped Ni-Zn ferrites, J. Magn. Magn Mater. 398 (2016) 90-95.

**Yadav R.S,** Kuritka I, Vilcakova J, Havlica J, Kalina L, Urb anek P, Machovsky M, Masar M, Holek M, Influence of La<sub>3p</sub> on structural, magnetic, dielectric, electrical and modulus spectroscopic characteristics of single phase CoFe<sub>2x</sub>La<sub>x</sub>O<sub>4</sub> nanoparticles, J. Mater. Sci. Mater. Electron. 28 **(2017)** 9139-9154.

**Yousuf M.A**, Baig M.M, Al-Khalli N.F, Khan M.A, Aboud M.F.A, Shakir I, Warsi M.F, The impact of yttrium cations (Y<sup>3+</sup>) on structural, spectral and dielectric properties of spinel manganese ferrite nanoparticles, Ceram. Int. 45 (8) (2019) 10936–10942.

**Zidi N**, Chaouchi A, D'Astorg S, Rguiti M, Courtois C, Dielectric and impedance spectroscopy characterizations of CuO added (Na<sub>0.5</sub>Bi<sub>0.50.94</sub>Ba<sub>0.06</sub>TiO<sub>3</sub>) lead-free piezoelectric ceramics, J. Alloys Compd. 590 (2014) 557-564.

# CHAPTER -VIII SUMMARY AND CONCLUSION

In recent years, nanosized ferrites have immense applications in various fields with fast development of microwave technology such as high frequency devices and their components, telecommunications devices, memory core devices, microwave absorption micro-oven, radar, antenna, sensor, magneto-resistive random-access memory (MRAM) devices, targeted magnetic tunnel junction and spintronics devices and also drug delivery. In electronic society, the usage of telecommunication and electronic equipment has increased due to the problem raised in electromagnetic interference [EMI] as it generates false image, reduces the life time and efficiency of the instruments and also destroy the safety operation of many electronic devices.

To overcome these problems, all electronic equipment's must be protected from electromagnetic damage. Now a days research has been done for the improvement of latest microwave shielding materials which include high efficiency, light weight, lifetime and high durability. Electromagnetic radiation [EMR] solves such problems and also satisfies the above-mentioned parameters. Therefore, electromagnetic absorbers are highly needed and broad ranges of application have been taken out. Some rare-earth element doping has been reported to play vital roles to amplify the magnetic, structural and electrical properties. These properties can be change through the cation distribution, size, shape, concentration and lattice sites. Spinel ferrites are one of the most absorbing materials in different forms such as paints, powder, ceramic filter and sheets, etc. The electrical and magnetic properties are superior when dopant of rare earth ions included.

In this work, rare earth doped nanoferrites synthesized by sol-gel method. The synthesized nanoferrites have been characterized through, X-ray diffraction (XRD) Field Emission Scanning Electron Microscopy (FESEM), Fourier Transform Infrared Spectroscopy (FT-IR), optical (UV-DRS and Raman spectroscopy), Magnetic studies (VSM) and Dielectric studies were analyzed. The major attention has been given to the investigation of magnetic and Dielectric properties of rare-earth doped nanoferrites in order to improve the performance of the same towards Electro Magnetic Radiation (EMR) applications.

This chapter describes the summary and conclusion of the findings in the present investigation and the promising future of the research work is also highlighted at the end of the chapter.

#### **SUMMARY**

This present investigation is aimed to synthesize and characterize the Lanthanides doped nanoferrites. In order to scrutinize the feasibility of microwave absorption, magnetic and electrical properties of the prepared nanoferrites were analysed. CoLa<sub>X</sub>Fe<sub>2-X</sub>O<sub>4</sub>, MnLa<sub>X</sub>Fe<sub>2-X</sub>O<sub>4</sub>, CoGd<sub>X</sub>Fe<sub>2-X</sub>O<sub>4</sub> and MnGd<sub>X</sub>Fe<sub>2-X</sub>O<sub>4</sub>(X=0.00, 0.02, 0.04, 0.06 and 0.08) nanoferrites were prepared using the sol-gel method. The prepared nanoferrites were investigated to examine their structural, optical, magnetic and electrical properties using X-ray diffraction (XRD), Field Emission Scanning Electron Microscopy (FESEM) coupled with energy-dispersive X-ray (EDAX) analysis, Fourier Transform Infrared Spectroscopy (FTIR), Ultra Violet-Diffuse Reflectance Spectroscopy (UV-DRS), Raman spectroscopy, X-ray Photoelectron

Spectroscopy (XPS), Vibrating Sample Magnetometer (VSM), electrochemical impedance spectroscopy and inductance capacitance and resistance (LCR) Hitester.

The following are the summary of the present investigation:

### Impact of Lanthanum ions on Magnetic and Dielectric properties of Cobalt Nanoferrites

- ❖ Lanthanum doped cobalt  $CoLa_xFe_{2-x}O_4$  nanaoferrites with various composition for X = 0.00, 0.02, 0.04, 0.06, 0.08 were synthesized using simple and most effective sol-gel method.
- ❖ XRD results revealed cubic spinel structure with an average crystallite size of 31 nm. FTIR analyses confirmed the presence of metal at 583 cm⁻¹ corresponding to stretching M-O bond respectively.
- ❖ The lattice constant and volume of unit cell were increases with increase of La³+ ions, whereas X-ray density and bulk density became inversely proportional to lattice constant.
- ❖ UV-diffuse reflectance spectra showed that the absorbance spectra of the CoLa<sub>x</sub>Fe<sub>2-x</sub>O<sub>4</sub> nanoferrites were varied from 226 to 222 nm. The value of indirect and direct energy bandgap varied from 1.73 to 2.06 eV and 1.45 to 1.56 eV. The obtained bandgap energy increased with increase of La<sup>3+</sup> concentrations.
- The obtained prepared nanaoferrites were identified with spherical morphology.
- ❖ XPS confirmed the presence of Co 2p, Fe 2p, La 3d and O 1s at octahedral
   [B] and tetrahedral [A] sites in CoLa<sub>x</sub>Fe<sub>2-x</sub>O<sub>4</sub> nanoferrites.
- ❖ The obtained VSM result showed that the prepared Lanthanum doped cobalt

- nanoferrites has got a soft ferromagnetic nature. The saturation magnetization from 97.35 to 75.84 emu/g decreases with increase of La<sup>3+</sup> concentration.
- ❖ The higher coercivity (1128 Oe) with dielectric constant of the Lanthanum doped cobalt spinel nanoferrites is favorable for the applications in magneto recording devices.
- ❖ Impedance spectroscopy is used to identify grain contributions and grain boundary contributions to conductivity and utilized to estimate electrical response of Lanthanum doped cobalt nanoferrites.
- ❖ The frequency dependant dielectric constant, complex dielectric constant and dielectric loss decreases with increase of La³+ ion. Behavior of dielectric constant and AC conductivity of pure and Lanthanum doped cobalt nanoferrites was found to follow Maxwell-Wagner's model.
- ❖ Hence the combination of structural, magnetic, electrical and optical activities makes CoLa<sub>x</sub>Fe<sub>2-x</sub>O<sub>4</sub> (X = 0.00 to 0.08) nanoferrites highly useful for reducing false signals in the electronic devices and its highly suitable for Microwave frequency applications.

## Dependance of Lanthanum ionson Structural, Magnetic and Electrical of Manganese based Spinel Nanoferrites

- ❖ Lanthanum doped Manganese nanoferrites were successfully synthesized by sol-gel method. These nanoferrites have cubic spinel structure with crystallite size from 26 to 12nm.
- ❖ The lattice constant and bulk density increased with increase of La<sup>3+</sup> ions, whereas X-ray density is inversely proportional to lattice constant and bulk density. The value of porosity decreases with increase of La<sup>3+</sup> ions.

- ❖ The absorption bands are noticed in the FTIR spectrum near 562 cm<sup>-1</sup>, which confirms tetrahedral and octahedral stretching of Metal-Oxygen bond.
- ❖ The bandgap values of the prepared Lanthanum doped manganese nanoferrites are 1.89 2.35 eV, which improve with respect to the band gap 1.25 1.38 eV values of Mn nanoferrites due to impact of La<sup>3+</sup> ions.
- ❖ FESEM with EDAX reveals that the prepare nanoferrites have spherical morphology with few agglomerations and present elemental peaks attained consistently in all the composition.
- ❖ The value of magnetic saturation is decreased from 81.5 to 51.3 emu/g and the value of coercivity increased from 105 to 517.32emu/g with increase of La³+ ions whereas it showed magnetic saturation inversely proportional to coercivity. VSM revealed that prepared nanoferrites are soft and ferromagnetic in nature.
- ❖ The dielectric constant and dielectric loss are decreased with increase of frequency and also dielectric constant and complex dielectric constant increased with increase of La<sup>3+</sup> ions.
- ❖ Impedance spectra reveal that the impedance response is over ruled by grain boundary behavior. The AC conductivity increases with increase of La<sup>3+</sup> ions.
- Hence, Lanthanum doped manganese nanoferrites are favorable for electromagnetic applications.

# Effect of Gd<sup>3+</sup> ions on Structural, Optical, Magnetic and Dielectric properties of $CoGdxFe_2-xO_4$ (0.00 $\leq X \geq$ 0.08) Nanoferrites

- ❖ The production of  $Gd^{3+}$  doped cobalt nanoferrites of a spinel crystal  $CoGd_XFe_{2-X}O_4$  (X = 0.00 to 0.08) via the sol-gel method.
- ❖ The impact of Gd³+ ion substitutions in cobalt nanoferrites on structural, functional, optical, magnetic, and dielectric properties were examined.
  The cubic spinel structure of these nanoferrites was confirmed by X-ray diffraction patterns.
- ❖ In cobalt nanoferrites, the average crystallite size falls as the number of Gd³+ ions increase. Because of the change in ionic radius, the lattice constant and unit cell dimension rise as the number of Gd³+ ions increase.
- ❖ The porosity reduces as the number of Gd<sup>3+</sup> ions increase, which is related to an increase in bulk density, but the surface area increases as the number of Gd<sup>3+</sup> ions fall, which is due to a reduction in crystallite size.
- The particles are spherical shaped grains with agglomeration, according to surface morphology.
- ❖ The performance of grain and grain boundaries towards capacitance and resistance was shown by the Cole-Cole plot using impedance spectroscopy, implying that grain boundary contribution is higher than grain contribution. With increasing frequency, the variation of the dielectric constant diminishes.
- ❖ It is thought that the addition of Gd had a substantial impact on the Maxwel-Wagner interfacial charge polarization model, which agreed with the Koop model.

Summary and Conclusion Page 240

- ❖ The values of dielectric constant are increased with increase of Gd³+ ions. The value of dielectric losses decreases with increase of Gd³+ ions. The results also reveals abnormal behavior of dielectric loss and the same is due to relaxation peak.
- ❖ AC conductivity increases with increase of frequency as a function of increase with Gd³+ ions concentration as the spinals undergone Verwey mechanism.
- ❖ The very low dielectric loss and minimum magnetic saturation of these prepared nanoferrites has potential application in magnetic recording devices, magnetic shielding and microwave absorption devices.
- ❖ Further, reported sol-gel technique provides cost effective and green synthesis alternative for large scale production for industrial products and also for environmental advantages.

# Influence of Gd<sup>3+</sup> ions on Structural, Optical, Magnetic and Dielectric properties of MnGdxFe<sub>2-x</sub>O<sub>4</sub>( $0.00 \le x \ge 0.08$ ) Nanoferrites

- ❖ In summary, we have successfully synthesized  $MnGd_xFe_{2-x}O_4$  (X = 0.00 to 0.08) nano ferrites using sol-gel technique.
- ❖ XRD pattern shows cubic spinel structure without any impurity peak. The crystallite size decreases from 26 to 13 with increases of Gd³+ ions. The Lattice constant increases with Gd³+ ions due to ionic radius.
- ❖ The optical bandgap was inversely proportional to the absorbance of wavelength which in the range of semiconductor materials.
- ❖ FESEM shows spherical shape with agglomeration. The purity of the composition was confirmed from EDAX.

Summary and Conclusion Page 241

- The formation of spinel ferrites was confirmed from the peak found from the FTIR spectra.
- Raman spectroscopy attains five active modes  $[2A_{1g} + 3T_{2g} + E_g]$ .
- ❖ Magnetic studies confirm S-shaped soft ferromagnetic material. The magnetic saturation decreases with the increase of Gd³+ ions due to a decrease in crystallite size. The coercivity increases with Gd³+ ions, depending on grain size, magneto- crystallinity anisotropy constant, porosity and strain. And also, it can be explained based on stoner Wohl forth theory.
- ❖ The Cole-Cole plot from impedance spectroscopy infers grain and grain boundaries towards capacitance and resistance, which denotes grain boundary greater than the grain contributions.
- ❖ The dielectric constant decreases with the frequency increase, which is explained based on the Maxwell-Wagner and Koop model. The value of the constant dielectric increases with the increase of  $Gd^{3+}$  ion. The highest value of dielectric constant attains at X = 0.08. The value of dielectric loss decreases with increases of  $Gd^{3+}$  ions.
- ❖ The results also express abnormal behavior dielectric loss. The low value of dielectric loss attains 0.08.
- ❖ AC conductivity linearly increases with the increase of frequency as well as increase with Gd³+ ions.
- ❖ The investigation of Gd doped manganese nano ferrites (X= 0.00 to 0.08) reveals that the very low dielectric loss, saturation and minimum coercivity has finds potential application in storage devices, microwave absorption devices and also it can be used for various electronic applications.

#### OVER ALL CONCLUSION

This is the conclusion and the achievements during in the due course of the investigation.

- ❖ The standard sol-gel method was used to prepare CoLa<sub>X</sub>Fe<sub>2-X</sub>O<sub>4</sub> and MnLa<sub>X</sub>Fe<sub>2-X</sub>O<sub>4</sub>nanoferrites and CoGd<sub>X</sub>Fe<sub>2-X</sub>O<sub>4</sub> and MnGd<sub>X</sub>Fe<sub>2-X</sub>O<sub>4</sub> was prepared.
- ❖ The complete characterization techniques such as XRD, UV-DRS/Raman Spectroscopy, FTIR, FESEM EDAX, XPS, LCR meter, Impedance Spectroscopy and VSM were carried out to explore the structural, optical, dielectric and magnetic properties of the prepared nanoferrites.
- ❖ A decrease in crystalline size [26 (X=0.00) to 13 (X=0.08) nm] and an increase in the Lattice constant [7.820 (X=0.00) to 8.928 (X=0.08) Å] were observed for MnGdxFe₂-xO₄ nanoferrites.
- ❖ The energy bandgap increased with an increased in the concentration of Lanthanides (MnGd<sub>x</sub>Fe<sub>2-x</sub>O<sub>4</sub>).
- ❖ A spherical-like morphology of the prepared nanoferrites was identified from FESEM and it was found that the particle size decreased with an increase in the concentration of Lanthanides (MnGd<sub>x</sub>Fe<sub>2-x</sub>O<sub>4</sub>).
- ❖ The saturation magnetization of the prepared nanoferrites was decreased with doping of Lanthanides (MnGd<sub>x</sub>Fe<sub>2-x</sub>O<sub>4</sub>).
- ❖ The reduction in saturation magnetization of Gadolinium doped Manganese nanoferrites may be attributed to the presence of a nonmagnetic polymer, which reduces particle—particle interactions and decreases the exchange coupling energy, which in turn reduces saturation magnetization.

- ❖ The VSM measurements indicated the S shaped soft ferromagnetic nature of the prepared nanoferrites was obtained.
- $\clubsuit$  An increase in Ε' (from 60407.81 (X=0.00) to 1574426.14 (X=0.08)) and decrease in tanδ (from 2.02 (X=0.00) to 1.91 (X=0.08)) were obtained for MnGd<sub>X</sub>Fe<sub>2-X</sub>O<sub>4</sub> nanoferrites.
- ❖ The dielectric constant of the prepared nanoferrites was increased with decrease of dielectric loss for MnGdxFe₂-xO₄.

Finally concluded that the Gadolinium doped Manganese nanoferrites exhibits better structural, magnetic and dielectric properties. Over all, it is suggested to improve the EMI shielding, and also, to reduce the interference of electromagnetic radiation from the telephone towers, ships and aircraft, etc.,

#### **FUTURE SCOPE OF THE WORK**

The following are the future scope of the present work:

- ❖ From the structural, optical, magnetic and dielectric properties of the Lanthanides doped nanoferrites, the EMI shielding ability can be evolved.
- ❖ The technology to reduce the interference of electromagnetic radiation from the telephone towers, ships and aircraft, etc., will be developed from the outcome of the present investigation.
- ❖ The obtained optical bandgap, impedance, dielectric constant, dielectric loss and AC conductivity of the nanoferrites will be suggested to design the Electromagnetic devices.

Summary and Conclusion Page 244





1.228

Elsevier

Create account Sign in

## Sources

Scopus Preview

Title	~	Enter title				Find sou	rces				
Title: Cer	ramics International	×									
	proved Citesco			20 TV V AV							×
whice calcu prev	h provides an indi ulation of CiteScor	CiteScore methodology to e cation of research impact, e, as well as retroactively fo ues have been removed and odology. >	earlier. The upd r all previous C	ated methodo iteScore years	logy will be ap	plied to the					
1 result					<b>业</b> Dov	vnload Scopus	Source List	(i) Learn m	ore about S	copus Sou	ırce List
☐ All ∨	Export to Exc	cel 🖾 Save to source list						View metri	cs for year:	2020	~
Sou	rce title $\psi$		CiteScore ↓	Highest percentile	Citations	Documents	% Cited $\downarrow$	SNIP ↓	SJR ↓	Publis	sher $\psi$

88% 34/292 Materials Chemistry

84,802

12,314

∧ Top of page

1 Ceramics International

Author search Sources



⑦ 🟦 Create account Sign in

## Sources

Title Enter title				Find sou	rces				
Title: Journal Of Materials Science: Materials In Electronics	×								
i Improved Citescore We have updated the CiteScore methodology to e which provides an indication of research impact, calculation of CiteScore, as well as retroactively fo previous CiteScore values have been removed and View CiteScore methodology. >	earlier. The upd r all previous C	ated methodolo iteScore years (i	ogy will be ap	plied to the					×
1 result  ☐ All ✓ ☐ Export to Excel ☐ Save to source list			<b>业</b> Dov	vnload Scopus	Source List	① Learn mo	ore about So	copus Source	e List
Source title ↓	CiteScore ↓	Highest percentile ↓	Citations 2017-20 ↓	Documents 2017-20 ↓	% Cited ↓	View metric	cs for year: SJR ↓	Publishe	er 🗸
Journal of Materials Science: Materials in Electronics	4.0	68% 222/693 Electrical and Electronic Engineering	36,024	8,903	74	0.651	0.489	Springer Nature	r

∧ Top of page

Author search Sources



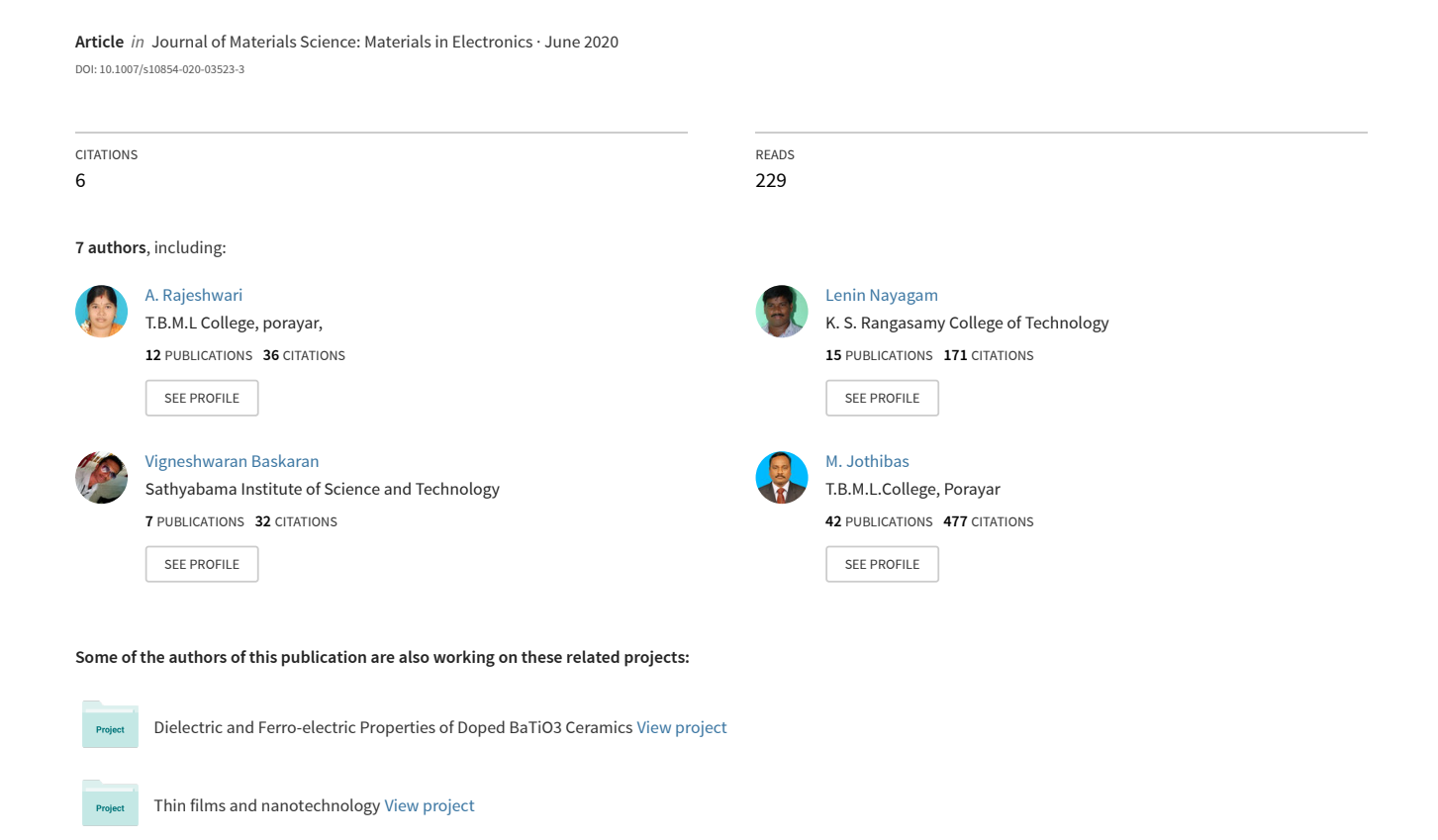
⑦ 🟦 Create account Sign in

## Sources

Title Enter title				Find sou	rces				
Title: Journal Of Materials Science: Materials In Electronics	×								
i Improved Citescore We have updated the CiteScore methodology to e which provides an indication of research impact, calculation of CiteScore, as well as retroactively fo previous CiteScore values have been removed and View CiteScore methodology. >	earlier. The upd r all previous C	ated methodolo iteScore years (i	ogy will be ap	plied to the					×
1 result  ☐ All ✓ ☐ Export to Excel ☐ Save to source list			<b>业</b> Dov	vnload Scopus	Source List	① Learn mo	ore about So	copus Source	e List
Source title ↓	CiteScore ↓	Highest percentile ↓	Citations 2017-20 ↓	Documents 2017-20 ↓	% Cited ↓	View metric	cs for year: SJR ↓	Publishe	er 🗸
Journal of Materials Science: Materials in Electronics	4.0	68% 222/693 Electrical and Electronic Engineering	36,024	8,903	74	0.651	0.489	Springer Nature	r

∧ Top of page

## Impact of lanthanum ions on magnetic and dielectric properties of cobalt nanoferrites





## Impact of lanthanum ions on magnetic and dielectric properties of cobalt nanoferrites

I. Kartharinal Punithavathy<sup>1</sup> • A. Rajeshwari<sup>1</sup> • S. Johnson Jeyakumar<sup>1</sup> • N. Lenin<sup>2</sup> • B. Vigneshwaran<sup>3</sup> • M. Jothibas<sup>1</sup> • B. Arunkumar<sup>1</sup>

Received: 28 March 2020 / Accepted: 28 April 2020 © Springer Science+Business Media, LLC, part of Springer Nature 2020

#### **Abstract**

Lanthanum-doped cobalt nanoferrites  $CoLa_xFe_{2-x}O_4$  (X=0.00 to 0.08) were synthesized by using sol–gel method. A cubic spinel structure was confirmed by using X-ray diffraction pattern. A band obtained at 583 cm<sup>-1</sup> recorded by Fourier transform infrared spectrum confirmed the presence of metal oxide spinel nanoferrites. The bandgap energy has increased with addition of  $La^{3+}$  ions by using ultraviolet diffuse reflectance spectrum. The grain boundary contribution is greater than that of grain contribution due to small crystal size, which was confirmed by an impedance analysis. The dielectric constant and dielectric losses decreased with increasing frequencies. The binding energy of La, Co, Fe and O were determined by X-ray photoelectron spectroscopy. The magnetic studies were analyzed through vibrating sample magnetometer. The hysteresis loop revealed the soft ferromagnetic nature.

#### 1 Introduction

Recently, spinel nanoferrites have been used in numerous technological and scientific applications [1], i.e., low loss magnetic core materials, hyperthermia, memory devices, drug delivery, antenna rods, gas sensors, microwave-absorbing materials, super capacitors, solar cell, and high-frequency devices [2–4]. Basic formula of spinel nanoferrites is AB<sub>2</sub>O<sub>4</sub>, where A and B represent a divalent and trivalent metal cations [5]. The spinel ferrites are classified into three types such as normal spinel structure, inverse spinel structure, and intermediate spinel structure. In normal spinel ferrites, divalent ions are at tetrahedral A-site and trivalent ions are in octahedral B-site; in inverse spinel structure, half of the trivalent ions are at B-site and half at A-site and the remaining ions are distributed in octahedral B-site, whereas intermediate spinel structure possesses the intermediate

stage between the normal and inverse spinel ferrites [6]. From the different spinel ferrite materials, CoFe<sub>2</sub>O<sub>4</sub> is the best challenging ferromagnetic material due to its better properties, such as high Curie temperature, high coercivity, reasonable saturation magnetization, high mechanical and chemical stability [7, 8]. Recent years, rare earth elements substituted spinel nanoferrites have special attention in developing their physical properties such as grain size and cation distribution at tetrahedral and octahedral sites [9, 10]. The spinel nanoferrites are the best advisable materials used for absorption of electromagnetic radiation (EMR) in different ways such as ceramic tiles, sheets, and powders [11]. Electromagnetic interference (EMI) has got most promising applications in communication systems such as radar systems, computers, and mobile phones [12, 13]. The EMI affects electronically controlled systems and also damages human health. It causes device interrupt, generate distorted images, increase clutter on radar due to system to system interruption during EMI [14]. To circumvent these EMI troubles, EMR is preferred, which has the ability of absorbing unwanted electromagnetic signals. Rare earth-doped nanoferrites have unique and important applications in electronic devices, transformer cores, magnetic recordings, radar signals, high-frequency circuits, and telecommunication. The doping of lanthanum (La<sup>3+</sup>) ions which are having unpaired electrons in the 4f orbital tends normally to nonmagnetic state. However, replacing smaller ionic radii Fe<sup>3+</sup>

Published online: 11 May 2020



<sup>☐</sup> I. Kartharinal Punithavathy profpunithaphysics@gmail.com

Department of Physics T.B.M.L College, Porayar, Nagapattinam 609307, India

<sup>&</sup>lt;sup>2</sup> Centre for Nano Science and Technology, K.S. Rangasamy College of Technology, Tiruchengode 637215, India

<sup>&</sup>lt;sup>3</sup> Centre for Nanoscience and Nanotechnology, International Research Centre, Sathyabama Institute of Science and Technology, Chennai 600119, India

ions into La<sup>3+</sup> ions at the octahedral site (B) to the ferrites leads to enhance the magnetic and electrical properties of the spinel nanoferrites used for microwave frequency applications [15–17]. The magnetic saturation ( $m_s$ ) decreases with an increase in the concentration of rare earth content in Li, Co, and Ni spinel nanoferrites [18]. Azadmanjiri et al. [12] describes, that the stability for transformer core where EMI is gently reduced and can avoid predicting false image in telecommunication system. Lanthanum-doped cobalt ferrites are synthesized by various techniques such as the sonication technique [17], mechanical milling technique [8], coprecipitate method [21], sonochemical method [1], hydrothermal method [19], and sol–gel technique [20]. The spinel nanoferrites were synthesized by sol–gel technique which overcomes the difficulties in co-precipitate technique [21].

In this study, lanthanum-doped cobalt nanoferrites CoLa<sub>X</sub>Fe<sub>2-X</sub>O<sub>4</sub> (X=0.00 to 0.08) were prepared by using sol–gel method. The obtained lanthanum-doped cobalt nanoferrites were characterized by X-ray diffraction (XRD) for phase and structural identification, ultraviolet diffuse reflectance spectroscopy (UV-DRS) to identify the optical properties, and Fourier transform infrared spectroscopy (FTIR) for checking the metal oxides presence. The field emission scanning electron microscopy (FESEM) and energy-dispersive X-ray analysis (EDX) were used to understand the surface morphology and elemental analysis. Magnetic and electrical properties were evolved using vibrating sample magnetometer (VSM) and Impedance spectroscopy. The obtained results were analyzed and utilized for the application of electronic devices in microwave frequency.

### 2 Materials and experimental procedure

#### 2.1 Materials

High pure grade Merck precursors such as cobalt nitrate  $(Co(NO_3)_2 \cdot 6H_2O)$ , lanthanum nitrate  $(La(NO_3)_3 \cdot 6H_2O)$ , ferric nitrate  $(Fe(NO_3)_3 \cdot 9H_2O)$ , ammonia  $(NH_4OH)$ , citric acid  $(C_6H_8O_7 \cdot H_2O)$ , and deionized water were used.

#### 2.2 Experimental procedure

The  $CoLa_XFe_{2-X}O_4$  (X=0.00, 0.02, 0.04, 0.06, 0.08) nanoferrites were prepared by sol-gel technique in the following approach. The measured precursors were dissolved with 100 ml of deionized water to obtain a uniform mixture of the precursor materials. The final mixture was continuously stirred at a temperature of 80 °C for 1 h. Further, ammonia was added drop wise to the ferrite solution to attain the pH value of 7. Finally the dark solution was obtained and dried in hot air oven at fixed temperature of 60 °C for 24 h. The dried nanoparticles were collected and sintered

in muffle furnace at 500 °C for 2 h. At next, sintered nanopowders were grinded for 15 min to obtain byproduct-free nanoparticles. Thus, obtained nanopowders were calcined at 1000 °C for 24 h. The schematic diagram for preparation of  $CoLa_xFe_{2-x}O_4$  nanoferrites is shown in Fig. 1.

## 2.3 Characterization of the CoLa<sub>X</sub>Fe<sub>2-X</sub>O<sub>4</sub> nanoferrites

The crystallite size and structural properties of the prepared  $CoLa_{\nu}Fe_{2-\nu}O_{\lambda}$  (X=0.00 to 0.08) nanoferrites were made by XRD (SHIMADZU-XRD 6000) technique with CuKα radiation source, at the  $2\theta$  range from  $20^{\circ}$  to  $80^{\circ}$ , operated at 40 kVand 30 mA. The chemical interaction and functional groups obtained in the prepared CoLa<sub>X</sub>Fe<sub>2-X</sub>O<sub>4</sub> nanoferrites were determined by FTIR spectra (SHIMADZU-UV 18,000) ranging from 4000 to 400 cm<sup>-1</sup> at RT (room temperature). The surface morphology and elemental composition were analyzed using FESEM with an EDAX (Quanta FEG 250). The optical properties of the synthesized samples were analyzed using an UV- DRS spectrum and the absorption wavelength was noted from 200 to 400 nm. The electrical property of the synthesized CoLa<sub>x</sub>Fe<sub>2-x</sub>O<sub>4</sub> nanoferrites was revealed using Impedance spectroscopy with the frequency range of Hz to 7 MHz at room temperature (30 °C) (Biologic SP-300), Silver coating was applied to the pellet for good Ohmic contact. X-ray photoelectron spectroscopic (XPS) studies were made using an

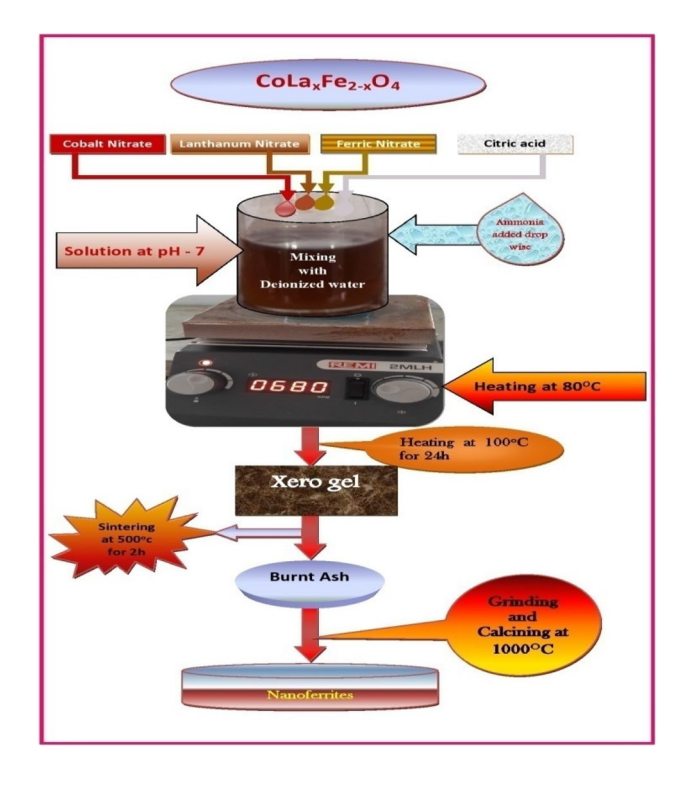


Fig. 1 Schematic diagram for preparation of  $CoLa_XFe_{2-X}O_4$  nanoferrites



(ALU-PHI5000) AUG spectrometer with monochromatic Al Ka (26.00 eV) radiation. Magnetic studies were assessed using VSM (Lakeshore VSM 7140) at room temperature (RT) with an applied magnetic field of -15 to +15 KOe.

#### 3 Results and discussion

#### 3.1 Structural analysis

XRD patterns of  $CoLa_XFe_{2-X}O_4$  for all the samples with series of X=0.00 to 0.08, calcined at 1000 °C are shown in Fig. 2. The obtained peaks are related to cubic spinel ferrites crystal structure and are matched with the standard JCPDS file no 22-1086. The peaks at 30.08°, 35.43°, 43.05°, 53.44°, and 56.97° correspond to the crystal planes (220), (311), (400), (422), and (511), respectively [22, 23]. The average crystal size of the synthesized nanoferrites was estimated using Debye's Scherrer equation [24].

$$D = \frac{k\lambda}{\beta Cos\theta} \tag{1}$$

where k is a Scherrer constant (0.9),  $\lambda$  is the wavelength of X-ray beam,  $\beta$  is the full width half maximum (FWHM),

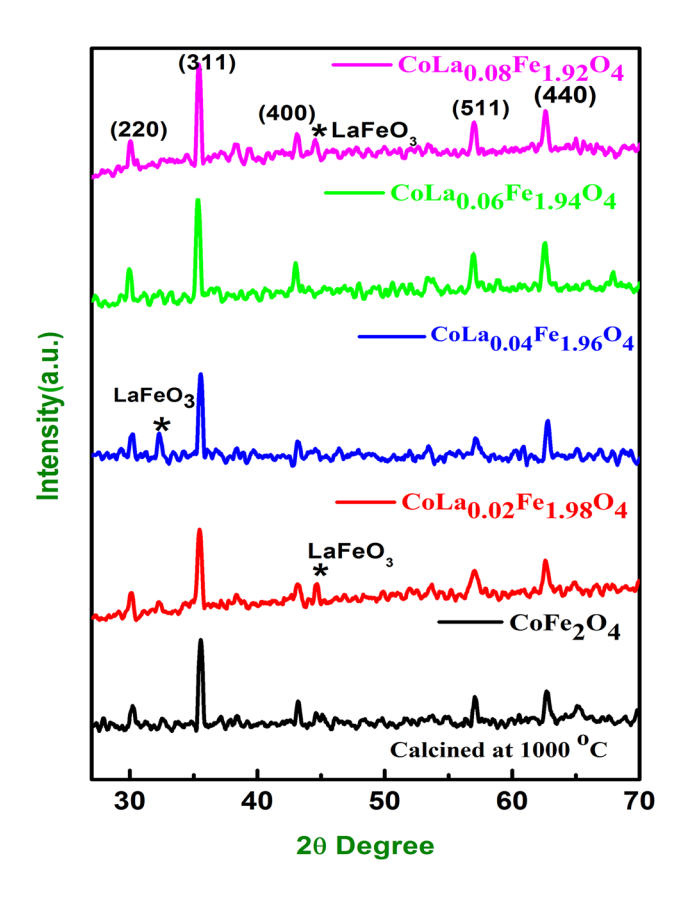


**Fig. 2** X-ray diffraction pattern of prepared  $CoLa_XFe_{2-X}O_4$  (X=0.00 to 0.08) nanoferrites calcined at 1000 °C

and  $\theta$  is the Braggs diffraction angle. The crystallite size of the ferrites decreases from 42 to 18 nm with increasing dopants concentration from X = 0.00 to 0.08. The La<sup>3+</sup> ion having ionic radius of 1.06 Å has larger ionic radii compared with Fe<sup>3+</sup> ionic radius 0.67 Å. Therefore, it is difficult to displace Fe<sup>3+</sup> ion in CoFe<sub>2</sub>O<sub>4</sub> spinel cubic nanoferrites. So, few La<sup>3+</sup> ions could present at grain boundaries. This larger ionic radius of La<sup>3+</sup> ions form pressure on the grains and therefore crystal size deceases with increasing La content [25]. The emergence of small amount of orthoferrite phase LaFeO<sub>3</sub> also appears with La<sup>3+</sup> content of (X=0.02, 0.04,0.08). The ionic radius of La<sup>3+</sup> ion is 1.06 Å, which is higher than that of the  $Fe^{3+}$  ion (0.67 Å), and hence, the amount of Fe<sup>3+</sup> ions replaced by La<sup>3+</sup> ions is limited and hence there is a solubility limit for the replacement of Fe<sup>3+</sup> ions by La<sup>3+</sup> ions. Thus, it is expected that an excess substitution of La<sup>3+</sup> ions tends to aggregate around the grain boundaries in the form of LaFeO<sub>3</sub>.

The lattice constant for the prepared nanoferrites is calculated using Nelson-relay function [26]:

$$a = d_{hkl}\sqrt{h^2 + k^2 + l^2} \tag{2}$$

where d is inter planar distance, a is the lattice constant, and hkl are Miller indices. The value of lattice constant is 8.37 Å which is in agreement with the reported value [27]. Lattice constant increases monotonically with increasing La<sup>3+</sup> ions which is due to the substitution of both Co<sup>2+</sup> ions with ionic radius of 0.78 Å and Fe<sup>3+</sup> ions with ionic radius of 0.64 Å by the larger La<sup>3+</sup> ions with ionic radius of 1.06 Å in Co–Fe–La spinel lattice [28]. The volume of unit cell increases from 587.3 to 600.9 Å with the increase in La<sup>3+</sup> concentration which occurs due to a increase in the lattice constant. X-ray density of the CoFe<sub>2</sub>O<sub>4</sub> nanoparticles was calculated using the following equation [28]:

$$d_x = \frac{Zm}{Na^3} \tag{3}$$

where  $N_{\rm a}$  is Avogadro's number, m is the molecular weight of the sample,  $a^3$  is the volume of the unit cell, and Z is the basic unit cell for the cubic spinel structure which contains 8 ions. X-ray density decreases from 5.685 to 5.403 g/cm<sup>3</sup> with an increase in La<sup>3+</sup> ion concentration in cobalt ferrite nanoparticles, which may possibly due to the increase in unit cell volume. The volume of the unit cell is inversely propositional to the X-ray density. The bulk density  $(d_{\rm B})$  was calculated using the mentioned equation [26]:

$$d_m = \frac{m}{\pi r^2 t} \tag{4}$$

where r is the radius of the pellet, m is the mass of the pellet, and t is the thickness of the pellet. The bulk density of lanthanum-doped cobalt nanoferrites was noticed to decrease



from 2.6085 to 2.0173 g/cm<sup>3</sup> with the increase of lanthanum ions. As compared to X-ray density, bulk density was less due to the presence of pores which mainly depend on calcined conditions [29]. The surface area (*S*) was estimated using the following expression [30]:

$$S = 6/d_X D \tag{5}$$

where  $d_X$  is the X-ray density and D is the crystallite size of the nanoparticles. The surface areas (S) are increased with an increase in La<sup>3+</sup> ions which attribute to a decrease in crystal size. The porosity (P) was calculated using the following relation [30]:

$$P = \left(1 - d_B/d_X\right) \% \tag{6}$$

The percentage of porosity increases from 5.0 to 6.4% which may be due to a decrease in bulk density with an increase in La<sup>3+</sup> concentrations. Structural parameters such as X-ray density, crystal size, dislocation density, microstrain, lattice constant, volume of unit cell, surface area, bulk density, and porosity were determined and are listed in Table1.

#### 3.2 Optical properties

The influence of lanthanum on cobalt nanoferrites was studied by using UV-DRS spectra is shown in Fig. 3. The UV-DRS spectrum has overcome UV-visible absorption spectroscopy in its capability to evaluate the optical properties of powdered nanoparticles. UV-visible absorption has larger scattering effect when compared to UV-DRS spectra [17]. The absorbance values are 226.6, 224.7, 223.3, 222.5, and 222.0 nm as shown in Fig. 3. The  $E_{\rm g}$  of the prepared nanoferrites was obtained energy-dependant relation as follows [17]:

$$E_g = \frac{hc}{\lambda} \tag{7}$$

where c is the velocity of light, h is the Planck's constant, and  $\lambda$  is the wavelength of the absorption.

The indirect and direct bandgap energy values of lanthanum-doped cobalt nanoferrites were calculated using the following relation [17]:

$$h\gamma\alpha = (h\gamma - E_{gap})^n \tag{8}$$

where  $\gamma$  is the frequency, h is the plank's constant,  $\alpha$  is the absorbance coefficient, and n is the different types of electronic transition (n = 1/2 and 2) for bandgap (indirect and direct) transition, respectively.

In Fig. 3a, direct bandgap energy demonstrates the Taue plot between  $(\alpha E_{\rm photon})^2$  vs  $E_{\rm phot}$  and the E values were 1.45, 1.50, 1.53, 1.55, and 1.56 eV. In Fig. 3b, indirect bandgap energy demonstrates the Taue plot between  $(\alpha)^{1/2}$  vs  $E_{\rm phot}$  and the bandgap energy values of prepared nanoferrites were 1.73, 1.86, 1.93, 1.97, and 2.06 eV, respectively.

The absorbance and bandgap energy values of the lanthanum-doped cobalt nanoferrites are listed in Table 2. The bandgap energy shifts from red region to blue region for doped La<sup>3+</sup> ions. These shifts are attributed to 3d-4s spin interchange between Fe ions and La ions. However, the lanthanum-doped cobalt nanoferrite bandgap energies vary based on the Brus equation [31].

#### 3.3 Functional group analysis

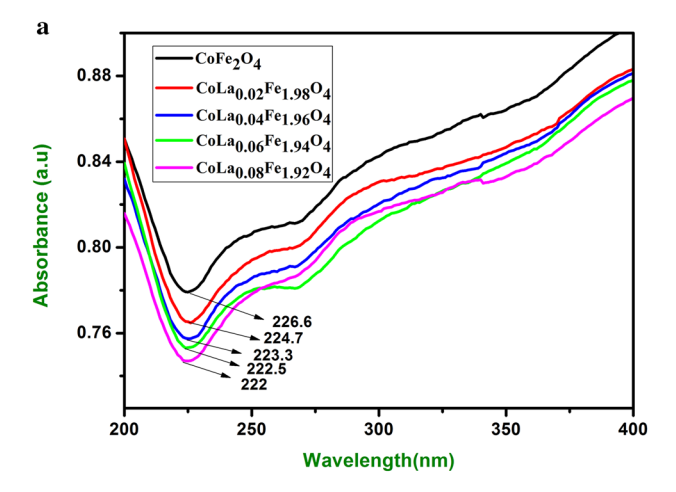
The FTIR spectra of prepared nanoferrites are depicted in Fig. 4. The transmittance spectra were obtained from the vibrational peaks appropriate to citric acid used in sol–gel technique which was acquired by stretching vibrations appropriate are to metal- oxygen band of around 583 cm<sup>-1</sup> to form spinel structure (Table 3).

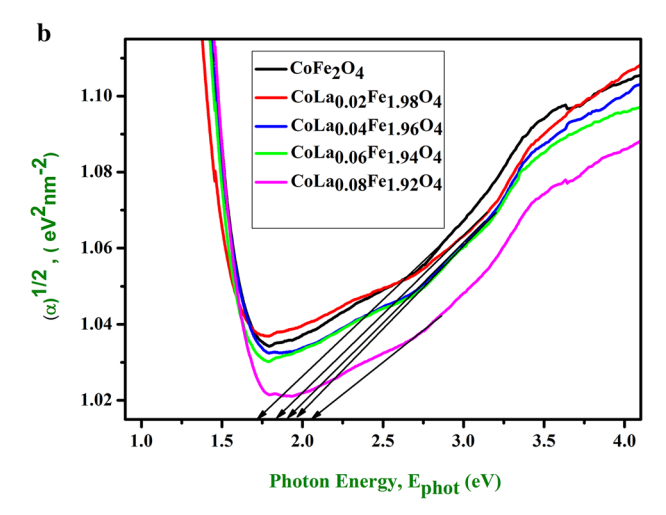
The broad and strong stretching peak obtained which indicates the O–H stretching due to the available water vapor in the prepared sample at 3437 cm<sup>-1</sup> [32]. The bending vibration of CH<sub>2</sub> carbon chain was observed with peak 2921 cm<sup>-1</sup>. The peaks are at 1745 cm<sup>-1</sup> corresponding to the C–H bending absorption of carboxyl group. Then 1149 cm<sup>-1</sup> is the C=O stretching vibration due to nitrogen group [33]. In these cubic structure ferrites Fe<sup>3+</sup> ions placed tetrahedral A-sites as well as octahedral B-sites.

Table 1 Structural parameters of prepared CoLa<sub>x</sub>Fe<sub>2-x</sub>O<sub>4</sub> (X=0.00 to 0.08) nanoferrites optimized calcination temperature at 1000 °C

Composition	Crystal size (D) (nm)	Dislocation density $(\delta)$ l/ $m^2 E + 15$	Micro strain $(\varepsilon)$ X10 <sup>-3</sup>	Lattice constant (a) Å	Volume of unit cell (a³) Å	X-ray density $(\rho_{XRD})$ (g/ cm <sup>3</sup> )	Surface area (S <sub>XRD</sub> ) (m <sup>2</sup> /g)	Bulk density (d <sub>B</sub> ) (g/cm <sup>3</sup> )	Porosity (%)
X = 0.00	42	0.55	0.849	8.37	587.30	5.68	25.12	2.68	5.0
X = 0.02	37	0.72	0.977	8.37	587.30	5.64	28.72	2.61	5.2
X = 0.04	34	0.85	1.058	8.40	593.95	5.54	31.83	2.57	5.3
X = 0.06	25	1.56	1.429	8.42	596.96	5.47	43.81	2.45	5.6
X = 0.08	18	2.85	1.933	8.43	600.99	5.40	61.68	2.01	6.4







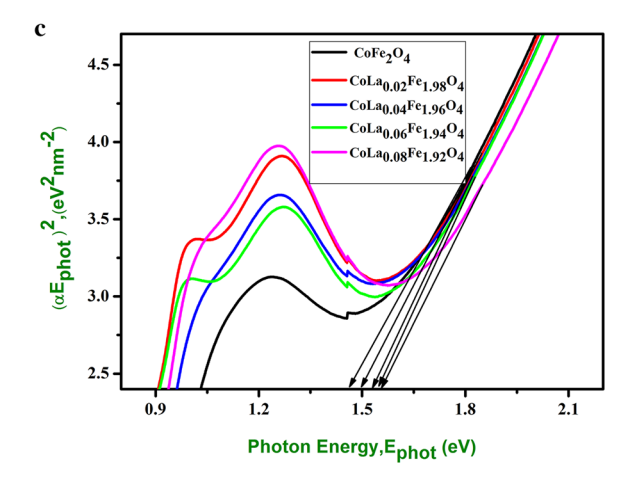


**Fig. 3** Absorbance spectra of prepared nanoferrites  $CoLa_XFe_{2-X}O_4$  (X=0.00 to 0.08) from UV-DRS spectra. **a** Indirect bandgap energy of prepared nanoferrites  $CoLa_XFe_{2-X}O_4$  (X=0.00 to 0.08) from UV-DRS spectra. **b** Direct bandgap energy of prepared nanoferrites  $CoLa_XFe_{2-X}O_4$  (X=0.00 to 0.08) from UV-DRS spectra

**Table 2** Optical parameters of prepared  $CoLa_XFe_{2-X}O_4$  (X=0.00 to 0.08) nanoferrites

Composition	Absorbance (nm)	Indirect band- gap energy (eV)	Direct band- gap energy (eV)
X = 0.00	226.6	1.73	1.45
X = 0.02	224.7	1.86	1.50
X = 0.04	223.3	1.93	1.53
X = 0.06	222.5	1.97	1.55
X = 0.08	222.0	2.06	1.56

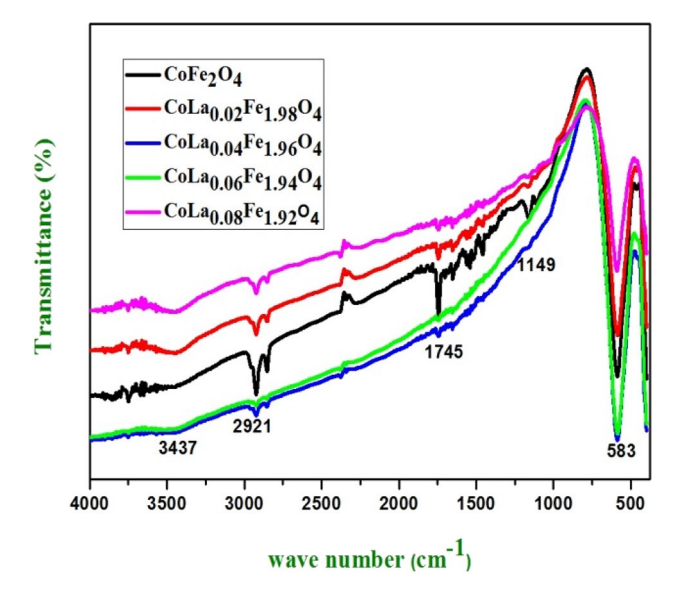


Fig. 4 FTIR spectra of prepared  $CoLa_XFe_{2-X}O_4$  (X=0.00 to 0.08) nanoferrites

#### 3.4 Surface morphology with EDAX

The FESEM images of lanthanum-doped cobalt nanoferrites were used to study surface morphology. Figure 5 denotes that the prepared nanoferrites were spherical in shape with some agglomeration. This agglomeration of grain structure was mainly due to small crystallite size, calcinating process and magnetic nature of all the crystallites form together and promotes cluster and also gets agglomerated [34, 35]. Magnetic force or weak Vander Waals bonds plays a major role in holding these agglomerations in contact [36]. In the obtained result, grain size was decreased with an increase in La<sup>3+</sup> ions. EDAX spectra of lanthanum-doped cobalt nanoferrites correspond to the elements Fe, O, Co, and La, which is presented in Fig. 5 (X = 0.02 to 0.08) where absent of La peaks is observed for (X = 0.00).



**Table 3** Functional parameters of prepared  $CoLa_XFe_{2-X}O_4$  (X=0.00 to 0.08) nanoferrites

S. no	Vibrational assignments	Experimental absorption (cm <sup>-1</sup> )				
		X = 0.00	X = 0.02	X = 0.04	X = 0.06	X = 0.08
1	Metal-oxygen stretching vibration	583	583	583	583	583
2	C=O stretching vibration	1149	1149	1149	1149	1149
3	C-H bending vibration of carboxyl group	1745	1745	1745	1745	1745
4	CH <sub>2</sub> bending vibration of carbon chain	2921	2921	2921	2921	2921
5	O-H stretching vibration	3437	3437	3437	3437	3437

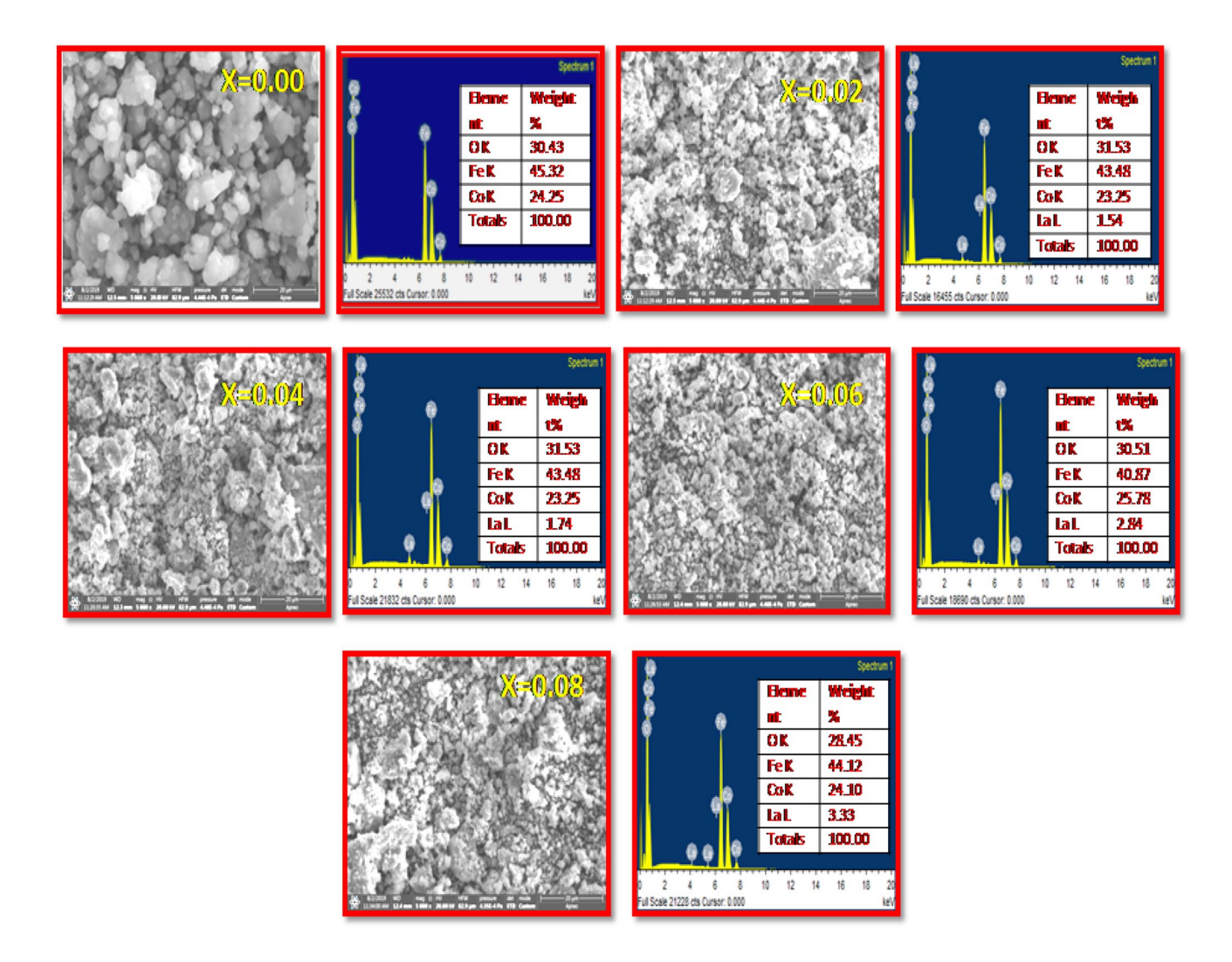


Fig. 5 FESEM with EDAX images of the prepared  $CoLa_XFe_{2-X}O_4$  (X=0.00 to 0.08) nanoferrites

#### 3.5 XPS studies

The X-ray photoelectron spectroscopy (XPS) analysis was used to investigate oxidation state and elemental composition of prepared nanoferrites. Figure 6 brings a wide scan spectrum of pure and lanthanum-doped cobalt nanoferrites in the range of 0–980 eV. In the long-range spectrum as in Fig. 6e, it can be clearly shown that the elemental and oxidation states of Co 2p, Fe 2p, La 3d, o 1s, and c 1s are present.

No other elements were found, which proves the purity of prepared nanoferrites. The narrow scan spectrum of O 1s shown in Fig. 6a clearly indicates a peak at 529.06, 535.76, and 535.96 eV for pure and lanthanum-doped cobalt nanoferrites. These obtained peaks were due to the presence of O<sup>2-</sup> in the nanoferrites [37, 38]. The narrow scan spectrum of O 1s shown in Fig. 6b, clearly indicate a peak at 529.06, 535.76 and 535.96 eV for pure and lanthanum doped cobalt nanoferrites. These obtained peaks were due to the presence



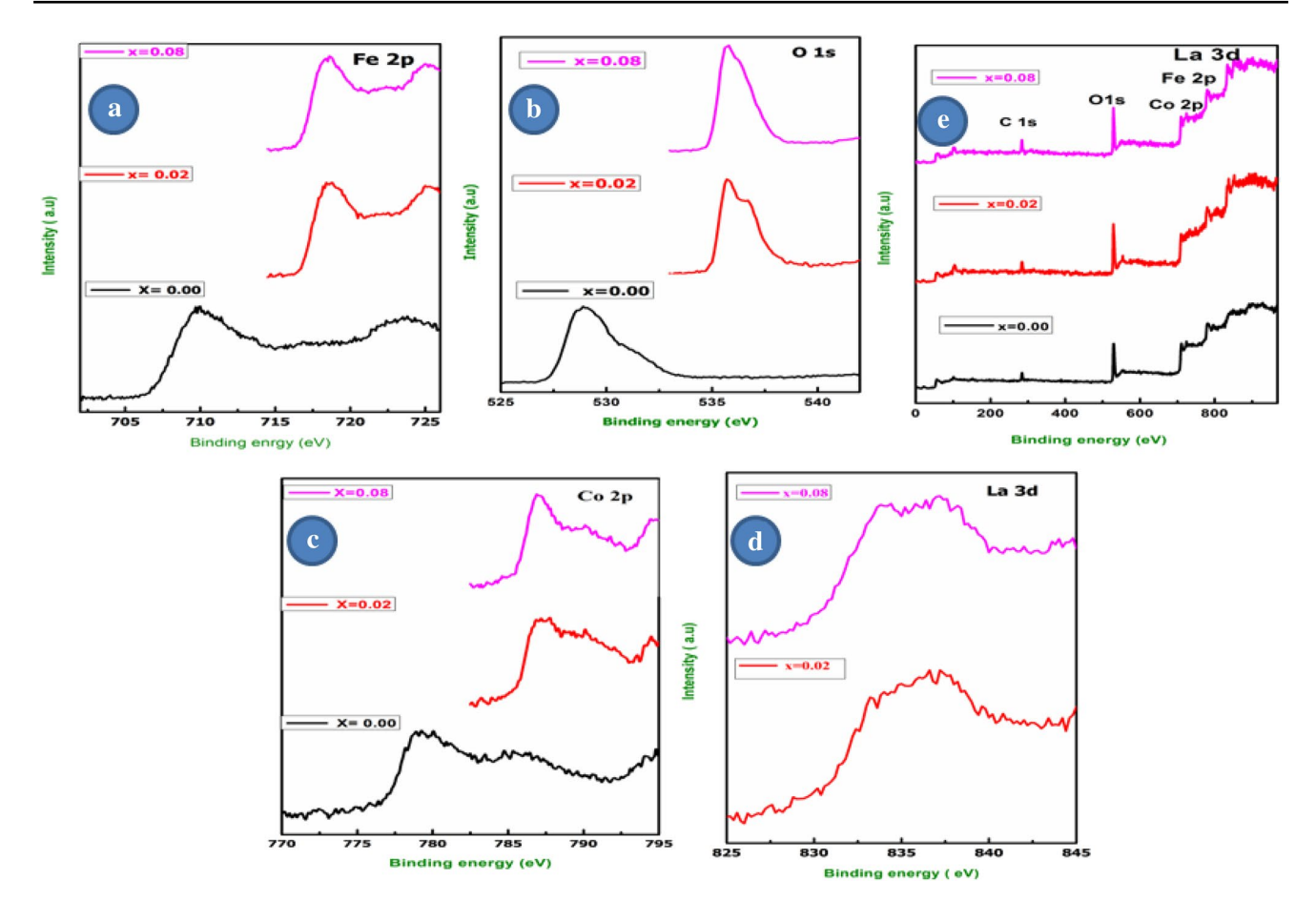


Fig. 6 XPS spectra of the prepared CoLa<sub>x</sub>Fe<sub>2-x</sub>O<sub>4</sub> (X = 0.00 to 0.08) nanoferrites

of  $O^{2-}$  in the nanoferrites [38, 39]. The narrow scan spectrum of Co 2p as noticed from Fig. 6c, and corresponding two peaks at 778.93 and  $786 \pm 0.4$  eV. Similarly 785.11 eV and  $790 \pm 15$  were present for Co  $2p^{3/2}$  and Co  $2p^{1/2}$ , which confirms the oxidation state of  $Co^{2+}$ . The narrow range spectrum of Fe 2p in nanoferrites revealed Fe  $2p^{3/2}$  and Fe  $2p^{1/2}$  binding energy peaks at 709.75 and 718  $\pm$  0.8eV for Fe  $2p^{3/2}$ , 723.54 and 725  $\pm$  14eV for Fe  $2p^{1/2}$  Fig. 6a, respectively. The peak at  $718 \pm 0.8$  eV is attained due to the Fe<sup>3+</sup> cation located at the octahedral site in the spinal ferrites, and the peak at  $725 \pm 14$  eV is attained due to the Fe<sup>2+</sup> cation located at the tetrahedral site in the spinal ferrites [39, 40]. From Fig. 6d, the narrow scan spectrum was obtained for La<sup>3+</sup> with binding energies of  $833.18 \pm 0.69$  eV for  $3d^{5/2}$ 

and  $837.20 \pm 0.12$  eV for  $3d^{3/2}$ . The obtained peaks were explained to the electron transfer of oxygen to the 4 f subshell of La<sup>3+</sup> ions due to photo-ionization process [38]. From XRD and XPS results, it was clearly noticed that the La<sup>3+</sup> ions were assimilated into Fe ions in cobalt nanoferrites. The observed binding energy of oxygen, cobalt, iron, and lanthanum is listed in Table 4.

#### 3.6 Magnetic properties

The M-H loop for prepared  $CoLa_XFe_{2-X}O_4$  nanoferrites have been plotted with magnetic field maximum of 15,000 Oe at room temperature by VSM. From Fig. 7, S shaped hysteresis loops shows the soft magnetic nature of the prepared

**Table 4** Binding energy of prepared  $CoLa_XFe_{2-X}O_4$  (X=0.00 to 0.08) nanoferrites

Composition	O 1s (eV)	Co 2p (eV)		Fe 2p (eV	)	La 3d (eV)		
		2p <sup>3/2</sup>	2p 1/2	2p <sup>3/2</sup>	2p 1/2	3d <sup>5/2</sup>	3d <sup>3/2</sup>	
X = 0.00	529.06	778.93	785.11	709.75	723.58	_	_	
X = 0.02	535.76	786.98	790.28	718.49	725.16	833.18	837.20	
X = 0.08	535.96	787.12	790.43	718.57	725.30	833.87	837.32	



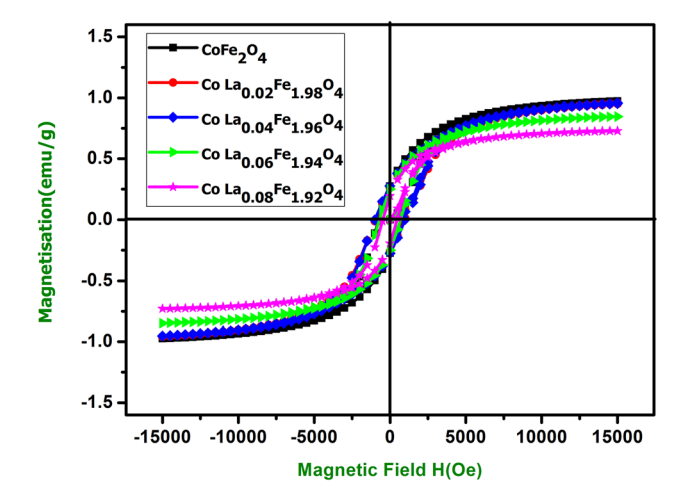


**Fig. 7** Hysteresis loop of the prepared  $CoLa_XFe_{2-X}O_4$  (X=0.00 to 0.08) nanoferrites

nanoferrites. The variation in magnetic parameters such as coercivity  $(H_C)$ , magnetic saturation  $(M_s)$ , retentivity  $(M_r)$ , and magnetic moment  $(\eta_B)$  for prepared nanoferrites have been revealed to be dependent of number of factors such as grain growth, anisotropy, density, A–B exchange interaction, surface spin effect, synthesis techniques, and chemical composition [41].

From magnetic hysteresis loops, it is understood that the inclusion of La³+ions promotes ferromagnetic nature. From Table 5, it is noticed the values of saturation magnetization decreases with an increase in La³+ ions in CoFe<sub>2</sub>O<sub>4</sub> nanoparticles which could be explained by Neel's sublattice model [42]. From the Neel's sub lattice model, the magnetic moment of ions on the A-site and B-site sublattices was aligned antiparallel to each other and their spins have a collinear structure. The magnetic moment was calculated by using the following equation:

$$\eta_{\rm B} = M_{\rm B} - M_{\rm A} \tag{9}$$

where  $M_A$  and  $M_B$  are [A] and [B] sublattices [43]. In general, magnetic super exchange interaction is based on the cation distribution between A-site and B-sites. This could

be attained due to their larger ionic radii. Therefore, suggesting that the nonmagnetic La<sup>3+</sup> could be replacing Fe<sup>3+</sup> ions from octahedral site (B) to tetrahedral site (A) [44]. Moreover, three types of exchange interaction would have happened between the magnetic ion at octahedral (B) and tetrahedral (A) sites in spinel structure such as AA interaction, BB interaction, AB interaction.

Out of three mentioned interactions, AB interaction predominates over rest of other two interactions [41]. Further, the increase in  $La^{3+}$  ions in  $CoLa_XFe_{2-X}O_4$  nanoparticles decreases the value of  $M_s$  from 97.35 to 75.84 emu/g with a decrease in crystal size from 42 to 18 nm, which results in the increase in the surface effect [43, 44]. Decreasing crystallite size due to the substitution of La<sup>3+</sup> trends to the increase in disordered spins which implies in the decrease in magnetic saturation. The value of coercivity increases from 736.33 to 1128.35 Oe with an increase in La<sup>3+</sup> ions depending on crystal size, magnetic crystallite, cation distribution, strain, porosity, and anisotropy [45]. According to Brown's relation, the coercivity is inversely proportional to the magnetic saturation. It was agreed for the prepared nanoferrites, where the coercivity increased with decreasing magnetic saturation for addition of La<sup>3+</sup> concentration. The anisotropy constant and squareness ratio were estimated by using the following equation [46, 47]:

$$\frac{M_{\rm r}}{M_{\rm s}} \tag{10}$$

$$K = \frac{H_c M_s}{0.98} \tag{11}$$

where  $M_r$  is the remanent magnetization or retentivity, K is the anisotropy constant. Further, Bohr magnetizations ( $\eta_B$ ) in magnetic moments ( $\mu_B$ ) were estimated from the following equation [47]:

$$\eta_{\rm B} = \frac{MXM_{\rm s}}{5585} \tag{12}$$

where X is the concentration and M is the molecular weight of  $La^{3+}$  ion content. The magnetic parameters such as magnetic saturation  $(M_s)$ , coercivity  $(H_c)$ , retentivity  $(M_r)$ ,

**Table 5** Magnetic parameters of prepared  $CoLa_XFe_{2-X}O_4$  (X = 0.00 to 0.08) nanoferrites

Composition	Magnetization $(M_s)$ (emu/g)	Remanent magnetization $(M_r)$ (emu/g)	Coercivity $(H_{c)}$ (Oe)	Squareness ratio $(M_r/M_s)$ (No unit)	Anisotropy constant (K) (Oe)	Bohr magneton $(\eta_B)$ $(\mu_B)$
X = 0.00	97.35	27.45	736.33	0.2819	73.14	0.4381
X = 0.02	95.62	26.75	958.91	0.2797	93.56	0.4273
X = 0.04	95.59	25.64	993.84	0.2683	96.90	0.4241
X = 0.06	94.66	25.04	1010.45	0.2645	63.60	0.3731
X = 0.08	75.84	19.45	1128.23	0.2564	34.94	0.3188



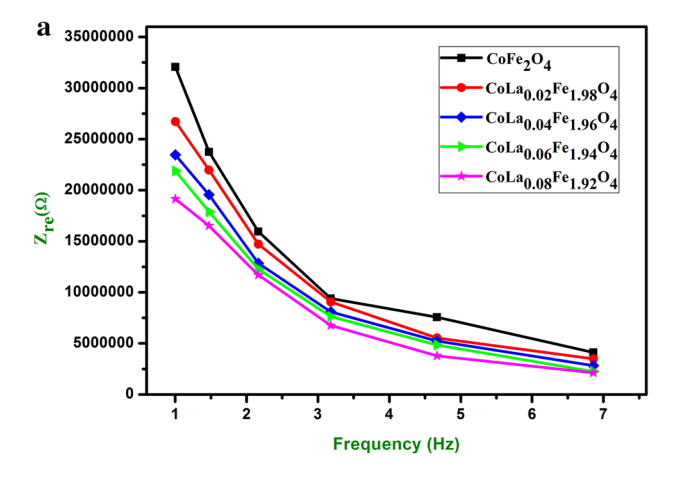
squareness ratio, anisotropic constant (k) and Bohr magnetron ( $n_{\beta}$ ) were noticed from M–H and measurements are listed in Table 5. This suggests that  $\text{CoLa}_X\text{Fe}_{2-X}\text{O}_4$  nanoferrites have spin arrangements which are better on the B-site, leading to decrease in (A–B interaction) [48, 49]. It was observed that the addition of La<sup>3+</sup> ions in cobalt matrix improved to get soft ferrite behavior with good saturation magnetization and it has good suitability for electromagnetic application [50]

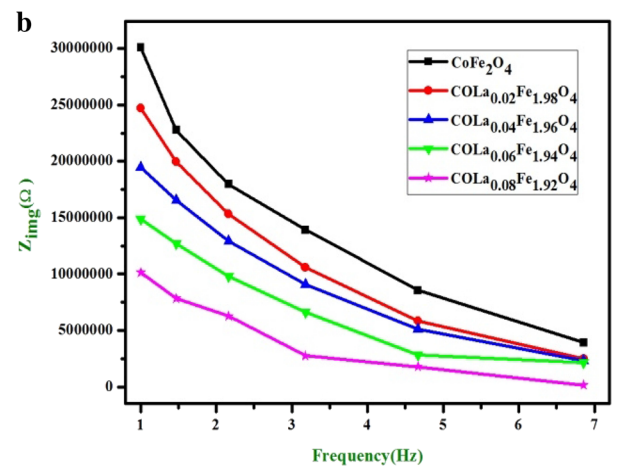
#### 3.7 Impedance analysis

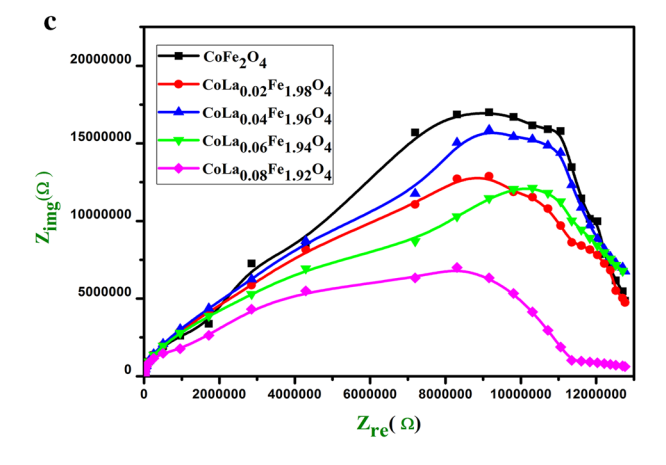
Impedance spectroscopy is a well-known technique for complete understanding of electrical properties of spinel type ferrites, whose properties depend on their ceramic texture, impedance of electrodes, distribution of dopants and grain and grain boundary contributions [51]. And it also provides information regarding imaginary and real components of the impedance property of a material. The Nyquist plot shows a complete contribution of grain and grain boundary resistance. Figure 8c shows that the applied frequency dependent imaginary (Z'') and real (Z')part of impedance decreased with an increase in frequency. It denotes an increase in a.c conductivity. The real part (Z') of the spectra values for all the prepared nanoparticles leads to lower values at higher frequency which implies release of space charges as a result of reduction in barrier properties of material [51]. In Fig. 8a, impedance vs frequency plot gives an indication of a increase in conduction with frequency, which infers that the ferrites behave like a semiconductor material [52].

Figure 8b, the imaginary part (Z'') of the La<sup>3+</sup>-doped cobalt nanoferrites decreases with an increase in applied frequency and then remains low at high frequency. The imaginary part (Z'') of the impedance spectra brings out relaxation peaks due to existence of space charge relaxation, associated with charge carries resulting from energy vacancies [53]. The Z'' also decreases with increasing frequency due to the decreasing loss in the imaginary part of the nanoferrites.

Nyquist plot of impedance spectra as function of frequency for  $CoLa_XFe_{2-X}O_4$  nanoferrites is shown in Fig. 8c. Clear semicircle arcs were formed in high frequency for all the prepared nanoferrites with series of (X=0.00 to 0.08) because of the grain and grain boundary contributions to the conductivity. This also indicates that because of small crystal size, the grain boundary contribution is higher than that of the grain contribution [54]. Furthermore, it is observed that the value of Z' and Z'' in the impedance spectra for cobalt decreases with increasing  $La^{3+}$  concentration and it depicts that the overall resistance of the  $La^{3+}$ -doped cobalt ferrite nanoparticles decreases, accordingly.







**Fig. 8 a** Real part of impedance spectra of prepared  $CoLa_XFe_{2-X}O_4$  (X=0.00 to 0.08) nanoferrites. **b** Imaginary part of impedance spectra of prepared  $CoLa_XFe_{2-X}O_4$  (X=0.00 to 0.08) nanoferrites. **c** Nyquist plots of prepared  $CoLa_XFe_{2-X}O_4$  (X=0.00 to 0.08) nanoferrites.



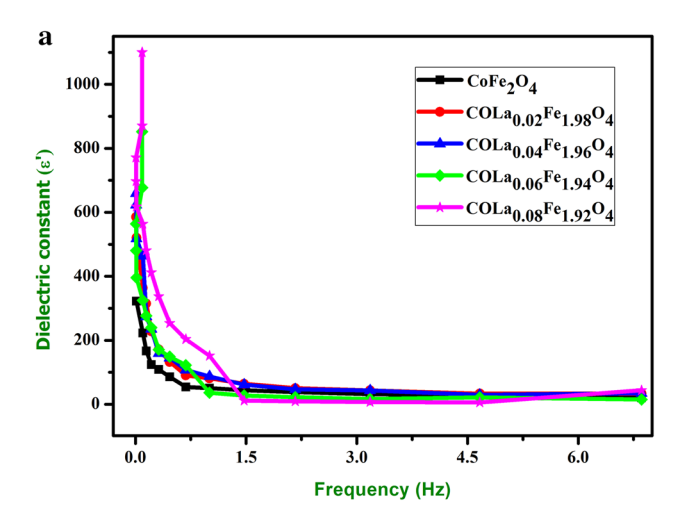
#### 3.8 Dielectric properties

#### 3.8.1 Dielectric constant

The variation of dielectric constant ( $\varepsilon'$ ) measured at the frequency in microhertz at RT for the prepared nanoferrites as shown in Fig. 9a. The dielectric constant decreases with an increase in lanthanum content as a mechanism for the electrical conduction, which is same that of dielectric polarization. The dielectric constant was calculated using the following equation [44]:

$$\varepsilon' = \frac{Cd}{\varepsilon_0 A} \tag{13}$$

where  $\varepsilon'$  is the dielectric constant, C is the capacitance of the pellet,  $\varepsilon_0$  is the permittivity of free space, A is the area of the CoLa<sub>X</sub>Fe<sub>2-X</sub>O<sub>4</sub> pellet, and d is the thickness of the pellet. The values of dielectric constant both  $\varepsilon'$  and  $\varepsilon''$  are higher



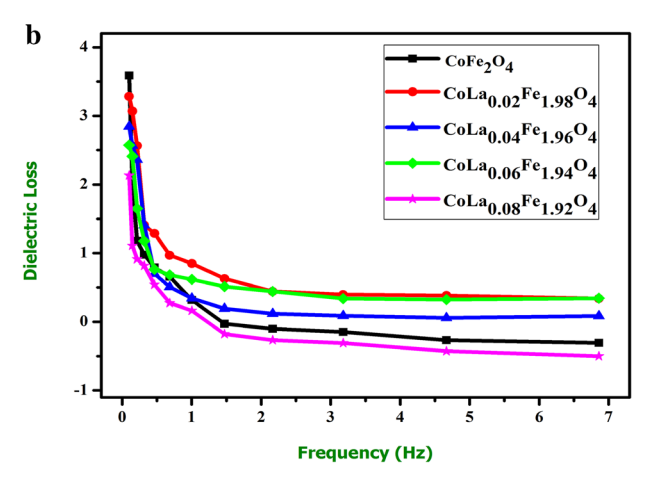


**Fig. 9** a Dielectric constant of the prepared  $CoLa_XFe_{2-X}O_4$  (X=0.00 to 0.08) nanoferrites, **b** Dielectric loss of the prepared  $CoLa_XFe_{2-X}O_4$  (X=0.00 to 0.08) nanoferrites



at lower frequency and then decreases with an increase in frequency for all the compositions (X = 0.00 to 0.08).

The obtained dielectric constant and complex dielectric constant values are 321, 585, 659, 852, and 1100 and 1150, 1921, 1874, 2190, and 2344 for all the compositions of X = 0.00, 0.02, 0.04, 0.06, and 0.08, respectively. The dielectric constants at lower frequency are based on some polarizations such as ionic, space charges, and interface [55, 56]. This type of behavior can be described based on Maxwell–Wagner interfacial polarization which is in agreement with Koop's theory [57]. According to the Maxwell–Wagner model, the dielectric constant was due to high conductivity grains and poor conductivity grain boundaries.

In  $CoLa_xFe_{2-x}O_4$  spinal ferrites, the formation of  $Fe^{2+}$ ions are due to interchange of electrons between Co<sup>2+</sup> and  $Fe^{3+}$  to generate a pair of  $Co^{3+}$  and  $Fe^{2+}$  ions [58]. The electron hopping between  $Fe^{2+} \leftrightarrow Fe^{3+}$  and hole hopping between  $Co^{3+} \leftrightarrow Co^{2+}$  ions and hence an applied electric field, the electrons pile up there, due to high resistance ultimately produces polarization. However, at high frequency the electron cannot move with fast changes due to the applied electric field because charge carries need sufficient time to transfer their orientation in react to the applied electric field. In general, the dielectric constant of any surface material depends on bulk polarization factor such dipolar, interfacial, ionic, and electronic polarizations. In certain polarizations, dipolar and interfacial polarizations are real for the noticed behavior in dielectric constant at lower frequency, while electronic polarization is held responsible in the high-frequency region [59]. The decrease in both  $\varepsilon''$  and  $\varepsilon'$  with frequency is due to the fact that any spices contributing to polarization is bound to slow the logging behind the applied field at high frequency [60, 61]. Interestingly dielectric constant values decreased by more than 50% from 1100 (X = 0.08) to 321 (X = 0.00) when the La<sup>3+</sup> increased less than 0.1% in  $CoLa_xFe_{2-x}O_4$ . The substitution of  $La^{3+}$ ions in CoLa<sub>x</sub>Fe<sub>2-x</sub>O<sub>4</sub> nanoferrites tends to have significant variation in  $\varepsilon'$  which improves the suitability of the nanoferrites for microwave frequency applications.

#### 3.8.2 Dielectric loss

The variation of dielectric loss or loss tangent with variation of frequency is shown in Fig. 9b. It is evidently noticed that the loss tangent decreases with an increase in La<sup>3+</sup> concentration. This can be mainly due to the increase in resistivity which results loss in tanδ. From the results, it is observed that the dielectric loss decreases with an increase in frequency at low frequency which decreased slowly in high-frequency region before it become almost independence of the frequency in the higher-frequency region.

The dielectric loss is formulated with high resistivity at low frequency which is playing major role. The dielectric

**Table 6** Dielectric parameters of prepared  $CoLa_XFe_{2-X}O_4$  (X = 0.00 to 0.08) nanoferrites

Composition	Dielectric constant $(\varepsilon')$	Dielectric loss $(\tan \delta)$	Complex dielectric constant $(\varepsilon'')$
X = 0.00	321	3.583	1150.14
X = 0.02	585	3.284	1921.44
X = 0.04	659	2.844	1874.19
X = 0.06	852	2.571	2190.49
X = 0.08	1100	2.131	2344.10

loss and complex dielectric constant of nanoferrites were calculated using following equations [62]:

$$\tan \delta = \frac{1}{2\pi f \varepsilon_0 \varepsilon'} \tag{14}$$

$$\varepsilon'' = \varepsilon' \tan \delta \tag{15}$$

The dielectric losses of the nanoferrites are 3.583, 3.284, 2.844, 2.571, and 2.131, respectively. The electron interchange between Fe<sup>2+</sup> and Fe<sup>3+</sup> required more energy and accordingly more energy ions due to high resistivity of grain boundaries [63]. Further, the electron interchange between Fe<sup>2+</sup> and Fe<sup>3+</sup> required loss of energy at high frequency of applied AC electric field which is equal to the hopping frequency of the charge carrier. The large amount of energy was thus recovered to transfer the oscillating ions and those by appearance of dielectric loss. The prepared material shows low dielectric loss is favorable for application in micro frequency devices. The electrical parameters such as dielectric constant, dielectric loss, and complex dielectrics are listed in Table 6.

#### 4 Conclusion

Lanthanum-doped cobalt  $CoLa_XFe_{2-X}O_4$  nanoferrites with various composition for X=0.00, 0.02, 0.04, 0.06, 0.08 were synthesized using simple and most effective sol-gel technique. XRD revealed cubic spinel structure with an average crystal size of 31 nm. FTIR analyses confirmed the presence of metal at 583 cm<sup>-1</sup> corresponding to stretching M–O bond, respectively. The lattice constant and volume of unit cell were increased with an increase in  $La^{3+}$  ions, whereas X-ray density and bulk density became inversely proportional to lattice constant. UV diffuse reflectance spectra showed that the absorbance spectra of the  $CoLa_XFe_{2-X}O_4$  nanoferrite were varied from 226 to 222 nm. The value of indirect and direct energy bandgap varied from 1.73 to 2.06 eV and 1.45 to 1.56 eV. The obtained bandgap energy increased with an increase in  $La^{3+}$  concentrations. The obtained prepared

nanoferrites were identified with spherical morphology. XPS confirmed the presence of Co 2p, Fe 2p, La 3d, and O 1s at octahedral [B] and tetrahedral [A] sites in CoLa<sub>x</sub>Fe<sub>2-x</sub>O<sub>4</sub> nanoferrites. The obtained VSM result showed that the prepared lanthanum-doped cobalt nanoferrites has got a soft ferromagnetic nature. The saturation magnetization from 97.35 to 75.84 emu/g decreases with an increase in La<sup>3+</sup> concentration. The higher coercivity (1128 Oe) with dielectric constant of the lanthanum-doped cobalt spinel nanoferrites is favorable for the applications in magneto recording devices. Impedance spectroscopy is used to identify grain contributions and grain boundary contributions to conductivity and utilized to estimate electrical response of lanthanum-doped cobalt nanoferrites. The frequencydependant dielectric constant, complex dielectric constant, and dielectric loss decreases with an increase in La<sup>3+</sup> ion. Behavior of dielectric constant and AC conductivity of pure and lanthanum-doped cobalt nanoferrites was found to follow Maxwell-Wagner's model. Hence the combination of structural, magnetic, electrical, and optical activities makes  $CoLa_xFe_{2-x}O_4$  (X = 0.00 to 0.08) nanoferrites highly useful for reducing false signals in the electronic devices and its highly suitable for microwave frequency applications.

#### References

- R.S. Yadava, I. Kuritkaa, J. Vilcakovaa, J. Havlicab, L. Kalinab, P. Urbaneka, M. Machovskya, D. Skodaa, M. Masara, M. Holeka, Sonochemical synthesis of Gd<sup>3+</sup> doped CoFe<sub>2</sub>O<sub>4</sub> spinel ferrite nanoparticlesand its physical properties. Ultrason. Sonochem. 40, 773–783 (2018)
- A. Kovalenko, R.S. Yadav, J. Pospisil, O. Zmeskal, D. Karashanova, P. Heinrichova, M. Vala, J. Havlica, M. Weiter, Towards improved efficiency of bulk-heterojunction. Solar cells using various spinel ferrite magnetic nanoparticles. Org. Electron. 39, 118–126 (2016)
- P.N. Anantharamaiah, P.A. Joy, Tuning of the magnetostrictive properties of cobalt ferrite by forced distribution of substituted divalent metal ions at different crystallographic sites. J. Appl. Phys. 121, 093904 (2017)
- X. Lasheras, M. Insausti, I. Gil de Muro, E. Garaio, F. Plazaola, M. Moros, L. De, J.M. de la Matteis, L.L. Fuente, Chemical synthesis and magnetic properties of monodisperse nickel ferrite nanoparticles for biomedical applications. J. Phys. Chem. C 120(6), 3492–3500 (2016)
- L. Kumar, M. Kar, Effect of La3+ substitution on the structural and magneto crystalline anisotropy of nanocrystalline cobalt ferrite (CoFe<sub>2-x</sub>La<sub>x</sub>O<sub>4</sub>). Ceram. Int. 438, 4771–4778 (2012)
- K. Pubby, S.S. Meena, S.M. Yusuf, S.B. Narang, Cobalt substituted nickel ferrites via Pechini's sol-gel route: X-band electromagnetic characterization. J. Magn. Magn. Mater. 466, 430–445 (2018)
- L.T. Lu, N.T. Dung, L.D. Tung, C.T. Thanh, O.K. Quy, N.V. Chuc, S. Maenosono, N.T.K. Thanh, Synthesis of magnetic cobalt ferrite nanoparticles with controlled morphology, mono dispersity and composition: the influence of solvent, surfactant, reductant and synthetic conditions. Nanoscale 7, 19596 (2015)



- 8. H. Widatallah, C. Johnson, A. Gismelseed, I. Al-Omari, S. Stewart, S. Al-Harthi, S. Thomas, H. Sitepu, Structural and magnetic studies of nanocrystalline Mg-doped Li0.5Fe2.5O4 particles prepared by mechanical milling. J. Phys. D 41, 165006 (2008)
- S.K. Gore, S.S. Jadhav, V.V. Jadhav, S.M. Patange, M. Naushad, R.S. Mane, K.H. Kim, The structural and magnetic properties of dual phase cobalt ferrite. Sci. Rep. 7, 2524 (2017)
- K.K. Bharathi, R.J. Tackett, C.E. Botez, C.V. Ramana, Coexistence of spin glassbehavior and long-range ferromagnetic ordering in La- and Dy-doped Co ferrite. J. Appl. Phys. 109, 07A510 (2011)
- N. Lenin, R.R. Kanna, K. Sakthipandi, A.S. Kumar, Structural, electrical and magnetic properties of NiLa<sub>x</sub>Fe<sub>2-x</sub>O<sub>4</sub> nanoferrites. Mater. Chem Phy. 212, 385–393 (2018)
- J. Azadmanjiri, H.K. Salehani, M.R. Barati, F. Farzan, Preparation and electromagnetic properties of Ni<sub>1-x</sub>Cu<sub>x</sub>Fe<sub>2</sub>O<sub>4</sub> nanoparticle ferrites by sol-gel auto combustion method. Mater. Lett. 61, 84–87 (2007)
- H. Wang, H. Guo, Y. Dai, D. Geng, Z. Han, D. Li, T. Yang, S. Ma, W. Liu, Z. Zhang, Optimal electromagnetic-wave absorption by enhanced dipole polarization inNi/C nanocapsules. Appl. Phys. Lett. 101, 083116 (2012)
- V. Chaudhari, S.E. Shirsath, M.L. Mane, R.H. Kadam, S.B. Shelke, D.R. Mane, Crystallographic, magnetic and electrical properties of Ni<sub>0.5</sub>Cu<sub>0.25</sub>Zn<sub>0.25</sub>La<sub>x</sub>Fe<sub>2-x</sub>O<sub>4</sub> nanoparticles fabricated by solgel method. J. Alloys Compd. 549, 213–220 (2013)
- P.K. Roy, J. Bera, Enhancement of the magnetic properties of Ni-Cu-Zn ferrites with the substitution of a small fraction of lanthanum for iron. Mater. Res. Bull. 42, 77–83 (2007)
- M.R. Kadam, R.P. Patil, P.P. Hankare, Investigations on structural, electrical andmagnetic properties of nickel substituted La-ferrites. Solid State Sci. 14, 964–970 (2012)
- R.R. Kanna, N. Lenin, K. Sakthipandi, M. Sivabharathy, Impact of Lanthanum on structural, optical, dielectric and magnetic properties of Mn1-xCuxFe1.85La0.15O4 spinel nanoferrites. Ceram. Int. 43, 15868–15879 (2017)
- K. Sakthipandi, V. Rajendrana, T. Jayakumar, B. Raj, P. Kulandivelu, Synthesis and on-line ultrasonic characterisation of bulk and nanocrystalline La068Sr032MnO3 perovskite manganite. J. Alloys Compd 509, 3457–3467 (2011)
- A.M. Anwar, Enhancement of electrical and magnetic properties of Cd<sup>2+</sup> doped Mn–Zn soft nanoferrites prepared by the sol–gel autocombustion method H. J. Magn. Magn. Mater. 333, 46–52 (2013)
- Z. Yan, J. Gao, Y. Li, M. Zhang, M. Guo, Hydrothermal synthesis and structure evolution of metal-doped magnesium ferrite from saprolite laterite. RSC Adv. 5, 92778–92787 (2015)
- J. de Vicente, A.V. Delgado, R.C. Plaza, J.D.G. Duran, F.G. Caballero, Stability of Cobalt ferrite colliodal particles. Effect of pH and applied magnetic fields. Langmuir 16, 7954–7961 (2000)
- F. Bensebaa, L. Zavaliche, P. Ecuyer, R.W. Cochrane, T. Veres, Microwave synthesis and characterization of co-ferrite nanoparticles. J Colloid Interface Sci 277, 104–110 (2004)
- S. Gaba, A. Kumar, P.S. Rana, M. Arora, Influence of La<sup>3+</sup> ion doping on physical properties of magnesium nanoferrites for microwave absorption application. J. Magn. Magn. Mater. S0304– 8853, 32557 (2017)
- B. Vigneshwaran, P. Kuppusami, A. Panda, A. Singh, H. Sreemoolanadhan, Microstructure and optical properties of Ba0.6Sr0.4TiO3 thin films prepared by pulsed laser deposition. Mater. Res. Express 5, 0664 (2018)
- A. Sattar, A.M. Samy, R.S. El-Ezza, A.E. Eatah, Effect of rareearth substitution on magnetic and electrical properties of Mn–Zn ferrites. Phys. Status Solid 193(1), 86–93 (2002)
- M.I. Ali, U. Islam, M.I. Hasan, M. Khan, M.N. Ashiq, Effect of Gd-substitution on physical and magnetic properties of

- Li1.2Mg0.4GdxFe(2-x)O4 ferrites. J Alloys Compd. **579**, 181–186 (2013)
- R.S. Yadav, J. Havlica, J. Masilko, L. Kalina, J. Wasserbauer, M. Hajduchova, V. Enev, I. Kuritka, Z. Kozakova, Impact of Nd<sup>3+</sup> in CoFe<sub>2</sub>O<sub>4</sub> spinel ferrite nanoparticles on cation distribution, structural and magnetic properties. J. Magn. Magn. Mater. 399, 109–117 (2015)
- J. Peng, M. Hojamberdiev, Y. Xu, B. Cao, J. Wang, H. Wu, Structural and Electrical Studies of MnGd<sub>x</sub>Fe<sub>2-x</sub>O<sub>4</sub> Nanoparticles. J. Magn. Magn. Mater. 323, 133–138 (2011)
- I. Ali, M. Ahmad, M.U. Islam, M.S. Awan, Substitution effects of La3+ ions on the structural and magnetic properties of Co2Y hexafterites synthesized by sol–gel autocombustion method (Springer, New York, 2013)
- E.R. Kumar, T. Arunkumar, T. Prakash, Heat treatment effects on structural and dielectric properties of Mn substituted CuFe<sub>2</sub>O<sub>4</sub> and ZnFe<sub>2</sub>O<sub>4</sub> nanoparticles. J. Superlatt. Microstruct. 85, 530–535 (2015)
- L. Saravanan, R. Jayavel, A. Pandurangan, J.H. Liu, H.Y. Miao, Synthesis, structural and optical properties of Sm<sup>3+</sup> and Nd<sup>3+</sup> doped cadmium sulfide nanocrystals. Mater. Res. Bull. 52, 128 (2014)
- P.P. Hankare, R.P. Patil, A.V. Jadhav, R.S. Pandav, K.M. Garadkar, R. Sasikala, A.K. Tripathi, Synthesis and characterization of nanocrystalline Ti-substituted Zn ferrite. J. Alloy. Compd. 509, 2160–2163 (2011)
- G. Mustafa, M.U. Islam, M. Ahmad, W. Zhang, Y. Jamil, A. Wahee, A.M. Hussain, Influence of the divalent and trivalent ions substitution on the structural and magnetic properties of Mg0.5-xCdxCo0.5Cr0.04TbyFe1.96-yO4 ferrites prepared by sol-gel method. J. Magn. Magn. Mater. 387, 147–154 (2015)
- P.P. Hankare, K.R. Sanadi, K.M. Garadkar, D.R. Patil, I.S. Mulla, Synthesis and characterization of nickel substituted cobalt ferrite nanoparticles by sol-gel auto-combustion method. J. Alloys Compd. 553, 383–388 (2013)
- J. Peng, M. Hojamberdiev, Y. Xu, B. Cao, J. Wang, H. Wu, Hydrothermal synthesis and magnetic properties of gadolinium-doped CoFe<sub>2</sub>O<sub>4</sub> nanoparticles. J. Magn. Magn. Mater. 323, 133–138 (2011)
- P.S. Aghav, V.N. Dhage, M.L. Mane, D.R. Shengule, R.G. Dorik, K.M. Jadhav, Effect of aluminium substitution on the structural and magnetic properties of cobalt ferrite synthesized by sol–gel auto combustion process. Phys. B 406, 4350–4354 (2011)
- M.H. Abdellatif, C. Innocenti, I. Liakos, A. Scarpellini, S. Marras, M. Salerno, Effect of Jahn-Tellerdistortion on the short range magnetic order in copper ferrite. J. Magn. Magn. Mater. 424, 402–409 (2017)
- S. Anandan, T. Selvamani, G.G. Prasad, A.M. Asiri, J.J. Wu, Magnetic and catalytic properties of inversespinel CuFe<sub>2</sub>O<sub>4</sub> nanoparticles. J. Magn. Magn. Mater. 43, 437–443 (2017)
- N. Venkatesha, S.M. Pudakalakatti, Y. Qurishi, H.S. Atreya, C. Srivastava, MnFe<sub>2</sub>O<sub>4</sub>-Fe<sub>3</sub>O<sub>4</sub> core-shell nanoparticles as potential contrast agent for magnetic resonance imaging. RSC Adv. 5, 97807–97815 (2015)
- Z.K. Karakas, R. Boncukcuoglu, I.H. Karakas, The effects of heat treatment on the synthesis of nickel ferrite (NiFe<sub>2</sub>O<sub>4</sub>) nanoparticles using the microwave assisted combustion method. J. Magn. Magn. Mater. 374, 298–306 (2015)
- R.S. Yadav, I. Kuritka, J. Vilcakova, J. Havlica, J. Masilko, L. Kalina, J. Tkacz, J. Svec, V. Enev, M. Hajduchov, Impact of grain size and structural changes on magnetic, dielectric, electrical, impedance and modulus spectroscopic characteristics of CoFe<sub>2</sub>O<sub>4</sub> nanoparticles synthesized by honey mediated sol-gel combustion method. Adv. Nat. Sci. 8, 045002 (2017)
- 42. H.S. Aziz, S. Rasheed, R.A. Khan, A. Rahim, J. Nisar, S.M. Shah, F. Iqbal, A.R. Khan, Evaluation of electrical, dielectric and



- magnetic characteristics of Al-La doped nickel spinel ferrites. RSC Adv. 6, 6589–6597 (2016)
- Y.K. Dasan, B.H. Guan, M.H.Z. Chuan, Influence of La<sup>3+</sup> substitution on structure, morphology and magnetic properties of nanocrystalline Ni-Zn ferrite. PLoS ONE 12(1), e0170075 (2017)
- 44. B. Santosh, N. Tsering, S. Mor, S. Bansal, S. Singhal, Structural, electrical, optical and magnetic properties of chromium substituted Co–Zn nanoferrites Co<sub>0.6</sub>Zn<sub>0.4</sub>Cr<sub>x</sub>Fe<sub>2x</sub>O<sub>4</sub> (0 6 x 6 1.0) prepared via sol–gel auto-combustion method. J. Mol. Struct. 1012, 162–167 (2012)
- S. Joshi, M. Kumar, S. Chhoker, A. Kumar, M. Singh, Effect of Gd<sup>3+</sup> substitution on structural, magnetic, dielectric and opticalproperties of nanocrystalline CoFe<sub>2</sub>O<sub>4</sub>. J. Magn. Magn. Mater. 426, 252–263 (2017)
- H. Anwar, A. Maqsood, Structural, magnetic and electrical properties of Cu substituted Mn Zn soft nanoferrites. J. Supercond. Nov. Magn. 25, 1913–1920 (2012)
- Y. Zhou, W. Chen, Y. Shen, X. Wu, W. Wu, J. Wu, Lattice strains and magnetic properties evolution of copper-magnesium ferrite with lithium substitution. J. Magn. Magn Mater. 396, 198–203 (2015)
- R. Tholkappiyan, K. Vishista, Influence of lanthanum on the optomagnetic properties of zinc ferrite prepared by combustion method. Phys. B 448, 177–183 (2014)
- K.K. Kefeni, T.A.M. Msagati, B.B. Mamba, Ferrite nanoparticles:synthesis, characterisation and applications in electronic device. Mater. Sci. Eng. B 215, 37–55 (2017)
- K. Lily, K. Kumari, R.N. Prasad, P. Choudhary, Impedance spectroscopy of (Na0.5Bi0.5) (Zr0.25Ti0.75)O3 lead-free ceramic. J. Alloy. Compd. 453, 325–331 (2008)
- M.A. Rahman, A.K.M.A. Hossain, Electrical transport properties of Mn–Ni–Zn ferrite using complex impedance spectroscopy. Phys. Scr. 89, 025803 (2014)
- R.V. Mangalaraja, S. Ananthakumar, P. Manohar, F.D. Gnanam, Magnetic, electrical and dielectric behaviour of Ni0.8Zn0.2Fe2O4 prepared through flash combustion technique. J. Magn. Magn. Mater. 253, 56–64 (2002)
- C. Murugesan, G. Chandrasekaran, Impact of Gd<sup>3+</sup>-substitution on the structural, magnetic and electrical properties of cobalt ferrite nanoparticles. RSC Adv. 5, 73714–73725 (2015)

- D.M. Jnaneshwara, D.N. Avadhani, B. Daruka Prasad, H. Nagabhushana, B.M. Nagabhushana, S.C. Sharma, S.C. Prashantha, C. Shivakumar, Role of Cu<sup>2+</sup> ions substitution in magnetic and conductivity behaviour of nano CoFe<sub>2</sub>O<sub>4</sub>. Spectrochim. Acta Part A 132, 256–262 (2014)
- J. Parashar, V.K. Saxena, D. Jyoti, K.B. Bhatnagar, Sharma, Dielectric behaviour of Zn substituted Cu nano-ferrites. J. Magn. Magn. Mater. 394, 105–110 (2015)
- D. Ravinder, P.V.B. Reddy, High-frequency dielectric behaviour of Li-Mg ferrites. Mater. Lett. 57, 4344–4350 (2003)
- G.R. Mohan, D. Ravinder, A.V.R. Reddy, B.S. Boyanov, Dielectric properties of polycrystalline mixed nickel–zinc ferrites. Mater. Lett. 40, 39–45 (1999)
- M.J. Iqbal, R.A. Khan, S. Mizukami, T. Miyazaki, Mossbauer, magnetic and microwave absorption characteristics of substituted W-type hexaferrites nanoparticles. Ceram. Int. 38, 4097–4103 (2012)
- R.K. Kotnala, Preparation and characterization chemistry of nanocrystalline NiCuZn ferrite. J. Alloys Compd. 549, 348–357 (2013)
- M.H. Alimuddin, S.E. Shirsath, S. Kumar, R. Kumar, A.S. Roy, J. Shah, R.K. Kotnala, Preparation and characterization chemistry of nano-crystalline NiCuZn ferrite. J. Alloys Compd. 549, 348–357 (2013)
- S.F. Mansour, Frequency and composition dependence on the dielectric properties for Mg–Zn ferrite. Egypt. J.Solids 28(2), 211–214 (2005)
- Z.C. Veji, S. Raki, S. Jankov, S. Skuban, A. Kapor, Dielectric properties and conductivity of zinc ferrite and zinc ferrite doped with yttrium. J. Alloy. Compd. 480, 241–245 (2009)
- S.A. Saafan, S.T. Assar, Dielectric behavior of nano-structured and bulk LiNiZn ferrite samples. J. Magn. Magn. Mater. 324, 2989–3001 (2012)

**Publisher's Note** Springer Nature remains neutral with regard to jurisdictional claims in published maps and institutional affiliations.



ELSEVIER

Contents lists available at ScienceDirect

#### Ceramics International

journal homepage: www.elsevier.com/locate/ceramint



### Dependance of lanthanum ions on structural, magnetic and electrical of manganese based spinel nanoferrites



Rajeshwari A.a, Kartharinal Punithavthy I.a,\*, Johnson Jeyakumar S.a, Lenin N.b, Vigneshwaran B.c

- <sup>a</sup> Department of Physics, T.B.M.L College, Porayar, 609 307, Nagapattinam, Tamil Nadu, India
- <sup>b</sup> Department of Nano Science and Technology, K.S. Rangasamy College of Technology, Tiruchengode, 637215, Tamil Nadu, India
- <sup>c</sup> Centre for Nanoscience & Technology, Sathyabama Institute of Science and Technology, Chennai, 600 119. Tamil Nadu, India

#### ARTICLE INFO

#### Keywords: Spinel ferrites Dielectric properties Grain boundaries Magnetization Optical properties

#### ABSTRACT

Lanthanum doped manganese spinel nanoferrites (MnLa<sub>X</sub>Fe<sub>2-X</sub>O<sub>4</sub>) with X = 0.00, 0.02, 0.04, 0.06 and 0.08 were fabricated by sol-gel method. The cubic phase was confirmed by using X-ray diffraction technique. FESEM revealed that the prepared samples attain highly stable spherical morphology. Energy dispersive X-ray spectra confirm the presence of Manganese (Mn), Lanthanum (La), Iron oxide (Fe) and oxygen (O) element in desired proportion. Ultra-violent diffuse reflectance spectroscopy shows that absorbance spectra were inversely proportional to band gap energy. Room temperature magnetic hysteresis curves expose the ferromagnetic behavior with decreases of saturation (M<sub>s</sub>) and increases of coercivity (Oe). The origin of ferromagnetism in La<sup>3+</sup> doped manganese nanoferrites were elaborated with reverence to the allocation of Mn<sup>2+</sup> and Fe<sup>3+</sup> ion within the spinel lattice. An impedance spectroscopy of the samples were analyzed in the frequency ranges from 0 to 7 MHz at room temperature reveals the resistance of the grains and grain boundary were found to increase with La<sup>3+</sup> ion. The dielectric constant and loss tangent decreases with increases of frequency. The obtained results confirm that the prepared samples were useful for better radiation-absorption properties.

#### 1. Introduction

Nanomaterials have been showing excellent chemical and physical properties due to their smaller crystal size, high surface area, quantum confinement effect and high calcined ability. Recently, ferrite nanoparticles are used in many applications such as technological and fundamental reason [1]. So that, these materials are of most challenging as magnetic memories, high density storage media, transformer cores, analogue devices, electron transport devices, electron magnetic interchange devices, choke coil and even in high - frequency device are derived [2-4]. The properties attained by these ferrites are based on their cation distribution and chemical composition and in Octahedral Bsites and tetrahedral A-Site [5]. Mn nanoferrites are one of the most important soft magnetic materials due to its high coercivity and low core losses [6]. The rare earth iron plays vital role to change its magnetic properties involves large magneto crystalline anisotropy; a high magnetostriction and magnetic moment on adding of La<sup>3+</sup> ions have high ionic radii at very low temperature because of its localized nature of 4f electrons [7]. La<sup>3+</sup> ions replace Fe<sup>3+</sup> ions at low concentration as they like to enter the octahedral site (B-site) [8,9]. Micro strains are developed due to variation in the ionic radii between La<sup>3+</sup> and Fe<sup>3+</sup> ions which may effect spinel structure that in turn influence the motion of domain wall. Lanthanum doped manganese nanoferrites are very helpful in preventing and extinguishing electromagnetic interference to electronic controlled system [10].

In recent years, the sol-gel method is used to prepare various mixed oxide, nanoporous oxides, nanoscale architectures, nanomaterials, inorganic and organic hybrids [11]. The sol-gel method has most admiring advantages such as small crystalline size and better homogeneity in the final product [12]. Samolia.et al. have reported magnetic and structural properties of Gd-doped Ni–Mn–Cr ferrites synthesized by solgel method and noticed that magnetization and coercivity decrease with the increase of  $\mathrm{Gd}^{3+}$  ions [13]. The rare earth element of  $\mathrm{Nd}^{3+}$  doped manganese zinc ferrite synthesized by using combustion method influence on the magnetic and structural properties and it is increase in saturation magnetization with increase of  $\mathrm{Nd}^{3+}$  ions [14]. Lanthanum doped manganese ferrites are prepared by enormous synthesize methods such as micro-emulsion auto-combustion, co-precipitation technique, wet chemical and sonication method [15–17]. Systematic studies on structural, electrical, optical and magnetic properties of  $\mathrm{La}^{3+}$ 

E-mail address: profpunithaphysics@gmail.com (I. Kartharinal Punithavthy).

<sup>\*</sup> Corresponding author.

ion doped Manganese nanoferrites prepared by sol-gel method could not be found yet. The present study, dependence of  $La^{3+}$  ions substitution on the structural, optical, magnetic and electrical properties of manganese nanoferrites with particular series (X = 0.00 to 0.08) was noticed.

In present study, Lanthanum doped manganese nanoferrites  $MnLa_XFe_{2-x}O_4$  (X=0.00 to 0.08) were prepared by sol-gel method. The obtained Lanthanum doped cobalt nanoferrites are characterized by X-ray diffraction (XRD) for phase and structural identification, Fourier transform infrared spectroscopy (FTIR) for to identify organic and also some inorganic materials, field emission scanning electron microscopy (FESEM) coupled with energy dispersive X-ray analysis (EDX) for surface morphology and elemental analysis, ultra violet (UV) diffuse reflectance spectroscopy (DRS) for optical properties and vibrating sample magnetometer (VSM) for magnetic measurements. The results are analyzed and the obtained results are identified towards utilized for the possible electronic devices in electromagnetic radiation applications.

#### 2. Experimental procedure

 $MnLa_XFe_{2-X}O_4$  (X = 0.00, 0.02, 0.04, 0.06 and 0.08) nanoferrites were synthesized by sol-gel method. The precursors such as Lanthanum nitrate (La(NO<sub>3</sub>)<sub>3</sub>·6H<sub>2</sub>O), ferric nitrate (Fe(NO<sub>3</sub>)<sub>3</sub>·9H<sub>2</sub>O), manganese nitrate (Mn(NO<sub>3</sub>)<sub>2</sub>·6H<sub>2</sub>O), ammonia (NH<sub>4</sub>OH), citric acid (C<sub>6</sub>H<sub>8</sub>O<sub>7</sub>·H<sub>2</sub>O) and deionized water were used to prepare Lanthanum doped manganese nanoferrites. The measured precursors were dissolved with 100 ml of deionized water to attain homogeneous mixture of the precursor. The mixed solution was continuously stirred at 80 °C for 1 h. Further ammonia was added drop by drop to the ferrite solution to attain the pH value of 7. Finally dark solution was collected and dried in a hot air oven at fixed temperature at 60 °C for 24 h. The amorphous powders were collected and sintered in muffle furnace at 500 °C for 2 h. Then the sintered nanopowders were grinded for 15 min to reach a fine powder. Thus obtained nanopowders were again well calcined at 1000 °C for 24 h. Finally, obtained nanoferrite powders were grinded well. The Flow chart for sample preparation of MnLa<sub>x</sub>Fe<sub>2-x</sub>O<sub>4</sub> nanoferrites was shown in Fig. 1.

#### 2.1. Characterization of MnLa<sub>X</sub>Fe<sub>2-X</sub>O<sub>4</sub> nanoferrites

The structural analysis of the prepared MnLa<sub>x</sub>Fe<sub>2-x</sub>O<sub>4</sub> (X = 0.00 to 0.08) nanoferrites were analyzed by XRD (SHIMADZU-XRD 6000) technique with CuK $\alpha$  radiation source is used to discover the prepared nanoferrites at the 2 $\theta$  range from 20° to 80°, operated at 40 kV and 30 mA. The functional groups and chemical interaction obtained in the prepared CoLa<sub>x</sub>Fe<sub>2-x</sub>O<sub>4</sub> nanoferrites were examined by FTIR spectra (SHIMADZU-UV 18,000) in the wave number ranges from 4000 to 400 cm<sup>-1</sup> at RT. The surface morphology and elemental composition were carried out using FESEM with an energy dispersive spectrum (Quanta FEG 250). The optical properties of the prepared samples were analyzed using the UV- DRS with absorption wavelength in the range of 200–400 nm. Impedance spectroscopy is used to examine the conductivity of the prepared CoLa<sub>x</sub>Fe<sub>2-x</sub>O<sub>4</sub> nanoferrites (Biologic SP-300). Magnetic studies were assessed using VSM (Lakeshore VSM 7140) at RT with a magnetic field of -15 to +15 KOe.

#### 3. Result and discussion

#### 3.1. Structural studies

Fig. 2 shows the structural XRD analysis of the Lanthanum doped manganese nanoferrites (MnLa<sub>X</sub>Fe<sub>2-X</sub>O<sub>4</sub>) with series X=0.00 to 0.08 calcined at 1000 °C. The peak positions appeared at 30.67°, 35.33°, 43.47°, 53.52° and 56.6° corresponds to (220), (311), (400), (422) and (333) planes respectively. All the obtained peaks are in good agreement

with JCPDS card no (74–24023) and it is also revealed that the synthesized nanoferrites are in cubic structure [18]. No other peaks related to either Lanthanum or other byproducts are observed. It confirms that the Lanthanum is doped in to the host Mn lattice. The average crystal sizes of the prepared nanoferrites are calculated using the well known Scherrer formula [19]:

$$D = \frac{K\lambda}{\beta Cos\theta}$$
 (1)

where K is a Scherrer constant (0.89),  $\lambda$ ,  $\beta$ ,  $\theta$  are the wavelength of x-ray used, Full Width at Half Maximum (FWHM) and Bragg's angle respectively. The crystallite size is calculated for the prepared nanoferrites which decreasing from 26 to 12 nm with increase of La³+ concentration from X = 0.00 to 0.08. The decreasing crystal sizes are mainly due to the difference in ionic radii of La³+ ions and Fe³+ ions [22]. Therefore, it is difficult to replace La³+ ion (1.06 Å) which has larger ionic radii as compared with Fe³+ ions (0.67 Å) on the lattice strain. At the same time of substitution La³+ ions to Fe³+ ions on the lattice strain, few of the La³+ ions may be settled on the grain boundaries and created pressure on the grain boundaries have arisen in smaller crystal size of La³+ doped Mn ferrites in comparison with Gd, La doped Mn–Zn ferrites [20,21]. The lattice constant for the prepared nanoferrites is estimated through Nelson-relay function [22];

$$a = d_{hkl} \sqrt{h^2 + k^2 + l^2} \tag{2}$$

where d is inter planer distance, hkl are Miller indices and 'a' is the lattice constant. The lattice constant increases linearly with increase of  ${\rm La}^{3+}$  ions for prepared nanoferrties. This may be due to  ${\rm La}^{3+}$  ions posses a significant affinity to replenish the octahedral site due to their larger ionic radii (1.06 Å) than the metal ion at the octahedral site  ${\rm Mn}^{2+}$  (0.83 Å) and consequently it occupies the octahedral sites [23]. The X-ray density was calculated by using the following equation [24];

$$d_x = \frac{Zm}{Na^3} \tag{3}$$

where m is the molecular weight of the sample N is Avogadro's number  $(6.022 \times 10^{23})$  (particles/mole)  $a^3$  is the volume of the unit cell, Z is the cubic unit cell which contains 8 atoms. X-ray density was decreases from 5.144 to 4.862 g/cm $^3$  with increase of La $^{3+}$  ions. This may be due to change in volume of unit cell and also X-ray density is inversely proportional to the volume of the unit cell. The strains in the unit cell of the crystal increased with substitution of La $^{3+}$  ions due to the induced crystalline anisotrophy [25]. The bulk density (d<sub>B</sub>) is evaluated using the mentioned equation [24];

$$d_m = \frac{m}{\pi r^2 t} \tag{4}$$

where r is the radius of the pellet, m is the mass of the pellet and t is thickness of the pellet. The smaller value of bulk density than the X-ray density may be attained due to the existence of pores in the prepared ferrites [26]. The doping of La ions activate the process in ferrites and leads to increase in density [27]. The increase in bulk density is due to difference in atomic weight of Lanthanum (138.90 amu) and manganese (54.93 amu). The surface area of the prepared nanoferrites is calculated using the following expression [24];

$$S = 6/d_X D (5)$$

where dis the X-ray density and D is the diameter of the particles. The surface area (S) increases from (44.85–102.16) which may be due to decrease in crystal size. The porosity  $(\rho)$  is calculated using following relation [28];

$$P = (1-d_B/d_X) \%$$
 (6)

The porosity decreases from 6.737 to 4.431% which attributed to the increase in bulk density with adding  ${\rm La}^{3+}$  ions. Hence  ${\rm D}_{\rm B}$  and  ${\rm d}_{\rm x}$  are the bulk and X-ray densities for the prepared sample. Structural

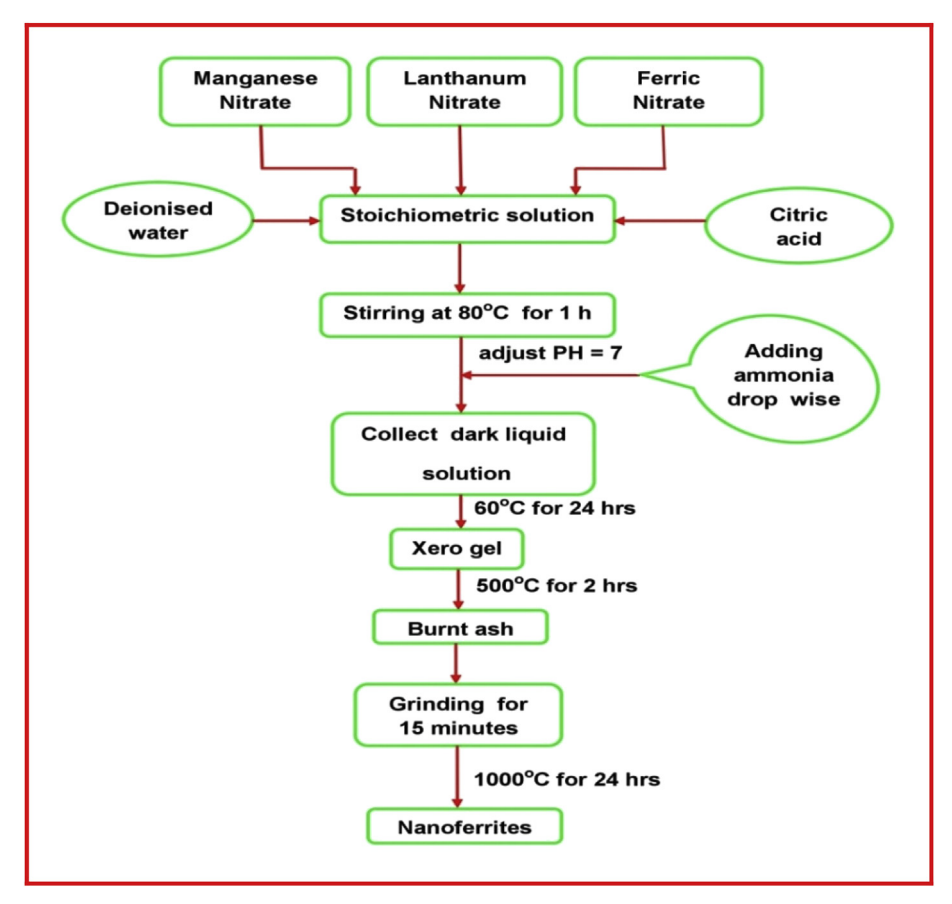


Fig. 1. Flow chart for the sample preparation of MnLa<sub>X</sub>Fe<sub>2-X</sub>O<sub>4</sub> nanoferrites.

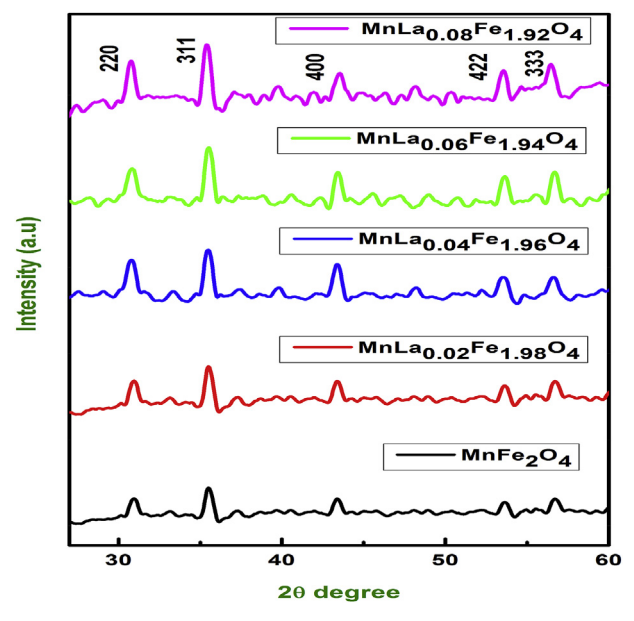


Fig. 2. X-ray diffraction pattern of prepared MnLa $_{\rm X}$  Fe $_{2 \cdot {\rm X}}$ O $_4$  (X = 0.00 to 0.08) nanoferrites calcined at 1000 °C.

parameters such as crystal size, dislocation density, micro strain, lattice constant volume of unit cells, surface area, bulk density, X-ray density and porosity are listed in Table 1.

#### 3.2. Functional group analysis

Fig. 3 shows the FTIR spectra of Lanthanum doped manganese

nanoferrites with different composition (X=0.00 to 0.08) recorded by vibrational appropriate in the region 4000-400 cm<sup>-1</sup> (shown in Table 2). FTIR spectra are performed to give information corresponding to the phase formation of spinel ferrites and other structural changes [29]. It proves that there are changes in secondary phase formations such as substitution of rare-earth ions in the spinel structure [30,31]. The band exists in the range of 583 cm<sup>-1</sup> may be due to the stretching vibration of metal oxygen in tetrahedral and octahedral sites. The band at 1366 cm<sup>-1</sup> represents for C–H bending bond due to carboxylic acid (Citric Acid). The wave number near at 2368 cm<sup>-1</sup> band is related C= N bond [32]. The broad and strong band of oxygen hydrogen stretching vibration of remaining water appeared at wave number 3187 cm<sup>-1</sup> [33].

#### 3.3. UV-DRS

The optical properties of prepared nanoferrties  $MnLa_XFe_{2.x}O_4$  with different composition X=0.00 to 0.08 were investigated using UV-diffuse reflectance measurement. The UV-DRS spectra recorded in the ranges from 200 to 400 nm can examine the band gap and electronic structure features. The optical absorbance is estimated using band gap energy (Eg) of the prepared Lanthanum doped manganese nanoferrties. The absorbance values are 228.12, 227.40, 226.10, 225.60 and 224.9 nm respectively with corresponding X=0.00 to 0.08 compositions. The direct and indirect band gap energy values of prepared nanoferrites are calculated using relation between the absorption coefficient and the band [34].

$$h\gamma\alpha = A\left(h\gamma - E_{gap}\right)^n\tag{8}$$

where  $\alpha$  is the absorption coefficient, h is Planck's constant,  $\gamma$  is the frequency of light, A is a proportional constant, and  $E_g$  is the band gap and exponent n is the different type electronic transition n=1/2 and

Table 1 Structural parameters of prepared  $MnLa_XFe_{2.X}O_4$  (X = 0.00 to 0.08) nanoferrites.

Composition	Crystal size (D) (nm)	Lattice constant (a) Å	Volume of unit cell $(a^3)$ Å	X-ray density (ρXRD) (g/cm <sup>3</sup> )	Surface area ( $S_{XRD}$ ) ( $m^2/g$ )	Bulk density ( $d_B$ ) (g/cm <sup>3</sup> )	Porosity (%)
X = 0.00	26	8.7117	661.16	5.1448	1.6786	44.85	6.737
X = 0.02	22	8.7515	670.26	5.0390	1.7888	54.12	6.450
X = 0.04	18	8.7613	672.52	4.9869	1.8768	66.84	6.236
X = 0.06	14	8.7777	676.30	4.9245	2.5383	87.03	4.845
X = 0.08	12	8.7945	680.19	4.8662	2.7078	102.16	4.431

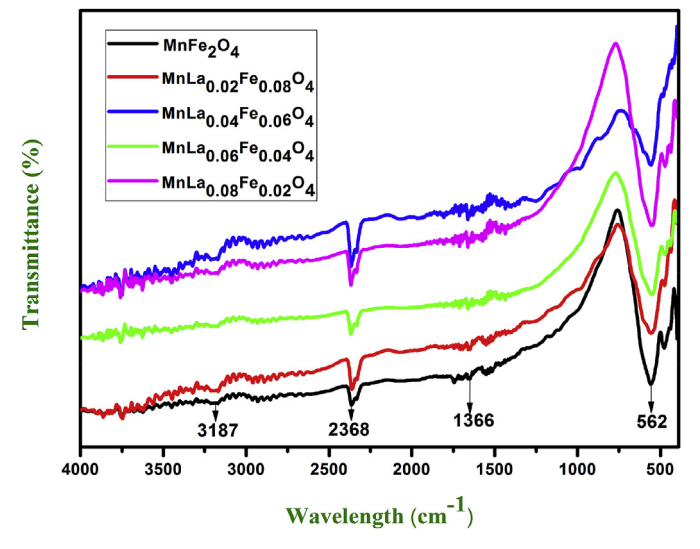


Fig. 3. FTIR spectra of prepared  $MnLa_XFe_{2.X}O_4$  (X = 0.00 to 0.08) nanoferrites.

n = 2 for direct and indirect band gap energy. In Fig. 4a associates the Tauc plot between  $(\alpha \ E_{photon})^2 \ V \ E_{photon}$  and the energy band gap values are 1.25, 1.26, 1.30, 1.34 and 1.38 eV respectively. The band gap value of prepared Lanthanum doped manganese nanoferrites increases with increase La<sup>3+</sup> ions concentration (X = 0.00 to 0.08). Fig. 4b demonstrates that the Tauc plot between  $(\alpha)^2$  vs  $E_{phot}$  and the indirect energy band gap values of prepared nanoferrites are 1.89,1.98, 2.13,2.27 and 2.35 eV respectively. The value of absorbance and bandgaps are listed in Table 3. The overview of result demonstrates that the improvement of energy levels or interface defects may be attributed to synergistic effect of Lanthanum with nanoferrites, and then recombination of decreased electron hole, which resulted in an increased band gap [35].

#### 3.4. FESEM with EDAX

The morphology of prepared samples is obtained by FESEM which is shown in Fig. 5. It reveals that spherical shape with uniform grain. This happened due to the diffusion of  ${\rm La}^{3+}$  ions mainly closer to the grain boundary, which exhibits ion and oxygen vacancies [37]. There is some agglomeration occurred is obtained due to typical magnetic attraction of the spinel ferrites [38]. Fig. 5. Depict EDAX spectra for a prepared

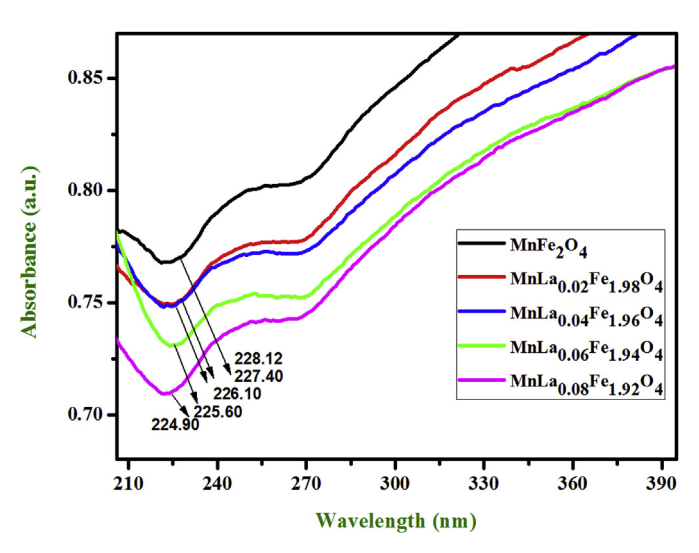


Fig. 4. Absorbance spectra of prepared  $MnLa_XFe_{2.X}O_4$  (x = 0.00 to 0.08) nanoferrites from UV-DRS spectra.

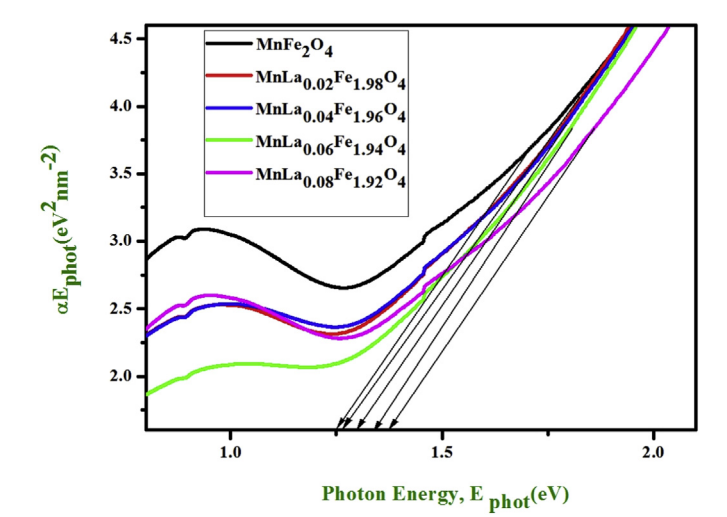


Fig. 4a. Direct bandgap energy of prepared  $MnLa_XFe_{2.X}O_4$  (X = 0.00 to 0.08) nanoferrites from UV-DRS spectra.

Table 2 Functional parameters of prepared  $MnLa_XFe_{2.X}O_4$  (X = 0.00 to 0.08) nanoferrites.

S·NO	Vibrational assignments	Experimental absorption (cm <sup>-1</sup> )					
		X = 0.00	X = 0.02	X = 0.04	X = 0.06	X = 0.08	
1	Metal - oxygen stretching vibration	562	562	562	562	562	
2	CH bending of carboxylic acid	1366	1366	1366	1366	1366	
3	Stretching vibration of C=N	2368	2368	2368	2368	2368	
4	O–H stretching vibration	3187	3187	3187	3187	3187	

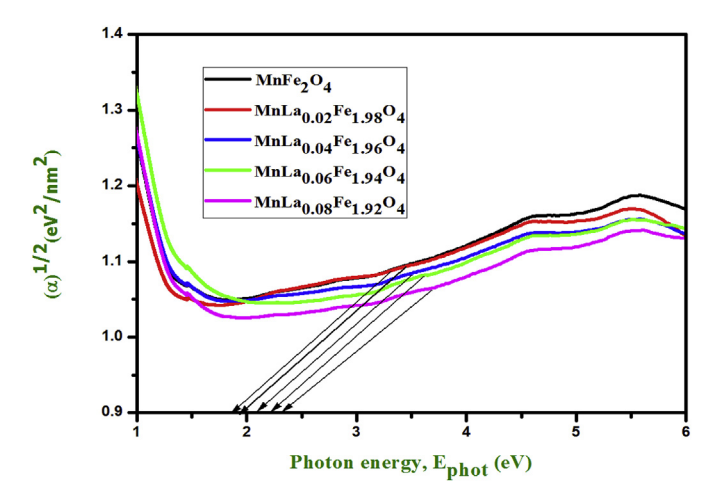


Fig. 4b. Indirect bandgap energy of  $MnLa_XFe_{2.X}O_4$  nanoferrites with series X=0.00 to 0.08 from UV-DRS spectra.

**Table 3** Optical parameters of prepared  $MnLa_XFe_{2.X}O_4$  (x = 0.00 to 0.08) nanoferrites.

Composition	Absorbance (nm)	Indirect bandgap energy (eV)	Direct bandgap energy (eV)
X = 0.00	228.12	1.89	1.25
X = 0.02	227.40	1.98	1.26
X = 0.04	226.10	2.13	1.30
X = 0.06	225.60	2.27	1.34
X = 0.08	224.90	2.35	1.38

sample confirms the presence of Mn, La, Fe and O with few impurities.

#### 3.5. Vibrating sample magnetometer

The M - H loop for the prepared Lanthanum doped manganese nanoferrites  $MnLa_XFe_{2\cdot X}O_4$  with series X=0.00 to 0.08 are plotted using vibrating sample magnetometer (VSM). All the hysteresis loops are scanned up to 15,000 (Oe), recorded at room temperature. The shape and width of loops are based on few factors such as calcinating temperature, chemical composition, porosity, cation distribution and grain size etc. Fig. 6, S shaped hysteresis loops promote soft and ferromagnetic natures for prepared ferrites. The magnetic saturation ( $M_S$ ) in manganese ferrites decreases with decrease of crystallite size due to increase of surface effect [39]. The values of saturation also decreases from 81.57 to 51.31 with increase in  $La^{3+}$  ions which is attributed to smaller magnetic moment of La (0 IB) than Fe (5 IB). In general magnetic moment of rare earth ions corresponds to 4f-electrons [40].

The structure at the surface is distressed and strain on the surface atom to promote various inter atomic distance, vacancies and low coordination numbers which implies splinter the bond exchange of the surface atoms promoted to spin disorder [41,42]. Magnetic saturation for spinel nanoferrites are adopted by the super exchange interaction between tetrahedral (A site) and Octahedral (B site) cations. Here three types of exchange interaction are placed between the magnetic ions at tetrahedral (A) and Octahedral (B) site in spinal structure such as A-A interaction, B-B interaction and A-B interactions. Among these A-B Interactions predominate the intra sub lattice than A-A and B-B interactions. The obtained A-B interaction is due to non-magnetic nature for La<sup>3+</sup> ions, which implies that exchange of ion interaction does not occur with closest neighbouring ions [43]. The values of coercivity 105 Oe to 517.37 Oe increases with increase of La<sup>3+</sup> ions for prepared

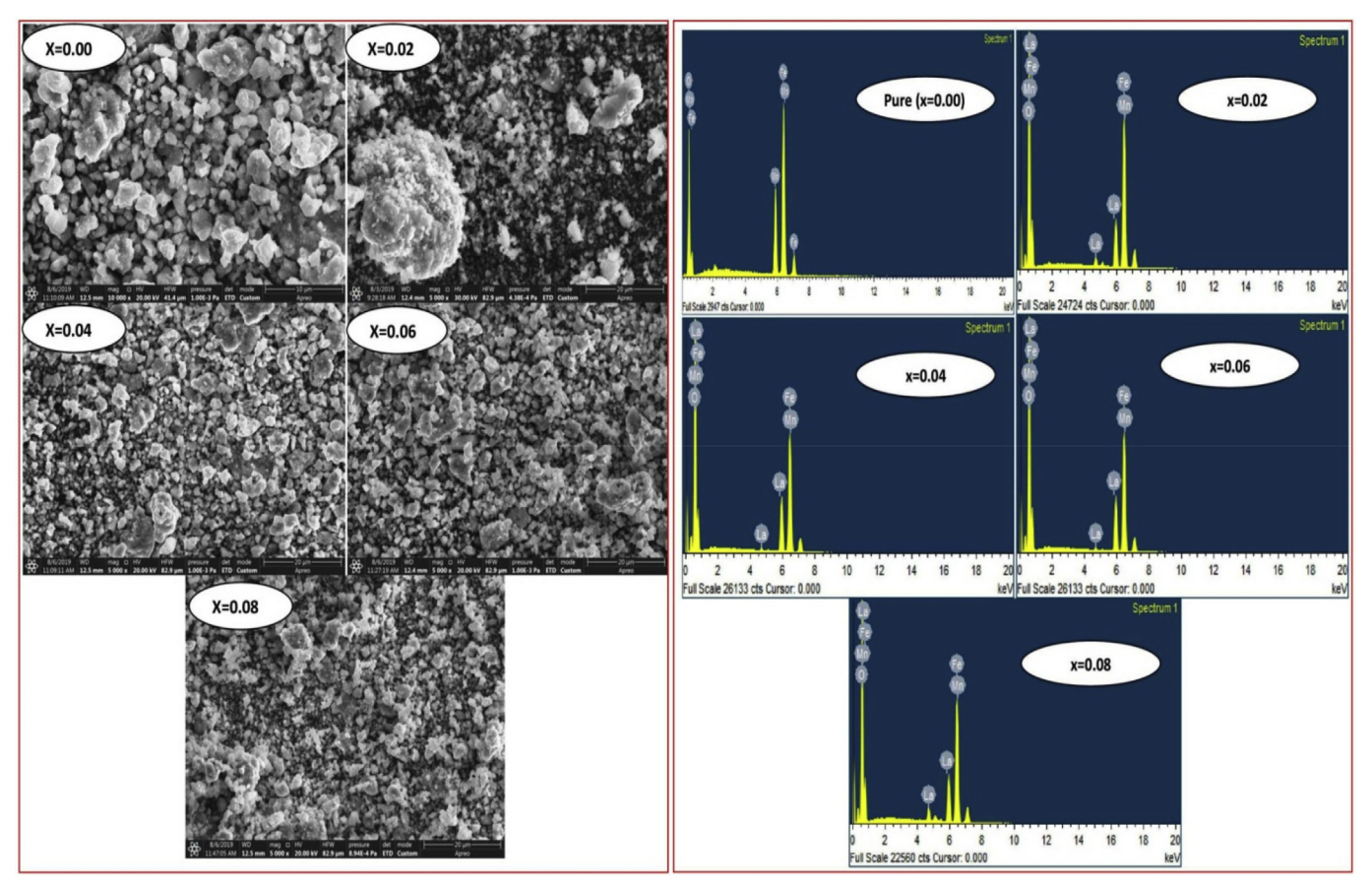


Fig. 5. FESEM with EDAX images of prepared  $MnLa_XFe_{2-X}O_4$  (X = 0.00 to 0.08) nanoferrites.

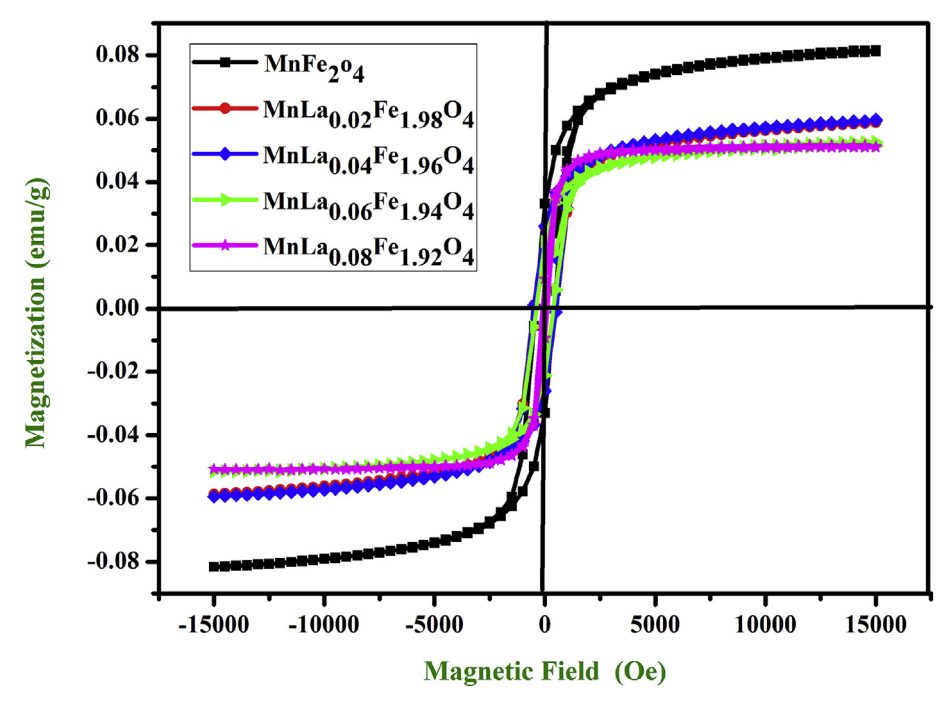


Fig. 6. Hysteresis loop of prepared  $MnLa_XFe_{2-X}O_4$  (X = 0.00 to 0.08) nanoferrites.

nanoferrites. This effect on coercivity based some factors like anisotrophy, magneto crystallinity, magnetic particle and domain size of the material etc [44]. The changes of coercivity with crystal size are due to the change in multi domain to single domain nature [44]. The magnetic saturation and coercivity is inversely proportional to each other through Brown's relation [45]. The present work agrees this relation of decreasing magnetic saturation to Lanthanum concentrations. Earlier reports have explained that the larger ionic radii of rare earth substitution in spinel ferrites have increased the coercivity [46]. The squareness ratio and anisotrophy constant of  $MnLa_xFe_{2-x}O_4$  (X = 0.00, 0.02, 0.04, 0.06 and 0.08) nanoferrites are evaluated through below mentioned equations [32].

$$Squareness ratio = \frac{M_r}{M_s}$$
 (10)

$$K = \frac{H_c M_s}{0.98} \tag{11}$$

where  $M_r$  is the remanent magnetization (or) retentivity, K is the anisotrophy constant and  $H_c$  is coercivity. The values of squareness ratio are less than 0.5 for all the prepared samples, which denotes uniaxial anisotropy contribution in the obtained nanoferrites [47]. Uniaxial anisotropy is a precondition for a hysteresis loop in ferromagnetic ferrites. Furthermore, Bohr Magnetization ( $\eta_\beta$ ) in magnetic moment ( $\mu_\beta$ ) is calculated using following equation [32].

$$\eta_B = \frac{MXM_s}{5585} \tag{12}$$

where x is the concentration and M is the molecular weight of La<sup>3+</sup> ion

substitution. The magnetic parameters such as magnetic saturation  $(M_s),$  retentivity  $(M_r),$  coercivity  $(H_c),$  squareness ratio  $(M_r/M_s),$  anisotrophy constant (K) and Bohr magnetron  $(\eta_\beta)$  are observed from M-H measurements as listed in Table 4. In the present study, the value of coercivity are few hundred Oersteds (Oe) of prepared Lanthanum doped manganese nanoferrites and with such a low values of coercivity nanoferrites materials are favorable for electromagnetic radiation materials [48].

#### 3.6. Impedance spectroscopy

Impedance spectroscopy is a useful technique which is widely used to separate real and imaginary part of the electrical parameter to propose the material's electrical properties. The impedance spectra values of prepared nanoferrites have capacitance and resistive components, Fig. 7c clearly shows that successive semicircle's represent electrical phenomena attributed to grain, grain boundaries and interfacial etc. In general, low frequency regions are effective in grain boundaries while the grains are effective in high frequency region. Thus appearing of semi circle in low frequency region enables the grain boundary contribution while grains are enabling to high frequency contribution. The real part (Z') of the spectra values for prepared nanoferrites are corresponds low frequency to high frequency in the range of 0–7 MHz at room temperature.

Fig. 7a implies to impedance in frequency graph is decreases with increase in applied frequency and then remain same at higher frequency. The constant Z' value at high frequency are promotes the dominant contribution from grain boundary. The low value at high

**Table 4** Magnetic parameters of prepared  $MnLa_XFe_{2.X}O_4$  (X = 0.00 to 0.08) nanoferrites.

Composition	Magnetization ( $M_s$ ) (emu/g)	Remanent magnetization $(M_{\rm r})$ $(emu/g)$	Coercivity (Hc) (Oe)	Squareness ratio $(M_r/M_s)$ (No unit)	Anisotropy constant (K) (Oe)	Bohr magneton ( $\eta B$ ) ( $\mu_{B)}$
x = 0.00	81.57	33.08	105.00	0.4055	87.39	0.3739
x = 0.02	59.56	26.03	392.55	0.4370	23.85	0.2711
x = 0.04	58.73	25.86	429.59	0.4403	25.74	0.2654
x = 0.06	52.00	21.15	516.93	0.4067	27.42	0.2334
x = 0.08	51.31	09.33	517.32	0.1818	27.08	0.2287

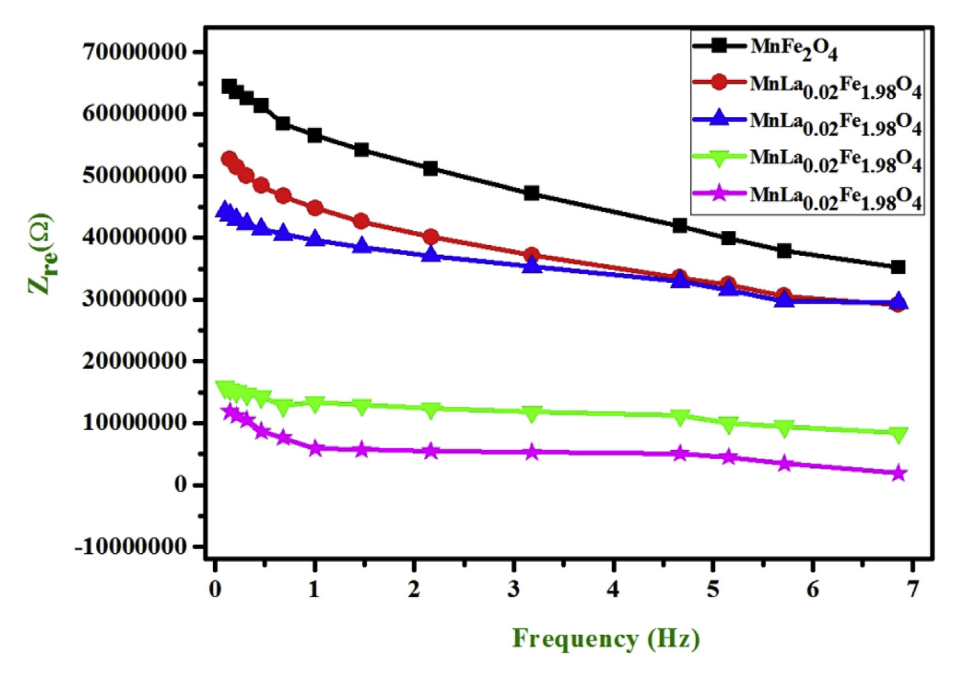


Fig. 7a. Real part of impedance spectra of prepared  $MnLa_XFe_{2-X}O_4$  (X = 0.00 to 0.08) nanoferrites.

frequency implies that release of space charges and an improvement of the mobility of charge carrier [49]. The imaginary part (Z") of the Lanthanum doped manganese nanoferrites represented in Fig. 7b. It decreases with increases of applied frequency and then merges at high frequency. The decrease in increasing frequency is due to the reduction loss in the resistive part of the prepared nanoferrites. The noticed peaks in the imaginary part (Z") are one due to existence of the space charge relaxation attributed with the charge carriers concluding from Oxygen vacancies [50].

The Nyquist plot of impedance spectra for prepared Lanthanum doped manganese nanoferrites with series (X = 0.00 to 0.08) are shown in Fig. 7c. The plot consists of clear semicircle arc which consists the grain and grain boundaries have contribution to the conductivity. These semicircles contain two types of relaxations with increase in La  $^{3+}$  ion

concentrations. The lower frequency side relaxation is attributed to grain boundary contribution and higher frequency grain contribution is mainly due to the effect of small crystal size from XRD. Furthermore, it is observed that the value of Nyquist plot decreases with increase of Lanthanum concentrations which implies that impedance is inversely proportional to the conductivity, as the conductivity increases with increase of La<sup>3+</sup> ion. Hence this is well corroborated from conductivity values [51].

#### 3.7. Dielectric properties

The dielectric behavior of iron (Fe) oxide is attributed to the electric dipole created due to the charge ion exchange interaction between the divalent and trivalent metal cations with in the spinel structure,

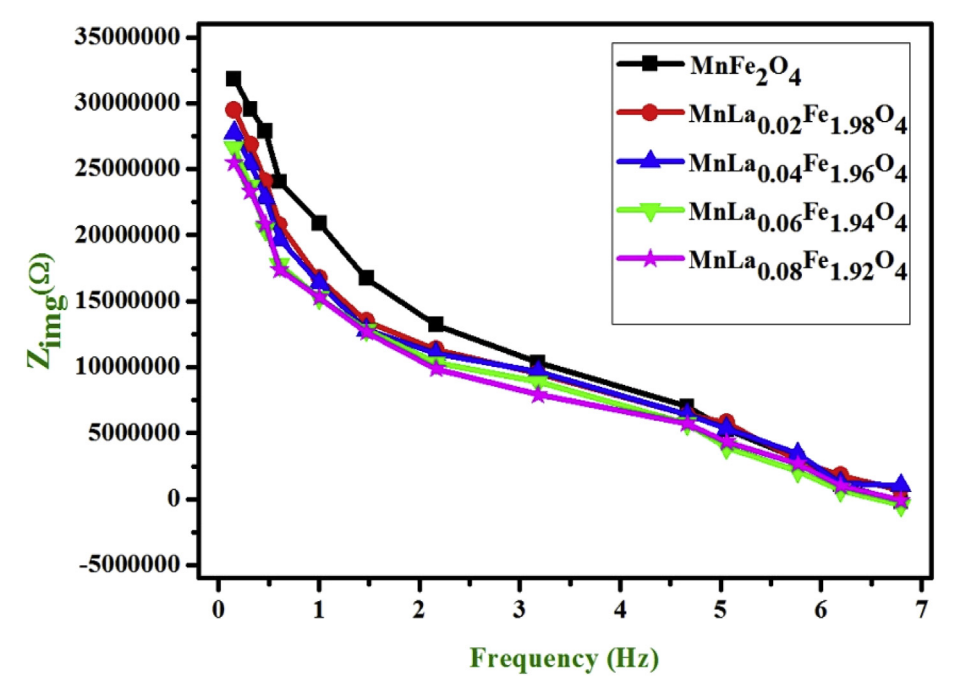


Fig. 7b. Imaginary part of impedance spectra of prepared  $MnLa_XFe_{2-X}O_4$  (X = 0.00 to 0.08) nanoferrites.

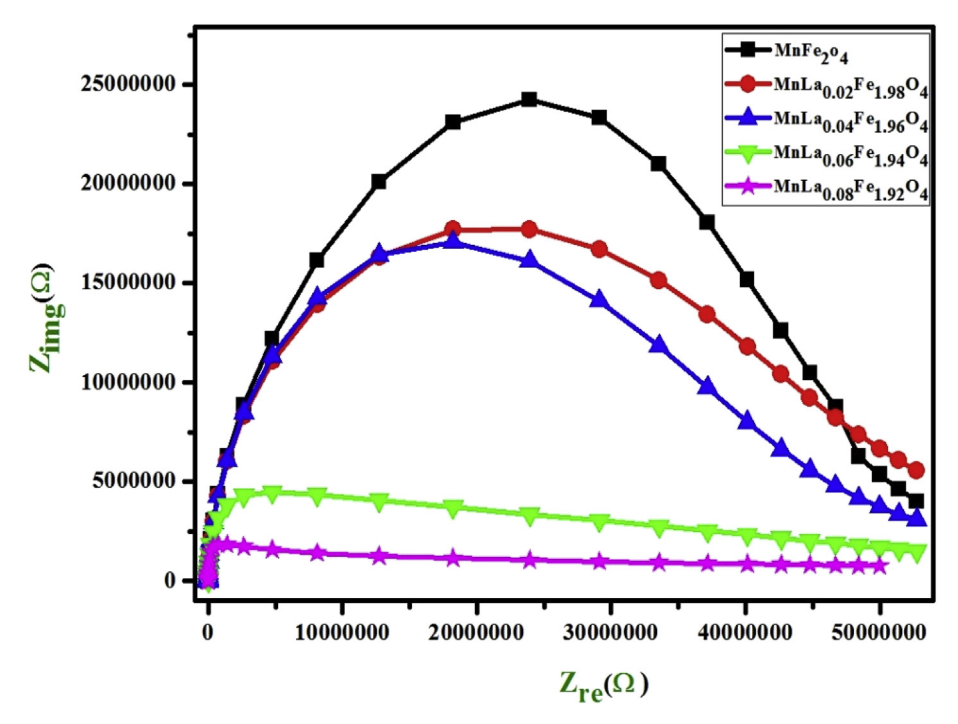


Fig. 7c. Nyquist plots of prepared  $MnLa_XFe_{2-X}O_4$  (X = 0.00 to 0.08) nanoferrites.

calcination temperature and time, method of preparation, chemical composition and occupancy of site in metal cation among the tetrahedral and octahedral sites on dielectric properties of ferrites [52,53]. The dielectric behavior of ferrites as a function of frequency gives important information of the behavior of the localized charge carriers and understanding the mechanism of dielectric polarization in ferrites [54].

3.7.1. Compositional effect on dielectric constant ( $\epsilon'$ ) and complex dielectric constant ( $\epsilon''$ )

The variation of dielectric constant ( $\epsilon$ ') and complex dielectric constant ( $\epsilon$ ") is measured at the frequency in range 0 –7 MHz for

Lanthanum doped manganese nanoferrites  $MnLa_XFe_{2-X}O_4$  with series X=0.00 to 0.08 at room temperature are depicted in Fig. 8a and 8b respectively. From the figure it can be noticed that both dielectric constant ( $\epsilon$ ') and complex dielectric constant ( $\epsilon$ ") increase with increase of  $La^{3+}$  ions concentration. The obtained results from electron interchange between  $Fe^{2+} \leftrightarrow Fe^{3+}$  in local displacement produce polarization of charges in these ferrites. Thus, it reveals number of ferrous ion on octahedral sites play a predominant in the process of conduction and dielectric polarization [55]. The hindrance of electron transfer between  $Fe^{2+}$  and  $Fe^{3+}$  ions are leading to decreases the polarization. The  $La^{3+}$  ion occupy octahedral sites owing to their larger ionic radius (1.06 Å).

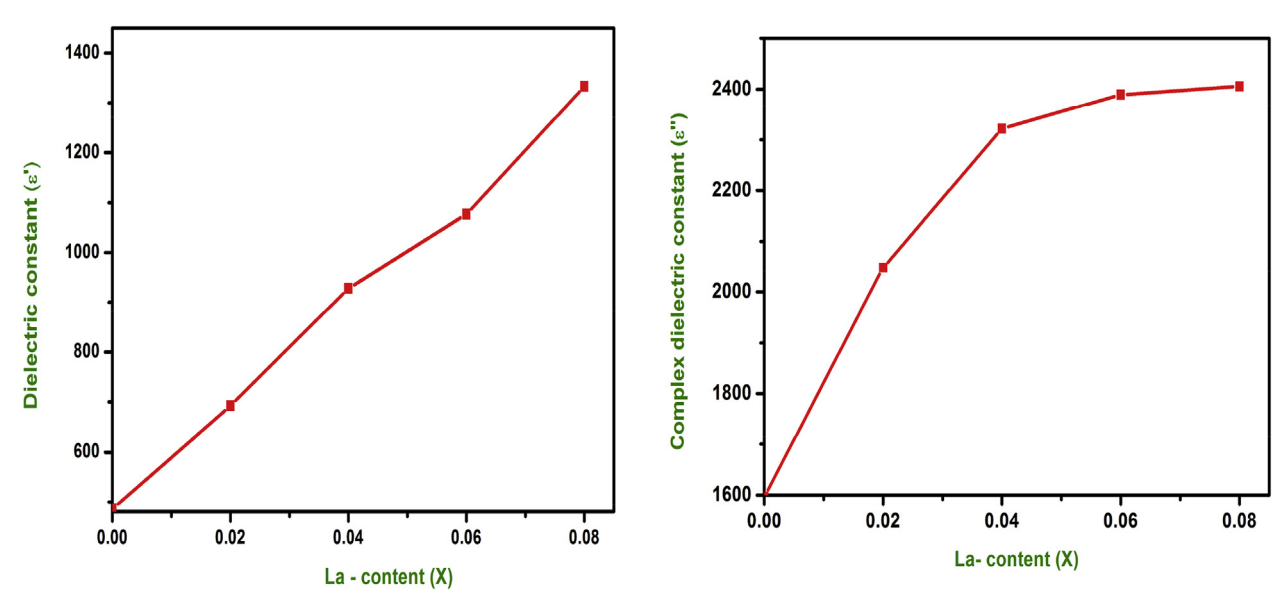


Fig. 8. (a,b). Dielectric constant and Complex dielectric constant of the prepared  $MnLa_XFe_{2\cdot X}O_4$  (X = 0.00 to 0.08) nanoferrites.

- c. Dielectric constant of the prepared MnLa  $_X$ Fe $_{2\cdot X}$ O $_4$  (X = 0.00 to 0.08) nanoferrites.
- d. Dielectric loss of prepared  $MnLa_XFe_{2-X}O_4$  (X = 0.00 to 0.08) nanoferrites.
- e. AC Conductivity vs Frequency of prepared  $MnLa_XFe_{2-X}O_4$  (X = 0.00 to 0.08) nanoferrites.
- f. AC Conductivity vs La-content of prepared  $MnLa_XFe_{2.X}O_4$  (X = 0.00 to 0.08) nanoferrites.

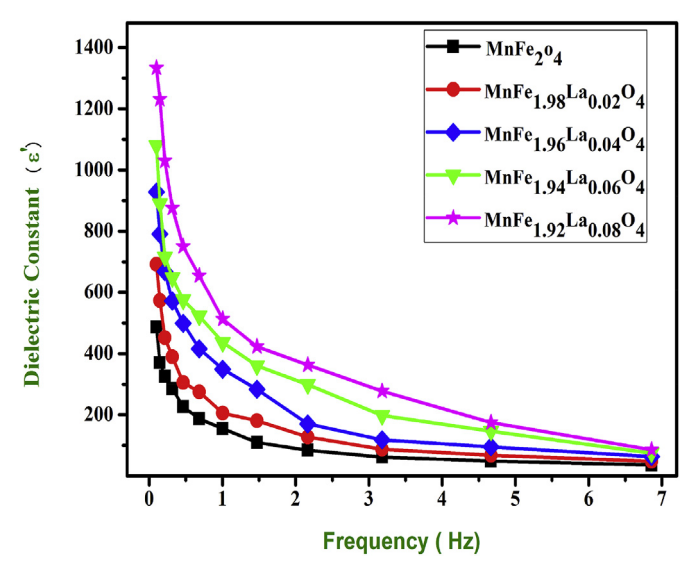


Fig. 8. (continued)

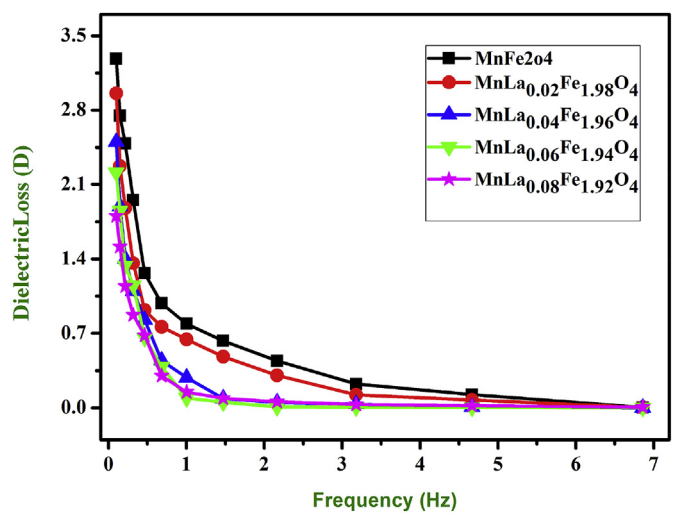


Fig. 8. (continued)

#### 3.7.2. Dielectric constant ( $\varepsilon$ ')

Fig. 8c. Shows the variation in the dielectric constant as a function of frequency for  $MnLa_XFe_{2.X}O_4$  nanoferrites with series X=0.00 to 0.8 at room temperature. The value of dielectric constant for high frequency region depend in the low frequency region while high frequency region it is frequency independents. The dielectric constants increase with increase of  $La^{3+}$  ions for prepared Lanthanum doped manganese nanoferrites which is evaluated using the following relation [32];

$$\varepsilon' = \frac{cd}{\varepsilon_0 A}$$
 (13)

where C is the capacitance of the pellet,  $\varepsilon_0$  is the permittivity of free space, A is the area of the pellet and d is the thickness of the pellet. The values of dielectric constant and complex dielectric constant are high at lower frequency and then decrease with increase in frequency for increasing La<sup>3+</sup> ions. The calculated dielectric constant values are 486, 692, 928, 1076 and 1333 with series  $X=0.00,\,0.02,\,0.04,\,0.06$  and 0.8 respectively. The dielectric constant values decrease with increase of frequencies. This dispersion behavior in the ferrites can be explained with Maxwell Wagner type interfacial polarization in compliance with Koop's phenomenological theory [56,57]. According to Maxwell - Wagner type, dielectric is constant of two layer non-uniform medium, where first layer denotes high conducting grains at higher frequency,

while second layer denotes poor conducting grain boundaries at low frequency [56]. The polarization can be occurred due to interchange of electrons between Fe<sup>2+</sup> and Fe<sup>3+</sup> on applying field in ferrites, which follows the behavior of conducting mechanism [58]. The decreasing polarization with increasing frequency leads to decrease in dielectric constant may be accumulated to decrease of electron exchange between Fe<sup>2+</sup> and Fe<sup>3+</sup> with applied field [58]. In spinel nanoferrites presence of La<sup>3+</sup> ions wish to occupy octahedral sites. Hopping between La<sup>3+</sup> and Fe<sup>3+</sup> increases at octahedral site with increase of La<sup>3+</sup> ion. Hopping of ion exchange between dissimilar metal is more effective in compared to similar metal ion [59]. This mechanism gets activated to intensify the conduction while there is an increase of La<sup>3+</sup> ions. Thus, the dielectric constant increases with La content.

#### 3.7.3. Dielectric loss

Variation of dielectric loss (or) tangent loss with frequency is depicted in Fig. 8d. From this it is clearly noticed that dielectric loss decreases with increase in frequency.

This indicates a strong association in dielectric process and conduction process [59]. The obtained dielectric loss decreases with increase of higher frequency. This dielectric loss may depend on certain factors such as composition, synthesis method and  ${\rm Fe}^{2+}$  content [56]. The dielectric loss and complex dielectric constant of prepared nanoferrites were estimated using the below mentioned relation [32].

$$\tan \delta = \frac{1}{2\pi f \epsilon_0 \epsilon'} \tag{14}$$

$$\varepsilon'' = \varepsilon' \tan \delta$$
 (15)

The obtained dielectric loss values of the prepared nanoferrites are 3.28, 2.95, 2.50, 2.21 and 1.80 respectively. The tangent loss decreases with increase of La³+ ions implies a decrease in total number of hopping mechanism, as tangent loss is directly proportional to number of dipole available for relaxation [60]. This is agreed with impedance analysis; where the increase of La³+ improves the resistive properties of materials thereby squash the Mn²+  $\leftrightarrow$  Mn³+ and Fe²+  $\leftrightarrow$  Fe³+ linkages [61]. Even at higher frequencies, tangent loss are small which promote the application of these prepared ferrites is suitable to electromagnetic devices.

#### 3.7.4. A.C conductivity

Fig. 8e. Shows a. c conductivity of prepared nanoferrites is shows increasing trend at low frequency region whereas the mentioned behavior is exhibit at high frequency range. Here, both Maxwell-Wagner model and Koop's phenomenological theories are confirms that ferrite material consists of conducting grains dispersive by resistive layer of grain boundary. This conduction process is related to the dielectric polarization [62]. So that, all the prepared nanoferrites are affected by grain boundaries with high resistance at low frequency region. However at high frequency region effect due to grain and increasing trend of hopping of charge carriers Fe<sup>2+</sup>- Fe<sup>3+</sup> at adjacent octahedral sites influence increasing conductivity [63].

Fig. 8f shows that the increase in a. c conductivity with increase of La $^{3+}$  ions. It reveals that the magnitude of electronic transfer is based on the concentration of Fe $^{3+}$ /Fe $^{2+}$  ion pairs located at B-sites [64]. From the graph, it is noticed that the a. c conductivity increases with increase of La $^{3+}$  ions monotonously. The value of a. c conductivity increases from 0.014 to 0.134 ( $\Omega cm^{-1}$ ) with increase of La $^{3+}$  ions (x = 0.00 to 0.08). The increase in a. c conductivity is due to decrease in porosity confirms from XRD. It is noticed that at low frequency a. c conductivity implies grain boundary contribution whereas high frequency can be attributed to the effect of grains [65,66]. The electrical parameters such as dielectric constant, dielectric Loss, complex dielectric constant and ac conductivity are listed in Table 5.

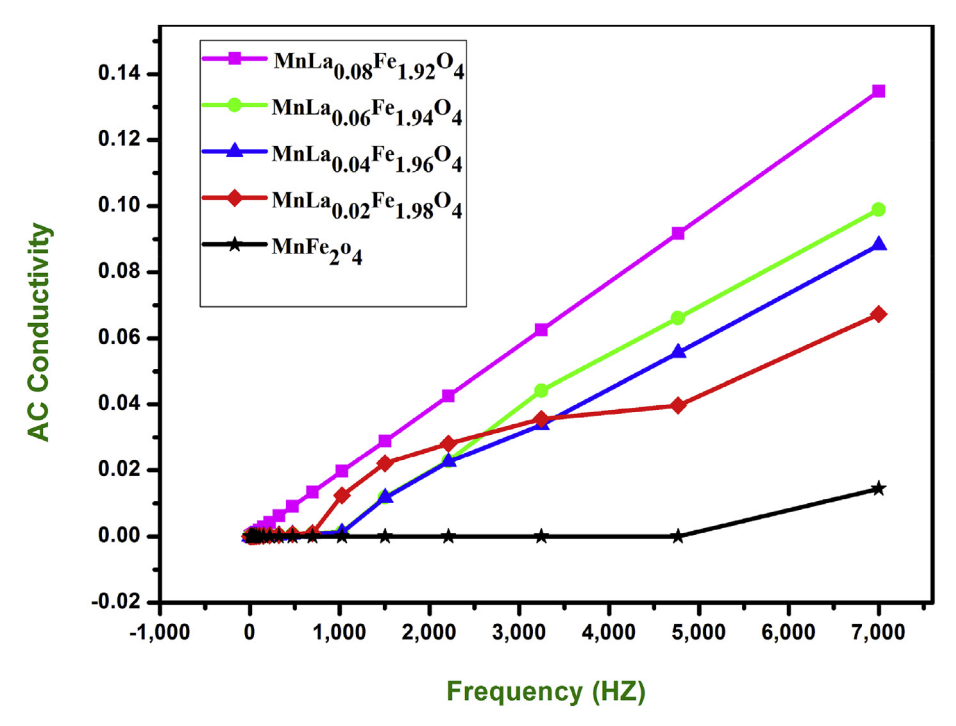


Fig. 8. (continued)

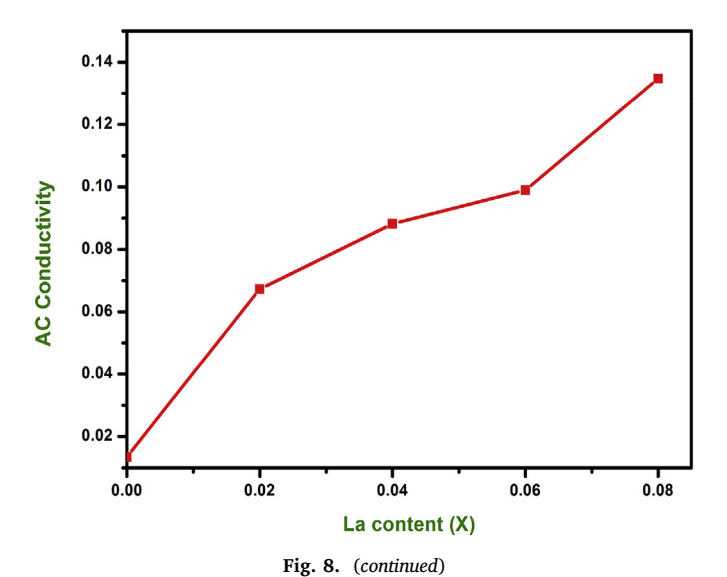


Table 5 Electrical parameters of prepared  $MnLa_XFe_{2.X}O_4$  (X = 0.00 to 0.08) nanoferrites.

Composition	Dielectric Constant ( $\epsilon'$ )	Dielectric Loss (tanδ) D	Complex dielectric constant $(\varepsilon'')$	AC Conductivity (ac) (Ωcm-1)
X = 0.00	486.08	3.2839	1595.97	0.0134
X = 0.02	692.37	2.9581	2048.09	0.0672
X = 0.04	928.15	2.5017	2321.95	0.0882
X = 0.06	1079.69	2.2128	2389.13	0.0989
X = 0.08	1333.49	1.8039	2405.48	0.1347

#### 4. Conclusion

Lanthanum doped Manganese nanoferrites were successfully synthesized by sol-gel method. These nanoferrites have cubic spinel structure with crystallite size from 26 to 12 nm. The lattice constant and

bulk density increased with increase of La<sup>3+</sup> ions, whereas X-ray density is inversely proportional to lattice constant and bulk density. The value of porosity decreases with increase of La3+ ions. The absorption bands are noticed in the FTIR spectrum near 562 cm<sup>-1</sup>, which confirms tetrahedral and octahedral stretching of Metal-Oxygen bond. The band gap values of the prepared Lanthanum doped manganese nanoferrites are 1.89-2.35 eV, which improve with respect to the band gap 1.25–1.38 eV values of Mn nanoferrites due to impact of La<sup>3+</sup> ions. FESEM with EDAX reveals that the prepare nanoferrites have spherical morphology with few agglomeration and present elemental peaks attained consistently in all the composition. The value of magnetic saturation are decreased from 81.5 to 51.3 emu/g and the value of coercivity increased from 105 to 517.32emu/g with increase of La3+ ions whereas it showed magnetic saturation inversely proportional to coercivity. VSM revealed that prepared nanoferrites are soft and ferromagnetic in nature. The dielectric constant and dielectric loss are decreased with increase of frequency and also dielectric constant and complex dielectric constant increased with increase of  ${\rm La}^{3+}$  ions. Impedance spectra reveal that the impedance response is over ruled by grain boundary behavior. The a. c conductivity increases with increase of La3+ ions. Hence, Lanthanum doped manganese nanoferrites are favorable for electromagnetic applications.

#### **Declaration of competing interest**

The authors declare that they have no known competing financial interests or personal relationships that could have appeared to influence the work reported in this paper.

# Appendix A. Supplementary data

Supplementary data to this article can be found online at https://doi.org/10.1016/j.ceramint.2019.11.180.

#### References

- $\hbox{[1]} \ \ \hbox{M.H. Kryder, Ultrahigh-density recording technologies, MRS Bull. 21 (1996) 17–19.}$
- [2] P. Samoila, L. Sacarescu, A.I. Borhan, D. Timpu, M. Grigoras, N. Lupu, M. Zaltariov, V. Harabagiu, Magnetic properties of nanosized Gd doped Ni–Mn–Cr ferrites

- prepared using the sol-gel autocombustion technique, J. Magn. Magn. Mater. 378 (2015) 92-97
- [3] G. Dixit, J.P. Singh, R.C. Srivastava, H.M. Agrawal, Magnetic resonance study of Ce and Gd doped NiFe2O4 nanoparticles, J. Magn. Magn. Mater. 324 (2012) 479–483.
- [4] M.A. Igbal, M. Islam, M.N. Ashiq, I. Ali, A. Iftikhar, H.M. Khan, Effect of Gdsubstitution on physical and magnetic properties of Li1.2Mg0.4Gd<sub>x</sub>Fe<sub>(2-x)</sub>O<sub>4</sub> ferrites, J. Alloy. Compd. 579 (2013) 181-186.
- Nitendar Kumar, Pran Kishan, Z.H. Zaidi, Effect of Mg Ti and Zn Ti substitutions on electrical and magnetic properties of Li ferrite, J. Magn. Magn. Mater. 184 (1998) 355\_357
- Katarzyna Winiarska, Irena Szczygieł, Roman Klimkiewicz, Manganese-zinc ferrite synthesis by the sol-gel autocombustion method. Effect of the precursor on the ferrite's catalytic properties, Ind. Eng. Chem. Res. 52 (2012) 353-361.
- [7] O.M. Hemeda, M.Z. Said, M.M. Barakat, Spectral and transport phenomena in Ni ferrite-substituted Gd O, J. Magn. Magn. Mater. 224 (2001) 132-142.
- [8] L. Nalbandian, A. Delimitis, V.T. Zaspalis, E.A. Deliyanni, D.N. Bakoyannakis, E.N. Peleka, Hydrothermally prepared nanocrystalline Mn-Zn ferrites: synthesis
- and characterization, Microporous Mesoporous Mater. 114 (2008) 465–473. J. Wang, C. Zeng, Z.M. Peng, Q.W. Chen, Synthesis and magnetic properties of  $\rm Zn_1$ . Mn<sub>x</sub>Fe<sub>2</sub>O<sub>4</sub> nanoparticles, Physica B 349 (2004) 124–128.
- [10] J.M. Hasting, L.M. Corliss, An antiferromagnetic transition in zinc ferrite, Phys. Rev. 102 (6) (1956) 1460.
- [11] C.N. Chinnasamy, A. Narayanasamy, N. Ponpandian, Magnetic properties of nanostructured ferromagnetic zinc ferrite, J. Phys. Condens. Matter 12 (2000) 7795.
- M. Yang, K.L. Yang, An Optimal low temperature tartrate precursor method for the synthesis of monophasic nanosized ZnFe<sub>2</sub>O<sub>4</sub>, J. Nanoparticle Res. 11 (2009) 1739.
- [13] P. Samoila, L. Sacarescu, A.I. Borhan, D. Timpu, M. Grigoras, N. Lupu, M. Zaltariov, V. Harabagiu, Magnetic properties of nanosized Gd doped Ni-Mn-Cr ferrites prepared using the sol-gel autocombustion technique, J. Magn. Magn. Mater. 378 (2015).
- [14] P.P. Naik, R.B. Tangsali, S.S. Meena, S.M. Yusuf, Influence of rare earth (Nd + 3) doping on structural and magnetic properties of nanocrystalline manganese-zinc ferrite, Mater. Chem. Phys. 191 (2017) 215–224.
- A. Shahul Hameed, H. Bahiraei, M.V. Reddy, M.Z. Shoushtari, J.J. Vittal, C.K. Ong, B.V.R. Chowdari, Lithium storage properties of pristine and (Mg, Cu) co doped ZnFe<sub>2</sub>O<sub>4</sub> nanoparticles, ACS Appl. Mater. Interfaces 6 (2014) 10744–10753.
- [16] G. Fan, J. Tong, F. Li, Visible-light-induced photocatalyst based on cobalt-doped zinc ferrite nanocrystals, Ind. Eng. Chem. Res. 51 (2012) 13639–13647.

  [17] P. Guo, L. Cui, Y. Wang, M. Lv, B. Wang, X.S. Zhao, Facile synthesis of ZnFe<sub>2</sub>O<sub>4</sub>
- nanoparticles with tunable magnetic and sensing properties, Langmuir 29 (2013) 8997-9003.
- [18] E.C. Devi, I. Soibam, Effect of Zn doping on the structural, electrical and magnetic properties of MnFe<sub>2</sub>O<sub>4</sub> nanoparticles, Indian J. Phys. 91 (2017) 861–867.
- [19] B. Vigneshwaran, P. Kuppusami, Arunkumar Panda, Akash Singh, H. Sreemoolanadhan, Microstructure and optical properties of Ba<sub>0.6</sub>Sr<sub>0.4</sub>TiO<sub>3</sub> thin films prepared by pulsed laser deposition, Mater. Res. Express 5 (2018) 066420.

  [20] Prashant Thakur, Rohit Sharma, Manoj Kumar, S.C. Katyal, Nagesh Negi, N. Thakur,
- Vineet Sharma, Pankaj Sharma, Superparamagnetic La doped Mn-Zn nano ferrites: dependence on dopant content and crystallite size, Mater. Res. Express 3 (2016)
- [21] Shahab Torkian, Ali Ghasemi, Reza Shoja Razavi, Structural and magnetic consequences of Mn0.6Zn0.4Fe<sub>2-x</sub>Gd<sub>x</sub>O<sub>4</sub> ferrite, J. Supercond. Nov. Magnetism 29 (2016) 1617-1625.
- [22] Irshad Ali, M.U. Islam, M. Ishaque, Hasan M. Khan, Muhammad Naeem Ashiq, M.U. Rana, Structural and magnetic properties of holmium substituted cobalt ferritessynthesized by chemical co-precipitation method, J. Magn. Magn. Mater. 324 (2012) 3773-3777.
- [23] Y. Zhang, D. Wen, Influence of RE/Mn (RE = La, Nd and Gd) ratios on the infrared absorption and emission properties of Co-Zn ferrites, Adv. Mater. Res. 218 (2011) 311-316
- [24] R. Tholkappiyan, K. Vishista, Influence of lanthanum on the optomagnetic properties of zinc ferrite prepared by combustion method, Physica B 448 (2014) 177-183.
- V. Chaudhari, S.E. Shirsath, M.L. Mane, R.H. Kadam, S.B. Shelke, D.R. Mane, [25] Crystallographic, magnetic and electrical properties of Ni0.5Cu0.25Zn0.25La<sub>x</sub>Fe<sub>2</sub>. <sub>x</sub>O<sub>4</sub> nanoparticles fabricated by sol-gel method, J. Alloy. Comp. 549 (2013) 213-220
- [26] N. Rezlescu, E. Rezlescu, P.D. Popa, L. rezlescu, Effect of rare-earth oxides on physical properties of Li-Zn ferrite, J. Alloy. Comp. 275–277 (1998) 657–659. [27] D.H. Bobade, S.M. Rathod, Maheshkumar L. Mane, Physica B 407 (2012)
- 3700-3704.
- [28] E. Ranjith Kumar, T. Arunkumar, T. Prakash, Heat treatment effects on structural and dielectric properties of Mn substituted CuFe<sub>2</sub>O<sub>4</sub> and ZnFe<sub>2</sub>O<sub>4</sub> nanoparticles, Superlattice Microstruct. 85 (2015) 530-535.
- [29] E.C. Devi, I. Soibam, Structural and optical characterization of MnFe<sub>2</sub>O<sub>4</sub> nanoparticles, Adv. Mater. Process. 2 (2017) 93-96.
- [30] S. Torkain, A. Ghasemi, R.S. Razavi, Structural and magnetic consequences of Mn0.6Zn0.4Fe<sub>2-x</sub>Gd<sub>x</sub>O<sub>4</sub> ferrite, J. Supercond. Nov. Magnetism 29 (2016)
- [31] R. Islam, M.A. Hakim, M.O. Rahman, H.N. Das, M.A. Mamun, Study of the structural, magnetic and electrical properties of Gd-substituted Mn-Zn mixed ferrites, J. Alloy. Comp. 559 (2013) 174–180.
- N. Gupta, P. Jain, R. Rana, S. Shrivastava, Current development in synthesis and characterization of nickel ferrite nanoparticle, Mater. Today Proc. 4 (2017) 342-349.
- Y. Köseoğlu, M. Bay, M. Tan, A. Baykal, H. Sözeri, R. Topkaya, N. Akdoğan, Magnetic and dielectric properties of Mn0.2Ni0.8Fe<sub>2</sub>O<sub>4</sub> nanoparticles synthesized by PEG-assisted hydrothermal method, J. Nanoparticle Res. 13 (2011) 2235-2244.

- [34] A.V. Mahulkar, C. Riedel, P.R. Gogate, U. Neis, A.B. Pandit, Effect of dissolved gas on efficacy of sonochemical reactors for microbial cell disruption: experimental and numerical analysis, Ultrason. Sonochem. 16 (2009) 635-643.
- D.V. Pinjari, A.B. Pandit, Cavitation milling of natural cellulose to nanofibrils, Ultrason. Sonochem. 17 (2010) 845-852.
- [37] Q. Xing, Z. Peng, C. Wang, Z. Fu, X. Fu, Doping effect of Y<sup>3+</sup> ions on the microstructural and electromagnetic properties of Mn–Zn ferrites, Physica B 407 (3) (2012) 388-392.
- [38] A.A. Al-Ghamdi, F.S. Al-Hazmi, L.S. Memesh, F.S. Shokr, L.M. Bronstein, Evolution of the structure, magnetic and optical properties of Ni1-xCuxFe2O4 spinel ferrites prepared by soft mechanochemical method, J. Alloy. Comp. 712 (2017) 82.

  [39] B.D. Cullity, Elements of X-Ray Diffraction, Addison-Wesley, Reading, MA, 1978.
- [40] S.E. Shirsath, M.L. Mane, Y. Yasukawa, X. Liu, A. Morisako, Self-ignited high
- temperature synthesis and enhanced super-exchange interactions of Ho<sup>3+-</sup> Mn<sup>2+-</sup>Fe<sup>3+-</sup>O<sub>2</sub> ferromagnetic nanoparticles, Phys. Chem. Chem. Phys. 16 (2014) 2347-2357.
- [41] Lawrence Kumar, Manoranjan Kar, Effect of La<sup>3+</sup> substitution on the structural and magnetocrystalline anisotropy of nanocrystalline cobalt ferrite, Ceram. Int. (2012) 4771-4782.
- [42] Pawan Kumar, S.K. Sharma, M. Knobel, M. Singh, Effect of La<sup>3+</sup> doping on the electric, dielectric and magnetic properties of cobalt ferrite processed by co precipitation technique, J. Alloy. Comp. 508 (2010) 115-118.
- M.A. John Jacob, Khadar, Investigation of mixed spinel structure of nanostructured nickel ferrite, J. Appl. Phys. 107 (2010) 114310-114320.
- [44] Mathew George, Swapna S. Nair, Asha Mary John, P.A. Joy, M.R. Anantharaman, Structural, magnetic and electrical properties of the sol-gel prepared Li0.5Fe2.5O<sub>4</sub> fine particles, J. Phys. D Appl. Phys. 39 (2006).
- [45] Razia Nongjai, Shakeel Khan, K. Asokan, Hilal Ahmed, Imran Khan, Magnetic and electrical properties of in doped cobalt ferrite nanoparticles, J. Appl. Phys. 112 (2012) 084321.
- [46] A.M. Pachpinde, M.M. Langade, K.S. Lohar, S.M. Patange, S.E. Shirsath, Impact of larger rare earth Pr<sup>3+</sup> ions on the physical properties of chemically derived Pr<sub>x</sub>CoFe <sub>2-x</sub>O<sub>4</sub> nanoparticles, Chem. Phys. 429 (2014) 20–26.
- [47] R. Tholkappiyan, K. Vishista, Structural, optical and magnetic properties of nanocrystalline Zinc ferrite particles from glycine assisted combustion: effect of Sr<sup>2+</sup> dopant, Mater. Sci. Semicond. Process. 40 (2015) 631.
- J. Azadmanjiri, S.A. Seyyed Ebrahimi, Influence of stoichiometry and calcination condition on the microstructure and phase constitution of NiFe2O4 powders pre pared by sol-gel autocombustion method, Phys. Status Solidi C 1 (12) (2004) 3414.
- M. Kooti, M. Afshari, Magnetic cobalt ferrite nanoparticles as an efficient catalyst for oxidation of alkenes, Sci. Iran. 19 (2012) 1991–1995.
- M. Azizar Rahman, A.K.M. Akther Hossain, Electrical transport properties of Mn– Ni-Zn ferrite using complex impedance spectroscopy, Phys. Scr. 89 (2014) 025803
- [51] C. Li, J. Wang, W. Su, H. Chen, W. Zhong, P. Zhang, Effect of Mn<sup>2+</sup> on the electrical nonlinearity of (Ni, Nb)-doped SnO2 varistors, Ceram. Int. 27 (2001) 655.
- C.V. Ramana, Y.D. Kolekar, K. Kamala Bharathi, B. Sinha, K. Ghosh, Correlation between structural, magnetic, and dielectric properties of manganese substituted cobalt ferrite, J. Appl. Phys. 114 (2013) 183907.
- [53] Rabia Pandit, K.K. Sharma, Pawanpreet Kaur, Ravi Kumar, Cation distribution controlled dielectric, electrical and magnetic behavior of In3+ substituted cobalt ferrites synthesized via solid-state reaction technique, Mater. Chem. Phys. 148 (2014) 988-999.
- [54] E. Pervaiz, I.H. Gul, Structural, electrical and magnetic studies of Gd<sup>3+</sup> doped cobalt ferrite nanoparticles, Int. J. Curr. Eng. Technol. 2 (2012) 377.

  [55] Tatina N. brusentosva, Viatcheslva D. kuznetsov, Synthesis and investigation of
- magnetic properties of substituted ferrite nanoparticles of spinel systemMn<sub>1</sub>-<sub>x</sub>Zn<sub>x</sub>[Fe<sub>2-y</sub>L<sub>y</sub>]O<sub>4</sub>, J. Magn. Magn. Mater. 311 (2007) 22–25.
- [56] Ping Hu, Hai-bo Yang, De-an Pan, Hua Wang, Jian-jun Tian, Shen-gen Zhang, Xinfeng Wang, Alex A. Volinsky, Heat treatment effects on microstructure and magnetic properties of Mn-Zn ferrite powders, J. Magn. Magn. Mater. 322 (2010) 173 - 177
- [57] Q.A. Pankhurst, J. Connolly, S.K. Jones, J.J. Dobson, Applications of magnetic nanoparticles in biomedicine, J. Phys. D Appl. Phys. 36 (2003) R167.
- Neuberger Tobias, Bernhard Schopf, Heinrich Hofmann, Margarete Hofmann, Brigitte von Rechenberg, Superparamagnetic nanoparticles for biomedical applications: possibilities and limitations of a new drug delivery system, J. Magn. Magn. Mater. 293 (2005) 483-496.
- [59] Bin Liu, Dieter K. Weller, Heat assisted magnetic recording film including superparamagnetic nanoparticles dispersed in an antiferromagnetic or ferrimagnetic matrix, issued January, U.S. Patent 7 (2) (2007) 158-346.
- [60] E. Iguchi, N. Kubota, T. Nakamori, N. Yamamoto, K.J. Lee, Polaronic conduction in n-type BaTiO3 doped with La2O3 or Gd2O3, Phys. Rev. B 43 (1991) 8646. Pawan Kumara, S.K. Sharma, M. Knobel, M. Singh, Effect of La<sup>3+</sup> doping on the
- electric, dielectric and magnetic properties of cobalt ferrite processed by Co-precipitation technique, J. Alloy. Comp. 508 (2010) 115.

  [62] C.G. Koops, On the Dispersion of resistivity and Dielectric constant of some semi-
- conductors at audiofrequencies, Phys. Rev. 83 (1951) 121.
- A.K.M. AktherHossain, M.A. Rahman, S.F.U. Farhad, B. Vilquinc, Hidekazu Tanaka, Effect of Li substitution on the magnetic properties of LixMg<sub>0.40</sub>Ni<sub>0.60-</sub> <sub>2x</sub>Fe2+xO<sub>4</sub>ferrites, Physica B 406 (2011) 1506–1512.
- [64] M.A. Elkestawy, AC conductivity and dielectric properties of , Zn 1-x CuxCr0.8 Fe1.2
- O<sub>4</sub> spinel ferrites, J. Alloy. Comp. 492 (2010) 616–620. [65] Navneet Singh, Ashish Agarwal, Sujata Sanghi, Dielectric relaxation,conductivitybehavior and magnetic properties of Mg substituted Zn-Li ferrites, Curr. Appl. Phys. 11 (2011) 783-789.
- [66] H. Bottger, V.V. Bryksin, Hopping Conduction in Solids, Akademie-Verlag, Berlin, 1985.



# CoGd<sub>X</sub>Fe<sub>2-X</sub>O<sub>4</sub> (0.00 $\leq$ X $\geq$ 0.08) nanoferrites: effect of Gd<sup>3+</sup> ions on structural, optical, magnetic, and dielectric properties

A. Rajeshwari<sup>1</sup>, I. Kartharinal Punithavathy<sup>1,\*</sup> , S. Johnson Jeyakumar<sup>1</sup>, M. Jothibas<sup>1</sup>, and S. Ajith Kumar<sup>2</sup>

**Received:** 22 September 2021 **Accepted:** 12 January 2022

© The Author(s), under exclusive licence to Springer Science+Business Media, LLC, part of Springer Nature 2022

# **ABSTRACT**

Nanoferrites possessing very low dielectric loss and minimum magnetic saturation value finds its potential application in magnetic recording devices, magnetic shielding and microwave absorption devices, etc., Gadolinium (Gd³+)-doped cobalt nanoferrites (CoGd<sub>X</sub>Fe<sub>2-X</sub>O<sub>4</sub>, where X=0.00, 0.02, 0.04, 0.06 and 0.08 mol%) were synthesized by effective sol–gel method. The structural effects of Gd doping in the nanoferrites were analyzed by X-ray diffraction (XRD), Raman and FT-IR spectroscopic techniques. With increasing doping (Gd³+) concentration, the magnetic hysteresis curves revealed soft ferromagnetic nature with increases in coercivity (O<sub>e</sub>) and decreases in saturation ( $M_{\rm s}$ ). The very low dielectric loss and minimum magnetic saturation have been obtained for synthesized nanoferrites about 13.03 emu/g and 0.028, respectively. The prepared sample shows prominent dielectric constant 32,630 and lowest electrical resistivity ranging from 0.29 to 0.42  $\Omega$  cm<sup>-1</sup>.

#### 1 Introduction

In recent years, nanosized ferrites have immense applications in various fields with fast development microwave technology such as high frequency devices and their component, telecommunications devices, memory core devices, microwave absorption micro-oven, radar, antenna, sensor, magneto-resistive random access memory (MRAM) devices, targeted

magnetic tunnel junction and spintronics devices and drug delivery [1–4]. In electronic society, the usage of telecommunication and electronic equipment's has increased due to the problem raised in electromagnetic interference [5] as it generates false image, reduces the life time and efficiency of the instruments and also destroy the safety operation of many electronic devices. To overcome these problems, all electronic equipment's must be aware of

Address correspondence to E-mail: profpunithaphysics@gmail.com

https://doi.org/10.1007/s10854-022-07775-z

Published online: 30 January 2022



<sup>&</sup>lt;sup>1</sup> Department of Physics, T.B.M.L College (Affiliated to Bharathidasan University, Tiruchirapalli-620024), Porayar, Nagapattinam, Tamil Nadu 609 307, India

<sup>&</sup>lt;sup>2</sup>Centre of Excellence for Energy Research, International Research Centre, Sathyabama Institute of Science and Technology, Chennai, Tamil Nadu 600 119, India

electromagnetic damage [5, 6]. Nowaday's research has been done for the improvement of latest microwave shielding materials which includes high efficiency, light weight, lifetime and high durability. Electromagnetic absorber solves such problems and also satisfies the above-mentioned parameters. Therefore, electromagnetic absorbers are highly needed and broad ranges of application have been taken out [7, 8]. Some rare-earth element doping has been reported to play vital roles to amplify the magnetic, structural and electrical properties. These properties can change based on the cation distribution, size, shape, concentration and lattice sites [9]. Spinel ferrites are one of the most absorbing materials in different forms such as paints, powder, ceramic filter and sheets. [10]. The electrical and magnetic properties are superior when dopant are rare-earth ions [11]. Various efforts have been taken to develop techniques for the synthesis of nanoferrites such as co-precipitation [12], sonochemical method [13], micro-emulsion technique [14], hydrothermal [15] and solvo thermal [16]. Among these, sol-gel method has emerged as a useful strategy for the preparation of nanoferrites. Sol-gel method allows to control both size through structural properties and also homogeneity of particles. However, doping of rare-earth along with large amount of Fe and some metal may result in unique properties [16]. To our knowledge, a few researchers discussed the study of Gd in Co ferrites. Moreover, an elaborated study of magnetic and dielectric properties for spinel nanoferrites has been reported very rarely.

In the current study,  $CoGd_XFe_{2-X}O_4$ -doped cobalt nanoferrites with various doping concentrations ( $X=0.00,\,0.02,\,0.04,\,0.06$  and 0.08 mol %) were synthesized by sol–gel method. The impact of Gd incorporation on interconnected features such as structural, morphological, optical, and magnetic properties were investigated. The primary goal of the produced Gd-doped cobalt nanoferrites (GNF) with varied doping concentrations is to improve electromagnetic microwave absorption.

# 2 Materials and experimental procedure

#### 2.1 Materials

A high-pure nitrate precursors of the Cobalt, Iron, Gadolinium and salts such as Gadolinium nitrate (Gd  $(NO_3)_3 \cdot 6H_2O)$ ), and the commercial reagents

Ammonia (NH<sub>4</sub>OH) and Citric acid ( $C_6H_8O_7 \cdot H_2O$ ) were purchased from Merck.

## 2.2 Experimental procedure

The  $CoGd_xFe_{2-x}O_4$  nanoferrites were synthesized by the well-known sol–gel technique. The stoichiometric amount of nitrate was weighed and dissolved in 100 ml of de-ionized water until a mixture of the precursors. Then the mixture was constantly stirred at 80 °C for 1 h. The ammonium hydroxide solution was further added into the precursor solution drop by drop until the pH value of 7. A dark sol suspension was obtained and the content was dried in oven at 60 °C for 24 h. The dried powder was kept for calcination in a muffle furnace at 500 °C for 2 h to obtain the by-products-free nanoparticles. The asprepared nanopowders were calcined at 1000 °C for 24 h. The schematic diagrams of preparation of  $CoGd_xFe_{2-x}O_4$  nanoferrites are shown in Fig. 1.

# 2.3 Characterization of the $CoGd_XFe_{2-X}O_4$ nanoferrites

The structural properties of the prepared CoLa<sub>x</sub>Fe<sub>2</sub>- $_{X}O_{4}$  (X = 0.00–0.08) nanoferrites were characterized by XRD (SHIMADZU-XRD 6000) with CuKα radiation source operated at 40 kV and 30 mA. The functional groups in the CoLa<sub>X</sub>Fe<sub>2-X</sub>O<sub>4</sub> nanoferrites were determined by FTIR spectra (SHIMADZU-UV 18,000) ranging from 4000 to 400 cm<sup>-1</sup>. The morphology and elemental investigation of the prepared material were analyzed using FESEM with an EDAX (Quanta FEG 250). The optical properties were analyzed using an UV- DRS for the prepared material. Raman spectroscopy studies were made using an (ALU-PHI5000) AUG spectrometer with monochromatic Al Ka and 26.00 eV radiation. Magnetic properties were analyzed using VSM (Lakeshore VSM 7140) with an applied magnetic field of -15,000 to +15,000 Oe at room temperature. The Impedance spectroscopy with the frequency range of 100 mHz-10 MHz at room temperature (30 °C) (Biologic SP-300) was used to determine the electrical properties. The bulk powders were mixed with 5% polyvinyl alcohol (PVA) as binder in a mortar and pestle. The powders were pelletized by applying uniaxial force using hydraulic press to obtain pellets with dimension of 10 mm diameter, and 1.5 mm thickness. The green bodies were sintered under air atmosphere at 1573 K for 6 h. The well-



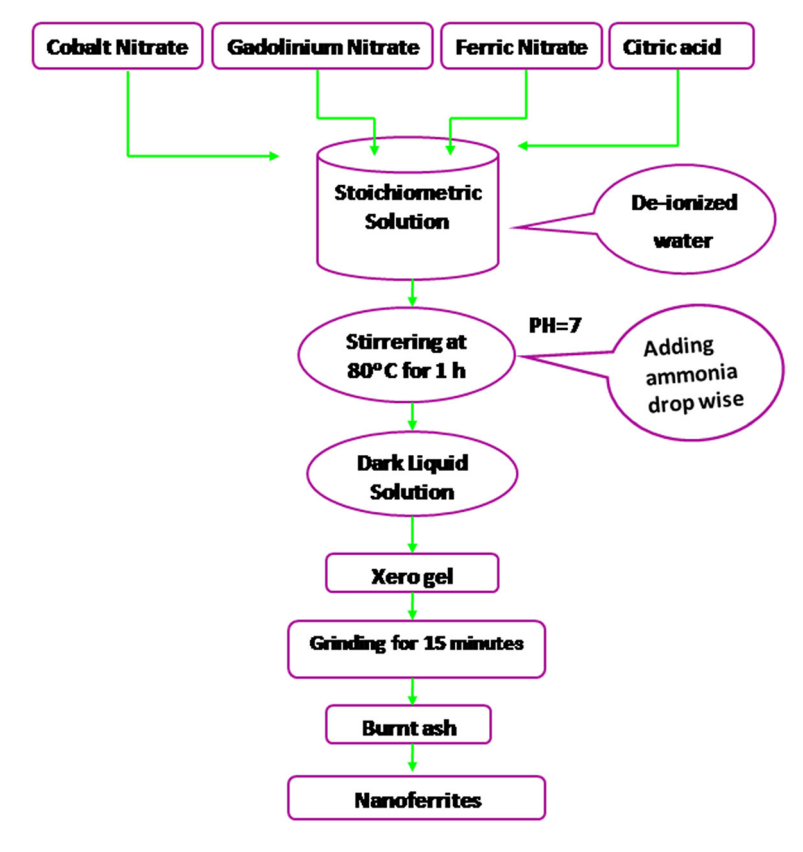


Fig. 1 Flow chart for the sample preparation of CoGd<sub>x</sub>Fe<sub>2-x</sub>O<sub>4</sub> nanoferrites

sintered pellets were polished using SiC abrasive sheets (1000 and 1500 grads) sheets in running water and ultrasonically cleaned in ethanol for 15 m. Density  $\rho$  = Mass/Volume g/cm². Relative sintered density  $R\rho$  (%) was measured by the ratio of green (before sintering) densities and sintered densities. The relative density  $R\rho$  of the samples were calculated to be  $\sim$  85%. The density of the sintered pellets has been measured by weight change method. The dried pellets further coated with silver paste on both sides and again dried  $\sim$  80 °C in hot air oven to make good electrical contact for impedance measurements.

#### 3 Results and discussion

#### 3.1 Structural analysis

XRD spectra of  $CoGd_XFe_{2-X}O_4$  (X = 0.00-0.08) are shown in Fig. 2. The observed reflections are (220), (311), (400), (422), and (511) of spinel ferrites which are matched to JCPDS card no 22-1056 [17]. The diffraction pattern confirms the formation of pure

cubic structure of the spinel ferrites, without any secondary impurities. The method used for preparation ensures the substitution of Gd<sup>3+</sup> ions into the spinel structure. The crystallite size was estimated from the basic Scherrer equation [18];

$$D = \frac{K\lambda}{\beta\cos\theta} \tag{1}$$

where D is the average crystallite size, l is the X-ray wavelength, b is the width of the X-ray peak on the 2q axis, normally measured as full width at half maximum (FWHM) after the error due to instrumental broadening has been properly corrected (subtraction of variances), q is the Bragg angle, and K is the so-called Scherrer constant. K depends on the crystallite shape and the size distribution, indices of the diffraction line, and the actual definition used for b whether FWHM or integral breadth [19]. K can have values anywhere from 0.62 and 2.08. In this paper, K = X.X was used. Further, microstrain in the crystallite or nanocrystal also affects the width b, which needs to be considered in an accurate analysis. Spatial fluctuations in the alloy composition can also



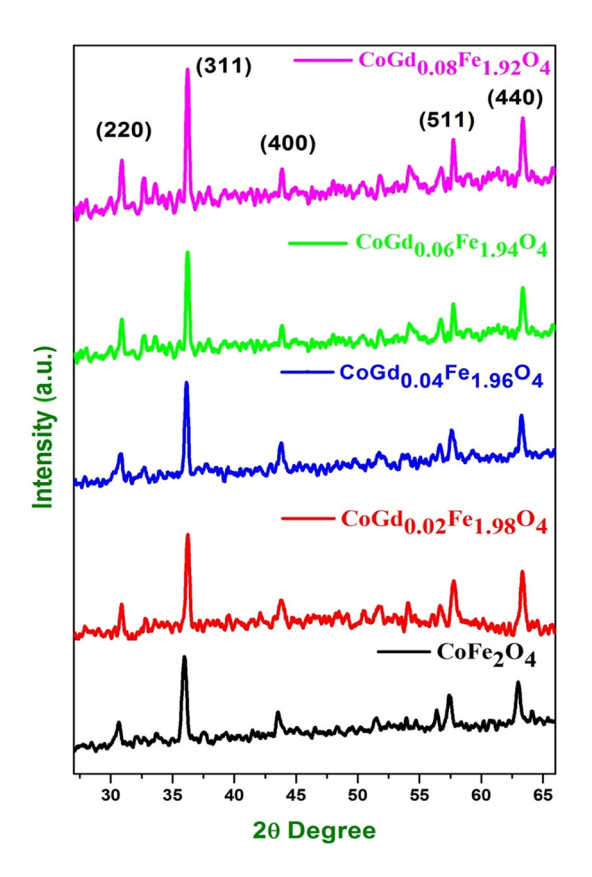
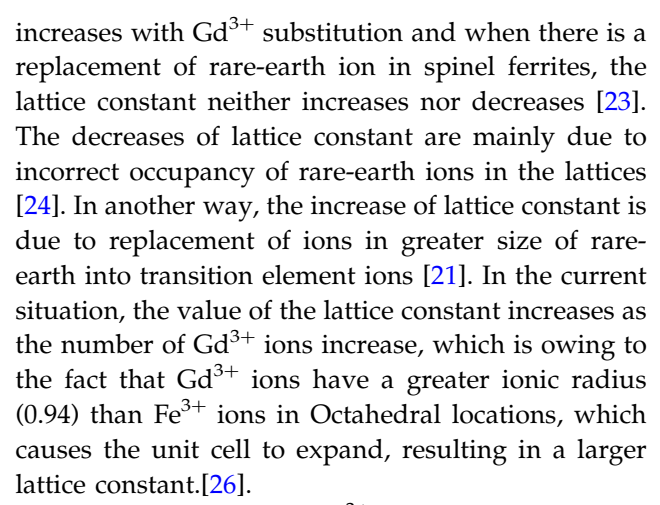


**Fig. 2** X-ray diffraction pattern of prepared  $CoGd_XFe_{2-X}O_4$  (X = 0.00-0.08) nanoferrites calcined at 1000 °C

affect the width. In this work, the calculated values of D represent estimates [20]. The average crystallite size of the nanoferrites decreases from 29 to 13 nm with increase of doping Gd<sup>3+</sup>. The obtained results reveal that the average crystallite size of the prepared ferrites is highly influenced by the concentration of Gd concentration. This implies that the substitution of Fe ions with Gd ions hinders the grain growth. It can also be explained based on the difference between the ionic radii of Gd<sup>3+</sup> and Fe<sup>3+</sup> ions. The ionic radius of  $Fe^{3+}$  ions (0.67 Å) is smaller than that of Gd<sup>3+</sup> ions (0.938 Å) and, the substitution of rareearth ions shows limited solubility in spinel lattice and higher grain growth [21]. The lattice constant of the prepared nanoferrites is calculated using below equation [22]:

$$a = d_{hkl}\sqrt{(h^2 + k^2 + l^2)}$$
 (2)

where d is inter atomic spacing, a is the lattice constant and (hkl) are miller indices. The lattice constant was in the range of 8.50 ( $\pm$  0.002)–8.59 ( $\pm$  0.002) Å (Table 1). It reveals that lattice constant



Thus, incorporation of Gd<sup>3+</sup> into cobalt nanoferrites was observed without any traces of secondary phase. X-ray density of Gd<sup>3+</sup> doped CoFe<sub>2</sub>O<sub>4</sub> nanoferrites were estimated by the following equation [22]:

$$d_x = Zm/Na^3 (3)$$

where Z is basic unit cell of cubic structure contains eight ions, m is molecular weight of the ferrites, N is Avogadro's number and  $a^3$  is volume of the unit cell. The observed X-ray density increases from 5.0 to 5.4 g/cm<sup>3</sup> with addition of  $Gd^{3+}$  ion and it can be ascribed to the fact that the atomic weight of  $Gd^{3+}$  is larger than that of Fe (55.84 g/mol). When the X-ray density increases the particles tend to acquire nanosize and tightly packed. The bulk density (dB) was calculated using specified equation [22]:

$$d_{\rm B} = m/\pi r^2 t \tag{4}$$

where t is thickness, r is radius and m denote pellet's mass. The result revealed that the bulk density increases from 1.7 to 2.7 g/cm<sup>3</sup> possibly as a result of pores in the prepared nanoferrites. The place of  $Gd^{3+}$  ions activate the calcinating condition thus trends to increase in densities [25]. The porosity (P) was estimated using following equation [22]:

$$P = (1 - d_B/d_X)\% (5)$$

where  $d_x$  and  $d_B$  are X-ray density and bulk density of the ferrites. Table1, the porosity percentage decreased from 6.9 to 4.7 with increase of  $Gd^{3+}$  ions which is due to increase in bulk density and also porosity behaves inversely proportional to each other. The surface area (S) of the sample was calculated using subsequent expression [22]:

$$S = 6/d_{\rm X}D\tag{6}$$



Composition	Crystallite size (nm) $(\pm 0.03)$	Lattice constant (a) Å (± 0.002)	Volume of unit cell (a³) Å	X-ray density (ρ <sub>XRD</sub> ) (g/cm <sup>3</sup> )	Bulk density (d <sub>B</sub> ) (g/cm <sup>3</sup> )	Surface area (S <sub>XRD</sub> ) (m <sup>2</sup> /g)	Porosity (%)
(G0) $X = 0.00$	29	8.50	615.5	5.0	1.7	38	6.9
(G2) $X = 0.02$	22	8.52	620.6	5.2	1.8	51	6.6
(G4) $X = 0.04$	19	8.56	626.3	5.2	1.9	60	6.2
(G6) $X = 0.06$	15	8.57	630.7	5.3	2.5	77	5.1
(G8) $X = 0.08$	13	8.60	650.0	5.4	2.7	90	4.7

**Table 1** Structural parameters of prepared  $CoGd_XFe_{2-X}O_4$  (X = 0.00–0.08) nanoferrites

where D is crystal size and  $d_X$  is the X-ray density of the ferrites. The surface area increases from 38 to 90 m<sup>2</sup>/g with addition of Gd<sup>3+</sup> ions are due to decrease in crystallite size. The results observed from all the structural parameters are listed in Table 1.

#### 3.2 FESEM with EDAX

The morphology studies can be determined using FESEM as in Fig. 3, which revealed that these nanoferrites have spherical in shape with few agglomerations which is due to the magnetic interactions between the particles increase in substitution of Gd<sup>3+</sup> ions [26]. It was noticed that the substitution of Gd<sup>3+</sup> ion had insignificant effect on the material morphology, but largely impact the average size of the ferrites, which implies that the average crystallite decreases with increase of dopant concentration [21].

EDAX analysis of CoGd<sub>x</sub>Fe<sub>2-x</sub>O<sub>4</sub> ferrites are shown in Fig. 4. It is clearly seen that there is no formation of secondary impurity elements in the composition. The spectra also indicate that the incorporation of Gd<sup>3+</sup> was well incorporated in the ferrites as the Gd<sup>3+</sup> peaks appear as the intensities increase with increase of Gd<sup>3+</sup> ions. It's worth mentioning that the atomic weight percentages are closely matched with the theoretical stoichiometry which corresponds expected ratio of the to the concentrations.

#### 3.3 FT-IR analysis

Infrared Radiation (IR) transmittance spectra of these nanoferrites series are shown in Fig. 5. The absorption of IR in molecular vibrations also confirms the formation of ferrites phase. The vibrational frequency at 585 cm<sup>-1</sup> represents stretching vibration of metaloxygen bond. The broad and strong stretching peak

at 3390 cm<sup>-1</sup> is due to stretching vibration of O–H bonds of water molecules coordinates to the ferrite structure [27].

The peak around at  $1495 \text{ cm}^{-1}$  is due to stretching vibration of nitrate (NO<sup>3-</sup>) which indicates that nitrate ions are present in the starting precursors of all the samples [28]. The peak appears around 2344 cm<sup>-1</sup> is due to stretching vibration C = H bond of CH<sub>3</sub> functional group [29]. The peak at 2935 cm<sup>-1</sup> was ascribed to symmetric and antisymmetric stretching modes of CH<sub>2</sub>, respectively [30]. All the repoted vibrational assignments was provided in the Table 2.

#### 3.4 Optical properties

The impact of  $Gd^{3+}$  doping on the optical properties of  $CoGd_XFe_{2-X}O_4$  was carried out through diffuse reflectance (DR) UV spectrometer in the wavelength range of 200–400 nm as shown in Fig. 6.

It can be clearly noticed that  $CoGd_XFe_{2-X}O_4$  nanoferrites exhibited absorption in the visible region. The absorption values of cobalt ferrites show visible light cut-off wavelength at 234 nm. As the  $Gd^{3+}$  ions increasing, the absorptions were observed as 233, 232, 231 and 230 nm, respectively. When compared to  $Gd^{3+}$  doped ferrites, pure cobalt nanoferrites show better visible light absorption.

The optical bandgap energy was calculated following expression [31];

$$h\gamma\alpha = (h\gamma - E_{gap})^n \tag{7}$$

where the absorption coefficient is  $\alpha$ , the frequency of light is denoted by  $\gamma$ , the planks constant is h, and the band gap is E<sub>g</sub>. For indirect and direct band gap energies, the exponents are 2 and  $\frac{1}{2}$ .

Figure 7 shows that the direct band gap energy values are found as 3.14, 3.27, 3.39, 3.46 and 3.61 eV,



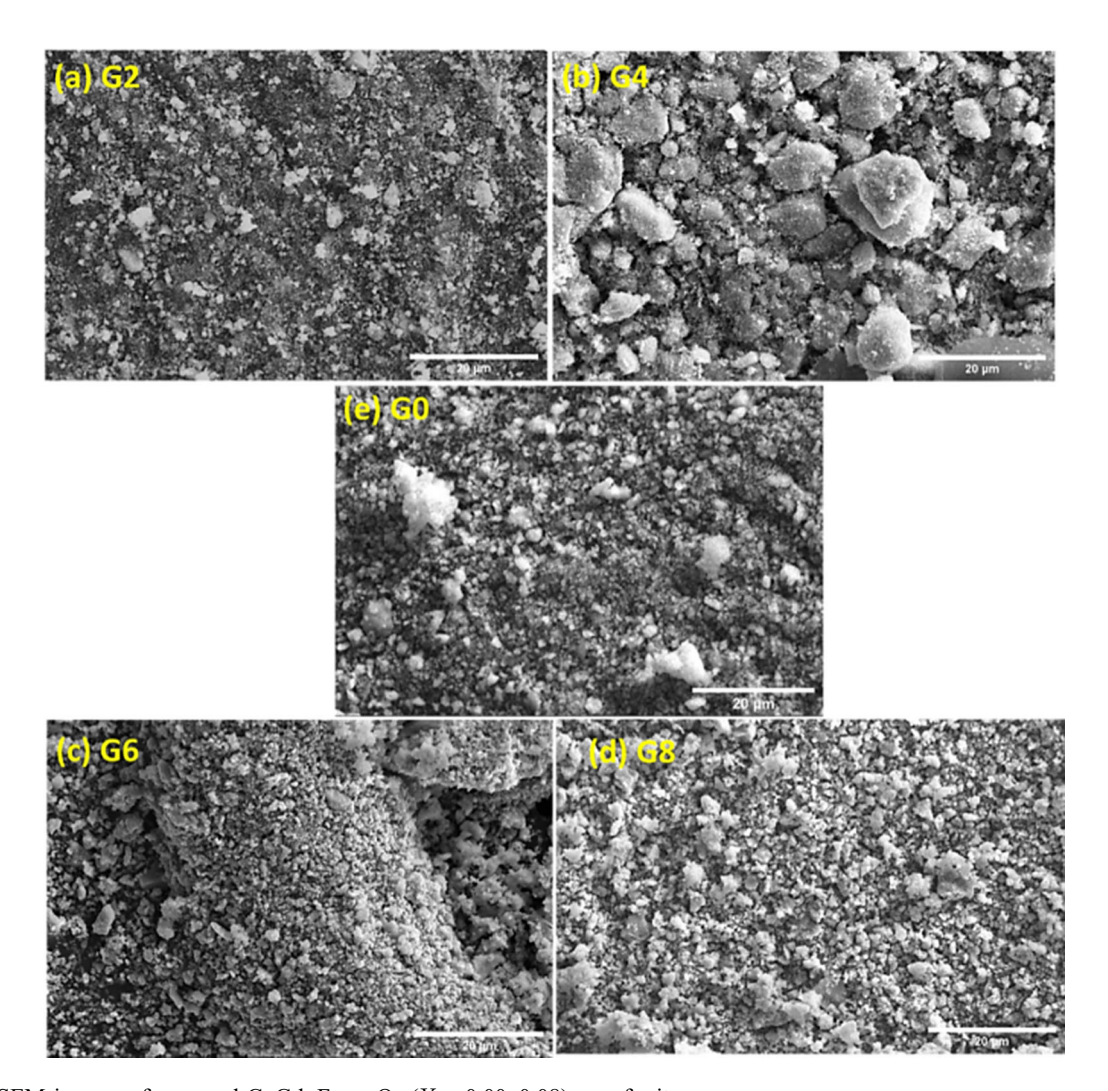


Fig. 3 FESEM images of prepared  $CoGd_XFe_{2-X}O_4$  (X = 0.00–0.08) nanoferrites

**Table 2** Functional parameters of prepared  $CoGd_XFe_{2-X}O_4$  (X = 0.00-0.08) nanoferrites

S.NO	Vibrational assignments	Experimental absorption (cm <sup>-1</sup> )						
		X = 0.00	X = 0.02	X = 0.04	X = 0.06	X = 0.08		
1	Metal-oxygen stretching vibration	585	585	585	585	585		
2	Stretching vibration of No <sub>3</sub>	1495	1495	1495	1495	1495		
3	Stretching vibration of $C = N$	2344	2344	2344	2344	2344		
4	C = H bending of carboxylic acid	2935	2935	2935	2935	2935		
5	O-H stretching vibration	3390	3390	330	3390	3390		

which are relatively high with previous reports [32]. Figure 8 shows that the indirect band gap values are 2.62, 2.73, 2.84, 2.96 and 3.09 eV respectively, which are also considerably higher values with previous reports [33].

The bandgap energy increased as the concentration of  $Gd^{3+}$  grew (X=0.00-0.08). This indicates an increase in energy level, which may be attributed to

the synergistic impact of the Gd<sup>3+</sup> ion, which reduces electron hole recombination and so increases the bandgap [34]. Table.3 shows that the bandgap value has increased which exhibits an inverse relationship between bandgap and crystallite size as the lattice parameter is increased. [35].



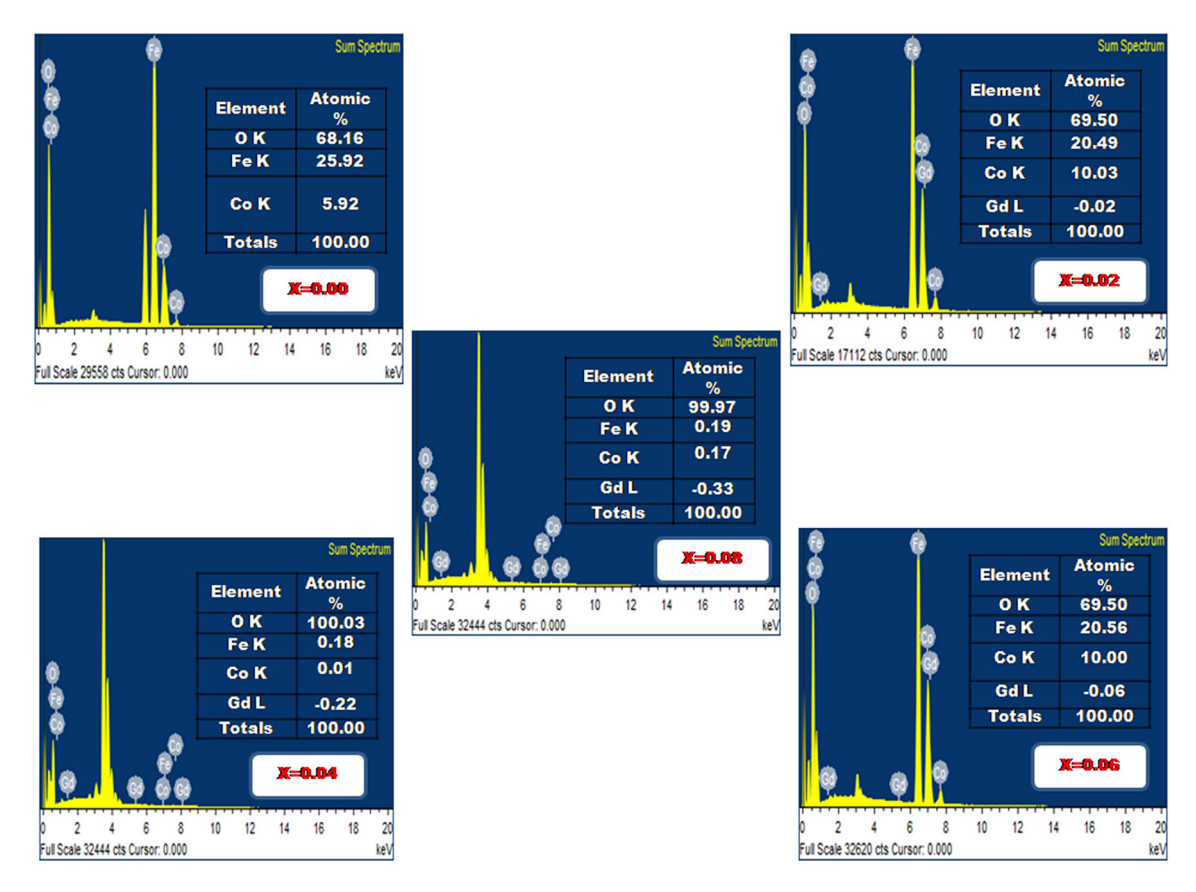
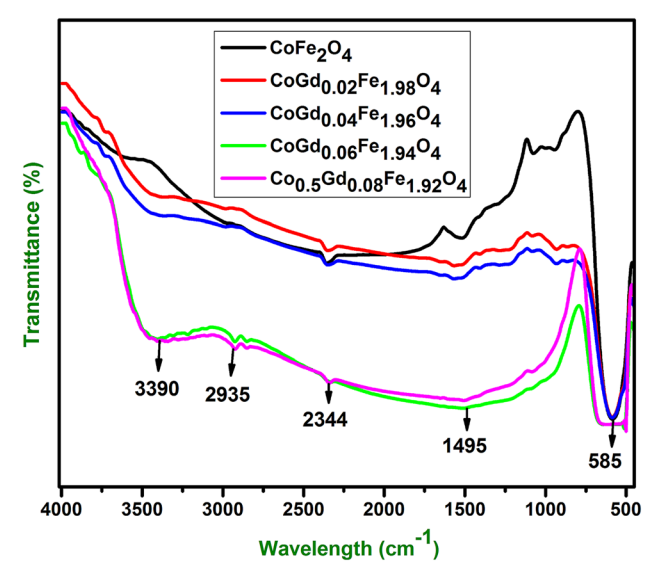


Fig. 4 EDAX images of prepared  $CoGd_XFe_{2-X}O_4$  (X = 0.00–0.08) nanoferrites



**Fig. 5** FTIR spectra of prepared  $CoGd_XFe_{2-X}O_4$  (X = 0.00-0.08) nanoferrites

## 3.5 Raman spectroscopy analysis

Raman spectroscopy analysis has been widely used to understand the key structural properties of the

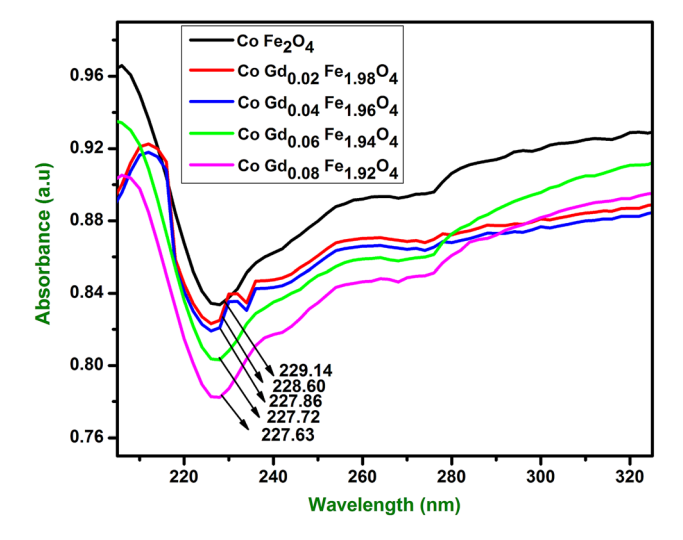


**Fig. 6** Absorbance spectra of prepared  $CoGd_XFe_{2-X}O_4$  (X = 0.00-0.08) nanoferrites from UV-DRS spectra

nanoparticles such as phase transition, structure and lattice distribution, spin-lattice, charge-lattice, couplings and magnetic ordering in nanoferrites [36]. Based on the group theory analysis of the lattice vibration, the cubic 3a spinel structure cobalt ferrite



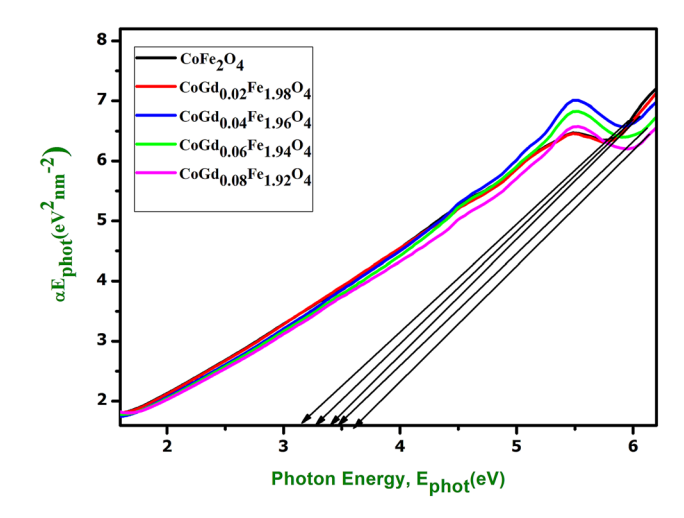


**Fig. 7** Direct bandgap energy of prepared  $CoGd_XFe_{2-X}O_4$  (X = 0.00-0.08) nanoferrites from UV-DRS spectra

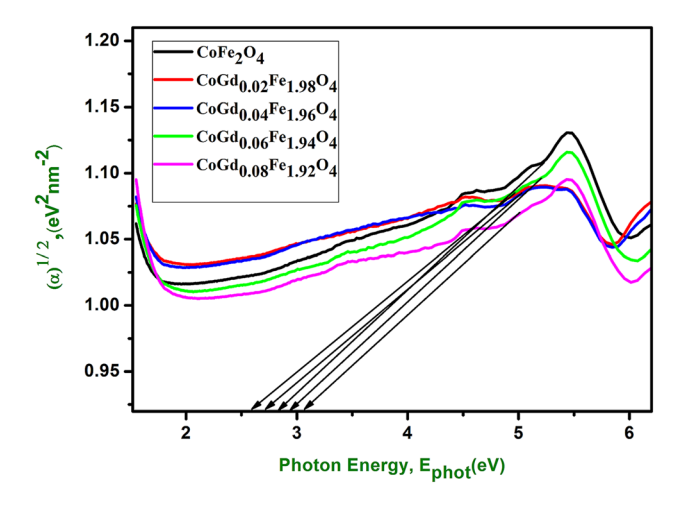


**Fig. 8** Indirect bandgap energy of  $CoGd_XFe_{2-X}O_4$  nanoferrites (X = 0.00-0.08) from UV-DRS spectra

has vibrational Raman active modes of vibrations  $(A_{1g} + E_g + 3T_{2g})$  [36, 37]. These modes are noticed due to the motion of anion and cation at A and B sites. The Raman spectra taken at room temperature in the Wavelength range of 200–800 cm<sup>-1</sup> at CoGd<sub>X</sub>-Fe<sub>2-X</sub>O<sub>4</sub> (X = 0.00–0.08) are shown in Fig. 9. The  $A_{1g}$ 

mode is organized to symmetric stretching of the oxygen atom, the T<sub>2g</sub> mode is associated to asymmetric stretching of oxygen atom with both octahedral and tetrahedral cation and Eg mode is organized to symmetric bending of oxygen atom [37]. The highest intensity of  $A_{1g}$  active mode split up into two modes  $(A_{1g})$  and  $(A_{2g})$  due to cation inversion [38]. The Raman modes at T<sub>2g</sub> and E<sub>g</sub> in the Gd-doped cobalt nanoferrites are at lower frequency region described the stability of the spinel structure. Table4 indicates the strong Raman mode above 600 cm<sup>-1</sup> represents to A<sub>1g</sub> mode and it can be associated to the symmetric stretching of oxygen atoms along with metal oxygen (M-O) and Fe-O bonds at tetrahedral sites. The Raman mode T<sub>2g</sub> (3) about 540 cm<sup>-1</sup> corresponds to 2 g asymmetric bending of oxygen atom,  $T_{2g}$  (2) mode around 465 cm<sup>-1</sup> corresponds to asymmetric stretching of M-O and Fe-O at Octahedral site and  $T_{2g}$  (1) Raman mode around 220 cm<sup>-1</sup> is assigned to translation motion of tetrahedral. The Raman active mode of  $E_g$  (1) are located at 310 cm<sup>-1</sup> is linked with symmetric bending of oxygen with metal ion [39].

In this study, the vibration modes above  $600 \text{ cm}^{-1}$  are associated with  $A_{1g}$  symmetry of metal-oxygen bond at tetrahedral sites. The doping of  $Gd^{3+}$  ions are expected to occupy at the octahedral sites [35] by exchange of  $Co^{2+}$  from octahedral to tetrahedral sites. And the vibrational frequency of Raman modes is moved to lower frequency region due to the crystallite size and cation redistribution of  $CoGd_XFe_{2-X}O_4$  (X = 0.00–0.08) nanoferrites.

## 3.6 Magnetic properties

Room temperature M-H loop study was carried out to analyze the magnetic behavior of  $CoGd_XFe_{2-X}O_4$  nanoferrites with applied magnetic field in the range of + 15,000 Oe as shown in Fig. 10. The magnetic behavior of S-shaped M-H hysteresis loops confirmed

**Table 3** Optical parameters of prepared  $CoGd_XFe_{2-X}O_4$  (X = 0.00-0.08) nanoferrites

Composition	Absorbance (nm)	Indirect band gap energy (eV)	Direct band gap energy (eV)
X = 0.00	234	3.14	2.62
X = 0.02	233	3.27	2.73
X = 0.04	232	3.39	2.84
X = 0.06	231	3.46	2.96
X = 0.08	230	3.61	3.09



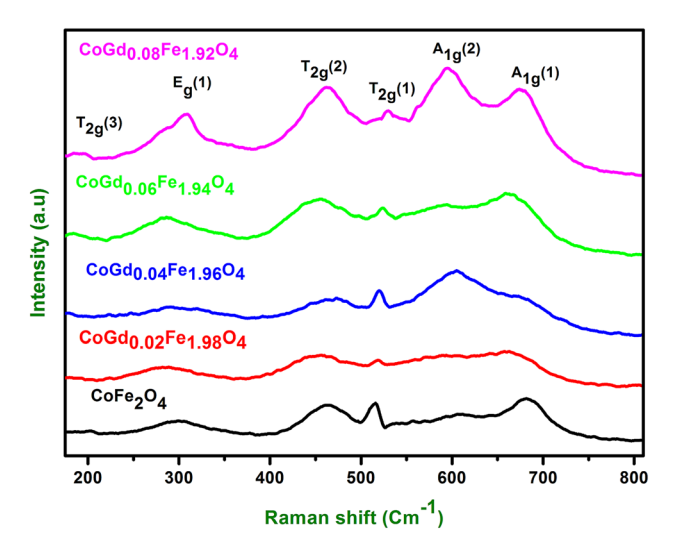


**Fig. 9** Raman studies of prepared  $CoGd_XFe_{2-X}O_4$  (X = 0.00-0.08) nanoferrites

soft magnetic nature which can be associated to cubic spinel nanoferrites [40].

The hysteresis curve exhibits ferromagnetic behavior. The cation distribution in tetrahedral and octahedral nanocrystalline materials, chemical composition, synthesis process, and crystallite size all influence the magnetic characteristics of the material [41, 42]. The magnetic parameters such as Retentivity  $(M_r)$ , Coercivity  $(H_C)$ , magnetic saturation  $(M_S)$ , Anisotropy constant (K), squareness ratio and magnetic moment are evolved from the hysteresis loop and the variation of each magnetic parameters are listed in Table 5. The magnetic saturation decreases from 26 to 13 (X = 0.00-0.08) with increment of Gd<sup>3+</sup> ions in the cobalt ferrites due to decrease of crystallite size. This could be readily due to the presence of magnetically inactive layers at particle surfaces, which can get more promoted as crystallite size decreases. This concept was explained from the theory of dead layer, i.e. core shell model [43].

In the core shell model, the magnetic particles are shielded inside the non-magnetic layer. And also, it can be discussed based on the changes in A-B

**Table 4** Raman studies of prepared  $CoGd_XFe_{2-X}O_4$  (X = 0.00-0.08) nanoferrites

Composition	A <sub>1g</sub> (1)	A <sub>1g</sub> (1)	T <sub>2g</sub> (1)	T <sub>2g</sub> (2)	E <sub>g</sub> (1)	T <sub>2g</sub> (3)
CoFe <sub>2</sub> O <sub>4</sub>	199	305	462	517	614	683
$CoGd_{0.02}Fe_{1.98}O_4$	222	284	450	520	604	666
$CoGd_{0.04}Fe_{1.96}O_4$	197	285	459	519	608	679
$CoGd_{0.06}Fe_{1.94}O_4$	207	291	455	524	601	668
$CoGd_{0.08}Fe_{1.92}O_4$	195	308	462	532	599	679

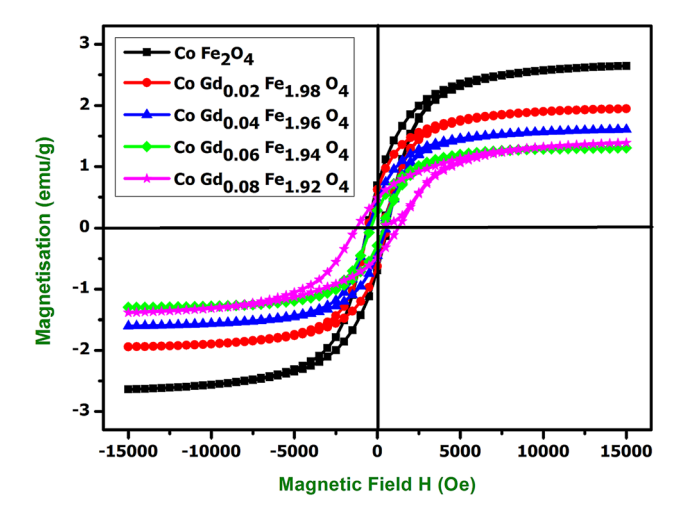


**Fig. 10** Hysteresis loop of prepared  $CoGd_XFe_{2-X}O_4$  (X = 0.00-0.08) nanoferrites

exchange interaction between Octahedral (B) and tetrahedral (A) sub lattices. The cubic structure of spinel nanoferrites has various crystallographic sublattices for magnetic ions, i.e. Octahedral (B) and tetrahedral (A). Three types of magnetic interaction are involved among the magnetic ions, i.e. AA interaction, BB interaction and AB interaction. In spinel nanoferrites, magnetic order is strong because of super-exchange interaction among the magnetic ions in the A and B sub lattices intermediate by oxygen ions. The surface effect for oxide nano material leads to decrease of magnetic saturation. The magnetic dead layer on the spin canting effect in the whole volume of the crystallite could be the reason for decrease in magnetic saturation [44].

Coercivity of the nanoparticles depends on defects, porosity, strain, synthesis process and magnetic crystalline anisotropy etc. The value of coercivity increased with increase of  $Gd^{3+}$  ions as the crystallite size decreased. It can be clarified based on the Stoner Wohlforth theory, the coercivity value is correlated to the anisotropy constant (K) by the expression [46];

Composition	$\begin{array}{c} \text{Magnetization} \\ \text{(M}_{s}\text{)} \\ \text{(emu/g)} \end{array}$	Remanent magnetization $(M_r)$ (emu/g)	Coercivityity (Hc) (Oe)	Squareness ratio $(M_r/M_s)$ (No unit)	Anisotropy constant ( <i>K</i> ) (Oe)	Bohr magneton $(\eta_B) (\mu_B)$
X = 0.00	26.0	69.3	394.5	0.33	106.3	0.33
X = 0.02	19.5	62.4	520.5	0.32	85.3	0.24
X = 0.04	16.0	48.1	564.5	0.30	84.3	0.20
X = 0.06	13.9	45.2	600.5	0.26	80.0	0.17
X = 0.08	13.0	28.7	609.5	0.22	79.8	0.16

**Table 5** Magnetic parameters of prepared  $CoGd_XFe_{2-X}O_4$  (X = 0.00-0.08) nanoferrites

$$H_c = 0.98 \times K/M_S \tag{8}$$

where K is the anisotropy constant,  $H_c$  is coercivity and  $M_s$  is magnetic saturation. In Table6, it is noticed that anisotropic constant increases with decrease of crystallite size from XRD, and it leads to an increase in coercivity. Based on this relation, Hc and K are inversely proportional to  $M_s$  which is constant with the results. The magnetic moment ( $\mu_B$ ) was estimated using relation [45]:

$$\eta_{\rm B} = M \times M_S / 5585 \tag{9}$$

where *M* is the molecular weight of Gd<sup>3+</sup> ions, *X* is the concentration. Because Gd<sup>3+</sup> has a higher ionic radius than Fe<sup>3+</sup>, the magnetic moment in cobalt nanoferrites decreases as the amount of Gd<sup>3+</sup> ion increases. This is due to less magnetic contact between B and A sites. The presence of rare-earth ions has been found to alter spin-orbit coupling. As Gd<sup>3+</sup> is a rare-earth cation, it causes collinear ferromagnetic arrangements on B sites to change into noncollinear ferromagnetic orders of spins. The majority of Co<sup>2+</sup> ions occupy B sites in CoFe<sub>2</sub>O<sub>4</sub> ferrites, with the remainder Co<sup>2+</sup> ions occupying A sites. As a result of the Gd<sup>3+</sup> ions occupying B sites, the collinear arrangements of spins are deformed, resulting in a

drop-in saturation. The fact that the squareness ratio was so low, suggested the presence of multidomain particles in these nanoferrites [46].

The addition of Gd<sup>3+</sup> ions in CoFe<sub>2</sub>O<sub>4</sub>, being as non-magnetic ion substitution in the spinel lattice, which decreases the magnetic exchange interaction between A and B site, leads to decrease in magnetic saturation. Smaller value of coercive field was achieved due to these nanoferrites which are applicable for magnetic shielding devices [47].

# 3.7 Impedance spectroscopy

Impedance spectroscopy is one of the most powerful tools for spectrum analysis which gives more information regarding real and imaginary part of an electrical component in nanoferrites and also effectively used for investigating electrical behaviors like electric, conductivity and relaxation characteristic in terms of the grain boundary and grain of the prepared nanoferrites.

#### 3.8 (a) Real part of impedance spectroscopy

The real part of impedance spectroscopy (z') as a function of frequency is shown in Fig. 11. From the

**Table 6** Dielectric parameters of prepared  $CoGd_XFe_{2-X}O_4$  (X = 0.00-0.08) nanoferrites

Composition	Dielectric constant $(\varepsilon')$	Dielectric loss $(\tan \delta)$	Complex dielectric constant ( $\epsilon$ ")	AC conductivity ( $\Omega$ ) (cm <sup>-1</sup> )
X = 0.00	949	1.13	1070	0.30
X = 0.02	1799	0.56	1002	0.32
X = 0.04	10,222	0.07	759	0.36
X = 0.06	14,588	0.06	817	0.39
X = 0.08	32,630	0.03	929	0.42



figure, real part (z') decreases with increase of frequency and then remains same at a higher frequency which implies increase in AC conductivity. The real part of impedance decreases with increase of Gd<sup>3+</sup> ions and then tends to merge at high frequency. This is occurring because release of space charge can lead to reduction in barrier properties for material [48].

# 3.9 (b) Imaginary part of impedance spectroscopy

The imaginary part of the impedance spectroscopy also decreases with increase of frequency and at last merges at higher frequency. The imaginary part of the impedance decreases with increasing of Gd<sup>3+</sup> ions and then the curve tends to merge at higher frequencies as shown in Fig. 12. The observed peak in the z" parts are due to existence of the space charge relaxation, undertaken with the space charge carriers infer from oxygen vacancies [49]. Space charge polarization is found to be higher when the material is composed with grain and grain boundaries.

# 3.10 (c) Cole-cole plot

Figure 13 shows the cole–cole plot for  $GdCo_XFe_{2-X}O_4$  with series of X = 0.00–0.08. The plot clearly shows semicircular arc, which denoted the electron interface grain boundary and grain contribution to the conductivity [50]. The material's grain conduction mechanism, which is produced by a parallel combination of grain capacitance and grain resistance, is responsible for the appearance of a semicircle in the high frequency region. The semicircle symbolizes the

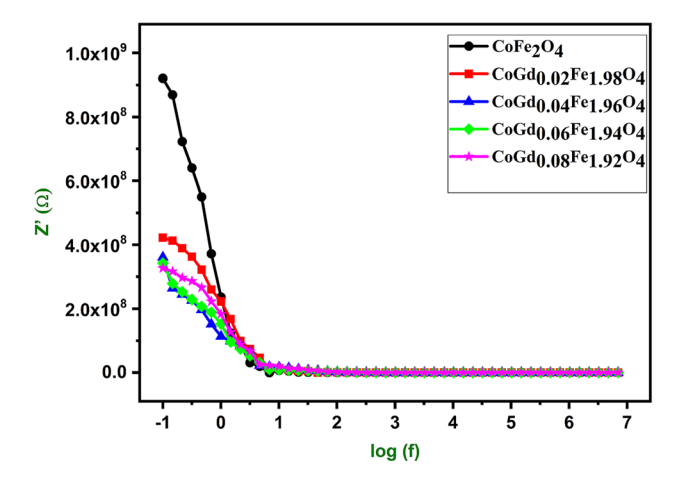


**Fig. 11** Real part of impedance spectra of prepared  $CoGd_XFe_{2-X}O_4$  (X=0.00-0.08) nanoferrites

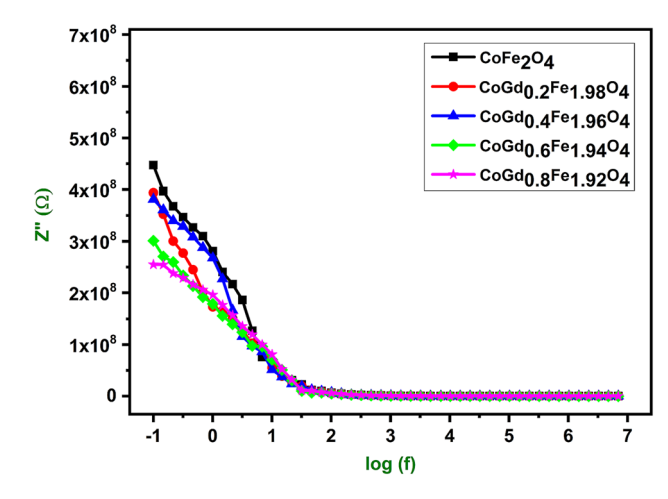
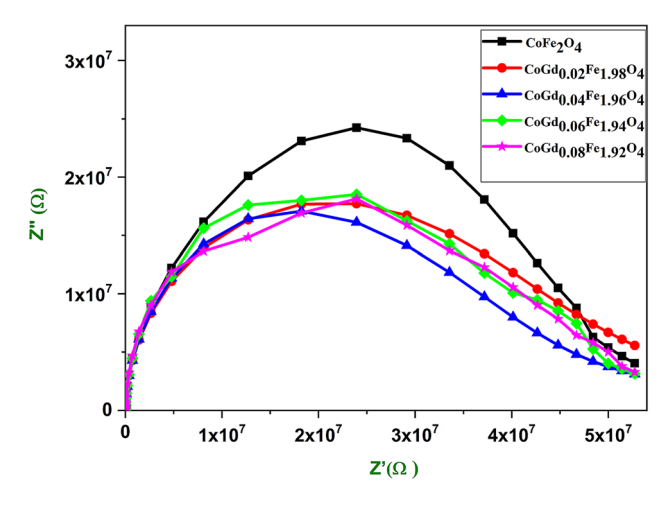


Fig. 12 Imaginary part of impedance spectra of prepared  $CoGd_XFe_{2-X}O_4$  (X = 0.00-0.08) nanoferrites

low frequency area and is created by grain boundary conduction in materials, which happens when the material's grain boundary capacitance and grain boundary resistance are coupled in parallel [51].

The observed semicircle was successfully fitted by the equivalent circuit model as shown in Fig. 14. In the present study, the major role in the conduction is observed to occur due to grain boundary contribution. Substitution of  $\mathrm{Gd}^{3+}$  ions in cobalt ferrites increases the grain boundary resistance, where  $R_{\mathrm{gb}}$  and  $R_{\mathrm{g}}$  are the resistance of the grain boundaries and grains.  $\mathrm{CPE}_{\mathrm{gb}}$  and  $\mathrm{CPE}_{\mathrm{g}}$  are constant phase element of grain boundaries and grains. This boundary is greater than that of the grain contribution which is occurred due to the effect of smaller crystallite size.



**Fig. 13** Nyquist plots of prepared  $CoGd_XFe_{2-X}O_4$  (X = 0.00-0.08) nanoferrites



#### 4 Dielectric studies

#### 4.1 (a) Dielectric constant ( $\epsilon'$ )

Figure 15 shows the dielectric constant ( $\varepsilon'$ ) measured to the material at the frequency range in 100 mHz-10 MHz at room temperature. With the increase in frequency, the dielectric constants decrease. The dielectric constant declines sharply at low frequencies, but becomes frequency independent at high frequencies. The Maxwell-Wagner model of interfacial polarization, which agrees with the Koop model, is used to explain the fluctuation in dielectric constant [52]. The structure of spinel ferrites is assumed to have strongly conducted layers as grains in an insulating matrix with poor conduction layers as grain borders, according to Maxwell-Wagner [53]. At low frequencies, grain boundaries are more active than grains; hence the dielectric constant is higher at low frequencies and rapidly drops as frequency increases [54]. As electrons are ready to reach the poor conducting phase grain boundaries under the influence of an applied AC electric field. As a result, these electrons clump together, causing space charge polarization.

As a result, the dielectric constant is high at low frequencies and drops as frequency increases. In spinel ferrites, the formation of  $Fe^{3+}$  ions occur due to the exchange of electrons between  $Co^{2+}$  and  $Fe^{3+}$  to join a pair of  $Co^{3+}$  and  $Fe^{2+}$  [55].

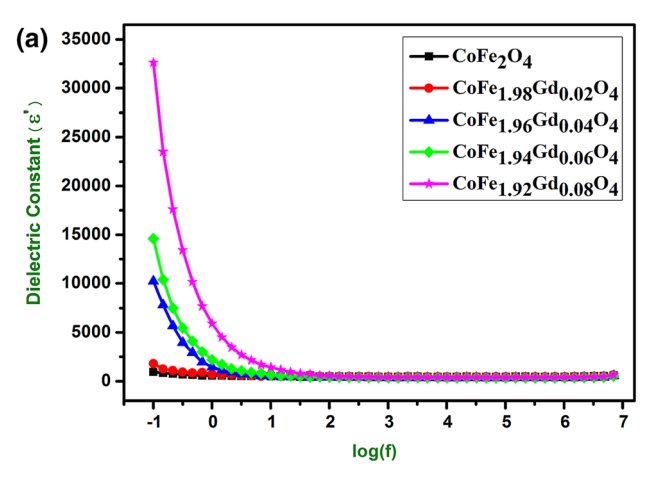
The electron transfer from Fe<sup>3+</sup> to Fe<sup>2+</sup> causes a local displacement of the electron in the direction of the applied field, which explains ferrites' polarization. The polarization diminishes with increasing frequency until it reaches a constant value. As crystallite sizes shrink to the nanoscale, space polarization becomes increasingly important in determining the material's dielectric constant [56]. The dielectric constant was evaluated using the below equation [49, 56]:

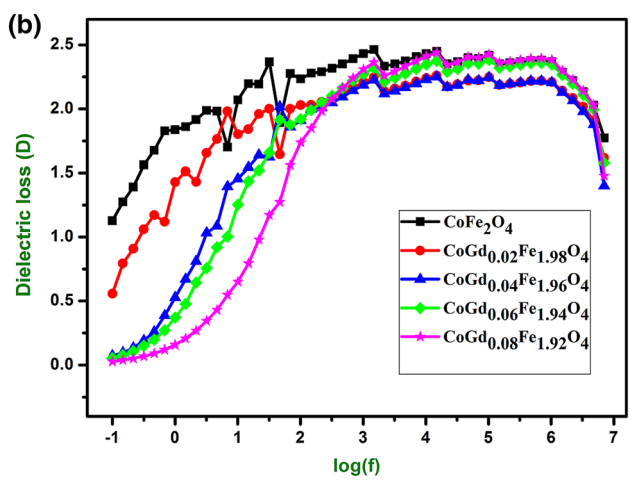
$$\varepsilon' = Cd/\varepsilon_0 A \tag{10}$$



**Fig. 14** Equivalent circuit model of prepared  $CoGd_XFe_{2-X}O_4$  (X = 0.00-0.08) nanoferrites







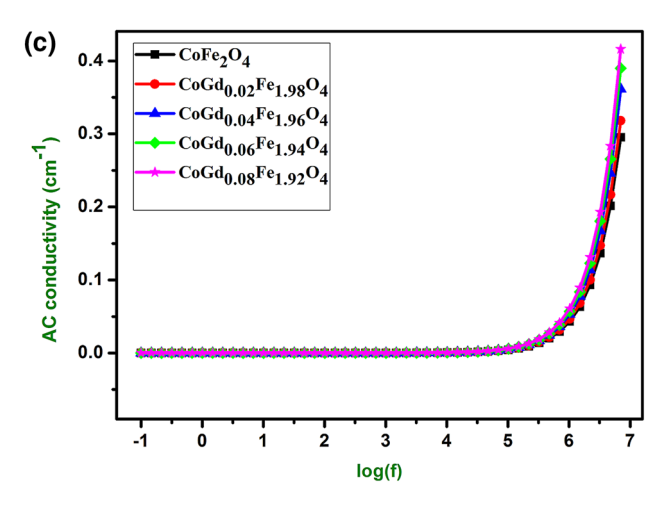


**Fig. 15 a** Dielectric constant of prepared  $CoGd_XFe_{2-X}O_4$  (X = 0.00-0.08) nanoferrites. **b** Dielectric loss of prepared  $CoGd_XFe_{2-X}O_4$  (X = 0.00-0.08) nanoferrites. **c** AC Conductivity vs Frequency of prepared  $CoGd_XFe_{2-X}O_4$  (X = 0.00-0.08) nanoferrites

where C is the capacitance, d is thickness of the cylindrical pellet, A is area of the circular pellet,  $\varepsilon_0$  is permittivity of free space. In Table 6, the value of dielectric constant 949, 1799, 10,223, 14,588 and 32,630 respectively increases with increase of  $Gd^{3+}$  ions. Furthermore, with increase of  $Gd^{3+}$  ions, the crystallite size decreases. Due to this, surface effects are increased the grain boundaries become highly active at lower frequency. The observed results showed increase in the value of dielectric constant for these samples.

#### 4.2 (b) Dielectric loss

The dielectric loss with respect to the frequency is shown in Fig. 15a. The dielectric losses are low at lower frequency and gradually increase with increase of frequency and also in the end, dielectric loss decreases at high frequency. This abnormal behavior of dielectric loss is due to dielectric relaxation peaks which could be described by Rezescu model [57]. In the view of Rezescu model, the dielectric relaxation peaks produce a combined involvement of N-type and P-type charge carriers. Beo et al. [58] stated that the small polarons created in a material also associate to the polarization in addition to the N-type charge carriers which exhibits to abnormal behavior of dielectric loss. Furthermore, the hopping frequency of localized charge carriers being linearly equal to the externally applied frequency and response occurring, resulting in the construction of the relaxation peak, can be linked to the establishment of the relaxation peak. The complex dielectric constant and dielectric loss are determined using the equations below [56]:

$$\tan \delta = 1/2\pi f \varepsilon_0 \varepsilon' \tag{11}$$

$$\varepsilon'' = \varepsilon' \tan \delta \tag{12}$$

The value of dielectric losses are 1.13, 0.56, 0.07, 0.06 and 0.03 which respectively decreases with increasing of Gd<sup>3+</sup> ions. The electron exchanges between Fe<sup>3+</sup> and Fe<sup>2+</sup> need more energy and accordingly more energy loss occur due to high resistivity in grain boundaries. Furthermore, the amount of energy recovered was used to transfer the oscillating ions and these leads to dielectric loss. The irregular phenomenon is in the impedance and loss tangent may raise due to the electrical relaxation process of charge carriers in the nanoferrites, which might have not influenced\controlled by certain Gd

doping levels. Because the relaxation has occurred due to the electrons/defects generated by incorporation of  $Gd^{3+}$  ions (aliovalent substitutions  $Gd^{3+}$   $\leftrightarrow$   $Fe^{2+}$ ). As the impedance plots shown single semicircle, the time constant ( $t = R \times C$ ), the distribution of relaxation time could be possible only if the movement of the ions over an extensive distance from the low frequency points. Therefore, the lower Gd concentration (0–0.06) might have struggled to maintain the relaxation as it doesn't have such defect environment in the crystal system.

# 4.3 (c) AC conductivity

Figure 15b shows the variation of Ac conductivity of the Gd<sup>3+</sup>-doped cobalt nanoferrites at various frequencies (100 mHz–10 MHz). In spinel nanoferrites, the conduction mechanism can be explained by the Verwey mechanism [59].

The conduction is due to electron hopping between ions of the same element with various valence states at the octahedral (B) site, according to this mechanism. The following equation can be used to describe electron migration [60]:

$$Co^{2+} + Fe^{3+} \leftrightarrow Co^{3+} + Fe^{2+}$$
 (13)

The migration of electron in between  $\mathrm{Fe^{3+}}$  and  $\mathrm{Fe^{2+}}$  present at the octahedral site in spinel ferrites is under the impact of applies Ac field and it owes to the electrical response of these ferrites. The electrical conductivity of nanoferrites is increased slowly at lower frequency, and then increases sharply at a higher frequency. Furthermore, in Table 6, an increase of conductivity in  $\mathrm{Fe^{3+}}$  ions at the octahedral sites with the doping of  $\mathrm{Gd^{3+}}$  ion in the cobalt ferrites play a major role in enhancing the Ac conductivity of  $\mathrm{CoGd_XFe_{2-X}O_4}$  nanoferrites (X = 0.00-0.08) [61–64]. The dielectric parameters such as dielectric constant, complex dielectric constant, dielectric loss and ac conductivity are listed in Table 6.

#### 5 Conclusions

The production of  $Gd^{3+}$ -doped cobalt nanoferrites of a spinel crystal  $CoGd_XFe_{2-X}O_4$  (X=0.00-0.08) via the sol-gel method is described briefly in this paper. The impact of  $Gd^{3+}$  ion substitutions in cobalt nanoferrites on structural, functional, optical, magnetic, and dielectric properties were examined. The



cubic spinel structure of these nanoferrites was confirmed by X-ray diffraction patterns. In cobalt nanoferrites, the average crystallite size falls as the number of Gd<sup>3+</sup> ions increase. Because of the change in ionic radius, the lattice constant and unit cell dimension rise as the number of Gd<sup>3+</sup> ions increase. The porosity reduces as the number of Gd<sup>3+</sup> ions increase, which is related to an increase in bulk density, but the surface area increases as the number of Gd<sup>3+</sup> ions fall, which is due to a reduction in crystallite size. The particles are spherical-shaped grains with agglomeration, according to surface morphology.

The performance of grain and grain boundaries towards capacitance and resistance was shown by the Cole-Cole plot using impedance spectroscopy, implying that grain boundary contribution is higher than grain contribution. With increasing frequency, the variation of the dielectric constant diminishes. It is thought that the addition of Gd<sup>3+</sup> had a substantial impact on the Maxwell-Wagner interfacial charge polarization model, which agreed with the Koop model. The values of dielectric constant are increased with increase of Gd<sup>3+</sup> ions. The value of dielectric losses decreases with increase of Gd<sup>3+</sup> ions. The result also reveals abnormal behavior of dielectric loss and the same is due to relaxation peak. AC conductivity increases with increase of frequency as a function of increase with Gd<sup>3+</sup> ions concentration as the spinels undergone Verwey mechanism. The very low dielectric loss and minimum magnetic saturation of these prepared nanoferrites has potential application in magnetic recording devices, magnetic shielding and microwave absorption devices. Further, reported solgel technique provides cost-effective and green synthesis alternative for large scale production for industrial products and also for environmental advantages.

#### **Author contributions**

IKP: project administration, writing—original draft preparation. AR: methodology, data curation. SJJ: investigation, conceptualization. MJ, SAK: resources.

# **Funding**

There is no funding for this study.



# Data availability

Not applicable.

# Code availability

Not applicable.

#### **Declarations**

**Conflict of interest** This research did not receive any specific grant from funding agencies in the public, commercial, or not-for-profit sectors.

#### References

- M. Rashad, E. Elsayed, M. Moharam, R. Abou-Shahba, A. Saba, Structure and magnetic properties of Ni<sub>x</sub>Zn<sub>1-x</sub>Fe<sub>2</sub>O<sub>4</sub> nanoparticles prepared through co-precipitation method.
   J. Alloy. Compd. 486(1–2), 759–767 (2009). https://doi.org/10.1016/j.jallcom.2009.07.051
- K.R. Krishna, K.V. Kumar, C. Ravindernathgupta, D. Ravinder, Magnetic properties of Ni-Zn ferrites by citrate gel method. Adv. Mater. Phys. Chem. 2(3), 149–154 (2012). h ttps://doi.org/10.4236/ampc.2012.23022
- S.M. El-Sheikh, M.M. Rashad, F.A. Harraz, Morphological investigation and magnetic properties of nickel zinc ferrite 1D nanostructures synthesized via thermal decomposition method. J. Nanopart. Res. 15(10), 1–11 (2013). https://doi. org/10.1007/s11051-013-1967-9
- K. Tanbir, M.P. Ghosh, R.K. Singh, S. Mukherjee, Gd-doped soft Mn–Zn nanoferrites: synthesis, microstructural, magnetic and dielectric characterizations. J. Mater. Sci.: Mater. Electron. (2020). https://doi.org/10.1007/s10854-020-02901-1
- S. Abbas, R. Chatterjee, A. Dixit, A. Kumar, T. Goel, Electromagnetic and microwave absorption properties of (Co<sup>2+</sup>–Si<sup>4+</sup>) substituted barium hexaferrites and its polymer composite. J. Appl. Phys. 101(7), 074105 (2007). https://doi.org/10.1063/1.2716379
- R.C. Che, L.M. Peng, X.F. Duan, Q. Chen, X.L. Liang, Microwave absorption enhancement and complex permittivity and permeability of Fe encapsulated within carbon nanotubes. Adv. Mater. 16(5), 401–405 (2004). https://doi.org/10.1002/ adma.200306460
- Y. Huang, N. Li, Y. Ma, F. Du, F. Li, X. He, X. Lin, H. Gao, Y. Chen, The influence of single-walled carbon nanotube structure on the electromagnetic interference shielding efficiency of its epoxy composites. Carbon 45(8), 1614–1621 (2007). https://doi.org/10.1016/j.carbon.2007.04.016

- J.J. Siddiqui, K. Zhu, J. Qiu, H. Ji, Sol–gel synthesis, characterization and microwave absorbing properties of nano sized spherical particles of La<sub>0.8</sub>Sr<sub>0.2</sub>Mn<sub>0.8</sub>Fe<sub>0.2</sub>O<sub>3</sub>. Mater. Res. Bull. 47(8), 1961–1967 (2012). https://doi.org/10.1016/j.materresbull.2012.04.017
- M. Meshram, N.K. Agrawal, B. Sinha, P. Misra, Characterization of M-type barium hexagonal ferrite-based wide band microwave absorber. J. Magn. Magn. Mater. 271(2–3), 207–214 (2004). https://doi.org/10.1016/j.jmmm.2003.09.045
- M.P. Ghosh, S. Mukherjee, Ce<sup>3+-</sup>doped nanocrystalline cobalt–zinc spinel ferrite: microstructural, magnetic, and optical characterizations. J. Mater. Sci.: Mater. Electron. (2020). https://doi.org/10.1007/s10854-020-03174-4
- N. Lenin, K. Sakthipandi, R.R. Kanna, G. Rajkumar, Electrical, magnetic and structural properties of polymer-blended lanthanum-added nickel nano-ferrites. Ceram. Int. 44(17), 21866–21873 (2018). https://doi.org/10.1016/j.ceramint.2018.08.295
- M. Ahmed, N. Okasha, R. Kershi, Influence of rare-earth ions on the structure and magnetic properties of barium W-type hexaferrite. J. Magn. Magn. Mater. 320(6), 1146–1150 (2008). https://doi.org/10.1016/j.jmmm.2007.11.014
- L. Phor, V. Kumar, Structural, thermomagnetic, and dielectric properties of Mn0.5Zn0.5GdxFe2–xO4 (x = 0, 0.025, 0.050, 0.075, and 0.1).
   J. Adv. Ceram. 9(2), 243–254 (2020). https://doi.org/10.1007/s40145-020-0364-y
- N. Lenin, R.R. Kanna, K. Sakthipandi, A.S. Kumar, Structural, electrical and magnetic properties of NiLa<sub>x</sub>Fe<sub>2-x</sub>O<sub>4</sub> nanoferrites. Mater. Chem. Phys. 212, 385–393 (2018). https://doi.org/10.1016/j.matchemphys.2018.03.062
- M. Junaid, M.A. Khan, Z.M. Hashmi, G. Nasar, N.A. Kattan, A. Laref, Structural, spectral, magnetic and dielectric properties of Bi substituted Li-Co spinel ferrites. J. Mol. Struct. 1221, 128859 (2020). https://doi.org/10.1016/j.molstruc.202 0.128859
- A.M. Bolarín-Miró, P. Vera-Serna, F. Sánchez-De Jesús, C.A. Cortés-Escobedo, A. Martínez-Luevanos, Mechanosynthesis and magnetic characterization of nanocrystalline manganese ferrites. J. Mater. Sci. Mater. Electron. 22(8), 1046–1052 (2011). https://doi.org/10.1007/s10854-010-0257-x
- N. Sivakumar, A. Narayanasamy, N. Ponpandian, G. Govindaraj, Grain size effect on the dielectric behavior of nanostructured Ni0.5 Zn0.5Fe2 O4. J. Appl. Phys. 101(8), 84116 (2007). https://doi.org/10.1063/1.2721379
- M. Ahmed, E. Ateia, F. Salem, Spectroscopic and electrical properties of Mg–Ti ferrite doped with different rare-earth elements. Phys. B 381(1–2), 144–155 (2006). https://doi.org/ 10.1016/j.physb.2005.12.265
- F. Bensebaa, F. Zavaliche, P. L'ecuyer, R. Cochrane, T. Veres, Microwave synthesis and characterization of Co-ferrite

- nanoparticles. J. Colloid Interface Sci. **277**(1), 104–110 (2004). https://doi.org/10.1016/j.jcis.2004.04.016
- P. Scherrer, Bestimmung der Grösse und der inneren Struktur von Kolloidteilchen mittels Röntgenstrahlen. Nachr. Ges. Wiss. Göttingen 26, 98 (1918)
- 21. J.I. Langford, A.J.C. Wilson, Scherrer after sixty years: a survey and some new results in the determination of crystallite size. J. Appl. Cryst. 11, 102 (1978)
- V. Uvarov, I. Popov, Metrological characterization of X-ray diffraction methods for determination of crystallite size in nano-scale materials. Mater. Charact. 85, 111 (2013)
- J. Peng, M. Hojamberdiev, Y. Xu, B. Cao, J. Wang, H. Wu, Hydrothermal synthesis and magnetic properties of gadolinium-doped CoFe<sub>2</sub>O<sub>4</sub> nanoparticles. J. Magn. Magn. Mater. 323(1), 133–137 (2011). https://doi.org/10.1016/j.jmmm.201 0.08.048
- 24. N. Lenin, A. Karthik, S.R. Srither, M. Sridharpanday, S. Surendhiran, M. Balasubramanian, Synthesis, structural and microwave absorption properties of Cr-doped zinc lanthanum nanoferrites Zn1-xCrxLa0.1Fe1.9O4 (x=0.09, 0.18, 0.27 and 0.36). Ceram. Int. 47, 34891–34898 (2021)
- N. Rezlescu, E. Rezlescu, C. Pasnicu, M. Craus, Effects of the rare-earth ions on some properties of a nickel-zinc ferrite.
   J. Phys.: Condens. Matter 6(29), 5707 (1994). https://doi.org/ 10.1088/0953-8984/6/29/013
- M.T. Rahman, C. Ramana, Gadolinium-substitution induced effects on the structure and AC electrical properties of cobalt ferrite. Ceram. Int. 40(9), 14533–14536 (2014). https://doi. org/10.1016/j.ceramint.2014.05.140
- Z. Peng, X. Fu, H. Ge, Z. Fu, C. Wang, L. Qi, H. Miao, Effect of Pr<sup>3+</sup> doping on magnetic and dielectric properties of Ni–Zn ferrites by "one-step synthesis." J. Magn. Magn. Mater. 323(20), 2513–2518 (2011). https://doi.org/10.1016/j.jmmm. 2011.05.033
- D. Bobade, S. Rathod, M.L. Mane, Sol–gel auto-combustion synthesis, structural and enhanced magnetic properties of Ni<sup>2+</sup> substituted nanocrystalline Mg–Zn spinel ferrite. Phys. B: Condens. Matter 407(18), 3700–3704 (2012). https://doi.org/10.1016/j.physb.2012.05.017
- J. Ghodake, R.C. Kambale, T. Shinde, P. Maskar, S. Suryavanshi, Magnetic and microwave absorbing properties of Co<sup>2+</sup> substituted nickel–zinc ferrites with the emphasis on initial permeability studies. J. Magn. Magn. Mater. 401, 938–942 (2016). https://doi.org/10.1016/j.jmmm.2015.11.009
- B. Purnama, A.T. Wijayanta, Effect of calcination temperature on structural and magnetic properties in cobalt ferrite nano particles. J. King Saud Univ.-Sci. 31(4), 956–960 (2019). https://doi.org/10.1016/j.jksus.2018.07.019
- 31. P. Sivakumar, R. Ramesh, A. Ramanand, S. Ponnusamy, C. Muthamizhchelvan, Preparation and properties of nickel



- ferrite (NiFe<sub>2</sub>O<sub>4</sub>) nanoparticles via sol–gel auto-combustion method. Mater. Res. Bull. **46**(12), 2204–2207 (2011). https://doi.org/10.1016/j.materresbull.2011.09.010
- Z. Wang, Y. Xie, P. Wang, Y. Ma, S. Jin, X. Liu, Microwave anneal effect on magnetic properties of Ni0.6Zn0.4Fe2O4 nano-particles prepared by conventional hydrothermal method. J. Magn. Magn. Mater. 323(23), 3121–3125 (2011). https://doi.org/10.1016/j.jmmm.2011.06.068
- L. Zhang, R. He, H.-C. Gu, Oleic acid coating on the monodisperse magnetite nanoparticles. Appl. Surf. Sci. 253(5), 2611–2617 (2006). https://doi.org/10.1016/j.apsusc.2 006.05.023
- 34. B. Vigneshwaran, P. Kuppusami, A. Panda, A. Singh, H. Sreemoolanadhan, Microstructure and optical properties of Ba<sub>0.6</sub>Sr<sub>0.4</sub>TiO<sub>3</sub> thin films prepared by pulsed laser deposition. Mater. Res. Exp. 5(6), 66420 (2018). https://doi.org/10.1088/2053-1591/aacb12
- S. Asiri, M. Sertkol, S. Guner, H. Gungunes, K. Batoo, T.A. Saleh, H. Sozeri, M.A. Almessiere, A. Manikandan, A. Baykal, Hydrothermal synthesis of Co<sub>y</sub>Zn<sub>y</sub>Mn<sub>1-2y</sub>Fe<sub>2</sub>O<sub>4</sub> nanoferrites: magneto-optical investigation. Ceram. Int. 44(5), 5751–5759 (2018). https://doi.org/10.1016/j.ceramint.2017.1 2.233
- T. Alves, H. Pessoni, A. Franco Jr., The effect of Y<sup>3+</sup> substitution on the structural, optical band-gap, and magnetic properties of cobalt ferrite nanoparticles. Phys. Chem. Chem. Phys. 19(25), 16395–16405 (2017). https://doi.org/10.1039/c7cp02167d
- X. Li, Y. Hou, Q. Zhao, L. Wang, A general, one-step and template-free synthesis of sphere-like zinc ferrite nanostructures with enhanced photocatalytic activity for dye degradation. J. Colloid Interface Sci. 358(1), 102–108 (2011). h ttps://doi.org/10.1016/j.jcis.2011.02.052
- G. Kumar, J. Shah, R. Kotnala, P. Dhiman, R. Rani, V.P. Singh, G. Garg, S.E. Shirsath, K.M. Batoo, M. Singh, Selfignited synthesis of Mg–Gd–Mn nanoferrites and impact of cation distribution on the dielectric properties. Ceram. Int. 40(9), 14509–14516 (2014). https://doi.org/10.1016/j.ceramint.2014.07.017
- R.S. Yadav, I. Kuritka, J. Vilcakova, J. Havlica, J. Masilko, L. Kalina, J. Tkacz, J. Svec, V. Enev, M. Hajdúchová, Impact of grain size and structural changes on magnetic, dielectric, electrical, impedance and modulus spectroscopic characteristics of CoFe<sub>2</sub>O<sub>4</sub> nanoparticles synthesized by honey mediated sol-gel combustion method. Adv. Nat. Sci.: Nanosci. Nanotechnol. 8(4), 045002 (2017). https://doi.org/10.1088/2043-6254/aa853a
- 40. T. Yu, Z. Shen, Y. Shi, J. Ding, Cation migration and magnetic ordering in spinel CoFe2O4 powder: micro-Raman

- scattering study. J. Phys.: Condens. Matter **14**(37), L613 (2002). https://doi.org/10.1088/0953-8984/14/37/101
- F.D. Saccone, S. Ferrari, D. Errandonea, F. Grinblat, V. Bilovol, S. Agouram, Cobalt ferrite nanoparticles under high pressure. J. Appl. Phys. 118(7), 075903 (2015). https://doi.org/10.1063/1.4928856
- A.V. Humbe, A.C. Nawle, A. Shinde, K. Jadhav, Impact of Jahn Teller ion on magnetic and semiconducting behaviour of Ni-Zn spinel ferrite synthesized by nitrate-citrate route.
   J. Alloys Compd. 691, 343–354 (2017). https://doi.org/10. 1016/j.jallcom.2016.08.199
- P. Liua, Z. Yaoa, J. Zhoua, Z. Yanga, L.B. Kongc, Small magnetic Co-doped NiZn ferrite/graphene nanocomposites and their dual-region microwave absorption performance.
   J. Mater. Chem. C (2016). https://doi.org/10.1039/C6TC03518C
- 44. M.C. Dimri, A. Verma, S.C. Kashyap, D. Dube, O. Thakur, C. Prakash, Structural, dielectric and magnetic properties of NiCuZn ferrite grown by citrate precursor method. Mater. Sci. Eng., B 133(1–3), 42–48 (2006). https://doi.org/10.1016/j.mseb.2006.04.043
- P. Lavanya Rathi, B. Ponraj, S. Deepa, Absorption-dominant microwave shielding properties of Sn0.2Fe2.8O4-graphite-PVDF ternary nanocomposite films. J. Phys. D: Appl. Phys. (2021). https://doi.org/10.1088/1361-6463/ac38e2
- P. Liu, Z. Yao, V.M. Ng, J. Zhou, L.B. Kong, K. Yue, Facile synthesis of ultrasmall Fe3O4 nanoparticles on MXenes for high microwave absorption performance. Compos. A Appl. Sci. Manuf. 115, 371–382 (2018)
- 47. S. Amiri, H. Shokrollahi, Magnetic and structural properties of RE doped Co-ferrite (RE: Nd, Eu, and Gd) nano-particles synthesized by co-precipitation. J. Magn. Magn. Mater. **345**, 18–23 (2013). https://doi.org/10.1016/j.jmmm.2013.05.030
- N. Kumari, V. Kumar, S. Khasa, Chemical synthesis and magnetic investigations on Cr3+ substituted Zn-ferrite superparamagnetic nano-particles. Ceram. Int. 41, 1907–1911 (2015). https://doi.org/10.1016/j.ceramint.2014.09.118
- P. Belavi, G. Chavan, L. Naik, R. Somashekar, R. Kotnala, Structural, electrical and magnetic properties of cadmium substituted nickel–copper ferrites. Mater. Chem. Phys. 132(1), 138–144 (2012). https://doi.org/10.1016/j.matchemphys.201 1.11.009
- A. Kadam, S. Shinde, S. Yadav, P. Patil, K. Rajpure, Structural, morphological, electrical and magnetic properties of Dy doped Ni–Co substitutional spinel ferrite. J. Magn. Magn. Mater. 329, 59–64 (2013). https://doi.org/10.1016/j.jmmm.2012.10.008
- 51. K. Kumari, K. Prasad, R. Choudhary, Impedance spectroscopy of (Na<sub>0.5</sub>Bi<sub>0.5</sub>)(Zr<sub>0.25</sub>Ti<sub>0.75</sub>)O<sub>3</sub> lead-free ceramic.



- J. Alloys Compd. **453**(1–2), 325–331 (2008). https://doi.org/ 10.1016/j.jallcom.2006.11.081
- M.A. Rahman, A.A. Hossain, Electrical transport properties of Mn–Ni–Zn ferrite using complex impedance spectroscopy. Phys. Scr. 89(2), 025803 (2014). https://doi.org/10.1088/003 1-8949/89/02/025803
- S. Ajith Kumar, P. Kuppusami, S. Amirthapandian, Y.-P. Fu, Effect of Sm co-doping on structural, mechanical and electrical properties of Gd doped ceria solid electrolytes for intermediate temperature solid oxide fuel cells. Int. J. Hydrog. Energy 45(54), 29690–29704 (2020). https://doi.org/10.1016/ j.ijhydene.2019.10.098
- 54. S.A. Kumar, P. Kuppusami, B. Vigneshwaran, Y.-P. Fu, Codoped ceria Ce<sub>0.8</sub>M<sub>0.1</sub>Gd<sub>0.1</sub>O<sub>2-δ</sub> (M= Sm<sup>3+</sup>, Sr<sup>2+</sup>, Ca<sup>2+</sup>) and codoped ceria–Na<sub>2</sub>CO<sub>3</sub> nanocomposite electrolytes for solid oxide fuel cells. ACS Appl. Nano Mater. 2(10), 6300–6311 (2019). https://doi.org/10.1021/acsanm.9b01282
- 55. M.D. Rahaman, M.D. Mia, M. Khan, A.A. Hossain, Study the effect of sintering temperature on structural, microstructural and electromagnetic properties of 10% Ca-doped Mn<sub>0.6</sub>Zn<sub>0.4</sub>Fe<sub>2</sub>O<sub>4</sub>. J. Magn. Magn. Mater. 404, 238–249 (2016). https://doi.org/10.1016/j.jmmm.2015.12.029
- J.C. Maxwell, Electricity and Magnetism (Dover, New York, 1954)
- R. Kambale, P. Shaikh, C. Bhosale, K. Rajpure, Y. Kolekar, Dielectric properties and complex impedance spectroscopy studies of mixed Ni–Co ferrites. Smart Mater. Struct. 18(8), 085014 (2009). https://doi.org/10.1088/0964-1726/18/8/ 085014
- 58. M.J. Iqbal, R.A. Khan, S. Mizukami, T. Miyazaki, Mössbauer, magnetic and microwave absorption characteristics of substituted W-type hexaferrites nanoparticles. Ceram. Int.

- 38(5), 4097–4103 (2012). https://doi.org/10.1016/j.ceramint. 2012.01.067
- B. Vigneshwaran, P. Kuppusami, S. Ajithkumar, H. Sreemoolanadhan, Study of low temperature-dependent structural, dielectric, and ferroelectric properties of BaxSr(1–x) TiO3 (x = 0.5, 0.6, 0.7) ceramics. J. Mater. Sci.: Mater. Electron. 31, 10446–10459 (2020). https://doi.org/10.1007/s10854-020-03593-3
- N. Rezlescu, E. Rezlescu, Dielectric properties of copper containing ferrites. Phys. Status Solidi (a) 23(2), 575–582 (1974). https://doi.org/10.1002/pssa.2210230229
- J. Bao, J. Zhou, Z. Yue, L. Li, Z. Gui, Dielectric behavior of Mn-substituted Co<sub>2</sub>Z hexaferrites. J. Magn. Magn. Mater. 250, 131–137 (2002). https://doi.org/10.1016/S0304-8853(0 2)00364-5
- M. Gabal, Y. Al Angari, F. Al-Agel, Cr-substituted Ni–Zn ferrites via oxalate decomposition. Structural, electrical and magnetic properties. J. Magn. Magn. Mater. 391, 108–115 (2015). https://doi.org/10.1016/j.jmmm.2015.04.115
- H.S. Aziz, S. Rasheed, R.A. Khan, A. Rahim, J. Nisar, S.M. Shah, F. Iqbal, A.R. Khan, Evaluation of electrical, dielectric and magnetic characteristics of Al–La doped nickel spinel ferrites. RSC Adv. 6(8), 6589–6597 (2016). https://doi.org/10.1039/C5RA20981A
- C. Murugesan, G. Chandrasekaran, Impact of Gd<sup>3+</sup> substitution on the structural, magnetic and electrical properties of cobalt ferrite nanoparticles. RSC Adv. 5(90), 73714–73725 (2015). https://doi.org/10.1039/C5RA14351A

**Publisher's Note** Springer Nature remains neutral with regard to jurisdictional claims in published maps and institutional affiliations.

